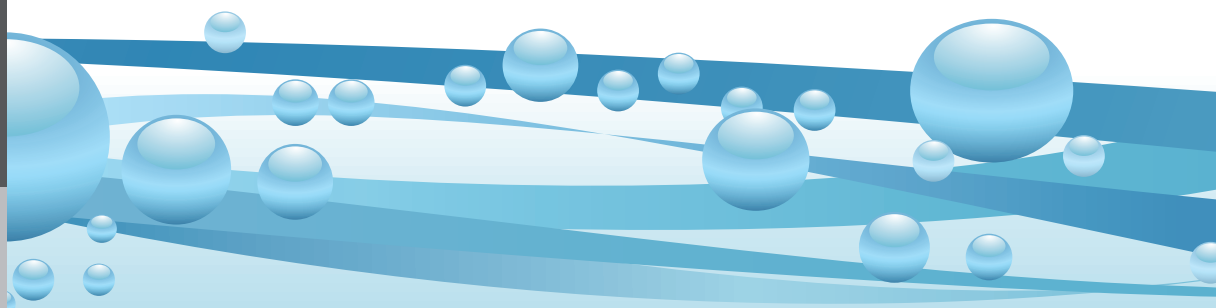

18th World Hydrogen Energy Conference 2010 – WHEC 2010 Proceedings

Parallel Sessions Book 3: Hydrogen Production Technologies – Part 2

Editors: Detlef Stolten, Thomas Grube

JÜLICH
FORSCHUNGSZENTRUM

Mitglied der Helmholtz-Gemeinschaft

18th World Hydrogen Energy Conference 2010 - WHEC 2010: Parallel Sessions Book 3: Hydrogen Production Technologies - Part 2

WHEC, May 16.-21. 2010, Essen

Detlef Stolten, Thomas Grube (Eds.)

Institute of Energy Research - Fuel Cells (IEF-3)

Guide to the Online Edition

Forschungszentrum Jülich GmbH, Zentralbibliothek, Verlag

Schriften des Forschungszentrums Jülich / Energy & Environment Vol. 78-3

978-3-89336-653-8 / 1866-1793

HP Hydrogen Production Technologies – Part 2

HP.3a Hydrogen from Renewable Electricity

Poster

HP.3b High-Temperature Electrolysis

Poster

HP.3c Alkaline Electrolysis

Poster

HP.3d PEM Electrolysis

Poster

HP.4a Reforming and Gasification - Fossil Energy Carriers

Poster

HP.4b Reforming and Gasification – Biomass

Poster

HP.5 Hydrogen-Separation Membranes

Poster

HP.6 Hydrogen Systems Assessment

Poster

HP.7 Photocatalysis

Poster

Schriften des Forschungszentrums Jülich
Energy & Environment Volume 78-3

Forschungszentrum Jülich GmbH
Institute of Energy Research (IEF)
Fuel Cells (IEF-3)

18th World Hydrogen Energy Conference 2010 – WHEC 2010

Parallel Sessions Book 3:
- Hydrogen Production Technologies – Part 2

Editors: Detlef Stolten, Thomas Grube

Schriften des Forschungszentrums Jülich
Energy & Environment Volume 78-3

ISSN 1866-1793 ISBN 978-3-89336-653-8

Bibliographic information published by the Deutsche Nationalbibliothek.
The Deutsche Nationalbibliothek lists this publication in the Deutsche Nationalbibliografie; detailed bibliographic data are available in the Internet at http://dnb.d-nb.de.

Vol. 78 Set (komplett)
ISBN 978-3-89336-657-6
Editors: Detlef Stolten, Thomas Grube, Bernd Emonts

Publisher and Distributor: Forschungszentrum Jülich GmbH
Zentralbibliothek
52425 Jülich
Phone +49 (0) 24 61 61-53 68 · Fax +49 (0) 24 61 61-61 03
e-mail: zb-publikation@fz-juelich.de
Internet: http://www.fz-juelich.de/zb

Cover Design: Grafische Medien, Forschungszentrum Jülich GmbH

Printer: Grafische Medien, Forschungszentrum Jülich GmbH

Schriften des Forschungszentrums Jülich
Reihe Energy & Environment Volume 78-3

ISSN 1866-1793
ISBN 978-3-89336-653-8

The complete volume ist freely available on the Internet on the Jülicher Open Access Server (JUWEL) at http://www.fz-juelich.de/zb/juwel

Book 3: Hydrogen Production Technologies – Part 2

Contents

Posters

Posters

Posters

Hydrogen Production: Fundamentals and Case Study Summaries

Kevin W. Harrison, Robert Remick, Gregory D. Martin, and Aaron Hoskin

Abstract

It is important that parties interested in hydrogen technologies standardize methods of evaluating the performance and efficiency of these technologies. A detailed description of the chemical and electrical processes for electrolysis and fuel cells is presented. Hydrogen and hydrocarbon fuels also pose a source of confusion about whether the efficiencies are based on the higher or lower heating value. A discussion of fundamental principles for fuel cell and electrolyzer systems is presented along with recommendations. Renewable hydrogen production is being researched across the globe to enable the environmental benefits of this energy carrier to be realized. The focus of many of these projects is coupling wind energy with hydrogen production (via water electrolysis) in an effort to use all available wind energy and to store that energy to be used during times of high electricity demand. Summaries of projects from Canada, Greece, Spain, United Kingdom and the United States are provided.

Wind-Hydrogen-Biomass – The Hybrid Power Plant of ENERTRAG AG

A. Miege, **T. Luschtinetz**, Fachhochschule Stralsund, Germany
M. Wenske, **F. Gamallo**, ENERTRAG AG, Germany

Abstract

The ENERTRAG Hybrid Power Plant is designed around the following components: three wind turbines of 2 MW each, an electrolyser of 500 kW, a hydrogen storage system, and two CHP units of 350 kW each, able to run with variable mixtures of biogas and hydrogen. The use of the electrolyser - acting as a deferrable load, and running under variable power - and the possibility of reconverting the hydrogen again into electricity will allow a feeding-in of the produced electricity to the grid, free of any of the changing characteristics of the wind power. Besides of that renewable electricity, the Hybrid Power Plant will also be able of delivering hydrogen as a clean fuel for the transport sector, as well as oxygen and heat. The project will show that renewable energy sources, like wind and solar, will be able, in the future, of producing back-up power without any support of fossil sources; and also of feeding electricity to the grid as a part of the base-load demand. As a first step towards this direction, the project has the goal of assuring that the energy production of the three wind turbines will be in accordance to the 24-h-forecasted wind power values.

1 Wind Energy within the Electrical Energy Mix

The natural variability of the instantaneous power supplied by wind turbines can seriously affect the stability of voltage and frequency in power grids. This influence largely depends on the penetration level (fraction of wind power present in the instantaneous energy mix), and will produce no noticeable consequences if maintained below a value of 10 % of installed capacity [1]. At present, this level has already been exceeded, and prognoses show that in 2020, in Germany, the electricity produced by renewable sources will even exceed the total demand during several hours a year [2].

In consequence, the base power generation demand will decrease, while intermediate and peak power generation demand will increase within the following years. However, even if only based on conventional sources, electricity systems – supply and demand – are inherently highly variable, and are influenced by a large number of planned and unplanned factors. The issue, therefore, is not one of variability or intermittence *per se*, but how to predict, manage and compensate variability, and what tools can be utilised to improve the grid efficiency by using additional energy storages [3, 4].

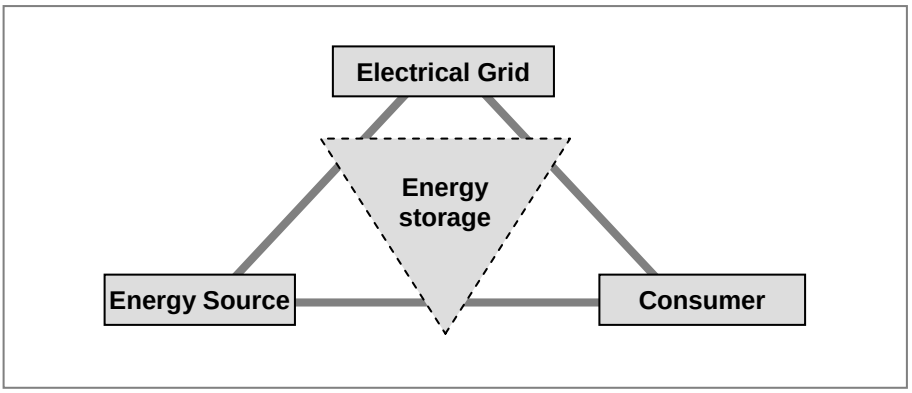

Figure 1: Integration of energy storages.

The already-established controls method and backup available for dealing with variable demand and supply are more than adequate for dealing with the additional variable supply such as wind power at penetration levels up to around 20 % of gross demand, depending on the nature of the specific system. For larger penetration levels, changes are needed both in the structure of the power systems and in their methods of operation, in order to be able of accommodating the further integration of wind energy.

2 Integration of Wind Energy by Coupling with Some Energy Storage System

A wind-hydrogen-system is designed as in the model of figure 3. In this case, the wind energy is partly converted into hydrogen by an electrolyser (PV5). As a fuel, it can also be sold to the market. This option could be a further step towards a global hydrogen infrastructure based on renewable energies.

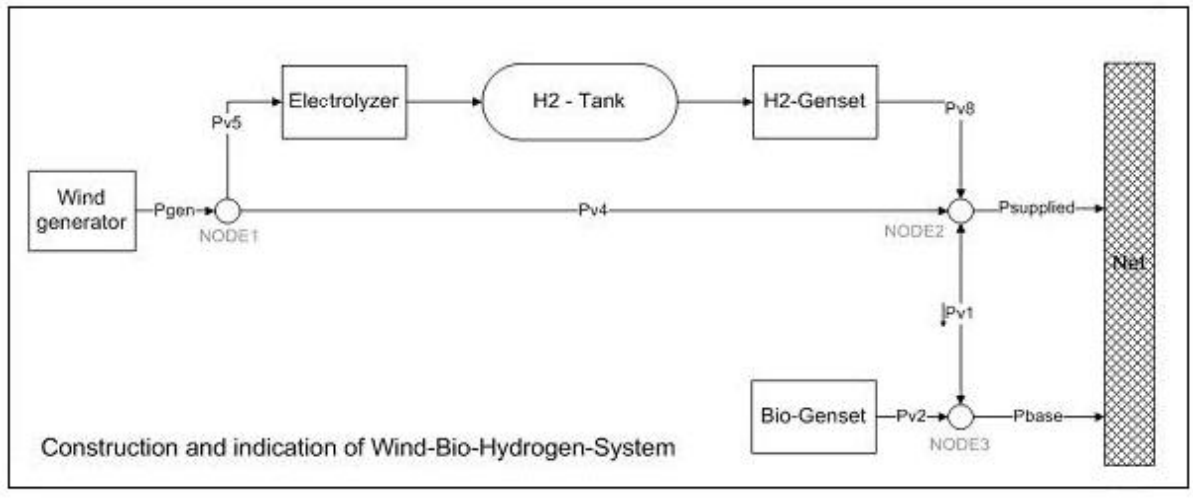

Figure 2: Configuration of model for H2-storage integration.

On the other hand, the hydrogen is used by a genset (PV8) to improve the electrical output characteristic of the overall system. Wind energy which is not used by the electrolyser is fed directly to the grid (PV4). A genset based on biogas works as the third power source (PV2) within that system. This power, in addition to a part of the wind power, forms the base power (node3) that is fed to the grid.

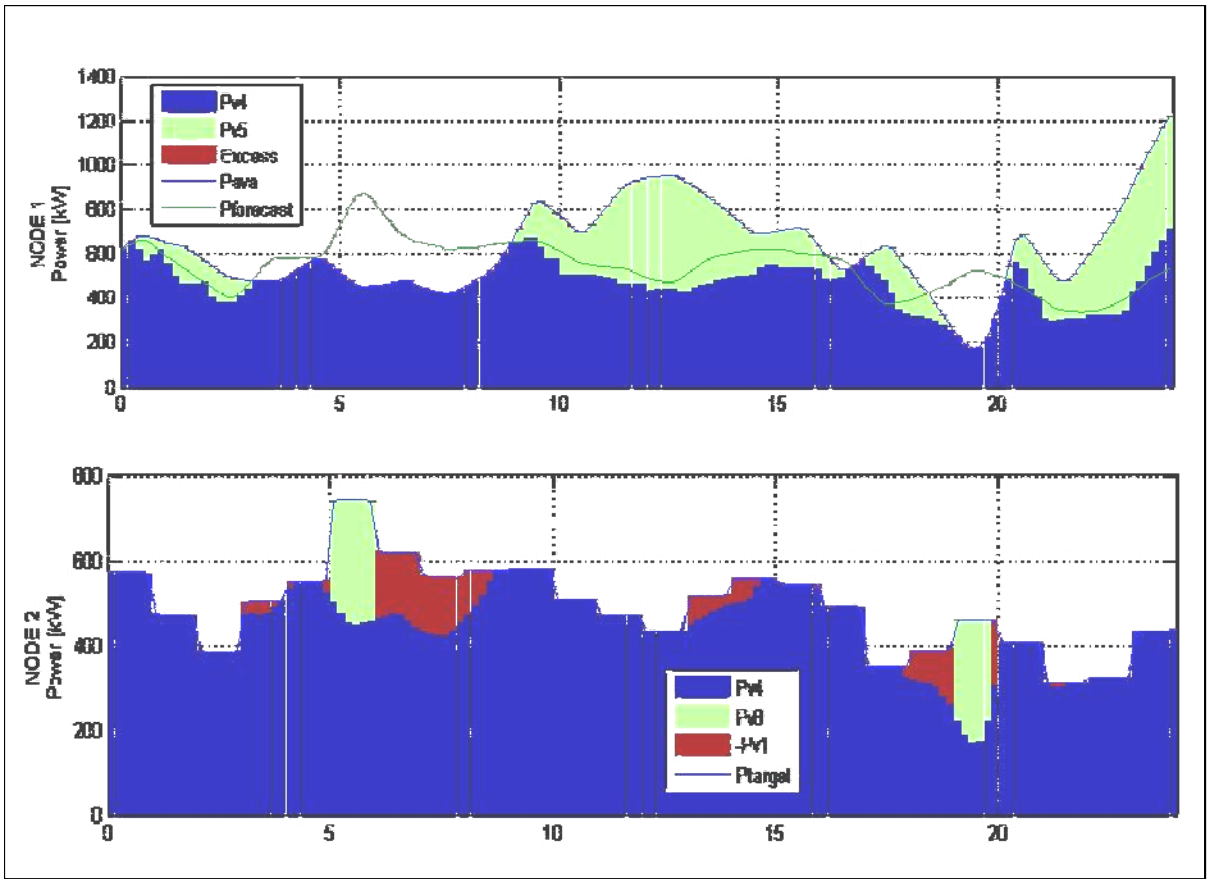

Figure 3: Simulation results for 24h.

The dynamic part of power supply (node2) is defined 24 hours ahead, taking into account wind forecast, H2-tank status and biogas potential. Related to the real wind power yield, the power difference is supplied by the gensets. The lower diagram in figure3 displays the situation for one day. Both gensets with a minimum activation level (step-in limit) are controlled following a priority class.

One strategy of hydrogen production is simulated in the upper diagram in figure 3. Within this day the power forecast and the real power input differs in positive and negative directions. The gaps are filled as explained before. The wind power above the target value is used by the electrolyser running under a variable power mode.

3 Practical Tests of Variable-power Electrolysis

Currently, the most extended electrolysis technology is that of the bipolar, alkaline units, using an aqueous solution of KOH, around 28 % v/v. The average efficiency of the currently available electrolysers is between 75 % and 80 % (HHV), even when efficiency values higher than 80 % under full power (up to 90 % at 20 % load) have been reached on experimental, industrial-sized units.

Despite being a long-term established industrial technology, the production of H_2 by electrolysis will still require some research, in order to be capable of dealing with the natural variability of the wind-generated power. Almost all the experience already acquired about water electrolysis is valid only for steady operation. The industrial utilisation of electrolysers is largely based on stable, nominal-power operation, with very seldom and controlled start and shut-down cycles, performed in comparatively extended time periods. So, the concrete experience in operating electrolysers under a non-steady power regime, with relatively sudden power fluctuations; still seems not to be enough for allowing this technology to widely enter the commercial market. Even when several wind-hydrogen pilot plants were already built and tested, definitive results were still not attained [5].

Some specific research works, however, showed that such a variable-power-mode operation is possible, if attention is paid to certain specific parameters. Further activities are currently being developed toward this direction.

From a theoretical point of view, there are no problems for the electrolysis process to be performed under variable power conditions. However, the behaviour of the real devices not only depend on the cell stack (the core of the electrolyser, where the water splitting takes place), but also on the dynamic characteristics of all the peripheral components. So, the real performance of the whole system, working under a service condition completely different from those for which the electrolyser was designed, is sometimes difficult to predict. Furthermore, the scale factor produces also an important difference: Small electrolysers, designed, for example, for laboratory service, or for small hydrogen supplies to industrial processes; present some technological differences with the large, production-oriented units. For this reason, experimental results obtained from small units, can difficultly be extrapolated to larger units, being the direct work on industrial-sized units a much better alternative.

4 The ENERTRAG Hybrid Power Plant

One of the technical goals to be achieved is the balance of the energy inputs and outputs over a certain time. Also, the overall grid situation has to be taken into consideration. The economical characteristics of the market are the second important group of aspects to focus on while operating a combined wind-hydrogen-system. Depending on the attainable price for electricity and for hydrogen, the more lucrative energy form should be produced at any moment. Furthermore, the price distribution pattern over a day or a week is considered in such a way that the periods of price peaks are preferred for the sale of electricity.

About two years ago, ENERTRAG AG, a leading company in the field of wind energy production, started, in cooperation with the University of Applied Sciences of Stralsund and some other academic institutions; the design of a hybrid power plant, comprising several wind turbines, a biogas generator, an electrolyser, and several other components; oriented to

balance the electrical output of the wind turbines in such a way that it could be easily admitted by the grid. The plant is already under construction, and it is expected to enter into full service in the upcoming year.

The hybrid power plant will be integrated in the ENERTRAG's own energy grid. So, during the periods when the grid cannot accept all the available wind power, the non-dispatchable surplus will be used for producing hydrogen, in order to reduce the net electricity offer, bringing it near to the demanded values.

On the opposite, during periods of high electricity demand, the hydrogen will be mixed with biogas, and used to fuel two 350 kW, high-efficiency CHP (combined-heat-and-power) units; in which it will be converted again into electricity, in a CO_2-neutral way, for serving the grid. Simultaneously, the CHP units will also produce heat, out of that hydrogen-biogas mixture, that will also be utilized.

In accordance to several different operation strategies, it will not only be possible to produce hydrogen for reconverting it into electricity, but also for furnishing some kind of external demand (i.e. the transportation sector). So, the hybrid power plant could be not only able of supplying electricity and heat, but also pure hydrogen to be used as fuel. The possibilities of using the co-generated oxygen (eventually for non-energetic purposes as waste water treatment, water purification, air enrichment, etc.) is also considered [6].

5 Summary

Hydrogen production, by means of water electrolysis, can undoubtedly offer a suitable alternative for dampening the severe power fluctuations that could take place in electrical grids having a high penetration of wind energy; consequently reducing or even avoiding the need of wind power curtailment. Such an operation mode could allow a wind park to deliver firm, ensured power to the grid, thus contributing to the stability of the whole system. The option of hydrogen production could be a further step towards a global hydrogen infrastructure [7] based on renewable energies.

Simulations show the benefits of such combined systems and allow testing in advance a variety of different operations modes. Tests and analysis under a variable power regime have been performed only at laboratory and pilot-project scales. For properly knowing the dynamical behaviour of such systems, long-term testing of industrial-sized units is necessary.

A factor seriously affecting a fast integration of the electrolysis technology to the energy market, is the fact that the current offer of industrial-scaled electrolysers is low (a comprehensive list of manufacturers can also be found at [8]). For this reason, prices are high, and delivery times may often be quite long.

Once the dynamic operation of electrolysers had been sufficiently tested, grid-independent wind-hydrogen systems could also be built, both for fuel supply and for decentralized cogeneration; attaining competitive costs.

References

[1] Deutsche Energie-Agentur GmbH, Energiewirtschaftliche Planung für die Netzintegration von Windenergie in Deutschland an Land und Offshore bis zum Jahr 2020, Köln, Februar 2005

[2] IWES, Dynamische Simulation der Stromversorgung in Deutschland nach dem Ausbauszenario der Erneuerbaren-Energien-Branche, Kassel 2009

[3] Lehmann, J.; Miege, A.; Sponholz, C; Luschtinetz, O. “Wasserstoff – Medium zur Speicherung von regenerativ erzeugter Elektroenergie, Untersuchungen zu Netzkapazität, Infrastruktur und Wirtschaftlichkeit in Mecklenburg-Vorpommern“. Studie des Instituts für Energie und Umwelt (IFEU) e.V. an der FH Stralsund, 2004 – 2005

[4] EWEA. “Large Integration of Wind Energy in the European Power Supply: analysis, issues and recommendations”. Brussels, Belgium, December 2005, http://www.ewea.org/fileadmin/ewea_documents/documents/publications/grid/051215_Grid_report.pdf

[5] Varkaraki and S. Thomas, Comparison of hydrogen storage options for wind hydrogen plants, Centre for Renewable Energy Sources, Greece, XVI. Symp. Nutzung regenerativer Energiequellen und Wasserstofftechnik, Stralsund 2009

[6] ENERTRAG AG. “ ENERTRAG Hybridkraftwerk – Kurzbeschreibung“ (in german language). Currently available under: http://www.enertrag.com/download/praesent/hybridkraftwerk_kurzinfo_090417.pdf, 12.01.2010

[7] LBST – Ludwig Bölkow Systemtechnik. “Hydrogen Filling Stations Worldwide“. http://www.h2stations.org/, 12.12.09

[8] Michael Wenske, Wasserstoff – Herstellung per Elektrolyse, XV. energie – symposium Nutzung regenerativer Energiequellen und Wasserstofftechnik, Stralsund 2008

Clean Hydrogen Production in Patagonia Argentina

Sergio Raballo, **Jorge Llera**, **Ariel Pérez**, **Juan C. Bolcich**, Hychico S.A., Argentina

Hychico is a company part of the CAPSA – Capex Argentine group, this group has been engaged in the Exploration and Exploitation of Oil and Gas and in the production of Electric Power and Liquefied Petroleum Gases in the Argentine Patagonia for over 30 years.

Focused on renewable energies, Hychico's objective is Hydrogen production from wind energy in Patagonia. The company's vision is that hydrogen will play a significant role in world energy demand as an energy vector, and that industries belonging to the energy sector must turn their efforts and resources towards the development of sustainable energies.

Hychico's Hydrogen Plant started operating in January 2009. It is located in the outskirts of the City of Comodoro Rivadavia, Province of Chubut, and it is the first phase of the "Large Scale Clean Hydrogen Production in Patagonia Argentina" pilot project. The second phase, which will start shortly, will be the start-up of a 6.3 MW wind park which will feed 0.8 MW to the hydrogen plant, the remaining output will be sold to the national interconnected electric system.

The significance of the wind resource in Patagonia [1], recorded in our measurement towers equipped with instruments meeting international standards, can be appreciated in Figure 1.

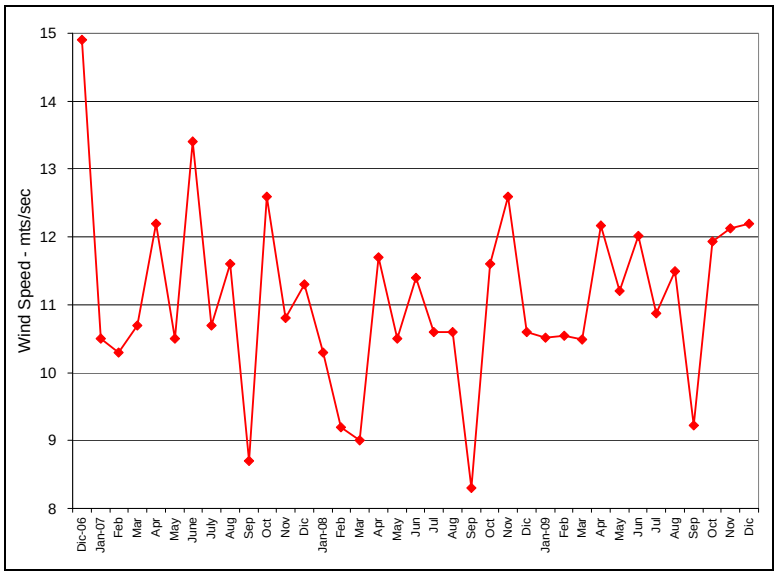

- Wind speed measured at 50m.
- 3-year Monthly Average Speed (Dec. 06 - Dec. 09): 11.1 m/sec., with a maximum of 14.9 m/sec.
- Net Average Capacity Factor: 47 %

Figure 1: Patagonian wind resource.

1 Hydrogen Plant

The plant has 2 hydrogen-producing electrolysers; this hydrogen is mixed with natural gas and used as fuel in a 1.4 MW Genset. In addition, there is a high pressure oxygen dispatch plant (220 bar) which supplies the local market.

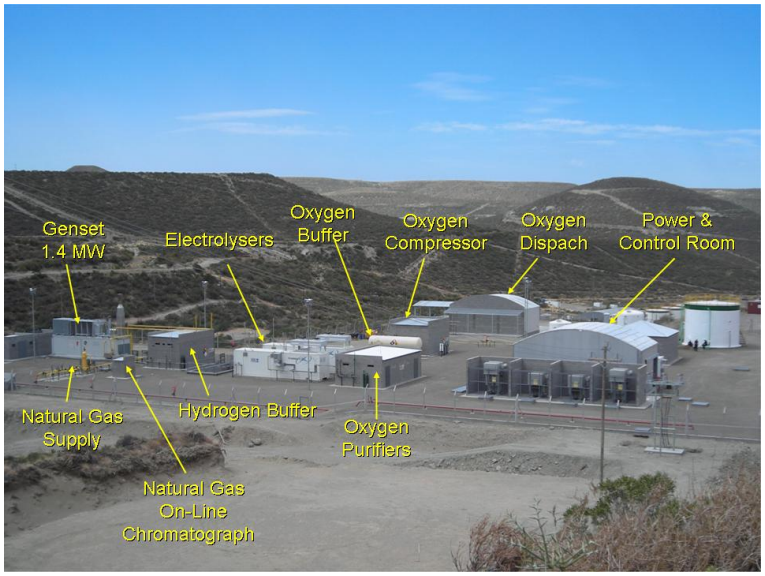

Both 325 kW electrolysers can operate up to a 10-bar pressure, producing a total flow of 120 Nm^3/h of H_2 and 60 Nm^3/h of O_2, both of them high purity gases (99.998 %). The produced H_2 is suitable to be used both in Internal Combustion Engines (ICE) and in Fuel Cells.

Figure 2: General view of the hydrogen plant.

The Genset has an ICE designed to operate with gases from biomass, pyrolysis, etc., and has been specially adapted to operate with rich and/or poor gas – hydrogen mixtures. It is worth mentioning that gases used are raw gases extracted from the Field, with no previous treatment. The rich gas has a 90% Methane content and the poor gas has a ~40% CO_2 content.

2 Results of the First Year of Operation

Genset: Rich Gas/H_2 Mixtures were used as fuel in the range 0-42% H_2 (vol).

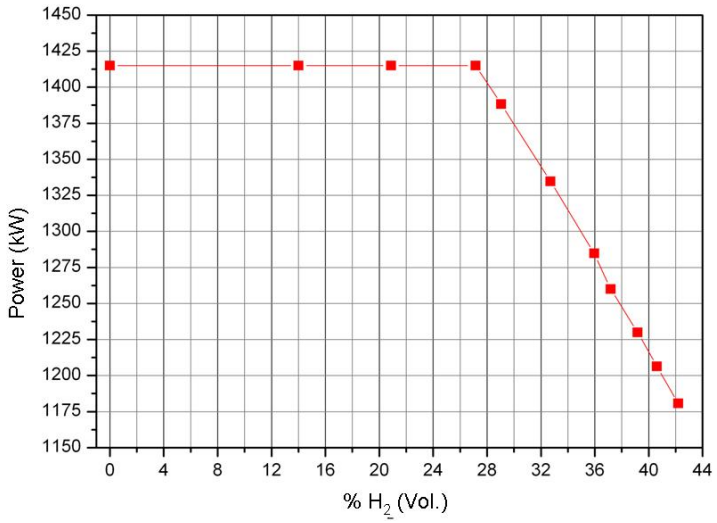

- In the range 0-27% H_2, the equipment was able to run at full power (1,415 kW).
- In the range 28-42% H_2, power was progressively reduced from 1,415 to 1,180 kW to avoid knocking.
- We consider that Max. Power (1,415 kW) could be increased at a higher (than 27%) H_2 content.
- We consider a higher (than 42%) H_2 content could be used.

Figure 3: Maximum Power vs. H_2 content.

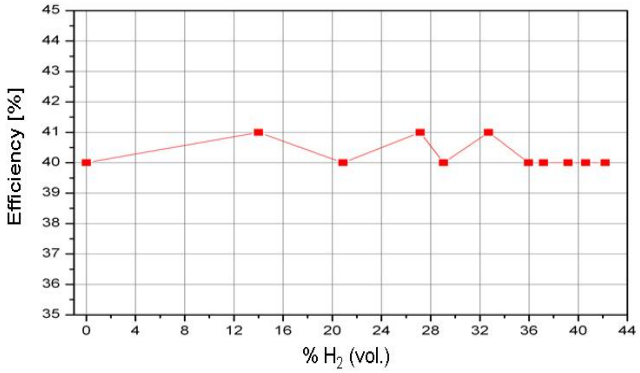

- An average thermal efficiency of 40-41% at maximum power was achieved.
- Everything indicates efficiency remains constant to H_2 incremental contents in the mixture.

Figure 4: Efficiency vs. H_2 content.

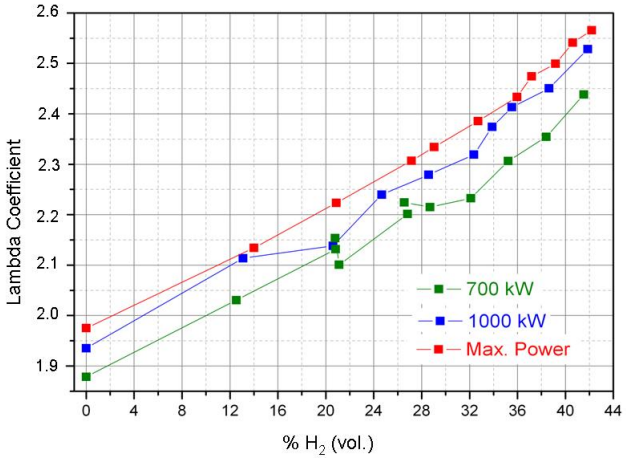

- H_2 content increase requires a greater amount of air in order to slow down flame speed and avoid knocking [2].
- Work was carried out within a 1.9-2.6 Lambda range.
- Lambda coefficient is proportional to H_2 content.
- For the same H_2 %, Lambda coefficient is higher at incremental powers.

Figure 5: Lambda vs. H_2 content.

We consider that higher Lambda values may be reached and consequently the H_2 content could be increased.

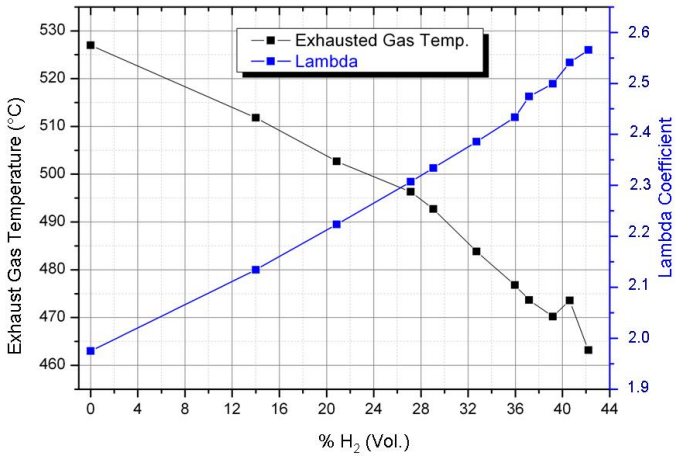

- Lambda incremental value (greater amount of air) with H_2 content means a reduction from 530 ºC to 460 ºC in exhaust gases temperature at maximum power.
- Exhaust gases temperature reduction allows the decrease of NOx and CO concentration [3].

Figure 6: Lambda vs. influence in exhaust gas temperature (max. power).

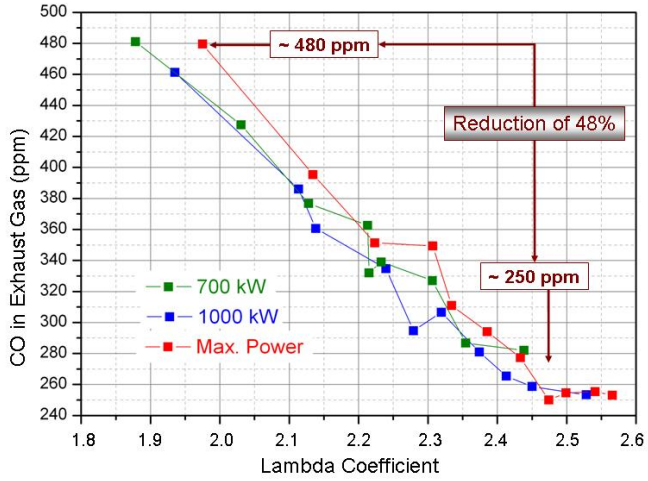

- Exhaust gases temperature reduction due to Lambda coefficient increase has brought about a 48% CO content reduction in exhaust gases.
- This CO content reduction is observed throughout the range of powers.

Figure 7: Lambda & its influence on CO reduction.

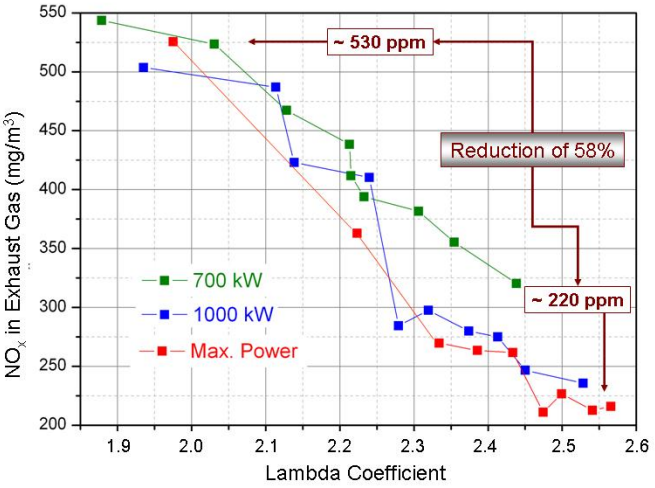

- Exhaust gases temperature reduction as a result of Lambda coefficient increase has brought about a 58% NOx content reduction in exhaust gases.
- Such NOx reduction is observed in the tested powers, i.e. 700 kW, 1,000 kW and Maximum Power.

Figure 8: Lambda vs. NOx reduction.

- As we approach the engine's rated power, a greater NOx content reduction is verified.

3 Genset: Conclusions and Next Steps (Year 2010)

- Rich Gas/H_2 Mixtures were used as fuel in the range 0-42% H_2 (Vol.).
- In the range 0-27% H_2 the equipment was able to run at full power (1,415 kW).
- In the range 28-42% H_2, power was progressively reduced from 1,415 to 1,180 kW.
- An average efficiency of 40% was achieved.
- The replacement of methane for H_2 in the mixture means a CO_2 reduction of approximately 1,000 Tons/year and a NOx reduction of approximately 15 Tons/year.
- Based on the technical possibility of further increasing Lambda coefficient, tests will be run aimed at:

- Keeping Genset Maximum Power even with mixtures with over 27% H_2 content.
- Increasing H_2 content above 42%.
- Reducing exhaust gases emissions.

- Tests will continue with Poor Gas and Hydrogen mixtures in order to evaluate the effect of higher CO_2 content in gas on the Genset's powers and emissions.
- The possibility of incorporating Pure Oxygen (from electrolysis process) in the Genset air feed, in order to observe its effects on efficiency and emissions, will be evaluated.

4 Electrolysers

- Electric consumption measurements were carried out on each cell stack.

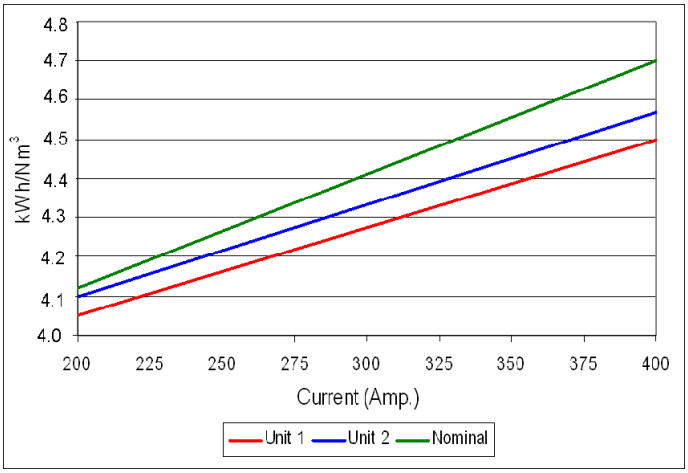

- The linear correlation among hydrogen production, current and consumed power is verified [4].
- Electrolysers' performance is obtained by integrating that of all cell stacks.
- 4.1 - 4.6 kWh/Nm3 specific consumption range.
- Electrolysers have shown a better performance to the one defined by the manufacturer.

Figure 9: Electrolysers average specific consumption.

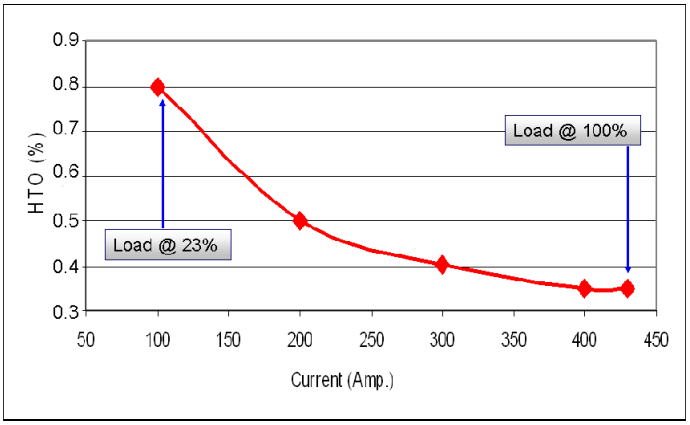

- Electrolysers are able to operate in the 23-100% range of maximum production.
- Cross contamination measurements are carried out (H_2 in O_2 and vice versa) in order to guarantee optimum quality and safety standards [5].
- Wide equipment Turn Down is favourable for Wind Turbine-power fluctuations.

Figure 10: Hydrogen concentration in oxygen line (HTO) in terms of production ratio.

5 Electrolysers: Conclusions and Next Steps (Year 2010)

- Specific consumption of 4.1 - 4.6 kWh/Nm^3 was achieved.
- H_2 and O_2 are produced at 99.998% purity, being H_2 suitable to be used both in ICE and Fuel Cells.
- A 90 Nm^3 H_2 buffer proved to be advantageous to this application, aimed at "softening" the electrochemical process inertia.
- 23-100 % Turn Down capacity was tested and we believe it could be increased considering HTO values obtained at lower production ratios.
- Equipment behaviour and gas purity will be determined in the whole range of operation.
- Available 3-year wind resource measurements will be used as input signal to the electrolysers, in order to simulate wind park behaviour.

6 General Conclusions and Hychico Goals

- Hychico has started up a high purity H_2 and O_2 production plant using electrolysis.
- Equipment applications and power match industrial scale with state-of-the-art technology.
- Hychico will continue to gather experience in H_2 state-of-the-art technology operation, also seeking to:
    - Carry out the Wind Park construction and its connection to electrolysers.
    - Develop Strategic Partners with Technology Expertise, thus assuring the concretion of ambitious projects.
    - Achieve a competitive advantage for Argentina, in a market that will be CLEAN and SUSTAINABLE energy-demanding in the medium term.

References

[1] K. Mönnich et ál. Wasserstoff aus Windenergie in Ost-Patagonien – Eine Machbarkeitsstudie-. DEWI Magazin N° 23, August 2003.

[2] L. Das. Hydrogen-Oxygen reaction mechanism and its implication to hydrogen engine combustion. Int. J. Hydrogen Energy. Vol. 21, N°8, pp. 703-715, 1996.

[3] F. Ma et ál. An investigation of optimum control of a spark ignition engine fueled by NG and hydrogen mixtures. Int. J. Hydrogen Energy. Vol. 33, pp. 7592-7606, 2008.

[4] H. Wendt and G. Bauer. Water-splitting methods in Hydrogen as an energy carrier: technologies, systems, economy by Carl-Jochen Winter and J. Nitsch, Springer-Verlag 1988.

[5] ISO/TR 15916. Basic considerations for the safety of hydrogen systems

Study of Hydrogen Production from Wind Power in Algeria

Lilia Aiche-Hamane, **Maiouf Belhamel**, **Boumedienne Benyoucef**, **Mustapha Hamane**, Centre for Development of Renewable Energies (CDER), BP62 Route de l'observatoire. Bouzaréah. 16040Alger, Algeria

Abstract

An overview of the potentiality of hydrogen production from wind power in Algeria has been given in this study. Wind resource assessment has been presented in cartographic form and windy sites have been identified for wind power application.

A system constituted by a wind turbine, an electrolyser and a power conditioning device have been proposed for the study of hydrogen production in the southwest region of Algeria.

For this purpose, the transient system simulation program (TRNSYS) have been used. The results obtained showed the sensitivity of hydrogen production to the wind resource trend and the importance of optimisation of the electrolyser according to the power produced by the wind turbine.

1 Introduction

Nowadays, wind energy is the fastest growing renewable energy sector in the world with annual growth of 29% in 2008[1] which represents 1.5 % of the global electricity consumption. Nevertheless, the instability caused by the wind turbines to the grid and the intermittence of the wind source, make necessary to develop efficient energy storage system.

Hydrogen as an energy vector, together with electrolyser and fuel cell technologies can provide a technical solution to this challenge. Additionally, the use of hydrogen for a clean transportation fuel will increase the need of renewable hydrogen generating.

However, one of the inherent drawbacks of wind power is that the wind velocity is highly intermittent, on a second by second basis, as well as hourly, daily, and even seasonally.

This inconvenient makes necessary to study the feasibility of wind-hydrogen systems according to the wind resource in order to choose the adequate wind turbine and electrolyser components at site installation [2].

The aim of this study is to provide necessary information for future use of wind power for hydrogen production in Algeria.

In the present work, a wind power hydrogen system is proposed. This system consists of wind turbine, AC/DC converter, electrolyser and hydrogen storage tanks.

The results obtained for regions situated in Algeria are presented in order to evaluate the viability of electrolytic hydrogen wind production systems.

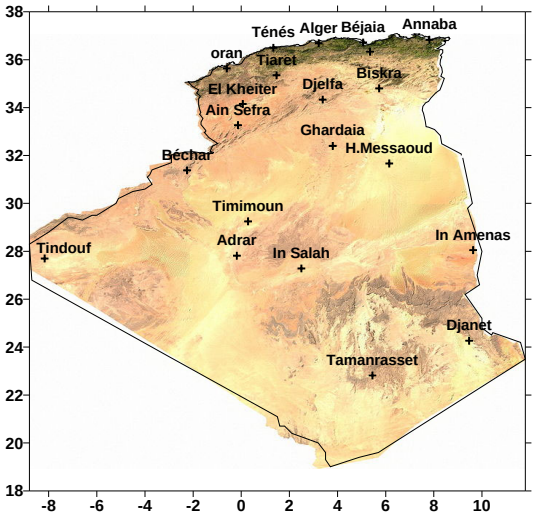

Figure 1: Geographical Topography of Algeria.

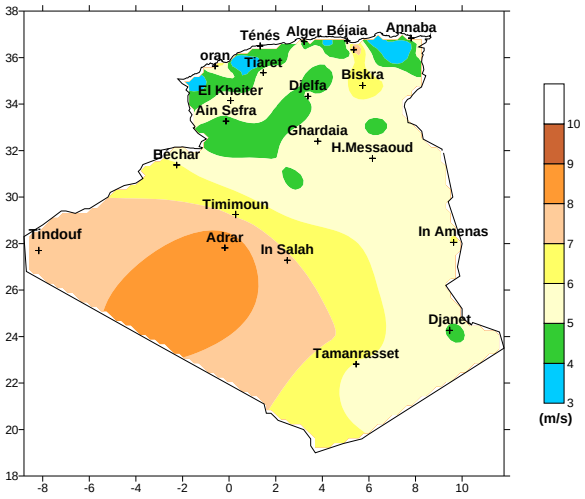

Figure 2: Annual wind speed distribution over Algeria at 50 m height.

2 Wind Energy Potential

Algeria is the second largest country in Africa and the first one in the Mediterranean region with 2.381.741 Km^2, located in the northern part sharing a vast coastline of about 1200 km along the Mediterranean Sea, with over four-fifths of its territory covered by the Sahara desert.

A study of the wind resource in Algeria has been carried out using wind data of 75 meteorological stations for a period of 11 years at 10 m height measurement [4].

The annual wind speed distribution at 50 m height plotted in Fig.2 indicates that the wind resource is very promising in Algeria. Areas that are potentially suitable for wind energy applications are dispersed throughout much of Algeria, particularly in the Sahara where the wind resource is more important on the whole area.

In the southwest including Béchar Timimoun, and Tamanrasset, the wind speed is greater than 6 m/s exceeds 7 m/s over Tindouf and In Salah and reaches 8 m/s throughout the big region of Adrar.

3 Hydrogen Production from Wind Power

A promising option for clean hydrogen production from wind power is electrolysis.

Electrolysis uses direct current (DC) electricity to split water into its basic elements of hydrogen and oxygen. Since this process uses only water as a source, it can produce up to 99.9995 % pure hydrogen and oxygen.

There are three principal types of water electrolyser: alkaline (referring to the nature of its liquid electrolyte), proton-exchange membrane (referring to its solid polymeric electrolyte), and solid-oxide (referring to its solid ceramic electrolyte). The alkaline and PEM electrolysers are well proven devices with thousands of units in operation, while the solid-oxide electrolyser is as yet unproven. The PEM electrolyser is particularly well suited to highly

distributed applications. The alkaline electrolyser currently dominates global production of electrolytic hydrogen.

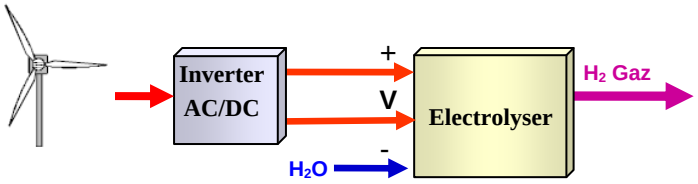

Figure 3: Wind hydrogen system production.

A system of hydrogen production from wind power has been proposed in this study. It consists of a wind turbine, an AC/DC converter and an alkaline electrolyser (fig.3). In this system, the AC output of the wind turbine is converted to a DC voltage suitable for electrolyser operation through an AC/DC converter.

The simulation of this system has been done using Hydrogems library developed by Ulleberg [7] and integrated in the transient system simulation program (TRNSYS) [8]. The simulation models for the wind turbine, AC/DC converter and electrolyser used have been tested and verified against measured data from the reference plant [7].

The wind turbine selected is of the type Nordex N54 which starts the power production at 4m/s and reaches the maximum rated output power of 1 MW at 14m/s at 70m hub height tower. A representation of the power output from the wind turbine as a function of wind speed is shown in fig.4.

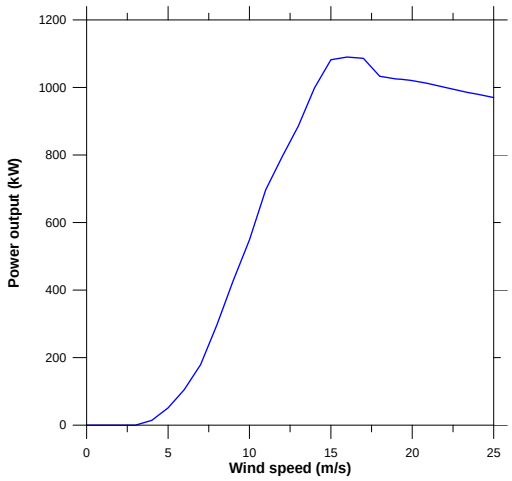

Figure 4: Power curve of the NordexN54 wind turbine.

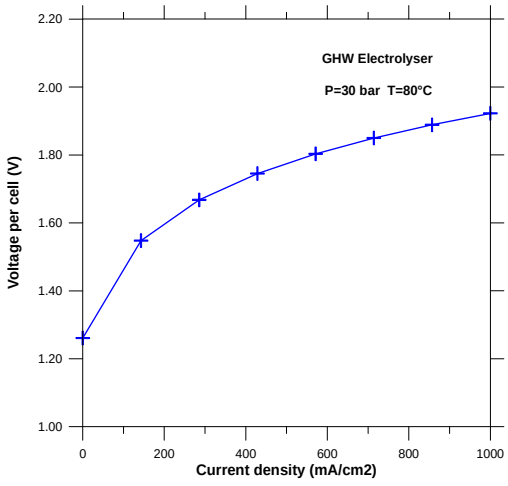

Figure 5: Voltage-current characteristics of the GHW electrolyser.

The characteristics of GHW alkaline electrolyser operating at 30 bars with a nominal temperature of 80°C were considered. The number of cells has been fixed to 200 cells in order to increase the power input of the electrolyser. The voltage-current curve of the GHW electrolyser used in the simulation is presented in fig.5.

4 Results and Discussion

The TRNSYS model has been used to simulate the hydrogen system production at six sites situated in the south west desert of Algeria. Wind speed data of these sites measured at 10m height have been used for the simulation. The annual rate production of hydrogen has been obtained and plotted in fig.6.

It appears clearly that hydrogen production is highest at Adrar because of its high wind speed while the lowest production is confirmed for Hassi Messaoud and Béchar. These results are obvious since hydrogen production depends on the power input in the electrolyser which is fed by the wind turbine.

It can be also noticed that hydrogen production is seven times greater in Adrar where the mean wind speed is 6 m/s than Béchar with 3.7 m/s mean wind speed. Thus, efficiency of wind hydrogen system production strongly depends on wind resource available at place.

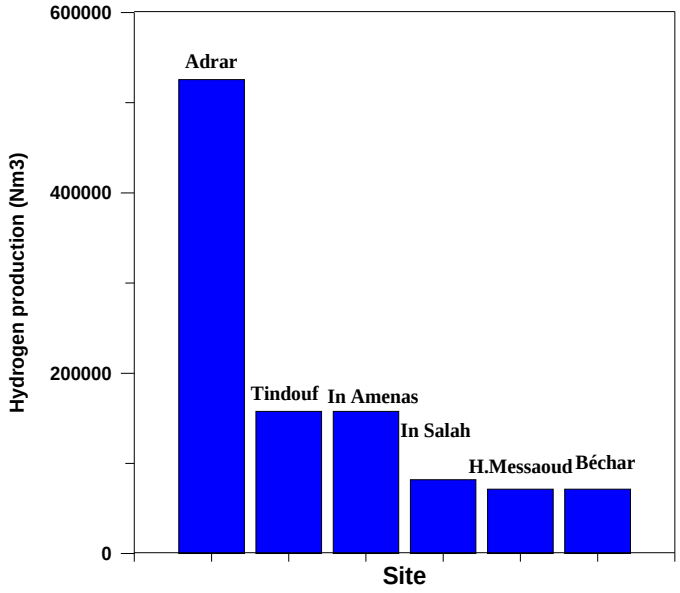

Figure.6: Annual hydrogen production from 1 MW wind turbine.

5 Conclusion

The purpose of this study is to give an overview of the feasibility development of wind-hydrogen systems in Algeria. The wind resource assessment has shown the big potentiality of wind power production in Algeria.

Furthermore, this contribution gives a simplified methodology to evaluate the potential viability of electrolytic hydrogen wind production systems.

In order to increase the efficiency of the wind-electrolyser system, it is primordial to optimise the wind turbine according to the wind potential available at site installation and choose than the right electrolyser according to the wind power produced.

The present study must be improved in future works by a techno-economic optimisation that takes into account the sizing and the cost of the different components of the system.

References

[1] World Wind Energy Association, Press Release, available on: www.wwindea.org , 2010.

[2] L.Aiche-Hamane, M.Belhamel, B.Benyoucef, M.Hamane,"Feasibility study of hydrogen production from wind power in the region of Ghardaia", International journal of hydrogen Energy 2009,34, 4947-4952.

[3] Available on: www.desertec.org, 2010.

[4] L. Aiche-Hamane L. "Contribution à l'élaboration de la carte du gisement énergétique éolien de l'Algérie". Mémoire de magister, institut de mécanique, université Saad Dahleb de Blida, Algérie, 2003.

[5] L.Aiche-Hamane, M.Belhamel, M.Hamane, 2008, "Estimation of hydrogen production from wind power in the south of Algeria", International Scientific Journal for Alternative Energy and Ecology ISJAEE, No. 5 (55), p 21-25.

[6] Available on: www.windpowermonthly.com/news/982260/Algeria-seals-deal-first-ever-wind-farm, 2010].

[7] O.Ulleberg, 1998, Stand-Alone Power Systems for the Future: Optimal Design, Operation & Control of Solar-Hydrogen Energy Systems. PhD thesis, Norwegian University of Science and Technology, Trondheim.

[8] SA Klein, WA Beckman, JW Mitchell et al, 2007, "TRNSYS—a transient system simulation program", Solar Energy Laboratory, University of Wisconsin, Madison.

[9] O. Ulleberg, 2003, "Modeling of advanced alkaline electrolysers: a system simulation approach", International Journal of Hydrogen Energy, Vol.28, pp. 21-33.

Novel Electric Generator Using Electroactive Polymer Artificial Muscle (EPAM)

Seiki Chiba, **Roy Kornbluh**, **Ron Pelrine**, SRI International, Japan
Mikio Waki, HYPER DRIVE Corporation, Japan

1 Introduction

Electroactive polymer artificial muscle (EPAM), known as dielectric elastomers in the literature, is being developed for a wide variety of actuator applications [1,2]. EPAM has also been shown to operate in reverse as a generator. As such, EPAM has several characteristics make it potentially well suited for power takeoff systems using wave, water current, wind, human motion, etc.:

1. High energy density allowing for minimal EPAM material quantities
2. Low material cost
3. High energy conversion efficiency independent of strain rate (frequency of operation)
4. Non-toxic and non-corrosion-susceptible materials

These characteristics suggest that EPAM can make a very simple and robust direct drive wave power system that is economically viable. Further, because the energy conversion principle of EPAM is capacitive in nature, the performance is largely size independent and devices can be made in sizes ranging from microwatts to megawatts. Indeed, EPAM has been considered for a variety of novel energy harvesting devices [3].

2 Background on Electroactive Polymer Artificial Muscle (EPAM)

Electroactive polymer artificial muscle (EPAM) is a new smart material with characteristics and properties not seen in other materials [4,5] that has been under development at SRI International since 1991. Currently, EPAM has moved from the research and development stage to the commercial domain with research and development on practical applications, and furthermore to the mass production stage.

EPAM has a very simple structure comprised of polymer films (elastomers) sandwiched by two electrodes made of a flexible and elastic material, and can operate as an electric control actuator.

The operating principle is to use the horizontal deformation of elastomers that is a consequence of the synergistic combination of an electrostatic force and a repulsive force between the electrodes generated when a voltage difference is applied between the two electrodes.

3 EPAM-Based Electric Generator

The operation principle in the generator mode is the transformation of mechanical energy into electric energy by deformation of the EPAM. Functionally, this mode resembles piezoelectricity, but its power generation mechanism is fundamentally different. With EPAM,

electric power can be generated even by a slow change in the EPAM shape, while for piezoelectric devices impulsive mechanical forces are needed to generate the electric power. Also, the amount of electric energy generated and conversion efficiency from mechanical to electrical energy can be greater than that from piezoelectricity [6]. Fig.1 shows the basic operating principal of EPAM power generation.

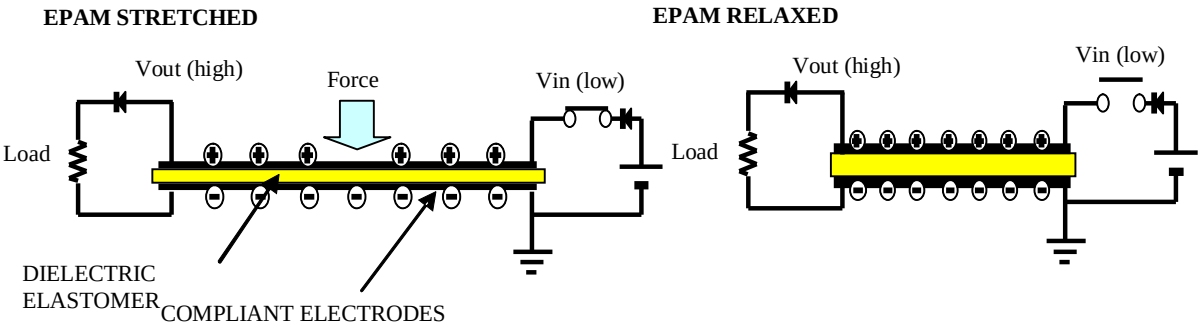

Figure 1: Operating Principle of EPAM Power Generation.

Application of mechanical energy to EPAM to stretch it causes compression in thickness and expansion of the surface area. At this moment, electrostatic energy is produced and stored on the polymer as electric charge. When the mechanical energy decreases, the recovery force of the EPAM acts to restore the original thickness and to decrease the in-plane area. At this time, the electric charge is pushed out to the electrode direction. This change in electric charge increases the voltage difference, resulting in an increase of electrostatic energy.

$$C = \varepsilon_0 \varepsilon A/t = \varepsilon_0 \varepsilon b/t^2 \qquad (1)$$

where ε_0 is the dielectric permittivity of free space, ε is the dielectric constant of the polymer film, A is the active polymer area, and t and b are the thickness and the volume of the polymer. The second equality in Equation (1) can be written because the volume of elastomer is essentially constant, i.e., $At = b$ = constant.

The energy output of an EPAM generator per cycle of stretching and contraction is

$$E = 0.5 C_1 V_b^2 (C_1/C_2 - 1) \qquad (2)$$

where C_1 and C_2 are the total capacitances of the dielectric elastomer films in the stretched and contracted states, respectively, and V_b is the bias voltage.

Considering then changes with respect to voltages, the electric charge Q on an EPAM film can be considered to be constant over a short period of time and in the basic circuit. Since $V = Q/C$, the voltages in the stretched state and the contracted state can be expressed as V_1 and V_2, respectively, and the following equation is obtained:

$$V_2 = Q/C_2 = (C_1/C_2)(Q/C_1) = (C_1/C_2) V_1 \qquad (3)$$

Since $C_2 < C_1$, the contracted voltage is higher than the stretched voltage, corresponding to the energy argument noted above. The higher voltage can be measured and compared with predictions based on the dielectric elastomer theory. In general, experimental data based on high impedance measurements are in excellent agreement with predictions. When the

conductivity is assumed to be preserved in the range of electric charging, Q remains constant.

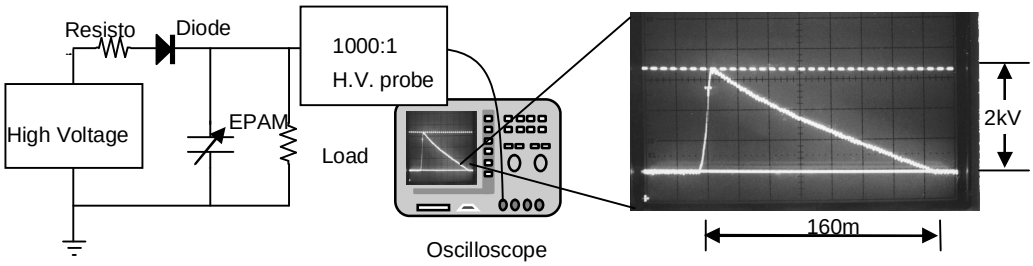

(a)Typical scope trace from EPAM contraction. (b) Measurement Circuit of Generated Energy

Figure 2: Voltage for EPAM Compression and Measurement Circuit.

Figure 2(a) shows a typical scope trace from EPAM contraction. Figure 2(b) shows a simplified circuit for oscilloscope measurement of voltage. Though the voltage wave generated for one impact has on the order of a few ms to several tens of ms for a piezo-electric element, in the case of EPAM it is on the order of 150-200 ms [7]. This is one of the significant characteristics of EPAM. The long power – generation pulse duration of EPAM can allow for the direct use of generated energy for activities such as lighting LEDs or as a power source for high-speed wireless devices. Due to both the long pulse duration and the high energy density of EPAM in power generation mode, mechanical energy can be effectively converted to electric energy even at low frequencies.

3.1 Wave generation

In August of 2007, we carried out ocean experiments on generating electric power from natural wave motion with the EPAM generator installed on a buoy [9]. These experiments were carried out on Tampa Bay, 1.6 km off the coast of St. Petersburg, Florida, at a water depth of about 5 m. Our objectives in these experiments were to:

1. Confirm that the EPAM can operate in the marine environment,
2. Demonstrate that electric power can be generated by natural wave motion,
3. Correlate the wave and buoy motion to the measured energy output of the EPAM generator.

The power generation unit used in the experiments (See Photo1.) was a cylindrical tube with a diameter of 40 cm and a height of 1.2 m. Inside the tube were two roll-type EPAM modules, each about 30 cm in diameter and 20 cm in height (in the stretched state). About 150 g of EPAM film (including electrodes) was used in each roll. The maximum measured electrical output capacity, verified in laboratory tests, was 12.5W for each roll. However, wave activity was minimal during the test period. Wave heights were on the order of few centimetres, which made it very difficult to carry out tests for wave-powered generators. On occasion the weather generated waves 10 centimetres high. Despite the low wave activity and non-ideal motion of the buoy, the generator was shown to function. Even with the small wave height of 10 centimetres, we were able to generate a peak power of 1.2 W with an average power of

0.25 W (See *Figure 3.). While this amount of power is small, we can extrapolate these numbers to estimate the potential of an EPAM generator mounted on a buoy.*

This measured energy output was in response to a voltage applied to the EPAM of approximately 2,000 V. By simply raising the applied voltage to the 6,000 V limit that the roll can withstand before risk of electrical failure, we can estimate that a peak power of 11 W and an average power of 2.2 W could have been generated under these same small wave conditions.

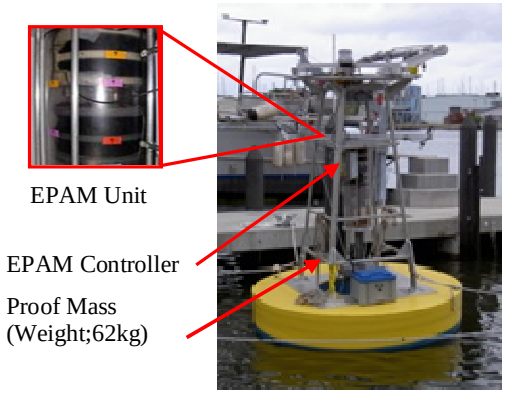

Photo 1: EPAM generator system on the test buoy.

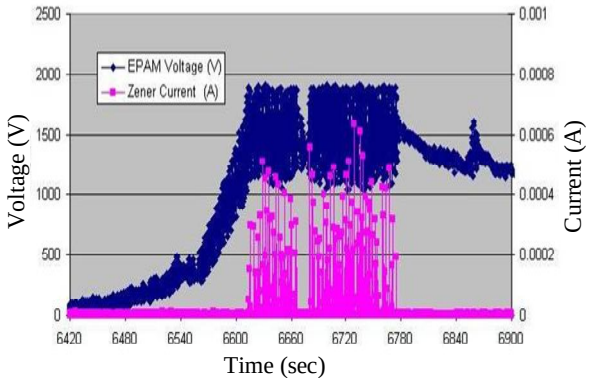

Figure 3: Electricity generated by ten centimetres waves.

Based on data from laboratory testing, we estimated that the energy conversion efficiency of EPAM generator is 70 – 75% (not including hydrodynamic losses).

In December 2008, oceanic tests were also carried out in California, USA, and it was confirmed that generated electric power was constantly stored in a battery.

An energy transduction technology that operates efficiently over a range of frequencies is important for practical energy harvesting devices such as ocean wave power generators. EPAM is based on the change in capacitive energy of a deformable dielectric and is a candidate for such applications. A simple scale model of EPAM-based wave energy harvesting system was tested in a wave tank over a range of wave periods from 0.7 to 3 seconds and wave heights of 3 cm and 6 cm. The energy output was found to be largely independent of wave period (See Figure 4.) [8].

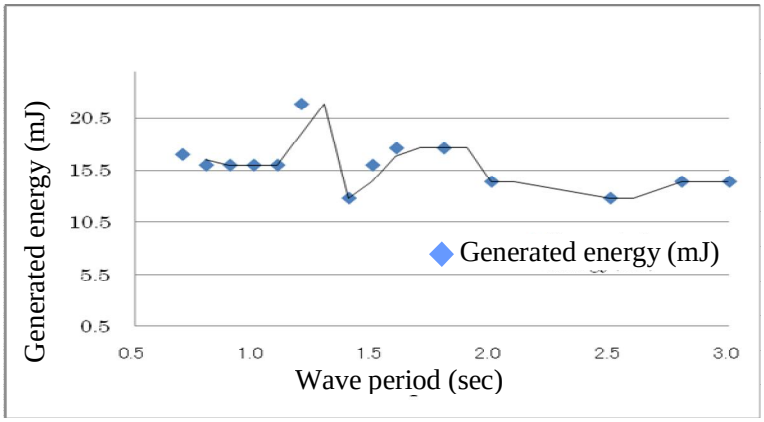

Figure 4: Generated energy as a function of wave period.

Conventional wave power generators have a tendency for a slight modification from the optimum natural period to cause a considerable decrease in generation efficiency, but the EPAM based generator produces stable generated electricity over a range from a short to a long period, which, on average, represents approximately 70% of the maximum value. This is the first case in the world where this kind of electric output has been shown to be possible.

3.2 Water current generation

An EPAM generator can be well suited for micro hydro [9]. As with wave power, the fact that EPAM can operate efficiently over a range of frequencies suggests that an EPAM generator can operate efficiently in the widely varying flow rates of many undammed streams and rivers. Since the EPAM material has a high energy density, EPAM generators do not require high-speed rotation from a converter. A simple structure that induces stretching and contracting of the EPAM is enough to generate electricity.

Photo 2 shows a water mill device that is 80 cm in diameter. This proof-of-principle device was tested in the laboratory. A small water pump (1.12 L/sec flow rate) was fixed to a test tank to move water that spun the waterwheel. The waterwheel was attached to a crankshaft with a push rod that was then attached to a diaphragm-type of EPAM device. The up and down motion of the push rod stretched and contracted the EPAM in the diaphragm. In this simple test, each turn of the wheel produced 5W of electricity.

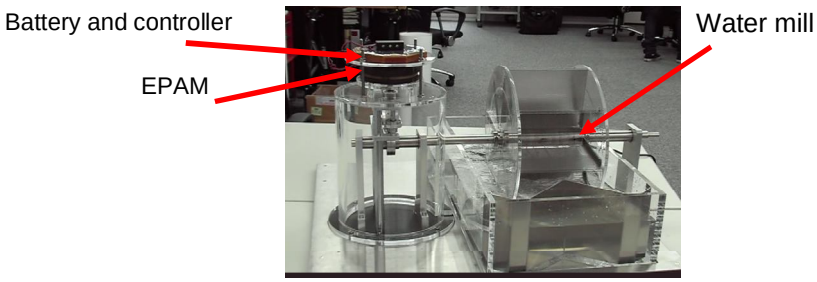

Photo 2: Water mill generator using EPAM.

3.3 Experiments for generation of hydrogen with EPAM generators

At the time of field tests for wave power generation, we also carried out experiments on hydrogen production. In the experiments, the generated energy was first stored in a small battery (12 V/600 mAh). This battery was connected to a hydrogen generation system via a DC-DC converter. The hydrogen generation equipment used in the experiments was a simple electrolytic cell that used nickel electrodes of a mesh of 0.1 mm (150 mm×100 mm). Instead of seawater, a 3% aqueous solution of sodium hydroxide was used as a raw material. Applied voltages were reduced to 3 V by the DC-DC converter. The hydrogen generation equipment used in the experiments was a simple electrolytic cell that used nickel electrodes of a mesh of 0.1 mm (150 mm×100 mm). Instead of seawater, a 3% aqueous solution of sodium hydroxide was used as a raw material. Applied voltages were reduced to 3 V by the DC-DC converter.

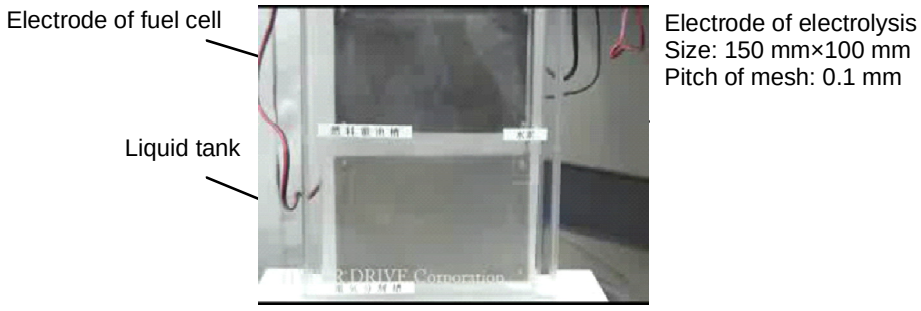

Photo 3: Hydrogen generation equipment by electrolysis.

As mentioned above, we have found that approximately 11 W can be obtained by waves of just 10 cm in height, thus enabling the generation of 1.76 litres of hydrogen in about one hour (estimated for charging and discharging battery efficiencies of 80%[11]). As with the production of electrical energy, the process could be scaled up by several orders of magnitude.

4 Analysis of Power Generation Cost and Future Development

Even without EPAM technology, ocean wave power is beginning to flourish in several countries. These ocean wave power systems typically use hydraulic pistons that are pumped by the wave action. The hydraulic fluid flows through a transmission and then a turbine to spin a rotary electromagnetic generator. When these systems are successfully developed for commercial use, the unit price of a power generation of kWh is estimated to be about 20 US Cents [9]. These wave power systems are typically designed for ocean waves exceeding 2 - 3 m in height. At significantly smaller wave heights, the systems become less economically attractive.

Because of its simplicity, efficiency, and size scalability, we believe that EPAM-based wave generator systems can be attractive not only for large wave applications but for many applications where the waves are much smaller. An estimate based on data from our sea trial demonstration experiments has shown that even in seas where the wave height is only 1 m throughout the year (e.g., the sea close to Japan), if there are spaces of approximately

350 m in length and 15 m in width, the establishment of a sea-based facility generating 6 MW of power is possible [1, 2]. This is a useful amount of power, be it for general use or for providing energy for nearby residential or industrial needs. The ability to produce the power where it is needed can eliminate the losses and costs associated with power transmission over long distances and make wave power even more attractive. The power generation efficiency estimated on the basis of the data obtained from in-tank experiments in 2006[3] and ocean demonstration experiments in 2007[7] and 2008 is approximately 19 US cents/kWh. In the near future, we expect that the electric power generation per unit mass or volume of EPAM material can double, and that the expected power generation cost per kilowatt-hour is 5 - 7.5 US cents. This value is comparable to that for fossil fuel thermal power plants. Of course, the wave power systems have the additional benefit of not releasing any pollution or greenhouse gasses.

Helping to address critical issues such as global warming through the enabling of effective harvesting of highly distributed natural power sources is clearly a great potential benefit of EPAM. We are expecting the EPAM generators may become one of the promising technologies、not only to produce the power, but also to produce hydrogen in ocean and deserts in future [10].

We plan to further investigate more effective structure and methods for water power transmission and realize a power generation unit of 2 kW in the near future. In late 2010, we plan to carry out full-scale ocean experiments using an improved buoy-mounted EPAM power generation unit that will enable the power output level of several hundred watts.

References

[1] R. Pelrine, R. Kornbluh, H. Prahlad, R. Heydt, and S. Chiba, “Micro and Nano Fluidic Devices Using Electroactive Polymer Artificial Muscle “, Proc., Tenth International Conference on Miniaturized System for Chemistry and Life Science, Vol.1, pp278-280, Tokyo, Japan, Nov. 5-9, 2006.

[2] S. Chiba, S. Stanford, R. Pelrine, R. Kornbluh, and H. Prahlad, “ Electroactive Polymer Artificial Muscle “, JRSJ, Vol. 24, No. 4, pp 38-42. 2006.

[3] S. Chiba, R. Pelrine, R. Kornbluh, H. Prahlad, S. Stanford, and J. Eckerle, “ New Opportunities in Electric Generation Using Electroactive Polymer Artificial Muscle (EPAM) “, J.Jpn. Inst. Energy, Vol. 86, No. 9, pp 38-42.pp 743-747, 2007.

[4] R. Pelrine, J. Eckerle and S. Chiba, “Review of Artificial Muscle Approaches”, (Invited) Proc. Third International Symposium on Micromachine and Human Science, Nagoya, Japan, pp 1–9, October 1992.

[5] R. Pelrine, R. Kornbluh, Q. Pei, and J. Joseph, “High Speed Electrically Actuated Elastomers with Over 100% Strain,” Science 287:5454, pp 836–839, 2000.

[6] R. Pelrine, R. Kornbluh, J. Eckerle, P. Jeuck, S. Oh, Q. Pei, and S. Stanford, “ Dielectric Elastomers: Generation Mode Fundametals and Applications “, Smart Structures and Matrials 2001: Electroactive Polymer Actuators and Devices, ed. Bar-Cohen, Proc., SPIE, Vol. 4329, pp 148-156, 2001.

[7] S. Chiba, M. Waki, R. Kormbluh, and R. Pelrine, “ Innovative Power Generators for Energy Harvesting Using Electroactive Polymer Artificial Muscles “, Electroactive

Polymer Actuators and Devices (EAPAD) 2008, ed. Y. Bar-Cohen, Proc. SPIE. Vol. 6927, 692715 (1-9), 2008.

[8] S. Chiba, M. Waki, K. Masuda, T. Ikoma, R. Kornbluh, and R. Pelrine, " Consistent Ocean Wave Energy Harvesting Using Electroactive polymer Artificial Muscle Generators ", Submitted to OES, IEEE.

[9] S. Chiba, R. Kornbluh, R. Pelrine, and M. Waki, "Low-cost Hydrogen Production From Electroactive Polymer Artificial Muscle Wave Power Generators", Proc. of World Hydrogen Energy Conference 2008, Brisbane, Australia, June 16-20, 2008.

[10] S. Chiba, M. Waki, R. Kornbluh, M. Waki, T. Yanagisawa and S. Yonemura,.Electroactive polymer artificial mucles (energy harvesting mode and high-efficiency actuation mode). Eco Design 2007, Tokyo, Japan, December 10-13, 2007.

A Renewable Energy Based Hydrogen Demonstration Park in Turkey – HYDEPARK

Nilüfer İlhan, **Atilla Ersöz**, TÜBİTAK Marmara Research Center Energy Institute 41470 Gebze Kocaeli, Turkey
Mete Çubukçu, Ege University Solar Energy Institute, 35100 Bornova İzmir, Turkey

Abstract
The main goal of this national project is to research hydrogen technologies and renewable energy applications. Solar and wind energy are utilized to obtain hydrogen via electrolysis, which can either be used in the fuel cell or stored in cylinders for further use. The management of all project work packages was carried by TÜBİTAK Marmara Research Center (MRC) Energy Institute (EI) with the support of the collaborators. The aim of this paper is to present the units of the renewable energy based hydrogen demonstration park, which is in the demonstration phase now and share the experimental results.

Keywords: Hydrogen, electrolysis, renewable energy, decentralized power production

1 Introduction

The world's increasing energy demand is mainly provided by the fossil fuels, whose amount decreases strictly; therefore researchers have focused on alternative clean energy sources and how to set them for practical usage economically. One of the methods to produce hydrogen which is one of the most favourable alternative energy carriers is water electrolysis, which can be feasible when integrated with the renewable energy sources [1]. Also hydrogen production by renewable energy can be realized as a decentralized power generation application, which becomes popular nowadays [2–6].

Hydrogen, in many respects, is a better fuel than the existing transportation fuels. In the long term, hydrogen could play a key role in adapting energy supply to energy demand as hydrogen has the potential for large-scale, even seasonal, energy storage [3]. For both transport and stationary applications, widespread production and a reliable hydrogen distribution system should be in place. The outlook for future markets for hydrogen as a fuel can be governed by two economic scenarios:

1. Hydrogen produced from fossil sources
2. Hydrogen produced from nonfossil sources.

While not currently practical, it appears that nonfossil energy sources will become dominant in the future. A long-sought goal of energy research has been a method to produce hydrogen fuel economically by using nonfossil fuels such as sunlight, wind and hydropower as the primary energy source [7]. Although production of hydrogen via the use of solar cells or wind turbines has been regarded as the cleanest and most desirable method, these processes do not supply enough hydrogen at the present stage.

2 General Description of Project

"Development of Hydrogen Production, Conversion and Storage Technologies – HYDEPARK" project, which was supported by the State Planning Organization of Turkey (DPT), started on June 1st, 2005 and completed by the end of 2007. The main goal of this national project was to research hydrogen technologies and renewable energy applications. The project had two segments of the laboratory studies such as indoor and outdoor applications. Indoor applications included the design and construction of reactor systems with the required sub-units for hydrogen production from methane and purification of syngas. On the other hand, hydrogen production via electrolysis by using renewable energy sources was investigated within the outdoor applications. Hydrogen could either be stored for further use or directly utilized by a fuel cell to obtain energy. The design, purchase and integration of all the units and sub-units were carried out by TÜBİTAK MRC EI. Finally a renewable energy based hydrogen production and storage system was established and now it is in the demonstration phase (Figure 1a).

Figure 1a: HYDEPARK demonstration park.

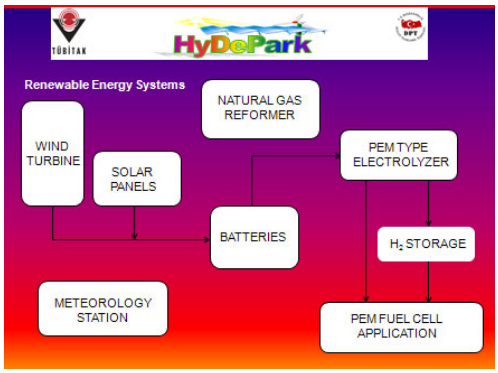

Figure 1b: System components.

3 Description of Components

As seen from Figure 1b, the main units of HYDEPARK demonstration park are solar panels, a wind turbine, batteries, an electrolyser, a hydrogen compressor, hydrogen storage cylinders, fuel cells and a meteorology station. Except the solar panels, the wind turbine and the meteorology station, all units are placed in two containers. There is also a natural gas reformer test unit in EI laboratory, which was designed and constructed in the scope of the indoor laboratory activities.

3.1 Photovoltaic (PV) panels

The photovoltaic system (Figure 2a) includes totally 145 PV panels and the total installed power is ~12 kW_p in the standard conditions (values correspond to 1000 W/m^2, 25°C and 1.5 air mass). 120 PV panels are CIS type thin film, which have 9.6 kW_p total with ~ 10.5% efficiency. 10 PV panels are multicrystalline type and they were produced by Ege University Solar Energy Institute which was one of the collaborator organizations. The multicrystalline solar power capacity is 1.2 kW_p total with ~ 13% efficiency. The rest 15 PV panels are monocrystalline type, which have ~ 1.1 kW_p installed capacity with ~ 14% efficiency.

3.2 Wind turbine

The wind turbine peak power is 5 kW_p which was produced by a national company (Figure 2b). The wind generator is a permanent magnet and a three-phase synchronous machine. The nominal power of the generator is 5 kVA and the rated rpm is 375 (the wind speed is 13 m/s). The DC output voltage is 45-60 V DC. This voltage can be easily used for 48 V batteries charging. There is also 220 VAC output voltage from the PWM inverter. The height of the pole is 15 m and the blade radius is 1.65 m. The wind turbine produces electricity in the range of 3–13 m/s wind speed.

Figure 2a: PV panels.

Figure2b: Wind turbine.

3.3 Batteries

All the generated renewable energy is stored in conventional stationary type lead acid batteries which were produced by a national company (Figure 3a). The designed DC busbar voltage is set to be 48V. Therefore 2V DC cells are connected serially in number of 24 in order to achieve this voltage. The capacity of the desired battery is calculated to be 1500Ah. The batteries are Low Maintenance Tubular Stationary (OPzS) which are a new version of common lead-acid batteries. The batteries have a long life of 10-15 years or more. The dimension of each battery (W x L x H) is 275 x 210 x 848 (mm). The weight with acid is 114.3 kg for each battery.

Figure 3a: Lead acid batteries.

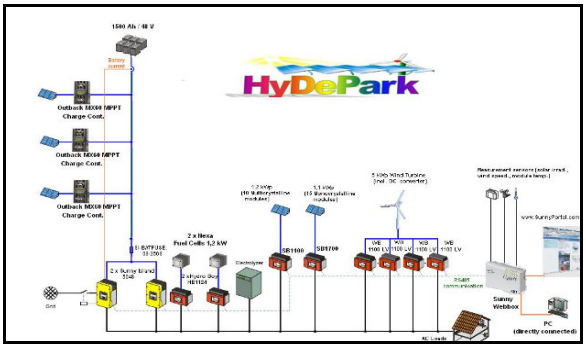

Figure 3b: Power conditioning layout of HYDEPARK.

3.4 Control units / converters / inverters

The system was designed to operate the electrolyser by the renewable energy source, so an AC bus was created since the electrolyser operates in 220 V and 50 Hz AC line (Figure 3b). The main important component of the system is a bidirectional inverter, which acts as a battery charger and an inverter. This unit supplies loads on the standalone grid side and charges battery banks with power that is provided by feeding electricity into the grid on the AC side. The bidirectional inverter unit achieves a maximum efficiency of more than 95%. The parallel operation of two bidirectional inverters on a single phase of a battery bank which has 48 V and 1500 Ah capacity enables to stand up a power supply for electrolyser load. The bidirectional inverter can also automatically deactivate loads if the battery does not have sufficient electrical energy available.

3.5 Proton exchange membrane (PEM) type electrolyser

The electrolyser is used to produce hydrogen by utilizing the electricity generated by the wind turbine and the PV panels (Figure 4a). The net hydrogen production rate of the electrolyser is 1.05 Nm^3/h with a delivery pressure of maximum 13.8 barg. The purity of the product hydrogen is 99.9995% and the power consumed is 6.7 kWh/Nm^3 H_2 (for optimal conditions). The electrolyser uses deionized water that should meet minimum of ASTM Type II requirements, to produce hydrogen and to actively cool the cell stack. A deionized water feeding system was purchased from a national company, since deionized water can be supplied from an already established system in TUBITAK MRC Campus. The electrolyser produces also oxygen in electrolysis process, which can be directly vented inside the container with small amounts of water condensate since the required ventilation was established. The electrolyser has a hydrogen vent port, which should be vented outside the container for safety. The product hydrogen port is separated into three lines, one of which goes to the hydrogen compressor to be pressurized, one goes to the vent, and the other one directly goes to the PEM fuel cell. Although electrolysis reaction needs DC current, the electrolyser is designed to be connected to the grid so it requires AC current. In this project, the electrolyser supplies the power from the batteries after converting/adjusting the current to AC, which also serves to buffer the electrolyser from power spikes. If a problem occurs with this system, electrolyser can be directly connected to the grid.

Figure 4a: PEM type electrolyser.

Figure4b: Hydrogen compressor.

3.6 Hydrogen compressor

The single-stage hydrogen compressor has a triple diaphragm construction, which isolates hydrogen from hydraulic oil (Figure 4b). All piping, tubing and wetted compressor parts are type 316 stainless steel which is corrosion-resistant. It has a 4 kW motor with a flameproof enclosure. It has a flow capacity of 4 Nm^3/h at maximum suction and it can compress hydrogen gas to provide a discharge pressure up to 103 bar (1450 psi). No water cooling is required. Hydrogen is fed to the compressor through a buffer tank with an inlet pressure of 7–10 bar. The pressurised hydrogen leaving the compressor is cooled through a heat exchanger before sent to the cylinders for storage.

3.7 Hydrogen storage cylinders

Hydrogen produced by the electrolysis is stored in high pressure cylinders in gas phase after pressurized by the compressor up to 103 bar. There are 12 cylinders placed in a stationary bundle and 4 individual cylinders which are ready to be carried to the laboratory in case of need (Figure 5a). Stored hydrogen in the cylinders can also be utilized in the fuel cell after the pressure is regulated. The stored hydrogen in the cylinders can be directly fed to the PEM fuel cells after regulating the pressure.

3.8 PEM fuel cell

PEM Fuel Cell is air-cooled and comprises all necessary fuel, electrical and control interfaces (Figure 5b). There are two power modules in this demonstration park. Each fuel cell module works at atmospheric pressure and generates up to 1200 Watt of unregulated DC electrical power from hydrogen and oxygen (air). All necessary auxiliary components including an air compressor, cooling fan, humidity exchanger, purge valve, pressure regulator and microprocessor controller are built into the system.

Figure 5a: Hydrogen cylinders.

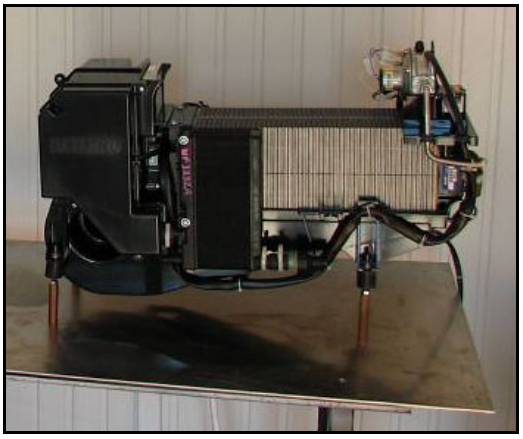

Figure 5b: PEM fuel cell.

4 Operational Experience and Performance

Since the main goal of HYDEPARK project was to obtain the electrolyser load from the renewable energy sources, the energy consumed by the electrolyser was considered to define the required renewable energy capacity. The energy consumption of the electrolyser is 6.7 kWh/Nm^3 H_2 and its net production rate is 1.05 Nm^3 H_2/h. This means that the electrolyser needs 7.04 kWh energy per hour. For 3 hours operation per day, the energy consumption is 21.12 kWh/day. When the electrolyser is operated 3 hours per day and 5 days per week, the daily hydrogen production is 3.15 Nm^3 and the yearly hydrogen production is 819 Nm^3.

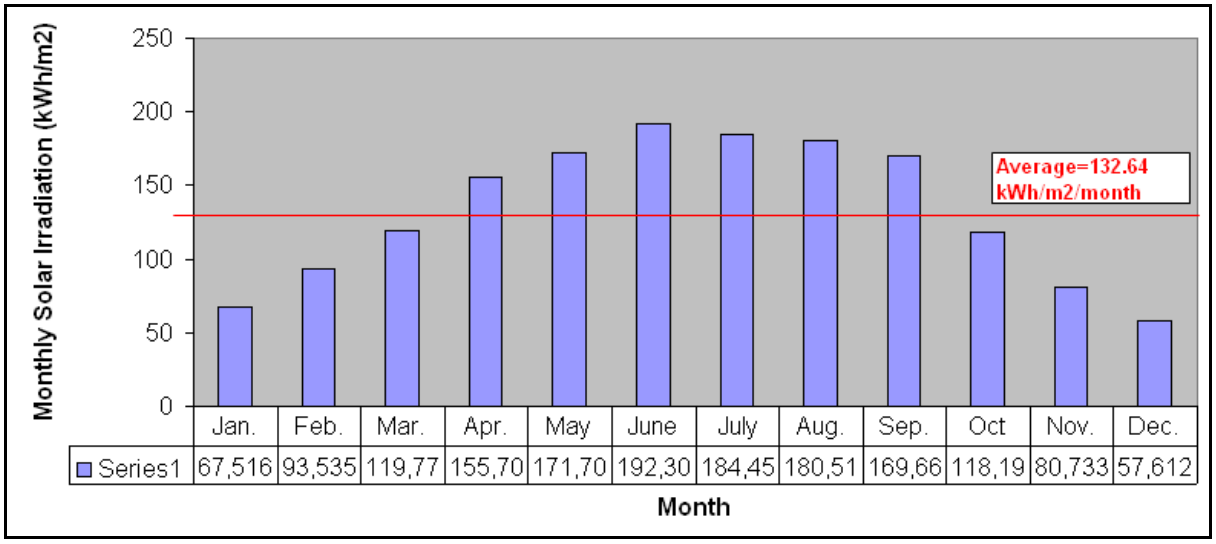

Figure 6: The monthly solar irradiation values in Gebze.

The location of the installation area is so important to define the energy potential on solar and wind energy sources. The solar irradiation and the wind speed are important factors for photovoltaic and wind power systems, respectively. At the beginning of the project, measurements of the reliable sources (the solar irradiation, module temperature and wind speed values) were used to calculate the system requirements. The capacity of the PV system was calculated to be sufficient for the operation of the electrolyser load. When the PV power capacity was not enough, the wind power would compensate the lack of it. The average daily solar radiation energy and the load consumption energies were taken as the essential parameters for solar system sizing (The yearly total solar irradiation is ~ 1.6 MWh/m^2 in Gebze).

Assuming that the PV rated efficiency was 13.5%, the battery efficiency was 70%, the mean inverter efficiency was 90%, the mean charge controller efficiency was 90%, the other components (wires, temperature losses in PV etc.) efficiency was 80% and then the total solar system efficiency was calculated to be ~ 6% (Other efficiencies such as wind turbine, fuel cell, and hydrogen storage etc. are not included in it). By using these values, the peak power of the PV generator was calculated to be approximately 12 kW_p.

Considering that the battery efficiency was 70%, 2 days in autonomy duration and the daily load consumption was 21.12 kWh, the essential battery capacity was calculated to be ~ 61

kWh. Therefore the battery capacity in Ah at 48 V battery voltage was ~ 1270 Ah. By regarding the additional energy supplies (wind turbine, fuel cell etc.), the storage battery bank was set up to be 48 V 1500 Ah.

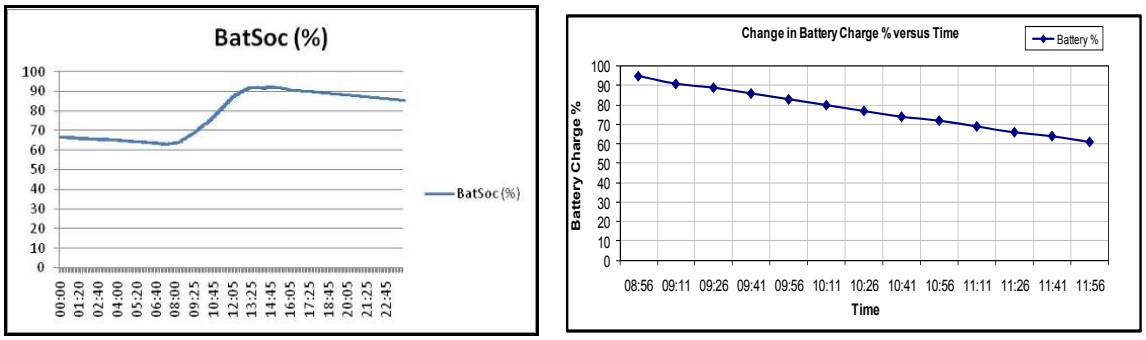

Figure 7: Battery charge and discharge versus time.

The operational parameters of the electrolyser can be monitored and stored by using its original PC program. Also it is possible to measure other system parameters and a PC system is set to view and save them. So efficiency of the individual systems and total system efficiency can be calculated and the system efficiency is found to be 9% according to the formula given below:

$$\eta_{system} = \eta_{PV} * \eta_{PCU} * \eta_B * \eta_o$$

where η_{system} is the system efficiency, η_{PV} is the PV efficiency (12.5%), η_{PCU} is the power conditioning unit efficiency (96%), η_B is the battery efficiency (75%) and η_o is the efficiency of others (98%).

5 Safety

Hydrogen is odourless, tasteless, colourless, and highly flammable. It is very combustible in the presence of oxygen and burns with a colourless flame. The lower explosive limit of hydrogen is 4% by volume [8]. Within the safety considerations of the electrolyser, a combustible gas sensor is located at the exit of the air purge stream to detect hydrogen. The sensor will cause an alarm and an automatic shutdown of the electrolyser when it detects the concentration of hydrogen within the purge air stream is in excess of 1.2%. If hydrogen leakage occurs due to any internal equipment failure, the indoor hydrogen detector safety circuit of the electrolyser will stop any further generation of hydrogen by automatically shutting down the electrolyser. A ventilation system was established to avoid the accumulation of hydrogen in the container in any case of leakage. Climatization of the container was realized due to the operational conditions of the electrolyser (5°C–40°C). Also the electrolyser shutdown circuits should not be bypassed. Hydrogen storage cylinders are placed outside the containers in a fixed position for safety reasons.

All inverters which are used in the project are compatible with all communication products and impressive with a high degree of protection (IP65). The robust enclosure design and high protection degree IP65 ensure secure operation even in extreme climatic conditions, both indoors and outdoors. The design also ensures over voltage protection on DC and AC sides.

Acknowledgements

Ege University Solar Energy Institute and Hatgrup are acknowledged for their help and support in our studies.

References

[1] Frano Barbir, “PEM electrolysis for production of hydrogen from renewable energy sources”, Solar Energy, Vol. 78, pp. 661–669, 2005.

[2] Ben Kroposki and Carolyn Elam, “Renewable Electrolysis Integrated System Development and Testing”, National Renewable Energy Laboratory, 2004. Presented at the 2004 DOE Hydrogen, Fuel Cells & Infrastructure Technologies Program Review.

[3] Rupert Gammon, Amitava Roy, John Barton and Matthew Little, “Hydrogen and Renewables Integration (HARI)”, CREST (Centre for Renewable Energy Systems Technology), Loughborough University, UK. http://ieahia.org/pdfs/HARI.pdf

[4] Torstein Våland, Willy Bartholdsen, Morten Ottestad and Magne Våge, “Grimstad Renewable Energy Park”, Agder University College, NO-4878 Grimstad, Norway. http://ieahia.org/pdfs/grimstad.pdf

[5] http://www.res2h2.com/

[6] Tapan K. Bose, Kodjo Agbossou, Mohan Kolhe and Jean Hamelin, “Stand-Alone Renewable Energy System Based on Hydrogen Production”, Institut de recherche sur l’hydrogène, Université du Québec à Trois-Rivières, Canada. http://ieahia.org/pdfs/res_uquebec.pdf

[7] Thomas L. Gibson and Nelson A. Kelly, “Optimization of solar powered hydrogen production using photovoltaic electrolysis devices”, International Journal of Hydrogen Energy, Vol. 33, pp. 5931–5940, 2008.

[8] http://www.isocinfo.com/DocumentRoot/13/Hydrogen.pdf

Analysis of the Impact of Hydrogen on Wind Power

Dennis Krieg, **Thomas Grube**, **Detlef Stolten**, Forschungszentrum Jülich GmbH, Germany

1 Motivation for Wind Power and Hydrogen

Due to environmental circumstances (climate change, security of energy supplies, etc.) a rethinking is needed in both energy and environmental policy.

There is a general consensus that the share of renewable energy sources will increase massively in the future.

Renewable energy sources can be divided into two groups. The first group can be used almost continuously, e.g. hydro, geothermal, biomass. The second group is characterized by intermittent energy supply, such as solar power and wind.

Due to the fact that the potential of the first group is too low, energy policy must focus on the second group, whose potential exceeds energy demand by far. Unfortunately, supply and demand for energy differ enormously, which consequently leads to the fact that the power supply needs to be adjusted [1].

Wind power is the most promising alternative due to its mature stage of development and the fact that it also tends to be economically attractive. It has almost achieved a level comparable to normal coal-fired power plants. At an average wind velocity of 25 km/h, the cost of electricity ranges between 4 and 6 ct/kWh [2, 3, 4].

The target of the policy is to increase the share of renewable energies up to 2020 by as much as 30% or even 40% [5, 6]. Wind is the most successful form with average growth rates of 30 to 40% (2005) per year [7].

The wind power capacity installed worldwide increased from 1.9 GW in 1990 to almost 60 GW in 2005. Hence wind power plants delivered roughly 125 TWh of electrical power (2005), which is around 0.7% of the global electrical output [7, 8].

Estimations of the general potential of wind power plants differ enormously depending on the assumptions made. The theoretical potential is estimated to be roughly 480,000 TWh whereas only 20,000 TWh seems to be technically available [7, 9]. This technical potential ranges up to 64,000 TWh [7, 10] or even 96,000 TWh [7, 11].

Surveys of 100 wind power plants have shown that the average capacity factor is roughly 24% (2003) [12, 13]. Due to the high degree of intermittency it is usually assumed that a penetration of 20 to 30% will affect the grids, even those that are very stable at the moment [5, 14].

With increasing wind penetration the share of curtailment, i.e. the share of power that cannot be applied to the grid, rises dramatically. Calculations have shown that more than 30% cannot be used in the case of 50% wind penetration on the market (=installed wind power capacity/total installed power capacity). Hence CO_2 savings will not be as high as expected [12].

Besides selling the electricity instantaneously on the market it can be converted into hydrogen via water electrolysis.

This hydrogen can be used to stabilize the grid (e.g. lack of current wind power) or it can be used as fuel within the transportation sector.

Water electrolysis is the most effective method to generate hydrogen by electricity and generally also one of the simplest methods. Several other advantages are listed in the following [2, 12, 15]:

- Mature and commercially available technology
- Reasonable efficiency (more than 70% based on HHV) with a power demand of about 4.3 kWh/Nm^3
- Both small and large applications feasible
- High degree of purity
- Small footprint and maintenance cost
- Application of off-peak power is possible in order to reduce electricity costs.
- Fast reaction: from 16% to 100% power input within 40 seconds.
- Possibility of producing CO_2-free hydrogen: conventional steam reforming: 6 – 11 kg CO_2/kg H_2

2 Stationary Storage

Hydrogen can be used to store excess electricity. This may be done in the case of low demand or abundant wind power. This hydrogen may then be re-converted into electricity if needed [15]. The efficiency of the energy chain is roughly 33% [1].

A recent survey calculated that one kWh would cost between € 0.43 and € 1.7 , assuming the same profit as if the power had been fed into the grid [16]. This is due to the high investment costs and the tremendous energy losses.

The authors assumed an electrolysis efficiency of 65% (based on HHV, comprising all losses) and a fuel cell efficiency of 36.4%. Internal combustion engines are cheaper to purchase (200 to 500 €/kW) in comparison to fuel cells (1000 to 2500 €/kW), but also less efficient (≤ 30%) [16].

More optimistic assumptions for an electrolyzer are investment costs of 1300 €/kW [17] and an efficiency of roughly 70%. For stationary fuel cells 50% seem to be adequate [1].

As mentioned above, wind power is a power source that fluctuates greatly. Hence storage is needed in order to [1]:

- compensate for temporary blackouts which might cause contractual penalties ,
- make the input more predictable

Due to the amount of energy losses (caused by every conversion step) as well as the enormous investment costs, hydrogen is seen as a technically feasible alternative to store excess electricity but not as an economically attractive option [1].

Depending on the size of the system, different alternatives are preferred. Lead or lithium batteries are preferable for small and medium-size systems (up to a few 100 kWh). Large systems (from a few MWh upwards) in contrast prefer compressed air storage etc., which leads to a decisive advantage in procurement costs [1].

3 Application in the Transport Sector

All renewable energy sources, except biomass, have in common that they cannot be used directly as fuel.

Nonetheless, via water electrolysis it is possible to produce a clean energy carrier which can be used as fuel [12].

Other methods, such as those mentioned above, are only able to provide “electricity in – electricity out” options [12, 18, 19].

The markets for hydrogen and its related technologies are potentially huge and hydrogen could, in the long term, replace most other fossil fuels [12].

Positive is also the high well-to-wheel-efficiency that can be achieved of 22 up to 33% At present, gasoline vehicles normally have an efficiency of 15% [20, 21].

It is estimated that after market introduction it will take 15 years before the first million fuel-cell vehicles are sold in the EU. After a further 10 years up to 12 million fuel-cell-driven cars might be in operation [22]. This is in keeping with the recently published EU strategy of achieving one to five million fuel-cell cars in 2020 [22, 23].

Hydrogen may be produced on site or at centralized facilities. Centralized production needs an appropriate distribution infrastructure. Hence trucks or pipelines should be taken into account.

Hydrogen is expected to be produced via steam reforming with natural gas and on-site electrolysis with wind power in the early stages. At this stage, all transport will be realized by trucks [24].

None of the needed technologies is expected to be technically very challenging. The only exception may be pipelines due to the fact that a large new infrastructure has to be constructed, which might cause some difficulties. Therefore pipelines are not expected before 2025 [24].

Examples of a well-performing application of hydrogen are the fuel-cell buses from ISE Corporation. They need 50 kg hydrogen, which is stored at 345 bar, for a range of 400 to 480 km [5].

4 Optimizing Hydrogen Production

Water electrolysis is a well-known process. It has been established for years, but the hydrogen produced is almost exclusively used for chemical applications (e.g. margarine production) or as a coolant. No appreciable quantity is used for energetic purposes in the sense of fuel (e.g. space industry).

Due to the fact that hydrogen has completely different properties (cost, purity, efficiency, etc.) as a chemical product and as a fuel, new efforts are needed to implement hydrogen on the market.

Therefore it is very important to calculate the appropriate capacity of the electrolyzer as well as the storage system.

Besides the well-known parameters, such as investment cost, operation and maintenance, etc., three parameters have a decisive influence on how electrolyzers should be used.

The first is the electricity price (which is time-variable), the second is the fuel price and the third one is the penalty to be paid if the agreed amount of electricity is not supplied to the grid.

Today it is obvious that operators of wind power plants will supply their electricity to the grid at any time. There are no incentives, such as greatly varying prices within one day, that could induce the operator to store the electricity in order to supply it to the grid when needed.

All other suppliers suffer from this situation because they have to adjust their electricity production according to the electricity input of wind power plants. The additional losses (due to partial load and overcapacities) will ultimately be paid by the consumers.

Hence some countries, e.g. Spain, have chosen to punish wind power plant operators if they supply less electricity than agreed and if they supply more electricity to the grid.

The amount of electricity is agreed upon roughly one day in advance.

Operators adjust their behavior depending on the three above-mentioned parameters. The promised amount of electricity will be slightly less than expected on the basis of the weather forecast in order to avoid penalties. Very high penalties will make operators supply very little electricity, so that they will (under all circumstances) be able to supply as much electricity to the grid as agreed. This extreme would lead to a permanent under-utilization, which would increase the attractiveness of storage capacity. The indirect energy losses, such as wasted electricity, could outweigh the loss due to the conversion chain.

The same might occur with respect to economic attractiveness. Investment costs for electrolyzers and fuel cells may be less than those due to the wasted electricity from the wind power plant, which is never used at full load.

Therefore hydrogen might be used to store excess electricity.

Calculations by Norwegian scientists have shown that hydrogen production costs are extremely dependent on the system. Grid-connected hydrogen production costs were estimated to be roughly 2.8 €/kg while hydrogen in an isolated system will cost twice as much (6.2 €/kg). Therefore the grid-connected system is assumed to be far more economically attractive [17].

The price difference is mainly due to the components that need to be much larger in an isolated system in order to prevent too much electricity from being wasted, which would make wind power itself economically very unattractive (and consequently the whole system).

Further analyses have shown that even marginal decreases in the costs of wind power plants, electrolyzer, etc. will reduce hydrogen production costs enormously [17].

References

[1] Ibrahim, H., Ilinca, A., Perron, J., (2008) Energy storage systems – Characteristics and comparisons. *Renewable & Sustainable Energy Reviews*, **12** (5), 1221-1250.

[2] Diéguez, P.M., Ursúa, A., Sanchis, P., Sopena, C., Guelbenzu, E., Gandia, L.M. (2008) Thermal performance of a commercial alkaline water electrolyzer: Experimental study and mathematical modeling. *Int. J. Hydrogen Energy*, **33** (24), 7338-7354.

[3] Bockris, J, O´M., Veziroglu, T. N. (2007) Estimates of the price of hydrogen as a medium for wind and solar source. *Int. J. Hydrogen Energy*, **32** (12), 1605-1610.

[4] Joselin Herbert, G. M., Iniyan, S., Sreevalsan, E., Rajapandian, S. (2007) A review of wind energy technologies. *Renewable & Sustainable Energy Reviews*, **11** (6), 1117-1145.

[5] Briguglio, N., Ferraro, M., Andaloro, L., Antonucci, V. (2008) New simulation tool helping a feasibility study for renewable hydrogen bus fleet in Messina. *Int. J. Hydrogen Energy*, **33** (12), 3077-3084.

[6] Zervos, A., Oral presentation at European renewable energy policy conference 2007, Brussels; 29-31 January 2007.

[7] Moriarty, P., Honnery, D. (2007) Intermittent renewable energy: The only future source of hydrogen? *Int. J. Hydrogen Energy*, **32** (12), 1616-1624.

[8] Anon. Plugging the gap: the diminishing resource. Wind Dir 2006; September 27-33.

[9] Intergovernmental Panel on Climate Change (IPCC). Climate Change 2001: mitigation. Cambridge, UK: Cambrigde University Press; 2001.

[10] Lenzen, M., Munksgaard, J. (2002) Energy and CO_2 life-cycle analyses of wind turbines – review and applications. *Renewable Energy*, **26**, 339-362.

[11] Keith, D., DeCarolis, J.F., Denkenberger, D.C., Lenschow, D.H., Malyshev, S.L., Pacala, S., et al. (2004) The influence of large-scale wind power on global climate. *PNAS*, **101** (46), 16115-16120.

[12] Troncoso, E., Newborough, M., (2007) Implementation and control of electrolyzers to achieve high penetrations of renewable power. *Int. J. Hydrogen Energy*, **32** (13), 2253-2268.

[13] www.eng.elkraft-system.dk

[14] McDowall J. (2006) Integrating energy storage with wind power in weak electricity grids. *J. Power Sources*, **162** (1), 959-964.

[15] Zhou, T., Francois, B. (2009) Modelling and controll design of hydrogen production process for an active hydrogen/wind hybrid power system. *Int. J. Hydrogen Energy*, **34** (1), 21-30.

[16] Bernal-Agustin, J. L., Dufo-López, R. (2008) Hourly energy management for grid-connected wind-hydrogen systems. *Int. J. Hydrogen Energy*, **33** (22), 6401-6413.

[17] Greiner, C. J., Korpas, M., Holen, A. T. (2007) A Norwegian case study on the production of hydrogen from wind power. *Int. J.Hydrogen Energy*, **32** (10-11), 1500-1507.

[18] Baxter, R. Energy storage, enabling a future for renewables? Renewable Energy World, July-August 2002.

[19] Merz and McLellan. Review of energy sources for power stations. Consultation document for the DTI, 1998.

[20] Qadradan, M., Saboohi, Y., Shayegan, J. (2008) A model for investigation of optimal hydrogen pathway, and evaluation of environmental impacts of hydrogen supply system. *Int. J. Hydrogen Energy*, **33** (24), 7314-7325.

[21] Fuel cell handbook. 7th ed. EG&G Technical Services, Inc.; November 2004. Under contract no. DE-AM26-99FT40575.

[22] Mulder, G., Hetland, J., Lenaers, G. (2007) Towards a sustainable hydrogen economy: Hydrogen pathways and infrastructure. *Int. J. Hydrogen Energy*. **32** (10-11), 1324-1331.

[23] HFP. “Deployment strategy”. European hydrogen & fuel cell technology platform, 2005, published on: www.hfpeurope.org/uploads/677/687/HFP_DS_Report_AUG2005.pdf.

[24] Seymour, E. H., Murray, L., Fernandes, R. (2008) Key Challenges to the introduction of hydrogen – European stakeholder views. *Int. J. Hydrogen Energy*, **33** (12), 3015-3020.

H_2 Production in Sotavento Wind Farm

Milagros Rey Porto, **Trinidad Carretero**, Gas Natural SDG S.A., Plaça del Gas 1, 08003 Barcelona, Spain
Mónica Aguado, **Raquel Garde**, Renewable Energy Grid Integration Department, National Renewable Energy Centre (CENER), Ciudad de la Innovación, 7, 31621 Sarriguren, Spain

Summary

This article aims to show a hydrogen production and conversion plant from wind power, the biggest of Spain, owned by Gas Natural.

1 Background

For decades, a series of progressive decrease in the reserves of fossil fuels and environmental problems associated with burning them have promoted the search for alternative energy, including renewable energies (EERR).

The use of EERR offers numerous advantages. The main ones include:

- They are inexhaustible
- Both production and consumption of energy are major emitters of greenhouse gases. The use of renewable energy, allows producing a low environmental impact.
- Statewide, they foster the decline of foreign energy dependence by providing a diversification of energy sources
- Contribute to improve and modernize the industrial base, the generation of employment and, therefore, regional development
- Distributed Generation Systems allows the point of generation being close to the consumption, and therefore to reduce electricity losses produced in transport and the necessity of transportation infrastructure.

Faced with all these advantages, the EERR have three major drawbacks:

- The great variability of renewable resources
- The difficulty of the production
- The difficulty of adjusting production to demand

Currently in Spain there are over 16,500 MW installed, this means a coverage greater than 12% of electricity demand.

Given the magnitude of wind power installed and the expected growth in the coming years, it is very important to mitigate and correct the weaknesses of wind power. It becomes imperative to manage the energy produced into the grid by wind turbines. Therefore, it is necessary to research and develop technologies to correct the variability of the resource and adjust the production to demand.

These technological developments are focused on the prediction and storage of wind power delivered to the grid.

The resolution of the problem of electricity storage on a large scale is one of the most important technological challenges to overcome in the field of electrical engineering. Currently there are various storage systems based on the amount of stored energy and storage time needed [1].

Energy storage can solve most problems associated with wind power:

1. The energy generated by wind farms is allowed to be managed, improving its selling price in the pool [2].
2. Wind energy production is possible to be adjusted to forecasts predictions as well as get a guarantee of wind production at peak electricity demand
3. The penetration level of wind power is allowed to be increased, once it becomes manageable. Using these systems the installed capacity could be increased in resource-rich sites: during times of high wind, wind power is stored, so the limit of the network is never reached and electricity is injecting into the grid in times of low wind production [3,4,5]
4. Allows implementing wind farms in remote locations but with high potential, reducing transmission costs.

2 Hydrogen as Storage System

This article presents an installation that utilizes the technology of H_2 as energy storage system.

The concept of generating H2 from wind born in 1923, when John BS, Haldane proposed the production of H_2 and O_2 from water using this type of energy [6]. Back in the 30s Hermann Honnef introduced the use of high-power wind turbines to generate H_2.[7] From the 60s is beginning to study the electrolysis using solar power and extend the studies of H2 generation from wind energy.[8, 9, 10, 11]

Hydrogen is an energy carrier, in other words there is no free in nature and must be obtained from a primary source, although there are numerous sources and hydrogen production technologies.

Thus, hydrogen is one of the energy carriers with greater environmental benefits because its combustion produces no emissions and its production will have a greater or lesser environmental impact in terms of the energy that is used to generate it.

Therefore, if obtained through renewable energy, the environmental impact it causes is minimal. It is for this reason that today there is great interest in developing projects that use hydrogen generated from renewable energy as energy storage.

The development of such facilities in each country is conditioned by the quality of the transport and distribution grid and existing legislation in terms of renewable energy and management.

Currently, there are two types of systems that use H_2 as energy storage of wind power. The former are island energy systems, whose primary objective is to satisfy the demands of a particular community with an island configuration of the grid. The others are integrated energy systems in the electrical grid, which aim to manage and optimize energy production from a wind farm, improving their capacity factor. Both approaches must be addressed from

different perspectives, because the objectives, and therefore the operation mode of the facility, are different.

Another objective of such facilities is the generation of H_2 as fuel using renewable sources instead of conventional natural gas reforming.

At present, there is some development of the study of such systems. In fact, the facilities currently available are directed mostly to study energy self-sufficiency of communities in island or the production of H_2 as fuel.

However, the installation presented here is one of the largest global capacity, where hydrogen is used in the energy management of the production of a wind farm. Therefore, it could be used as a platform for the development of tests and studies in this type of facility.

3 Sotavento Wind Farm

The facility is located in the Sotavento wind farm in the municipality of Xermade (Lugo), at its border with the municipality of Monfero (A Coruña). This has a rated capacity of 17.56 MW with 24 wind turbines of 5 different technologies (Figure 1).

This project was born thanks to a framework agreement between Gas Natural and the Department of Innovation, Industry and Trade of the Xunta de Galicia for the development of renewable energy. In 2008 an agreement with the National Renewable Energy Center (CENER) was signed by Gas Natural to study, analyze and characterize the plant.

The facility uses the surplus electricity generated by the wind farm, in other words the excess of energy produced over than expected to generate hydrogen with an electrolyser. This breaks down water using electricity (electrolysis) in four stacks of electrolytic cells, generating separate H_2 and O_2.

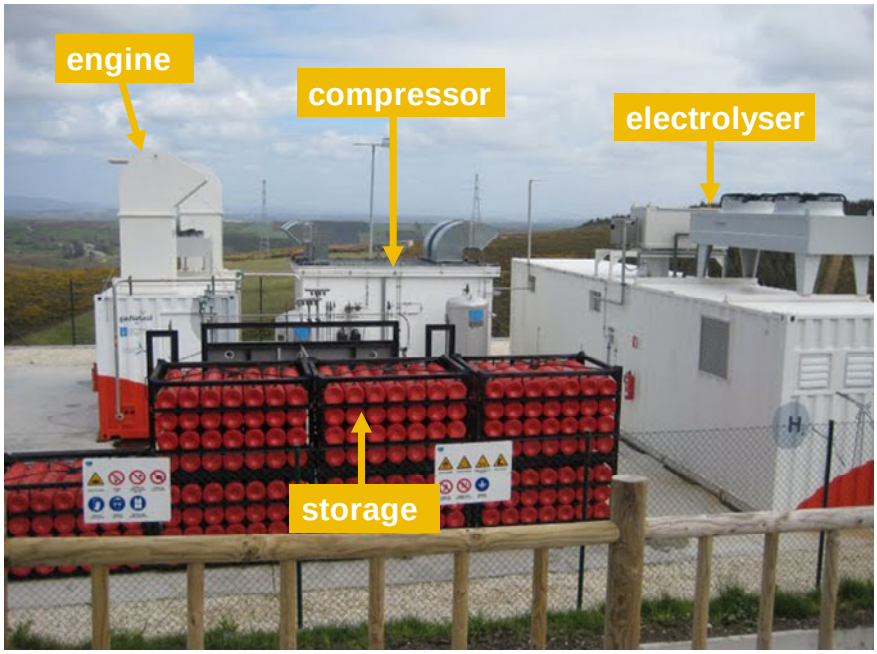

Figure 1: Photography of the H_2 facility.

Figure 2 contains the main equipments of this installation: electrolyser, compressor, H_2 storage and H_2 engine.

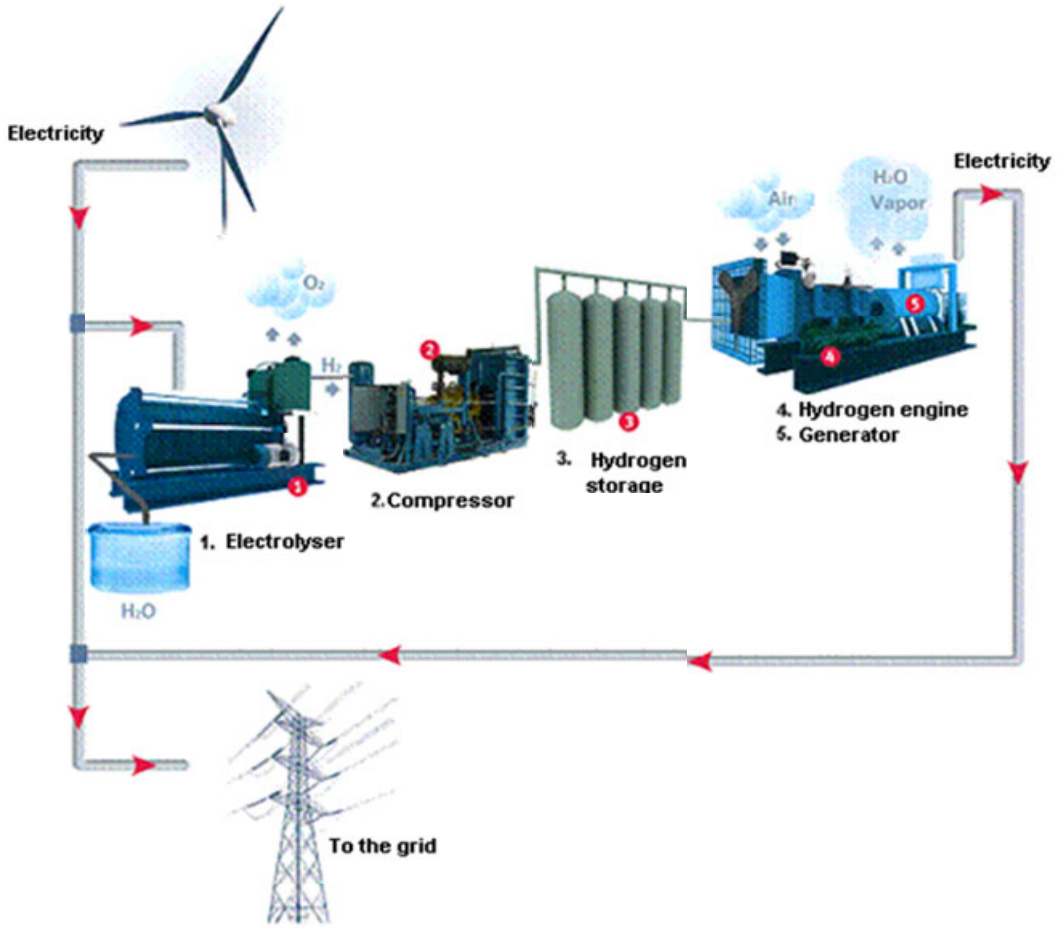

Figure 2: Scheme of the H_2 facility.

The O_2, that is not going to be used in this process is vented to the air and the H_2, produced at a rate of 60 Nm^3/h and a pressure of 10 bar, goes through a process of purification and drying to obtain a purity higher than 99.99%.

To increase storage capacity, the H_2 generated is compressed to 200 bar in two compressor groups supporting up to 61.8 Nm^3/h at 4 bar.

The storage system at 200 bar is composed by 7 blocks of 28 bottles each, with a maximum capacity of 1.725 Nm^3. These blocks are interconnected forming two groups of H_2 storage, with the possibility of isolation of each group.

The H_2 stored can be used in a 55 kW engine in case of energy deficit, that is, if the amount of energy produced by wind turbines in the wind farm is less than that is expected to generate.

The engine has a consumption of up to 70 Nm^3/h of H_2 at a pressure of 25-60 mbar H_2. The compressed H_2 at 200 bar, is decompressed in a first stage to 14 bar and a second until the suction pressure of engine.

The electrolyser Hydrogenics is mounted in a container consisting of three separate rooms: the process plant, control room and electric power and ancillary items room.

Figure 3: Photograph of the exterior of the electrolyser.

There are four cell stacks in the process plant. These consist of a series of interconnected electrolytic cells. Each contains the cathode, the anode and an inorganic ion-exchange membrane (patented technology IMET). The membrane prevents contact and reaction between O_2 and H_2 produced in the electrodes. As electrolyte is used a basic aqueous solution of KOH 30%. The process occurs at a pressure of 10 bar.

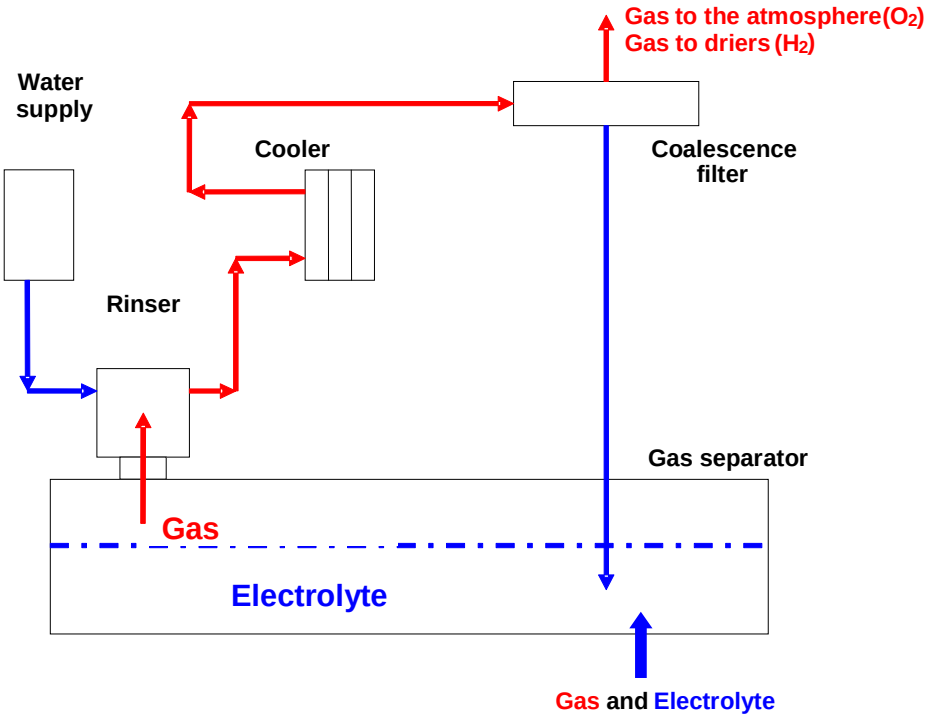

Figure 4: Operating diagram of the electrolyser.

The control room contains the electrical board; two closets EPS (Electrolyser Power Supply) and the control system of the unit.

The electrolyser power system comprises four AC to DC converters. Those four converters are grouped two to two and are fed by two lines.

All components of the compression plant are located inside a soundproof booth for outdoor installation, with ventilation and heating system. The piston compressor has of two groups Bauer Model HFS 15.4-13-DUO II.

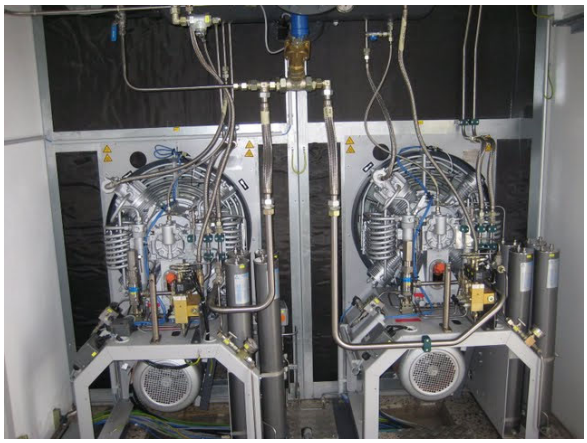

Figure 5: Photography inside the compressor.

The motor-generator Continental Energy Systems of 55 kW, which uses hydrogen as fuel, is mounted on rigid base structure and has a radiator for heat dissipation, gas pipeline and control system. The H2 engine consumes a maximum rate of 70 Nm^3 H_2/h. The whole team is in a soundproof container.

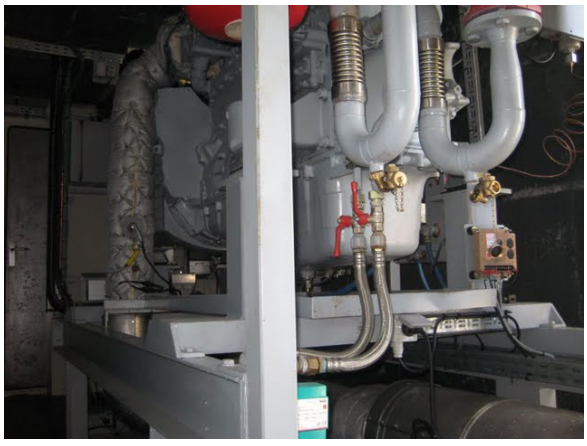

Figure 6: Photography inside the motor-generator group.

Each system has its own control system. In this project we have developed an integrated communications system. We use MODBUS as communication protocol and integrate signals from the engine, compressor, electrolyser and network into a common server.

The control system has a visualization software that allows the sending of orders by the operator and displaying the status of all equipment and variables involved in the operation of the facility. In addition, there is an acquisition of historical data.

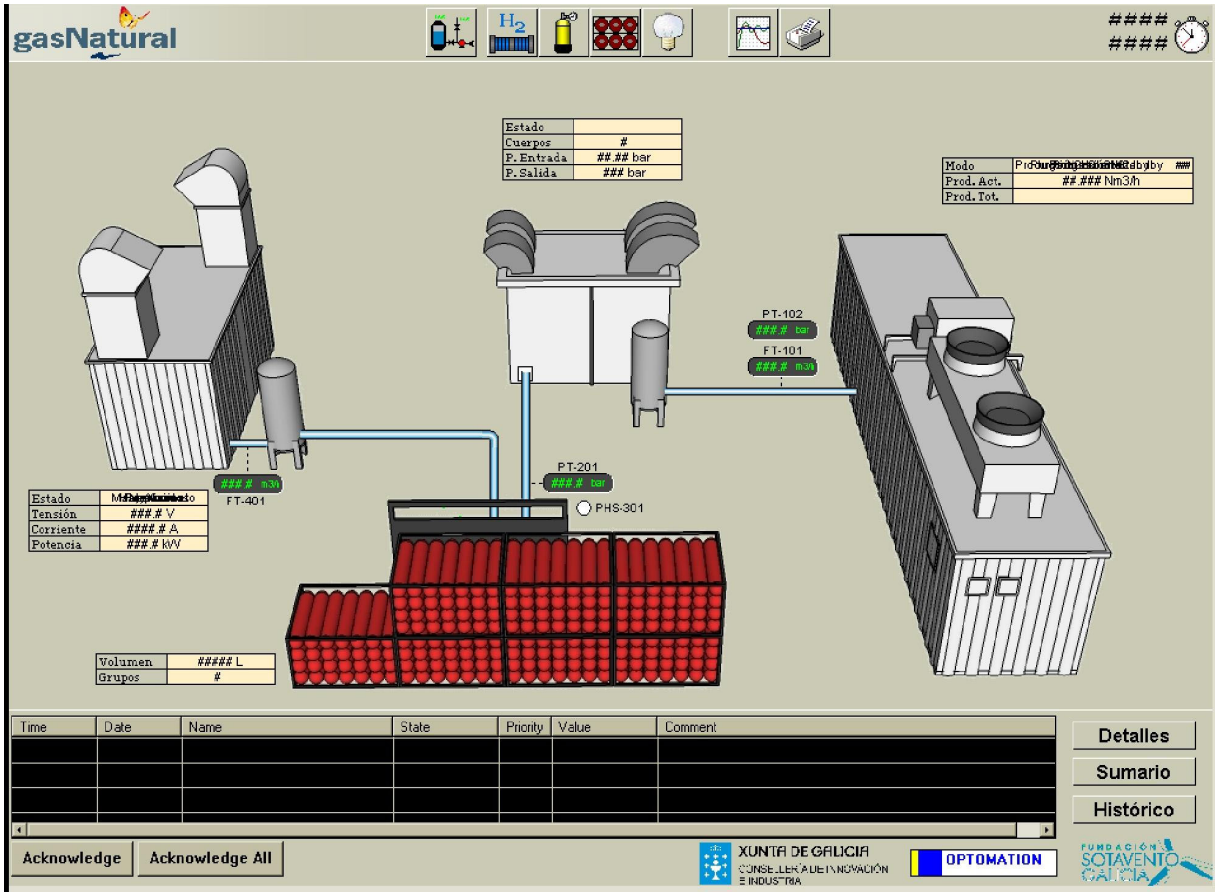

Figure 7: Main Screen control system.

Nowadays the installation is operating successfully in order to model the behaviour of each system component and integrate its operations, working with diverse wind generation scenarios and using different management strategies.

References

[1] http://www.energias-renovables.com/paginas/Contenidosecciones.asp?ID=9&Cod=16982&Tipo=&Nombre=E%C3%B3lica

[2] J.L. Bernal-Agustín, R. Dufo-López, L. Correas-Usón, I. Aso-Aguarta, “Analysis of a wind-hydrogen system connected to the electrical grid”, World Renewable Energy Congress X and Exhibition, 2008

[3] L. Fingersh “Optimized hydrogen and electricity generation from wind”. Technical report, NREL/TP-500-34364. National Renewable Energy Laboratory (NEREL), 2003.

[4] M. Korpas, C. Greiner, “Opportunities for hydrogen production in connection with wind power in weak grids”, Renewable Energy, 33, 1119-1208, 2008.

[5] M. Korpas, “Hydrogen energy storage for gird-connected wind farms”, Proceedings of the IASTED International Conference, Power and Energy Systems, Greece, 2001.

[6] J. B. S. Haldane, “DAEDALUS or Science and the Future.” Cambridge, 1923.

[7] P. Hoffman, “Tomorrow’s Energy - Hydrogen, Fuel Cells, and the Prospects for a Cleaner Planet,” The MIT Press, 2001.

[8] M. Dubey, “Hydrogen From Wind - A Clean Energy System,” Alternative Energy Sources, Vol. 8 Hydrogen Energy, pp.3551-3561, 1978.

[9] H. De Battista, R. Mantz, F. Garelli “Power conditioning for a wind-hydrogen energy system", Journal of Power Sources, Vol. 155, pp.478-486, 2005.

[10] S. Kelouwani, K. Agbossou, and R. Chahine, "Model for energy conversion in renewable energy system with hydrogen storage", Journal of Power Sources, Vol. 140, pp.392-399, 2004.

[11] S. Sherif, F. Barbir, and T. Veziroglu, "Wind energy and the hydrogen economy - review of the technology", Solar Energy, Vol 78, pp.647-660, 2005.

Project RH_2-WKA – Making Wind Energy a Steady Power Source

Martin Weiße, WIND-projekt Ingenieur- und Projektentwicklungsgesellschaft mbH, Boergerende, Germany

1 Summary

RH_2-WKA aims at the development and operation of a wind farm as an adjustable power plant. To attain that goal an energy storage system has to be integrated into the wind farm. The production, storage and power reconversion of the storage medium are regulated by demand. The storage cycle will enable the operator to store discontinuously available wind energy independently of time and - via the power reconversion unit - feed power back into the grid later at a constant rate. The project initiators, WIND-WASSERSTOFF-projekt GmbH & Co. KG (WiWa) and WIND-projekt Ingenieur- und Projektentwicklungsgesellschaft mbH (WIND-projekt), are sure that Wind-Hydrogen-Systems (WHS) will be one possible solution in this regard.

WiWa is responsible for the project management in RH_2-WKA and is going to operate the planned innovative energy park consisting of approximately 30 wind turbines and one hydrogen based energy storage unit. The project development is undertaken by WIND-projekt who also came up with the initial project idea and did the preliminary planning.

The project implementation area will be approx. 120 km north of Berlin in the federal state of Mecklenburg-Western Pomerania. The singularity of RH_2-WKA is defined by the interaction of the pure hydrogen-based (100 %) and CO_2-free energy system directly fed with electricity by a wind farm, its size and the integration of local energy consumers.

Similar projects which have been realized are for instance HyWindBalance (Germany) and Utsira (Norway). One thing they all have in common with each other is a power class in lower kW level.

Table 1: Advantages of RH_2-WKA at a glance.

Advantages of RH_2-WKA at a glance:
Technical ▪ self-supply of power for the wind turbines ▪ link between different energy branches ▪ hydrogen production unit as controllable system load ▪ optimized efficiency through multi-stage power reconversion unit
Commercial ▪ independence from energy resources that are subject to fluctuating prices and uncertain availability (e.g. biogas) ▪ preparation for the market of balancing energy

Environment protection and sustainability ▪ CO_2-free power storage circle on hydrogen basis ▪ CO_2-free hydrogen production ▪ sustainable, demand based and decentralized heat and power supply based on wind energy (CHP)
External effects ▪ long-term stable and predictable energy costs for local consumers ▪ creating new and qualified jobs ▪ strengthening the public acceptance of wind energy and hydrogen ▪ strengthening the domestic innovation basis by using new technologies and integrating manufacturers and service providers from Germany ▪ starting point for equalized wind power on decentralized level
Project planning ▪ advanced level of knowledge as basis for similar projects ▪ stepwise project implementation

2 Project Initiators

Project initiators of RH_2-Werder/Kessin/Altentreptow[1] (RH_2-WKA) are the WIND-WASSERSTOFF-projekt GmbH & Co. KG (WiWa) as well as the WIND-projekt Ingenieur- und Projektentwicklungsgesellschaft mbH (WIND-projekt). WiWa is responsible for the project management and is going to operate the planned innovative energy park consisting of approximately 30 wind turbines and one hydrogen based energy storage unit. The project development is undertaken by WIND-projekt who also came up with the initial project idea and did the preliminary planning.

WIND-projekt is an independent engineering company headquartered in Börgerende (county Bad Doberan/Federal State Mecklenburg-Western Pomerania). It deals exclusively with the planning, realization and operation of wind turbines and other regenerative energy systems as well as with the topic of energy storage. The company was founded in 1994. From the very beginning its aim has been the realization of an "affordable kilowatt hour" based on a clean power generation.

The company's success is reflected in the development of the already realized projects. Altogether more than 150 onshore wind turbines with an installed power of round about 200 MW were planned and built. In addition, WIND-projekt could successfully finish the planning for the offshore wind farms *Baltic I* (2006) and *Kriegersflak I* (2005) + *II* (2006) with approx. 230 wind turbines and a total capacity of around 1,000 MW. In 2006 the company initiated the installation of the first offshore wind turbine in the German Baltic Sea. For the latter WIND-projekt has been doing the technical operation management since then.

[1] RH_2® - *Renewable Hydrogen* as synonym for hydrogen made of renewable energies

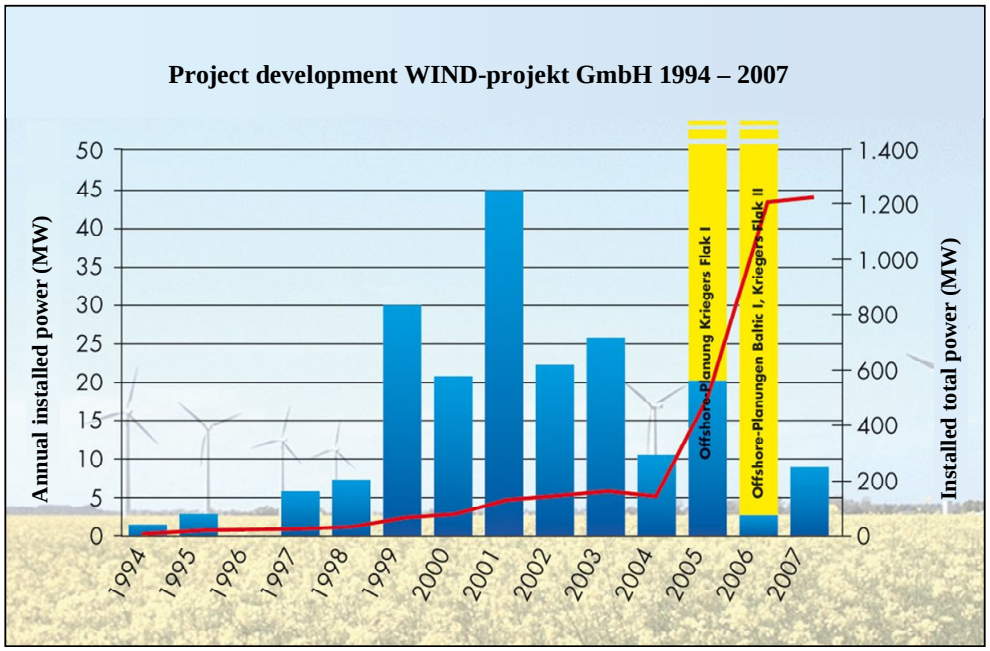

Figure 1: Project development WIND-projekt GmbH.

3 Problems to Solve

With increasingly powerful wind farms and the accompanying rising wind power feed-in into the power grid new challenges for operators and energy providers arise. Primarily these are:

- Balancing of fluctuating power production
- Integration of powerful (offshore) wind farms into the power grid
- Increasing requirements for grid management
- Bottlenecks in the power grid capacity
- Enlargement of energy storage capacities

Beside answers to the aforementioned problems the solutions must be affordable for the consumers on the one side and sustainable on the other side. The initiators are sure that Wind-Hydrogen-Systems (WHS) will be one possible solution.

4 Project Objectives

RH_2-WKA aims at the development and operation of a wind farm as an adjustable power plant. To attain that goal an energy storage system has to be integrated into the wind farm. The production, storage and reconversion of the storage medium are regulated by demand. The storage cycle will enable the operator to store discontinuously available wind energy independently of time and - via the power reconversion unit - feed power back into the grid later at a constant rate.

WiWa intends to develop, build and operate a practical and marketable solution that is free of CO_2. That's one of several reasons why the company decided to use hydrogen as energy carrier. The operation period is separated in different phases. In the first step the storage

system is going to be optimized and shall supply the power needs of the wind turbines themselves. That allows the operator to run a self-contained energy system in the sense that the wind farm is still power supplier to the grid but not consumer anymore. The main aim of the second step is the supply of local consumers with electricity, heat, hydrogen and oxygen. In addition, RH_2-WKA is used as preparation for similar projects or projects that aim to supply control energy from renewable sources (final stage of development).

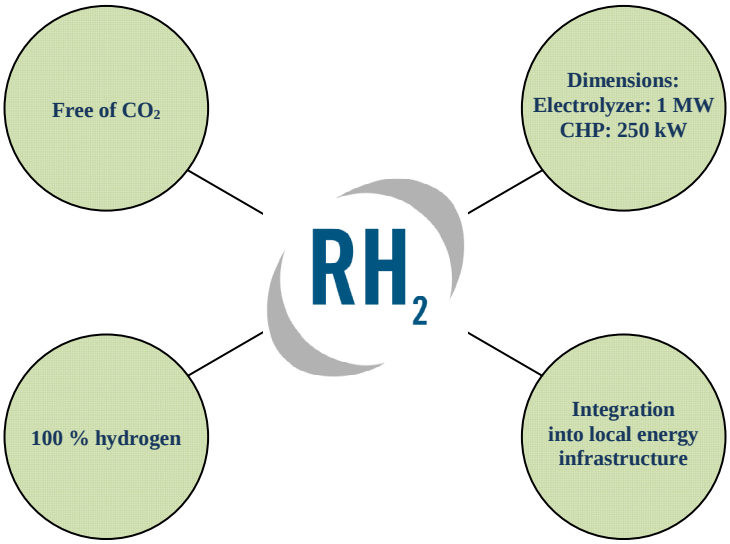

Figure 2: Singularity of RH_2-WKA.

The singularity of RH_2-WKA is defined by the interaction of the pure hydrogen-based (100 %) and CO_2-free energy system directly fed with electricity by a wind farm, its size and the integration of local energy consumers.

For economic and ecological reasons the use of the system's heat is planned (combined heat and power generation). Thus, the overall efficiency of the plant shall be maximized.

The first construction measures are planned for the 2nd quarter of 2011.

RH_2-WKA is going to be partly funded by the "National Innovation Programme for Hydrogen and Fuel Cell Technology" (NIP).

Table 2: Innovations created by the RH_2-WKA project.

Innovations created by the RH_2-WKA project:
▪ Development of an intelligent control software between wind turbines and H_2-storage circle ▪ Development of a modular hydrogen power reconversion unit in the 250 kW class ▪ Development of a measuring and control software for the entire hydrogen system ▪ Development of an energy storage system which produces no CO_2 ▪ Integration of a sustainable energy storage system into an already existing energy supply structure based on fossil energy sources ▪ Direct storage of wind power without using the power grid

5 Hydrogen-Storage-System RH_2-WKA

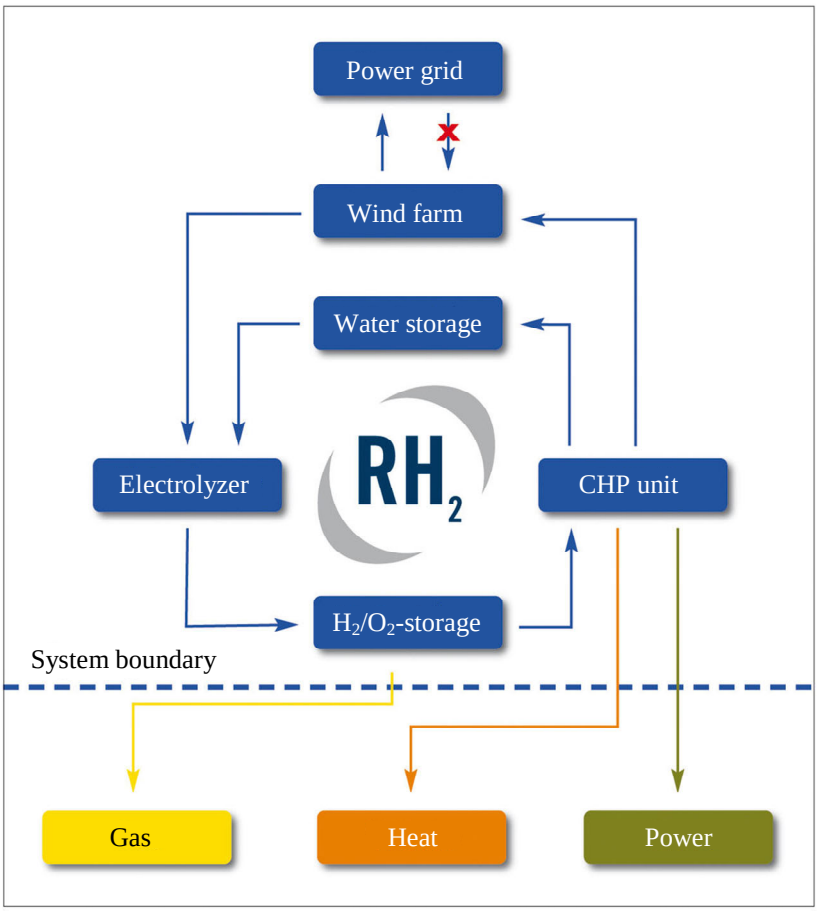

Figure 3: Drawing of the Wind-Hydrogen-System in RH_2-WKA.

The loop contains the production, compression, storage and power reconversion of pure hydrogen (purity 5.0). Oxygen (purity 2.5) is a by-product within the process and can be used internally or externally if needed. The final energy forms (after the reconversion of hydrogen) are electricity and heat (CHP). In addition, gaseous hydrogen can be taken out of the storage unit for external needs. It is planned to recycle the fumes of the CHP unit, which is mainly water vapour, to make it available again to the electrolysis (via water storage).

Table 3: Components of the hydrogen system.

Component	Capacity/size
Electrolyser	1.000 kW (ca. 200 Nm³/h)
Hydrogen compressor	300 bar
Hydrogen storage tanks	ca. 9.500 Nm³
CHP	250 kW_{el} (ca. 400 kW_{th})

6 Project Area RH_2-WKA

Figure 4: Project area of RH_2-WKA.

The project implementation area will be between the communities Altentreptow, Werder, Kessin and Grapzow, which are located approx. 120 km north of Berlin in the federal state of Mecklenburg-Western Pomerania. At this location WiWa plans the installation of a wind farm with a total installed capacity of up to 170 MW. A great deal of it is going to be provided by wind turbines with a rated power of 5 MW each and above. This fact allows the collection of important data regarding the control behaviour of powerful turbines in connection to an additive energy storage system at an early stage. This becomes increasingly important as the turbines in planned offshore wind farms are similar to those foreseen for the RH_2-WKA project.

Table 4: Advantages of the project location.

Advantages of project location:
▪ very good wind regime at coastal hinterland ▪ close to motorway A 20: - fast connection to Berlin, Hamburg, Isle of Rügen - easy and quick supply of potential H_2-fuelling stations possible - well suited transport route for wind and hydrogen components (e.g. multi-MW-class wind turbines and electrolyser) ▪ natural gas pipeline crosses area ▪ local consumers for power, heat and hydrogen available ▪ adequate space for extension available ▪ wind farm with offshore characteristics (total power, turbine power, spatial dimensions) ▪ direct connection to 380 kV-transmission grid

Contact

WIND-WASSERSTOFF-projekt GmbH & Co. KG
Seestraße 71 A
18211 Börgerende
Germany
Homepage: www.wiwa-projekt.de

General Manager:
Dipl.-Ing. C. Schmidt
Tel. +49 (0)38203-9126 0
Fax: +49 (0)38203-75313
e-mail: c.schmidt@wind-projekt.de

WIND-projekt Ingenieur- und Projektentwicklungsgesellschaft mbH
Seestraße 71 A
18211 Börgerende
Germany
Homepage: www.wind-projekt.de

Project Manager Hydrogen RH_2-WKA:
Dipl.-Geographer M. Weiße
Department for Hydrogen Technology
Tel. +49 (0)38203-9126 26
Fax: +49 (0)38203-75313
e-mail: m.weisse@wind-projekt.de

Project Manager Wind RH_2-WKA:
Dipl.-Ing. M. Heinicke
Department for Wind Energy
Tel. +49 (0)38203-9126 17
Fax: +49 (0)38203-75313
e-mail: m.heinicke@wind-projekt.de

High-Temperature Water Electrolysis Using Planar Solid Oxide Fuel Cell Technology: A Review

Mohsine Zahid, Josef Schefold, and Annabelle Brisse

Abstract

The present global hydrogen demand is met to a large extent by hydrogen from fossil fuels, but hydrogen production via water electrolysis has always been an alternative for production, in niche applications or, on a larger scale, when the electric energy required for the electrolysis reaction was readily available. Conventional alkaline electrolysis or electrolysis with proton-exchange membrane fuel cells are technologically mature processes but limited in energy efficiency to 60–80%. Hydrogen production via water electrolysis could play an increasingly important role in future, for industrial and transportation application and also as a means for storing energy from renewable sources, as a consequence of cost and availability limitations of fossil fuels, if a higher energetic efficiency can be reached. Water electrolysis at high temperature using protonic or ionic conducting electrolytes constitutes an advanced concept aimed at increased electrical-to-chemical energy conversion efficiency. At high temperature (600–900°C), higher efficiencies are achievable owing to favorable thermodynamic conditions and also because of improved kinetics for the electrode reactions, even without the use of precious metal catalysts. The thermodynamic reason for higher efficiencies is a decrease in the molar Gibbs energy of the reaction with increasing temperature while the molar enthalpy remains essentially unchanged. Reversible operation of solid oxide fuel cells as H_2O electrolyzer cells (SOECs) is well known from pioneering work in the 1980s on tubular cells. In recent years, renewed interest has arisen in SOECs, driven by the availability of (tubular or planar) cells with improved performance at lower temperatures. In this chapter, the current state of research on SOECs is briefly summarized, the main actors in the field are mentioned, and potential hurdles for the future development are identified.

Recent Progress in the Development of Solid Oxide Electrolyzers at ECN

Jan Pieter Ouweltjes, **Loek Berkeveld**, **Bert Rietveld**, Energy Research Centre of the Netherland (ECN), The Netherlands

1 Introduction

ECN has been active in the development of high-temperature electrolyzers since the year 2006. The experimental research has been focusing on the evaluation of different concepts for high-temperature electrolysis. The investigated cell designs were based on solid oxide fuel cell technology. From the experimental research it became clear that hydrogen electrode supported cells were potentially the preferred option, as the ohmic losses across the electrolyte were considerably lower than those obtained with electrolyte supported cells. The use of hydrogen electrode supported cells was however not straightforward. A potential drawback of using this cell technology was the occurrence of mass transport limitations in the porous mechanical support depending on its porosity and tortuosity, which limited the operating window with respect to feed gas composition and steam utilization [1]. Later, it was shown that the operating window was considerably improved by increasing the porosity of the 500 µm thick mechanical support from 30 to 40 vol%. The increased porosity allowed for operation at 70% steam utilization, yielding 93% electrical efficiency at 850°C. Operation at current densities higher than 0.5 Acm^{-2} was however still problematic [2].

In contrast to the difficulties encountered with hydrogen electrode supported cells, it became clear that electrolyte supported cells did not suffer from mass transport limitations. This allowed for electrolyzer operation at much higher current density than would be possible with hydrogen electrode supported cells. This is why ECN, as a partner in the European project RelHy, adopted electrolyte supported cell technology for operation at the targeted current density of 1 Acm^{-2}. This paper summarizes the achievements that were recently been obtained on electrolyte supported cells within the RelHy consortium.

2 Experimental

The aim of the experimental research was to develop an electrolyte supported electrolyzer cell that can be operated at 800°C, -1 Acm^{-2} current density and 60% steam utilization. The adopted electrolyte composition was $Sc_{0.20}Ce_{0.01}Zr_{0.79}O_{2-\delta}$ (10Sc1CeSZ), a ceramic oxide that exhibits considerably higher ionic conductivity than the yttria doped zirconias at 800°C [3]. The investigated electrolyte substrates were made by conventional tape casting. The 10Sc1CeSZ powder was purchased at Daiichi Kigenso Kagaku Kogyo Corporation, Japan. The powder was processed to slurry by mixing with a proprietary binder system, and ball milling was used for homogenization. The tape casting was done at two different blade heights in order to produce substrates with different thicknesses. After tape casting, the resulting tapes were cut to the right size, and sintered in air at 1400°C for 1 h. The size of the

electrolyte substrates was 108x108 mm^2. The resulting thicknesses were 115 and 215 µm, respectively.

The electrodes that were applied onto the electrolytes were deposited by means of screen printing and were 90x90 mm^2 in size. First, an approximately 5 µm thick layer of $Y_{0.2}Ce_{0.8}O_{2-\delta}$ (YDC, Praxair Specialty Ceramics) was applied at the oxygen electrode side of the electrolyte, and this layer was sintered at 1400°C 1 h. Next, the hydrogen electrode was applied. This electrode was composed of three layers. First, an approximately 5 µm thick layer consisting of $Gd_{0.4}Ce_{0.6}O_{2-\delta}$ (Praxair) was applied. On top of that an approximately 15 µm thick composite of 65 w% NiO and 35 w% $Gd_{0.1}Ce_{0.9}O_{2-\delta}$ (Praxair) was put. And finally, an approximately 20 µm thick layer of NiO (Mallinckrodt Baker) was put on top. The hydrogen electrode was then sintered at 1250°C for 1 h. Then, an approximately 70 µm thick $La_{0.6}Sr_{0.4}Co_{0.2}Fe_{0.8}O_{3-\delta}$ or LSCF (Praxair, including a heat treatment at 1100°C for 1 h) was applied on top of the YDC coating to act as oxygen electrode, and the assembly was given its final heat treatment at 1100°C for 1 h.

The prepared cells were tested in a test set-up that allowed for testing in both fuel cell mode and electrolyzer mode. The cell housing was made of dense alumina and included parallel flow channels in counter-flow arrangement. Current collection at the oxygen electrode was done by means of platinum mesh, and current collection at the hydrogen electrode was done with nickel mesh. The gas flows, including steam, were controlled by means of Bronkhorst flow controllers. The hydrogen electrode compartment of the cell housing was sealed by double layer gold/glass seal, which required heating to 1000°C prior to electrochemical testing to establish gas tightness. The glass bars were made of Schott G018-251 glass. In order to check for gas tightness of the hydrogen electrode compartment, the exhaust flow rate of the hydrogen electrode was measured. This was done by means of a gas flow meter (Bronkhorst), after drying the exhaust flow of the hydrogen electrode exhaust by Peltier cooling. The applied clamping force during the experiments was 0.2 $kgcm^{-2}$ for all test cells. This was achieved by putting weights on a spindle that rested on top of the cell housing. DC electrical loading was established with a Kikusui PLZ1004W in conjunction with a Delta Elektronika SM15-200D power supply. The cell voltage was recorded by means of a Keithley voltmeter. Electrochemical impedance spectroscopy measurements were performed with a Gamry FC500 potentiostat between 100 kHz and 0.1 Hz. The used AC amplitude varied with DC load; until 20 A DC load, an amplitude of 1 A was used, between 20 and 60 A DC load, the amplitude was 2 A, and above 60 A DC load, the amplitude was increased to 3 A. The obtained impedance spectra were fitted to an equivalent circuit using the computer program Echem Analyst.

The procedure followed during the cell tests comprised the following steps:

- Heating to 1000°C cell temperature with a 30°C h^{-1} ramp and 2 h dwell time, and followed by cooling to 800°C, while feeding the hydrogen electrode with 1000 ml min^{-1} nitrogen and feeding the oxygen electrode with N_2-O_2 80-20vol%
- Reduction of the hydrogen electrode by stepwise replacing the nitrogen flow with H_2-4%H_2O
- Cell operation in fuel cell mode during 24 h at 1 A cm^{-2}, at 56% hydrogen utilization and 47% oxygen utilization

- Electrochemical characterization (j-V curve, impedance spectroscopy)
- Change the hydrogen electrode feed to 1000 ml min^{-1} H_2 + 1000 ml min^{-1} H_2O
- Cell operation in fuel cell mode during 24 h at 1 A cm^{-2}, at 56% hydrogen utilization and 47% oxygen utilization
- Electrochemical characterization (j-V curve, impedance spectroscopy)
- Cell operation in electrolyzer mode during 300 h at 1 A cm^{-2}, at 60% steam utilization
- Electrochemical characterization (j-V curve, impedance spectroscopy)
- Cell operation in electrolyzer mode at 1 A cm^{-2}, at 60% steam utilization for undetermined time period
- Electrochemical characterization (j-V curve, impedance spectroscopy)
- Cell cooling with 4% hydrogen in N_2 at the hydrogen electrode and N_2-O_2 80-20 vol% at the oxygen electrode

3 Results

Figure 1 shows the j-V behaviour of the tested cells in electrolyzer mode, while feeding the hydrogen electrode with H_2-50%H_2O at the hydrogen electrode and the oxygen electrode with N_2-O_2 80-20 vol%. No current limiting behaviour was observed beyond 60%. Furthermore, a striking similarity in j-V behaviour between both cells with 215 µm thick electrolyte can be observed. This indicates good reproducibility of the cell performance in electrolyzer mode.

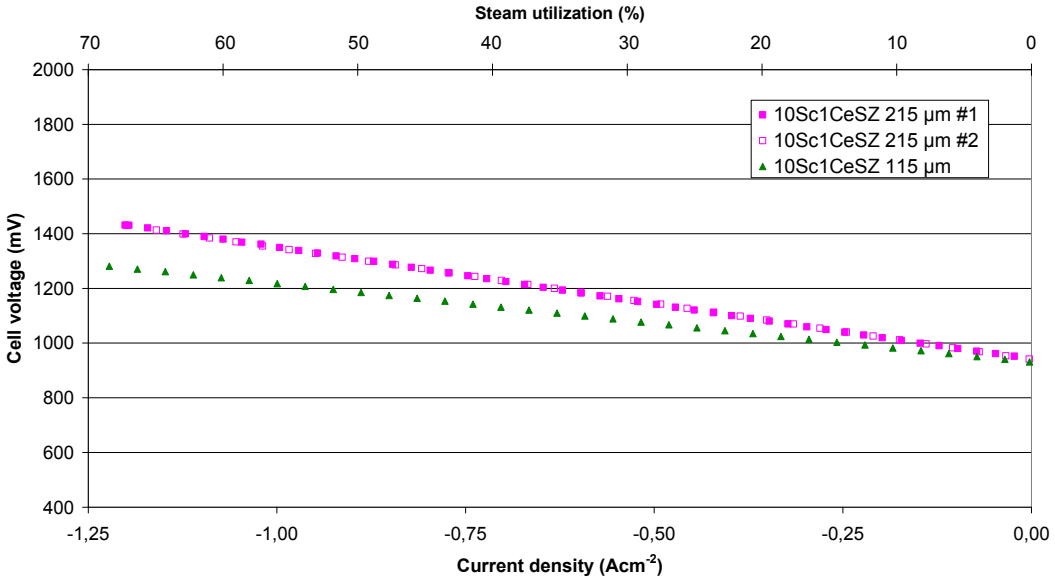

Figure 1: j-V behaviour in electrolyzer mode at 800°C, feeding H_2-H_2O 50-50 vol% to the hydrogen electrode and N_2-O_2 80-20 vol% to the oxygen electrode.

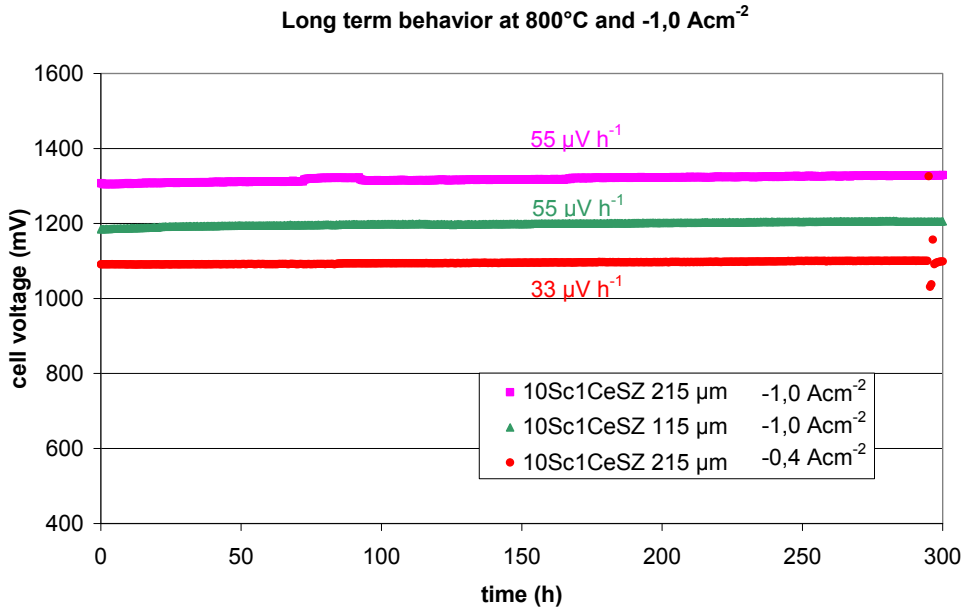

Figure 2: Long term behaviour in electrolyzer mode at 800°C, feeding H_2-H_2O 50-50 vol% to the hydrogen electrode and N_2-O_2 80-20 vol% to the oxygen electrode.

The long term behaviour of the cells in electrolyzer mode is shown in figure 2. For the cells operated at -1 Acm^{-2}, comparable degradation rates were observed. The cell that was operated at a modest current density of -0.4 Acm^{-2} exhibited a lower degradation rate.

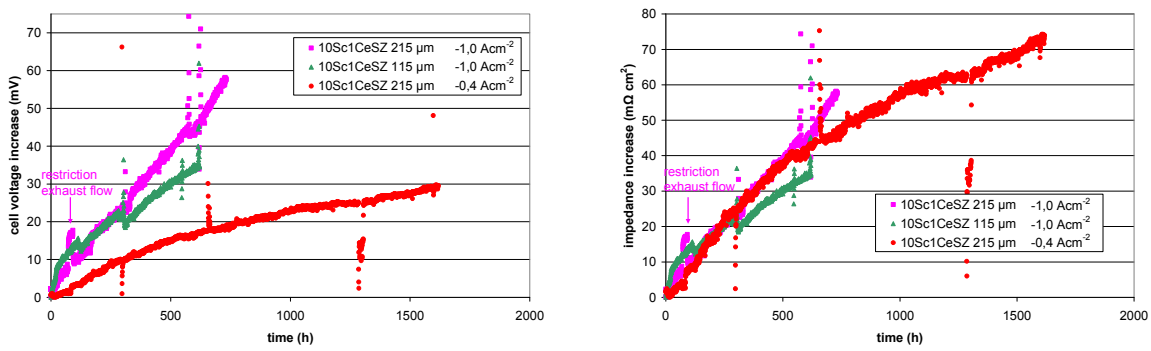

Figure 3: Long term behaviour in electrolyzer mode at 800°C, feeding H_2-H_2O 50-50 vol% to the hydrogen electrode and N_2-O_2 80-20 vol% to the oxygen electrode.

In order to get further insight in the degradation behaviour of the cells, Figure 3 was produced. At the left hand side, the voltage increase with time is shown, while at the right hand side, the increase of the internal resistance (i.e., cell voltage increase divided by operating current density) with time is shown. This makes clear that the lower degradation rate of the cell operated at the modest current density of -0.4 A cm^{-2} is related to the operating current density, not to better stability of the cell internal resistance.

Something else that can be seen in figure 3 is that the durability graphs were prone too several artefacts. First, an artefact was observed in the cell voltage of one of the cells. This

was probably caused by malfunctioning of the Peltier cooler which allowed condensed water to restrict the exhaust flow. Furthermore, it was observed that j-V measurements sometimes had a long term impact on the cell voltage. It is unlikely that this is related to temporary effects such as a temperature change induced by a change in Joule heat during the j-V measurement. More likely, the long term effect is caused by rearrangement of the electrical contact between the current collecting meshes due to thermal stresses released during the j-V measurement.

In order to deconvolute the impedance spectra that have been recorded throughout the tests, additional measurements have been carried out on the cell with 215 µm thick 10Sc1CeSZ electrolyte that was operated at -1.0 Acm^{-2}. At 800°C, impedance spectra were recorded at fixed current density as a function of the hydrogen electrode and oxygen electrode gas feeds. Furthermore, impedance spectra were recorded at 750, 700 and 650°C as a function of current density and oxygen electrode gas feed (either N_2-O_2 80-20 vol% or O_2 100 vol%). These measurements made clear that the polarization resistance exists of four different contributions, here denoted Rp1, Rp2, Rp3 and Rp4. See, for example, the impedance spectra depicted in figure 4. Polarization term Rp1 has a typical turnover frequency of between 15 kHz (650°C). Polarization term Rp2 has a turnover frequency of between 300 Hz (650°C). Polarization terms Rp1 and Rp2 were inseparable above 700°C, so separate interpretation was only possible at 650 and 700°C, whereas above 700°C only the sum of Rp1 and Rp2 was considered. Polarization resistance Rp3 had a turnover frequency of about 30 Hz (650-800°C). Polarization resistance Rp4 had a turnover frequency of 1.5 Hz (650-800°C). Besides the polarization terms Rp1 until Rp4, the impedance spectra comprised a serial resistance Rs, which is a summation of the ohmic losses existing in the cell, prominently the ionic resistance of the electrolyte. The complete equivalent circuit used during the fitting exercise is shown in figure 5. Next to the resistors mentioned, it comprised four capacitances in parallel with the polarization resistances, and at 750 and 800°C, an inductance L that was induced by the wiring between the potentiostat and the cell.

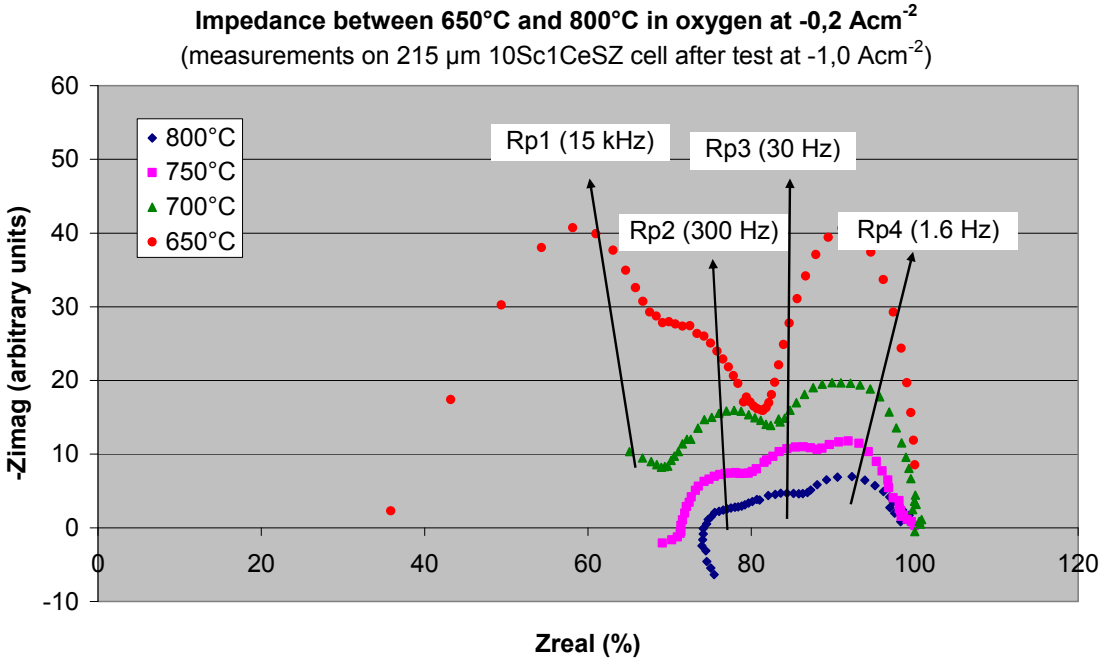

Figure 4: **Impedance spectra recorded on the cell with 215 µm thick 10Sc1CeSZ electrolyte as a function of operation temperature, under H_2-50%H_2O and N_2-O_2 80-20% gas feeds, at -0.25 A cm^{-2}.**

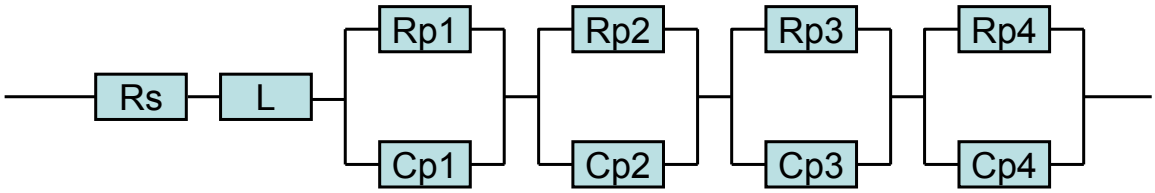

Figure 5: **Equivalent circuit used to fit the obtained impedance spectra. Below 750°C, the inductance L was visible in the impedance spectra and therefore omitted in the equivalent circuit. Above 700°C, the spectra were fitted with only three polarization repetitions.**

Figure 6 shows the values for Rs, Rp1+2, Rp3 and Rp4 for the three tested cells, obtained after approximately 300 h testing. The lower serial resistance Rs for the cell with the thinnest electrolyte is clearly the result of the lower electrolyte resistance, but not in a completely linear fashion. This indicates that Rs is not only related to the lower bulk resistance but also to other, unknown, ohmic losses. Furthermore, it can be seen that the polarization contributions were more or less comparable. Somewhat lower polarization resistance can be observed for the cell with 115 µm thick electrolyte which, in comparison with figure 3, could indicate that at the start of the test under electrolyzer conditions, the polarization resistance values were more comparable than after 300 h operation. There are however no initial impedance data available that could confirm this. Something else that can be seen from figure 5 is that both cells with 215 µm thick electrolyte have similar internal resistance. This

indicates that operation at -1.0 A cm^{-2} for 300 h has no detrimental effect on the internal resistance, compared to operation at -0.4 A cm^{-2}.

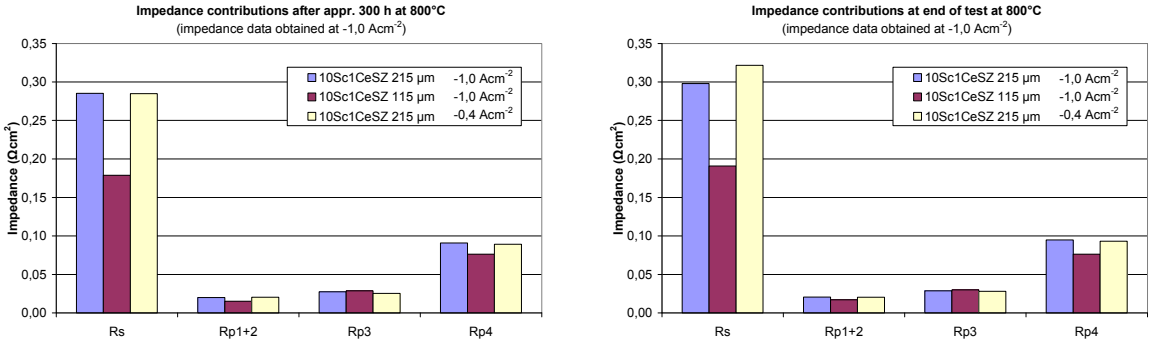

Figure 6: Impedance contributions after 300 h operation (left hand side) and at the end of the test in electrolyzer mode (right hand side).

Figure 7 shows how the resistance contributions evolved after 300 h operation under electrolyzer conditions. It makes clear that degradation is prominently related to an increase of the ohmic losses. Remarkably, the cell operated at -0.4 A cm^{-2} shows the largest increase of Rs. This could be caused by increased bulk resistivity of the electrolyte itself, but also by reduced electrochemical activity of the electrodes, which restricts the electrolyte surface area that is active in oxygen ion exchange. In order to identify the cause of the increase, it is therefore worthwhile to study the increase of the polarization resistances in more detail. For this reason, figure 8 was made, which gives the relative increase of the respective resistance contributions. This time, it can be seen that, although the polarization resistance values itself are modest, they do exhibit a considerable increase with time. It can be observed that the cells operated at -1,0 A cm^{-2} exhibit a considerably higher increase in the polarization term Rp1+2 in comparison with the cell operated at -0,4 A cm^{-2}. The other polarization terms do not show a clear dependency on electrolyte thickness or operating current density. Figure 9, that arranges the impedance contributions as a function of cell operation time, however makes clear that the polarization terms Rs, Rp3 and Rp4 rather increase with time than with operating current density. From the available data it cannot be determined whether the increase with time has a linear or a logarithmic dependency.

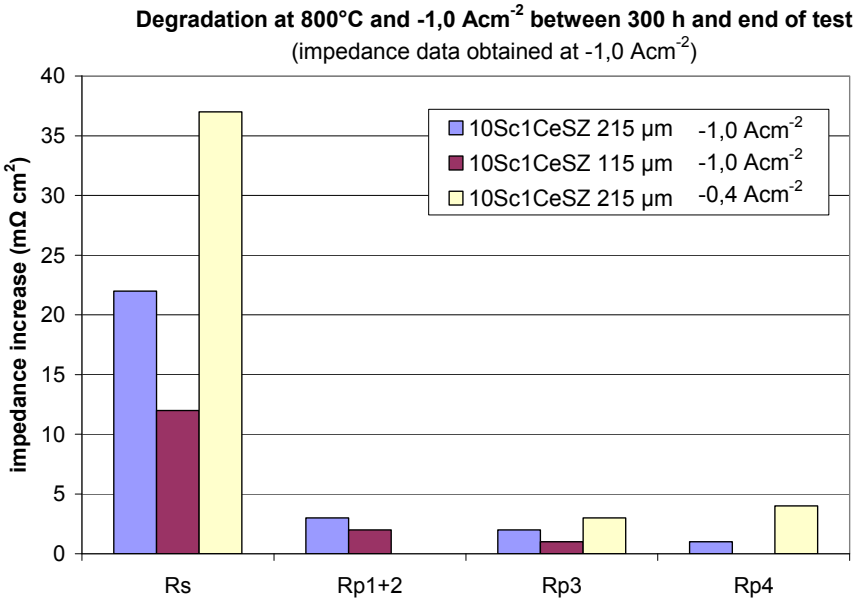

Figure 7: Impedance increase in Ωcm^2 between the first electrochemical characterization session after 300 h and the characterization session at the end of the test.

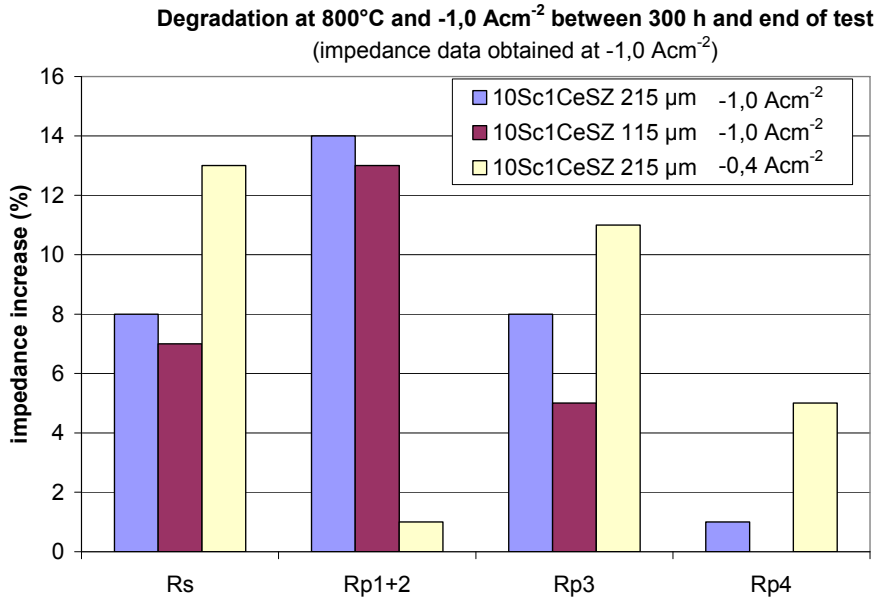

Figure 8: Impedance increase in % between the first electrochemical characterization session after 300 h and the characterization session at the end of the test.

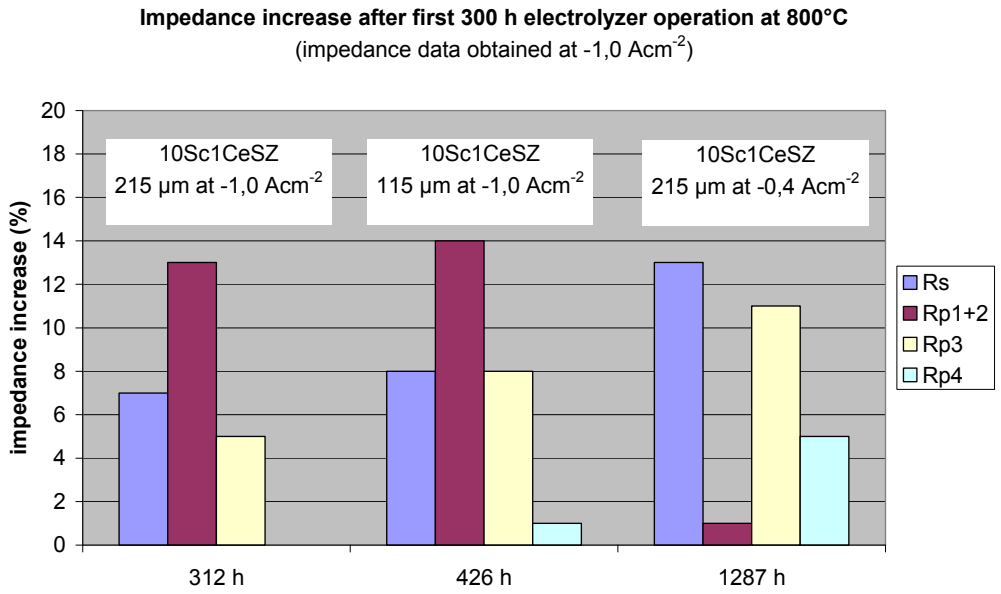

Figure 9: Impedance increase between the first electrochemical characterization session and the characterization session at the end of the test.

Figure 10 shows several graphs that have been produced in order to reveal the dependency of the polarization contributions to the oxygen electrode gas feed and the hydrogen electrode gas feed. This made clear that:

- Polarization resistance Rp4 (turnover frequency at 1.6 Hz) is dependent on both the hydrogen electrode gas feed (increasing resistance with increasing pH_2O) and the oxygen electrode gas feed (decreasing resistance with decreasing pO_2). It can be observed that Rp4 shows a hyperbolic dependency on current load in fuel cell mode and electrolyzer mode. This indicates that Rp4 is a summation of mass transport limited processes occurring at the hydrogen electrode and the oxygen electrode.
- Polarization resistance Rp3 (turnover frequency at 30 Hz) is weakly dependent on pH_2O, more prominently on the pO_2, and not dependent on current density. This indicates that Rp3 is related to a bulk rate limiting process in the oxygen electrode.
- Polarization resistance Rp2 (turnover frequency at 300 Hz) is strongly dependent on pO_2 (in particular this was observed at 650°C). This indicates that Rp2 is related to a bulk rate limiting process in the oxygen electrode.
- Polarization resistance Rp1 (turnover frequency at 15 kHz) is not dependent on the oxygen electrode gas feed. It has not been determined if Rp1 is dependent on the hydrogen electrode feed. But as the sum of Rp1 and Rp2 has been shown as function of both the pH_2O and pO_2, while Rp2 is hardly dependent on pH_2O, it is likely that Rp1 is related to a bulk rate limiting process in the hydrogen electrode.

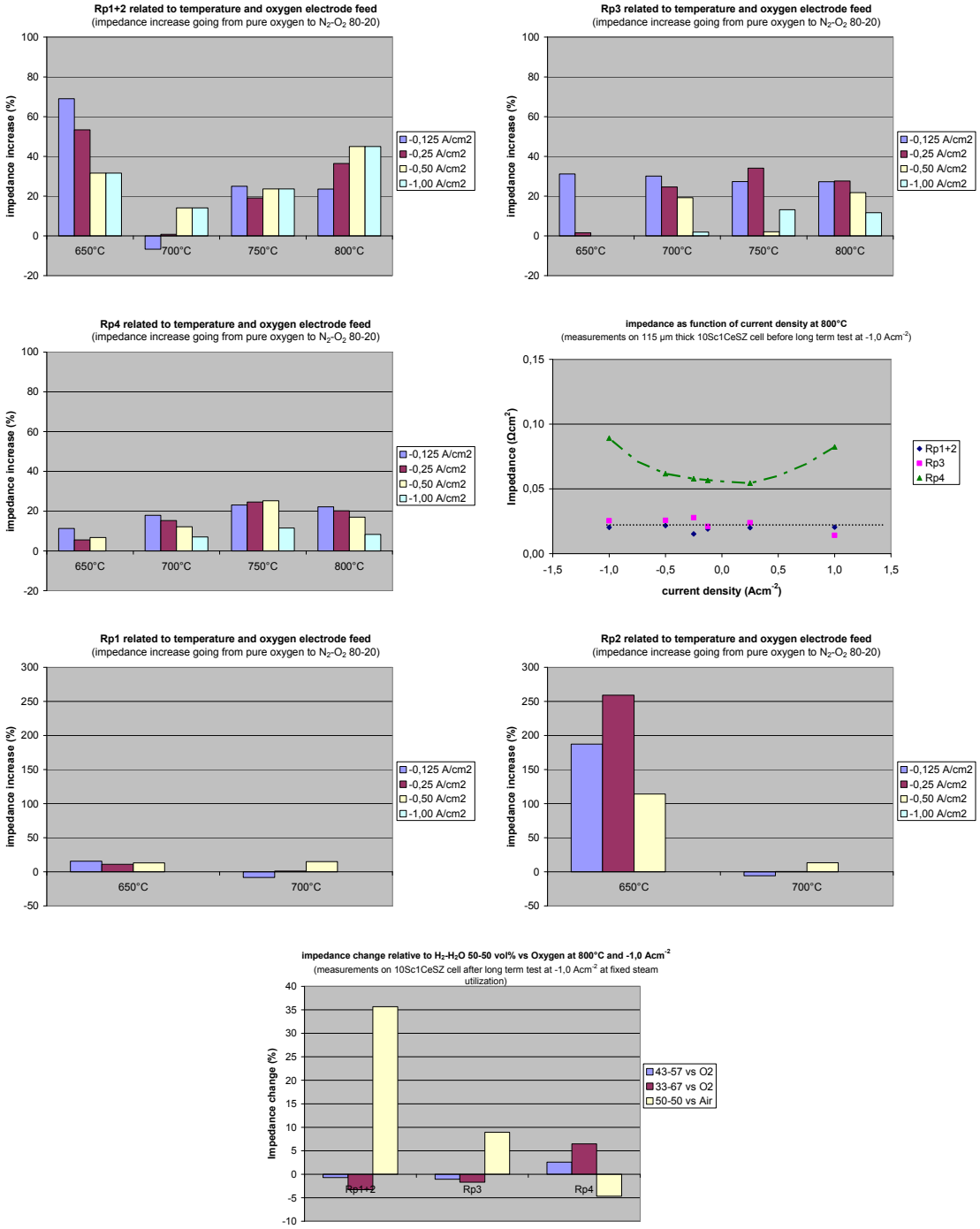

Figure 10: Polarization contributions Rp1, Rp2 (or the sum of Rp1 and Rp2), Rp3 and Rp4 as a function of temperature, operation current density, hydrogen electrode feed composition and oxygen electrode feed composition.

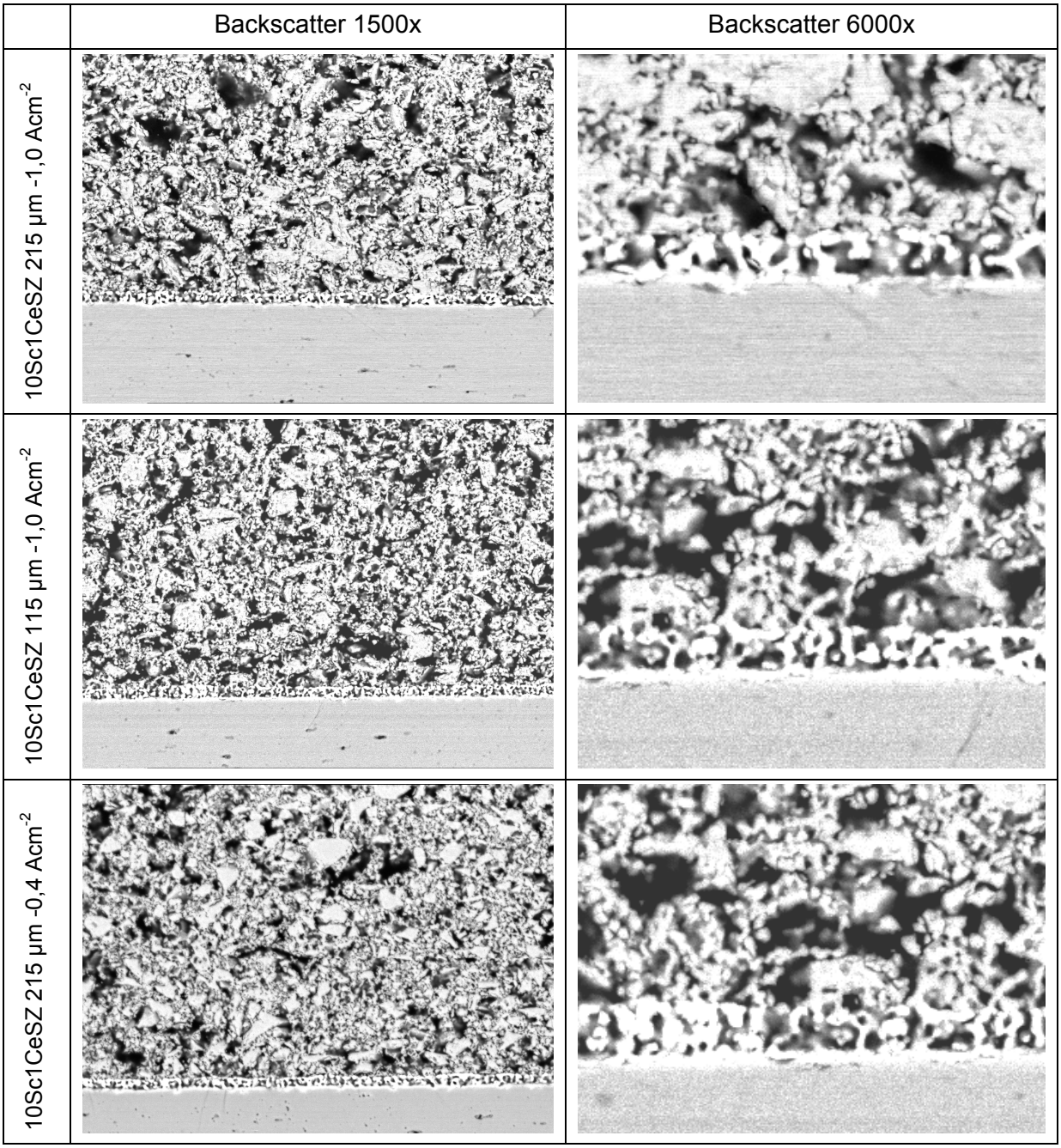

Figure 11: Scanning electron micrographs of the oxygen electrodes after testing. At the bottom of the micrographs, the 10Sc1CeSZ electrolyte can be seen. On top of the electrolyte, an approximately 5 µm thick porous YDC layer can be distinguished. Finally, on top of the YDC layer the porous, approximately 70 µm thick LSCF layer can be seen.

Figure 11 shows micrographs of the tested oxygen electrodes. The microstructures have been assessed with respect to LSCF grain size, 10Sc1CeSZ / YDC and YDC / LSCF interface adherence and thickness of the diffusion layer that has formed at the 10Sc1CeSZ / YDC interface. This revealed no significant differences that could be related to the two

observed degradation phenomena observed with impedance spectroscopy. Maybe the answer for the degradation phenomena is a more subtle one. In a previous paper from our group, it has been proposed that oxygen ion conducting perovskites such as LSCF could be prone to decreased oxygen desorption kinetics from the LSCF grains in electrolyzer mode, or decreased oxygen ion mobility in the bulk of the grains [2], but more investigation would be needed to obtain more certainty to that respect.

4 Conclusions

This paper summarizes the results that have been obtained at ECN on electrolyte supported solid oxide electrolyzer cells operated at 800°C and -1,0 Acm^{-2} current load. From long term electrochemical test under conditions similar to those aimed by the European project RelHy, the long term stability of the cells has been assessed and valuable insight in degradation phenomena at such high current load has been obtained. From impedance analysis that has been carried out throughout the tests it has become clear that the long term stability of electrolyte supported cells operated at -1.0 A cm^{-2} is related to two degradation phenomena occurring at the oxygen electrode. The first is reflected in an increase of polarization resistance at a turnover frequency of 300 Hz, which is only weakly existent at an operating current density of -0,4 A cm^{-2}, but strongly existent at -1,0 A cm^{-2}. The second degradation mechanism is reflected in an increase of polarization resistance at a turnover frequency of 30 Hz. This degradation phenomenon is not dependent on operation current density but on the electrolyzer operation time. The performed post test analyses, that focused on the microstructures, diffusion layer thicknesses and adherences between the interfaces at the oxygen electrode side of the cells, did not reveal the cause of the degradation phenomena.

Acknowledgements

This work is part of the RelHy project funded by the European Commission in the 7th Framework Program (Grant Agreement 213009).

References

[1] J.P. Ouweltjes, M.M.A. van Tuel, F.P.F. van Berkel, G. Rietveld, *Solid Oxide Electrolyzers for Efficient Hydrogen Production*, in: 10th International Symposium on Solid Oxide Fuel Cells (SOFC-X), June 2007, Nara, Japan, p. 933

[2] J.P. Ouweltjes, M. van Tuel, F. van Berkel, G. Rietveld, *Electrical Efficiency and Electrochemical Stability of Cathode Supported Electrolyzers*, in: Proceedings 9th European Solid Oxide Fuel Cell Forum, June 30 - July 3, 2009, Lucerne, Switzerland

[3] D.-S. Lee, W.S. Kim, S.H. Choi, J. Kim, H.-W. Lee, J.-H. Lee, Sol. St. Ionics 176 (2005) 33.

Durability and Efficiency of High Temperature Steam Electrolysis as Studied in the RelHy Project

Florence Lefebvre-Joud, Commissariat à l'Energie Atomique (CEA-LITEN), France
Annabelle Brisse, European Institute for Energy Research (EIFER), Germany
Jacob Bowen, Risoe NL / Danish Technical University (Risoe-DTU), Denmark
Jan Pieter Ouweltjes, Energy Research Centre of the Netherlands (ECN), The Netherlands

1 Introduction

High Temperature Steam Electrolysis (HTSE) stands for a promising process for large-scale centralised hydrogen production and is also considered since the 1970s as an excellent perspective for efficient use of renewable energy sources [1,2]. Most of the water electrolysis technologies to date have used alkaline or acidic electrolyte systems with typical system efficiencies within the 55-75% range and current density typically around 0.3-0.4 A/cm^2 corresponding to 10-15 mgH_2cm^{-2} hr^{-1} [3-6].

Electrolysers based on solid-oxide cell technology offer the possibility of using heat generated from various sources in order to reduce the electric energy input and enhance the electrolysis efficiency. This had been demonstrated in the 80's by Dornier using tubular ceramic cells but for economical reasons no further development had been made. Nowadays, with environmental threatens, it is again considered as a promising carbon free hydrogen production mean and many R&D programs have recently being re-started worldwide [7,8]. However, HTE technology will be competitive regarding alkaline or PEM technologies only if an increase of the electrolyser life time can be obtained (> 3 years).

If hydrogen production rates as high as 100 $mgH_2cm^{-2}hr^{-1}$ have recently been reported at 950°C with planar cells by [9,10] it has also been shown that the higher the performances the higher the degradation rates, especially in stack environment [11-12].

Main sources of degradation affecting the solid oxide electrolyser cells and stack lifetime are due to the high operating temperature (800 – 950°C). They have been studied and analysed in [13-18] and are principally:

- Delamination of O_2-electrode and bond layer on steam/O_2-electrode side,
- Poisoning of reaction sites due to Contaminants (Ni, Cr, Si, etc.),
- Loss of electrical/ionic conductivity of electrolyte,
- Mechanical break of the cell due to thermal cycling.

The RelHy project (www.RelHy.eu) launched in 2008 with 7 European partners from universities, technical research centres and industry, aims at reaching a satisfactory compromise between performance and durability and to demonstrate it at the electrolyser stack level. For such a purpose it is organised for identifying most detrimental degradation mechanisms at the scale of the single cell, the single repeating unit (SRU) and the short stack and for proposing solutions to overcome them.

2 Approach

Common test protocol has been established that comprises a first stage in the SOFC mode to reduce the hydrogen electrode and check the quality of the sample; a second stage in the SOEC mode at increasing steam partial pressures (from 50% to 90%) being repeated at 800°C, 850°C and 750°C; finally an endurance stage at 800°C and at current density below 1.5V but as close as possible to 1 $A.cm^{-2}$.

Common SRU to be distributed among the partners for testing have been developed (Figure 1). The main motivation for its design was to be as close as possible to the TOFC short stack design, to be easily mounted and instrumented by all the partners, to be easily simulated to assist data analysis. The 5-cell short stack (Figure 1) is based on the Alpha design by TOFC, it can accept planar cathode and electrolyte supported cells and has metallic interconnects.

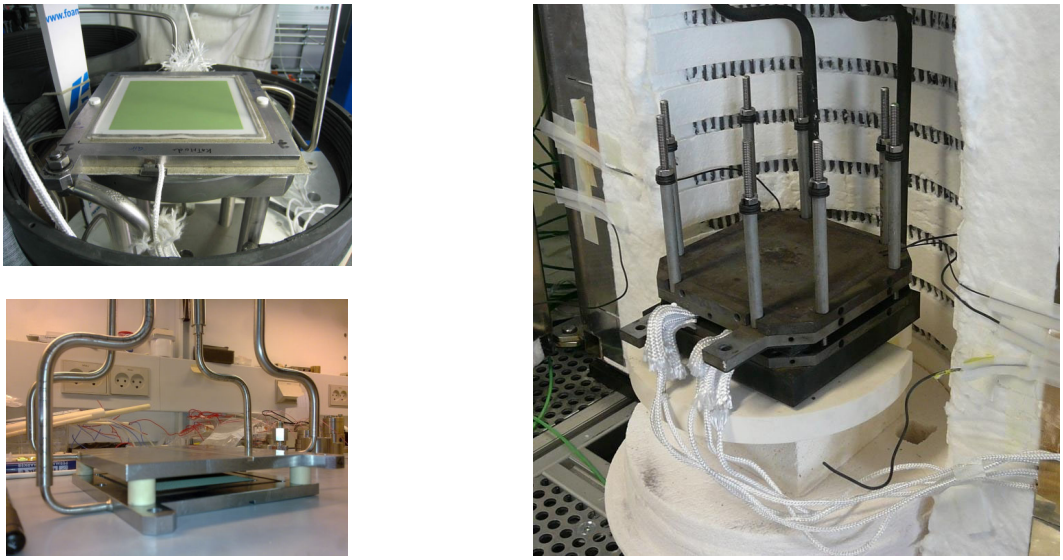

Figure 1: SRU upon mounting and 5-cell short stack ready for testing.

Tests are simulated by FE-CFD models integrating inputs from micro-modelling for data analysis, and extensive post-test characterisations is achieved to complement the analysis and identify the origin of degradation.

A first batch of materials chosen as representative of current state of the art has been tested in order to establish a reference basis within the project and to evaluate reproducibility within SRUs and between single cells, SRUs and short stacks. These reference materials include cathode supported cells Ni-YSZ/8YSZ/LSM-YSZ fabricated at Risoe-DTU and electrolyte supported cells Ni-CGO/3YSZ /LSCF fabricated at ECN. Interconnects are made with CROFER with LSM coating at the anode side and Ni based coating at the cathode side. For sealing reproducibility between testing laboratories, slurry options have been eliminated and the use of pre-sintered glass bars has been preferred.

3 Experimental Results

Performance and durability results of the reference materials have been obtained at the three levels considered with the two types of cells (Figure 2).

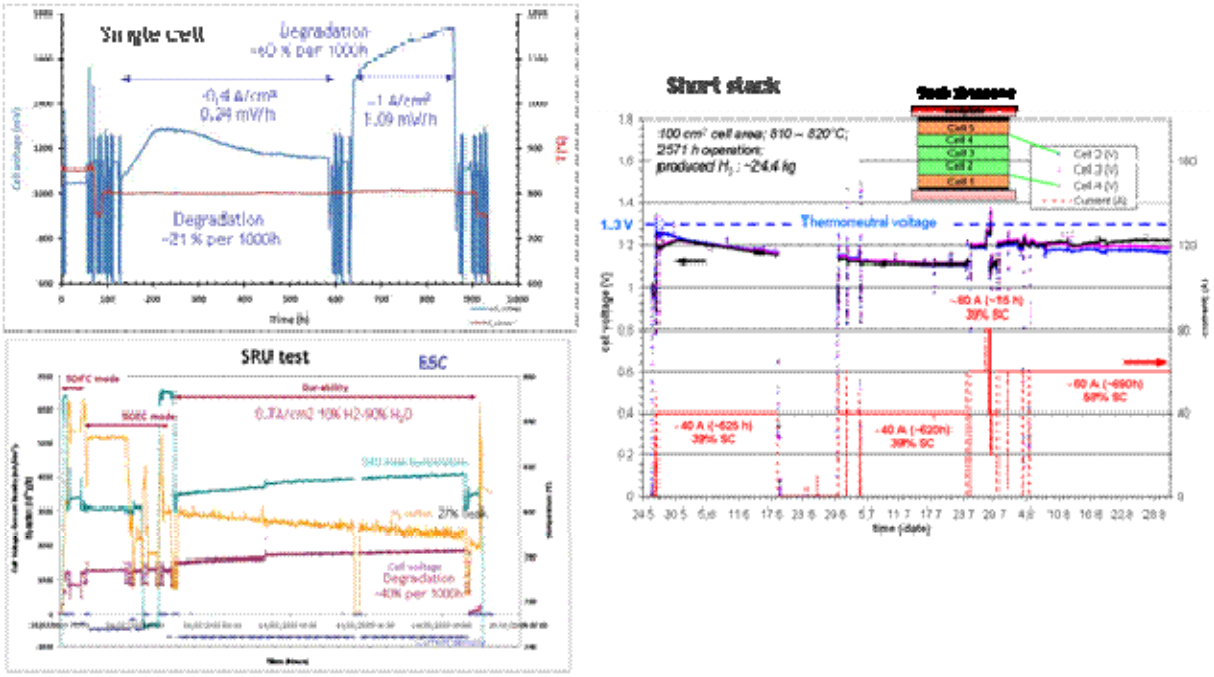

Figure 2: Duration tests at the single cell, the SRU and the short stack levels.

Scaling up from single electrolyser cell to short stack leads to different behaviour regarding performance and durability.

Regarding initial performances (Figure 3a), a tendency to degrade initial ASR when leaving grids for interconnect and single interconnects for short stack is observed; However, when comparing similar tests, a certain discrepancy is obtained at the single cell level as well as at the SRU level. Further tests have shown that satisfactory reproducibility between initial performances (at both levels) can be obtained when strictly controlling every operation parameter (Figure 3b); this being much harder in the SOEC operation mode than in the SOFC one.

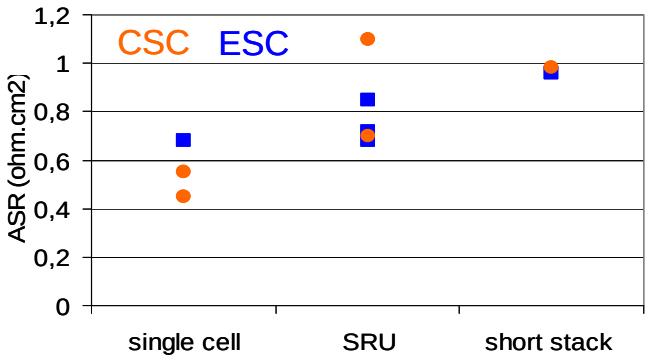

Figure 3a: ASR measured when starting SOEC operation at 800°C on both types of cells (ESC and CSC).

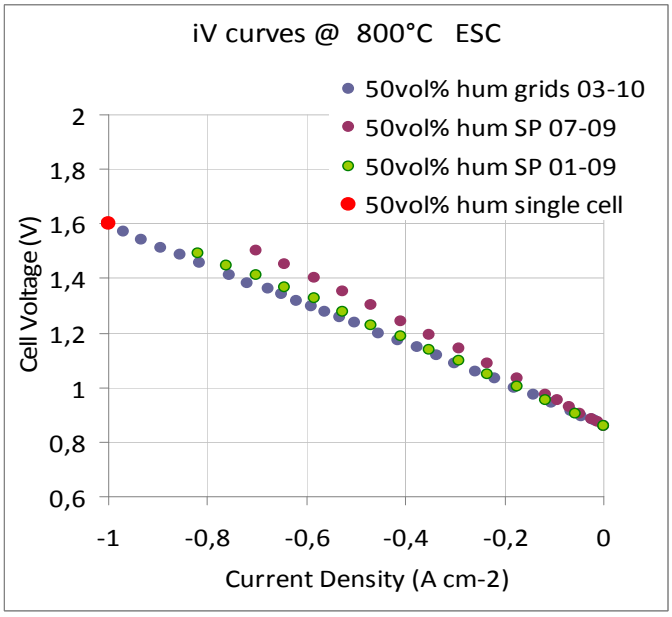

Figure 3b: Initial polarisation curves measured on an ESC at 800°C.
The same ASR (0.7Ω.cm^2) can be obtained in a single cell test (red point) and in SRU tests (blue and green). Poor control of the electrical contact within the SRU leads to higher ASR (purple)

Regarding degradation, as an illustration, all results obtained on CSC are gathered on Figure 4. No clear tendency can be obtained since each result has its own “story”. High degradation rates are obtained on single cells even at moderate current density and appear to be highly sensitive to test benches; high degradation rate has been obtained on a SRU at low current density that had poor initial ASR whereas more promising result has been obtained at 1A cm^{-2} with a SRU having a very good initial ASR. Low degradation rate is obtained at moderate current density at the stack level although initial ASR was not optimal. According to these results first order operation parameters on degradation are proposed to be:

- Electrical contacts within the single cell / SRU / stack since major differences have been obtained between the durability of similar cells with different initial ASR values;
- Steam generation and feeding since significant degradation events are always observed to be linked with steam feeding incident;
- Operation voltage that is found to be the most important parameter. Very low degradation rates (3% per 1000h) have been obtained at the stack level with cells operated below the thermo neutral voltage. On the contrary, at the single cell and the SRU level, operation above the thermo-neutral voltage have most of the time produced degradation rates higher than 10% / 1000h.

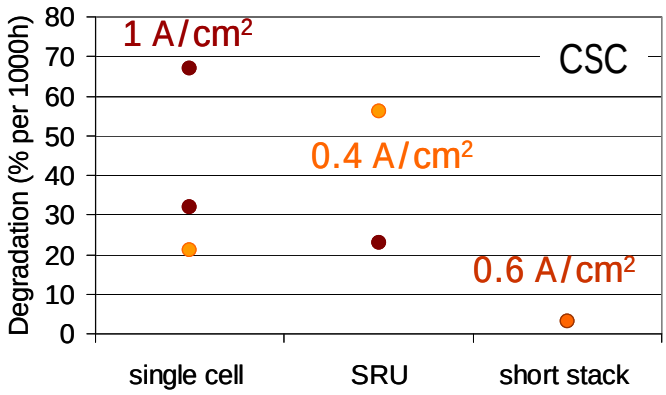

Figure 4: Degradation rates estimated over few hundred to 1 thousand hours of operation at 800°C on cathode supported cells.

4 Conclusion

Performance and durability results over few hundreds to thousand hours have been obtained on reference ESC and CSC following a specific testing protocol.

Good performance results could be obtained, as well as good durability at the stack level among 1000 hours.

Reproducibility between similar tests was found to be hard obtaining but main controlling parameters could be identified that are i) the electrical contacts with cells, ii) steam generation and feeding, iii) operation voltage.

Acknowledgments

The authors would like to mention and warmly acknowledge the essential participations of Marie Petitjean from CEA, Josef Schefold from EIFER, Bert Rietveld from ECN and Jens Ulrik Nielsen from TOFC to this work.

This work is part of the Relhy project funded by the European Commission in the 7th Framework Program (Grant Agreement 213009)

References

[1] M.M. Eisenstadt, K. E. Cox, Hydrogen production from solar energy, 1975 ; 17 :59-65

[2] Costogue E.N., Yasui R.K., Performance data for a terrestrial solar photovolatic/water electrolysis experiment, Solar Energy, 1977; 19 :205-10

[3] K. McHugh, Hydrogen production methods MPR-WP-0001, MPR Associates, Inc., Alexandria, Virginia, USA (2005)

[4] S.P.S. Badwal, S. Giddey and F.T. Ciacchi, Hydrogen and oxygen generation with polymer electrolyte membrane (PEM) based electrolytic technology, Ionics 12 (1) (2006), pp. 7–14

[5] P. Millet, F. Andolfatto and R. Durand, Design and performance of a solid polymer electrolyte water electrolyser, Int J Hydrogen Energy 21 (2) (1996), pp. 87–93

[6] M. Newborough, A report on electrolysers, future markets and the prospects for ITM Power Ltd's electrolyser technology

[7] Nuclear Hydrogen DOE USA

[8] European Fuel Cell and Hydrogen Joint Undertaking

[9] M. Mogensen, S. H. Jensen, A. Hauch, I. Chorkendorff, and T. Jacobsen. Lucerne (2006).

[10] S. H Jensen, P.H. Larsen, and M. Mogensen, Inter. J. Hydrogen Energy (2008).

[11] A. Brisse, J. Schefold, M. Zahid Inter. J. of Hydrogen Energy Vol 33, 5375, (2008)

[12] A. Brisse, A. Hauch, M. Mogensen, G. Schiller, U. Vogt, M. Zahid, Proceeding of the WHEC 2008 Brisbane Australia (2008).

[13] Manohar S. Sohal Degradation in Solid Oxide Cells During High Temperature Electrolysis, May 2009, Idaho National Laboratory, Idaho Falls, Idaho 83415, http://www.inl.gov, Prepared for the U.S. Department of Energy Office of Nuclear Energy Under DOE Idaho Operations Office Contract DE AC07-05ID14517

[14] A. Hauch, “Solid Oxide Electrolysis Cells – Performance and Durability,” Ph.D. Thesis,Technical University of Denmark, Risø National Laboratory, Roskilde, Denmark

[15] A. Hagen, R. Barfod, P. Hendriksen and Y. Liu, Effect of operational conditions on long-term stability of SOFCs , Proc.SOFC IX 1 (2005), pp. 503–513

[16] J.R. Mawdsley et al. Post-Test Evaluation of the Oxygen Electrode from a Solid Oxide Electrolysis Stack and Electrode Materials Development, AIChE Meeting, Salt Lake City, UT, November 5-9, 2007.

[17] J. R. Mawdsley, J. David Carter, et al. Post-test evaluation of oxygen electrodes from solid oxide electrolysis stacks. International Journal of Hydrogen Energy 34(9): 4198-4207.

[18] A. Hagen, R. Barfod, P. V. Hendriksen, Y. L. Liu and S. Ramousse, Degradation of Anode Supported SOFCs as a Function of Temperature and Current Load, J. Electrochemical Society,153(6), 2006, A1165-A1171

Research Progress of HTSE for Hydrogen Production Using Planar SOEC Technology at INET

Yu Bo, **Zhang Wenqiang**, **Xu Jingming**, Institute of Nuclear and New Energy Technology, Tsinghua University, Beijing 100084, China

1 Introduction

With the rapid growth of energy consumption, large-scale hydrogen production is becoming more and more of a concern worldwide in recent years [1]. High temperature electrolysis (HTE), which is the highly efficient electrolysis of steam at high temperature and utilizes the heat and electrical power supplied simultaneously by advanced nuclear reactor, provides a very promising way for massive production of hydrogen in the future [2]. Planar solid oxide electrolysis cell (SOEC) technology is being developed because it has the best potential for high efficiency due to minimized voltage and current losses [3]. Furthermore, Modular design of the stack can increase the system flexibility and reliability. The module can be standardized and controlled individually.

The R&D of HTSE technology was initiated in INET of Tsinghua University from 2005 as one of the approaches in National Key Special Projects for HTGR which aims at promoting highly efficient and sustainable application of nuclear process heat in the future. In the past several years, the research team mainly focused on preliminary investigation, feasibility study, equipment development and fundamental researches [4]. Three bench equipments special for the study of HTSE process, SOEC stack and components have been designed and constructed. In addition, the research group made rapid progress in the development of novel anode materials, effective microstructure control of cathode, short stack and theoretically quantitative analysis of hydrogen production efficiency through HTSE coupled with HTGR [5].

2 HTSE Development at INET

2.1 Program schedule

The proposed R&D plan on HTSE includes four-stages: 1) From 2008 to 2009, construction of HTSE test facilities and process verification, 2) From 2010 to 2012, bench-scaled experimental study with hydrogen production yield of 60L/h, 3) From 2013 to 2020, the design of pilot-scaled equipments and the pilot scale test with hydrogen production yield of 5 Nm^3/h as well as R&D on the coupling technology with HTGR, 4) Commercial demonstration after 2020.

2.2 R&D on HTSE

2.2.1 Key materials and preparation process of Solid Oxide Electrolytic Cells (SOEC)

Main fundamental researches involved in HTSE key materials had been made comprehensively, including as follows. 1) Two key issues need to be solved in the material preparation process were identified according to the special requirements of HTSE (under high temperature, high humidity, strong oxidation and reduction atmosphere). One is to ensure the porous electrodes and the dense electrolyte, the other is to ensure the flatness. 2) The preparation process of the electrolytic cells were studied, which mainly included two parts, namely, the tape casting process of hydrogen electrode and electrolyte, and screen printing process of oxygen electrode. Through experimental of powder selection, pore selection, dry condition, and sintering procedure, the preparation process was determined and the flat hydrogen electrode supported cells was prepared. For oxygen electrode, the synthesis process was identified and LSM20-YSZ composite oxygen electrode had been prepared based on the systematic investigation of several preparation methods, 3) On the basis of the previous work, the preparation process of the whole electrolytic cells was ultimately determined. The single cells by size 7cm × 7cm were successfully developed, which qualified the requirements suitable for stack assembly. The above research work laid good foundation for the development and following test of stacks.

2.2.2 Development of HTSE stack testing facility and SOEC components evaluation facility

At first, the stack testing requirements were made clear and the main test function was determined. On this basis, the overall design of the stack testing system was completed. The designed testing systems included four parts: gas supply system, steam circulation loop, reaction unit, and testing & control system. According to the purpose and function of various parts, the difficulties were analyzed and the corresponding solutions were proposed. During the design and construction process, the key problems of steam control were solved. Currently, steam quantitative production, accurate measurement and online monitoring can be carried out. The hydrogen production performance and electrochemical performance can be tested. In addition, the main testing methods and the operating procedure were determined.

Figure 1: HTSE online stack testing facility.

Figure 1 shows the lab-scale HTSE stack testing facility that can be used to simulate the actual running condition of HTSE and to study the thermal hydrogen and electrical hydrogen transformation process. Argon is being used as a carrier gas to control the steam-hydrogen ratio being fed to the button cell in the furnace. The dewpoint temperatures of the feed stream and the exiting stream are directly measured to determine the amount of hydrogen produced by the stack. For safety reasons, the oxygen is diluted with air before being exhausted.

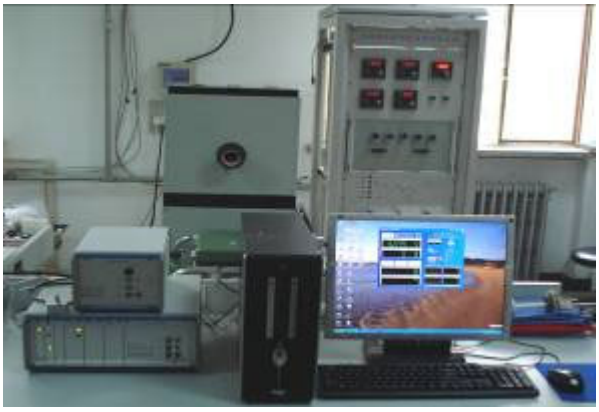

Figure 2: High temperature electrochemical analyzer.

Figure 2 shows the overall view of the high temperature electrochemical analyzer we developed special for material study and performance evaluation of SOEC components. All the connecting wires and sample holders in the system are made of platinum, so it works well even at 1200°C. The most difficult part of this equipment is sample holder, it has several major challenges. First is how to realize the weld of metal and ceramic. The second is seal issue and the third is ventilation and heat insulation. Different testing function needs different sample holder design. We can achieve multifunction tests by several unique designs. The equipment obtained the 18th Prominent Contribution Award for Laboratory Construction of Tsinghua University due to its stable operation, rapid response, high accuracy and unique property for operation both under strongly oxidizing steam and reducing hydrogen atmospheres.

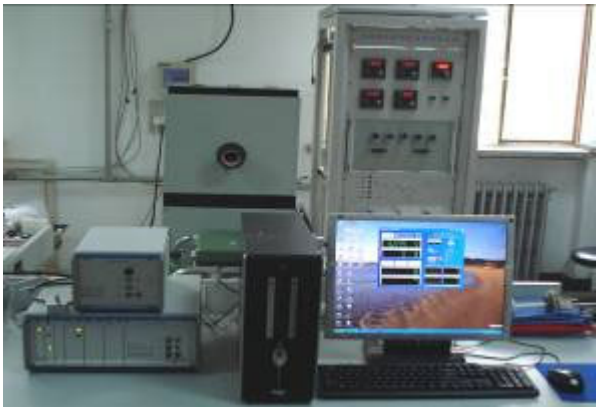

Figure 2: High temperature electrochemical analyzer.

The above two equipments are the basement for our study of HTSE technology and SOEC material. Through these, we can not only optimize the hydrogen production process but also reveal the mechanism and the essential we concerned.

2.2.3 Design, manufacture and assembly of SOEC stack

Stack design and assembly are core technologies of HTSE development. On the analysis of requirements of electrical, electrochemical, thermal and mechanical properties for planar stacks, as well as on the comprehensive consideration of seal ring, bipolar plates, end plates, the mode of gas flow channel, punching and pressure devices, the design scheme was initially proposed, which consists of seven parts, including electrolytic cell, bipolar plates, seal rings, top and bottom panels, top and bottom clips. During the experiments, difficulties such as sealing problems, material matching, electrical connection and other issues were solved successively. After improvement and modification, the stack performance had been greatly enhanced and the final design was determined. Figure 3 shows the photo of the assembled stack.

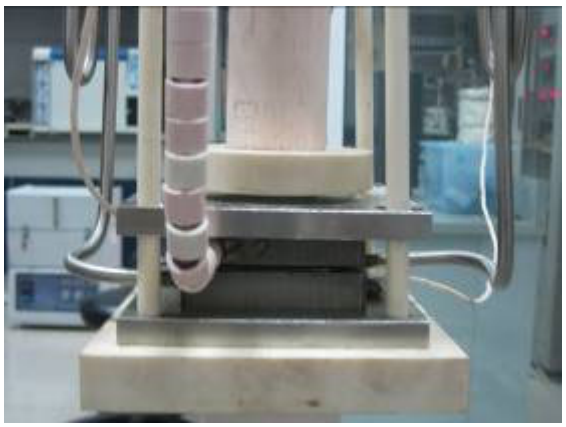

Figure 3: The assembled SOEC stack with three cells.

2.2.4 Performance test of SOEC stack

According to the final design, stacks with one cell, three cells and five cells were assembled respectively and the electrolytic experiments were carried out. The testing results were summarized and the problems appeared during the test were discussed and carefully analyzed. The stack test results had been fully met project requirements, exceeding technical specifications planed in the target. The detailed test results are listed as follows. Under constant current electrolysis with low current of 800mA, as for the stack with one cell: the hydrogen production rate of 0.33L/h and stable running of 50h. As for three-cell stack: the hydrogen production rate of 1.00L/h and stable running of 6h. As for five-cell stack: the hydrogen production rate of 1.67L/h and stable running of 40h as shown in Fig.4. Under high current of 2.4A, the stack with one cell can run stably for 5h and the hydrogen production rate is 1L/h. As for the stack with 5 cells, the voltage is up to 9.00V and it can run stably for 3h with an average hydrogen production rate of 5.2L/h.

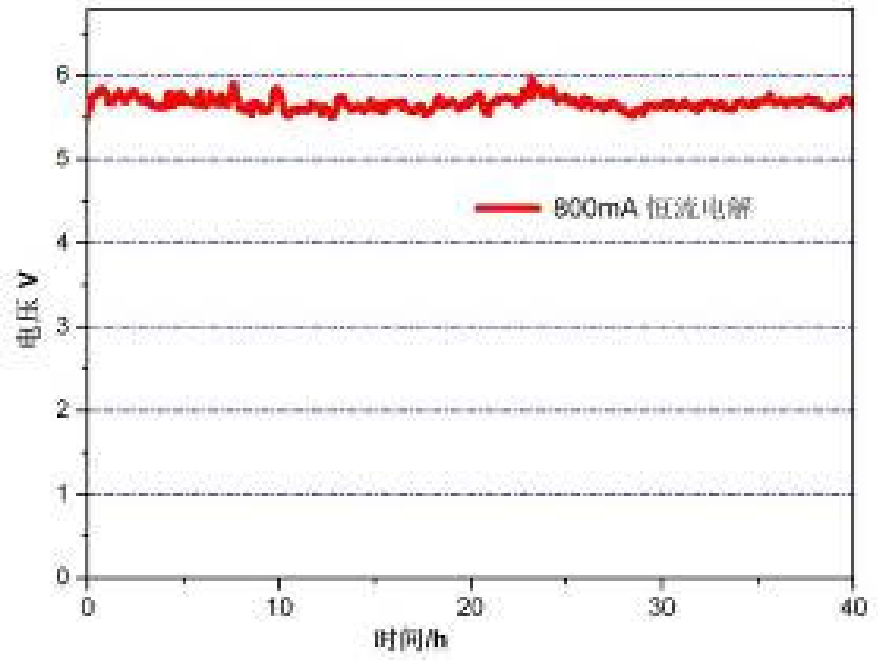

Figure 4: The stack with 5 cells runs for 40 hours without degradation at 850°C.

The results of stack test show that the preparation technology of thin ceramic electrodes by size 7cm×7cm, the manufacture technology of SOEC cell and the assembly process had been mastered, which make solid ground for the continuing research of HTSE in the future.

2.2.5 Quantitative Analysis of Hydrogen Production Efficiency through HTSE technology

Until now, few studies have been conducted on the practical limits for the overall conversion efficiency of the HTSE system. So the objective of this work is to examine the theoretical efficiency of the HTSE system and determine the quantitative and qualitative effects of various factors on the overall efficiency of the HTSE system in detail [6]. The result is listed in Table 1. The $\eta_{overall}$ of the HTGR coupled with the HTSE system were expected to increase from 31% to the maximum of 59% at 1000°C, which is above two times higher than that of the conventional alkaline water electrolysis.

Table 1: Overall system efficiencies under various conditions.

η_{es}	$\eta_{overall}$				
	$\eta_{th}=50\%$	$\eta_{th}=60\%$	$\eta_{th}=70\%$	$\eta_{th}=80\%$	$\eta_{th}=90\%$
$T=500\,^{\circ}C$ ($\eta_{el}=40\%$)					
60%	0.3704	0.3530	0.3415	0.3334	0.3273
80%	0.3961	0.3935	0.3917	0.3903	0.3892
100%	0.4132	0.4226	0.4295	0.4348	0.4391
$T=600\,^{\circ}C$ ($\eta_{el}=42\%$)					
60%	0.3971	0.3790	0.3671	0.3586	0.3523
80%	0.4186	0.4174	0.4166	0.4160	0.4155
100%	0.4327	0.4445	0.4533	0.4602	0.4656
$T=700\,^{\circ}C$ ($\eta_{el}=45\%$)					
60%	0.4360	0.4165	0.4037	0.3945	0.3877
80%	0.4504	0.4510	0.4515	0.4518	0.4520
100%	0.4595	0.4746	0.4860	0.4949	0.5020
$T=800\,^{\circ}C$ ($\eta_{el}=48\%$)					
60%	0.4746	0.4544	0.4409	0.4313	0.4242
80%	0.4807	0.4837	0.4859	0.4875	0.4888
100%	0.4845	0.5032	0.5175	0.5288	0.5379
$T=900\,^{\circ}C$ ($\eta_{el}=50\%$)					
60%	0.5000	0.4805	0.4675	0.4582	0.4513
80%	0.5000	0.5057	0.5099	0.5130	0.5155
100%	0.5000	0.5221	0.5392	0.5527	0.5637
$T=1000\,^{\circ}C$ ($\eta_{el}=52\%$)					
60%	0.5243	0.5062	0.4941	0.4854	0.4788
80%	0.5180	0.5268	0.5333	0.5383	0.5422
100%	0.5143	0.5400	0.5600	0.5760	0.5890

3 Conclusion

China has launched development of nuclear hydrogen production technology. The R&D on the technology was initiated as a component of China's HTR-PM Demonstration Nuclear Power Plant Project. The promising research results of HTSE in developed countries highlight the fact that it can be a suitable process for the next decades to consider massive production of hydrogen. The R&D on HTSE processes is being conducted at INET. It is expected to commercialize nuclear production of hydrogen after 2020, and therefore the coming decade is a critical period to realize the target. Many challenges exist and comprehensive international cooperation is desired.

Acknowledgements

This paper is jointly supported by the National S&T Major Project (Grant No. ZX06901) and NSFC (Grant No. 20803039)

Reference

[1] Charles W. F., Future hydrogen markets for large-scale hydrogen production systems, International Journal of Hydrogen Energy (2007), 431-439.

[2] Carl M. S, James E. O, Keith G. C. et al, High-temperature electrolysis for large-scale hydrogen production from nuclear energy – Experimental investigations, International Journal of Hydrogen Energy doi:10.1016/j.ijhydene.2009.10.045

[3] Anne Hauch，Sune Dalgaard Ebbesen，Søren Højgaard，et al,Highly efficient high temperature electrolysis, Journal of Materials Chemistry, 2008, l8(20), 2331-2340

[4] Yu B, Zhang W Q, Xu J M, et al. Status and research of highly efficient hydrogen production through high temperature steam electrolysis at INET, International Journal of Hydrogen Energy, doi: 10.10 16/ j.ijhydene. 2009.05.037.

[5] Bo Y, Zhang W Q, Xu J M, Microstructural characterization and electrochemical properties of $Ba_{0.5}Sr_{0.5}Co_{0.8}Fe_{0.2}O_{3-\delta}$ and its application for anode of SOEC, International Journal of Hydrogen Energy (2008), 6873-6877.

[6] LIU M Y, YU B*, CHEN J, XU J M. Thermodynamic analysis of the efficiency of high-temperature steam electrolysis system for hydrogen production, J. Power Source, 2008, 177(2):493-499.

Impact of the Heat Source Selection on the High Temperature Electrolysis Performances and Economic Competitiveness

Rodrigo Rivera Tinoco, CEA, DEN, I-tésé and CEP, MINES ParisTech, France
Christine Mansilla, CEA, DEN, I-tésé, France
Chakib Bouallou, CEP, MINES ParisTech, France

1 Introduction

Among the different processes under development throughout the world, high temperature electrolysis (HTE) seems to be a promising one to carry out massive hydrogen production in the medium to long term. Contrary to the well known alkaline process, hydrogen is to be produced from water steam inside high temperature electrolysis cells, which requires less electric energy than the electrochemical reaction in liquid phase. A relevant advantage of HTE is then the enhancement of process efficiency by direct use of heat for steam generation. In this work we will not detail the diverse operating modes of electrolysis cells, but we will study the possible heat sources that could supply high temperature electrolysis with the needed thermal energy input to evaporate the water stream. After having sorted out the heat sources that would be relevant in a massive hydrogen production context, their impact is assessed, taking into account the following characteristics: available temperature and pressure, and thermal energy cost.

2 Selection of the Heat Source

We first examine the possible heat sources that could provide enough heat to massively produce hydrogen. Up to now nuclear reactors (high temperature and sodium fast ones) and geothermal energy had been considered [1]-[[3]. This study aims at widening this scope through a screening according to four criteria:

- The greenhouse gas mitigation as a priority in a sustainable development context,
- The resource availability so that the process can be operated continuously,
- The heat source capacity to enable large hydrogen production,
- The maturity to allow production in the medium term.

Several potential heat sources did not pass the screening: slurry incineration from wastewater treatment plant demonstrated a low potential and cement kiln smoke was found to be too scattered. Finally four heat sources were selected. They can be divided into two categories:

- The ones involving incineration units: combustion of biomass or domestic wastes [4]-[6],
- The development of techniques to produce steam by using the European Pressurized nuclear Reactor (EPR) and Sodium Fast nuclear Reactor (SFR) [5]-[6].

In the incineration units, the steam needed to reach a defined rate of hydrogen is generated inside the combustion chamber. We assumed that the required vaporization and overheating energy is totally supplied by the fuel considered (biomass or domestic waste). The incineration costs were estimated as a function of the fuel flow in the furnace, its Low Heating Value, and the related incineration operation costs. From these results, the water steam production cost was assessed as a function of the incineration unit size [4]-[6].

As regards the EPR, steam is generated in the secondary loop that usually feeds the turbines with saturated steam in order to generate electricity. Coupling of EPR with HTE assumes drawing off part of the steam which is generated in this loop and introducing it directly into the heat exchanger network to feed the process [5]-[6].

The steam production through a SFR also appeals to drawing off the steam from the tertiary steam loop. Three steam generation techniques have been suggested [6]. Due to safety issues, it is strongly recommended not to generate additional steam by adding more exchangers on the sodium loops. For these last two cases, the thermal energy cost was estimated by assuming a 40 €/MWh electricity cost and by assessing the impact of the steam drawing-off on the heat-to-electricity conversion efficiency.

The heat cost together with the thermal source characteristics are gathered in the following table:

Heat source	**Steam temperature (K)**	**Steam pressure (MPa)**	**Thermal energy cost (€/MWh)**
Biomass	623	2.0	16.5
Domestic waste	713	4.0	21.5
EPR (1)	523	4.0	12.8
EPR (2)	503	3.0	12.8
SFR	484	2.0	15.6

3 Impact of the Heat Source Characteristics

The coupling between the heat source and the HTE process is performed in each case and optimised in order to estimate the lowest hydrogen production cost. The latter is estimated through a simplified levelized production cost model that enables identifying major trends. The optimisation is carried out by means of a FORTRAN program of a modified version of the “Adaptive Random Search Method” [7].

The results are presented in the following figure, by classifying the heat source according to the hydrogen production cost. One should not focus on the figures – which very much depend on the implemented model and related assumptions – but on the general trends.

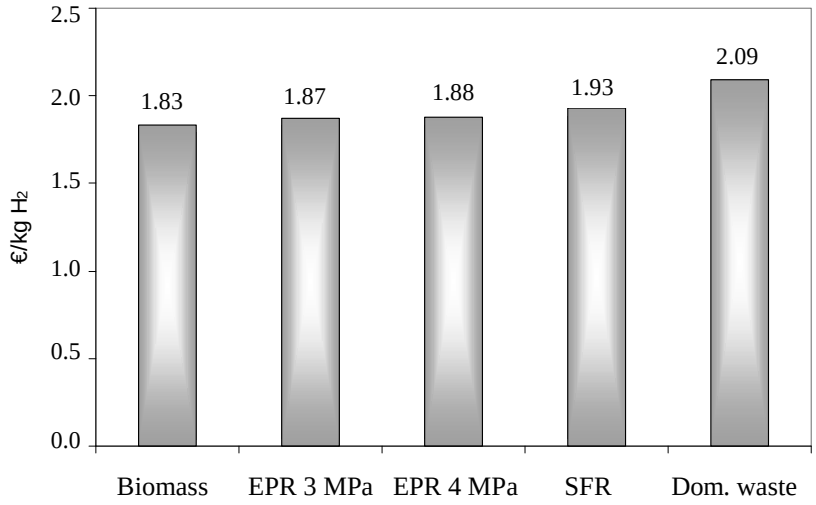

Figure 1: Hydrogen production cost for the selected heat sources, classified by increasing hydrogen production cost.

It first can be noticed that the influence of the heat source on the final production cost is not high. Then let us underline that the heat source that is characterized by the highest available temperature (i.e. domestic waste incineration) also corresponds to the highest hydrogen production cost. This is explained by the fact that besides being characterized by the highest temperature, incineration of domestic waste is also the most expensive thermal energy source (cf. Figure 2).

When comparing the SFR and biomass couplings it can be observed that higher temperatures can lead to diminish the production cost if it does not imply more expensive heat: biomass heat is around 140K hotter than SFR's for a slight overcost and the hydrogen production cost is lower for the biomass coupling. Achieving low hydrogen production costs implies a compromise between low cost thermal energy source and high temperature steam.

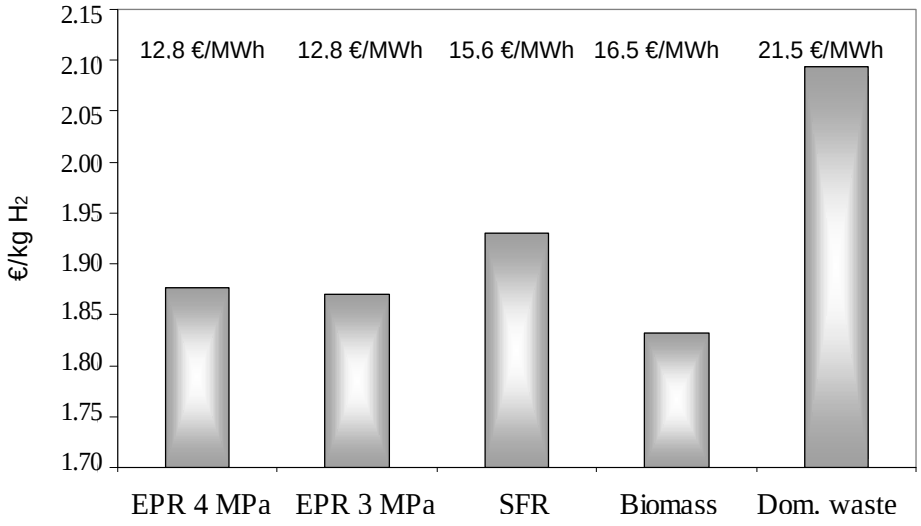

Figure 2: Hydrogen production cost for the selected heat sources, classified according to the thermal energy cost.

Finally, by comparing the two EPR couplings, it can be seen that the heat source pressure does not have a major influence on the hydrogen production cost, within the studied interval.

4 Conclusion

Through the use of a simplified economic model, the impact of the temperature, pressure and thermal energy cost of the heat source on the process competitiveness was assessed. Results show that medium temperature thermal energy sources could be coupled to the High Temperature Electrolysis process without involving strong overcosts. An overall deviation of ±8% was found on the results for the sources here presented, according to the implemented model. Therefore massive hydrogen production through High Temperature Electrolysis could be envisaged considering the use of a wide scope of thermal energy sources.

The thermal energy source needs to demonstrate a compromise between low heat costs and high temperatures: high heat source temperatures favour lower hydrogen costs, but only if the corresponding heat cost is not sharply increased. However, it is not a heavy constraint since the influence of the heat source on the hydrogen production cost is limited.

References

[1] O'Brien JE., Stoots CM., Hartvigsen JJ., Herring JS. Performance of planar high-temperature electrolysis stacks for hydrogen production from nuclear energy. International Topical Meeting on Nuclear Reactor Thermal Hydraulics No11, 2007;158(2):118-131. Avignon , FRANCE (02/10/2005)

[2] Sigurvinsson J., Mansilla C., Lovera P., Werkoff F. Can high temperature steam electrolysis function with geothermal heat? International Journal of Hydrogen Energy, 2007;32(9):1174-1182.

[3] McKellar MG., O'Brien JE., Herring JS. Commercial Scale performance predictions for High Temperature Electrolysis plants three advanced reactor types. DOE/INL-EXT 07 13575.

[4] Rivera-Tinoco R., Mansilla C., Bouallou C., Werkoff F. On the Possibilities of Producing Hydrogen by High Temperature Electrolysis of Water Steam Supplied from Biomass or Waste Incineration Units. International Journal of Green Energy, 2008;5(5):388-404.

[5] Rivera Tinoco, R., Mansilla, C., Werkoff, F., Bouallou, C. (2008b). Techno-economic study of hydrogen production by High Temperature Electrolysis coupled with an EPR, SFR or HTR – Water steam production and coupling possibilities. International Journal of Nuclear Hydrogen Production and Applications 1(3): 249-266.

[6] Rivera Tinoco, R. (2009). Etude Technico-économique de la production d'hydrogène par Electrolyse Haute Température à partir de différentes sources d'énergie thermique. Mines ParisTech. PhD Thesis. France.

[7] Salcedo R., Gonçalves M J., Feyo de Azevedo S. An improved random-search algorithm for non-linear optimization. Computers & Chemical Engineering, 1990;14(10):1111-1126.

Alkaline Electrolysis – Introduction and Overview

Detlef Stolten and Dennis Krieg

Abstract

This review describes the principles and history of electrolysis and elucidates the reasons for the development of certain varieties of electrolyzers, namely alkaline electrolyzers, solid polymer electrolyzers, high-temperature electrolyzers, and high-pressure electrolyzers, by outlining the physical and electrochemical basics applying to electrolysis. Materials, design, and operating conditions for alkaline electrolysis are described in further detail, concluding with a brief discussion of the status of electrolysis today.

Hydrogen Evolution on Ni Electrode during Synthetic Tap Water Electrolysis

Yanko Petrov, **Frank de Bruijn**, Energy Research Centre of the Netherlands
Jean-Pierre Schosger, Institute for Energy, JRC
Zdravko Stoynov, Institute of Electrochemistry and Energy Systems, BAS

1 Introduction

Electrolysis is a key technology in the production of hydrogen from renewable sources, especially those that generate electricity, such as solar, wind and hydroelectric power. While hydrogen producing electrolysers are industrially available [1, 2], these are especially aimed at the production of hydrogen as a chemical, not as an energy carrier. For the large scale application of hydrogen as an energy carrier for automotive applications, the hydrogen cost, energy efficiency of the electrolyser and the resulting hydrogen quality are key factors that need more attention. The need for ultrapure water in the present generation electrolysers is another factor that contributes to cost and hinders widespread introduction.

The current research attempts to investigate the influence of the contaminants in the tap water on the hydrogen as well as oxygen evolution reaction (HER/OER) on Ni electrodes.

2 Experimental

The electrochemical set up used in this study was three electrode Pyrex glass cell employing a large platinum basket as CE (counter electrode), a solid Nickel cylindrical electrode as WE (work electrode), and a reference electrode (RE) connected to the cell by a bridge allowing to keep the RE at room temperature. The solutions were prepared from p.a. grade chemicals and distilled 18 $M\Omega.cm^{-2}$ water, with 1 $mol.dm^{-3}$ KOH added to increase the conductivity. The synthetic tap water was prepared by different salts in the proper concentration according to the recipe obtained from a water monitoring laboratory in the Netherlands (N. V. PWN Waterleidingbedrijf Noord-Holland, location Bergen) [3]. The electrochemical equipment used was a Solartron SI 1287 electrochemical interface coupled with FRA SI 1255 frequency response analyzer. The temperature of the cell was controlled by a thermostat with accuracy within ± 1 C^{o}. The gas phase was analyzed by a gas-chromatograph while the electrode surface structure was studied with the help of scanning electron-microscope using SEM and EDX techniques.

3 Results and Discussion

Fig 1. shows the steady-state polarization curves of the Ni electrode in 1 $mol.dm^{-3}$ KOH pW and sTW at 298 and 353 K for HER. The difference in the performance between the two media is due to the influence of the impurities in the sTW on the electrode kinetics. As the WE in the case of HER is negatively charged only cations may take part in the electrochemical reaction at the electrode/electrolyte interface. However, it is known that anions, especially those from the halogen elements group, can undergo chemical adsorption

on the electrode surface under similar conditions. As result they block the active sites of the WE where the electrochemical reaction occurs. In such case, at identical current densities the potential of the partially covered with chemisorbed species WE will be higher. On the contrary, at one and the same potential the current density of WE will be lower.

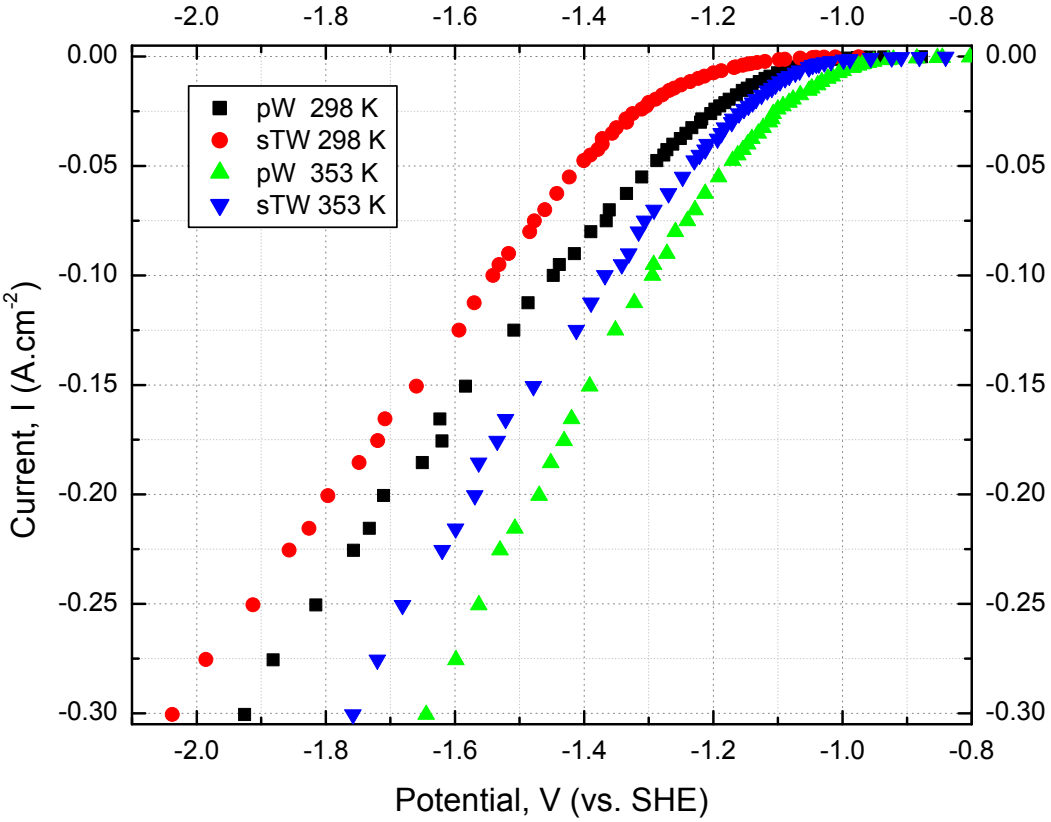

Figure 1: Polarization curves of Ni electrode in 1 mol.dm^{-3} KOH pure water (pW) and synthetic tap water (sTW) at two different temperatures.

Fig. 2 shows the SEM images of the WE surface composition after polarization tests. The results from EDX analyses are summarized in Table 1. The presence of Cl, S, Na, Mg as well as the higher content of C and O in the case of sTW can only be attributed to their presence in the bulk electrolyte as impurities. As expected, the latter two elements are also identified for pure water, because CO_2 from the air is easily dissolved in an alkaline solution.

Table 1: Quantified results from the EDX spectrum from Fig.2.

Weight %	C	O	Na	Mg	Si	S	Cl	K	Fe	Zn	Pb	Ca	Cr	Ti	Ni
pW	8.44	6.61			0.92			0.11	7.43		0.86	0.06	0.06	0.13	75.27
sTW	39.82	15.39	2.97	0.03	1.13	0.25	2.19	3.00	28.73	1.7	4.78				

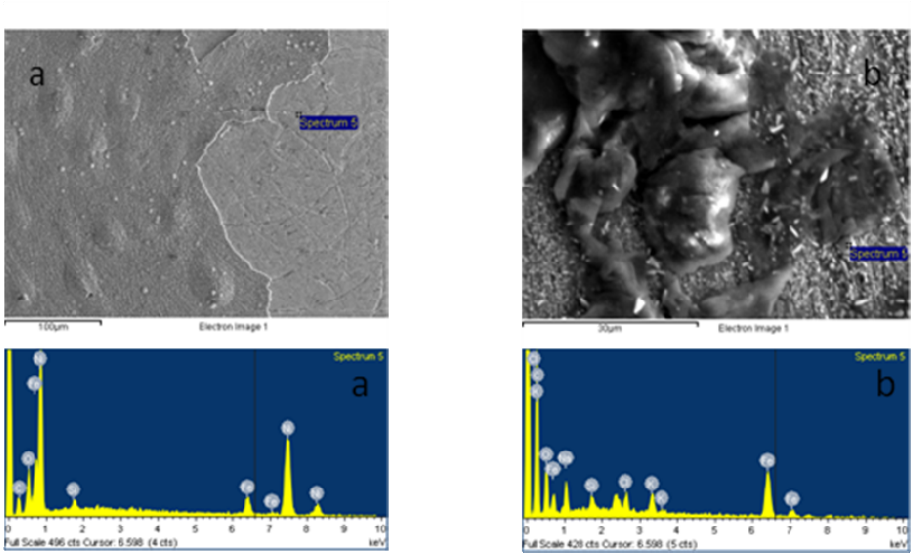

Figure 2: SEM and EDX spectrum images of Ni electrode after steady-state polarization in a) pure water + 1 mol.dm^{-3} KOH, b) synthetic tap water + 1 mol.dm^{-3} KOH.

Electrochemical Impedance Spectroscopy (EIS) measurements show that the systems under study display only one semi-circle in the impedance complex-plane, which is slightly distorted (Fig. 3). EIS complex-plane plots were approximated through R_s/CPE/R_{ct} equivalent circuit, where R_s represents the solution resistance, R_{ct} is the charge-transfer resistance related to the electrode kinetic and CPE is a frequency dependent parameter used instead of C_{dl} - pure double layer capacitance in case of surface inhomogeneities. Only R_{ct} gives information about the electrochemical rate of the reaction – the smaller the value of the R_{ct} the higher the rate is. This can be easily recognized on Fig. 3 since R_{ct} is defined in general as the diameter of the semi-circle [4]. R_{ct} of pure water is smaller compared with the sTW system which is in good agreement with the polarization measurement results.

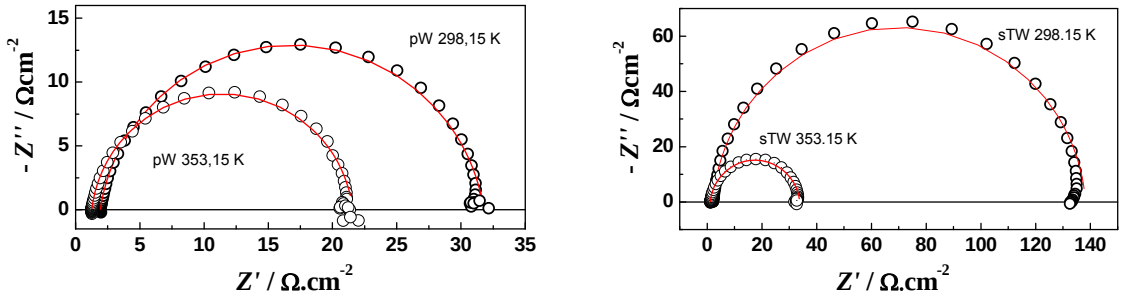

Figure 3: Complex-plane plots of Ni electrode in pure (pW) and synthetic tap water (sTW) at 298 and 353 K at constant potential -1.022 V vs. SHE.

The existence of only one semi-circle in both cases also indicates that the impurities in sTW do not participate in the charge-transfer reaction. If a log1/R_{ct} is plotted against E, it should yield a slope identical to the one obtained from steady-state curves. This is shown on Fig 4. The small difference in the values of the Tafel slope at one and the same temperature

suggests that the mechanism of HER in sTW is the same as in pW within the potential region under investigation.

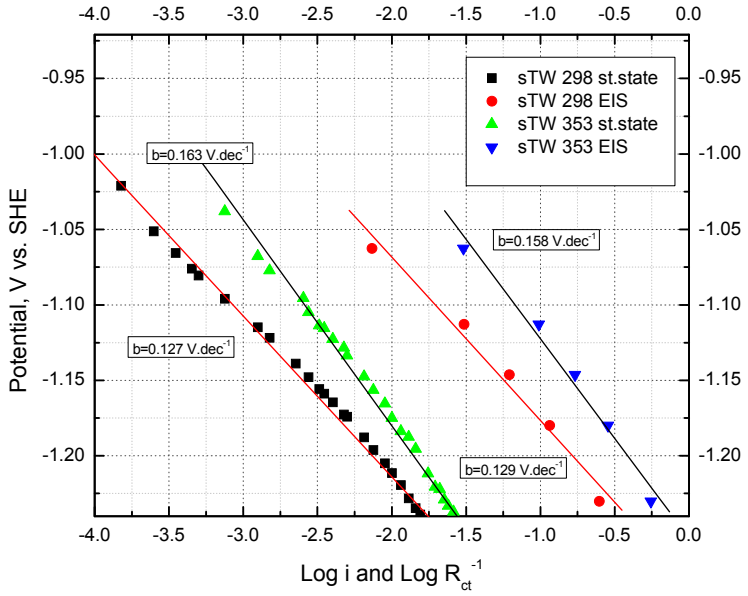

Figure 4: Comparison of the Tafel slopes obtained from steady-state and EIS techniques in sTW at 298 and 353 K.

The steady-state measurements usually cannot account for the stability of the system's performance with time. That is why long-term stability tests are performed to check the deviation of the parameters of interest under continuous operation conditions.

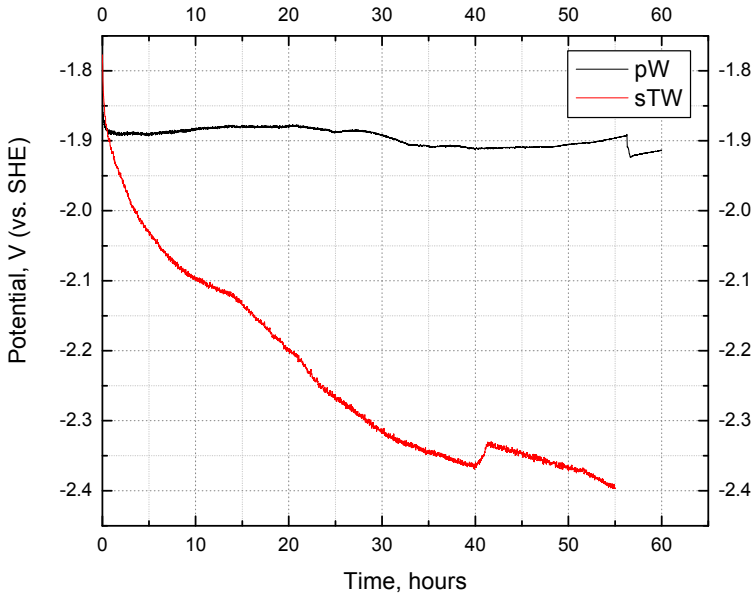

Figure 5: Stability test for Ni electrode in 1 mol.dm^{-3} KOH pure water (pW) and synthetic tap water (sTW) at 298 K and constant current density of 0,25 A.cm^{-2}.

Fig. 5 shows the performance of the Ni electrode in pW and sTW under polarization at a constant current of 0.25 A.cm^{-2} within 55 hours. In the case of pW the potential quickly reaches a steady value and remains almost unchanged for the whole period. This behaviour is not observed for sTW, whose potential continuously moves to more negative values. This fact could be due to the formation of $Ca(OH)_2$ or $Mg(OH)_2$ precipitates on the electrode surface. It is known that at pH higher than 10.7~11 Mg^{2+} or Ca^{2+} ions, if present in the solution, tend to form scales at the metallic surface of the electrode and later grow onto neutral surfaces in the form of hydroxides [5].

For the practical application on an electrochemical process it is important to lower the cost of the process itself and also to keep all other costs as low as possible for obtaining minimum price end products of interest. In this manner the purity of the products obtained is of great importance.

Using a gas-chromatograph attached directly to the electrochemical cell an attempt was made to analyze the gas phase for the most likely gases expected i.e. H_2, O_2, CO_2, CO, SO_x, NO_x, N_2 and H_2S. It has to be noted that no additional attempt to separate the anodic and cathodic compartments of the cell was made except that a glass tube positioned around the WE was mounted on the cell top thus allowing the formed gas bubbles to leave the cell body. In this manner gases evolved from the WE were driven to the gas-chromatograph and analyzed. With this experimental setup the quantity of the hydrogen obtained at 0.5 A.cm^{-2} is ca. 94~95% and 93% the latter being the result from sTW (Fig. 6). The rest is a mix of an O_2 and N_2. What is worth noting is that only CO_2 was detected in quantity in the range under 0.02 %V. No traces of CO which is known to play the crucial role in poisoning PEMWE electro-catalysts were detected.

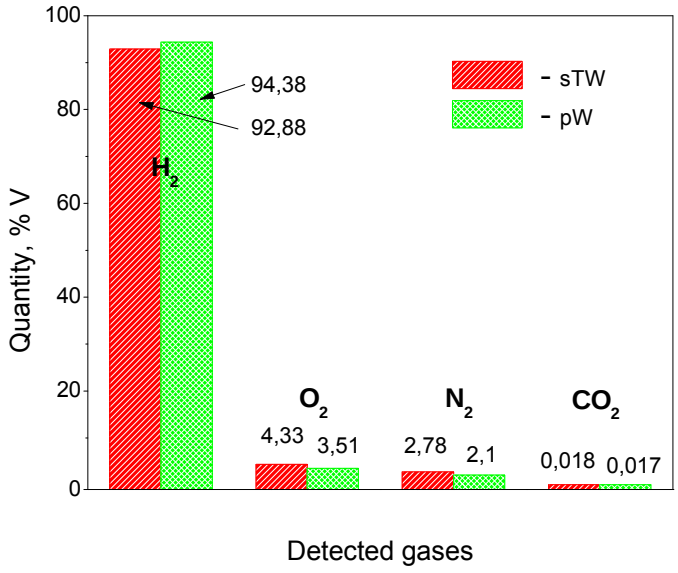

Figure 6: Gas analysis results.

Using the same experimental procedures Oxygen Evolution Reaction (OER) was also investigated. The experimental findings are discussed in details in the presentation.

4 Conclusion

The obtained results lead to the conclusion that impurities contained in synthetic tap water undergo chemical adsorption on the WE surface and block the active sites for the electrochemical reaction (HER) resulting in increased energy consumption. They do not take part in the electrochemical reaction whose mechanism seems to be the same in both media (pW and sTW). The purity of the obtained gas product at identical experimental conditions is almost equal. No stable potential was registered during the stability test within 55 hours which is probably due to additional formation of deposits on the WE surface. Having in mind all the above conclusions synthetic tap water electrolysis could enable energy storage in distributed off-grid application by simple conversion of available water using intermittent, renewable electricity.

References:

[1] Gandia L. M., O.R., Ursua A., Sanchis P., Dieguez P. M.,, Renewable hydrogen production: Performance of an alkaline water electrolyzer working under emulated wind conditions. Energy & Fuels, 2007. **21**: p. 1699-1706.

[2] Barbir F., PEM electrolysis for production of hydrogen from renewable energy sources. Solar Energy, 2005. **78**: p. 661-669.

[3] Water quality measurement 2nd quarter 2006, Location Bergen, NL; downloaded from www.pwn.nl.

[4] Bard A. J., Faulkner L. R., Electrochemical methods: Fundamentals and Applications, 2nd edition, Wiley, 2001, p. 385

[5] Bennett J. E., Electrodes for generation of hydrogen and oxygen from seawater. Int. J. Hydrogen Energy, 1980, **5:** p. 401-408

Study of SO_2-Depolarized Water Electrolysis

Anu Lokkiluoto, **Michael Gasik**, **Tuomo Kuikka**, Aalto University Foundation
School of Science and Technology, Finland

1 Introduction

Hydrogen is a promising energy carrier, which has the potential to replace fossil fuels used as power source of vehicles. There is, however, no large scale, cost-effective, environmentally attractive hydrogen production process available for commercialization today. One of the best alternatives of hydrogen production is the so-called hybrid sulphur cycle (HyS), which is also known as Westinghouse process. The Nuclear Hydrogen Initiative of The US DOE has identified the hybrid sulphur cycle together with sulphur-iodine cycle as the first priority cycles [1]. According to the calculations carried out within the IEA HIA Task 25, of these two processes, the HyS is the more favourable one.

In the low-temperature part of the HyS, sulphur dioxide depolarized electrolysis (SDE) is used, where hydrogen and sulphuric acid are produced as products of the reaction between water and dissolved SO_2. The advantage of the SDE is based on the fact that the reversible voltage E^o of the net reaction (1)

$$SO_2\,(aq) + 2H_2O \rightarrow H_2SO_4\,(aq) + H_2\,(g) \qquad (1)$$

is only 0.158 V at 25 °C [2], versus the theoretical E^o = 1.23 V needed for conventional water electrolysis (alkaline or PEM). In laboratory scale tests, the realized cell voltage has been 0.5-1.2 V depending on the current density versus 1.85 – 2.05 V of the commercial alkaline electrolysis. Thus the HyS process takes only 30 - 40% of the electric energy needed for direct water splitting by conventional electrolysis. A review by O' Brien et al. concerning the electrochemistry of oxidation of SO_2 in SDE was published recently. [3]

Research groups at the Savannah River National Laboratory (SRNL) and at the University of South Carolina (USC) have studied recently the SDE. Both research groups have used PEM electrolyser with carbon bipolar plates/flow channels and Pt/C electrodes (MEA structure). These were the materials used also by the original Westinghouse group. [4] At SRNL, SO_2 dissolved in H_2SO_4 is used as the anolyte, and water is fed to the cathode. [1] The electrolyser has been operated also in dry cathode mode. [5] At USC, they have used gaseous feed of SO_2 to the anode, while liquid water is fed to the cathode. [6]

The aim of this study was to identify the possible technical obstacles in respect to materials stability in production process of H_2 by SO_2-depolarized electrolysis. Metallic materials have good strength to weight ratio, are easily formed and joined and have good heat transfer properties. For engineering purposes, it is usually desirable to use metal alloys whenever possible. From the materials point of view, the SDE is very challenging due to the corrosiveness of the electrolytes used (mixtures of sulphuric acid and SO_2). Compared to the

time of the original Westinghouse studies, new metallic corrosion resistant alloys exist nowadays.

A bench-scale flow-through electrolysis cell with an active area of 0.01 m^2 and a test facility with necessary auxiliary equipment were built. With this facility, one-week-long tests were carried out. In addition to these tests, corrosion resistance testing of the coated electrode materials was carried out in a dedicated autoclave. The electrochemical behaviour of the possible bipolar plate/electrode materials was investigated also with linear sweep voltammetry.

The materials studied included uncoated stainless steel 904L and TiN- and gold coatings on steel 904L. Stainless steel 904L has good corrosion resistance in sulphuric acid solutions. The corrosion resistance of stainless steels is due to the formation of dense, protective passive layer. All metals, which corrosion resistance is based on their passive behaviour, have also high surface resistance. For bipolar plates/electrodes, high surface conductivity would be beneficial. Coatings can be used to modify surface properties, and conductive coatings like TiN and gold have been widely studied for PEM fuel cell applications. [7]

2 Experimental Methods and Materials

The materials studied included uncoated stainless steel 904L and TiN- and gold coatings on steel 904L. Disc-shaped samples (~15 mm x 2mm) were used both in linear sweep voltammetry and autoclave experiments. The samples were polished first with SiC paper, grades 240, 400 and 1200, and after that with 6, 3 and 1 µm diamond pastes. TiN and gold-coatings were then manufactured using proprietary low-temperature PVD-method. Thickness of the TiN coating was ~1 µm and thickness of the gold coating was 50±20 nm. A bulk gold electrode with the same dimensions as the samples was prepared from a commercial (24K - 999) gold sheet. The same coating process was used also for the electrodes of the bench-scale electrolyser.

3 Linear Sweep Voltammetry

Linear sweep voltammetry (LSV) is a versatile electrochemical method, which enables simultaneous study of the effects of applied potential, solution composition and temperature. In LSV, the potential applied of the sample is changed, and the current response is recorded. The resulting voltammogram (i-E-curve) shows the electrochemically active and passive potential regions.

The samples were studied at both oxidizing (anodic) and reducing (cathodic) potentials in H_2SO_4-SO_2-solutions at room temperature. The cathodic scans without SO_2 correspond to the cathode side of the SDE cell, and the anodic scans with SO_2 correspond to the anode side. The counter electrode was a platinum flag. The reference electrode was an SCE protected with a special glass jacket in a separated compartment connected with the main cell by a salt bridge. The 1000 ml cell was made of glass, and it had a gas-tight Teflon-lid, the test equipment is shown in figure 1.

Testing was carried out in 15 and 40 wt-% sulphuric acid with and without S(IV) additions. The solution was de-aerated prior experiments with instrument grade N_2 at least for 30 min.

Magnetic stirring was used during the experiments and de-aerating. The amount of SO_2/HSO_3^- was analysed by iodometric back-titration.

The sweep rate was 20 mV/s. The potential ranges of the experiments were -300…+1900 mV (anodic scans without SO_2), +200…+1900 mV (anodic scans with SO_2), and -800…0 mV vs. SCE (cathodic scans). The anodic scan with SO_2 was started at 0.2 V vs. SCE to avoid reduction of SO_2. The open circuit potential (OCP) was measured at the beginning of each experiment mostly to check the connections.

Figure 1: Three-electrode cell used in LSV test.

4 LSV Results

In figure 2, the behaviour of gold coated electrodes is shown on hydrogen scale. The cathodic side (without SO_2) corresponds to the cathode of the SO_2 depolarized electrolysis, and the anode side (with SO_2) corresponds to the anode. In a process corresponding to figure 2, the cell voltage would be ca. 0.8 V.

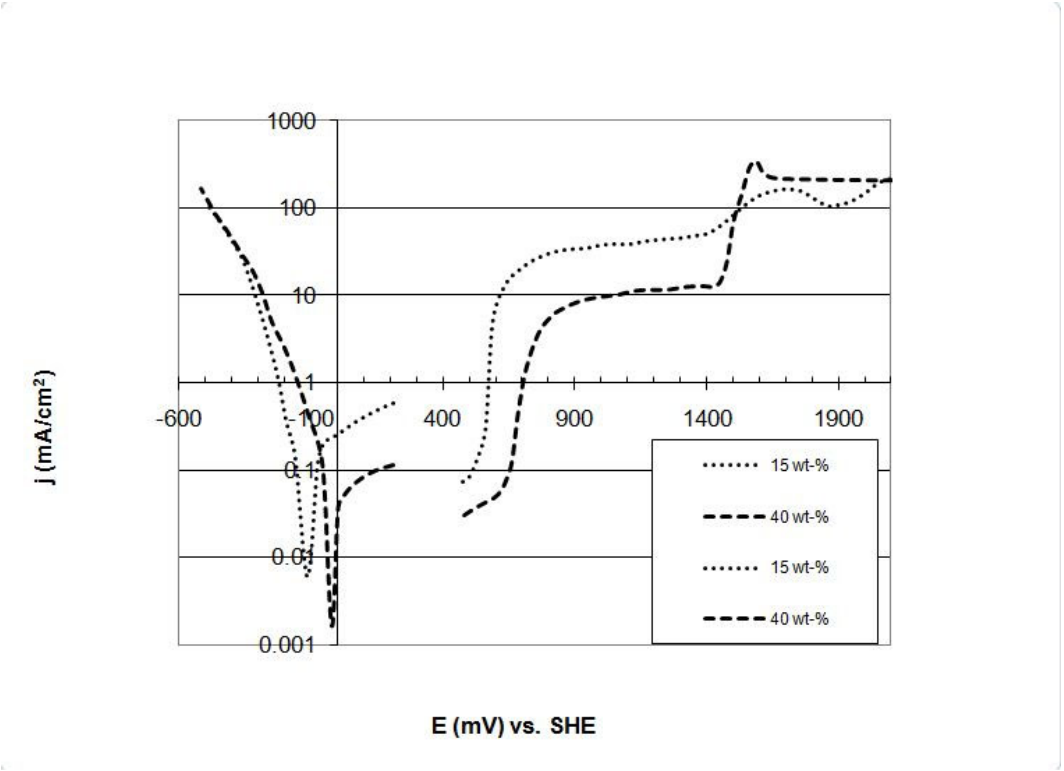

Figure 2: Au-coated 904 L. T= 25 °C, 15 and 40 wt-% sulphuric acid, v=20 mV/s.

5 Autoclave Materials Stability Tests

The autoclave corrosion testing was realized in parallel [8]. A special autoclave system was retrofitted and adapted to monitor the parameters listed below. Test equipment is shown in figure 3.

Atmosphere: N_2 <10 bar, SO_2 <2.8 bar

Temperature: RT to 100 °C

Stirrer: RPM from 40 upwards with 16 specimens

Total volume: 30 litres

Material: Special coatings + plastic in-bag for vessel protection.

Two test series were performed in the autoclave. The first series was performed in a sulphuric acid - nitrogen environment and the second in a sulphuric acid - sulphur dioxide environment. The sulphuric acid concentrations were 50 and 80 wt-% and test temperatures were 30 and 50 °C. These conditions are expected to be the most severe for the TiN coating and extreme conditions of the electrolyser.

Each test consisted of 8 specimens, which included duplicate samples of all the specimen types, with duration of two weeks.

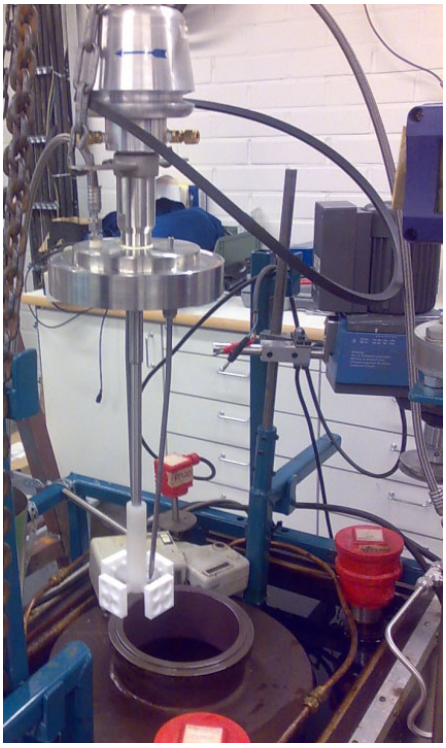

Figure 3: Photograph of the autoclave test equipment.

6 Autoclave Results

Samples were studied by optical and SEM microscopy. Also reference samples of both coatings and bare 904L were analyzed. All specimens were weighed before and after the experiments, but mass losses were not significant enough for any conclusions to be made. In figure 4, optical micrographs of gold coated samples tested in 50 wt-% sulphuric acid are shown.

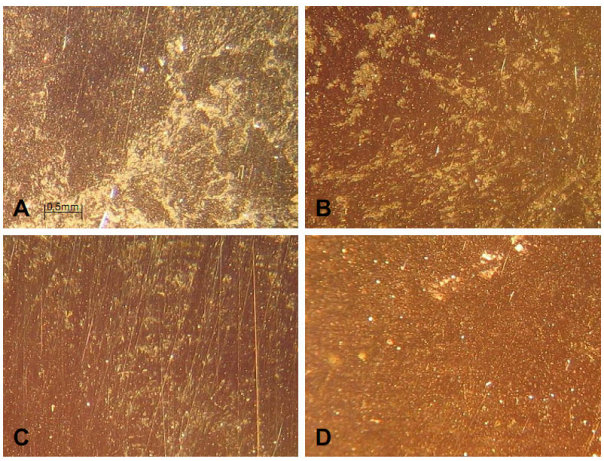

Figure 4: Au-coated 904L in 50 wt-% sulphuric acid. A=30 ºC, N_2; B=30 ºC, SO_2; C=50 ºC, N_2 and D=50 ºC, SO_2.

The gold coating showed no signs of corrosion when studied by optical microscopy.

7 Bench-scale Electrolyser

The bench-scale electrolyser test facility can be seen in figure 5. The active area of the electrolyser is 0.01 m^2. It was purchased from ElectroCell [9].

Figure 5: The bench-scale electrolyser test facility.

Two longer time-scale galvanostatic experiments were carried out at room temperature with current of 10 A, which corresponds 1 kA/m^2. The electrolyte flow rates were 60 – 80 l/h.

The first test was started by adding approximately 80 g/l of SO_2 to the anolyte, of which 70% was readily dissolved. No SO_2 was added during the experiments, so the test was carried out in a batch mode. The amount of SO_2 added corresponded to the solubility of SO_2 in sulphuric acid solution of that concentration and temperature and the test was continued until nearly all the SO_2 was consumed.

8 Bench-scale Electrolyser Results

The depolarization effect of SO_2 was ~0.65 V with gold-coated electrodes, similar to one observed in LSV experiments (figure 2).

9 Conclusions

The corrosion performance of all of the tested materials was better in sulfuric-acid with SO_2 than in pure sulphuric acid solution. This is most likely caused by the reducing nature of SO_2 under these particular conditions.

The corrosion resistance of 904L can be enhanced with gold coating. Thin gold coatings were stable in the conditions of SO_2 depolarized electrolysis at least in the short time scale (up to 14 days) of these experiments. Novel TiN-coatings tested do not seem to be suitable

for SO_2 depolarized electrolysis, but they had a good corrosion resistance against sulphuric acid, compared to the older crystalline TiN-coatings. This was the case at low temperatures and lower acid concentrations used in the tests.

In the SO_2 depolarized electrolysis tests, the depolarizing effect of SO_2 was 0.6 - 0.7 V with gold coated 904 L electrodes. The gold coated anode showed catalytic activity towards SO_2 oxidation. With gold coatings, it might be possible to avoid the use of Pt catalysts in the SDE.

Acknowledgements

Support from Tekes (Finnish Funding Agency for Technology and Innovation) and IEA HIA Task 25 is gratefully acknowledged.

References

[1] Gorensek, M.B., Summers, W.A. Hybrid sulfur flow sheets using PEM electrolysis and a bayonet decomposition reactor. International Journal of Hydrogen Energy. 34(2009) pp. 4097 – 4114.

[2] Gorensek, M.B, Staser, J.A., Stanford, T.G, Weidner, J.W. A thermodynamic analysis of the SO_2/H_2SO_4 system in SO_2-depolarized electrolysis. International Journal of Hydrogen Energy. 34(2009) pp. 6089 – 6095.

[3] O'Brien, J.A., Hinkley, J.T., Donne, S.W., Lindquist, S-E. The electrochemical oxidation of aqueous sulfur dioxide: A critical review of work with respect to the hybrid sulfur cycle. Electrochimica Acta 55(2010) pp. 573 – 591.

[4] Lu, P.W.T. Technological aspects of sulfur dioxide depolarized electrolysis for hydrogen production. International Journal of Hydrogen Energy 8(1983)10 pp. 773 – 781.

[5] Steimke, J.L., Steeper, T.J. Characterization Testing and Analysis of Single Cell SO_2 Depolarized Electrolyzer. Research report WSRC-STI-2006-00120. 2006, 56 p.

[6] Staser, J.A., Weidner, J.W. Effect of water transport on the production of hydrogen and sulfuric acid. Journal of Electrochemical Society 159(2009)1 pp. B16 – 21.

[7] de las Heras, N., Roberts, E.P.I., Langton, R., Hodgson, D.R. A review of metal separator plate materials suitable for automotive PEM fuel cells. Energy & Environmental Science 2(2009) pp. 206 – 214.

[8] Kuikka, T. The corrosion resistance of PVD coatings in H_2SO_4 environment. Masters's thesis, Aalto University Foundation School of Science and Technology. 2010. 44 p.

[9] http://www.electrocell.com/ (15.1.2010)

Flexible Production of Hydrogen from Sun and Wind: Challenges and Experiences

Hans Jörg Fell, **Petr Chladek**, Hydrogen Technologies, N-3908 Porsgrunn, Norway
Oddmund Wallevik, **Stein Trygve Briskeby**, Statoil, Research Centre Porsgrunn, N-3908 Porsgrunn, Norway

1 Introduction

With the looming threat of global climate change and progressing depletion of fossil fuels, renewable power sources, especially wind and solar, experienced an economic boom in the past decade [1, 2]. Both wind and sun supply significant amount of electrical power without generating any pollution during the operation. Unfortunately, both sources generate power of intermittent nature, regardless of the demand, which consequently stresses the existing electrical grid.

To mitigate this drawback, renewable energy needs to be converted into a storable intermediate, which could be used in the times of electricity peaks or alternatively used as a fuel for vehicles. The energy carrier of choice is hydrogen produced by water electrolysis [3, 4].

Water electrolysis is a well-established method of producing hydrogen and an ideal candidate due to the general availability of water, scalability of the electrolysis plant and zero-emission production of hydrogen. Traditionally, in industrial applications electrolysers are connected to the grid and operated under stable conditions. Renewable energy sources by contrast, supply intermittent power leading to new requirements to the electrolysers [5-8]. Conventional electrolysers tend to utilize only a fraction of the available renewable power due to a number of reasons: long start-up times, inability to follow rapidly changing power input and last but not least limited operating range in terms of capacity. The latter can be attributed to a reduced hydrogen gas quality at low power input.

We have demonstrated previously the feasibility of running a 1 Nm^3/h PEM electrolyser on emulated intermittent wind power [9]. Pursuing this route the research on the coupling of renewable energies to water electrolysis has now been taken a step further. In this study, performed by Statoils Research Centre in Porsgrunn, we have tested a prototype of a new pressurized alkaline electrolyser from Hydrogen Technologies operating under emulated power profiles from renewable energy sources. The electrolyser has shown excellent load-following capabilities opening for new possibilities in using excess renewable energy efficiently.

2 Experimental

The Energy Park with a hydrogen refuelling station at Statoils Research Center in Porsgrunn, Norway is a laboratory for testing and qualifying technologies and components for renewable energy production and energy storage (Figure 1). The Energy Park consists of two 6 kW wind turbines from Proven Energy and two 2.5 kW mono-crystalline silicon solar panels with

sun tracking from SolarWorld. A 70 kWh lead-acid battery bank from Suntek has been installed for energy storage means. The Energy Park can be run as a stand-alone system using a 48 V DC grid, or it can deliver excess energy to the mains 230 V AC grid. A simplified layout of the Energy Park and hydrogen refuelling station is presented in Figure 2. The latest addition to the Energy Park is a pressurized alkaline electrolyser from Hydrogen Technologies, which has been coupled to the wind turbines and solar panels and can be operated under intermittent power conditions. The produced hydrogen serves fuelling purposes at the hydrogen station supplying the local hydrogen vehicle fleet of 9 Toyota Prius H2-ICE. The hydrogen refuelling station is an integral part of the Norwegian hydrogen highway system, HyNor [10].

With the electrolyser connected to the grid any power input profile can be emulated with a time resolution of 1 second. The system can be run on three different emulated operation modes, either on wind power, on wind and photovoltaic (PV) or on PV solely.

In this study we have chosen to operate the electrolyser firstly on a wind power profile and secondly on a photovoltaic power input. The power input was capped by scaling to about 45% of the name plate capacity in order to test the electrolyser in the most demanding regime i.e., at low power input yielding a low hydrogen production.

Figure 1: Energy Park and hydrogen refuelling station with the solar panels and wind turbines.

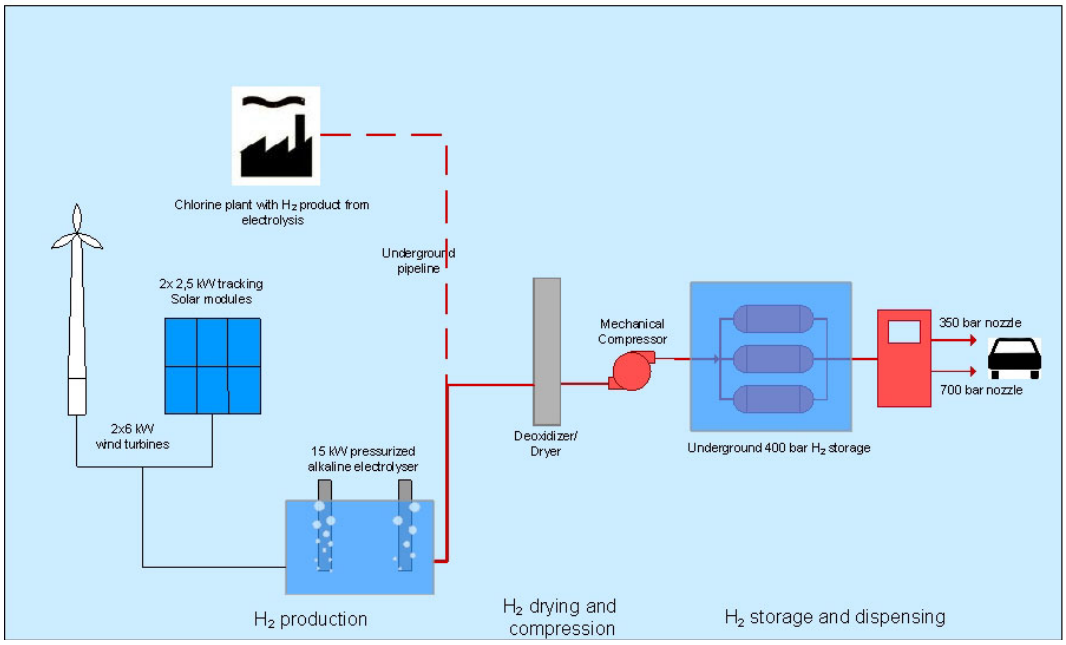

Figure 2: Schematic of Energy Park in Porsgrunn, Norway.

The technical specifications for the pressurized alkaline electrolyser are given in Table 1.

Table 1: Technical specifications for the alkaline electrolyser.

System	Alkaline, 30% KOH
Capacity	3.4 Nm^3/h
Pressure (max)	12 bar
Number of cells	10
Operation range, % of total capacity	12 %– 100%
Response time	< 1s
Operation temperature	60 °C

3 Results and Discussion

Figure 3 shows a short period of electrolyser operation under intermittent power. The green line shows the emulated power produced by the wind turbine with a resolution of 1 s. This power is converted to a current according to the specifications of the electrolyser stack. The converted current is used as a set-point in the power supply (blue line in Figure 3). The measured current is given as the red line. As seen in the Figure 3, a very fast response to the applied set point is observed proving the excellent load-following abilities of the unit. The control system is set to force a set point of 0 A as soon as the power supplied by the wind turbines becomes lower than a critical value. This value corresponds to an electrolyser current of 80 A, and is used to assure that the gas quality remains within the specified safe boundaries. Below 80 A the electrolyser enters a standby mode, maintaining operational pressure. As soon as the power production reaches acceptable levels again, hydrogen

production resumes at once. Such a forced pause in production can be seen between ~120 and 190 s in the figure.

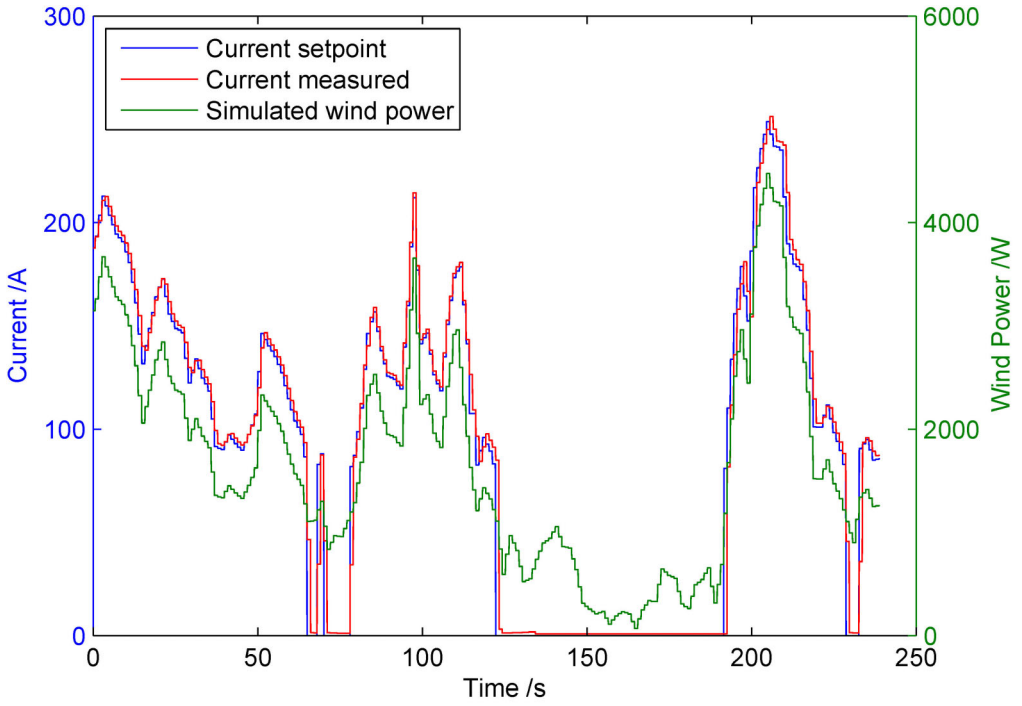

Figure 3: Operation characteristics of electrolyser under intermittent operation on emulated wind profile. The wind data has a resolution of 1 s^{-1}.

The ability of the system to resume hydrogen production even after long stand-by periods is shown in Figure 4. After a longer period with poor wind conditions and no hydrogen production, the electrolyser is responding immediately when the power produced by the wind turbine exceeds the critical limit. Before the system is started up at t~ 0.4 h, the hydrogen content in oxygen exceeds 1.5 %, Further deterioration of gas quality is experienced, due to a low initial power input. After ~0.6 h the wind conditions stabilize, the electrolyser is operated continuously between 20 and 40 % of maximum load and consequently the gas quality improves to a level well below 1 % H_2 in O_2. In general, the purity of the produced gases decreases with decreasing production rate. The gas quality is compromised by secondary electrolysis, gas crossover through the diaphragm and gas mixing due to mixing of anolyte and catholyte in the lye circuit. The operating conditions for the electrolyser in this regime are very demanding with power input ranging from 10% to 45% of the nameplate capacity. However, it is noteworthy, that even in this regime, the electrolysers performs very well and the hydrogen content in oxygen remains far below the LEL of 4%. Equipping the electrolyser with completely separate lye handling systems would improve the gas quality and thus broadening the operational range even further.

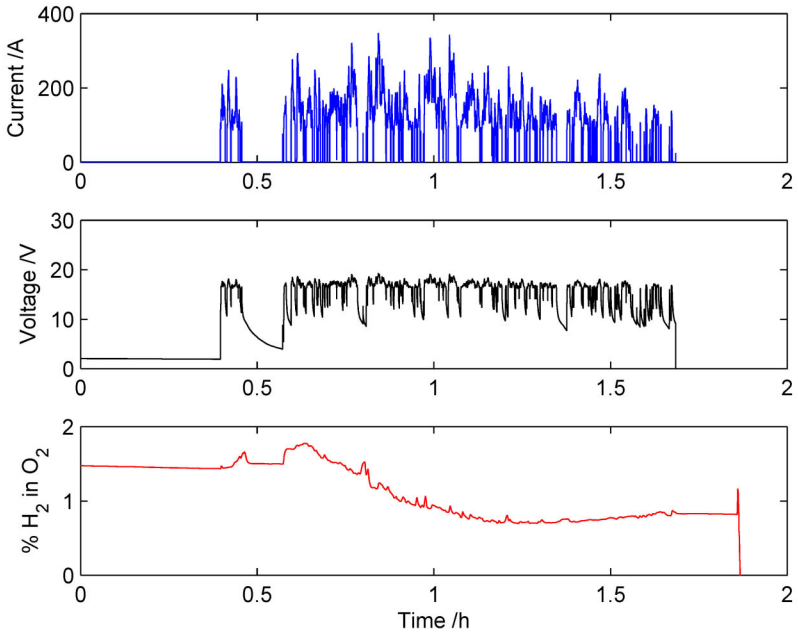

Figure 4: Start-up and operation after prolonged stand-by.

Figure 5 shows the difference in operation on PV and emulated wind power. During the first 0.4 hours the electrolyser is operated on the emulated wind profile. The operation is of intermittent nature switching the operational mode of the electrolysers between hydrogen production and stand-by. At t ~0.4 h the operation is switched to PV mode. As can be clearly seen, the production profile exhibits a far less transient behaviour illustrating the differences in requirements for an electrolyser running on wind versus solar energy.

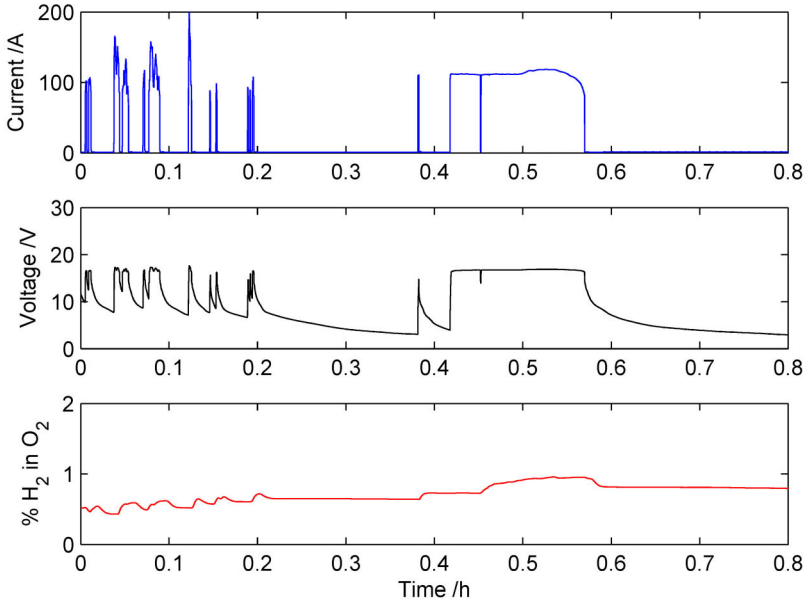

Figure 5: Operational characteristics of electrolyser running on emulated wind power. At t~0.42 h power is supplied from the PV panels in the Energy Park.

4 Conclusion

We have demonstrated a pressurized alkaline electrolyser that has crossed the traditional technology boundaries associated with the coupling of renewable energy and water electrolysis. With a quick response time (<1s) and a broad operational range (10-100%), the system has proven its ability to capture the fast variations in energy production associated with wind energy. Compared to earlier generations of alkaline electrolysers [11], this technology marks a technological breakthrough in the coupling of renewable energy and hydrogen generation. In the near future the electrolyser will be connected directly to the wind turbines and solar panels and its performance will be verified by long-term testing.

Acknowledgements

This work has been performed by staff at Statoils Research Center in Porsgrunn, Norway and was initiated by Torgeir Nakken. Audun Furumo and Stein Solum are acknowledged for their excellent work completing the experimental setup.

References

[1] World Wind Energy Association. World Wind Energy Report, 10 March 2010. See: http://www.wwindea.org/home/images/stories/worldwindenergyreport2009_s.pdf.

[2] Sandia National Laboratory. Photovoltaics research and development program info – PV roadmap: solar-electric vision, goals, and targets. See: http://photovoltaics.sandia.gov/docs/PVRMChapter_4.htm.

[3] John Barton and Rupert Gammon, The production of hydrogen fuel from renewable sources and its role in grid operations, Journal of Power Sources, in press http://dx.doi.org/10.1016/j.jpowsour.2009.12.100

[4] F. Barbir Energy 34 (2009) 308-312.

[5] Ø. Ulleberg, T. Nakken, A. Eté, Int. J. Hydrogen Energy 35 (2010) 1841-1852

[6] J.G. García Clúa, H. De Battista, R. J. Mantz Int. J. Hydrogen Energy 30 (2010) 1-7.

[7] K. Agbossou, R. Chahine, J. Hamelin, F. Laurencelle, A. Anouar, J.-M. St-Arnaud, T.K. Bose J. Power Sources 96 (2001) 168-172.

[8] F. Barbir Solar Energy 78 (2005) 661-669.

[9] P.J. S. Vie, Ø. Ulleberg, H. J. Fell, E. Rasten, Development of a Prototype PEM-electrolyser for Distributed renewable Energy Systems: Testing under Emulated Wind Power Conditions, WHEC2008

[10] HyNor, http:// www.hynor.no; 2010

[11] Hydrogen Technologies, product presentation see: www.electrolysers.com

Photovoltaic Hydrogen Production with Commercial Alkaline Electrolysers

A. Ursúa, **J. López**, **E. Gubía**, **L. Marroyo**, **P. Sanchis**, Department of Electric and Electronic Engineering, Public University of Navarra, Campus Arrosadía, 31006 Pamplona, Spain

Abstract

Renewable energy sources and Electrolysis generate the so-called green Hydrogen, a zero-emission and potentially fossil fuel independent energy source. However, the inherent variability of the renewable energy sources implies a mode of operation for which most current electrolysers have not been designed. This paper analyses the operation of a water electrolyser fed with photovoltaic (PV) generator electric profile. The system, Integrated by a 1 Nm^3/h Hydrogenics alkaline electrolyser and a 5100 W PV generator with 60 BP585 modules, is installed at the Public University of Navarra (Spain). The PV generator profile fed to the electrolyser is emulated by a custom-made apparatus designed and built by the authors of this paper. The profile is designed according to real irradiance data measured by a calibration cell. The irradiance data are converted to the electric power profile that the PV generator would have delivered in case of having been connected to the electrolyser by means of a DC/DC converter with maximum power point tracking (MPPT). Finally, from previously measured power-current electrolyser characteristic curves, the current profile to be delivered to the electrolyser is obtained and programmed to the electronic device.

The electrolyser was tested for two types of days. During the first day, the irradiance was very stable, whereas during the second day, the irradiance was very variable. The experimental results show an average power consumption rate and an efficiency of 4908 Wh/Nm^3 and 72.1%, on the first day, and 4842 Wh/Nm^3 and 73.3% on the second day. The electrolyser performance was particularly good in spite of the high variability of the electric supply of the second day.

Keywords: water electrolysis, hydrogen, photovoltaic energy, power supply.

1 Introduction

Renewable energies currently represent one of the firmest options of a sustainable energy future both for developed countries (like Germany, Japan, United States, Spain and Denmark) and emerging economies (like China and India). In the Spanish case, renewable energy sources reached quotes of 24% of the power generation in 2008 [1], and are projected to reach 30.3% in 2010. Until recently, most of this renewable energy came from wind farming; however, PV plants are rapidly growing, especially in Spain, reaching quotes close to 3500 MW installed at the end of 2008. The situation is similar in Germany and other developed countries.

Currently, the grid integration of the renewable energies implies certain problems due to their inherent variability. In this context, hydrogen generating systems might play a relevant part stabilizing and reducing this variability. Electrolysers coupled with renewable energy sources would need to operate in a completely different way than they currently do. These electrolysers might have to work under variable and dynamic feeding profiles.

Despite the fact that research on hydrogen and PV energy is relatively recent, there are already numerous literature references to studies of both real and theoretical prototype systems, generally isolated [2]-[5]. These systems usually show the experimental feasibility of hydrogen production and PV energy integration and set the base for the up-scaling effort. This paper contributes to the study of the behaviour of an electrolysis system fed with a PV profile, going one step beyond the study of its technical variability. The present study analyses the functioning of an alkaline electrolyser fed by a PV generator power profile highly variable.

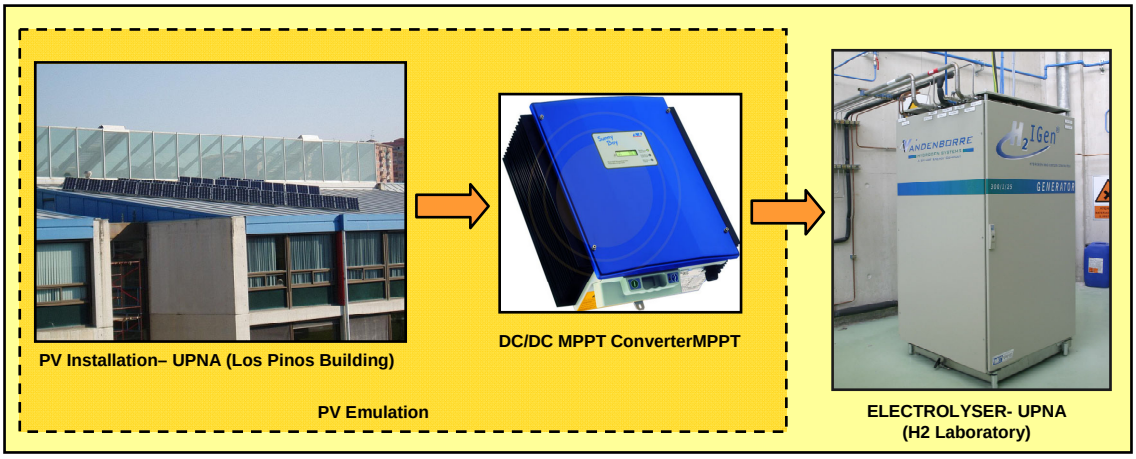

Figure 1: Scheme of the system under analysis.

Figure 1 shows the system under analysis. The system includes a PV system located at the Public University of Navarra Campus (UPNA), a DC/DC converter equipped with maximum power point tracking (MPPT) and an alkaline electrolyser. Considering the variability of PV energy, the system is analyzed at a laboratory scale by means of an emulated PV generator electric profile. As shown in Figure 2, the emulator is an electronic device designed and developed by the authors of this paper with three major functions [6]:

1. To characterize and model alkaline electrolysers
2. To emulate the electric behaviour of renewable energies, particularly, wind and PV, to feed electrolysers and to analyze their response to renewable power supply profiles
3. To emulate different electric profiles from various power supply topologies to evaluate and to compare the influence of the conversion stage on the behaviour and the efficiency of an electrolyser

The 10 kW nominal power emulator enables the simulation of current and voltages up to 250 A and 70 V. It has already been tested to evaluate the functioning of a wind powered

electrolyser [7] as well as to compare the efficiency of the electrolyser under various feeding source topologies [8]. In this paper, the device is used to characterize the electrolyser under analysis and to study the electrolyser behaviour if fed by a PV energy source.

The micro-controller of the system enables to customize the electrolyser feeding profile, to sensor and to monitor variables, to manage the data logging and to program the protection actions according to the selected recorded variables. The system has been validated by simulation and experimental tests under different functioning settings [8] and the system capacity to emulate highly variable power sources has previously been demonstrated for renewable and particularly for PV systems.

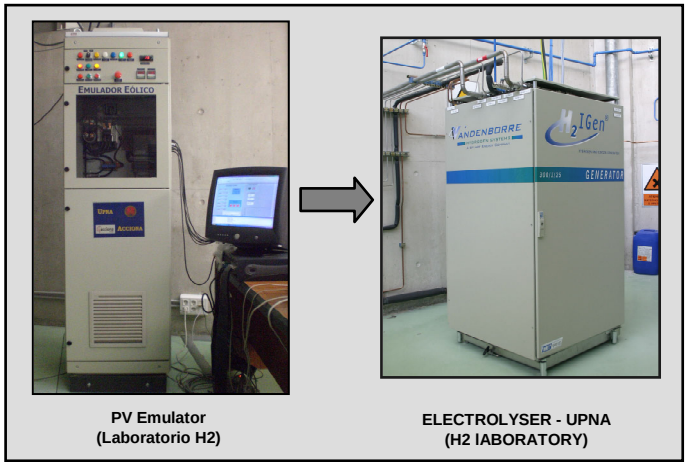

Figure 2: Electronic apparatus to emulate the PV system.

2 Test of an Alkaline Electrolyser Fed by a PV Solar Energy Profile

2.1 System description and characterization

This paper deals with the analysis of the system pictured in Figure 1. The system consists of a PV generator and an alkaline electrolyser to produce hydrogen. Both devices are installed at the Public University of Navarra (UPNA) Campus. The PV modules are installed on the roof of the Los Pinos building (Department of Electric and Electronic Engineering) and are oriented to the South, tilted 30º from the ground. The PV generator, of a peak power of 5100 W, consists of 60 modules BP585.

The PV system is modular, and is arranged on 15 branches with 4 modules connected in series each. The module electric specifications under standard conditions (T_S = 25ºC and E_S = 1000 W/m^2) are: a peak power P_{MS} = 85 W with a current I_{MS} = 4.7 A and a voltage V_{MS} = 18 V, a short-circuit current I_{SCS} = 5 A, an open circuit voltage V_{OCS} = 22 V, an average efficiency of 13.5% and a power variability coefficient as a function of temperature γ = -0.5%/ºC.

To characterize the electric behaviour of the PV generator, the current-voltage I-V characteristic curve of a module has been analytically modelled according to the 5 parameters that characterize the single exponential equation. Figure 3 shows the

characteristic I-V and P-V curves of a BP585 module under standard conditions. The electric characteristics calculated concur with the maker specifications.

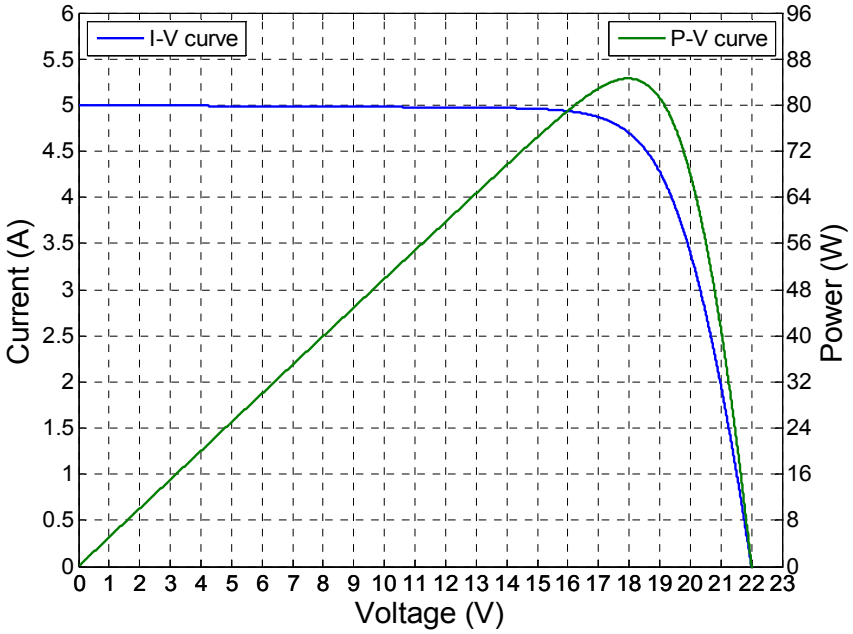

Figure 3: Characterization of the PV BP585 module: I-V and P-V curves under standard conditions.

The electrolyser is a H2 IGen 300/1/25 Hydrogenics model. The apparatus is located at the Hydrogen Laboratory of the UPNA. It is an alkaline electrolyser; the working pressure range goes from 5 to 26 bar and the temperature working range from 2ºC to 65ºC. The electrolysis bipolar stack consists of 22 round cells of 300 cm^2 each, connected in series. Each cell consists of two electrodes (an anode and a cathode) separated by an ion exchange inorganic membrane, assembled on a zero-gap configuration. On a zero-gap configuration the distance between the elements of the stack is minimized in order to maximize its efficiency. The electrolyte is a KOH 30% wg. solution. To maintain the conductivity of the water of the process bellow 5 µS/cm an ion exchange resin bed was set in place. This particular electrolyser model does not require pumps either to recirculate the electrolyte or to replenish water. The nominal hydrogen production rate is 1 Nm^3/h, which is equivalent to a 120 A DC current. The hydrogen production rate ranges from 25% (30 A DC) to 100% (120 A DC). Last, the stack energy consumption rate is 4.3 kWh/Nm^3, whereas the complete system energy consumption rate (including balance of plant and instrumentation) is 4.9 kWh/Nm^3.

The experimental characterization of the electric behaviour of the electrolyser was carried out using the electronic equipment described on Section 1. During the tests the current was swept from 0 A to 120 A (nominal current) at temperatures ranging from 15ºC to 65ºC and the pressure was kept constant at 20 bar. Each test measured both the current and the

power of both the stack and the electrolyser. Figure 4 shows the evolution of the power-current (P-I) curves of the electrolyser as a function of temperature.

As shown in Figure 4, as the temperature raises the power consumption decreases, being this effect more noticeable at low temperatures. This trend, especially at high currents (from 50 A to 120 A), is due to the variability of the electrolyte conductivity with temperature. The electrolyte conductivity is directly proportional to the temperature, and as the conductivity of the electrolyte increases the process energy losses decrease. Illustratively, at 120 A the electrolyser power consumption is 5.6% higher at 15ºC (4765 W) than at 65ºC (4495 W).

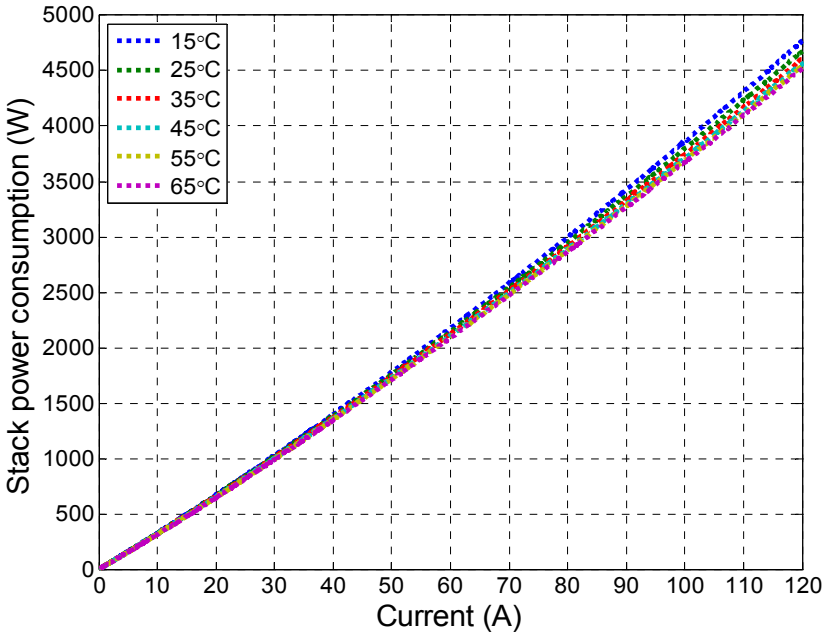

Figure 4: Electrolyser electric behaviour (P-I) as a function of temperature at 20bar.

2.2 Methodology

In order to analyze the electrochemical behaviour of an alkaline electrolyser coupled with a PV power supply, the electrolyser was fed by the supply emulator, assuming the PV generator was connected to a DC/DC MPPT converter as previously shown in Figure 1.

To emulate the PV supply source, the irradiance incident on the PV generator was measured indirectly by means of the short-circuit current I_{SC} of a permanently short-circuited module previously calibrated. Thus, using the digital power meter WT1600, the I_{SC} data were recorded at a frequency of 1 s and stored on a database. The irradiance E at time t can be calculated as:

$$E = \frac{I_{SC}\, E_S}{I_{SCS}} \tag{1}$$

Once the irradiance is known, the maximum power P_M injected to the electrolyser by the DC/DC MPPT converter can be calculated. The PV generator temperature is required. This temperature was obtained from the ETSIA-UPNA meteorological station measurements. The generator PV module working temperature is calculated from the outdoors temperature, T_a, and the irradiance, E, according to:

$$T_m = T_a + \left(\frac{TONC - 20^{\circ}C}{800\ Wm^{-2}} \right) E \tag{2}$$

where TONC is the nominal operation temperature of the modules (47ºC).

Finally, the maximum power P_M is calculated according to the following equation which accounts for the effects of irradiance and ambience temperature upon the power under standard conditions:

$$P_M = N_P\ P_{MS} \left(\frac{E}{E_S} \right) \left(\frac{100 + \gamma\ (T_m - T_S)}{100} \right) \tag{3}$$

where N_P is the number of modules of the PV generator, 59 in this case (since 1 was used to measure the I_{SC}).

To emulate a PV energy source, the renewable energy source emulator has to feed the electrolyser with the P_M calculated according to equation (3), hence the current to be supplied by the emulator to the electrolyser needs to be calculated. The electrolyser characteristic P-I curve can be expressed according to [9]:

$$P_E = (V_{rev} + r(T_E)\ I_E + s(T_E) \log(t(T_E)\ I_E + 1))\ I_E \tag{4}$$

where P_E and I_E are the electric variables of the electrolysis stack and V_{rev} is the reversible voltage. Parameters r, s, and t, depend on the process temperature (T_E) and are obtained adjusting the P-I curves shown in Figure 4 to equation (4) by non-linear numerical analysis methods. From here, the current that the emulator needs to feed the electrolyser (I_E) is calculated by equalizing the PV power to the electrolyser power ($P_E = P_M$) and then solving equation (4) by numerical iteration.

The calculations described in this section were programmed onto the micro-processor of the emulator system and are calculated online in real time, using the experimental vectors I_{SC} and T_a as seeds. The stack temperature in real time needs to be known in order to calculate the reference current ($I_{ref} = I_E$) to emulate at each instant (1 s).

2.3 Results and Discussion

To evaluate the electrolyser response to various working conditions of the PV generator, two particular days of 2007 were simulated: March 11th (1st day) and April 5th (2nd day). The experimental data (I_{SC} y T_a) were measured from 7:00a.m till 20:00p.m. Figure 5 shows the

measured irradiance of both dates. Noticeably, the 1st day was selected because of its unusual irradiance stability; whereas the 2nd day was selected for the opposite reason, since it was a day of particularly high irradiance variability. It can be observed, the foreseeable evolution of the irradiance with the sunlight, and in the 2nd day case, the high irradiance variability due to cloudiness. The variability registered along the 2nd day peaks at 800 W/m^2 (ranging from 300 W/m^2 to 1100 W/m^2) at 12:30pm in less than a minute.

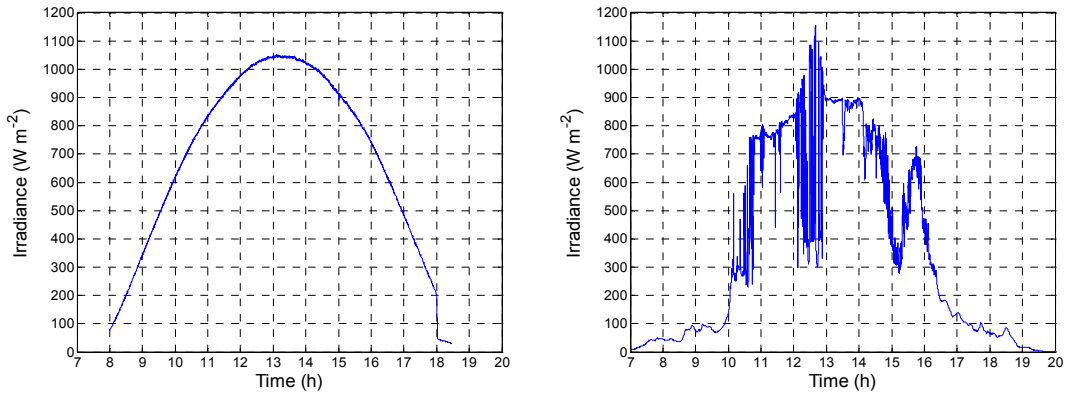

Figure 5: Irradiance. Left: March 11th (1st day). Right: April 5th (2nd day).

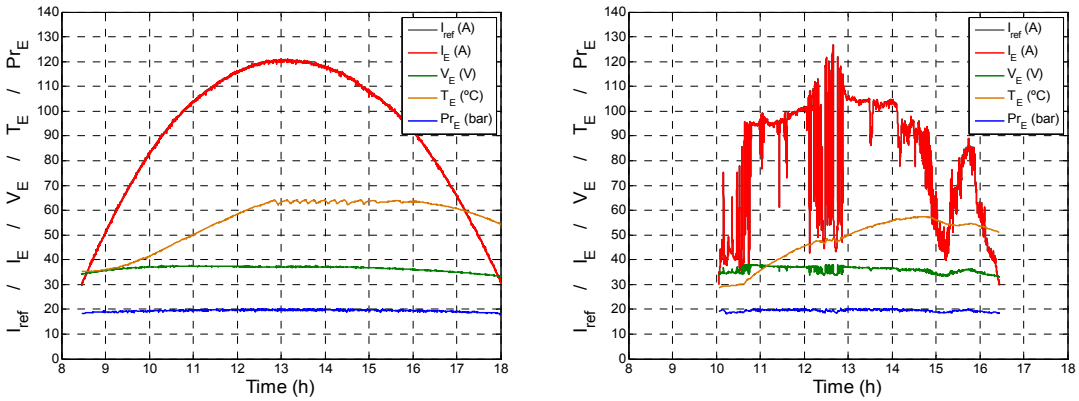

Figure 6: PV tests on both days (Left: 1st day; Right: 2nd day). Reference current (I_{ref}), current (I_E), and voltage (V_E) of the electrolysis stack; temperature (T_E) and pressure (P_{rE}) of the process.

Figure 6 shows the reference current (I_{ref}), the electrolyser electrical variables (I_E and V_E) and the evolution of the temperature T_E and the pressure P_{rE} of the electrolytic process during the tests of both days. First, it can be observed that the graphs depict how the PV energy source has been satisfactory simulated, since I_E, which profile is similar to the irradiance profile, consistently tracks the reference current (I_{ref} is overlapped by I_E). Due to the low limit of the electrolyser functioning settings (corresponding to I_E=30A), hydrogen is produced from 8:27a.m until 17:55p.m during the 1st day, and from 10:03a.m until the 16:27p.m on the 2nd

day. The voltage V_E varies similarly to the current due to the electrolyser ohmic behaviour. During the tests, the pressure is kept relatively stable at about 19.5 bar, with a variability of ±1 bar intrinsic to the process; however, the temperature evolution is coupled with the current I_E (actually, with the power) but slower dynamics.

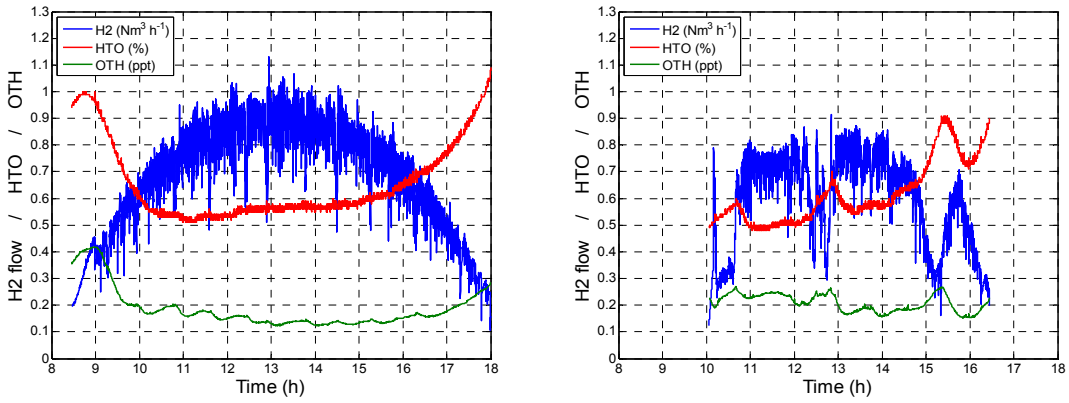

Figure 7: PV Energy source tests for both days (Left: 1st day; Right: 2nd day). Hydrogen production rate (H2), Oxygen purity (HTO) and Hydrogen purity (OTH).

Figure 7 shows the hydrogen production rate (H2) during the PV energy source emulation for both days, as well as the gas purity (Hydrogen: OTH; Oxygen: HTO). It can be observed, how the H2 production rate trails the current profile on Figure 6 although with strong variations of the amplitude due to the repetitive opening and closing of the valves regulating the electrolyte level in the electrolyser. It can also be noted, comparing Figures 6 and 7, that the hydrogen dynamics are decoupled from the I_E, since the electrical dynamics can be significantly faster than those associated to fluids. Concerning the purity of the gases, note how the OTH and HTO trends are inversely proportional to the hydrogen production. The higher the H2 production rate is, the more rapidly the gases are displaced from the stack and the less time the gases stay in the anodic and cathodic compartments; thus, the lower the mixing of the gases diffused through the gas separator membrane is. On the 1st day, the OTH ranges from 0.13 – 0.42 ppt (part per thousand), and HTO ranges from 0.52 to 1.1%. On the 2nd day, OTH ranges from 0.16 – 0.25 ppt, and HTO ranges from 0.5 to 0.9%. Comparing the gas impurity data along the various tests, it is concluded that the HTO is about 40 times higher than the OTH during the 1st day; and about 30 times higher during the 2nd day. The difference between the gas purities is due to the significantly higher diffusion coefficient of hydrogen through the gas separator membrane of the electrolytic cells than oxygen, because it is such a smaller particle (2 g/mol of hydrogen versus 16 g/mol of oxygen).

Last, the average energy consumption rate per Nm^3 (C_E) and efficiency were calculated (η_E). The stack C_E was calculated according to:

$$C_E = \frac{\int_0^{\Delta t} I_E \, V_E \, dt}{\int_0^{\Delta t} H2 \, dt} \quad (5)$$

where Δt is the test time elapsed (9h and 28' on the 1st day; and 6h and 24' on the 2nd day). The efficiency (η_E) was calculated based on the hydrogen high heating value (*HHV*, 3.5 kWh/Nm^3)*:*

$$\eta_E = 100 \frac{\text{HHV of } 1\text{Nm}^3}{C_E} \quad (6)$$

The results obtained on the test carried out during the 1st day; that is to say, with low irradiance variability, yielded: C_E = 4908 Wh/Nm^3 and η_E = 72.1%. Whereas the results on the 2nd day yielded: C_E = 4842 Wh/Nm^3 y η_E = 73.3%. Comparing both sets of results, it can be concluded that the variability of the working conditions has not negatively affected the electrolyser behaviour. The electrolyser dynamics is coupled to the variations but do not affect the energy efficiency. The minimal difference on the efficiency rate obtained is a result of the electrolyser functioning dependence on the instant current value applied. Finally, it is noteworthy that in any case, the efficiency of both tests was high.

3 Conclusions

This paper studies the behaviour of a 1 Nm^3/h alkaline electrolyser fed by a 5.1 kW PV system. The PV profile is emulated by a custom-made electronic device, capable as well of characterizing and modelling the electrolyser.

The PV supply profile is defined according to real irradiance measurements that are applied to a real PV installation to calculate what the actual generated electric power would be. The electronic device accordingly emulates the PV profile and feeds it to the electrolyser.0

The simulation was carried out for two different days, representative of fundamentally different working conditions. During the first day, the irradiance barely fluctuates; whereas during the second day, the irradiance is highly variable. The experimental results show how the electrolyser is capable of producing hydrogen even under a highly fluctuating electrical supply. The electrolyser behaviour is satisfactory. The electrolyser efficiency is high and none of the electrolyser production restrictions and protections is set off, despite the fact that the electrolyser is not designed, a priori, to be coupled with renewable energy sources, especially if they present a high variability.

Acknowledgements

The authors are thankful to the companies INGETEAM and ACCIONA Biocombustibles, and more in particular to J.Pérez and E.Guelbenzu, as well as to the Spanish Ministry of Science and Innovation (DPI2006-15703-C02-02) for sponsoring this project.

References

[1] Informe 2008, Red Eléctrica de España (Report 2008, Spanish Transmission System Operator), www.ree.es

[2] N. A. Kelly, T. L. Gibson, D. B. Ouwerkerk, “A solar-powered, high-efficiency hydrogen fuelling system using high-pressure electrolysis of water: design and initial result”, Int. J. Hydrogen Energy, vol. 33, pp. 2747-2764, 2008.

[3] J. G. G. Clúa, R. J. Mantz, H. De Battista, “Hybrid control of photovoltaic-hydrogen energy system,” Int. J. Hydrogen Energy, vol. 33, pp. 3455-3459, 2008.

[4] B. Paul, J. Andrews, “Optimal coupling of photovoltaic array to PEM electrolysers in solar-hydrogen systems for remote area power supply”, Int. J. Hydrogen Energy, vol. 33, pp. 490-498, 2008.

[5] A. Contreras, R. Guirado, T. N. Veziroglu, “Design and simulation of the power control systems of a plant for the generation of hydrogen via electrolysis, using photovoltaic solar energy”, Int. J. Hydrogen Energy, vol. 32, pp. 4635-4640, 2007.

[6] E. Guelbenzu, P. Sanchis, A. Ursúa, L. Marroyo, L. M. Gandía, P. M. Diéguez, Internacional Patent Appl. Nr. WO2007/057493, Applicant Acciona Biocombustibles.

[7] L. M. Gandía, R. Oroz, A. Ursúa, P. Sanchis, P. M. Diéguez, “Renewable hydrogen production: performance of an alkaline water electrolyser working under emulated wind conditions”, Energy & Fuels, vol. 21, pp. 1699-1706, 2007.

[8] A. Ursúa, L. Marroyo, E. Gubía, L. M. Gandía, P. M. Diéguez, P. Sanchis, “Influence of the power supply on the energy efficiency of an alkaline water electrolyser”, Int. J. Hydrogen Energy, vol. 34, pp. 3221-3233, 2009.

[9] O. Ulleberg,” Modeling of advanced alkaline electrolysers: a system simulation approach”, Int. J. Hydrogen Energy, vol. 28, pp. 21-33, 2003.

Polymer Electrolyte Membrane (PEM) Water Electrolysis

Tom Smolinka, Sebastian Rau, and Christopher Hebling

Abstract

Water electrolysis represents one of the simplest approaches to produce hydrogen and oxygen in a zero-pollution process by using electricity for the electrochemical decomposition of water. In Polymer Electrolyte Membrane (PEM) electrolysis cells, an acidic ionomer is used as the electrolyte. During the past decade, considerable progress has been made to advance this technology. Today, PEM electrolyzers can be regarded as a well-established industrial technology and are close to broader commercialization. An overview of the technical implementation of PEM water electrolysis is given in this chapter. Efficiency values and a selection of materials will be presented for a single cell and at the stack level. Lifetimes and degradation mechanisms will be considered. Finally, production rates and the power consumption for the system will be discussed.

A Review and Current Evaluation of a Decade of Concentrated PEM Fuel Cell Development at Hydrogenics 2000 to 2010

Mark Kammerer, Hydrogenics GmbH, Germany

A reality for many fuel cell systems developers in the first decade in the current millennium has been the existence of very many successful prototype projects from a technical standpoint, but relatively few commercial fuel cell product introductions. Apart from some beginnings of market volume breakthroughs in the portable fuel cell and specialized telecom back-up sectors, the same can be said about the stationary market growth. The inhibitors to commercialization have been not any one factor, but many obstacles requiring hurdling on the way to meeting the market acceptance thresholds. The list of necessary criteria to fulfill spans categories from performance and durability, to manufacturability, reliability and maintainability, to certification and safety, to cost.

Over the past decade, one by one, many of the challenges have been solved, and one-by-one, the barriers have been peeled away to a point now in 2010 one can argue, in a several early markets, there remains one barrier: price point. In some markets it can be argued that there remain no barriers except social inertia.

1 Durability and Stack Development

At the beginning of the decade many PEM developers celebrated reaching 100's of hours of operation, and by the middle of the decade, ambitious targets of 5 000 hours by 2010 necessary for the personal automotive application were set. Now in 2010 the automotive targets have been surpassed. 10 000 h is now a published expected lifetime by several stack manufacturers.

In figure 1, the progress of the H2X 500 Series (500 cm^2 nominal active area) stack is presented, showing more than 5-fold increase in power density per cell and a 500-fold increase in tested operation over the 10 year period. Currently there are no major limitations yet encountered which would prevent further durability improvements into the future.

	501 Series	505 Series	505.2 Series	506.5 Series	506.6 Series
Peak Power	3 kW	6 kW	14 kW	15 kW	20 kW
Power Density	50 W/cell	100 W/cell	233 W/cell	250 W/cell	330 W/cell
Pressure	Medium	Medium	Low	Low	Low
Temperature	80 ºC	80 ºC	65 ºC	≤ 60°C	≤ 70°C
Humidification	Full	Full	Partial	Zero	Zero
Durability	20 hrs	400 hrs	4 000 hrs	8 000 hrs	10 000 hrs

Figure 1: History of Hydrogenics FC Stack Development.

In figure 2, the improvements in durability results of the stacks in test stands running duty cycles from real world applications shows very good improvements for the stacks running on humidified (saturated) input gases towards the 5 000 h target.

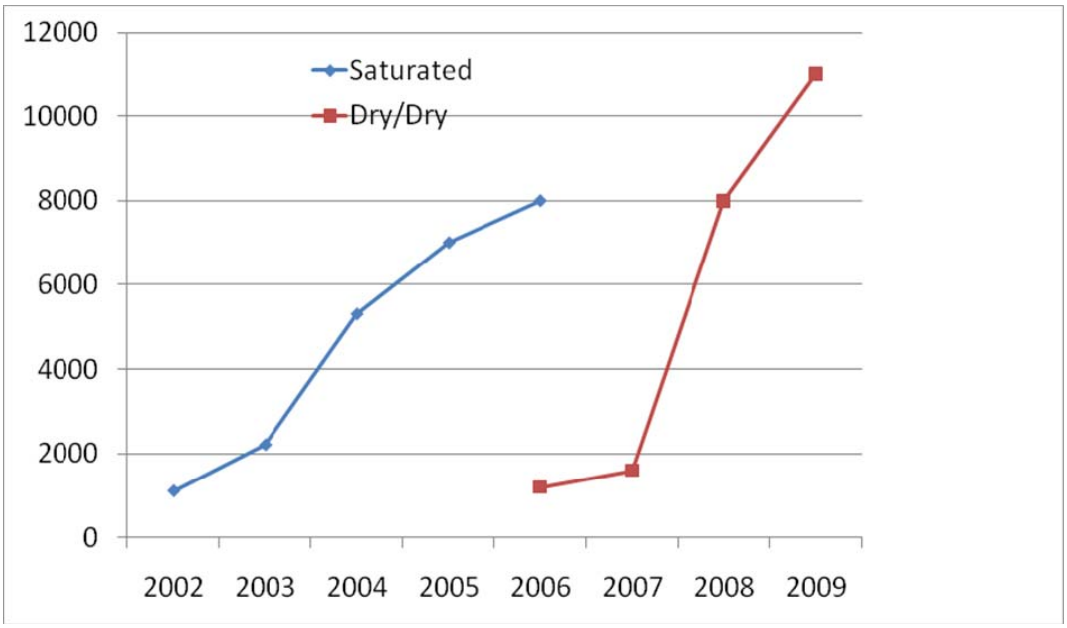

Figure 2: H2X stack lifetime – humidified vs. non-humidified.

Removing the humidifying components and running dry on the anode and cathode inlets was initially decided for back-up applications with low required run-times, but improvements in the MEA's allowed continued improvements, while simplifying the operational requirements of the stack resulting in a more simple and therefore cost-effective and reliable system. 10 000 hours is now possible.

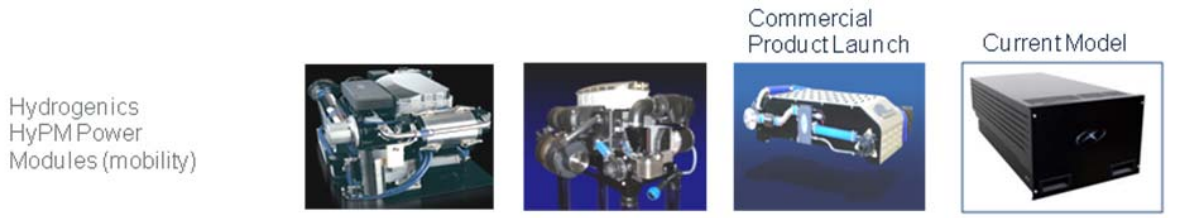

	2001	2002	2003	2009
Stack Pressure	High	High	Low	Low
Power	25 kW	25 kW	20 kW	16.5 kW
System Mass Power Density	290 kg **86 W/kg**	200 kg **125 W/kg**	170 kg **117 W/kg**	92 kg **180 W/kg**
System Volume Power Density	365 L **68 W/L**	340 L **73 W/L**	180 L **111 W/L**	133 L **124 W/L**
System Efficiency	45…38%	45…38%	54…40%	**54…48%**
Major Components	25	19	8	6
Onboard water	Required	Required	Not required. With Ca and An saturators.	**Not required** **No saturators**

Figure 3: Fuel cell system development – Hydrogenics HyPM™ Power Module.

2 System Development

On the system level, also dramatic improvements have been made over the last decade. Power densities have doubled, both by weight and by volume, while efficiencies have increased and system complexity has decreased, by eliminating major components, resulting on a more cost-effective, compact and more reliable system.

In November 2002 the commercial product launch of the 10 kW fuel cell power module was announced, called the HyPM 10 and deliveries to customers commenced in 2003. The concept was one module – many applications, but by 2005 it was clear that the model should be split in to two versions; a version for stationary rack-mount, optimized for backup-power applications, and a version for applications requiring maximum durability, especially mobile applications. The XR (eXtended Run back-up) and HD (Heavy Duty, High Durability) family had been started. The rated power was in creased from 10 kW to 12 kW, and in 2006 further power level sizes were introduced, followed by two compact mobile versions based on the compact 200 cm^2 stack. Following is the current line-up today in 2010 (Figures 4 and 5).

	XR 4	XR 8	XR 12	XR-L 4	XR-L 8	XR-L 12
Rated Power (kW)	4.5	8.5	12.5	4.5	8.5	12.5
Peak Power (kW)	5.5	9.5	14.5	5.5	9.5	14.5
Voltage (VDC)	30-38	24-38	37-57	30-38	24-38	37-57
Dimensions (cm)	87x50x32	87x50x32	96x50x32	87x50x32	87x50x32	96x50x32
Volume (L)	139	139	154	139	139	154
Mass (kg)	80	80	90	80	80	90
Expected lifetime (h)	1 000+	1 000+	1 000+	10 000+	10 000+	10 000+

Figure 4: 2010 HyPM™ XR Stationary Power Module Family.

	HD 4-200	HD 8-200	HD 4-500	HD 8-500	HD 12-500	HD 16-500	HD 33	HD 100
Rated Power (kW)	4.5	8.5	4.5	8.5	12.5	16.5	33	100
Peak Power (kW)	5.5	9.5	5.5	9.5	14.5	18.5	37	110
Voltage (VDC)	58-79	48-79	20-40	20-40	36-57	48-76	80-160	240-480
Dimensions (cm)	85x36x25	85x36x25	79x45x30	79x45x30	94x45x30	96x51x41	115x105x45	150x115x85
Volume (L)	77	77	78	78	127	201	543	1140
Mass (kg)	75	75	105	105	78	92	325	750
Expected lifetime (h)	10 000+	10 000+	10 000+	10 000+	10 000+	10 000+	10 000+	10 000+

Figure 5: 2010 HyPM™ HD Mobile Power Module Family.

3 Reliability

Absolutely critical, besides durability is reliability. The fuel cell system must start each any every time without fail. Based on accelerated start-up/shutdown testing – the worst punishment for a PEM fuel cell – 6000 cycles were achieved, which means in practice essentially unlimited start-ups and shutdowns.

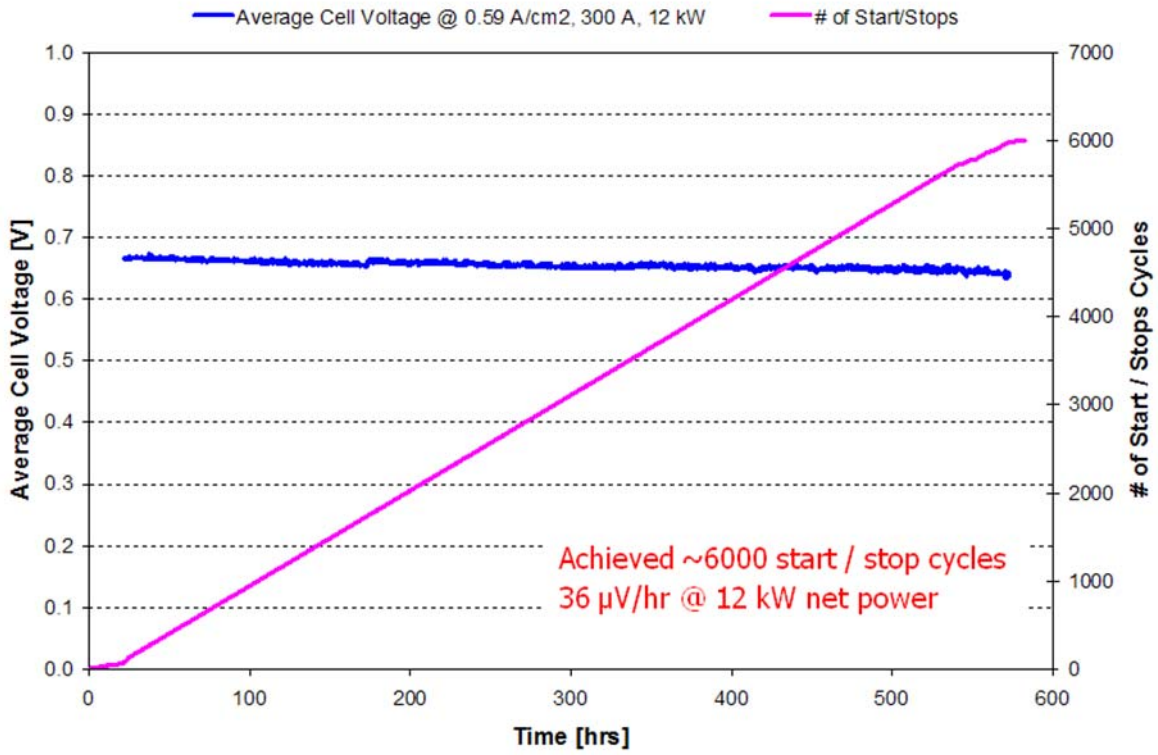

Figure 6: Accelerated Start/Stop Cycle Test results establishing unlimited start/stops.

4 Field Reliability Experience

Reliability has also been proven empirically in an extremely wide range of vehicles, applications and geographies [1]. In material handling and fleet vehicles a wide range of alpha followed by beta prototypes have been realized, which help evaluate and seed future markets, establish certification measures, validate the technology, provide maintenance data and experience and feed back into product improvements. The first alpha prototype demos from Hydrogenics were in 2005, and currently more than 60 forklifts are operating with HyPM fuel cells in real commercial service in North America and Europe [2-4].

In transit bus applications progress beyond 10 000 hours of expected stack lifetime is necessary, with cost reduction – which is largely but not entirely tied to the volume of production. Stack cost reduction, eventually leading to a tolerable frequency of stack renewal will allow feasibility of exchanging stacks in the system's lifetime to achieve the 40 000 h or 50 000 h typical of diesel engines in commercial vehicle today. Diesel-Hybrid

and CNG-Hybrid developments are paving the way for adding Fuel Cells to the Hybrids. Fuel Cell Plug-in scenarios may also play a significant role.

In stationary power Hydrogenics HyPM XR FCPM's are commercialized in the Datacenter [5] and Telecom UPS [6,7] sectors and the Data center configuration assembled with HD Long-Life stack technology is finding its place in standby prime power for renewable energy applications.

References

[1] Hickham Air Force Base: Fuel Cell Vehicles: Early Implementation Experience, Technical Report, NREL/TP-560-42233, Leslie Eudy, National Renewable Energy Laboratory, Kevin Chandler, Battelle, October 2007, http://www.nrel.gov/hydrogen/pdfs/42233.pdf

[2] Hamburg Sagt „Ja" zum Wasserstoff (Hamburg says „Yes" to Hydrogen), Annual report 2009 Hamburg Airport: http://www.airport.de/resources/downloads/GB_2009_web(5).pdf Page 39 (PDF Page 22).

[3] Linde MH liefert erste Stapler mit Brennstoffzelle aus (Linde MH deliveres the first Forklifts with Fuel Cells), Press Release 20.01.2010: http://www.linde-mh.de/de/countrysite/news_infoservice_1/newspressedetails_1216.html

[4] Linde Material Handling stellt ersten alltagstauglichen Brennstoffzellengabelstapler vor (Linde Material Handling presents the first everyday-suited Fuel Cell Forklifts), Press Article, May 2010: http://www.linde-mh.de/de/countrysite/news_infoservice_1/newsinfos.html

[5] APC Announces Next Generation Fuel Cell Product for Data Centers, Press Release, August 19, 2008 http://www.apc.com/site/press_center/index.cfm/apc-announces-next-generation-fuel-cell-product-for-data-centers/

[6] Andrew Fuel Cell Outdoor Cabinets, Product Website, http://www.commscope.com/andrew/eng/product/cabinet_enclosure/pbuc/1207153_17208.html

[7] Fuel Cell Technology: An Emerging Solution for Back-Up Power to Replace or Supplement the Traditional Solutions, Paper INTELEC 2010, R Szasz, MTS Allstream; J Lemos, Hydrogenics

Recent Advances in the Development of Unitized Regenerative Fuel cells based on PEM technology

Alireza Ranjbari, **Pierre Millet**, University of Paris 11, France
Serguey Grigoriev, **Vladimir Fateev**, Kurchatov Institute, Russia

Abstract

Unitized Regenerative Fuel Cells (URFC) are reversible electrochemical devices which can alternatively operate as a water electrolyser or a H_2/O_2 (air) fuel cell. Results reported in this communication are related to R&D on bi-functional electrocatalysts and stack development. Pt-Ir mixtures have been used as anodic catalyst for water and hydrogen oxidation. Carbon-supported platinum has been used for hydrogen evolution and oxygen reduction. A two-cell stack with 250 cm^2 active area electrodes has been assembled and successfully tested. Electrochemical performances are close to those obtained with conventional water electrolysers and H_2/O_2 fuel cells. Typical cell voltages of 1.55 and 0.70 V have been recorded at a current density of 0.2 $A.cm^{-2}$, during respectively water electrolysis and H_2/O_2 fuel cell operation.

1 Introduction

Proton Exchange Membrane (PEM) technology can be used for the development of unitized regenerative fuel cells (URFCs) operating either as water electrolysers (WE) or as H_2/O_2 fuel cells (FC) [1-4]. In conventional PEM water electrolysis technology, platinum is used as electrocatalyst for the hydrogen evolution reaction (HER) at the cathode and iridium (metal or oxide) is used as electrocatalyst for the oxygen evolution reaction (OER) at the anode. In conventional H_2/O_2 PEM fuel cell technology, platinum is used as electrocatalyst for both the hydrogen oxidation reactions (HOR) at the negative and for the oxygen reduction reaction (ORR) at the positive. Platinum group metals can thus be used as electrocatalysts in PEM-URFCs, but there are some specific problems to be handled to turn efficient water electrolysis cells and fuel cells into efficient URFCs. Potentially, there are two different designs for reversible cells: (i) one is using truly reversible oxygen and hydrogen electrodes and (ii) the other is using electrodes which do not change their redox function when the mode of operation is switched from electrolysis to fuel cell. Results reported here concern the second design which was found to be the most efficient although gas management is more complicated [5]. As in electrolysers and fuel cells, reversible cells can be stacked into a stack to adjust the gas and electric power productions of the URFC to process requirements. Basic components of PEM reversible cells are (i) solid polymer electrolyte (membrane), (ii) anodic and cathodic electrocatalytic layers, (iii) gas diffusion electrodes (GDE), and also separating bipolar plates. The purpose of the work reported in this communication was double. First, to develop efficient PEM-URFCs with low platinum-group-metals loadings and improved life time performances during cycling. To achieve this goal, bi-functional electrocatalytic layers and specific GDEs were developed and optimized for operation in both electrolysis and fuel cell modes. Then, to obtain a proof-of-concept using large surface area electrodes (250 cm^2) and

stack configuration (2 cells). These results were obtained in the course of the GenHyPEM STREP program supported by the European Commission.

2 Results and Discussions

2.1 Lab-scale results

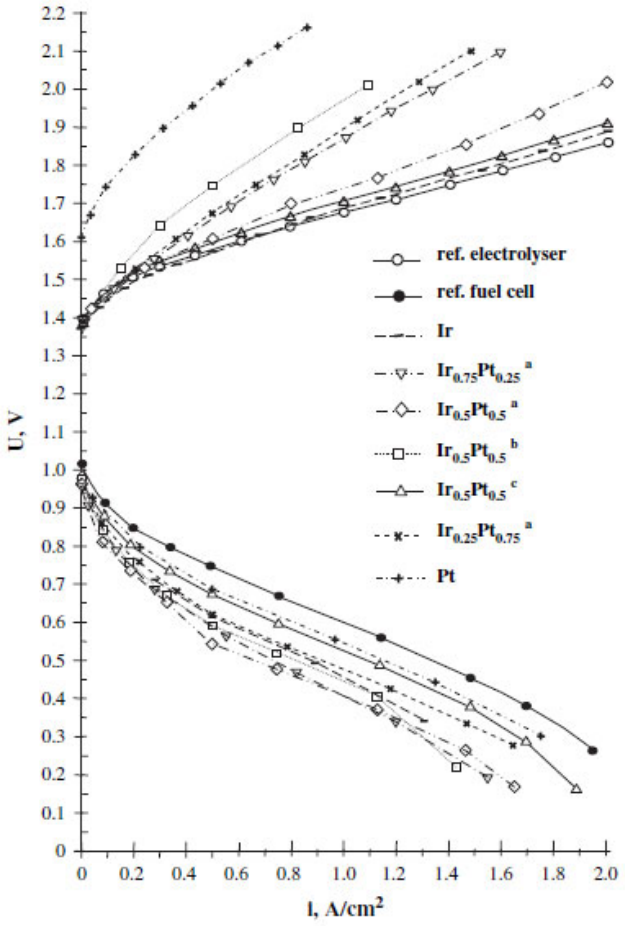

FC mode:

T_{cell} = 80°C, P_{H2} = 2.8 bar and P_{O2} = 3.0 bar; humidification temperature for H_2 = 85°C;

H_2 and O_2 flow rates : 160 ml min^{-1};

WE mode:

T_{cell} = 90°C; P_{H2} = P_{O2} = 1 bar.

Figure 1: Current–voltage relationships measured using a reference electrolysis cell (o), a reference PEM fuel cell (•), and reversible cells with anodes made of various Ir_xPt_y catalytic compositions. S=7 cm^2.

Membrane electrode assemblies (MEAs) used for operation in the PEM-URFC were firstly optimized at the lab scale (7 cm^2 monocell), using different catalysts. Typical polarization curves measured on a conventional PEM-WE cell (o) and on a conventional H_2/O_2 PEM-FC (•) are plotted in figure 1 for reference. Current-voltage polarization curves measured in both WE and FC modes using a URFC monocell are also plotted in figure 1. Pt40/Vulcan®XC-72 mixtures were used at the cathode (for the HER and the ORR) and Pt-Ir mixtures of various compositions have been tested as bi-functional electrocatalysts at the anode. As a general trend, homogeneous Pt-Ir mixtures did not provide satisfactory results, electrochemical performances being largely inferior to those measured on references cells. Best performances were obtained using a first thin and porous layer of metallic iridium deposited

directly against the SPE and a second layer of platinum placed on top. Using this two-layer structure, best current-voltage performances were obtained using 50 wt.% Pt and 50 wt.% Ir, both in WE and FC modes. As can be seen from figure 1, when proper catalytic compositions are used, electrochemical performances close to those measured on individual electrolysis cells and fuel cells are measured.

2.2 Two-cell stack performances

A two-cell stack URFC with two MEAs (250 cm^2 each) has been developed and tested. Nafion 117 was used as solid polymer electrolyte. A 3 mm thick titanium foil was used as bipolar plate to separate the two cells. Internal cell design has been optimized to improve the hydrodynamics of water-gas mixtures (electrolysis operation) and distribution of gases (fuel cell operation). During water electrolysis experiments, the URFC was directly powered using a 250A-50V DC power supply. A specific automated test station was used to measure stationary polarization curves. During H_2/O_2 fuel cell experiments, humidified H_2 and O_2 gases were provided by a PEM water electrolyser in the 1 to 10 bar pressure range. It was thus possible to adjust gas flows and input pressures to analyze their impact on the performances of the URFC. Typical polarization curves measured on this two-cell stack are plotted in figure 2 (circles). They are compared to those obtained on conventional cells of similar size. Although less efficient performances were obtained with the stack, encouraging results were measured under steady state conditions.

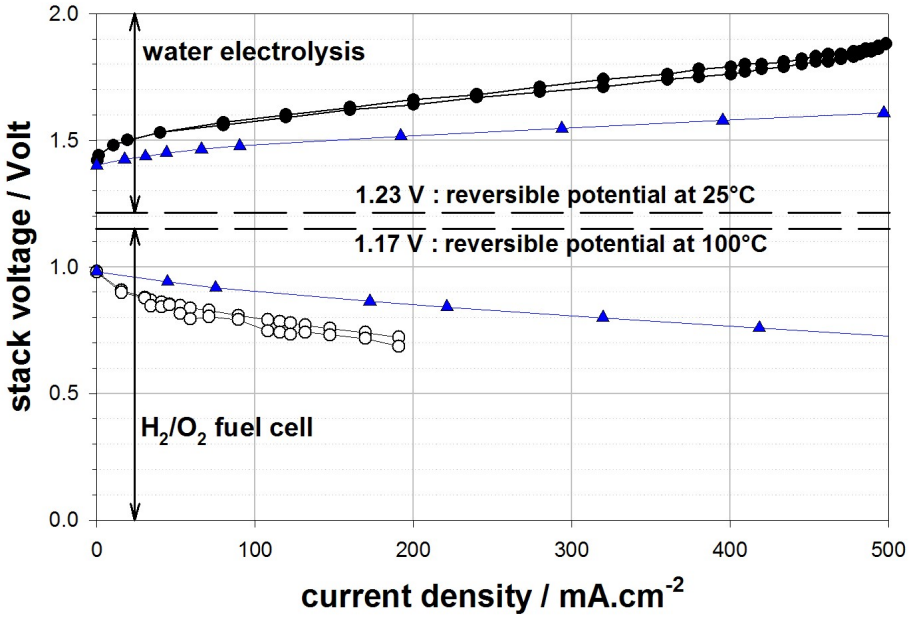

Figure 2: Individual polarisation curves measured on the two-cell PEM URFC (S = 250 cm^2): (●) water electrolysis; T = 51°C; (o) H_2/O_2 fuel cell; T = 80°C; (▲) WE and FC reference curves; T = 80°C.

2.3 Alternative WE and FC operation

The development of URFCs that can maintain their performances during a significant number of alternative cycles is also very challenging. A simple experimental protocol has been used to assess the capability of the URFC stack to maintain its electrochemical performances on the long-term (≈ 100 cycles, 30 minutes long at *ca.* 500 $mA.cm^{-2}$). Results, the detail of which cannot be reported within the format of this communication, show that electrochemical performances in stationary conditions of operation remain mostly stable. However, several minutes are required to stabilize performances after switching from WE to FC modes and conversely.

3 Conclusion and Perspectives

Some results obtained on Unitized Regenerative Fuel Cells in the course of the EC-supported GenHyPEM project are presented in this paper. The development and characterisation of electrodes where similar redox processes (reduction or oxidation) are taking place during water electrolysis and fuel cell experiments have been privileged. Lab-scale results obtained on 7 cm^2 reversible cells with optimized electrocatalytic compositions are encouraging, showing rather high electrochemical performances close to those obtained on conventional water electrolysis and H_2/O_2 cells. Best cell performances, both in electrolysis and fuel cell modes, were obtained with Pt-Ir black bi-layers, when the Ir-layer is directly facing the membrane. The use of porous titanium as anodic gas diffusion electrode during fuel cell experiments provides similar current-voltage performances to those obtained with conventional carbon cloth electrode. Carbon cloth or paper demonstrated a sufficient stability at the cathode. Stable and reproducible results have been obtained over several tens of cycles, alternating water electrolysis and H_2/O_2 experiments at a constant current density of 500 $mA.cm^{-2}$. The possibility of using other electrocatalysts (Pt and mixed oxides, such as nanostructured $Ru_xIr_ySn_{1-x-y}O_2$) is still under investigation. A two-cell stack with 250 cm^2 MEAs has been developed and tested. Encouraging performances have been obtained during both water electrolysis and fuel cell experiments. Experiments have been conducted over a limited (≈ 100) number of operating cycles. No significant loss of performances was observed though.

Acknowledgements

This work has been financially supported by the European Commission (GenHyPEM project 019802), by the UK Royal Society (International Joint Projects 2006/R4), by the Federal Agency for Science and Innovations of the Russian Federation within the framework of the Federal Principal Scientific-Technical Programme “Researches and development on priority directions in development of scientific technological complex of Russia for 2007-2012”, and by the Global Energy International Prize Non-Profit Foundation (Grant No. MG-2008/04/3).

References

[1] J.S. Bone, S. Gilman, L.W. Niedrach, M.D. Read. Ion-exchange regenerative fuel cells. In: Proceedings of the 15th Annual Power Source Conf., p. 47-49, Ft. Monmouth, N. J.; May 9-11, 1961.

[2] S. Hauff, K. Bolwin. System mass optimization of hydrogen/oxygen based regenerative fuel cells for geosynchronous space missions. J Power Sources 38 (1992) 303-15.

[3] F. Mitlitsky, B. Myers, A.H. Weisberg. Regenerative Fuel Cell Systems. Energy & Fuels 12-1 (1998) 56-71.

[4] F. Mitlitsky, B. Myers, A.H. Weisberg, T.M. Molter, W.F. Smith. Reversible (unitized) PEM fuel cell devices. Fuel Cells Bulletin 2 (1999) 6-11.

New Composite Membranes for Application in a PEM Electrolyser

Jesús Ferre, **Sergio Mollá**, **Jessica Calleja**, **Leire Zubizarreta**,
Energy Technology Institute (ITE), Av. Juan de la Cierva 24, Parque Tecnológico de Valencia, 46980 Paterna-Valencia, Spain

1 Introduction

Water electrolysers using proton exchange membranes (PEM) offer high prospective potentialities for the production of pure hydrogen. This application can produce hydrogen from energy sources and can contribute to reduce CO_2 emissions [1]. The performance of a PEM electrolyser is strongly related to the characteristics of the membrane and electrodes assembly, membrane electrode assembly (MEA), where the electrochemical reaction takes place. Generally, Nafion® membrane, a perfluorinated sulfocationic polymer, is used as proton conductive polymer electrolyte in PEM electrolyser systems. To improve some drawbacks of Nafion® polymer, composite membranes using additional reinforcements such as metal oxides or other reactive has been added to the Nafion polymer [2].

Particularly interesting are Nafion®-conducting polymer composites in which the ionomer, besides behaving as host network for the conducting polymer, provides doping anions and protons, both being essential to electronic conductivity in polyaniline (PANI) [3-4]. Composites of Nafion-PANI have shown good conductivity properties, and moreover, it has shown the possibility to work at high temperature, which means an increment in the performance of reaction [5-6].

In this work, PANI intercalations have been produced by in-situ polymerization of aniline in Nafion®. Membranes with different polymerization times were synthesized at ambient temperature to evaluate the optimum thickness of PANI layer. In this sense, two acid solutions containing an oxidant and aniline respectively were contacted with both faces of a commercial Nafion® membrane.

The properties of the obtained membranes were characterized by different techniques. Water uptake and the ion-exchange capacity (IEC) were determined in the different membranes. Impedance spectroscopy measurements were used to obtain the impedance of membranes and to calculate the protonic conductivity.

Finally, a test bench with a two-cell electrolyser was developed in order to study the performance of the Nafion-PANI membranes was evaluated in a two-cell electrolyser. A range of temperatures between 50-90ºC was used to determine the polarization curves.

The results obtained show that the reaction time of polymerization of aniline affects to the final properties of the membranes, furthermore these properties directly influence on the membrane performance in an electrolyser.

2 Experimental and results

2.1 Polyaniline synthesis

The composite membranes of Nafion-PANI were prepared by means of aniline polymerization within the Nafion network in acid medium. A vertically fixed membrane of Nafion N115 was placed between solutions of 0.01 M $FeCl_3$ in 0.5 M H_2SO_4, and 0.01 M aniline in 0.5 M H_2SO_4, as schematically shown in Figure 1. In acid medium, aniline exists as phenylammonium cations acting as counterions for the sulfonic groups, thus being protons in the membrane exchanged with aniline cations (An^+). Fe^{3+} ions act as redox-catalyst oxidizing aniline. The colour intensity depends on the balance between oxidized (doped) and reduced (undoped) forms of polyaniline and the exposure duration in working solutions [3]. Composite membranes were obtained using different polymerization times and ambient temperature.

The membranes were equilibrated in a 2M HCl solution overnight. The acidic membranes were further washed several times with distilled water.

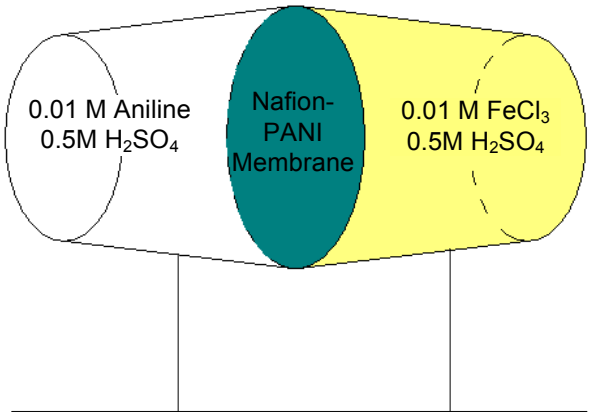

Figure 1: Diagram of reactive system used for polymerization of aniline in the Nafion® network. The membrane was vertically placed between two solutions.

Table 1: Water uptake and ion-exchange capacity (IEC) of Nafion and Nafion-PANI membranes with different polymerization times.

Membrane ($t_{polymerization}$)	Water uptake (kg water/kg wet membrane)	IEC (equiv. H^+/kg wet membrane)
Nafion	0.28	0.92
PANI 1h	0.24	0.91
PANI 5h	0.24	0.88
PANI 8h	0.28	0.85
PANI 24h	0.22	0.72
PANI 168h	0.20	0.64

2.2 Water uptake

A piece of washed membrane was dried at 90ºC during one hour, determining the dry mass of membrane. Then the piece of membrane was submerged in distilled water at 70ºC during one hour and afterwards superficially dried by gently blotting filter paper and weighed. The values of water uptake are collected in Table 1 and show that this parameter is practically independent on the aniline content of the composite membranes. Similar results have recently been reported for alike membranes [3-7].

2.3 Ion-exchange capacity

The washed membranes were equilibrated with a 2 M sodium chloride solution; the protons were exchanged by sodium cations and then titrated with a 0.01 M sodium hydroxide solution. The values of the ion-exchange capacities of the membranes are given in Table 1, and show that this parameter decreases with the aniline polymerization time, decreasing in linear mode during the first 24 hours.

2.4 Impedance spectroscopy measurements

The electrochemical technique of impedance spectroscopy is based on the analysis of response of an electrochemical system (the membrane) with the application of alternating current with variable frequency. This response is the impedance, a complex variable, which is represented through the modulus value, $|Z|$, and the phase angle, Φ, versus the frequency, a representation known as Bode diagram. The fundaments of this technique can be consulted in [3].

This study was realized for several membranes using different temperatures, i.e. 25, 50, 70 and 90 ºC. In Figure 2 it is shown the Bode diagram for different membranes at 70ºC. In this chart it can be observed that the value of modulus of impedance approaches to a constant value when the phase angle approaches to zero. The value of impedance in this plateau is the corresponding to protonic conductivity by the expression:

$$\sigma = \frac{L}{R \cdot A} \tag{1}$$

In this expression, R is the impedance modulus, L is the membrane thickness and A is the membrane area.

The conductivity values for different membranes at temperatures between 25-90ºC are shown in Table 2. It is observed that the conductivity rises with temperature, furthermore the maximum values were mainly obtained with the Nafion-PANI membrane prepared with 5 hours of polymerization time.

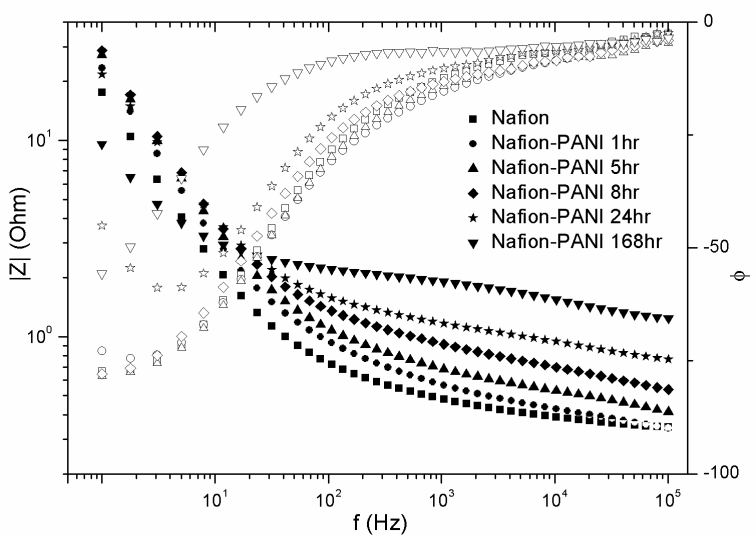

Figure 2: Bode diagram for different membranes at 70ºC. Filled and open symbols represent, respectively, the impedance modulus and the out of phase angle.

Table 2: Values of protonic conductivity, in S/m, as a function of temperature for Nafion-PANI membranes with different polymerization times.

$t_{polim.}$ (hr)	25ºC	50ºC	70ºC	90ºC
Nafion	2.4	2.3	3.8	3.5
PANI 1h	2.8	2.9	3.8	3.6
PANI 5h	3.4	2.8	3.3	4.9
PANI 8h	1.9	2.5	2.8	2.7
PANI 24h	1.7	2.6	2.1	2.8
PANI 168h	0.7	1.0	1.2	1.1

2.5 Electrolyser performance

The performance of the composite membranes in electrolysis operation was evaluated in a two-cell electrolyser with a circular active area of 28 cm^2. The electrolyser was mounted in a test bench developed to this aim and fed with ultrapure water. The tests were carried out at different temperatures, i.e. 50, 70, 80 and 90ºC, using membranes prepared with different aniline polymerization times, i.e. 3, 5, 8 and 10 hours. The membranes were coated with catalyst layers made up of Pt/C on the cathode and Iridium on the anode, deposited by FuMA-Tech GmbH (St. Ingbert, Germany), which are reported as suitable catalysts for electrolytic water splitting [8, 9].

The polarization curves were obtained with catalyst coated Nafion-PANI membranes as well as with a pristine Nafion® membrane for comparison. Voltage was stepwise incremented and current intensity recorded up to 6 V.

An interesting parameter is the specific energy consumption ES, which is defined as the amount of electricity (in kWh) required for the production of a given amount (for example one cubic meter) of hydrogen. It is expressed in units of kWh/Nm^3 [10]. In Figure 3 it is shown the evolution of this parameter versus the current density for the studied membranes at 70ºC.

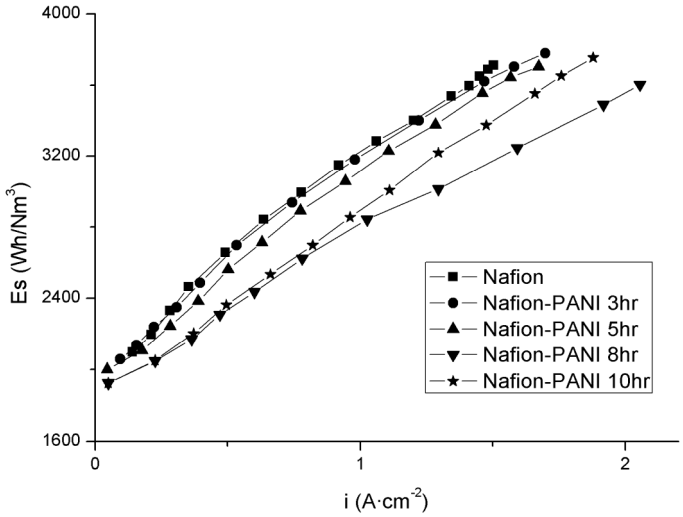

Figure 3: Specific energy consumption versus current density measured at 70ºC using different membranes.

The obtained results indicate that the quantity of polyaniline in Nafion, as a function of polymerization time, improves the electrolyser performance, although above 8 hours this effect is reversed.

3 Conclusions

The composite membranes of Nafion-PANI produced by in-situ aniline polymerization in the Nafion® network increase some properties as compared with pristine Nafion®. Their application in water electrolysis using PEM technology involves an increase in the system performance, due to the enhancement in membrane conductivity by the intercalations of conducting polymer in the structure.

The rise of the electrolyser performance is conditioned by the polymerization time used to obtain each membrane. The maximum value of performance was obtained at 8 hours of reaction time, however the maximum of conductivity was obtained at 5 hours. This indicates that the optimal point must be located within this range of polymerization times.

Acknowledgements

This work was supported by the European Regional Development Fund (ERDF) and the Ministry of Science and Innovation (Spain) in the context of the National Plan for Scientific research, Development and Innovation 2009-2011 (EPEMET: project ref. PID-590000-2009-9).

References

[1] F. Barbir, Solar Energy 78 (2005) 661–669.

[2] V. Antonucci, A. Di Blasi, V. Baglio, R. Ornelas, F. Matteucci, J. Ledesma-Garcia, L. Arriaga, A. Arico, Electrochimica Acta 53 (2008) 7350–7356.

[3] V. Compañ, E. Riande, F. Fernandez-Carretero, N. Berezina, and A. Sytcheva, J. of Membrane Science 318 (2008) 255–263.

[4] M. Fabrizio, G. Mengoli, M. Musiani, and F. Paolucci, J. of Electroanalytical Chemistry 300 (1991) 23–34.

[5] S. Tan, D. Bélanger, J. Phys. Chem 109 (2005) 23480-23490.

[6] K.W Lai, P.D. Beattie, F.P. Orfino, E. Simon, S. Holdcroft, Electrochimica Acta 44 (1999) 2559-2569.

[7] C.-Y. Chen, J.I. Garnica-Rodriguez, M.C. Duke, R.F. Dalla Costa, A.L. Dicks, J.C. Diniz da Costa, J. Power Sources 166 (2007) 324.

[8] S.A. Grigoriev, V.I Porembsky, V.N. Fateev, Int. J. of Hydrogen Energy 31 (2006) 171-175.

[9] A. Marshall, B. Borresen. G. Hagen, Tsypkin, R. Tunold, Energy 32 (2007) 431-436.

[10] P. Millet, R. Ngameni, S.A. Grigoriev, F. Brisset, A. Ranjbari, C. Etiévant, International Journal of Hydrogen Energy (2009) 1-10.

PEM Electrolyzer with Nano-structured Electrodes for High Efficient Hydrogen Production

S. Rau, **J. Colom Tomás**, **T. Smolinka**, Fraunhofer Institute for Solar Energy Systems ISE, Heidenhofstrasse 2, 79110 Freiburg, Germany
R.E. Fuentes, **J.W. Weidner**, University of South Carolina, Center for Electrochemical Engineering, Columbia, SC 29208, USA

1 Introduction

Hydrogen as a secondary energy carrier can play an important role in our future energy economy. Hydrogen can be stored, transported in tanks or pipe lines, is clean burning, and can be directly and efficiently converted into electricity using fuel cells. However, the major barrier is how to generate and supply pure hydrogen directly. One of the most efficient and simple ways to obtain hydrogen with high purity is the proton exchange membrane (PEM) water electrolysis. The main advantages against alkaline and steam water electrolysis is the high efficiency, compact design and fast response time against fluctuating energy supply. Therefore coupling of renewable energies with PEM electrolyzers is more and more regarded because hydrogen from PEM water electrolysis can match energy demand with energy supply.

For using PEM water electrolysis only water and electricity is necessary to produce hydrogen as well as oxygen as a by-product. The core component of every PEM water electrolyzer is the electrode membrane assembly, the so-called MEA. The membrane is only conductive for protons and works furthermore as a gas separator to avoid gas mixing inside the cell. Unfortunately PEM water electrolyzers suffer from membrane degradation and high costs of membrane and catalyst production. Currently, one of the main challenges is the large overpotential at typical current densities at the anode, where oxygen evolution reaction (OER) occurs. The OER depends strongly on the chemical and structural properties of the surface, being mainly determined by the interactions between a metal or metal oxide on the surface. The metal or its oxide used should be stable and conductive. These catalysts are usually unsupported because of the high corrosive conditions at the anode. Based on heterogeneous catalysis, a support is chosen to enhance the catalyst and promote the desired reaction. In electrochemical systems carbon support is chosen because of its high conductivity, rather than enhancement of activity. Since the anode of the water electrolyzer is operated at potentials higher than 0.9 V, carbon can corrode [1]. This corrosion can create a loss of electrical contact necessary for the transport of electrons, thus decreasing the performance. Also, platinum can increase the rate of corrosion of carbon [2]. Due to these limitations, research activities are underway to find a support that can be stable at high potentials and can help with the kinetics of the oxygen evolution reaction.

Some supports used in heterogeneous catalysis are composed of metal oxides, not only because of activity towards the selected reaction, but also because they are inert and non-corrosive. Specifically, titanium dioxide has been investigated for catalytic applications and

has been proved that its anatase structure is a more active catalyst for oxidizing hydroxil compounds, than its other structures rutile and brookite. The problem with titanium dioxide, as it is with metal oxides, presents a barrier for the conduction of electrons at low temperatures. Morris *et al.* [3] studied mixtures of NbO_2 and TiO_2 sintered at high temperatures to form $Nb_{0.1}Ti_{0.9}O_2$, but the material becomes the more stable and less catalytically active rutile structure. Chen *et al.* [4] measured the conductivity of this material and found a conductivity of 0.2-1.2 S/cm and a surface area of 1.4 m^2/g. We have refined the synthesis method of $Nb_{0.1}Ti_{0.9}O_2$ (here referred to as Nb-TiO_2) [5] and used it to deposit nanoparticles for the OER.

2 Results and Discussion

To examine the crystal structure of the pure TiO_2 (obtained from Sigma-Aldrich) and Nb-TiO_2 (synthesized via the method by Fuentes *et al.* [5]) support materials, X-ray diffraction (XRD) was performed on a Rigaku 405S5. The XRD patterns were compared with reference spectra using the software JADE (Materials Data, Inc.). Figure 1 presents the XRD spectra for Nb-TiO_2. The vertical blue lines in the spectrum represent the XRD peaks for anatase Titania using JADE. The parameter for anatase matches every peak demonstrating a good anatase TiO_2 structure. No other crystalline phases were detected in the sample, including distinct niobium oxides structures. For the same synthesis in Cassiers *et al.* [6], the crystal phases obtained for TiO_2 were a mixture of anatase and rutile. For our synthesis method, it appears that the addition of niobium into the synthesis procedure helps to maintain and preserve the anatase structure.

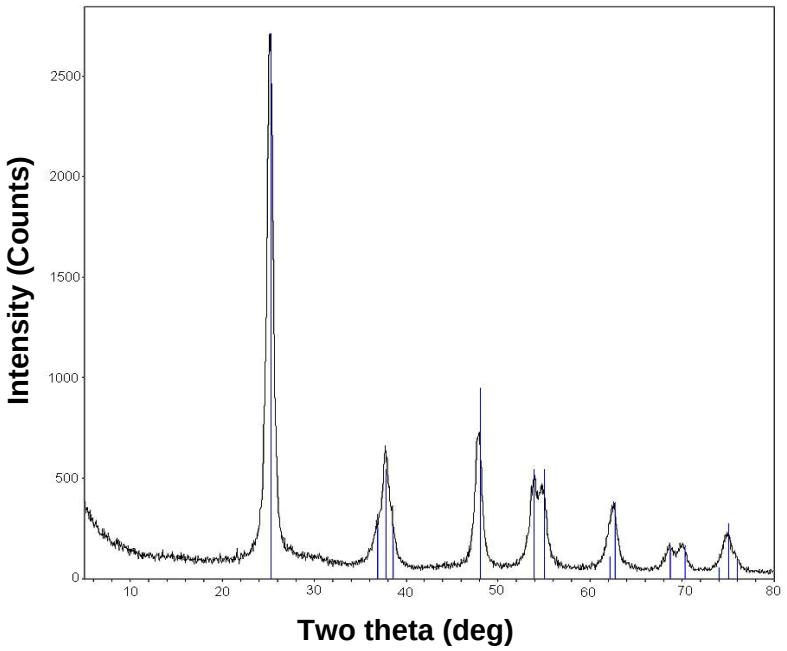

Figure 1: X-Ray Diffraction data for Nb-TiO_2. The blue lines represent the guidelines for anatase TiO_2.

Furthermore Brunauer-Emmett-Teller (BET) surface areas measurements were performed using a Nova 2000 High speed gas adsorption analyzer. The surface areas were obtained using liquid nitrogen at 77 K and a 6 point BET was used for calculating the specific surface area. The adsorbate used for BET was nitrogen gas. For anatase Nb-TiO_2, the surface area was 197 m^2/g, which is only 16% lower than the surface area of carbon Vulcan XC-72R (usually the support of commercial catalysts for fuel cells). However, this surface area is sufficiently lower than the 613 m^2/g for pure TiO_2 reported by Cassiers *et al.* [6]. However, their material contained a mixture of anatase and rutile. The pure TiO_2 anatase obtained from Sigma-Aldrich had a surface area of 166 m^2/g. We also prepared a rutile form of Nb-TiO_2 by raising the anatase form to 1000°C for 5 hours. The resulting surface area decreased to 5.0 m^2/g. The pure TiO_2 rutile obtained from Sigma-Aldrich had a surface area of 273 m^2/g.

A series of electrical conductivity tests, shown in Figure 2, were performed using different platinum weight percent to determine how the quantity of a conductive metal affects the conductivity of the composite electrode (i.e., Pt plus Nb-TiO_2 support). Platinum metal was used in this measurement for convenience.

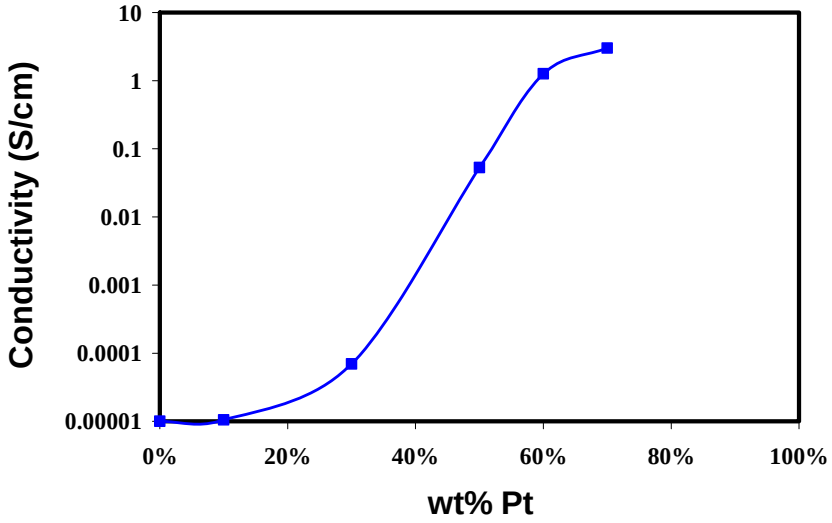

Figure 2: Conductivity of the composite electrode (i.e., Pt plus Nb-TiO_2 support) as a function of the weight percent loading of platinum.

Increasing the Pt loading to 60% increased the conductivity of the composite electrode from 10^{-5} to 1.26 S/cm. These results indicate that the mixture of metal particles and oxide material creates a significantly less resistive path for the transportation of electrons.

To examine the particle-size distribution of bimetallic nanoparticles on the oxide supports, high resolution transmission electron microscopy (HRTEM) images were obtained and shown in Figure 3. These images are for 60 wt% PtRu on commercial anatase (A) and rutile (B) TiO_2. The bright rounded images are the bimetallic metals, platinum and ruthenium and the dark areas are the TiO_2. The anatase TiO_2 particles are round in shape with a particle size in diameter of 10 to 15 nm. The TiO_2 in its rutile form are presented in a more elliptical shape with higher particle size than anatase TiO_2. Generally at this high loading, the particles

are well dispersed in all the supports. Average particle size was determined and a histogram is also presented in Figure 3 next to HRTEM images. Around 100 particles were measured for each material and the average particle size determined for 60% PtRu/TiO_2 anatase (A) was 1.36 ± 0.29 nm and for 60% PtRu/TiO_2 rutile (B) was 1.77 ± 0.34 nm.

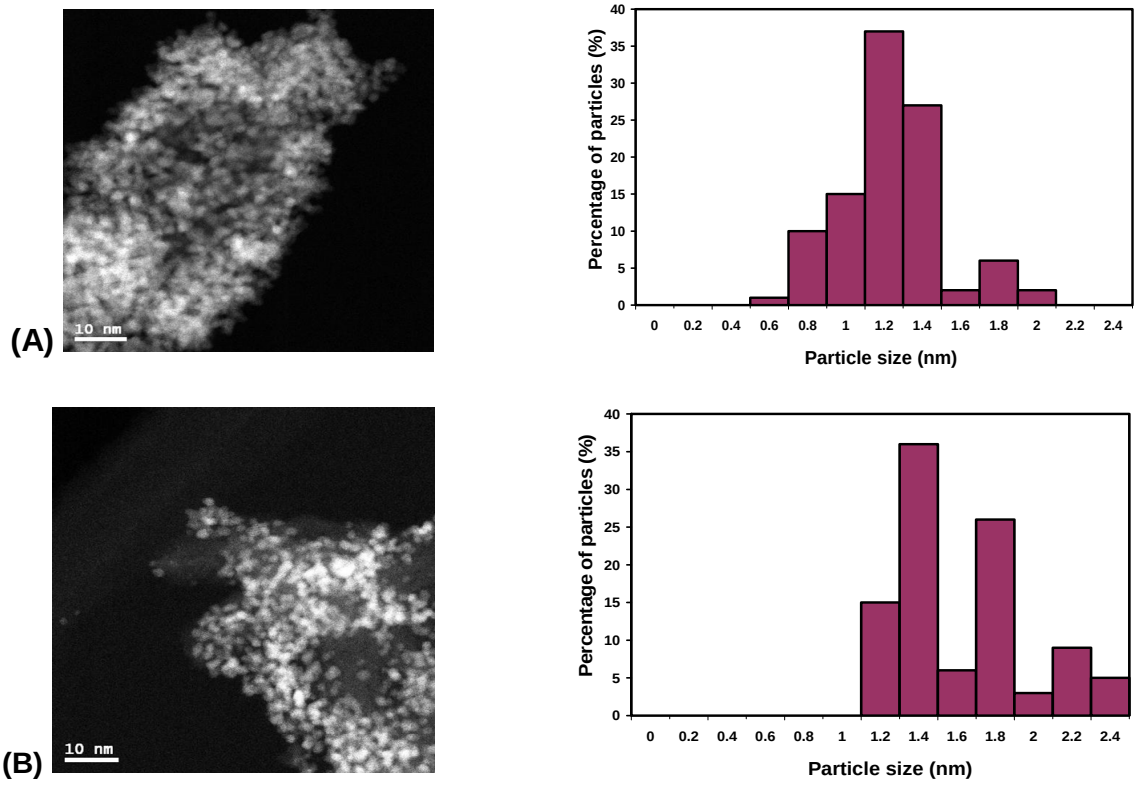

Figure 3: HRTEM images and Histograms of (A) 60 wt% PtRu on anatase TiO_2 and (B) 60 wt% PtRu on rutile TiO_2.

3 Benchmark Measurements

Performance and durability tests in PEM electrolyzers are necessary to compare these novel nano-structured materials with state-of-the-art MEAs. Therefore benchmark measurements from commercial MEAs are performed under different conditions like temperature and pressure variations. Benchmark measurements were performed in a 25 cm² single test cell. The test cell was delivered with deionized water on the anode and cathode side using a circulation pump. Under atmospheric pressure different temperature dependent curves are shown in Figure 4 in a galvanostatic mode. A titanium sinter plate with 75-100 µm spheric powder size as a current collector was used. The best cell performance was achieved by operating temperature of 343 K due to the faster kinetics of the reactions. Here 1.83 V can be obtained by current density of 1 A/cm^2. Marshall *et al.* [7] reported that voltage of 1.57 V at 1 A/cm^2 and 353 K are possible with $Ir_{0.6}Ru_{0.4}O_2$ anode and a 20 wt% Pt/C cathode. Figure 5 presents benchmark measurements for different operating pressures up to 50 bar by 343 K. It is clearly shown that higher pressures lead to higher voltage values, whereas the

difference with 15 mV by 1 A/cm^2 between 1 bar and 10 bar is rather small. The highest voltage with 2.11 V at 1 A/cm^2 is measured at a pressure of 50 bar, which yields in 14.1% higher cell performance comparable to atmospheric pressure.

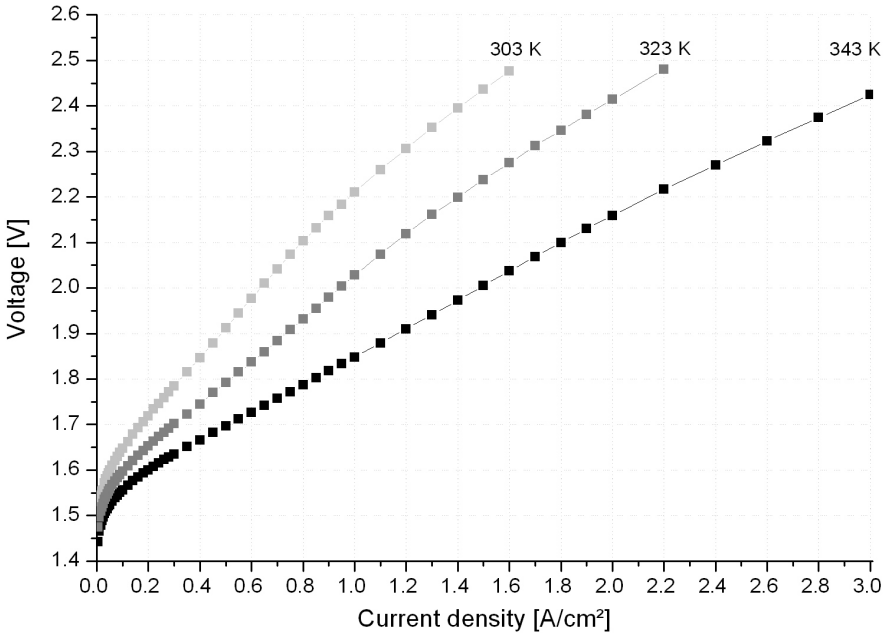

Figure 4: Polarization curve of a 200 µm benchmark CCM Fumea® from FuMA-Tech using different operating temperatures and 0.1 MPa.

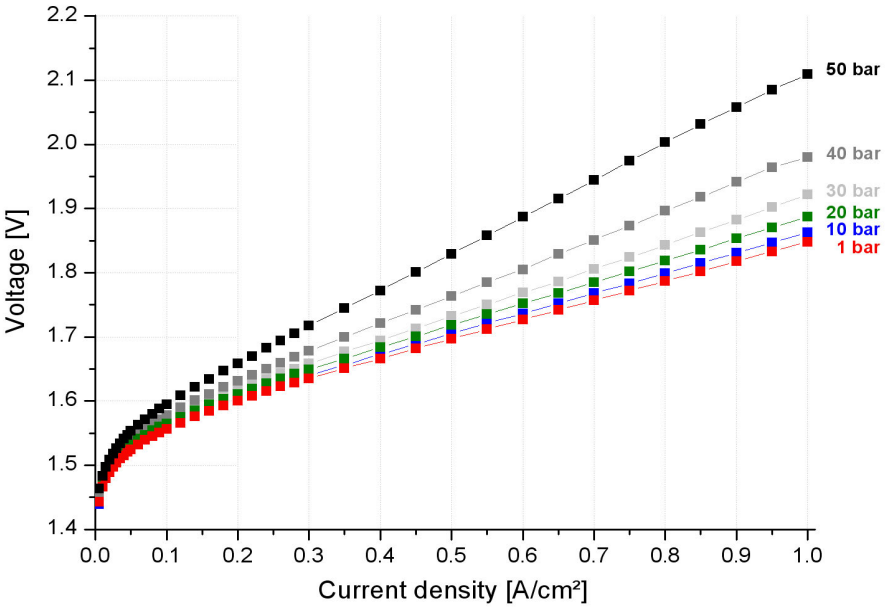

Figure 5: Polarization curve of a 200 µm benchmark CCM Fumea® from FuMA-Tech using different operating pressures and 343 K.

4 Conclusion

A Nb-TiO_2 support was synthesized with anatase and rutile crystalline structures. Since the Nb and Ti have similar ionic radius it is suggested that Nb is incorporated into the lattice. A surface-area analysis for the synthesized anatase Nb-TiO_2 gave 197 m^2/g, which is only 16% lower than carbon Vulcan XC-72R. The surface area was 19% higher than commercial anatase TiO_2. The surface area of the synthesize rutile Nb-TiO_2 was only 5.0 m^2/g. Particles with 60 wt% PtRu on anatase TiO_2 are round in shape, whereas 60 wt% PtRu on rutile TiO_2 have a more elliptical shape with higher particle size. For benchmarking, a high pressure 25 cm^2 electrolysis cell was constructed. First cell performance using commercial MEA showed a voltage of 1.83 V at 1 A/cm^2 and 343 K. With the same current density a voltage of 2.11 V was obtained by operating pressure of 50 bar. Further work is necessary to compare the new developed materials in a PEM electrolysis cell with benchmark measurements.

Acknowledgement

This work was partly founded by E.ON International Research Initiative to support projects for finding solutions in nanotechnology for energy supply.

References

[1] Young, A. P., Stumper, J., and Gyenge, E. (2009) Characterizing the Structural Degradation in a PEMFC Cathode Catalyst Layer: Carbon Corrosion. Journal of The Electrochemical Society, 156 (8), B913–B922.

[2] Roen, L. M., Paik, C. H., and Jarvi, T. D. (2004) Electrocatalytic Corrosion of Carbon Support in PEMFC Cathodes. Electrochemical and Solid-State Letters, 7 (1), A19–A22.

[3] Morris, D., Dou, Y., Rebane, J., Mitchell, C. E. J., Egdell, R. G., D., Law, S. L., Vittadini, A., and Casarin, M. (2000) Photoemission and STM Study of the Electronic Structure of Nb-Doped TiO2. Physical Review B, 61 (20), 13445–13457.

[4] Chen, G. Y., Bare, S. R., and Mallouk, T. E. (2002) Development of Supported Bifunctional Electrocatalysts for Unitized Regenerative Fuel Cells. Journal of The Electrochemical Society, 149 (8), A1092–A1099.

[5] Fuentes, R. E., García, B. L., and Weidner J. W. (2009) Effect of TiO2 Crystal Structure on the Activity of Pt-Ru towards Electrochemical Oxidation of Methanol. Journal of Electrochemical Society, submitted, March 2010.

[6] Cassiers, K., Linssen, T., Mathieu, M., Bai, Y. Q., Zhu, H. Y., Cool, P., and Vansant, E. F. (2004) Surfactant-directed synthesis of mesoporous titania with nanocrystalline anatase walls and remarkable thermal stability. The Journal of Physical Chemistry B, 108 (12), 3713–3721.

[7] Marshall, A., Sunde, S., Tsypkin, M., and Tunold, R. (2007) Performance of a PEM water electrolysis cell using IrxRuyTazO2 electrocatalysts for the oxygen evolution electrode. International Journal of Hydrogen Energy, 32 (13), 2320–2324.

Reforming and Gasification – Fossil Energy Carriers

Jens Rostrup-Nielsen

Abstract

This chapter summarizes the basic technologies available for the manufacture of hydrogen from fossil fuels followed by a description of important state-of-the-art flow schemes and potential alternatives. Finally, aspects of future applications for fuel cells and for synfuels are discussed.

Hydrogen Production by Supercritical Water Gasification of Alkaline Black Liquor

Changqing Cao, **Liejin Guo**, **Yunan Chen**, **Youjun Lu**, Xi'an Jiaotong University, Xi'an, China

1 Introduction

Black liquor (BL) is a large pollution resource to the environment; it mainly contains alkali wastes, lignin and its derivatives which is hard to degrade. Tomlinson recovery progress is the main method to treat black liquor in the world in nowadays and has 80 years long usage history, but it still has some weaknesses, such as the low efficiency and some safety and environmental problems [1-3]. Supercritical water gasification (SCWG) is an innovative thermo-chemical method for converting biomass and organic wastes into hydrogen-rich gaseous products. SCWG of black liquor has several advantages, for example, compared with other biomass gasification technologies such as air gasification and steam gasification, SCWG can directly deal with the wet biomass without drying. For black liquor always contains above 80 % moisture, SCWG can be much more efficient than other gasification technologies. On the other hand, the alkali salt contained in black liquor is reported to be a kind of effective catalyst for SCWG, which can promote water-gas shift reaction in supercritical water and increase the H_2 content of the gaseous product and decrease the CO content [4-7].

There is no report on SCWG of black liquor in large scale continuous type reactors so far. In present work, we conducted the experiments of black liquor SCWG in a continuous SCWG system developed in State Key laboratory of Multiphase Flow in Power Engineering (SKLMF). The influence of the main operating parameters and the distribution of alkali metal were investigated, a kinetic equation for COD (chemical oxygen demand) removal in SCWG was also achieved in this work.

2 Experimental

The black liquor from wheat straw soda pulping process was achieved from Hanxing paper mill in Shaanxi province of China, and the air-dried basis (a. d.) content of the black liquor is 9.5 %. The results of proximate and ultimate analysis, the heating value and pH value of the black liquor were listed in table 1.

Table 1: The properties of black liquor (a. d.).

Ultimate analysis (%, a. d.)					Proximate analysis (%, a. d.)				LHV (MJ/Kg)	pH
C	H	O	N	S	M	A	V	FC	11.30	11.3
33.43	2.77	32.86	0.23	0.13	3.2	27.38	49.32	20.1		

The experiments were conducted in a continuous SCWG system developed in SKLMF. In this system, quick heating rate of black liquor can be realized by mixing with the preheated

water before the reactor, and thus can advance the SCWG [4, 8]. The temperature was controlled by a PID temperature control system and the temperature deviation was ±5 °C. The fluid temperature in the reactor was measured by K-type thermocouples as the reaction temperature. The detailed description of this system can be found in our previous paper [9].

The gaseous products were analyzed in Agilent 7890A gas chromatograph with a thermal conductivity detector. The sodium content, COD(chemical oxygen demand) concentration and pH value of the aqueous samples were determined by ICP-AES, spectrophotometer method and glass electrode method respectively.

3 Results and Discussion

3.1 The influence of operating parameter

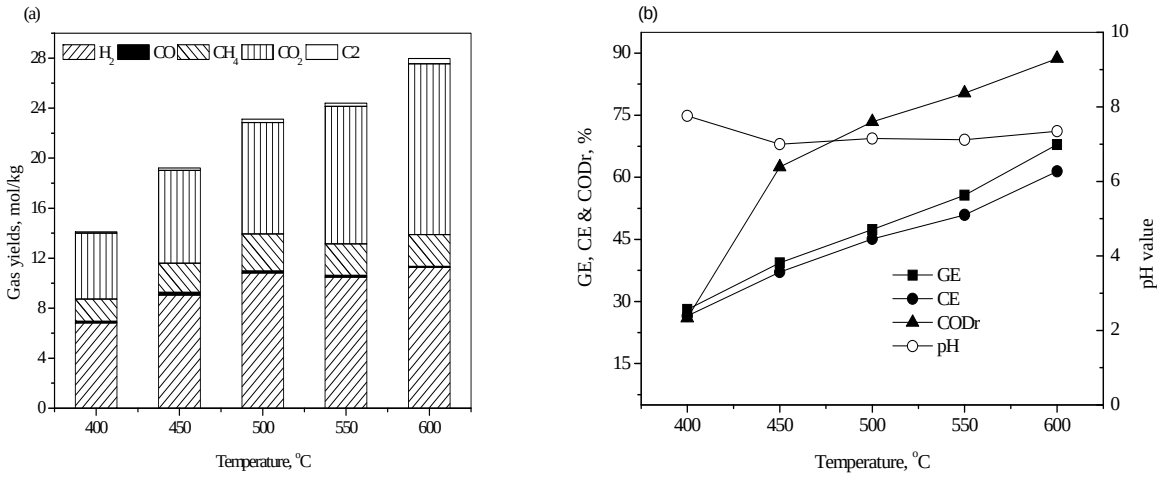

Figure 1: The influence of the temperature on black liquor SCWG (25 MPa, 5 kg/h, 9.5 %BL).

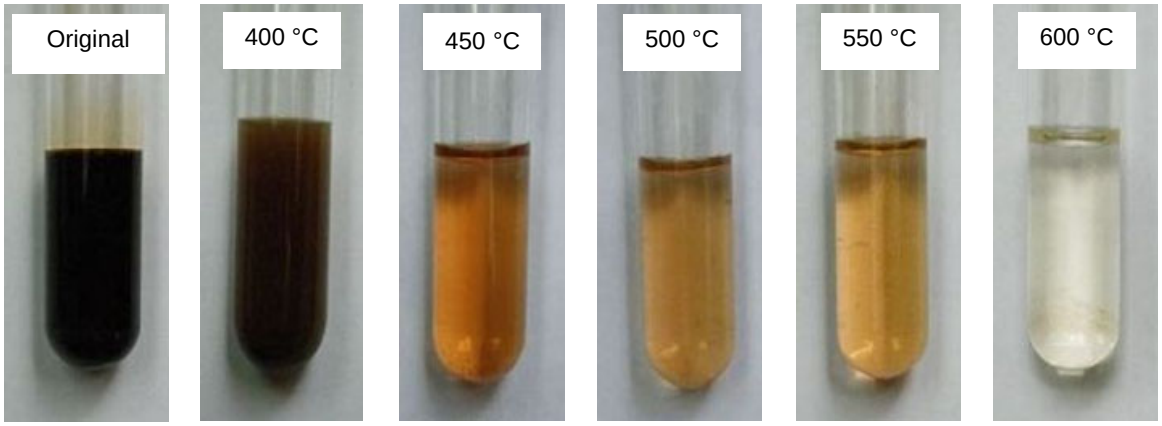

Figure 2: The photos of original BL and liquid residue at different reaction temperatures (25 MPa, 5 kg/h, 9.5 %).

The influence of temperature in the range of 400 °C~600 °C on SCWG of black liquor was investigated in the pressure of 25 MPa, the flow rate of 5 kg/h and the 9.5 % black liquor concentration. It can be seen from fig.1 that with the temperature increasing from 400 °C to 600 °C, the total gas yield, gasification efficiency, carbon gasification efficiency and COD removal efficiency increased from 14.1 mol/kg, 28.05 %, 26.5 %, and 25.97 % to 27.97 mol/kg, 67.89 %, 61.45 % and 88.69 % respectively. These results showed that temperature is a key operating parameter for black liquor SCWG and the increase of temperature can significantly enhance the gasification process.

Fig.2 shows the photos of original black liquor and the liquid residue at different reaction temperatures. It can be seen in fig.2 that the color of liquid residue after SCWG was much lighter than the black liquor. The color became lighter in higher reaction temperature and in 600 °C, the liquid residue became very clear. The pH values of the liquid residue were all decreased and close to neutral which is in the range of 7~7.8, which indicated that SCWG can weaken the alkalinity of black liquor and reduce its environmental contamination.

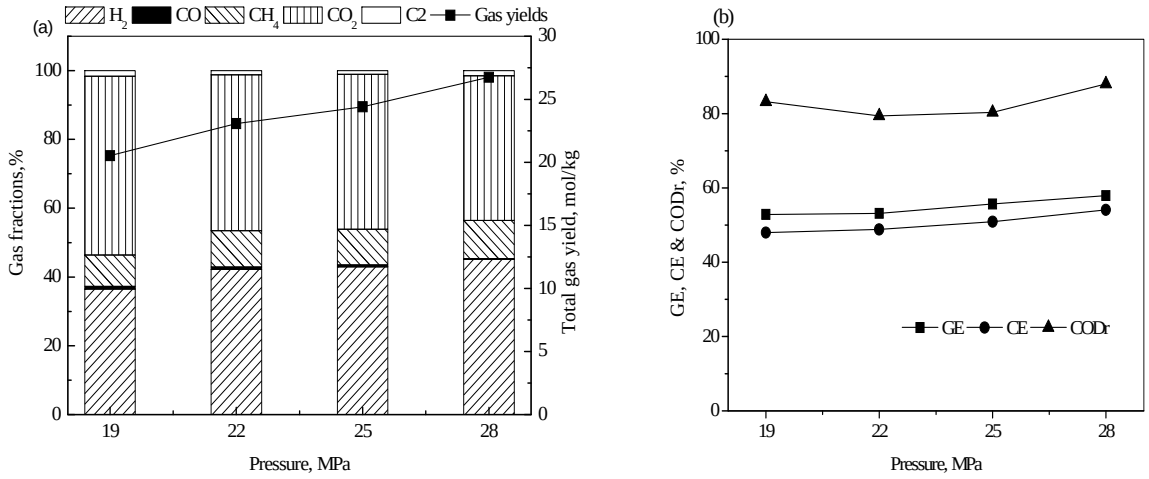

Figure 3: The influence of the pressure on black liquor SCWG (550 °C, 5 kg/h, 9.5 % BL).

The influence of pressure in the range of 19-28 MPa on black liquor SCWG was investigated. The results are shown in fig.3. It can be seen that with the pressure increased from 19 MPa to 28 MPa, the gas fractions of the gaseous products had no significant change. The total gas yield, the gasification efficiency and carbon gasification efficiency only increased slightly. The similar result was reported by Demirbas [10] in SCWG of fruit shell. He suggested that increasing of pressure increased the mass transfer and solvent diffusion rates of water and thus increased the efficiency of the SCWG.

The investigation of the influence of flow rate on supercritical water gasification of black liquor was done in the temperature of 500 °C, the pressure of 25 MPa and the black liquor concentration of 9.5 %. As shown in fig.4, with the flow rate increased from 3 kg/h to 7 kg/h, the total gas yield, the gasification efficiency and the COD removal efficiency decreased from 24.96 mol/kg, 54.05 % and 83.56 % to 20.97 mol/kg, 42.5 % and 70.84 % respectively, while the fractions of the gaseous products had no apparent change with the variation of the flow rate. From the results above, we inferred that SCWG has two steps: (1) the decomposition of

the feedstock and the production of original gases; (2) the reactions between the original gases which can change the composition of the gaseous product. From the above results, we speculated that it need longer residence time to complete step (1), while the reactions in step (2) were so quick that they were not influenced by the change of the residence time. So with longer residence time, which is corresponding to the smaller flow rate, more gases were produced while the composition had no apparent change with the flow rate.

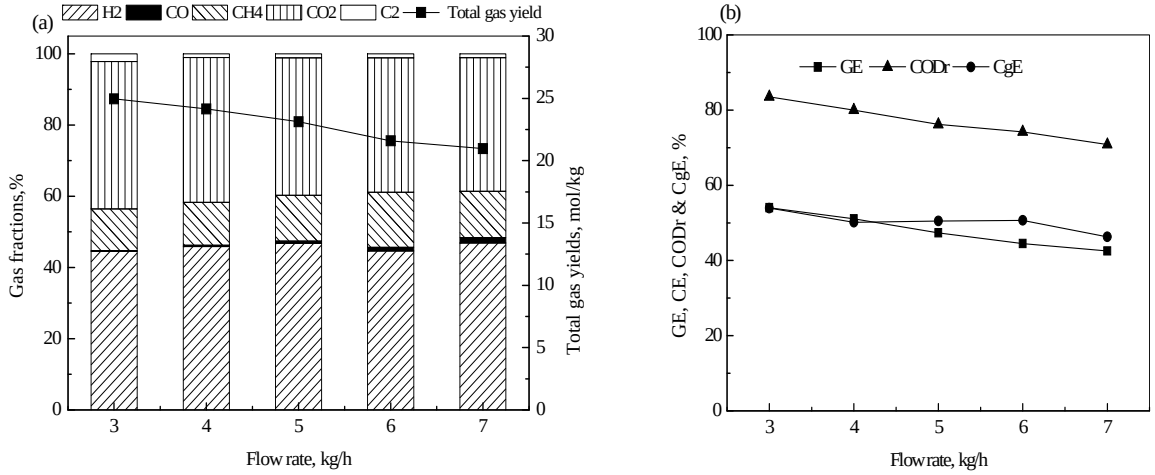

Figure 4: The influence of flow rates on black liquor SCWG (500 °C, 25 MPa, 9.5 % BL).

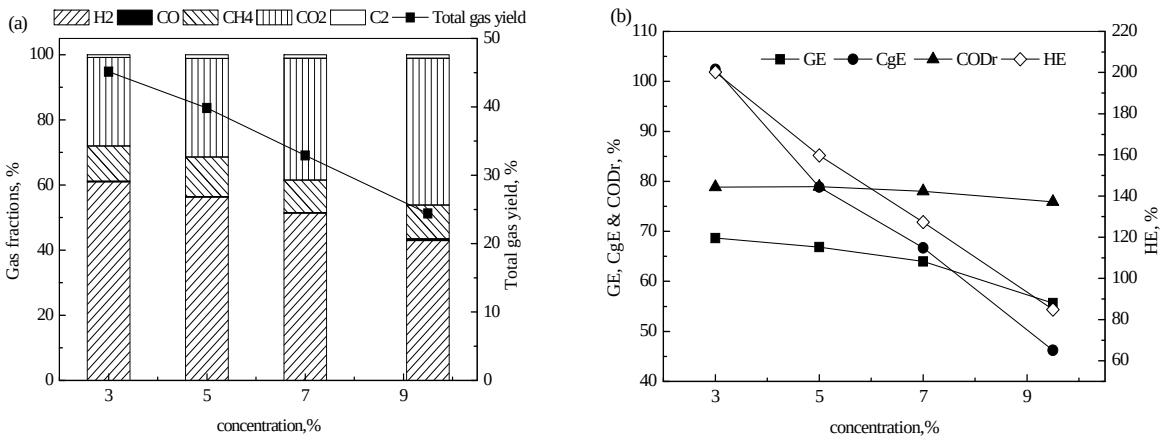

Figure 5: The influence of concentrations on black liquor SCWG (550 °C, 25 MPa, 5 kg/h).

The different concentrations of black liquor were achieved by diluting the primary black liquor with calculated amounts of de-ionized water and gasification at the same experimental condition (550 °C, 25 MPa, 5 kg/h). The results are shown in fig. 5. When the feed concentration decreased from the primary concentration (9.5 %) to 3 %, the fraction of H_2 in the gaseous product increased from 42.95 % to 61.02 %. The total gas yield almost doubled from 24.41 mol/kg to 45.15mol/kg, the gasification efficiency increased from 55.67 % to 68.66 %, and the hydrogen gasification efficiency increased from 84.9 % to 200.23 %. All these results indicated that the dilution of the black liquor favours SCWG. It is also shown in fig.5 that the hydrogen gasification efficiencies were all above 100 % with the concentration

below 7 %. We attributed these results to the participation of water in the reaction and some of the hydrogen in the gaseous product come from the water.

3.2 The distribution of alkali metal

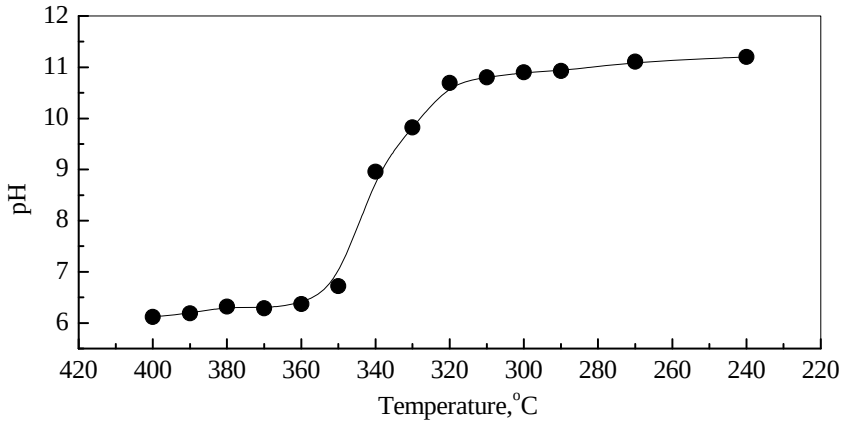

Figure 6: pH values of the effluent in the cooling progress after the complete of experiment.

In the cooling process after the reaction, it was found that as the fluid was cooled to below 360 °C, the pH value of the effluent increased and reached around 11 below 320 °C. The sodium content of the cooling effluent at the temperature of 330 °C examined by ICP-AES is 3165.5 mg/L while that of the liquid residue is 29.4 mg/L in the reaction progress. This result is supposed to be corresponded with the solubility of water around the critical point. As reported by J. W. Tester [11], supercritical water at low density is a poor solvent for ionic species like inorganic salts. We speculated that the sodium salt was condensed in the reactor in reaction process. When the temperature decreased in the cooling process, the sodium salts dissolved in the water and flowed out with the water. So the pH value increased with the decreasing of the temperature.

3.3 Kinetic study of black liquor SCWG

Pseudo first-order reaction was assumed for the COD removal in SCWG and confirmed by the reaction results at the reaction temperatures of 450 °C, 475 °C, 500 °C, 550 °C. The reaction rate constants at different temperatures were obtained by the least squares fitting method and they were in the range of 0.04-0.23 S^{-1} at the temperatures of 450 °C~550 °C. With the reaction rate constant in different temperature, the activation energy and the pre-exponential factor were calculated and they are 74.38±6.02 kJ/mol and $10^{4.05\pm0.41}S^{-1}$ respectively, so the Arrhenius equation of black liquor SCWG can be described as below:

$$k=10^{4.05\pm0.41}\exp(74.38\pm6.02\ /RT)\ (s^{-1}) \quad (1)$$

4 Summary

Black liquor was gasified continuously in supercritical water successfully and the main gaseous products were H_2, CO_2 and CH_4 with little amount of CO, C_2H_4 and C_2H_6. The increase of the temperature and the decrease of the flow rate and black liquor concentration enhanced SCWG of black liquor. The change of the system pressure had limited influence on the gasification effect. The maximal COD removal efficiency of 88.69 % was obtained at the temperature of 600 °C. The pH values of the aqueous residue were all decreased to the range of 6.4~8 while the pH value of cooling effluence below 360 °C increased to about 11 and the sodium content was much higher than that in the aqueous residue. The reaction rate for COD degradation in supercritical water was obtained by assuming pseudo first order reaction. And the activation energy and pre-exponential for COD removal in SCWG were 74.38kJ/mol and $1.11\times10^4\ s^{-1}$ respectively.

Acknowledgements

This work was financially supported by the National Natural Science Foundation of China (Contracted No. 50821064) and the National Basic Research Program of China (Contracted No. 2009CB220000).

Nomenclature

GE: gasification efficiency, the mass of product gas/the mass of BL,%

CE: carbon gasification efficiency, the carbon in product gas/the carbon in BL,%

CODr: COD removal efficiency, 1-COD concentration in liquid residue/COD concentration in BL,%

CgE: cold gas efficiency, LHV of product gas/LHV of BL,%

HE: hydrogen gasification efficiency, the hydrogen in product gas/the carbon in BL,%

References

[1] G. Gea, M. B. Murillo, J. Arauzo and W. J. Frederick, Energy & Fuels 17, 46 (Jan-Feb, 2003).

[2] G. Gea, M. B. Murillo, J. L. Sanchez and J. Arauzo, Industrial & Engineering Chemistry Research 42, 5782 (Nov 12, 2003).

[3] P. J. Hurley, Chemical Engineering Progress 76, 43 (1980).

[4] A. Sinag, A. Kruse and J. Rathert, Industrial & Engineering Chemistry Research 43, 502 (Jan 21, 2004).

[5] M. Watanabe, H. Inomata, M. Osada, T. Sato, T. Adschiri and K. Arai, Fuel 82, 545 (Mar, 2003).

[6] A. Kruse and M. Faquir, Chemical Engineering & Technology 30, 749 (Jun, 2007).

[7] J. M. L. Penninger and M. Rep, International Journal of Hydrogen Energy 31, 1597 (Sep, 2006).

[8] M. Modell, Mechanical Engineering 99, 108 (1977).

[9] L. J. Guo, Y. J. Lu, X. M. Zhang, C. M. Ji, Y. Guan and A. X. Pei, Catalysis Today 129, 275 (2007).

[10] A. Demirbas, International Journal of Hydrogen Energy 29, 1237 (Sep, 2004).

[11] J. W. Tester, A. M. P, M. M. DiPippo, K. Sako, M. T. Reagan, T. Arias and W. A. Peters, The Journal of Supercritical Fluids 13, 225 (1998).

Environmental Impact Comparison of Steam Methane Reformation and Thermochemical Processes of Hydrogen Production

G. F. Naterer, **O. Jaber**, **I. Dincer**, University of Ontario Institute of Technology, Oshawa, Ontario, Canada

Abstract

This paper compares the environmental impact of various processes of hydrogen production, particularly steam methane reforming (SMR) and the copper-chlorine (Cu-Cl) and modified sulfur-iodine (S-I) thermochemical cycles. Natural gas is used as the energy source for each of the different methods. Also, an integrated Cu-Cl and SMR plant is examined to show the reduction of greenhouse gas emissions by modifying existing SMR plants with thermochemical processes. The analysis shows that the thermochemical Cu-Cl cycle out-performs the other conventional methods of hydrogen production, with lower fuel requirements and carbon dioxide emissions.

1 Introduction

Various methods and technologies currently exist for producing hydrogen. However, most of these are based on reforming of fossil fuels and thus emit carbon dioxide to the atmosphere [1-3]. Water electrolysis accounts for about 3 % of the world's total hydrogen production. It is an environmentally friendly method, provided the source of electricity is clean. However, it is very energy intensive and it has relatively low efficiencies, especially when the efficiency of the generated electricity from a thermal power plant is taken into account. Thermochemical water splitting cycles are clean and more efficient alternatives to produce hydrogen, and they can be driven by various types of energy sources (i.e., nuclear, solar, geothermal or conventional fossil fuels). They can be linked with nuclear power plants for hydrogen production [4, 5]. Currently, active research around the world is being conducted for sulfur-iodine (S-I), copper-chlorine (Cu-Cl) and hydrogen sulfur cycles [6-11].

Unlike coal gasification and SMR (steam-methan reforming), thermochemical cycles use water as the feedstock for hydrogen, not fossil fuels. Thermochemical cycles can be linked to various types of energy sources, so they offer great flexibility and sustainability. The heat requirements of the Cu-Cl thermochemical cycle have been presented by Wang et al. [8, 9]. The cycle efficiency was found to be 46 % in Ref. [9]. The Cu-Cl cycle can operate at relatively low temperatures below 550 ^{o}C, whereas the S-I thermochemical cycle requires high temperature nuclear reactors with temperatures up to 900 ^{o}C.

This paper investigates the potential benefits of linking SMR and natural gas supplies with thermochemical cycles, in order to reduce greenhouse gas emissions and costs of conventional methods of hydrogen production. The paper specifically examines the feasibility of linking SMR with Cu-Cl and S-I thermochemical cycles and their potential comparisons,

with respect to water and fuel requirements, as well as greenhouse gas emissions and cost comparisons.

2 Processes of Hydrogen Production

Hydrogen can be produced from a range of processes, i.e., reforming of fossil fuels, electrolysis, thermochemical water splitting, or biological hydrogen production. Currently, steam methane reforming (SMR) is the most widely used process to produce hydrogen, followed by other reforming methods such as coal gasification. Carbon-based methods emit large quantities of carbon dioxide, which motivates the need to develop alternative and sustainable methods of generating hydrogen. Thermochemical cycles, particularly the Cu-Cl and S-I cycles, are among the most promising large-scale alternatives.

Steam methane reforming consists of four main steps: desulfurization, catalytic reforming, CO conversion, and gas separation [2]. Figure 1 shows a schematic of an SMR plant. In the desulfurization step, sulfur-organic compounds in natural gas are converted to H_2S by a catalytic hydrogenation reaction. Then it is scrubbed by a ZnO bed to produce ZnS and H_2O. The removal of sulfur from natural gas is required because it poisons the catalyst used in the next step. In the catalytic reforming step, natural gas and steam react at a temperature of about 900 °C to produce hydrogen and CO through the following endothermic reaction:

$$CH_4 + H_2O \rightarrow 3H_2 + CO \quad (1)$$

The products of the first step continue to the third step, where CO and steam react again in an exothermic reaction to produce more hydrogen as follows.

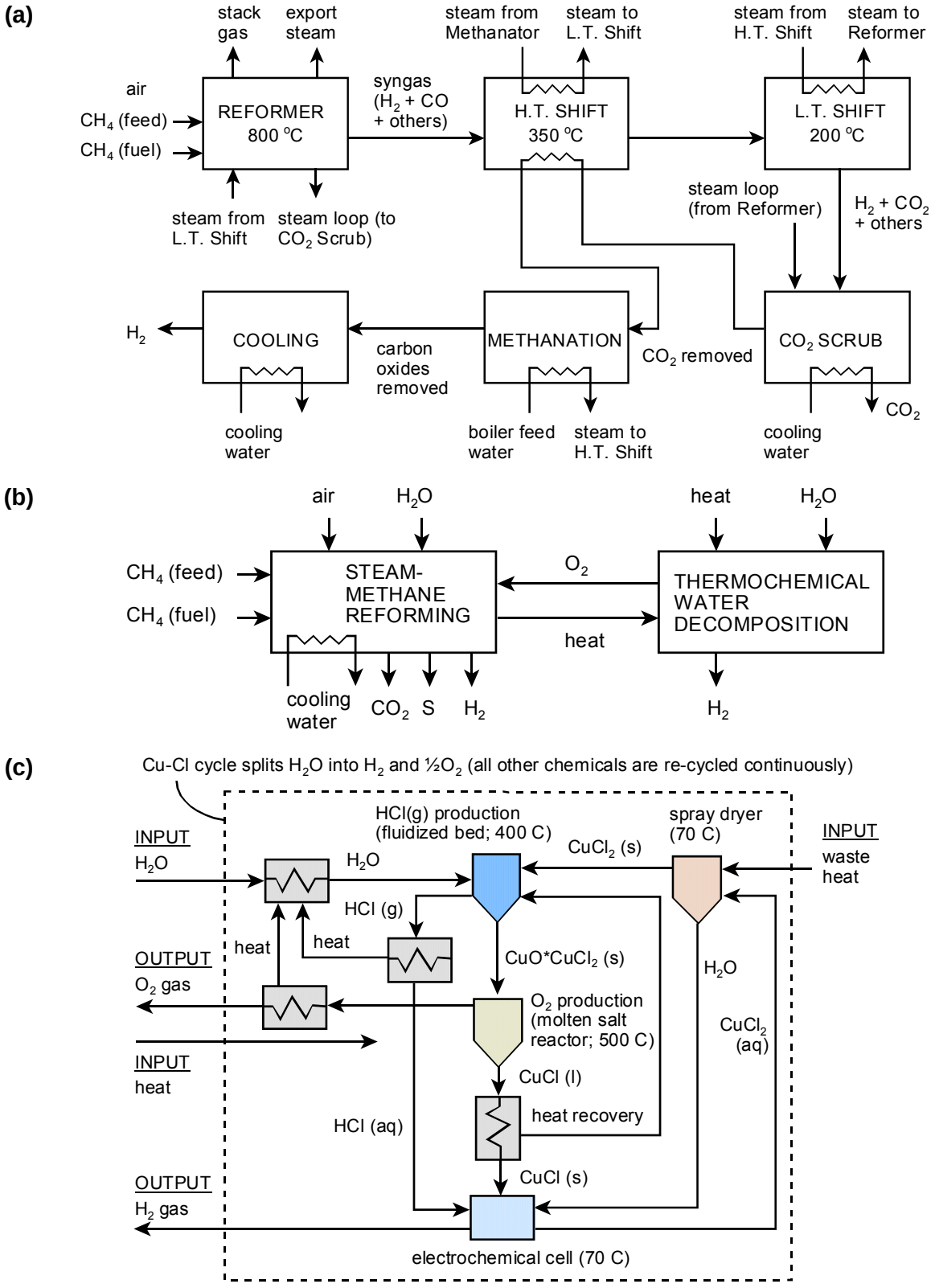

Figure 1: (a) SMR plant, (b) integrated SMR / Cu-Cl and (c) Cu-Cl cycle.

Table 1: Steps and chemical reactions in the Cu-Cl cycle.

Step	Reaction	Temp. Range (°C)	Feed/Output*	
1	$2CuCl(aq) + 2HCl(aq) \rightarrow H_2(g) + 2CuCl_2(aq)$	<100 (electrolysis)	Feed: Output:	Aqueous CuCl and HCl + V + Q H_2 + $CuCl_2$ (aq)
2	$CuCl_2(aq) \rightarrow CuCl_2(s)$	<100	Feed: Output:	Slurry containing HCl and $CuCl_2$ + Q Granular $CuCl_2$ + H_2O/HCl vapours
3	$2CuCl_2(s) + H_2O(g) \rightarrow CuO*CuCl_2(s) + 2HCl(g)$	400	Feed: Output:	Powder/granular $CuCl_2$ + $H_2O(g)$ + Q Powder/granular $CuO*CuCl_2$ + 2HCl (g)
4	$CuO*CuCl_2(s) \rightarrow 2CuCl(l) + 1/2O_2(g)$	500	Feed: Output:	Powder/granular CuO* $CuCl_2(s)$ + Q Molten CuCl salt + oxygen
* Q = thermal energy, V = electrical energy				

$$CO + H_2O \rightarrow H_2 + CO_2 \quad (2)$$

This reaction is usually carried out in two sub-steps, to make sure all CO is converted to CO_2. The final step is a separation and purification step. Hydrogen is separated from the gas mixture, either by solvents that absorb the acid CO_2, or by adsorption beds that have molecular sieves of suitable pore size.

The Cu-Cl cycle has been investigated by the Argonne National Laboratory [12] and Atomic Energy of Canada Limited [13] for hydrogen production with Super-Critical Water Reactors (SCWR). The cycle consists of four main steps (see Table 1 and Figure 1), wherein either a physical or chemical processes occurs in each step. Complete separation of hydrogen and oxygen from water is the net result. The first step in the Cu-Cl cycle is the CuCl / HCl electrolyzer to produce hydrogen, followed by the second step which removes water from the exiting $CuCl_2$ solution by spray drying. Then the third step produces HCl gas and copper oxychloride within a fluidized bed reactor at about 400 °C. In the fourth oxygen production step, copper oxychloride decomposes and releases oxygen at a temperature of 500 °C. The product of the oxygen step, molten CuCl, is cooled, solidified, dissolved in HCl, and moved to the electrolyzer to complete the cycle, and repeat the processes.

The S-I cycle consists of three reactions; sulfuric acid decomposition reaction where oxygen is produced; a Bunsen reaction where the sulfuric and hydrioidic acids are produced by reacting iodine and sulfur dioxide; and finally the hydrogen production reaction where hydrogen is released from the hydrioidic acid. This cycle requires higher temperatures than the Cu-Cl cycle, typically over 900 °C. The efficiency of the cycle is similar to values reported for the Cu-Cl cycle [8].

Another process to be examined in this paper is integration of SMR with a thermochemical cycle (see Fig. 1). This is particularly advantageous to reduce CO_2 emissions, improve efficiency and potentially reduce costs of hydrogen production. There are a number of potential advantages of integrating SMR and thermochemical processes, such as reduced

methane consumption, since the oxygen supply from the thermochemical cycle is not accompanied by nitrogen in air, which requires heating. There is potentially significant reduction of CO_2, NOx and other GHG emissions. Such potential benefits are examined numerically for comparison purposes.

3 Results and Discussion

To find the energy needs of SMR, the results of Rosen [8] will be used. For an SMR plant, about 67 % of the total natural gas is used in the reforming reaction, while 33 % is used to supply the heat requirements of the process. In the SMR processes, 1 mole of natural gas feed will supply 4 moles of hydrogen. By multiplying by the ratio of the fuel needed to the feed fuel, one obtains the required amount of natural gas as fuel to produce one mole of hydrogen. The results for these calculations are shown in Table 2. The total natural gas input is more than the required energy input because the analysis takes into account the natural gas needed for the reforming reaction.

Table 2: Summary of different process results.

Process	Conventional SMR	Conventional Cu-Cl cycle	Cu-Cl with oxygen recovery	Modified S-I cycle
Maximum Temperature (°C)	900	530	530	900
Fuel requirement (mole CH_4 / mole H_2 produced)	0.12	0.26	0.25	1.70
Total natural gas input (mole CH_4 / mole H_2 produced)	0.37	0.26	0.25	1.70
Water consumption (mole H_2O / mole H_2 produced)	0.50	1.00	1.00	1.00
Carbon dioxide emissions (mole CO_2 / mole H_2 produced)	0.37	0.26	0.25	1.70

For the Cu-Cl thermochemical cycle, after considering heat recovery within the cycle, it was found that the cycle needs 149 kJ/mol H_2 [9]. The amount of thermal energy needed to supply reactions occurring at temperatures of around 530 °C from combusting one mole of natural gas with 140 % theoretical air was determined. Then the energy required to produce one mole of hydrogen can be found. Table 2 shows a summary of the results for the Cu-Cl cycle. From the table, the energy input to the cycle and the total natural gas requirements are equal, as the Cu-Cl cycle does not require any natural gas internally, unlike SMR. All of the produced hydrogen from the Cu-Cl cycle comes from splitting of water, as no hydrogen is produced from the natural gas, which explains why the water requirement for this cycle is higher than SMR.

For the Cu-Cl thermochemical cycle with internal oxygen recovery, upon splitting water in the Cu-Cl cycle, oxygen is also released along with hydrogen. For every mole of hydrogen produced by the Cu-Cl cycle, there is half of a mole of oxygen produced as well. If this amount of oxygen can be supplied to the combustion reaction with incoming outside air, it

would reduce the amount of fuel needed to supply the heat requirements. This case has been analyzed and the results are shown in Table 2. It can be observed that the natural gas requirements and the carbon dioxide emissions have both been reduced by 5 % compared to the Cu-Cl cycle without any oxygen recovery. Considering the modified S-I Cycle, the same analysis has been performed as with the previous cases. This cycle is characterized by its high heat of reactions, especially at low temperatures. Again the case of heat recovery has been assumed and combustion occurs with 140 % theoretical air. The results are also shown in Table 2. It can be observed that the energy requirements for this cycle are high, due to the high heat of reactions.

4 Conclusions

This paper has found that the Cu-Cl cycle is the most attractive method for producing hydrogen in terms of fuel requirements, carbon dioxide emissions and cost. It has the lowest fuel requirements and carbon emissions, including about 40 % less natural gas than SMR, without considering oxygen recovery. Another promising method is to integrate the Cu-Cl cycle with existing SMR plants to operate in an integrated mode. The costs of producing hydrogen can be reduced and the overall performance of the plant can then be improved. The integrated process is a step towards more sustainable hydrogen production. The fuel requirements of the modified S-I cycle are higher, as well as the carbon dioxide emissions and costs. A sensitivity analysis has showed that the total cost of producing hydrogen was more sensitive to the fluctuations in natural gas price than changes in the carbon capture price. The sensitivity of the total cost to the fluctuations in fuel price is about 4 times the sensitivity of the total cost to the fluctuation in the carbon dioxide capture cost.

Acknowledgements

Financial support from Atomic Energy of Canada Limited and Ontario Research Fund is gratefully acknowledged.

References

[1] Rosen, M. A., “Thermodynamic investigation of hydrogen production by steam methane reforming”, International Journal of Hydrogen energy, 16 (1991) 207 – 217

[2] Gupta, R. B., “Hydrogen fuel: production, transport and storage”, CRC Press, (2009)

[3] De Jong, M., Rienders, A.H.M.E., Kok, J., Westendorp, G., “Optimizing a steam methane reformer for hydrogen production”, Int. J. Hydrogen energy, 34 (2009) 285

[4] Rosen, M. A., “Thermodynamic comparison of hydrogen production processes”, International Journal of Hydrogen energy, 21 (1996) 349 – 365

[5] Rosen M. A., Scott, D. S., “Comparative efficiency assessment for a range of hydrogen production processes”, Int. Journal of Hydrogen energy, 23 (1998) 653 – 659

[6] Yildiz B., Kazimi, M., “Efficiency of hydrogen production systems using alternative nuclear energy technologies”, Int. Journal of Hydrogen Eenergy, 31 (2006) 77 – 92

[7] Lewis, M., Serban, M., Basco, J. K., “Hydrogen production at <550C using a low temperature thermochemical cycle”, ANS/ENS Exposition, Nov. 2003, New Orleans

[8] Wang, Z., Gabriel, K., Naterer, G. F., “Thermochemical process heat requirements of the copper-chlorine cycle for nuclear based hydrogen production”, 29th conference of the Canadian nuclear society, (2008)

[9] Naterer, G. F., Gabriel, K., Wang, Z., Daggupati, V., Gravelsins, R., “Thermochemical hydrogen production with a copper-chlorine cycle. I: Oxygen released from copper oxychloride decomposition”, International Journal of Hydrogen Energy, 33 (2008) 5439 – 5450

[10] Naterer, G. F., Gabriel, K., Wang, Z. L., Daggupati, V. N., Gravelsins, R., “Thermochemical hydrogen production with a copper-chlorine cycle. II: Flashing and drying of aqueous cupric chloride”, Int. J. of Hydrogen Energy, 33 (2008) 5451 – 5459

[11] Wang, Z., Naterer, G. F., Gabriel, K., “Multiphase reactor scale-up for Cu-Cl thermochemical hydrogen production”, Int. J. Hydrogen Energy, 33 (2008) 6934 - 6946

[12] Lewis, M., Taylor, A., “High Temperature Thermochemical Processes, DOE Hydrogen Program”, Annual Progress Report, Washington, DC, 2006, p 182 - 185

[13] Stolberg, L., Boniface, H., McMahon, S., Suppiah, S., York, S., “Development of the Electrolysis Reactions involved in the Cu-Cl Thermochemical Cycle”, International Conference on Hydrogen Production, May 3 – 6, (2009), Oshawa, Canada

Upscaling of a 500 kW Solar Gasification Plant

A. Vidal[*], **T. Denk**, PSA-CIEMAT, Tabernas (Almería), Spain
L. Steinfeld, ETH Zurich, Zurich and PSI, Villigen, Switzerland
L. Zacarías, PDVSA INTEVEP, Caracas, Venezuela

Abstract

Research in recent years has demonstrated the efficient use of solar thermal energy for driving endothermic chemical reforming reactions in which hydrocarbons are reacted to form syngas. This process produces not only a highly useful and transportable end product, but also results in the storage of a significant fraction of solar energy in the chemical bonds of the fuel molecules.

The steam-gasification of petroleum derivatives and residues using concentrated solar radiation is proposed as a viable alternative to solar hydrogen production. PDVSA, CIEMAT and ETH are carrying out a joint project with the goal to develop and test a 500 kW plant for steam gasification of petcoke. This report summarizes the major accomplishments and challenges of upscaling the installation at the SSPS-tower of the Plataforma Solar de Almería.

1 Introduction

The use of high temperature solar heat to drive the endothermic reaction associated with coal gasification has been suggested and investigated in the last 20 years [1]. The advantages of supplying solar energy for process heat are three-fold: (1) Calorific value of the feedstock is upgraded, (2) Gaseous products are not contaminated by the by products of combustion; and (3) Discharge of pollutants to the environment is avoided. An important example of such hybridization is the endothermic steam-gasification of petroleum derivatives and residues (petcoke) to synthesis gas (syngas), represented by the simplified net reaction:

$$CH_xO_y + (1-y)H_2O \rightarrow (\frac{x}{2} + 1 - y)H_2 + CO$$

where *x* and *y* are the elemental molar ratios of H/C and O/C in petroleum tar, respectively.

The project of solar petroleum coke gasification is a joint cooperation between the company Petróleos de Venezuela (PDVSA), the Eidgenössische Technische Hochschule (ETH) in Zurich / Switzerland, and the Centro de Investigaciones Energéticas, MedioAmbientales y Tecnológicas (Ciemat) in Spain. The primary goal is to develop a clean technology for the solar gasification of petroleum coke and other heavy hydrocarbons.

* Corresponding author, email: alfonso.vidal@ciemat.es

The project is divided into three phases. In a first step, after performing in-depth studies of the thermodynamic and kinetic behaviour, a small prototype was tested in the Solar Furnace of PSI / Switzerland. Goal was to demonstrate the feasibility of the solar gasification, to determine critical process parameters, to identify possible difficulties, and finally to get a solid data base for the scale up step in phase 2. In phase 2, the design, construction, and operation of a 500 kW reactor are foreseen. In phase 3 finally, a 50 MW solar gasification plant located in Venezuela will be designed.

2 Reactor Design and Fabrication

A scheme of the reactor configuration is depicted in Fig. 1. The reactor design is one of the most important factor in development of solar gasification technology. Unlike in methane reforming all feeds are gases, petcoke gasification involves a solid and thus the design of solar driven coal gasification is much more technically-challenging.

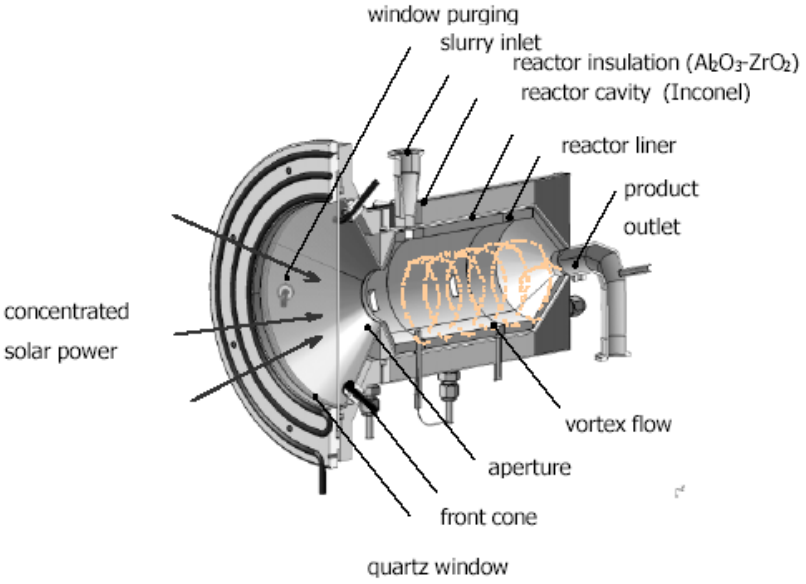

Figure 1: Schematic of the solar reactor-receiver.

A direct absorption concept with a cylindrical cavity receiver is used to perform the chemical reaction. The details of reactor design has been previously presented in [2,3].

The feasibility of petcoke-water slurry concept, demonstrated in the 5 kW solar reactor at Paul Scherrer Institute (Switzerland) [4], has been the optimum for up-scaling. The full entrainment of the particles requires relatively high gas velocities which are provided by pneumatically transportation of steam. With this arrangement, the coke particles are directly exposed to the high-flux solar irradiation, providing efficient heat transfer directly to the reaction site. Solar energy absorbed by the reactants is used to raise their temperature to above 1300 K and drive the gasification reaction.

3 The 500 kW SYNPET Solar Gasification Plant

The installation of the 500 kW Solar Gasification Plant has been located at the 40m-level of the SSPS-tower at the Plataforma Solar de Almería. The facility collects direct solar radiation by means of a field of 91 39.3-m^2-surface heliostats distributed in a 150-x-70-m north field into 16 rows. The heliostats have a nominal reflectivity of 87 % and the maximum thermal power delivered by the field onto the receiver aperture is 2,7 MW. In a previous paper the performance that can be expected from the receiver has been calculated starting from average irradiance of SSPS/CRS heliostat field along the year [5].

A complete description of the solar gasification plant is given hereinafter. The test bed consists of the following elements: coke pneumatic transport, coke feeder, slurry mixer, heat exchanger, water separator, and torch which were previously defined. Auxiliary components like water supply, power supply, measurement devices, and security systems will complete the installation.

A certification procedure following ATEX Directive was included in our installation for the purpose of advancing the technology to commercialization. The Directive applies to all equipment and systems for use in potentially explosive atmospheres. The plant is designed to utilize about 50 kg/h of petcoke (dry basis). A special unit based on pneumatic conveyor to feed finely ground coke (particle size less than 100 μm) from the ground has been installed. The coke reacts with steam at a temperature of 1100 – 1300 ºC to produce a raw fuel gas and ungasified material.

The outlet syngas is cooled by a water-cooled heat exchanger, which is used as an indirect method of thermal balance. A standard heat-exchanger was adapted to the special characteristics of these processes which are fouling and temperature limitations of present materials and designs. In a final separator tank, the water content of syngas is condensed. Most of the residual solids from gasification fall into this device or in a water trap placed after. The remaining part of the gas will be burned in a torch.

A small amount of the gas is separated for chemical analysis in a gas chromatograph and/or infrared gas measurement system. Extra steam flow to keep the window cool and clean from particles was actually supplied by an electrical evaporator with a capacity of about 60 kg/h. For this plant a syngas production of around 100 to 180 kg/h has been estimated.

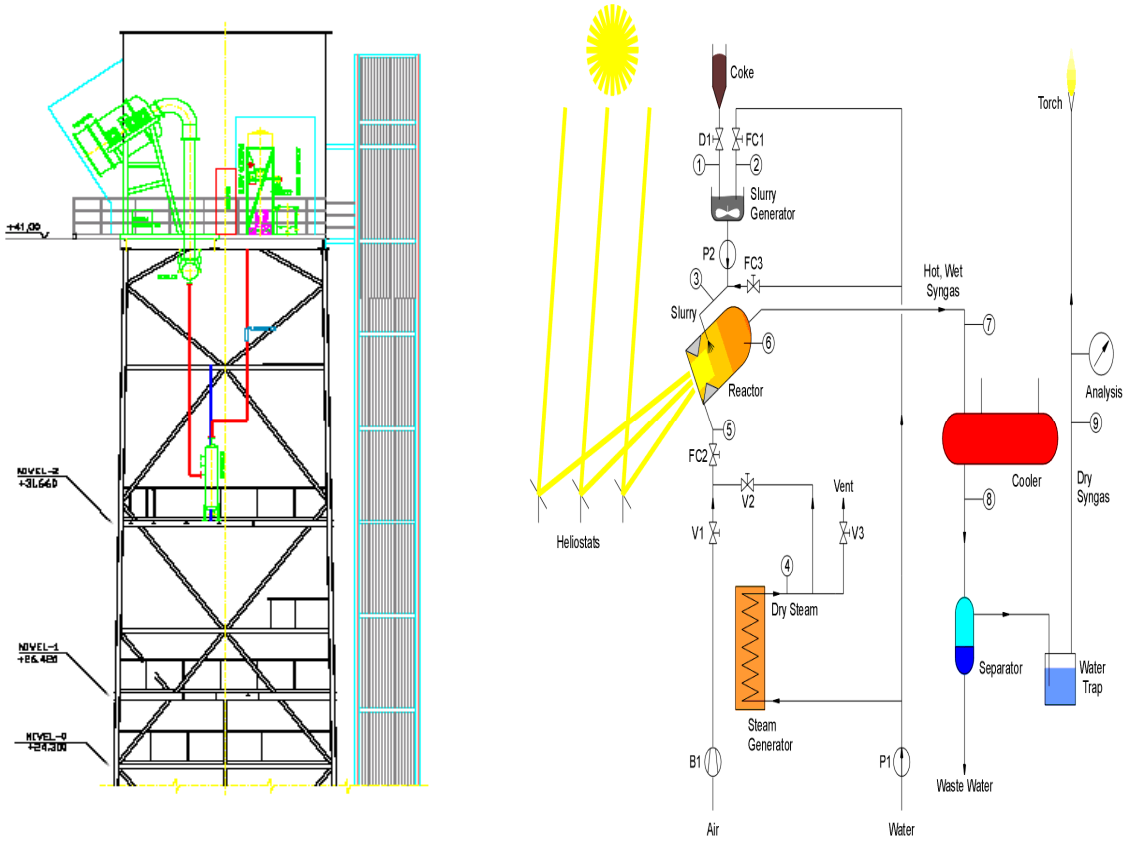

Figure 2: Right view of the tower and system layout.

For evaluation of SYNPET solar receiver and plant performance the system is equipped with the following sensors: thermocouples (receiver, inlet and outlet, insulation, vessel, heat exchangers, etc.), mass flow meters (water, steam, syngas, etc), pressure transducers, etc. A SCADA System monitors and controls the process variables (about 850 variables). Data acquisition begins at the PLC level and includes meter readings and equipment status reports that are communicated to SCADA as required. All the data will be recorded by the control room on the ground.

It is planned to start the experimental campaign of the solar installation at the SSPS tower of Plataforma Solar de Almería in summer 2010.

A conceptual layout of a commercial 50 MWth gasification plant in Venezuela will complete this project. Results of the testing campaign will provide input to the pre-design of the gasification plant in Venezuela. The test data will be evaluated and compared with simulation tools in order to verify the calculations and to identify potential problems. The major components of a solar petcoke reforming plant will be analysed to assess their impact on the conceptual layout of the plant. For the upstream part of the gasification loop, the operation with different gaseous feedstocks (natural gas, weak gas, bio-gas, landfill gas), and concepts for gas cleaning and gas treatment will all be assessed.

References

[1] Epstein, M., Spiewak, I., Funken, K-H and Ortner, J. Review of the technology for solar gasification of carbonoceus materials. ASME International Solar Energy Conference, S. Francisco, March 1994, 79-91.

[2] Z'Graggen A., Haueter P., Trommer D., Romero M., de Jesus J.C., Steinfeld A. (2005) Hydrogen production by steam-gasification of petroleum coke using concentrated solar power - II. Reactor design, testing, and modeling, Int. J. Hydrogen Energy, Vol. 31, pp 797-811, 2006.

[3] Z'Graggen A., Steinfeld A., "Hydrogen Production by Steam-Gasification of Carbonaceous Materials using Concentrated Solar Energy – V. Reactor modeling, optimization, and scale-up", *International Journal of Hydrogen Energ*y, Vol. 33, pp. 5484-5492, 2008.

[4] Z'Graggen A., Haueter P., Maag G., Vidal A., Romero M., Steinfeld A., "Hydrogen Production by Steam-Gasification of Petroleum Coke using Concentrated Solar Power − III. Reactor experimentation with slurry feeding", International Journal of Hydrogen Energy, Vol. 32, pp. 992-996, 2007.

[5] Thorsten Denk, Philipp Haueter, Alfonso Vidal, Luís Zacarías and Antonio Valverde. Upscaling of a solar powered reactor for CO2-free syngas and hydrogen production by steam gasification of petroleum coke. 13th International Symposium on Concentrating Solar Power and Chemical Energy Technologies. June 20, 2006. Seville. Spain.

RWE's IGCC-CCS-Project – A Way towards a Coal-based Hydrogen Technology

Dietmar Keller, **Johannes Ewers**, **Frank Schwendig**, RWE Power AG, Germany

1 „Where will the hydrogen in Germany come from by 2050?"

In 2009 a study [1] conducted on behalf of the German ministry of transport, building and urban affairs dealt with the question, where the hydrogen needed in Germany will be originating from within a time period until 2050. Three scenarios were investigated focusing on different assumptions concerning the development of energy use in Germany. The moderate scenario is a "business as usual" scenario assuming conservative aims to reduce greenhouse gas emissions including only small efficiency increases and only small increases in the use of renewable energies. Opposed to that, the climate scenario is characterized by stringent guidelines concerning the reduction of CO_2 emissions up to -80 % in 2050 (basis 1990). The third scenario assumes a drastic shortage of resources connected with a strong increase of prices for primary energy carriers. All investigated scenarios predict a rise in the use of hydrogen as energy carrier. For the production of hydrogen wind energy is estimated to play an important role in all time horizons. Moreover, in the long term, also coal with or without carbon capture and storage technology will be a major primary energy carrier for hydrogen synthesis with a share of about 30 – 50 % of the overall future H_2 production. To be able to cover this demand of coal for hydrogen production, it is beneficial to have a secure source of low-priced coal.

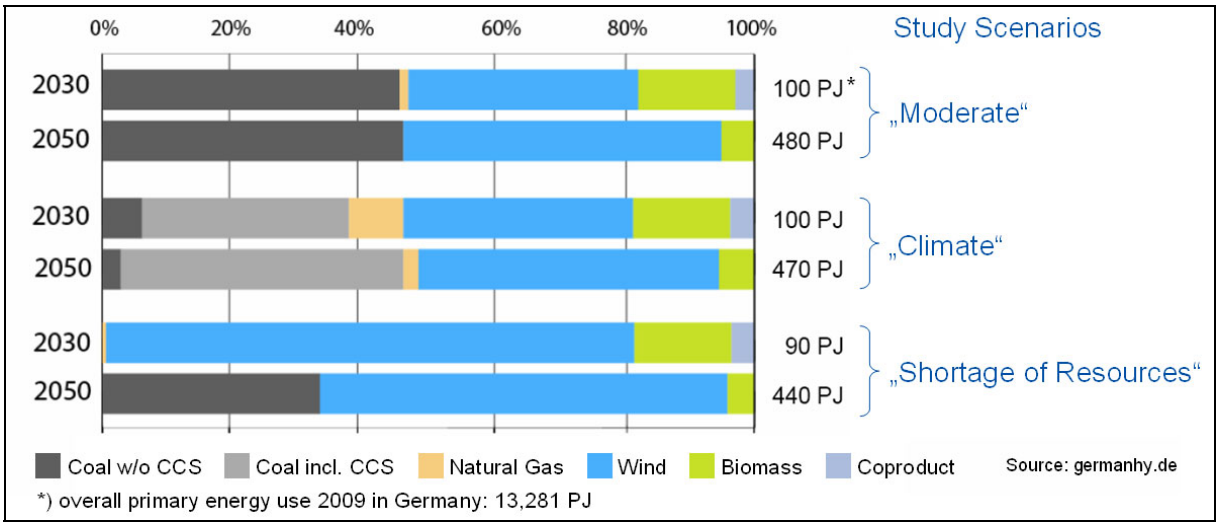

Figure 1: Shares of primary energy carriers in future H_2 production [2].

2 RWE's Rhenish Lignite Mining Area

RWE is operating three open cast lignite mines in Germany. About 3.4 bn t of approved lignite reserves are currently available in the mines Hambach, Garzweiler and Inden in North Rhine-Westphalia. The actual lignite production is about 92 Mt / a. Thereof, 9 Mt / a are processed in the refinement factories producing dry lignite in the form of coal briquettes or coal dust for industrial use and heating applications in private households. Among the approved lignite reserves, a potential of about 35 bn t of lignite have been explored. At the level of today's production rate, these reserves can contribute to secure the primary energy supply for further 350 years – a vast primary energy carrier source. RWE's lignite fired power plants are directly connected to the open cast mines via an own railway net. This way coal can be supplied independently to the power plants and factories. The overall installed capacity for power generation at 5 power plant sites is about 11 GW_{el}. The Rhenish lignite mines offer a secure national energy supply for different energy applications including potential conversion routes of lignite to chemical products or energy carriers for mobile applications.

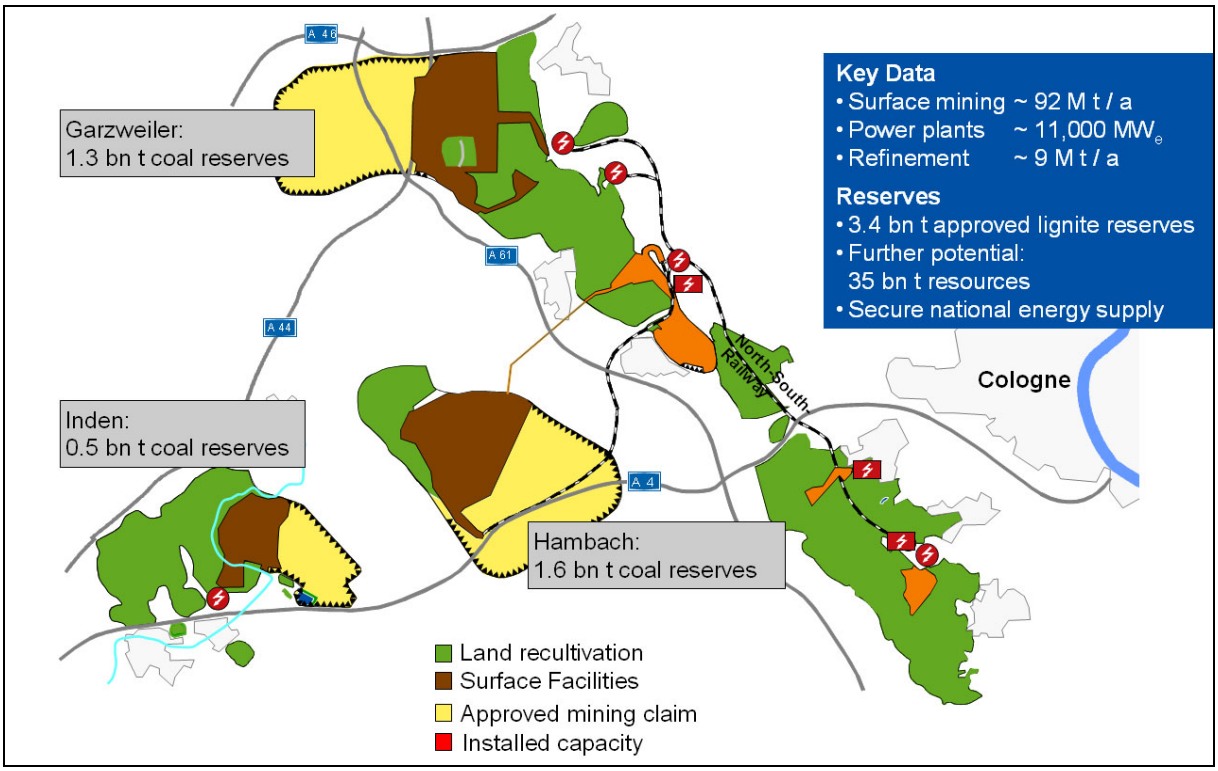

Figure 2: RWE's Rhenish lignite area is a large domestic energy reserve.

3 Gasification is Key to Multiple Products with Climate-friendly Use of Lignite

The conversion of lignite or coal in general was already realized in the 19th century for lightning applications and later on also for heating and cooking in private households. In the 20th century coal gasification was mainly used in crisis situations, when the supply of oil was no more ensured. Today large gasification capacities are still in operation in South Africa, where the national coal reserves are used to produce fuels. Having large coal reserves, but

less oil and gas deposits China and India are developing many gasification projects to produce chemicals and different energy carriers. Gasification technology for the conversion of coal to synthesis gas ($CO + H_2$) is the door opener to a whole bunch of products needed in industrialized countries. It is an interesting opportunity for countries having large world market price independent coal deposits to reach a certain independence from foreign energy imports. Moreover, the conversion of coal to synthesis gas opens the possibility to use coal in a climate friendly way since the implementation of the CCS technology to the gasification and further conversion of synthesis gas to the desired products is easily possible.

Downstream the coal gasification the produced raw synthesis gas is conditioned further for the following process. In this step the ratio CO/H_2 is adjusted according to the requirements of the applied syntheses. CO_2 scrubbing is usually added to the process to capture CO_2 that can be stored or used in other applications afterwards. In this way one ton of lignite will yield approximately 0.86 MWh of power, 580m³ H_2, 180 m³ CH_4, 270 kg methanol or 140 l of fuels by applying an IGCC-CCS-process, a pressure shift adsorption, a methanisation, a methanol syntheses or a Fisher-Tropsch process after gas conditioning, respectively.

4 RWE's Clean Coal Power Strategy

Innovative coal technologies are as indispensable to climate protection as coal is to satisfying the world's thirst for energy. With its clean coal power strategy, RWE faces the challenge of preventing climate change and is now introducing further elements of this strategy. In this respect, carbon capture and storage (CCS) plays a key role if more substantial CO_2 reductions are to be achieved than possible by merely increasing efficiencies. If this vision is to become reality, expertise, great commitment and a high willingness to take risks are required to implement a technological quantum leap.

The development of coal-fired power plants with CCS strengthens Germany's position as a technology leader, secures export potential for manufacturers and jobs in industry. The 450 MW IGCC-CCS project is part of RWE's overall strategy aimed at developing and implementing clean coal power.

On a broad basis – in line with the energy mix in the generation portfolio – innovation lines with different horizons are being pursued both for lignite and hard coal.

RWE has launched a large-scale renewal program for coal- and natural gas-based power plants that involves using cutting-edge technology to increase efficiency for the sake of climate protection. Examples for the use of coal are the BoA 2&3 new-build projects at the Neurath power plant and the two hard coal-fired twin units at the Westfalen power plant and in Eemshaven in the Netherlands. The total new-build capacity amounts to 5,400 MW with corresponding capital costs of € 6.2 bn.

In a second horizon, RWE is developing technologies in collaboration with partners that permit efficiencies to be further increased beyond today's high level. The focus is on demonstrating the WTA (lignite pre-drying) technology, which was developed by RWE to dry moist lignite on the prototype plant at BoA 1 in Niederaussem, and on the test plant for the 700 °C technology; both lines of development will increase the efficiency of lignite fired power plants up to values of over 50 %. For these projects, RWE Power will expend approx. € 60 million.

The 450 MW IGCC-CCS project based on an integrated gasification combined cycle process is part of the third horizon, focusing on the capture and storage of the CO_2 emitted by fossil-fired power plants. In parallel, we will develop CO_2 scrubbing technologies for conventional power plants in pilot plants with the primary goal of retrofitting advanced power plants to achieve a substantial cut in carbon emissions.

The overall aim of RWE's Clean Coal Power Strategy is the continuous renewal of the power plant fleet using state-of-the-art technology that ensures both competitiveness and security of supply while protecting the climate, thus making RWE's generation business fit for the future.

5 The IGCC-CCS Project

Following the project announcement in 2006, its concept was developed and specified in all process areas and its viability verified. RWE Power – which is responsible in the Group for electricity generation in Germany – is in charge of power plant matters, while RWE Dea, which is responsible for the exploration and production of crude oil and natural gas, works on the CO_2 pipeline and storage facilities. This work goes hand in hand with our intensive efforts to establish the necessary underlying conditions, such as a regulatory framework for CCS and a communication concept for informing authorities and the public.

A combined-cycle power plant with integrated coal gasification (IGCC) was chosen as the power plant technology to be used. The use of a modern gas turbine of the F class enables the plant to achieve a gross electric capacity of approx. 450 MW. About 90 % of the CO_2 produced in the power plant will be captured, compressed, and transported via a pipeline to a storage facility. In this way 2.6 m t CO_2 per year will be stored safely over the long term.

We plan the IGCC-CCS power plant at RWE’s Goldenberg power plant location in Hürth close to Cologne. The location thus resumes RWE / Rheinbraun's earlier gasification activities in connection with the development of HTW (High Temperature Winkler) gasification. It is already connected with our large lignite opencast mines via railway. For the IGCC power plant, parts of the existing infrastructure of the site can be used. Different studies have been assigned to investigate the viability of routing options for the connection of the power plant to the grid. To secure enough space for the construction of the power plant RWE has started to buy different areas adjacent to the existing RWE power plant site.

6 Process Description

Rhenish lignite from our own opencast mines serves as the fuel for the IGCC-CCS power plant. In a first process step, its moisture content is reduced from approx. 55 % to 12 % using RWE's own WTA drying technology. Subsequently, the lignite is ground by roller mills according to gasification requirements. An entrained-flow gasification with a thermal overall capacity of approx. 1,000 MW, operated at a pressure of approx. 40 bar, is employed for gasification. The hot, CO/H_2-rich raw gas is quenched to approx. 200 °C using water. The resulting high portion of steam is used in the subsequent shift stage to convert the CO into more hydrogen and CO_2.

The hydrogen-rich gas after the H_2S/CO_2 separation process is conditioned with N_2 from the air separation unit and if necessary with steam to create moderate combustion conditions and meet the legal requirements for NO_X values. The conditioned fuel gas is used to

generate electricity in the combined cycle power plant (CCPP) unit. The capacity of the gas turbine (F class), which has a share of approx. 300 MW in the total electricity generation capacity of 455 MW, determines the capacity of the overall process. The „First of its kind“ character of new technologies impacts the overall IGCC performance. The reliable interaction between individual process units shall be demonstrated.

7 RWE's Lignite Drying Technology

When power is generated in an integrated coal gasification combined-cycle power plant, lignite pre-drying is a matter of principle. At this point, an energetically efficient drying process can contribute to further efficiency enhancement. As an advanced method for processing and drying lignite, the WTA technology (WTA = German abbreviation for fluidized-bed drying with internal waste heat utilization) is applied to the RWE IGCC power plant. It contributes significantly to optimizing the energy efficiency and reducing emissions of the overall process. The WTA lignite drying technique has been developed by RWE. The first commercial scale drying unit is right now commissioned at RWE's Niederaussem power station. The lessons learned are identified and implemented. The continuous drying operation is safe.

The WTA technology is based on the principle of a stationary fluidized bed with low expansion operating at a slightly elevated pressure. The raw coal enters the dryer after running through a milling system reducing the grain sizes from 0 – 80 mm to 0 – 2 mm. The energy required for drying is supplied via heat exchangers that are integrated in the fluidized bed dryer and heated with steam. Drying takes place in nearly 100 % water steam atmosphere which is slightly superheated. Compared to other drying processes, lignite drying in a steam atmosphere has the advantage, among others, that the evaporated coal water can be condensed isothermally and, hence, utilized in an energy efficient way.

For the 450 MW IGCC power plant 2 drying units, having a raw lignite input of about 350 t/h and a dry lignite output of approx. 170 t/h, need to be utilized. To realize an environment-friendly use of freshwater, the condensed water from the WTA dryer will be used as quench water in the gasification process.

For the IGCC project, mechanical vapor recompression, realized as an open heat pump process, for heating the dryer is applied. The evaporated water from the coal is recompressed to about 4 bar, so that the vapor can be used to heat the heat exchangers installed inside the drier. The sensible heat of the produced vapor condensate is used for preheating the raw lignite. Part of the vapor is recirculated and employed for fluidizing the bed.

8 Coal Gasification

As gasification technology, an entrained flow gasification with subsequent water quench has been chosen for the IGCC power plant. It is envisaged to have a gasification process with an overall thermal power of approx. 1000 MW_{th}. The actual amount of CO-H_2-gas production is defined by the demand of the F-class gas turbine that is about 250,000 Nm^3 / h. The use of a direct water quench system has a positive effect on the overall efficiency. The water that is needed in the following CO-shift is added directly to the raw gas stream, instead of being heated by a raw gas cooler system and afterwards being let into the gas stream. The produced raw gas ex gasifier therefore consists of about 57 vol.-% steam.

Within the gasifier, the very fine milled dry lignite from the WTA will be partly combusted in sub-stoichiometric atmosphere at a pressure of about 40 bar to a raw gas containing mainly carbon monoxide and hydrogen. The high pressure in the gasifier enables the process to have no intermediate compressor for the fuel in front of the gas turbine. Oxygen is provided by an air separation unit. Due to temperatures of about 1500 °C, within the gasifier the ash contents of the coal melt and drop from the reaction chamber through the quench zone, where it solidifies again, into a water bath at the bottom of the gasifier. The raw gas is cooled down in the quench zone to about 200 °C in a water-saturated state.

The entrained flow gasification is the worldwide most often used gasification technology. The existing large experiences in this technology are beneficial for the IGCC-CCS project. But nevertheless, the process parameters in this project ask for further technological developments regarding a scale up to the required thermal power for the fuel demand of the gas turbine and an increase in the process pressure from usually about 25 – 30 bar to 40 bar. Also the water quench technology has so far not been used with IGCC power plants.

9 Gas turbine Technology

To be able to demonstrate the IGCC-CCS technology with the highest possible efficiencies an advanced F-class gas turbine with a power output of approx. 300 MW was chosen. As one of the major components in the IGCC plant the gas turbine determines the design of the whole process significantly. With the chosen F-class technology it could be possible to realize a one train concept including the design of auxiliary components like the air separation unit, gas treatment facilities as well as CO_2 scrubbing and compression. Main process parameters influenced by the gas turbine are gasification pressure as well as fuel quantity and quality.

By separating the CO_2 from the fuel gas of the gas turbine, a gas with very high hydrogen content of about 83 vol.-% is generated. Due to the high flame velocity and reactivity of hydrogen, the fuel gas needs to be preconditioned with nitrogen and / or water to ensure a safe control of the combustion and to limit the formation of NO_X components. Compared to e.g. methane, the resulting hydrogen plus diluent fuel has a significant smaller lower heating value. Therefore, the mass flow of hydrogen-rich fuel gases will be increased by about 20 % compared to natural gas fired gas turbines and subsequently can produce up to 20 % more power if the other turbine parts, i.e. compressor and hot gas path permit this increased mass flow. The high water content in the flue gases produces a more intensive heat transfer in the turbine section, which needs to be considered in the gas turbine design. To be able to meet

emission requirements, extensive tests to validate the operational range of the gas turbine combustion system need to be conducted. Furthermore it will be a major objective to raise the efficiency of the gas turbine by investigating the possibilities of low diluent combustion systems for future IGCC applications.

10 Market Potential and Profitability of Gasification Products

Not only technical challenges need to be addressed when realizing coal gasification projects. Also the market potential and market access of possible products has to be assessed. While it is relatively easy to access a wholesale market as new producer, it will be much more difficult to enter a business with small open market trade volumes. Looking at basic market characteristics of coal gasification products it is obvious, that the volume of synthetic natural gas (CH_4) and fuels for mobile applications (diesel / gasoline) in Germany is in principle large enough for a new producer to enter the market. Further more, it can be assumed that there will be a strong long term demand for these products. In contrast to this, the market volume of hydrogen is relatively small. There is a primarily industrial market where only 5 % of the produced H_2 is sold on the open market. Usually hydrogen is targeted produced where it is needed. Accessing this market will be only possible if usual market prices can be underpriced in situations where long term contracts are running out or new consumer markets are opened.

The methanol market is primarily driven by world market prices. Having a demand of about 45 m t per year worldwide, the actual production capacities are exceeding this demand. Moreover it is expected, that massive new build capacities in China and Middle East will go onstream in the next years.

A short study conducted by RWE estimated the ratios of market prices to required sales prices of gasification products. No product option reached the profitability threshold. The presented ratios for different products are only for illustrative purposes. They represent a certain market condition at a certain time for the German market. All in all it can be summarized, that oil market prices are the decisive parameter for the profitability of different products. World market independent lignite reserves usually offer earlier profitability than coal purchased abroad. Further influencing factors that can vary significantly by time are regional product market, CO_2 allowances and equipment prices.

11 Conclusions

For the expected hydrogen demand in the following 40 years, coal will be, next to different other sources like wind energy, an important energy source especially in the long term. Gasification technology can contribute to an effective production of hydrogen from coal that can also be realized in a climate friendly way if carbon capture and storage techniques are applied to the processes. The lignite reserves in Germany present an important option for an emerging hydrogen economy that is independent of world market prices and can offer security of supply. The profitability of hydrogen and other coal derived products depends highly on oil and gas prices as well as on the local market situation. Overall, coal gasification technologies and domestic coal reserves offer the opportunity to support an emerging hydrogen economy significantly.

References

[1] www.germanhy.de: GermanHy – Studie zur Frage „Woher kommt der Wasserstoff in Deutschland bis 2050?“, Im Auftrag des Bundesministeriums für Verkehr, Bau und Stadtentwicklung (BMVBS) und in Zusammenarbeit mit der Nationalen Organisation Wasserstoff-und Brennstoffzellentechnologie (NOW), Abschlussbericht.

[2] www.germanhy.de: GermanHy – Studie zur Frage „Woher kommt der Wasserstoff in Deutschland bis 2050?“, Im Auftrag des Bundesministeriums für Verkehr, Bau und Stadtentwicklung (BMVBS) und in Zusammenarbeit mit der Nationalen Organisation Wasserstoff- und Brennstoffzellentechnologie (NOW), Zusammenfassung der Ergebnisse anlässlich der Abschlussveranstaltung GermanHy am 26. Juni 2008.

Coal Gasification for Hydrogen Production Using Nuclear Energy

Werner von Lensa[*]**, Karl Verfondern,** Institute of Energy Research – Safety Research and Reactor Technology (IEF-6), Forschungszentrum Jülich GmbH, Jülich, Germany

Abstract

The most abundant fossil fuel on Earth is coal. Up-to-now coal is mainly used for electricity production and will continue to play this important role in the near and mid-term. However, coal could also substitute oil and gas by coal gasification or coal liquefaction techniques. The necessary process heat could be supplied by nuclear energy to save fossil energy resources and to lower carbon emissions to the environment. In Germany, comprehensive R&D activities were conducted in the past to investigate the utilization of nuclear energy in the heat-intensive processes of coal gasification for the large-scale production of hydrogen, synthetic natural gas and synthetic liquid fuels, respectively. Different methods of gasification for the two types of coal existing in Germany have been developed, i.e. steam gasification of hard coal and hydrogasification of lignite. Both processes were successfully demonstrated on pilot plant scale under simulated nuclear conditions.

1 Coal – More Than Just a Fuel to be Burnt

Despite of its abundant resources on earth, the conversion of coal to gaseous or liquid fuels has been commercially applied, only in a limited scale. In the 1970s, with the first oil crisis, coal resources were assumed to become a more central role and coal conversion programs were started as a contribution to an away-from-oil policy. Extensive experimental and theoretical studies included coal gasification, coal liquefaction, and advanced combustion systems aiming at improved methods for the generation of Synthetic Natural Gas (SNG), liquid hydrocarbons, and other raw materials for the chemical industries. Numerous coal gasification projects were launched to investigate various processes, on pilot plant scale [1, 2]. However, interest in coal refinement faded away again with low oil prices, since 1980s.

2 Coal Conversion Processes supported by Nuclear Energy

The conversion of coal into a gas is realized by means of a gasification agent, which reacts with the coal at temperatures > 800 °C. The gasification agent is either steam (steam coal gasification) or hydrogen (hydrogasification). Both processes have in common that high pressures are needed to achieve a high methane yield, whereas for an optimal synthesis gas production, high temperatures and low pressures are required. The gas-cooled nuclear High-

[*] Corresponding author, email: w.von.lensa@fz-juelich.de

Temperature Gas-Cooled Reactor (HTGR) is capable to provide the process heat at the required temperature level up to the range of 900-950 °C.

2.1 Steam coal gasification

Steam gasification of coal is a mature and well established technology practiced on industrial scale. In the conventional steam coal gasification processes, a part of the coal is partially oxidized to provide the necessary process heat. In the heterogeneous water gas reaction, the residual organic solids are converted to synthesis gas with 'steam' as the agent. The gasification reaction with is given by the heterogeneous water gas reaction:

$$C + H_2O \rightarrow H_2 + CO \qquad -118.5 \text{ kJ/mol C}$$

The homogeneous water gas (shift) reaction allows a further increase of the H_2 fraction. It is followed by a methanation step if the desired end product is SNG.

Gasification processes are classified according to the type of reactor. The principal lines mainly used today are those by Lurgi (since 1931), Winkler (since 1922), Koppers-Totzek (since 1941). They all were developed in Germany and exist at a large commercial scale.

1. In the Lurgi pressure gasification, a solid bed of coal moving from top to bottom is gasified by adding steam and oxygen from the bottom at a pressure of 1.5-3 MPa. Coal is inserted in smaller pieces. The counter-current flow arrangement leads to higher conversion rates and thermal efficiencies. The amount of methane generated is depending on pressure, temperature, the oxygen-to-steam ratio, reactivity of the coal, and the contents of volatile substances in the coal. The Sasol company in South Africa is the world's largest commercial applier of coal conversion technology operating gasification reactors which are able to produce 65,000 Nm^3/h of dry gas with a raw coal throughput of 54 t/h [2].
2. The High Temperature Winkler (HTW) process takes place in a fluidized bed where fine-grain coal is reacted with oxygen and steam. The fluidized bed has no reaction zones, but rather forms a homogeneous distribution of solids. The temperature must be below the ash melting point to prevent a softening and agglomeration of the ash, which would lead to a collapse of the fluidized bed. Characteristics are the simple coal pre-treatment, low oxygen consumption and good performance over a broad load range. Industrial scale is at ~60,000 Nm^3/h.
3. The Koppers-Totzek process runs in a flue stream gasifier at very high temperatures above the ash melting point. Dry coal dust is mixed with steam and oxygen/air and gasified at atmospheric pressure, in an autothermal way. The reaction zone is limited to the flame area with a co-current flow of coal and gasification agent. It has the advantage that tar formation is suppressed and other organic substances are destroyed. The conversion rate is at almost 100 %. Industrial plant capacities are in the order of 50,000 Nm^3/h.

Numerous modified process variants have been developed aiming at an adjustment of the feedstock quality, an optimization of the product gas composition and, of course, an

efficiency improvement. Variants differ by temperature and pressure range, grain size of the coal, and residence time. Coal conversion is estimated to be around 95 % and the total efficiency (based on higher heating value) to be ~ 70 %. Main issues of coal gasification are the handling of solid material streams and the large amounts of CO_2, SO_2, and ash requiring a complex cleaning system [1]. Emissions of carbon dioxide can be suppressed, if a CO_2-emission-free, external heat source is applied (allothermal gasification). For example, with an HTGR, the heat provided by the hot helium coolant can be introduced indirectly into the gas generator, another part being used for the steam production, and the rest still usable for electricity production.

2.2 Hydrogasification

In the hydrogasification process of coal, hydrogen is added to convert the coal into a methane-rich raw gas, in an exothermic reaction. This is ideal for the production of substitute natural gas (SNG). The hydrogen can be provided either by taking the coke left from the hydrogasification and convert it with oxygen and steam in an HTW process, or by taking a part of the produced methane for steam reforming. Both processes need high temperatures, which could be provided by nuclear energy, in an allothermal process. The gasification reaction with the agent 'hydrogen' and the main product methane is:

$$C + 2\,H_2 \rightarrow CH_4 \qquad +87.5\ \text{kJ/mol C}$$

Kinetics of the process are more complex compared to steam gasification. The advantage of hydrogasification compared with steam coal gasification is its 200 K lower pre-heating temperature which reduces potential corrosive attack. A major drawback, however, is the low conversion rate, i.e., the large amount of residual coke of up to 40 %. In contrast to steam gasification, the hydrogasification process still needs to be demonstrated at a larger commercial scale.

3 Nuclear Process Heat for Coal Gasification

3.1 Drivers for nuclear coal refinement

There are several drivers for nuclear energy to be introduced as a primary heat source into the coal gasification process [3]:

- In the conventional gasification process, a significant additional amount of feedstock is necessary to provide process heat at the required temperature level. Substitution of the process heat by nuclear energy would allow resource savings of up to 40 %.
  A respective reduction in CO_2 and other, coal-specific emissions will be achieved, at the same time.
- The conversion to liquid hydrocarbons will reduce dependency on oil imports and diversify energy supply.
- If cost of nuclear heat is sufficiently low, it may help to stabilise fluctuating energy cost.

3.2 The Prototype Nuclear Process Heat (PNP) Project

In Germany, the concept of the pebble-bed HTGR has been developed and became subject of various projects. Motivation for the PNP project was to take advantage of the large resources of both energy carriers coal and uranium and to create an additional use on the process heat market, for the coal. HTGR are characterized, among other features, by their operation at an average coolant exit temperature of up to 950 °C [4], due to the fully ceramic core and fuel elements. The maximum operational temperature of HTGR is mainly determined by the capabilities of metallic materials for heat exchangers. As most chemical processes are performed at lower pressures some adaptation of the reactor design and of the chemical process has been necessary, because HTGR normally operate at pressures of 4-9 MPa. Heat transfer under varying operational load conditions, hot gas mixing in the core bottom, or the lifetime of hot gas thermal insulation have been comprehensively investigated in extensive experiments.

The project started with an integrated arrangement of the core and the heat exchangers in a Prestressed-Concrete Reactor Pressure Vessel (PCRV), with a maximum power of 3000 MWth per unit. This concept was afterwards changed towards modular HTGR with a power size of 170-200 MWth per unit to allow for a passive decay heat removal in case of an accident. A particular safety significance has connection between the vessels for the nuclear heat source and for the steam generator or heat exchanger. This connection has to be designed as pressure vessel according to the leak-before-break principle, where the early detection of a leakage would allow the immediate plant shutdown. An underground placement of the nuclear unit might be recommended to ensure an enhanced protection against fire, aircraft crash or atmospheric explosions of gas clouds in the adjacent coal conversion facilities.

3.3 Coupling between nuclear and chemical plant

For the nuclear steam coal gasification process, it was foreseen that the heat from the reactor coolant be transferred to an additional intermediate circuit via a helium-helium intermediate heat exchanger (He-He IHX). Two different He-He IHX components were constructed by German companies, one with a helical tube bundle and the other one with U-tubes, designed for a power level (~125 MW) representative for large and medium-sized plants. Both components were tested with 950 °C helium on the primary side [5], at a 10 MW scale. For the PNP nuclear hydrogasification of coal, it was foreseen to place the steam-methane reformer directly into the primary circuit of the HTGR. The nuclear steam reformer component was tested as part of the EVA-ADAM system at FZJ, an energy transportation system based on nuclear steam reforming and methanation processes.

3.4 Nuclear steam gasification of coal

A new component for nuclear steam coal gasification was the gas generator with allothermal heating. Tests were conducted with a gas generator on semi-technical scale with a fluidized bed of about 1 m^2 base area and a height of up to 4 m, laid out for a coal throughput of ~200 kg/h. Different from the conventional concept, coal was gasified indirectly by means of

a tube-type immersion heat exchanger which was placed into the fluidized bed to transfer heat from a separate helium circuit to simulate nuclear conditions [6].

The semi-technical plant was used for testing components, feeding devices, insulation, investigating broad ranges of operating conditions, and applying different types of coal. Since the temperature provided by the helium is limited, catalytic coal gasification was also investigated in the semi-technical plant and enhanced reaction rates were observed. The catalyst, however, was found to be not effective until a certain threshold value, also corrosion effects were enhanced. The semi-technical plant was in hot operation for approx. 26,600 hours with more than 13,600 hours under gasification conditions (750-850 °C, 2-4 MPa). Maximum capacity was 0.5 t/h of coal, the total quantity of gasified coal was 2400 t [6, 7].

The commercial-size gas generator was foreseen to have a thermal power of 340 MW. It was designed, unlike the semi-technical plant, as a horizontal pressure vessel (Figure) to contain a fluidized bed with the shape of a long-stretched channel to allow for long residence times. It consisted of four parts (modules). Coal is introduced through several inlets in the first module; the gasification zone spreads over the other three modules. In the fourth module, the remaining ash is cooled and removed. Each module contains steam inlets in the bottom section and an immersion heat exchanger bundle, through which heat is transferred from the hot helium to the fluidized bed.

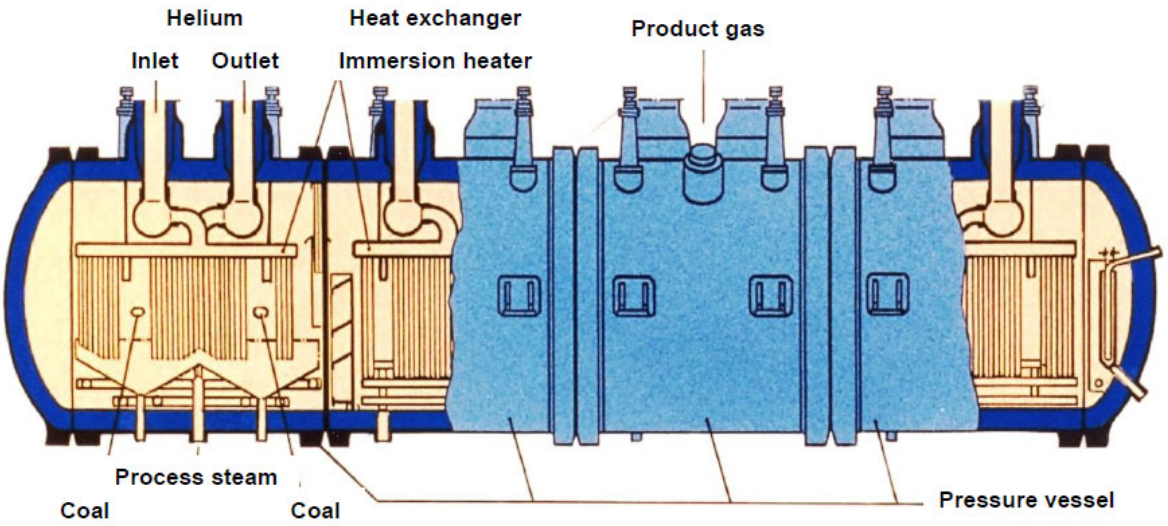

Figure: Schematic of an industrial-scale gas generator for nuclear steam coal gasification.

3.5 Nuclear hydrogasification of coal

The hydrogasification process can also be combined with a nuclear heat source. But unlike the steam coal gasification, the nuclear heat is not coupled directly into the gasification reactor [8]. One variant is steam-methane reforming, where a part of the product gas methane is drawn off and the high temperature nuclear heat is used for the endothermic reforming reaction. In a second variant, the nuclear heat is taken to pre-heat the hydrogen

produced during the gasification process itself (water gas shift reaction) to 800-950 °C. Nuclear heat is also used for steam production and the residual power for electricity generation. Compared to the first variant, it has a simpler process scheme. A drawback is the fact that high gasification pressures (8 MPa) are needed.

Between 1976 and 1982, the Rheinische Braunkohlenwerke, Wesseling, investigated the hydrogasification process in a 1.5 MW semi-technical test facility with both lignite and hard coal [8, 9, 10]. The reactor of 8 m height contained a fluidized bed with 0.2 m diameter where hydrogen was injected as gasification agent. The hydrogen was electrically pre-heated to 750 °C and could, if necessary, be further heated to 1000 °C by partial combustion. Operational parameters could be varied in a broader range. A part of the hydrogen was used as a carrier medium for the coal input.

The test facility was operated for about 27,000 h with more than 12,000 h under gasification conditions. The throughput was 320 kg/h of lignite or 160 kg/h of hard coal, the total quantity gasified was 1800 t.

From 1983 to 1985, a follow-up pilot plant was operated over 8300 h, with half of the time under coal gasification conditions with high availability. It included, unlike the semi-technical plant, all post-processing components of gas treatment up to the stage of SNG production. The plant had a throughput of 9.6 t/h corresponding to a total power of 50 MW. Gasification of more than 17,000 t of brown coal was made to yield a total of 11 million Nm^3 of SNG, whose fraction in the raw gas was between 22 and 36 %. The SNG production was at a rate of up to 6400 Nm^3/h.

4 Summary and Conclusions

Within the frame of the PNP project, comprehensive R&D activities on nuclear coal gasification were conducted in Germany in a cooperation between the Research Center Jülich and partners from the coal and nuclear industries. The results can be summarized as follows:

- The use of nuclear primary energy promises a saving of ~40 % of the coal resources, increase the specific SNG output, and reduce specific emissions of carbon and other pollutants to the atmosphere, respectively. As a transition step, process steam could be supplied from a nuclear heat source for use in conventional steam coal gasification.
- Special importance for process heat projects had the 45 MWt AVR test reactor in Jülich, which was operated between 1967 and 1988. It became the world's first pebble-bed reactor to successfully achieving a coolant outlet temperature of 950 °C proving the feasibility of the pebble-bed HTGR concept under high temperature process heat conditions with a high availability. (The same helium outlet temperatures are currently demonstrated for the Japanese block reactor HTTR as well.)
- Nuclear coal gasification is considered to be a complementary option in the energy supply strategy and may help to significantly reduce the dependency on oil and natural gas imports.

- A wide variety of coal gasification processes has been developed and demonstrated in the past, which are differently appropriate depending on user requirements, plant size, and coal characteristics.
- Allothermal steam coal gasification with both main types of coal in Germany, hard coal and lignite, was demonstrated in numerous experiments. The new major components that needed to be developed were the gas generator and the steam methane reformer.
- The operation of the semi-technical plants confirmed the technical feasibility of allothermal, continuous coal gasification under the nuclear conditions of a process heat HTGR.
- By the manufacture and successful operation of high temperature heat-exchanging and heat-transporting components on the 10 MW power level under simulated nuclear conditions in KVK and other related test facilities, valuable practical experience with high-temperature helium plants on a representative scale was acquired. Both IHX types were considered appropriate to be designed for a power of 170 MW and an operation time of 140,000 h at 950 °C.
- A key problem remained the selection of appropriate high temperature materials for the heat exchanging components such as steam reformer and He-He intermediate heat exchanger, but also for the gas generator in the case of catalytic coal gasification.

The idea of constructing a PNP prototype plant was abandoned at the beginning of the 1990s, when economic analyses had shown that competitiveness of nuclear SNG from expensive German coal with the cheap oil and gas available on the world markets was not given. Therefore, further funding and developments for both lines, steam gasification and hydrogasification were terminated.

Future activities could take benefit from a re-evaluation of the studies conducted in the past on HTGR process heat applications by comparing against current technologies and market conditions. The goal should be to select promising applications under the current industrial practice within existing and evolving markets. Superior safety features and high reliability are considered to be prerequisites for the introduction of nuclear process heat and nuclear combined heat and power generation.

References

[1] FRANCK, H.-G., and KNOP, A., Kohleveredlung an der Schwelle der 80er Jahre, Die Naturwissenschaften 67:421-430, 1980.

[2] TEGGERS, H., and JÜNTGEN, H., Stand der Kohlevergasung zur Erzeugung von Brenngas und Synthesegas, Erdöl und Kohle – Erdgas 37:163-174, 1984.

[3] MESSERSCHMIDT, H., Die Bedeutung nuklearer Verfahren für die Kohlenveredlung, Atomwirtschaft, August/September 1981.

[4] SCHULTEN, R., et al., Industriekraftwerk mit Hochtemperaturreaktor PR 500 – “OTTO-Prinzip” zur Erzeugung von Prozessdampf, Report Jül-941-RG, Jülich, Germany, 1973.

[5] HARTH, R., JANSING, W., TEUBNER, H., Experience Gained from the EVA II and KVK Operation, Nuclear Engineering and. Design 121:173-182, 1990.

[6] KIRCHHOFF, R., et al., Operation of a Semi-Technical Pilot Plant for Nuclear Aided Steam Gasification of Coal, Nuclear Engineering and. Design 78:233-239, 1984.

[7] KUBIAK, H., VAN HEEK, K. H., ZIEGLER, A., Nukleare Kohlevergasung – Erreichter Stand, Einschätzung und Nutzung der Ergebnisse, Fortschritte in der Energietechnik, Monographien des Forschungszentrums Jülich, Vol. 8, Jülich, Germany, 1993.

[8] SCHRADER, L., STRAUSS, W., TEGGERS, H., The Application of Nuclear Process Heat for HydroGasification of Coal, Nuclear Engineering and. Design 34:51-57, 1975.

[9] FLADERER, R., SCHRADER, L., Hydrierende Vergasung von Kohle – Neuere Betriebsergebnisse, Chem.-Ing.-Tech. 54:884-892, 1982.

[10] SCHARF, H.-J., SCHRADER, L., TEGGERS, H. Results from the Operation of a Semitechnical Test Plant for Brown Coal Hydrogasification, Nuclear Engineering and. Design 78:223-231, 1984.

Hydrogen Production by Thermal Cracking of Methane – Investigation of Reaction Conditions

Michael Wullenkord*, **Karl-Heinz Funken**, **Christian Sattler**, **Robert Pitz-Paal**,
Deutsches Zentrum für Luft- und Raumfahrt e.V. (DLR) / Solar Research, Germany

1 Introduction

The solar-thermal decomposition of methane represents a process, which allows the combined production of hydrogen and particulate carbon without generating CO_2-emissions. Solar radiation provides the heat necessary to run the cracking reactions. Different reactors have been used for solar operation (cf. e.g. [1], [2], [3]). The knowledge of reaction kinetics is essential for the design of reactors and plant operations. Although a lot of research has already been done in this field, a coherent and comprehensive characterization has not been reported in literature, yet. In order to learn more about the dependencies of the dissociation on the reaction conditions, numerous kinetic experiments have been carried out in the laboratories of DLR employing a tubular alumina reactor.

2 Experiments without Seeding

The nominal temperature of the electric tube furnace, which was used to heat the reactor, ranged from 1200 °C to 1600 °C, while the gas mixture fed into the reactor comprised a molar fraction of methane (in argon) between 2 % and 10 %.The full spectrum of conversion of methane and yield of hydrogen at a total pressure close to 1 bar was considered by variation of the residence time as shown in Figure 1 a and b. Different initial molar fractions of methane result in a moderate diversity of values for the conversion and the yield regarding similar reaction condition. The residence time is here defined as the time needed by the entering molar flow to pass through the heated volume of the reactor, characterized by the inner diameter of the reactor and the heated length of the tube furnace. For the calculation of the residence time it is assumed, that the heated volume holds the nominal temperature of the tube furnace and that the pressure equals the pressure measured at the inlet of the reactor. Beside the desired products, hydrogen and carbon, intermediates could be found at the reactor outlet, predominantly the C_2-hydrocarbons ethane, ethene, and ethyne. Maximum yields of 0.972 % for ethane, 4.71 % for ethene, and 59.5 % for ethyne were observed.

The sum of the molar fractions of argon, methane, hydrogen, and the C_2-hydrocarbons satisfies approximately 100 % taking the range of uncertainty of the measurands into account. Besides roughly all hydrogen atoms inserted to the system in form of the methane flow can be found in the considered compounds of the product flow.

* Corresponding author, email: michael.wullenkord@dlr.de

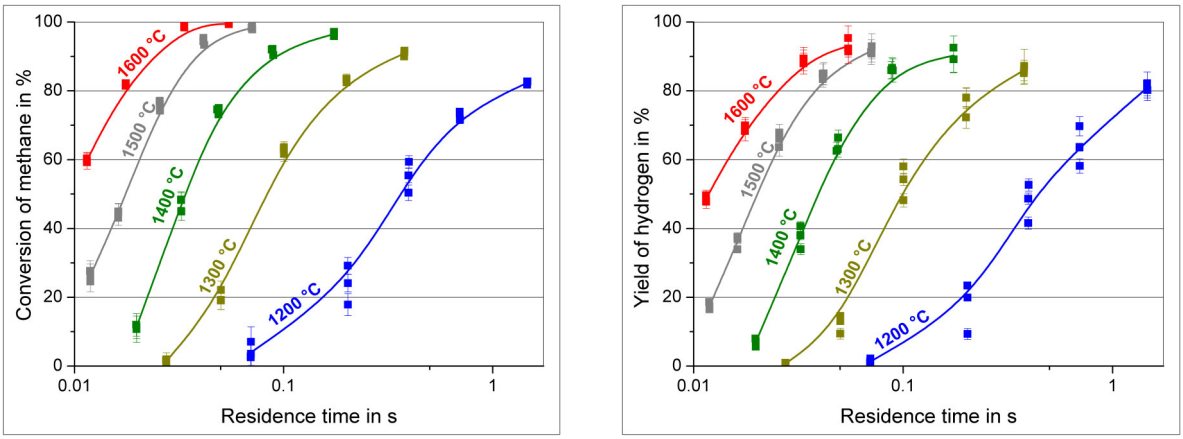

(a) (b)

Figure 1: Conversion of methane (a) and yield of hydrogen (b) as a function of the residence time and the nominal furnace temperature, dilution gas: argon, initial molar fraction of methane: between 2 % and 10 %.

3 Modeling the Reactor

Reactions in the test reactor were simulated employing a flow model and a kinetic model in order to extract kinetic parameters, which are the activation energy, the pre-exponential factor, and the reaction order for the four reactions. One of the main influencing factors concerning the kinetics is the temperature. For every combination of furnace temperature and residence time axial temperature profiles were measured using a thermocouple type S, which was stepwise moved through the reactor operated with a pure argon stream. The gained information was used to determine profiles for the wall temperature. With temperature profiles of the wall and velocity profiles at the entrance of the reactor temperature inside the whole reactor as well as flow lines were calculated utilizing the software COMSOL Multiphysics. A nested tube reactor model was chosen to approximate the laminar flow conditions inside the reactor. Reaction rates and finally leaving molar flows were obtained for discretized parts of the nested tube reactors. Each reaction step was followed by an ideal diffusion step in radial direction, equalizing molar fractions of the different species at the outlet of the considered discretized part. The kinetic model comprised the dehydrogenation reactions of methane, ethane, ethene, and ethyne (cp. [4]) and followed

$$2\ CH_4\ (g) \rightarrow C_2H_6\ (g) + H_2\ (g) \quad (1)$$
$$C_2H_6\ (g) \rightarrow C_2H_4\ (g) + H_2\ (g) \quad (2)$$
$$C_2H_4\ (g) \rightarrow C_2H_2\ (g) + H_2\ (g) \quad (3)$$
$$C_2H_2\ (g) \rightarrow 2\ \text{“C”}\ (s) + H_2\ (g) \quad (4)$$

Employing best fit kinetic parameters found by an optimization tool fairly good agreement for the conversion of methane and the yield of hydrogen between experimental results and output of the simplified model could be achieved. However the performance of the model offers potential for improvement. The dissociation of the species is not only the result of homogeneous reactions, but a combination of homogeneous and heterogeneous effects.

Thus an implementation of heterogeneous reactions will enhance the quality of a model of the thermal decomposition of methane. Heterogeneous effects occur on generated carbon particles – literature indicates rate-increasing effects of carbon-based catalysts (cp. e.g. [5], [6], [7]) – as well as on the surface of the reactor, which in operation in partly covered by carbon deposition. Additional experiments have been carried out, in order to learn about heterogeneous effects.

4 C-balance and Characterization of Samples

The latest experiments repeating selected reaction conditions, allow the balance of the amount of C-atoms. In contrast to the H-balance, the C-balance shows that about 25 %, and up to 50 %, of carbon atoms are contained in compounds of the product gas, which have not been considered in this work. As a result the presence of a low amount of substances with high C/H-ratios is probable. Without the consideration of further C-rich fractions the amount of particulate carbon is overestimated and, consequently, likewise the surface area provided for reactions. For the C-balance samples of carbon were obtained by removing carbon deposition from the inner wall of the reactor and from the filter element. In most carbon samples from the reactor not only black particulate carbon was found but also thin layers of shiny gray pyrocarbon (see Figure 2 a), which have the curved shape of the inner reactor wall. Some samples of carbon located in the filter show a slightly yellow color, which confirm the presence of high molecular by-products (see Figure 2 b). The BET-surface of particles found in the reactor range between 6.9 m^2/g and 56.4 m^2/g, whereas the range for particles found in the filter is characterized by higher values between 22.3 m^2/g and 139.1 m^2/g. Some samples show very similar specific surface areas to commercial carbon blacks.

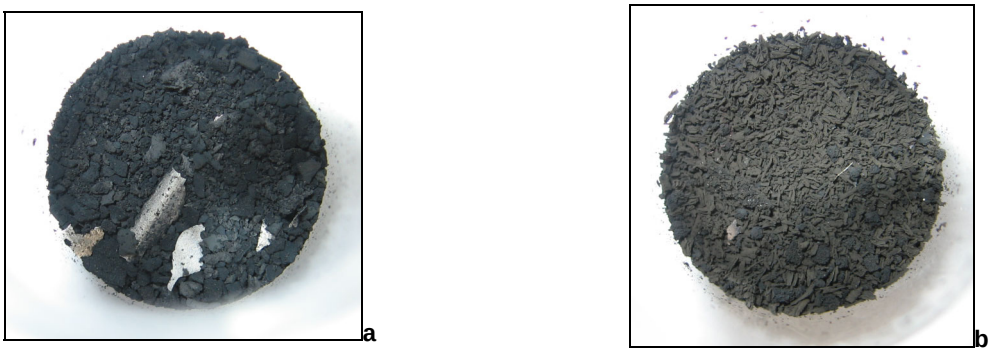

Figure 2: Examples of carbon samples: removed from the reactor wall (a) and removed from the filter (b).

5 Experiments with Particle Seeding

Experiments with carbon particle seeding of the inlet gas were carried out employing a recently developed apparatus, in order to expand data regarding heterogeneous effects. The material used for seeding was “Super P”, a commercial carbon black produced by Timcal, featuring a typical particle size of 40 nm and a specific surface area of 62 m^2/g (BET) (cp. [8]). The specific surface area of “Super P” has the same order of magnitude as most values for extracted samples from the reactor and the filter. The chosen reaction conditions were a

nominal furnace temperature of 1400 °C and a total volume flow of 3800 sccm (referring to standard conditions 0 °C and 1.01325 bar) consisting of 5 % methane in argon. The reference case without seeding corresponds to a calculated conversion of 48.2 % and 38.0 % yield of hydrogen. By adding a mass flow of about 5.24 g/h “Super P” the conversion of methane and the yield of hydrogen could be increased by 18 % and 33 %, respectively, compared to the reference case without seeding. The yields of ethane and ethene decreased by 40 % and 25 %, respectively, whereas the yield of ethyne rose slightly by about 4 % (see Figure 3 a). The related yields of hydrogen and C_2-hydrocarbons increased from 1.38 to 1.81. Thus obviously carbon particle seeding effects the dissociation of methane promoting the formation of the desired product hydrogen. Seeding influences the conditions inside the reactor in different ways, providing additional surface area for heterogeneous reactions and improving the heat transport between the reactor wall and the flow through the reactor.

The theoretical mass flow of generated carbon particles equals about 1.3 g/h for the reference case. In contrast to this calculation regarding the considered reaction condition without seeding the fraction of carbon atoms in not identified compounds of the product flow equals more than 20 %, leading to a practically negligible mass flow of generated particles. Therefore it is admissible to state, that major part of particles present in the reactor was contributed by particles, which were seeded. The surface area of added particles in the heated volume of the reactor can be approximated employing the mass flow, the residence time and the specific surface area (BET) of “Super P”. The theoretical surface area inside the reactor arises from the sum of the surface area of added particles and the geometrical surface area of the reactor, which equals about 0.0063 m^2. In Figure 3 b conversion and yields of the considered components of the product flow are depicted as a function of the theoretical surface area inside the reactor.

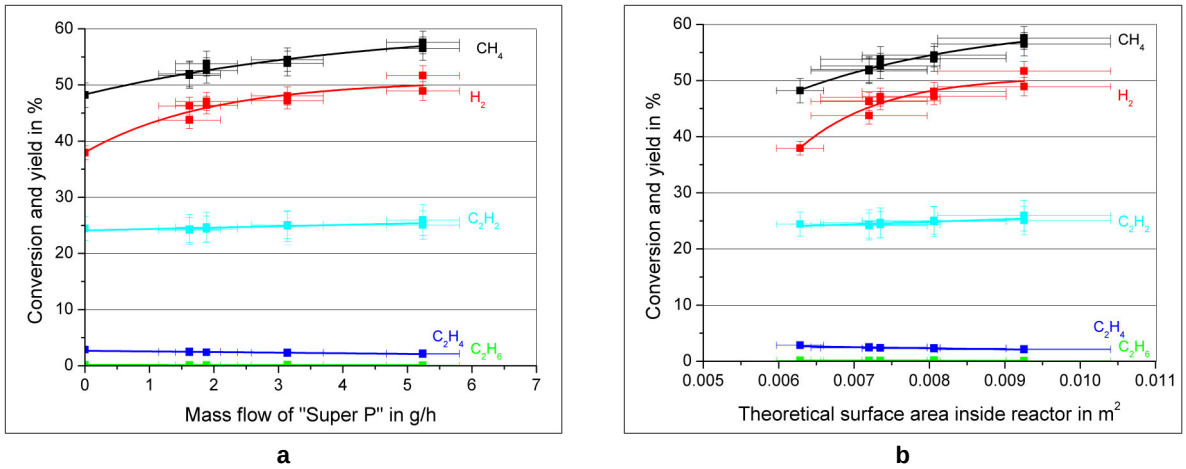

a b

Figure 3: Conversion of methane and yield of hydrogen, ethane, ethene, and ethyne as a function of the mass flow of added carbon black (a) and the theoretical surface area inside the reactor (b), nominal furnace temperature: 1400 °C, dilution gas: argon, initial total standard volume flow: 3800 sccm, initial molar fraction of methane: 5 %, pressure approximately 1.02 bar.

The diagram suggests that the surface area provided for reactions strongly affects the reaction rates, even though the influence of particle seeding is partly based on an improved heat transfer. Since the reactor wall provides surface area in the same order of magnitude as added particles, the wall should be considered as a preferred location for reactions. The specific surface area of carbon deposition found in the reactor and the filter is often similar (or even higher) compared to figures of “Super P”, indicating that also the surface of generated particles serves as reaction sites.

6 Summary and Conclusions

The thermal dissociation of methane comprises the presence not only of the final products hydrogen and carbon, but also of intermediates such as the C_2-hydrocarbons. A kinetic model considering the stepwise dehydrogenation from methane to finally hydrogen and carbon with the intermediates ethane, ethene and ethyne leads to fairly good agreement between results of the experiments and simulations concerning the conversion of methane and the yield of hydrogen. In order to learn about heterogeneous effects and to identify ways to improve the performance of the model for the thermal dissociation of methane further experiments were carried out. It was realized that remarkable fraction of C-atoms were located in compounds of the product flow with high C/H-ratios, which have not been considered in this work. Seeding of the inlet gas with carbon black results in an increase of both, conversion of methane and yield of hydrogen. It is suggested that the surface of the reactor as well as the surface of particles serve as reaction sites.

Acknowledgements

The authors would like to thank the European Commission for co-funding the project SOLHYCARB in the sixth framework program (SES6 019770). The authors would also like to thank Timcal Ltd. represented by Dr. Eusebiu Grivei for the provision with “Super P” and for the measurement of BET surfaces as well as Beatrice Förster and Tom Maibauer for their important contributions to the project.

References

[1] S. Rodat, S. Abanades, et al. (2009). "Hydrogen production from solar thermal dissociation of natural gas: development of a 10 kW solar chemical reactor prototype." Solar Energy 83(9): 1599-1610.

[2] G. Maag, G. Zanganeh, et al. (2009). "Solar thermal cracking of methane in a particle-flow reactor for the co-production of hydrogen and carbon." International Journal of Hydrogen Energy 34(18): 7676-7685.

[3] M. Kogan and A. Kogan (2003). "Production of hydrogen and carbon by solar thermal methane splitting. I. The unseeded reactor." International Journal of Hydrogen Energy 28(11): 1187-1198.

[4] M. H. Back and R. A. Back (1983). Thermal Decomposition and Reactions of Methane. Pyrolysis. THEORY AND INDUSTRIAL PRACTICE. L. F. Albright, B. L. Crynes and W. H. Corcoran. New York, Academic Press, Inc.: 1-24.

[5] K. L. Lee, S. Y. Lee, et al. (2004). "Catalytic decomposition of methane over carbon blacks for CO_2-free hydrogen production." Carbon 42: 2641-2648.

[6] N. Muradov, F. Smith, et al. (2005). "Catalytic activity of carbons for methane decomposition reaction." Catalysis Today 102: 225-233.

[7] R. Moliner, I. Suelves, et al. (2005). "Thermocatalytic decomposition of methane over activated carbons: influence of textural properties and surface chemistry." International Journal of Hydrogen Energy 30: 293-300.

[8] Timcal Ltd. (2008).Technical Data Sheet. Super P. Conductive Carbon Black. Version 12/08. Bodio, Switzerland, Timcal Ltd., http://www.timcal.com. 12 March 2010.

Development of Fuel Cell Systems for Aircraft Applications Based on Synthetic Fuels

J. Pasel, **R.C. Samsun, F. Scharf**, **C. Döll**, **R. Peters**, **D. Stolten**,
Forschungszentrum Jülich GmbH, Jülich, Germany

Abstract

At present, in the aviation sector considerable scientific project work deals with the development of fuel cell systems based on synthetic fuels to be integrated in future aircraft. The benefits of fuel cell systems in aircraft are various. They offer the possibility to simplify the aircraft layout. Important systems, i.e. the gas turbine powered auxiliary power unit (APU) for electricity supply, the fuel tank inerting system and the water tank, can be substituted by one single system, the fuel cell system. Additionally, the energy demand for ice protection can be covered assisted by fuel cell systems. These measures reduce the consumption of jet fuel, increase aircraft efficiency and allow the operation at low emissions. Additionally, the costs for aircraft related investments, for aircraft maintenance and operation can be reduced. On the background of regular discussions about environmental concerns (global warming) of kerosene Jet A-1 and its availability, which might be restricted in a few years, the aircraft industry is keen to employ synthetic, sulfur-free fuels such as Fischer-Tropsch fuels. These comprise Bio-To-Liquid and Gas-To-Liquid fuels. Within this field of research the Institute of Energy Research (IEF-3) in Jülich develops complete and compact fuel cell systems based on the autothermal reforming of these kinds of fuels in cooperation with industry. This paper reports about this work.

1 Synthetic Fuels

XtL (“Anything to Liquid”) is the general term for high value liquid hydrocarbon fuels synthesized from synthesis gas. Furthermore the abbreviations CtL (“Coal to Liquid”), GtL (“Gas to Liquid”) and BtL (“Biomass to Liquid”) are commonly used to refer to the feedstock materials applied for the production of the synthesis gas. The conversion of synthesis gas to hydrocarbon fuel with similar properties as petroleum diesel, gasoline or jet fuel can be realized with different processing routes: the Fischer-Tropsch (FT) process consists of a catalytic polymerization step which forms straight chain hydrocarbons that are converted to the desired final products during the following upgrade processing. Another process route called MtSynfuel produces methanol as a multi-purpose and storable intermediate product which can be chemically converted to XtL fuel. In contrast to conventional petroleum fuels XtL products are almost free of sulfur and aromatic compounds. Nevertheless it can be necessary to blend XtL with conventional fuel to meet the existing transportation fuel specifications [1-3].

In Jülich recently, four different synthetic fuels were ordered, which were produced via the “Gas to Liquid” technology. Their physical and chemical properties are summarized in Table 1. The fuel in the fifth line in Table 1 is produced by the “Bio to Liquid” process and is based on palm oil. All synthetic fuels have in common that they reveal a very low aromatics and

sulfur content. Only Shell MDS Kerosene from Table 1 can be classified as jet fuel with a quite narrow boiling range between 150 °C and 200 °C. All other synthetic fuels are so-called diesel fuels. Former experiments in Jülich compared the boiling ranges of conventional diesel fuels with those of synthetic fuels. They showed that the boiling range of synthetic fuels proceeds on a plainly lower level. That means that the critical step within each reforming unit, i.e. the complete evaporation of the fuel, is expected to be significantly easier when employing synthetic fuels.

Table 1: Different synthetic fuels to be used for autothermal reforming.

	Lower heating Value		**Density**	**Sulfur content**	**Aromatics**	**Boiling Range**
	MJ/kg	MJ/l	kg/m^3	ppm	vol.%	
Shell MDS Kerosene	-	-	737	< 3	< 0,1	150 °C - 200 °C
Shell GTL Fuel (Winter Grade)	-	-	778	< 3	< 0,1	210 °C - 318 °C
Shell GTL Fuel (Summer Grade)	-	-	781	< 3	< 0,1	204 °C - 356 °C
EcoPar Diesel			798	< 1	< 0,5	268 °C - 378 °C
NExBTL	44	43	775 – 785	≈ 0	≈ 0	260 °C (10%) – 300 °C (95%)

2 System Layout

As can be seen in Figure 1, a compact system design is possible by integrating heat exchangers in the reactors in order to recover reaction heat for educt conditioning. The reformer is operated with cold air and fuel. The heat input for fuel evaporation comes from superheated steam which is fed into the reformer with a temperature of 480 °C. A part of the required water for reforming is evaporated and slightly superheated in the integrated heat exchanger of the catalytic burner. The residual cold water flow is then mixed with this slightly superheated steam resulting in saturated steam. The integrated heat exchanger of the reformer is designed in such a way, that the saturated steam is superheated to the required temperature level. At the same time the reformate is cooled down to the temperature level, which is required at the entrance of the high temperature shift stage. The cooling between the shift stages is carried out using water quench. This strategy eliminates the necessity of a further heat exchanger and at the same time shifts the equilibrium towards CO reduction in the low temperature shift stage. After the shift reactor the reformate is cooled down to the inlet temperature of the fuel cell anode. At the same time, air for the cathode is heated up. After the electrochemical conversion in the fuel cell stack, the anode tail gas is directly fed into the catalytic burner. The catalytic burner enables a low emission operation of the system and supplies heat for educt conditioning as discussed above. Water autonomy is provided using the exhaust gas coolers and condensers after the cathode and the catalytic burner.

According to the outside and design conditions, additional water can be produced to be used in aircraft.

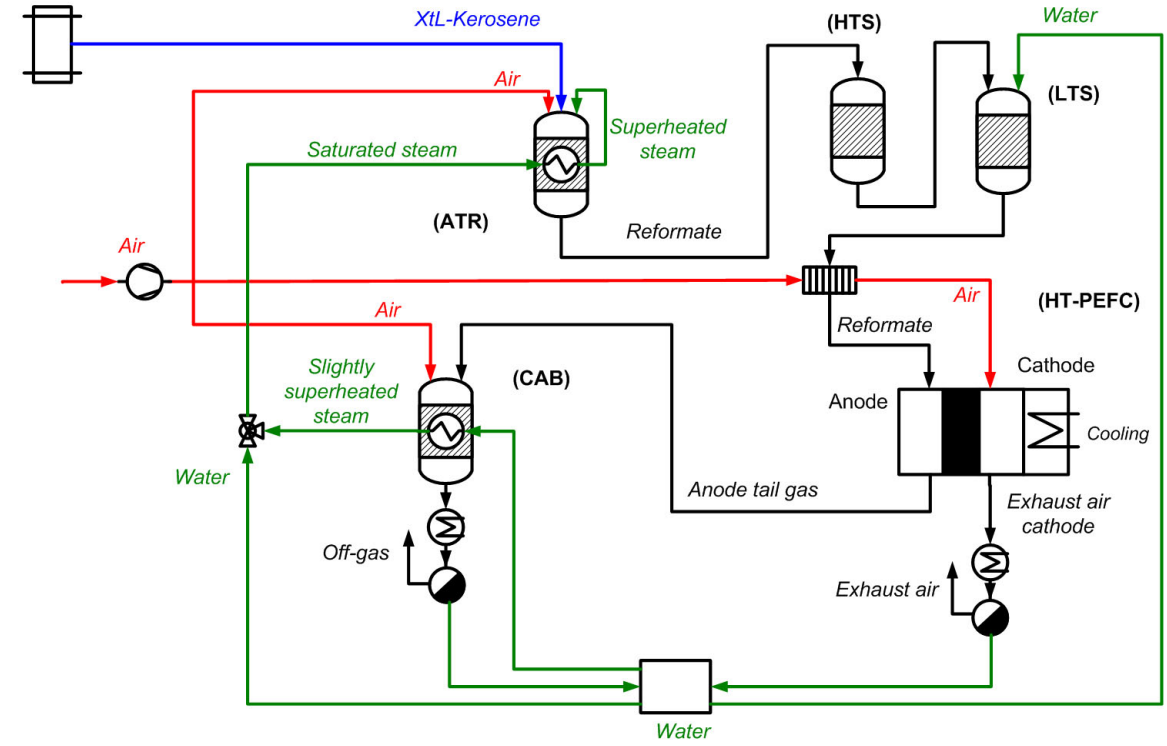

Figure 1: Flow sheet of the high temperature Polymer Electrolyte Fuel Cell (HT-PEFC) system based on autothermal reforming of synthetic fuels. ATR: Autothermal reformer, HTS: High temperature water-gas-shift reactor, LTS: Low temperature water-gas-shift reactor, CAB: Catalytic burner.

3 Component Development and Design

3.1 Autothermal reformer

The actual autothermal reformer of the Forschungszentrum Jülich of the ninth generation (ATR 9.2) is shown in Figure 2. Experimental results with former ATR generations (ATR 7 and ATR 8) are given in [4,5]. ATR 9.2 is specifically designed for the conversion of synthetic fuels and can produce a molar hydrogen flow with a thermal power of 28 kW. CFD simulations of ATR 9.2 aimed at a special design of the air injection device of the reformer. Figure 3 shows the results of these simulations. The mass fraction of oxygen in a mixture of steam, vaporized fuel and air is displayed. The red spots in Figure 3 indicate those positions, at which air is injected in the mixing chamber of the reformer. It becomes obvious from Figure 3 that due to the geometry of the air injection device strong turbulences occur very close to the air injection point. Thereby, the majority of oxygen molecules flow in direction of the catalyst of the reformer on the right hand side of Figure 3. The concentration of oxygen in the catalyst is very homogeneous. Simultaneously however, a low mass fraction of oxygen also flows in that part of the reformer, in which already a mixture of steam and vaporized fuel

prevails being injected via the fuel nozzle on the left hand side of the reformer. By this means, a homogeneous, slightly exothermic pre-reaction between oxygen and fuel in the mixing chamber is favored, which eases the complete evaporation of the fuel. This pre-reaction is supported by employing synthetic fuels, which consist of more lower boiling, aliphatic components in comparison to conventional fuels.

Moreover, ATR 9.2 in Figure 2 shows the following characteristics, which partly represent advancements in comparison to former ATR generations:

- An integrated heat exchanger device for producing steam by using the reaction enthalpy from the reforming reaction
- A one-fluid-nozzle (diameter of the drilling: 0.2 mm) for fuel injection. The nozzle is cooled and replaceable.
- For the first time, the mixing chamber of ATR 9.2 was made from sheet metal. In former ATR generations ceramics were used. This shift offers the potential to manufacture the mixing chamber more easily.
- In former ATR generations a cyclone was integrated into the mixing chamber, in which carbonaceous deposits being produced during the ATR process were collected. This cyclone was omitted in the case of ATR 9.2 since synthetic fuels consist of more lower boiling, aliphatic components in comparison to conventional fuels, which have a clearly weaker tendency towards the formation of carbonaceous deposits.
- The reaction chamber, in which the catalytic reforming reaction takes place at temperatures between 800 °C and 1000 °C, was also made from metal sheet. In former ATR generations turned tubes were used for that means. This shift offers the chance to reduce costs to a large extent during manufacturing if huge numbers of the reformer are considered.

Figure 2: Autothermal reformer of the ninth generation (ATR 9.2) of Forschungszentrum Jülich

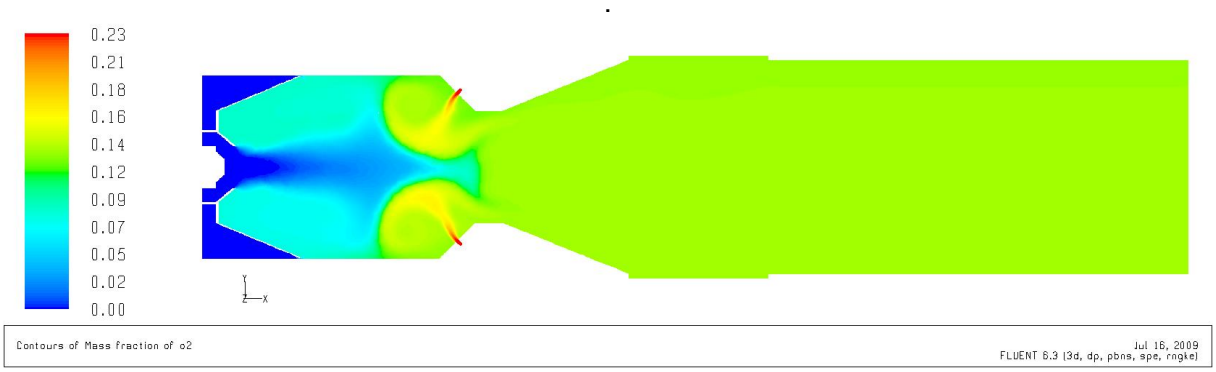

Figure 3: Simulation of air injection into the mixing chamber of ATR 9.2, mass fraction of oxygen in the mixing chamber (left) and the catalyst of the reformer (right).

3.2 Water-Gas-Shift reactor

The actual water-gas-shift reactor of the Forschungszentrum Jülich of the fourth generation (WGS 4) is shown as a model in Figure 4 on the left hand side. It well fits to the thermal power class of ATR 9.2 of 28 kW.

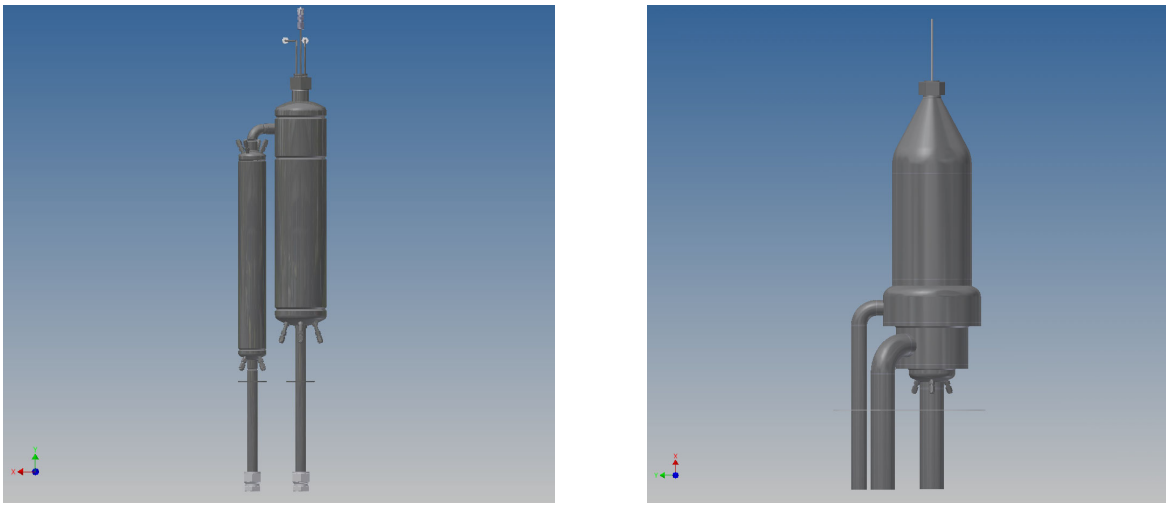

Figure 4: Models of the water-gas-shift reactor of the fourth generation (WGS 4, left) and of the catalytic burner of the third generation (CAB 3, right) of the Forschungszentrum Jülich, each with a thermal power of 28 kW.

The function of a water-gas-shift reactor within a fuel cell system is to reduce the concentration of carbon monoxide in the product gas of the autothermal reforming from approx. 8 vol.% to 1 vol.%. WGS 4 is a two-stage reactor. In the high temperature shift stage (HTS) the reaction runs in the temperature range between 400 °C and 450 °C. Carbon monoxide reacts with water giving carbon dioxide and hydrogen. In the HTS carbon monoxide conversion is thermodynamically controlled with a maximum of about 60 %. After

the HTS the reformate is cooled down to 300 °C by injecting water at ambient temperature. In the low temperature shift stage (LTS) the residual carbon monoxide molecules again react with water into hydrogen and carbon monoxide with a maximum conversion of approx. 85 %. In the LTS the reaction is kinetically controlled and proceeds in the temperature range between 300 °C and 330 °C. By these means, the carbon monoxide concentration in the reformate is reduced to approx. 1 vol.%. So, the reformate can be fed to the anode of a high temperature Polymer Electrolyte Fuel Cell (HT-PEFC).

3.3 Catalytic burner

The function of a catalytic burner in a fuel cell system is to catalytically convert the flammable components of the off-gas of a fuel cell anode (H_2, CO, CH_4) into H_2O and CO_2. Thereby, reaction enthalpy is released, which is used for the production of steam. Figure 4 on the right hand side shows the model of the catalytic burner of the third generation (CAB 3) of the Forschungszentrum Jülich. It again well fits to the power class of ATR 9.2.

During the design of CAB 3 it became obvious that CFD simulations have to be performed to optimize the process of water evaporation. In Jülich´s catalytic burner the stream of water to be vaporized is injected at ambient temperature via a one-fluid nozzle onto a so-called deflecting surface. The deflecting surface itself is heated by the enthalpy flow of the off-gas of the catalytic combustion, which proceeds in a cylindrical reaction zone underneath the deflecting surface. Thereby, a minor part of the water stream directly vaporizes, while the majority forms a water film on the deflecting surface. Then, this water films drains off into an annular gap, which is also heated by the enthalpy flow from the catalytic combustion. In the annular gap the residual water stream should completely vaporize. Figure 5 shows CFD simulations, which illustrate the way, in which the water film drains off a plane, a Klöpper head and a hemispherical head at 30 ° inclination of the catalytic burner. Such inclination most probably occurs during operation of a catalytic burner on-board aircraft. It becomes obvious from Figure 5 that in the case of a plane the water film drains off into only one third of the annular gap, while using a Klöpper head more than one half of the perimeter was exploited. In the case of a hemispherical head however, the simulation shows that almost the whole perimeter of the annular gap is available for the water film to drain off. Based on these results, the deflecting surface inside the catalytic burner CAB 3 was constructed as a hemispherical head.

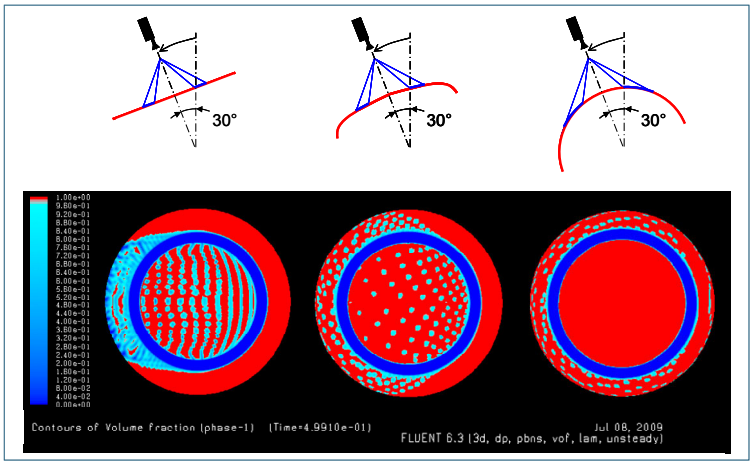

Figure 5: CFD simulations showing in which way the water film drains off a plane, a Klöpper head and a hemispherical head at 30 ° inclination.

Acknowledgements

The work was partly financed by the German Federal Ministry of Economics and Technology within the National Aerospace Research Programme (LuFo IV-2).

References

[1] Pabst, K.; Schaub, G.; Lüft, M.; Velji, A.: Neuartige Kraftstoffe und zukünftige Abgasemissionen bei Kraftfahrzeugen – eine Übersicht. Report by order of „Landesanstalt für Umwelt, Messungen und Naturschutz Baden-Württemberg“, 2007

[2] Schaub, G., Unruh, D.; Synthetische Kohlenwasserstoff-Kraftstoffe und Minderung fossiler CO_2-Emissionen. In: VDI-Berichte 1704 : Innovative Fahrzeugantriebe, Düsseldorf: VDI-Verlag, 2002

[3] Chevron Corporation: Alternative jet fuels : Abbendum 1 to Aviation Fuels Technical Review 2006

[4] Pasel J.; Meißner J.; Porš Z.; Samsun R.C.; Tschauder A.; Peters R., Int. J. Hydrogen Energy, 32 (2007) 4847 - 4858

[5] Pasel J.; Latz J.; Porš Z.; Meißner J.; Samsun R.C.; Tschauder A.; Peters R., ECS Transactions 12 (1) (2008) 589 - 600

Fuel Cell Methanol Reformer System for Submarines

Stefan Krummrich, Howaldtswerke-Deutsche Werft GmbH, Germany

1 Introduction

After the successful market introduction of Fuel Cell powered submarines, HDW is ahead of the market in the field of conventional submarines equipped with Air-Independent propulsion (AIP) systems. Today HDW offers different types of submarines including fuel cell systems like the classes U212A (Germany, Italy) or the class 214. All these submarines are based on fuel cell systems with metal hydride storage cylinders for the hydrogen.

In the recent decades conventional submarines were based on diesel-electric propulsion with lead batteries for submerged operation. Improvements to these systems have been gradually since WW II, small steps leading to improvements mainly in the field of signatures of the submarine. But still the snorkel operation to recharge the batteries is mandatory at least every few days.

In Comparison submarines equipped with Fuel Cells offer remarkable operational advantages. The AIP-equipped submarines can stay submerged during operation for a much longer time than before at similar performance regarding noise level. This is caused by the fact that fuel cells produce electrical energy without any moving parts, similar to a battery.

Generally the requirements of the AIP Systems in addition to the enlarged submerged operation period are as follows:

- high efficiency (low heat discharge to sea water)
- low noise level
- low magnetic signature
- small size
- low weight
- low effort for maintenance / no extra crew

Fuel cells have been under development by Howaldtswerke-Deutsche Werft for more than 20 years. In 1988 first sea tests were performed with a fuel cell plant in the submarine U1. Today four submarines of Class U212A are in service at the German Navy. Furthermore several export contracts could be realised, also with some submarines already in operation. Compared to other applications, fuel cells in submarines made its way because of the enormous customer benefit they offer. The development was based on a completely new approach, not on the replacement of any existing system [1].

2 Proven Technology

The system installed onboard the HDW submarines today consists of the components shown in Figure 1.

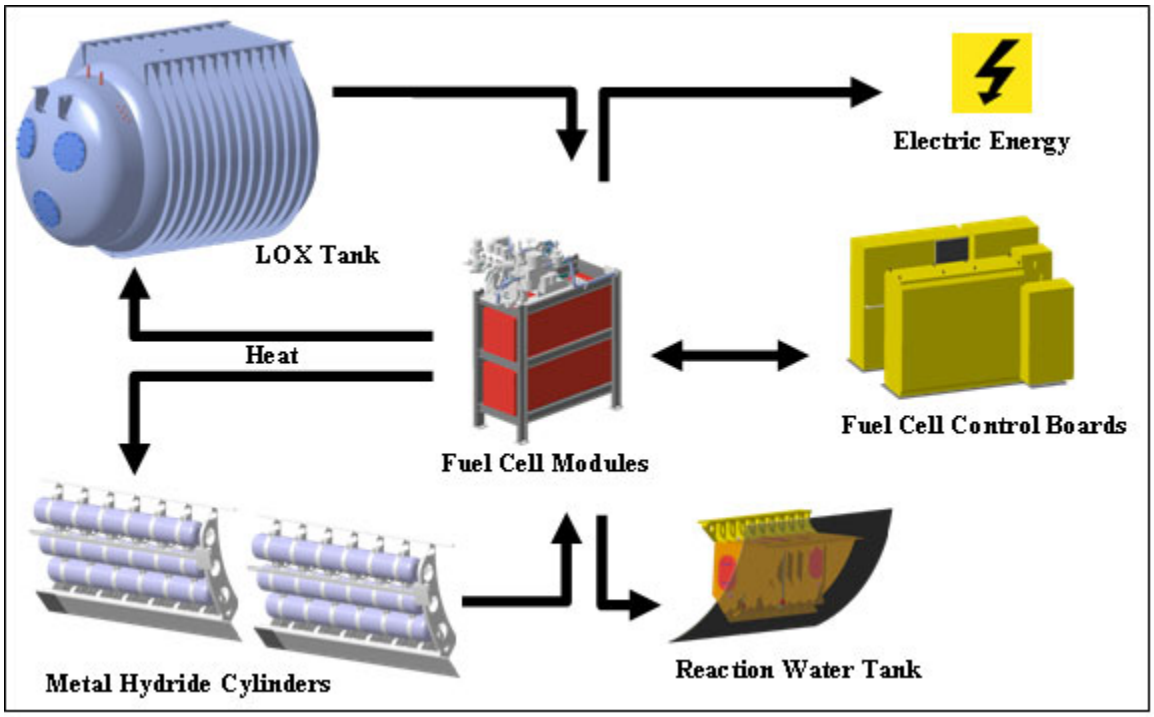

Figure 1: Overview about Fuel Cell System components.

The PEM fuel cells deliver the electrical energy for the boats power network system via a DC/DC-converter. The waste heat from the fuel cell is used to release the hydrogen from the metal hydride storage cylinders and to evaporate liquid oxygen for the operation of the H_2/O_2 fuel cells. The reaction water is collected onboard to prevent the need for weight compensation with sea water. In case of Class 209 and 214, two Siemens FCM 120 Fuel Cells are used, with 240 kW maximum system power output [2].

In total the system has a very high electrical efficiency of up to 60 %, and offers many benefits regarding submarine specific requirements.

3 Reasons for Reforming onboard Submarines

Even if the existing fuel cell system offers many advantages, the tendency in submarine development goes to higher amounts of stored AIP-Energy. The system based on metal hydride storage is relatively heavy, resulting in the fact that the amount of hydrogen stored onboard is limited by the size of the submarine, having in mind the principle of Archimedes.

Generally liquid fuels have high volumetric and gravimetric energy content and are easy to handle. These advantages in combination with the fuel cells performance motivated HDW to start with the development of a reformer system for onboard hydrogen production [3].

4 Choice of Feedstock

The choice of the best fuel for a reformer system for submarines has great influence not only on the system design, but also on the submarines design and performance. Generally the feedstock for a reformer system can be hydrocarbon or alcohol. Compared to the storage of pure hydrogen, this implies the production of CO_2 onboard. As CO_2 cannot be stored onboard like e.g. the product water of the fuel cell, it has to be discharged into the surrounding sea. To realize a weight balanced system (principle of Archimedes), the lost weight of the CO_2 has to be compensated with sea water.

The reformer has to be operated with fuel + oxygen (+ water). The oxygen is stored onboard as a liquid in a cryogenic tank. This LOX-tank is the dominant component regarding system size. Consequently, the oxygen consumption of the AIP-System is very important and should be kept as low as possible. Considering the entire AIP-System, the chemical products are water (H_2O) and carbon dioxide (CO_2). Therefore, the ratio of H to C in the chemical structure should be high, because the oxidation of C requires more oxygen then the oxidation of H. Furthermore the overall system efficiency is of importance for the oxygen consumption, and of course for the fuel consumption.

Further factors are important for the choice of feedstock are the worldwide availability, the safety (handling etc.), the purity (avoidance of additional adsorbers etc.) and the reforming temperature to keep the reformer easy.

Summarized the requirements for the feedstock are:

- high hydrogen content in the chemical structure
- high efficiency of the reforming process
- worldwide availability
- easy storage onboard
- easy handling for e.g. refuelling
- easy reformation

HDW has considered three feedstocks for submarine reforming: Diesel ($C_{13.57}H_{27.14}$) Ethanol (C_2H_5OH) and Methanol (CH_3OH). The final choice was made for Methanol because of the following reasons4:

- H/C ratio is highest for Methanol
- highest efficiency of reforming process
- very easy reformation (T app. 250 °C; for Diesel > 850 °C, for Ethanol >700 °C required)
- worldwide availability
- high purity (no sulphur etc.)

5 System Configuration

At the beginning of the development the requirements for the reformers have been defined. A major requirement was the operation based on the existing and proven Siemens Fuel Cells. Furthermore the exhaust gas (CO_2) pressure should be high, to enable the discharge of exhaust gas into the surrounding seawater without the need for an additional exhaust gas

compressor. Of major importance was the overall system efficiency and the reliability and availability of the system.

Based on these requirements, the choice was a methanol steam reformer system operated at elevated pressure. The hydrogen purification is performed with a membrane purification unit. The required thermal energy is produced in a high-pressure oxygen burner. An overview about the process is shown in Figure 2.

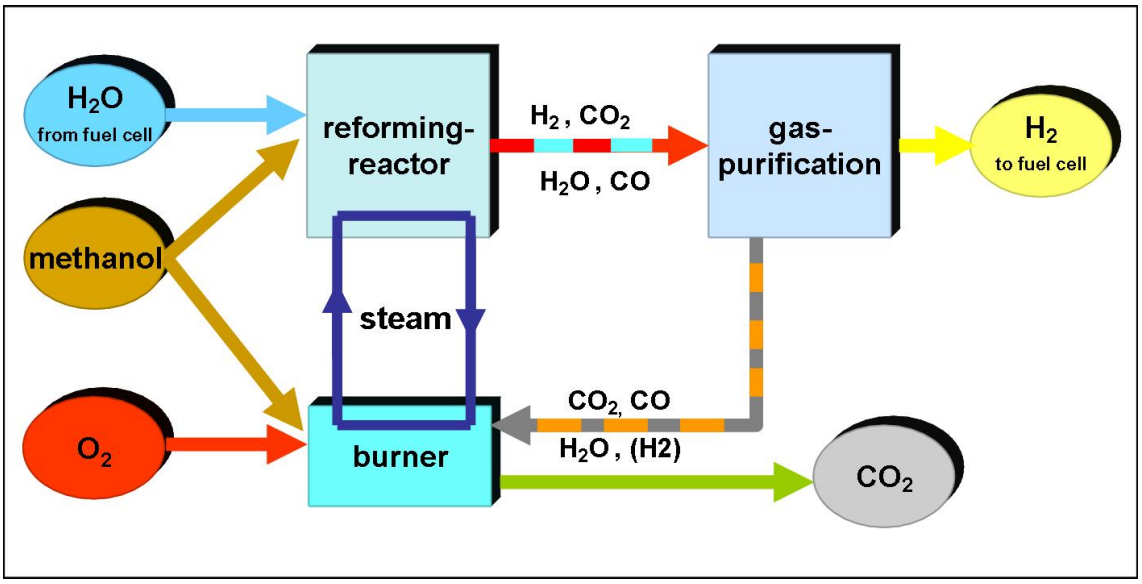

Figure 2: Overview of Methanol Reformer System.

The methanol is mixed with water, evaporated and fed to the steam reformer. The reforming reactor is heated by a boiling water cycle. The methanol-water mixture is converted into a hydrogen-rich gas mixture at typical methanol reforming temperatures. This reformate gas is further processed in a gas purification unit. The major fraction of hydrogen is separated and can be fed directly to the Siemens Fuel Cell. The rest of the reformate gas is burned, to provide the required heat for the reforming process. The only product gas from the reformer is CO_2 at elevated pressure, the H_2O in the exhaust gas is condensed and reused internally.

The methanol reformer itself will be operated in an encapsulation comprising several safety features, to prevent the crew from any harmful gases and liquids.

6 Status of Development

The reformer development at HDW started many years ago under the assumption that the German Navy would choose reformer technology for their second batch of Class 212 Submarines. After the decision to stay with the metal hydride storage cylinders, the development of reformer systems for submarines has been performed with reduced resources. Today the efforts have been increased again, to have the chance to offer the system to potential costumers worldwide.

HDW operates a full size functional demonstrator in the test facilities in Kiel. The demonstrator has formerly been built up with COTS components – most of the components used cannot be applied onboard a submarine. Now single components and systems are

developed and installed to achieve a submarine-proven design, and to test them under real process conditions in the functional demonstrator.

The major milestone in 2009 was the realisation and testing of a new gas purification. The purification unit has passed a shock test under operating conditions (temperature, and pressure difference) as part of military approval of the component. Furthermore the performance of the unit could be verified. The hydrogen is of a very high purity, the requirement of the Siemens Fuel Cell is fulfilled. In February 2010 the Reformer has been coupled with a submarine fuel cell with very good results – no difference in fuel cell performance could be detected compared to Hydrogen from the cryogenic storage tank at HDW.

The test runs with the reformer showed a very high efficiency of the system. The efficiency (H_{u_H2} / H_{u_CH3OH}) was measured to be >90 %.

The system integration has been worked out, a picture of the unit is shown in Figure 3. Another picture including the encapsulation is shown in Figure 4.

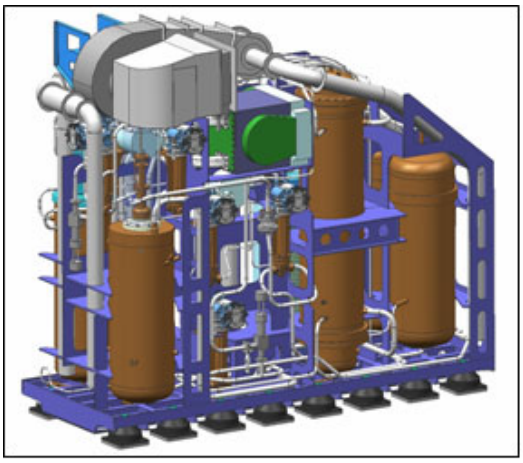

Figure 3: Methanol Reformer System

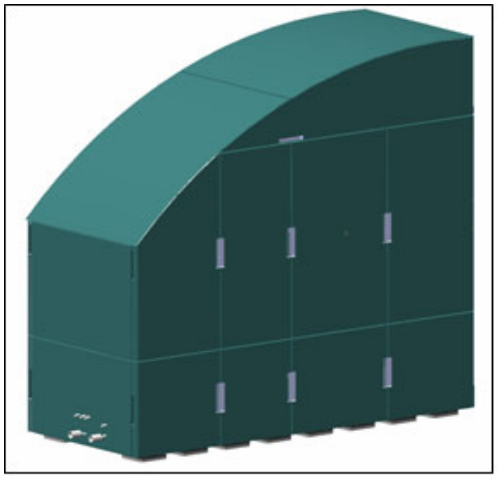

Figure 4: Encapsulation of MRS

7 Outlook

The reformer system will be further developed to meet all demands for onboard operation. During a reconstruction period in this year the heat integration will be further improved, and the valves in the plant will be replaced.

The operation of Reformer with fuel cell will be extended to implement and test a new DC/DC-converter.

Further major steps in the development will be the operation of the reformer system together with an exhaust gas treatment unit, to discharge CO_2 directly into the surrounding seawater.

All these further steps will bring the Fuel Cell Methanol Reformer System closer to application. With this technology HDW offers a second option of Fuel Cell AIP solution, that will confirm the leadership of HDW in AIP-Systems for submarines.

References

[1] Pommer, H.; Hauschildt, P.; Teppner, R. and Hartung, W. (2006) - Air Independent Propulsion System for Submarines. *ThyssenKrupp techforum 01/2006*

[2] Hammerschmidt, A. (2006) - Fuel Cell Propulsion of Submarines. *Advanced Naval Propulsion Symposium 2006*

[3] Psoma, A.; Sattler, G. (2002) - Fuel cell systems for submarines: from the first idea to serial production. *Journal of Power Sources, Volume 106*

[4] Kolb, G. (2008) – Fuel Processing for Fuel Cells. *Wiley-VCH*

Versatile Fuel Processor for Oxidative Steam Reforming and Catalytic Partial Oxidation of Various Liquid Fuels

Thomas Aicher, **Robert Szolak**, Fraunhofer ISE, Heidenhofstr. 2, D-79110 Freiburg, Germany
Lothar Griesser, Griesser Engineering, Hadlaubstrasse 83/b5, CH-8006 Zürich, Switzerland

1 Introduction

Oxidative steam reforming (ATR) and catalytic partial oxidation (CPOX) are reforming processes widely used for on-board hydrogen production in fuel cell systems for off-grid, portable/mobile applications. These reforming processes allow dynamic operation with liquid fuels. Critical challenges in reforming liquid fuels pose the complex nature of the fuels containing various coke precursors, the prevention of combustion in the vaporizer/pre-heater section due to low auto-ignition temperatures, and the creation of homogeneous mixture of air and fuel.

This contribution presents a novel process to transfer a wide range of liquid hydrocarbons and alcohols into the gaseous phase, thus facilitating mixture preparation for reforming and combustion applications. The presented proprietary process transfers any liquid fuel (including diesel) into the gaseous phase and supplies the mixture to the reforming reactor where it is converted into a hydrogen rich gas (synthesis gas) without the formation of carbon or residues. The principle underlying this process is to evaporate the fuel from its surface by radiant heat transferred from a hot metal catalyst coated mesh rather than from a hot heat exchanger wall in contact with the liquid fuel (see Figure 1). For more details please refer to Aicher and Griesser [1]. The vaporized fuel is mixed with additional reforming air and partially oxidized in a CPOX catalyst, as shown in Figure 1. At this point an air/steam mixture can be supplied instead, thus increasing the hydrogen yield of the reforming process by operating it in an oxidative steam reforming mode. The reforming catalyst can be a packed bed or a monolith.

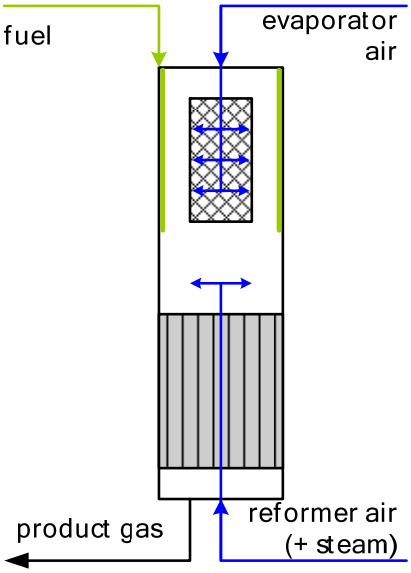

Figure 1: Sketch of the proprietary fuel evaporator reformer.

2 Carbon Formation

During the process design phase carbon formation was considered by investigating the thermodynamic equilibrium of carbon formation. Carbon formation depends on the oxygen-to-steam ratio (O/C) of the feed streams and reactor temperature. We performed process simulations of the CPOX process for hydrocarbons (iso-octane) with the commercial software package ChemCAD®. In order to determine critical carbon formation temperatures we calculated the equilibrium gas composition of a CPOX reactor for various oxygen-to-carbon ratios (O/C). By minimizing the Gibbs Free Energy the temperature could be obtained where only trace amounts of solid carbon (mol fraction > 1e-6) are predicted as a possible product. Figure 2 shows predicted minimum carbon formation temperatures in the gas phase over the O/C ratio of the reactor feed.

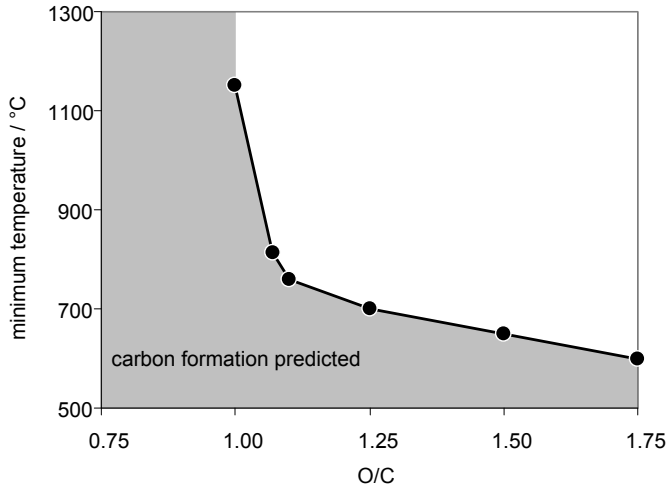

Figure 2: Calculated minimum temperature for diesel CPOX to avoid carbon formation.

When looking at the data you notice two contrary effects. From an operations standpoint you would like to reduce the amount of air supplied to the reactor in order to increase your reformer efficiency – the less fuel you combust and the better your reactor is insulated the higher the fuel efficiency. On the other hand, lowering the O/C increases the minimum temperature required to avoid carbon formation posing extra strains on the materials. Therefore, a happy medium has to be established, which lies somewhere between 1.1 and 1.3.

3 Experimental Results

Experimental investigations of the novel evaporator reformer reactor were performed. Test runs with commercial diesel (containing 16 ppm_w sulfur) and kerosene (5 ppm_w sulfur) will be presented for CPOX and ATR operation.

As an example, Figure 3 presents measured gas composition and reactor temperatures for operation of the reactor with diesel flow rates of 0.5 to 5.0 kW (based on the LHV of diesel). With increasing load, O/C was lower because heat losses became less dominant. With decreasing O/C, hydrogen and carbon monoxide concentration increase, while the carbon dioxide concentration decreases. In all cases the measured gas compositions are in close agreement with the thermodynamic equilibrium (not shown in Figure 3). Carbon deposits were never observed during inspection of the reactor internals after each test run. In addition, the concentration of unsaturated hydrocarbons, for instance ethylene, is very low (not shown in Figure 3). This implies that in the reforming catalyst no carbon was formed or deposited.

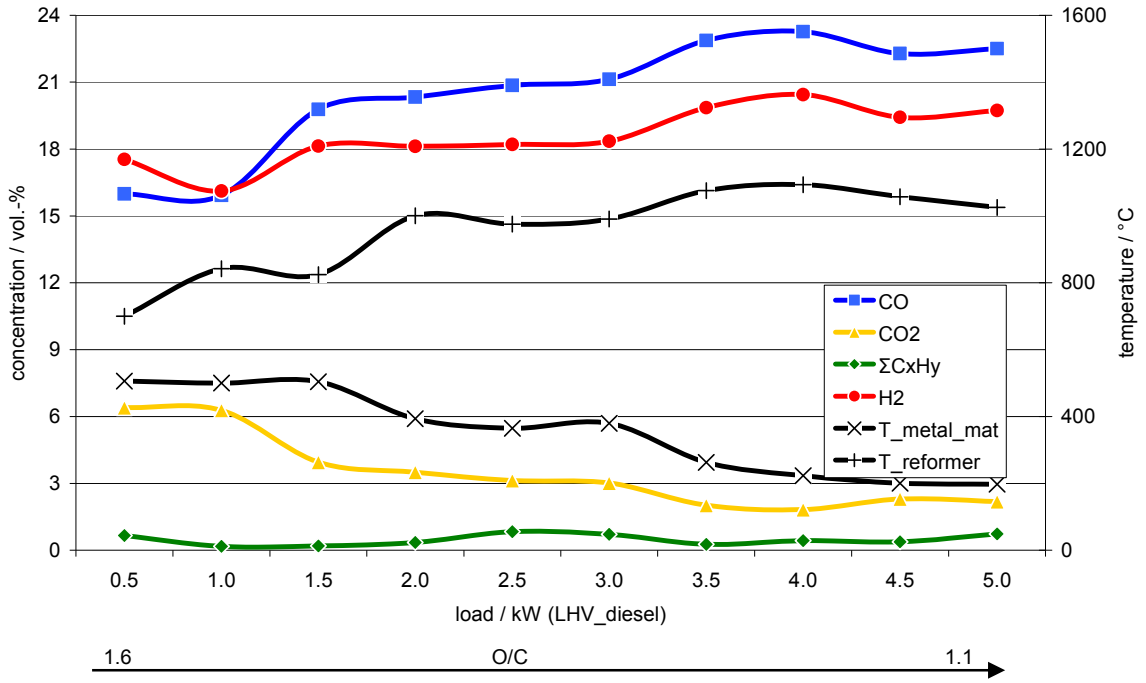

Figure 3: Gas composition and reactor temperatures measured for reactor loads between 0.5 and 5.0 kW (LHV_diesel).

In another set of experiments the impact of load changes on the reactor performance as well as the influence of higher sulfur concentrations in the diesel fuel was investigated. During load changes the air flow to the reactor has to be controlled in order to keep the CPOX reactor temperature below a maximum value of about 1000-1050 °C to avoid sintering of the catalyst. The investigations show that the system reacts immediately to load changes of 1.5 kW.

To elucidate the influence of sulfur on the evaporator reformer performance, two test series were conducted. First, three different diesel feeds with 16, 50 and 100 ppm_w sulfur were prepared and supplied to the reactor. The tests were done for two different diesel flow rates (1.5 and 3.0 kW). While the impact on the reformer temperature is negligible, the increase in sulfur reduces the concentration of carbon monoxide and hydrogen by approximately 10 % when increasing sulfur content from 16 to 100 ppm_w. The concentrations of methane and higher hydrocarbons show a slight increase. These effects are less pronounced at the higher diesel flow rate, i.e. 3.0 kW (see Fig. 4).

For the lower diesel flow rate the impact of sulfur on the performance over an extended period of time was investigated as well. Therefore, diesel with about 100 ppm_w sulfur was fed to the reactor for about 10 hours (see Fig. 4). Hydrogen and carbon monoxide concentration decline significantly from about 17.1 and 20.3 mol-% to about 15.3 and 18.7 mol-%, respectively. It was surprising that this deterioration in performance disappeared after purging with air for half an hour during shut down to ensure that no liquid hydrocarbons gather on the evaporator catalyst.

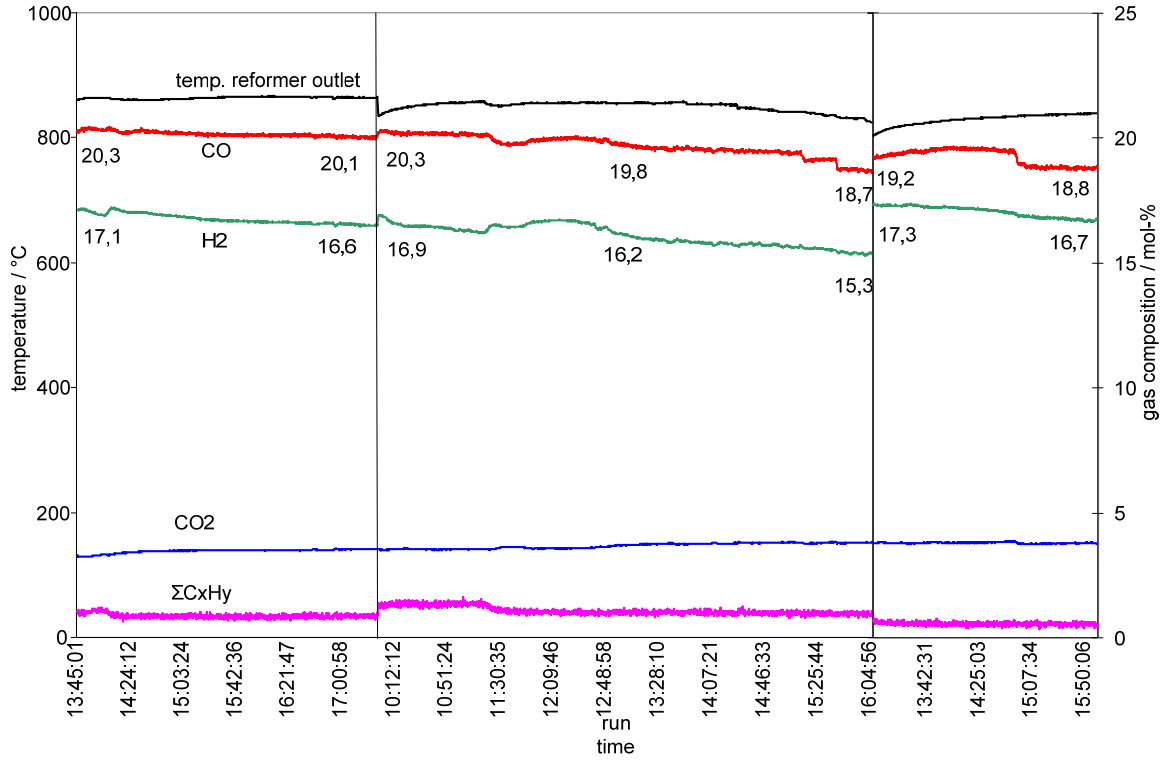

Figure 4: Impact of sulfur on diesel CPOX operation with 1.5 kW (LHV_diesel).

References

[1] T. Aicher, L. Griesser, J. Power Sources, 165 (2007) 210-216

Integration of a Natural Gas Fuel Processor for Residential PEM Fuel Cell Based Micro Cogeneration Application

Nilüfer İlhan, **Atilla Ersöz**, **Göktuğ Nezihi Özyönüm**, **Murat Baranak**, TÜBİTAK
Marmara Research Center Energy Institute 41470 Gebze Kocaeli, Turkey

Abstract

Fuel cell based cogeneration systems, which supply thermal energy and electricity simultaneously, are very promising for the near future commercial stationary applications, especially for residential power generation. The natural gas is the most suitable fuel for this application due to existing infrastructure and cost. The aim of this paper is to summarize the achievements of natural gas processor integration within "Fuel Cell based Micro Cogeneration System" project which is supported under TUBITAK Support Programme for Research Projects of Public Institutions. In this project 5 kW_e and 30 kW_t power are produced by fuel cell and catalytic combustion systems respectively. Sub systems such as fuel processing for hydrogen production, catalytic combustion, PEM fuel cell, power conditioning and control systems have been designed, manufactured and integrated for cogeneration application. Then a test program for the operation of the system has been performed. This paper presents the main experimental results on autothermal reforming of natural gas and gas clean-up systems concerning the requirements of PEM fuel cell system. It has been found that design parameters of the fuel processor were very important but operational parameters of the system were crucial for system performance.

Key words: Hydrogen, natural gas, reforming, micro cogeneration

1 Introduction

Coal and gas power plants which are the common centralized energy generation applications operate with 25–50% efficiency and cause high amount of greenhouse gas emissions [1, 2]. Decentralized power production, which is one of the most important research areas in advanced and clean energy technologies, supplies the energy demand by small scale systems established near the consumption area. The most important advantages of this method are the utilization of the alternative and renewable energy sources, availability for cogeneration, high efficiency (up to 90%), reduction in emission levels and avoidance of energy loss in transmission and distribution lines [3]. Micro turbines, internal combustion engines, Stirling engines and fuel cells are used for small scale electricity production [3]. Fuel cell systems are very efficient, reliable, silent and environment-friendly technologies and can be utilized in micro cogeneration systems on which intensive research has been conducted all over the world. Fuel cell based micro cogeneration systems, which supply thermal energy and electricity simultaneously, are very promising technologies for the near future stationary decentralized power generation applications. As well as the first prototypes were developed, the studies in this area still continue due to its importance from the point of clean energy [1-5].

2 Fuel Cell Based MiCro CoGeneraTIon SYstem

“Fuel Cell based Micro Cogeneration System” project, which has been conducted under TÜBİTAK Support Programme for Research Projects of Public Institutions by a consortium that includes TÜBİTAK Marmara Research Center Energy Institute, İstanbul Technical University, Kocaeli University and Türk Demirdöküm Fabrikaları A. Ş., has started on July 15, 2006 and is planned to be completed by the end of 2010. The aim of the project is to develop a 5 kWe Polymer Electrolyte Membrane (PEM) fuel cell based micro cogeneration system prototype to utilize the natural gas as a fuel to generate electricity and heat simultaneously for residential applications. The main units of the prototype are given below (Figure 1a):

- Hydrogen production unit via autothermal reforming of natural gas in a capacity range compatible with a 5 kW_e PEM fuel cell system,
- Gas clean up reactors for high and low temperature water-gas shift and preferential oxidation reactions,
- 5 kW_t catalytic burner unit for combustion of the anode-off gas of fuel cell,
- 30 kW_t natural gas burner for thermal power,
- 5 kW_e PEM fuel cell module and system,
- The control and power conditioning systems.

Firstly, requirements of main and sub-units of the hydrogen production and gas clean-up system were determined by process simulations. The most critical parameters for catalytic reactors were studied. Design and construction of reactors were realized according to the optimum operating conditions. Finally, reactors and sub-units were integrated to obtain a prototype unit (Figure 1b).

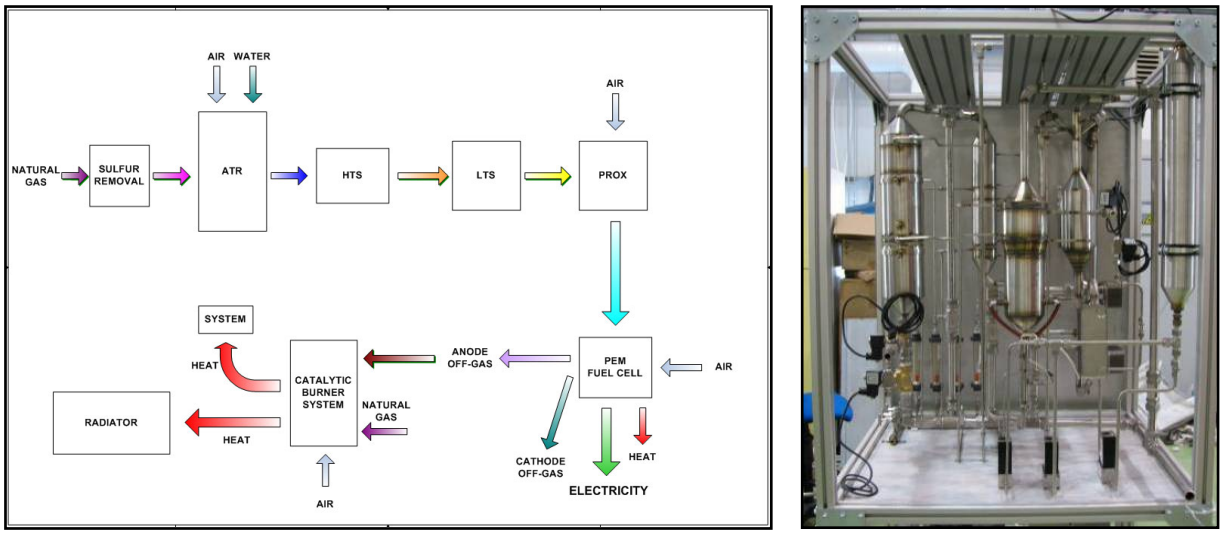

a) b)

Figure 1: a) Process flow diagram b) Process experimental set-up.

2.1 Autothermal reforming (ATR) unit

In this study, autothermal reforming of natural gas (NG) was studied in a catalytic reactor. NG consisted of ~ 90% methane (CH_4) and the main goal of this reaction was to convert CH_4 to obtain a syngas rich in hydrogen (H_2) with the lowest amount of CO formation. The selected primary operating variables in ATR reactor were temperature of the preheated fuel/air/steam mixture, steam-to-carbon (S/C) ratio, oxygen-to-carbon (O_2/C) ratio and reforming temperature (T_{ATR}). O_2/C ratio range was studied between 0.5–0.6, while a considerably wide S/C ratio range (2.0–3.0) was selected to see the effect on H_2 yield since lower S/C ratios could favor soot and coke formation which was not desired in catalytic operations. Figure 2 and Figure 3 show the effect of O_2/C ratio (at S/C = 3) and S/C ratio (at O_2/C = 0.55) on CH_4 conversion, H_2 and CO production rate at adiabatic conditions respectively.

In Figure 2, effect of O_2/C ratio on CH_4 conversion, CO and H_2 formation at constant S/C ratio of 3 can be seen. Increasing O_2/C ratio resulted in increasing CO and decreasing H_2 formations at constant S/C ratio. If O_2/C ratio was increased from 0.5 to 0.6, the H_2 concentration decreased from 45% to 40% at the reactor outlet stream. The CH_4 conversion was also positively affected by increasing O_2/C ratio at constant S/C ratio of 3. The conversion of CH_4 was observed around 99% at O_2/C ratio of 0.6, while it was decreased to 93% as O_2/C ratio decreased to 0.5.

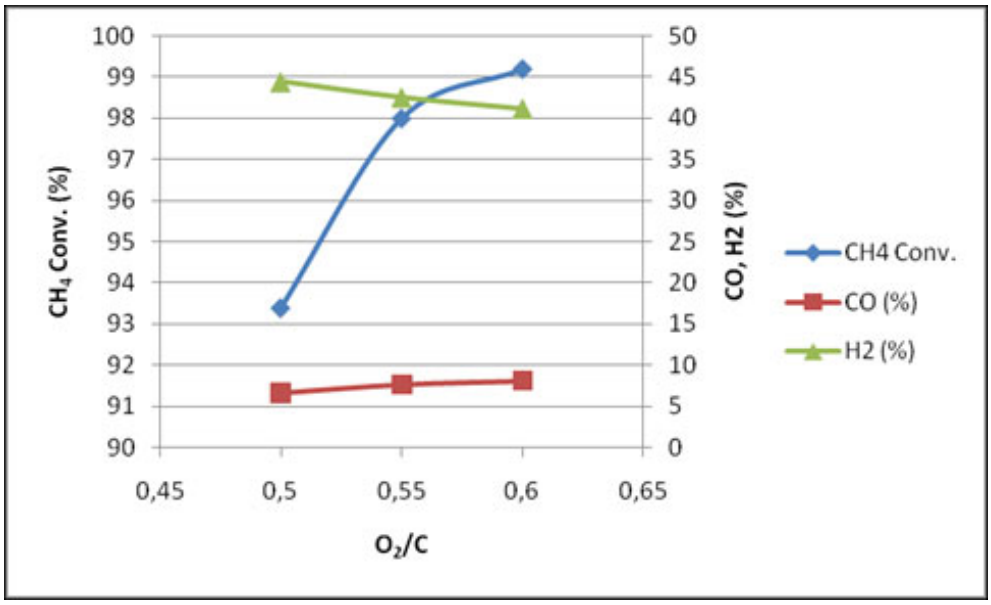

Figure 2: Effect of O_2/C ratio on CH_4 conversion, CO and H_2% composition (S/C = 3).

In Figure 3, the effect of S/C ratio on CH_4 conversion, CO and H_2 formation at constant O_2/C ratio of 0.55 is seen. The effect of S/C ratio on H_2 production was more pronounced at moderate O_2/C ratio of 0.55 and increasing the S/C ratio favored H_2 formation. On the other hand CO formation was depressed at higher S/C ratios and decreased as S/C ratio was increased. CH_4 conversion seemed to be slightly increased as S/C ratio was increased.

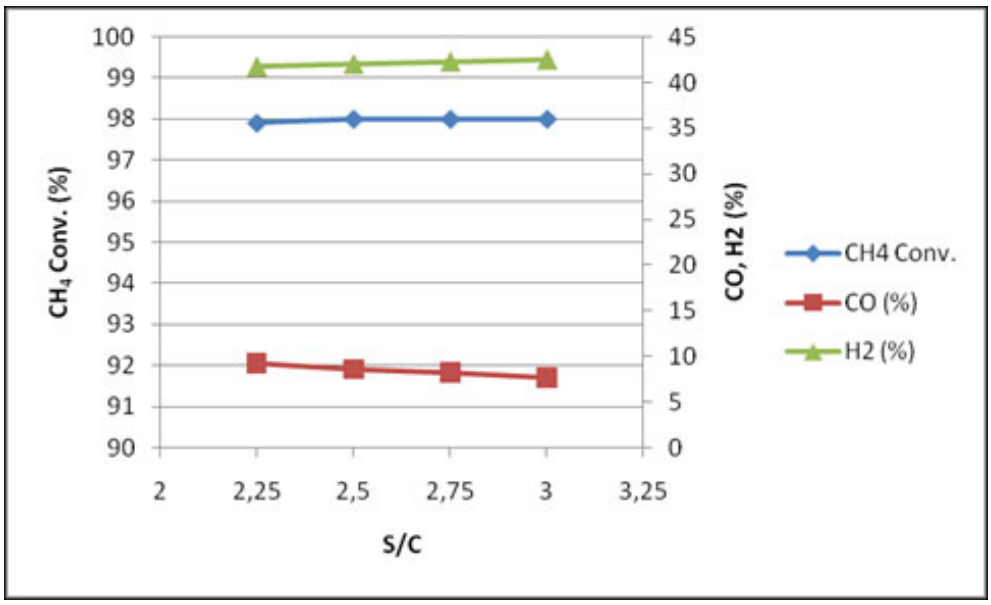

Figure 3: Effect of S/C on CH_4 conversion, CO and H_2% composition (O_2/C = 0.55).

2.2 Gas clean up unit

Since fuel cell anode catalyst is deactivated by the CO concentration in the downstream of ATR, CO concentration should be gradually decreased to below 1% by high and low temperature water-gas shift reactors (HTS, LTS) and then to below 10 ppm by preferential oxidation (PrOx) reactors [6, 7].

Commercial catalysts were used for gas clean up (HTS, LTS, PrOx) reactors. Since the steam feed flow rate was optimized in order to maximize ATR performance and the amount of the unreacted steam in ATR downstream was enough for the HTS and LTS reactions, there is no additional water feeding to these reactors. So the only studied operating parameter for HTS and LTS was the feed temperature of the reactor. During the HTS tests, the effect of feed temperature on CO conversion was studied and the optimum operating temperature was determined to be 400°C at which maximum CO conversion of 69% was obtained as seen from Figure 4.

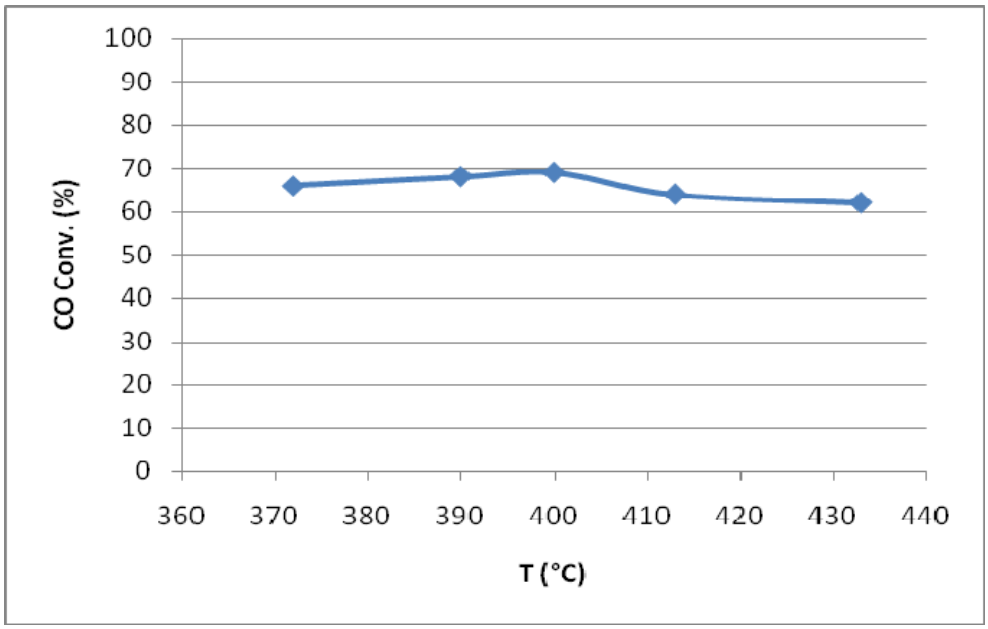

Figure 4: Effect of feed temperature on CO conversion in HTS reactor.

The effect of feed temperature on CO conversion in the LTS reactor was studied and the maximum CO conversion of 60.2% was obtained at 298°C as seen in Figure 5. At these conditions, CO concentration was ~ 0.5%, which was suitable to be fed to PrOx reactors.

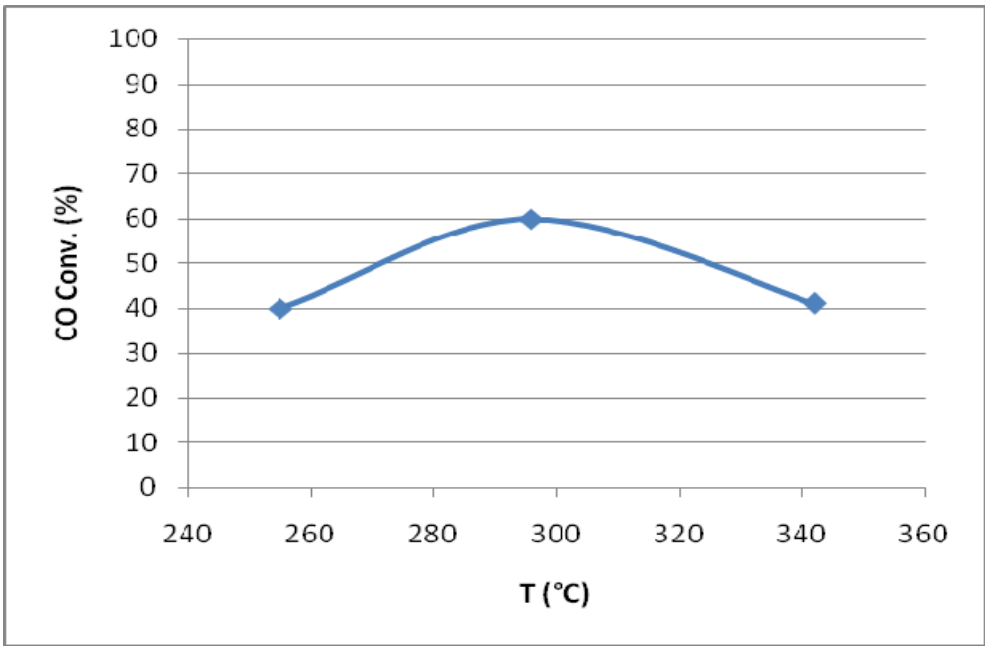

Figure 5: Effect of feed temperature on CO conversion in LTS reactor.

CO conversion, selectivity, H_2 and CO composition at the outlet of the first stage of PrOx reactors (PrOx-1) at various air to fuel ratios (λ) were investigated. For the commercial PrOx

catalyst used, λ values between 2–2.8 were studied for PrOx-1 during the tests. Since the PrOx-1 reactor outlet contained trace amounts of CO (ppm level), an online infrared CO analyzer was used to measure CO amount and a gas chromatography was used to measure the other components. The outlet CO content was reduced to 250 ppm at the determined optimum value of λ.

During the tests of the second stage of PrOx reactors (PrOx-2), the air feed to the PrOx-1 reactor was adjusted to provide the determined optimum value of λ. CO conversion, selectivity, H_2 and CO composition at the outlet of the PrOx-2 reactor at various λ values were investigated. During the tests, in order to reduce the CO content of the PrOx-2 reactor outlet which would be fed to the PEM fuel cell, excess air was fed to the PrOx-2 reactor compared to the PrOx-1. Although the CO conversion was very high, the CO selectivity was estimated to be low since the excess air also reacted with some H_2 beside CO in the PrOx-2 reactor. However, the excess air feed (above the stoichiometric ratio) was not resulted in an unacceptable H_2 loss since the CO content at the inlet of the PrOx-2 reactor was very low. The outlet CO content was reduced down to 4 ppm which was acceptable to be fed to the PEM fuel cell.

3 Conclusion

In this paper, the main experimental results on autothermal reforming of NG and gas clean-up systems concerning the requirements of PEM fuel cell system have been presented. It has been found that design parameters of fuel processor were very important but operational parameters of the system were crucial for system performance and PEM fuel cell requirements.

In this study commercial catalysts were used in all the reactors. For autothermal reforming of NG, O_2/C ratio was studied between 0.5–0.6, while S/C ratio was studied between 2.0–3.0 to observe their effects on CH_4 conversion, CO and H_2 formation. As a result of the experiments, it was observed that increase in S/C ratio at constant O_2/C ratio increased the CH_4 conversion and H_2 production, while decreased the CO production. On the other hand, increase in O_2/C ratio at constant S/C ratio increased the CH_4 conversion and CO production, while decreased the H_2 production. For the HTS reactor, the feed temperature was optimized to be 400°C at which maximum CO conversion of 69% was obtained. In the downstream of the LTS reactor, the amount of CO was reduced down to 0.5% at 298°C at which maximum CO conversion of 60.2% was obtained. Even though the effect of inlet temperature on CO conversion can be obviously seen, the efficiencies of HTS and LTS reactors were not high enough. After the catalysts were replaced with the new ones, CO conversion was increased for both reactors. CO conversion, CO selectivity, H_2 and CO composition at the outlet of the PrOx-1 and PrOx-2 reactors at various air to fuel ratios (λ) were investigated. The optimum values of λ were determined for both reactors that resulted in 250 ppm CO content in the PrOx-1 outlet and 4 ppm CO content in the PrOx-2 outlet which was acceptable to be fed to the PEM fuel cell.

Acknowledgements

This study has been realized within the “Fuel Cell based Micro Cogeneration System” project, whose project number is 105G127 and which is conducted under TÜBİTAK Support

Programme for Research Projects of Public Institutions (1007). General Directorate of Electrical Power Resources Survey and Development Administration as the customer and TÜBİTAK are greatly acknowledged for their support.

References

[1] Kume, Y., “Environment-friendly clean energy, Natural gas fired cogeneration, Current status and future overview in Japan”, The Japan Gas Association.

[2] Millicer, H., “Transformational Energy Futures, Efficient and clean energy for the world”, Ceramic Fuel Cells Limited.

[3] Alanne,. K. and A. Saari, “Sustainable small-scale CHPtechnologies for buildings: the basis for multi-perspective decision-making”, *Renewable and Sustainable Energy Reviews*, Vol. 8, pp. 401–431, 2004.

[4] Bernsen, E., “The perspective of future cogeneration development in Poland and in the common European market, CHP sector in liberalised energy markets - working solutions”, Conference Warsaw, 10 May 2006.

[5] Kalam, A., “Cogeneration and distributed resources”, Victoria University.

[6] Mariño, F., C. Descorme and D. Duprez, “Noble metal catalysts for the preferential oxidation of carbon monoxide in the presence of hydrogen (PROX)”, *Applied Catalysis B: Environmental*, Vol. 54, pp. 59–66, 2004.

[7] Avgouropoulos, G., T. Ioannides, C. H. Papadopoulou, J. Batista, S. Hocevar and H. K. Matralis, “A comparative study of Pt/γ-Al_2O_3, Au/α-Fe_2O_3 and CuO–CeO_2 catalysts for the selective oxidation of carbon monoxide in excess hydrogen”, *Catalysis Today*, Vol. 75, pp. 157–167, 2002.

Mass-Production Issues of Micro-structured Fuel Processors for Distributed Energy Generation

Gunther Kolb, Helmut Pennemann, David Tiemann, Institut für Mikrotechnik Mainz GmbH, Mainz, Germany

1 Introduction

Future sustainable and distributed energy generation will rely in many cases on fuel cell technology. To address the critical issue of hydrogen supply fuel processing of fossil and renewable fuels is a viable option [1].

Because fuel processor/ fuel cell systems for mobile applications are going to be a future mass product, production techniques are required, which allow high volume production at competitive pricing. Development of complete fuel processors for alcohol and hydrocarbon fuels is on its way at IMM applying micro-structured plate heat-exchanger technology. The power range of these systems reaches from 100 W_{el} [2] to 5 kW_{el} [3-5], while larger systems are under development [6]. All production steps required to build a fuel processor are currently addressed at IMM to meet the demands of future mass production and will be discussed below.

2 Microchannel Fabrication

The first step is the introduction of micro-channels into the metal foils, which are made from stainless steels or aluminum. Rapid prototyping techniques such as wet chemical etching of stainless steel or aluminium foils are established for the fabrication of micro-channels. Etching techniques might be suited for mass production already, depending on the number of units produced and on the size of the components. Cheaper techniques such as rolling or embossing are alternatives. One advantage of the embossing procedure compared to etching is, that the thickness of the metal sheets can be reduced significantly, because no material is removed during the shaping process and hence the thickness of the plate remains the same. Fig.1 shows an example of embossed plates and of a small-scale heat-exchanger fabricated by embossing and laser welding. In this first trial the plates were still embossed individually and then stacked manually together with other plates, which were cut by laser-cutting.

However, the embossing procedure alone is not sufficient to fabricate a heat-exchanger out of metal sheets in a fully automated manner. Actually such a shaping procedure is composed of 8-10 individual shaping steps, which could be realized in a follow-on composite tool. Such a tool would combine embossing, punching and folding steps. An endless coil of the metal sheet would then be transported through that tool.

A simpler version of such a tool, which integrates only the punching and embossing steps has been designed but not fabricated to-date (see Fig.2).

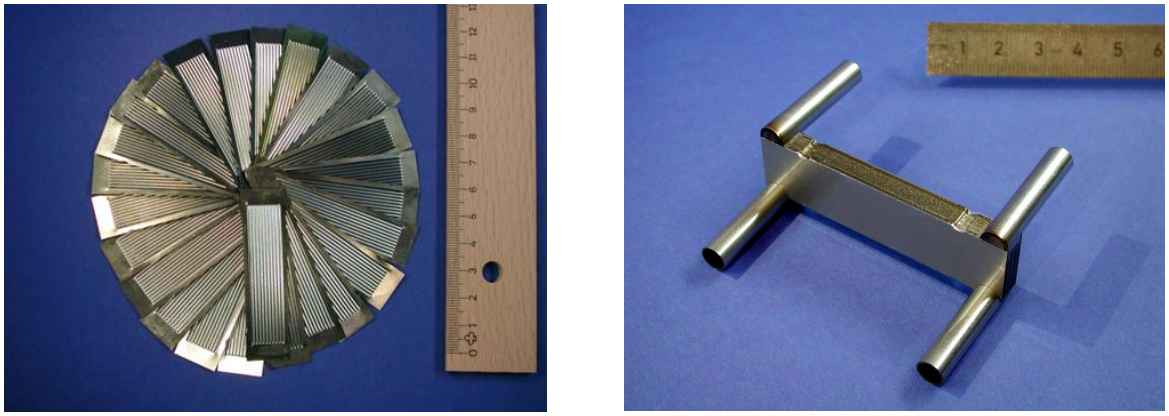

Figure 1: Micro-structured steel foils fabricated by embossing (left); embossed and laser-welded heat-exchanger (right).

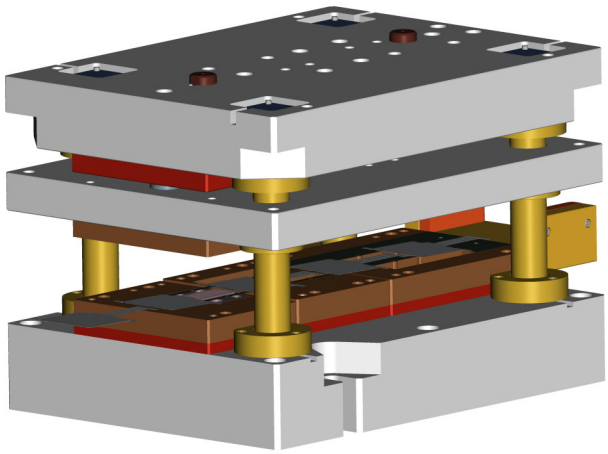

Figure 2: Follow-on composite tool for punching and embossing.

3 Catalyst Coating

The next step is the coating of catalysts into the micro-channels, which turns the plate heat-exchangers into chemical reactors. For the prototype reactors, a manual wash-coating procedure is applied [7]. However, this method includes the masking of the areas not to be coated by tape material, coating of the plate with the catalyst or catalyst carrier slurry (excess slurry is removed) and in some cases even the impregnation of the active species onto the alumina wash-coat in the micro-channels. In the latter case, two temperature treatment (calcination) steps are required to get the finished catalyst.

Different automated coating techniques have been investigated at IMM in the past, among them a coating machine, which more or less mimicked the manual procedure of filling the channels with a surplus of slurry and mechanical removal of the excess. More promising techniques under investigation were spray coating and screen printing. The former procedure, however, still requires masking of the areas not to be coated and generates

substantial losses of catalyst material. Therefore screen printing of the catalysts onto the plates was finally chosen as optimum method.

The development of the screen-printing procedure required a careful choice and combination of ingredients added to the catalyst slurry to achieve amongst others features such as the thixotropic behavior required for screen printing. The preservation of the catalytic activity and stability despite the changes of the slurry formulation is of course mandatory and requires experimental verification, which could be achieved in the current case by 1,000 hours activity tests for the catalyst formulations under development. Fig.2 shows examples of micro-channels coated by screen printing.

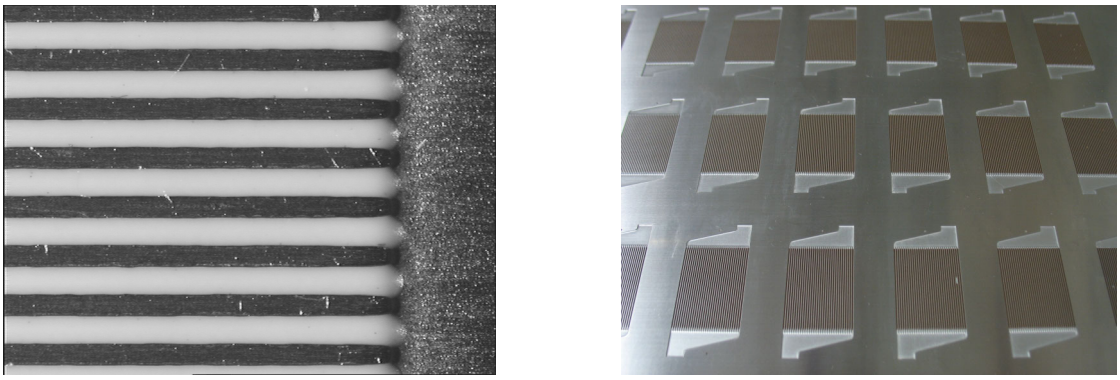

Figure 3: Microchannels coated with catalyst by screen-printing; single plate coated with catalyst slurry (left); sheet with multiple coated plates (right).

4 Joining Techniques

Finally the reactors and heat-exchangers need to be sealed by automated procedures such as laser welding or brazing. The reactors produced by these means are one-way products.

While brazing especially of aluminium is an established technique for plate heat-exchangers in the field of automotive and other mobile applications, it might well impair the performance of the catalyst coatings owing to the elevated temperatures required. Another issue is the release of organic material during the brazing procedure which might well impair catalyst durability.

Therefore a local input of heat, which does not increase the temperature of the catalytic coating significantly such as laser welding is the preferred option. Recently continuous wave (CW) disk and fiber lasers have entered the market, which had been dominated by CO_2-lasers before, as powerful tools for welding of metals. The continuous impact of a high amount of energy on a very small spot of e.g. 25 µm diameter even allows dynamic beam shaping by applying scanner technology. This results in superior quality of the welding seams at sufficient welding depth and high welding speed in the range of several m/min (see Fig.1). Long term welding trials performed with a 1 kW disc laser at IMM revealed superior quality of the welding seams at a length of one thousand meters without any defects. These trials are currently ongoing.

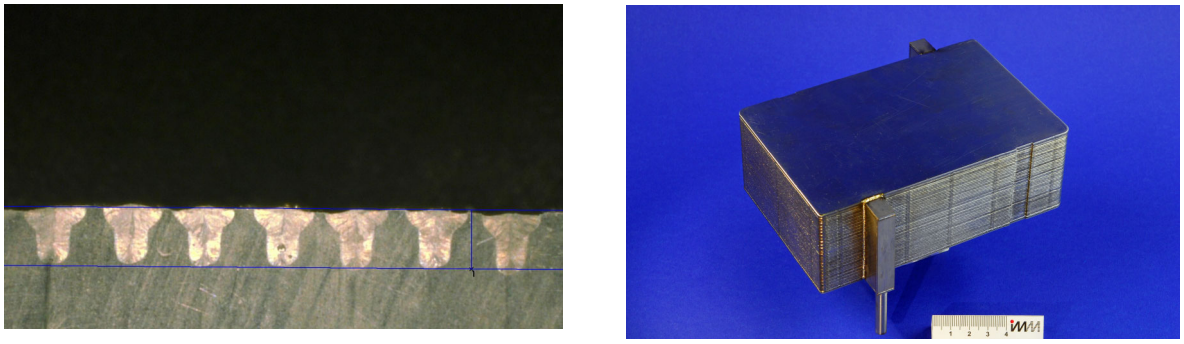

Figure 4: Welding seams of 1 mm thickness achieved at high temperature stainless steel 1.4841 (AISI 314)(left); plate stack joined by laser welding (right).

References

[1] G. Kolb Fuel Processing for Fuel Cells, 1 ed.; Wiley-VCH: Weinheim, 2008.

[2] G. Kolb; K.-P. Schelhaas; M. Wichert; J. Burfeind; C. Hesske; G. Bandlamudi. Chem. Eng. Technol. 2009, 32, 1739.

[3] M. O'Connell; G. Kolb; K. P. Schelhaas; J. Schürer; D. Tiemann; A. Ziogas; V. Hessel. Int. J. Hydrogen Energy 2009, 34, 6290.

[4] M. O'Connell; G. Kolb; K. P. Schelhaas; J. Schuerer; D. Tiemann; A. Ziogas; V. Hessel. Int. J. Hydrogen Energy 2010, 35, 2317.

[5] M. O'Connell; ; G. Kolb; ; K.-P. Schelhaas; ; J. Schuerer; D. Tiemann; ; S. Keller; ; D. Reinhard; ; V. Hessel; . Ind. Eng. Chem. Res. 2010, submitted for publication.

[6] G. Kolb; Y. Men; K. P. Schelhaas; D. Tiemann; R. Zapf; J. Wilhelm. Ind. Eng. Chem. Res. 2010, submitted for publication.

[7] R. Zapf; C. Becker-Willinger; K. Berresheim; H. Holz; H. Gnaser; V. Hessel; G. Kolb; P. Löb; A.-K. Pannwitt; A. Ziogas. Chemical Engineering Research and Development 2003, A 81, 721.

Experimental and Theoretical Studies of Solar Steam Reforming Assisted by Molten Salts

Alberto Giaconia, **Isabelle Labach**, **Giampaolo Caputo**, **Salvatore Sau**, Italian National Agency for New Technologies, Energy and Sustainable Economic Development (ENEA), Italy

1 Introduction

Steam reforming of methane is today the mostly used industrial process for hydrogen production, covering about 48 % of hydrogen demand. The process is based on two catalytic reactions:

$CH_4 + H_2O \rightarrow CO + 3H_2$ (1) (SMR, $\Delta H_{298\,K} = +206$ kJ/mol)

$CO + H_2O \rightarrow CO_2 + H_2$ (2) (WGS, $\Delta H_{298\,K} = -41$ kJ/mol)

Reaction (1) is usually carried out at 800-1000 °C in a tubular catalytic reactor placed in an industrial furnace. Hydrogen yield is afterwards maximized in one or two water-gas-shift (WGS) (2) reactors operating at lower temperatures (200-500 °C).

The whole process requires heat to power the highly endothermic SMR reaction (1), generate reactant steam, and drive purification units (e.g. CO_2 separation). This process heat is usually provided burning a fraction of the natural gas (NG) supply [1].

Alternatively, high-temperature carbon-free heat sources, like solar or nuclear, can be used to power the whole thermochemical process: in this way environmental benefits in terms of reduction of CO_2 emissions can be achieved, together with a corresponding reduction of methane consumption, as represented in Figure 1.

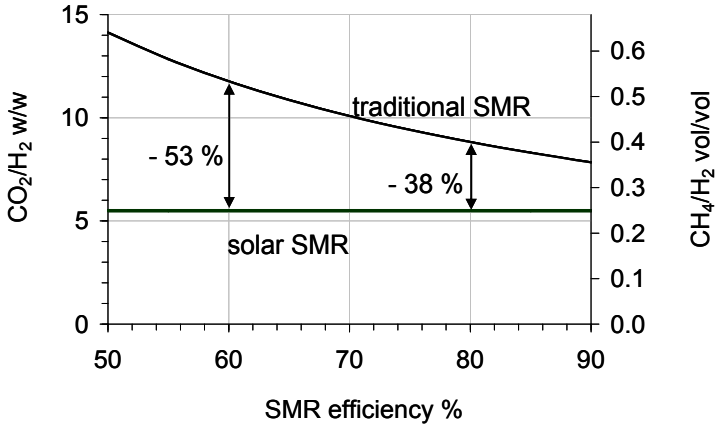

Figure 1: Comparison between conventional and solar SMR in terms of specific CO_2 emissions related to overall process thermal efficiency.

Given the lower NG demand, the solar (or nuclear) route is less sensible to NG price and availability. Therefore, due to possible increase of NG price, we can expect for the near future a hydrogen production cost from solar SMR competitive with the traditional process [2].

Solar SMR can be directly carried out in a high-temperature solar receiver reactor set on a tower [2]. This technology enables reactor operation at suitable temperature levels for the SMR reaction (1), but effectiveness is strictly linked to instant solar radiation fluctuations and night/day cycles.

In this paper it is presented an alternative solar SMR technology, studied by ENEA in the framework of the "Solar Thermodynamic Project". This innovative route makes use of a molten salts stream as heat transfer fluid and storage medium to drive the SMR process under steady state and designed conditions. Main R&D issues deal with the lower operating temperatures (450-550 °C) than the conventional route (800-1000 °C): this results in thermodynamic limits of SMR reaction (1), but also allows to lower material concerns and to drive SMR (1) and WGS reactions simultaneously.

Preliminary theoretical analysis and experimental programs are overviewed.

2 Process Description

Molten nitrate mixtures ($NaNO_3/KNO_3$ 60/40 w/w) up to 565 °C have been proved as suitable heat carriers and storage medium for concentrating solar power (CSP) plants. Particularly, ENEA has recently demonstrated their use in an innovative solar trough technology (a 5 MW_e demonstration plant has been built in Sicily, and will be started in the next months).

This system is also suitable to steadily power themochemical processes up to 550 °C [3], and steam reforming of methane (from NG or biogas) is an interesting option.

In Figure 2 is shown a general process scheme. During solar radiation hours the molten salts (MS), flowed through the solar receiver of the CSP plant, are heated up to about 550 °C and stored in a "hot" tank. The CSP plant with heat storage tanks is dimensioned to supply 24 h/24 h heat at constant rate to the thermochemical plant; a back up heater (powered by an auxiliary fuel, e.g. biomass or biogas) is often integrated in the MS loop to ensure constant heat supply even after long cloudy periods. MS are first sent to the SMR + WGS reactor, consisting of a shell and tube heat exchanger with the inner tubes packed with the catalyst (Figure 3). Residual sensible heat of MS is used to power the feed gas pre-heater (Pr-Htr), steam generator (Steam-Gn), and downstream separation units. Due to thermodynamic limits resulting from reaction temperatures lower than 550 °C, a CH_4/H_2 gas mixture will be obtained after cooling and water removal by condensation (GL-Sep) and CO_x removal (e.g. methanation and CO_2 adsorption in regenerative amine solution cycles).

Hydrogen can be recovered and purified from the outlet CH_4/H_2 mixture (e.g. by PSA) and methane recycled. Otherwise, the hydrogen-containing methane (often referred as HCNG) is a valuable energetic product for several applications [4]: it was demonstrated that, within certain composition limits (5-30 $\%_{vol}$ of H_2), pure NG replacement with HCNG in internal combustion engines (ICE) has some environmental benefits in terms of local pollution; the use of a renewable source for hydrogen generation leads to additional environmental

benefits even to the global level. Residual MS sensible heat (to 290 °C) can be used for the co-generation of solar electricity by steam cycles [5].

It is noteworthy that the gas fueled industrial SMR furnace of the industrial process is replaced by more compact and modular heat exchangers with improved scale down capabilities. This makes the SMR process more efficient at the small-medium scale, and eliminates flue gas emissions of the chemical plant.

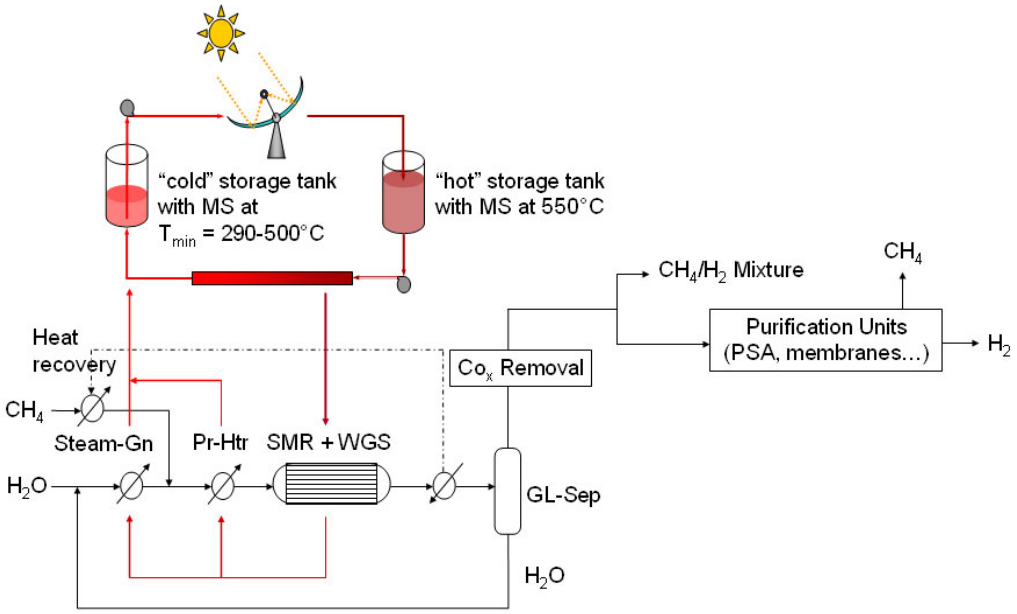

Figure 2: Simplified scheme of the SMR process powered by a concentrating solar plant using molten salts (MS) as heat transfer fluid.

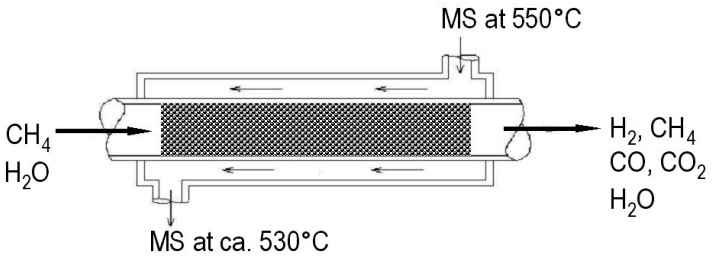

Figure 3: Methane steam reforming packed-bed reactor using molten salts (MS) as heat transfer fluid.

3 Preliminary Results and Application

MS assisted solar SMR has been analyzed by means of suitable mathematical models for catalytic steam reformers (specifically developed by the University "La Sapienza" - Rome), and the ASPEN Plus process simulator for flowsheet development with mass and energy balances. A parametrical analysis of several chemical process configurations was carried out

at nominal pressures of 10 and 20 bar, and 2.2 mol/mol steam-to-carbon ratio into SMR reactor inlet.

In order to shift methane conversion above the thermodynamic limits, H_2 selective membranes or CO_2 Sorption Enhanced Reforming Process (SERP) can be applied. Particularly, we first considered a process configuration involving a single reactor followed by conventional CH_4/H_2 separation units (e.g. PSA). This benchmark configuration was compared with advanced process scheme consisting of SMR reactors set in series with intermediate membrane units for H_2 removal. Permeated hydrogen was assumed extracted by a vacuum pump whose duty was accounted in the energy balance. In Figure 4 is represented the overall thermal energy demanded to the CSP plant with the number of reaction/membrane stages in series: by increasing single-pass methane conversion and hydrogen output rate, membrane exploitation leads to a significant energy efficiency increase of the thermochemical process. Therefore, membranes make the chemical plant more complex but significantly reduce the costs for the CSP plant.

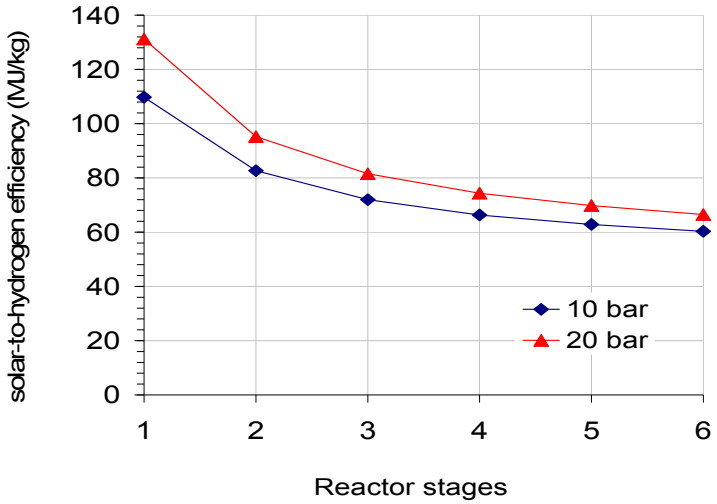

Figure 4: Thermal energy demand by the thermochemical process per kg of hydrogen produced using different reaction/membrane stages in series.

It is noteworthy that the reactor/membrane units train is fairly equivalent to a single integrated membrane reactor, i.e. a reactor equipped with the membrane tube set inside the catalytic bed [6]: the use of membranes working at temperatures close to SMR reactor temperatures (530-550 °C) should allow us to design compact membrane reformers powered by molten salts at 550 °C, with results fairly equivalent to those plotted in Figure 4.

Research and development activities in ENEA are now focused on experimental validation of these theoretical results, and engineering studies to process optimization.

First, suitable catalysts must be identified for methane steam reforming in the temperature range of 450-550 °C. Both commercial and home-made supported catalysts are investigated. Catalyst long-term stability (i.e. constant H_2 production rate over at least 200 hours operation), activity and selectivity (WGS reaction effectiveness) is determined under different operating conditions like temperature (450-550 °C), pressure (1-20 bar), steam-to-carbon

ratio, space velocity. Besides identification of the most promising catalyst, this preliminary study allows determination of the effect of process parameters for subsequent reactor design.

Moreover, performances of H_2-selective membranes are investigated in terms of selectivity and permeability under representative process conditions.

Afterwards, a MS-heated SMR prototype will be designed, constructed and integrated in the Molten Salts Experimental test facility (MOSE plant) in ENEA-Casaccia research center. In case of an integrated membrane reactor, an engineering challenge is the fitting of the rates of the three controlling physical-chemical mechanisms, i.e. mass transport through the membrane, reaction kinetics, and heat transfer from MS to reacting gas mixture.

Some of these activities will be carried out in the framework of the upcoming MET.I.SOL. project (founded by the Italian Ministry for the Environment), mainly focused on methane/hydrogen mixtures thermochemical production from solar energy, on-board storage and utilization in ICE vehicles. This project will be coordinated by Fiat Motors and several partners from Italian Industries, Regional Energy Agencies, Private Enterprises, Universities, and Research Organizations.

4 Summary

The pathway to hydrogen generation entirely from renewable energy and material sources probably goes by a transitional period with the utilization of hybrid fossil/renewable integrated systems.

Solar steam reforming of methane is set in this context, specifically suited for a country like Italy whose actual energy policy is mainly based on the imported NG, but also characterized by convenient solar radiation levels in the Southern Regions.

A new solar SMR process is being developed by ENEA, using molten nitrates as solar heat carriers and storage medium at about 550 °C. The potential of this process have been proved theoretically by process simulation studies. Engineering and experimental activities aimed to the development of a prototype apparatus are now in progress in ENEA's laboratories.

It is remarkable that the developed technology (MS powered SMR) can find interesting impact in the industrial chemistry wherever it is convenient decoupling the heat demanding reactor from the heat source. For example, this practice allows multi-fuel and power source exploitation (e.g. coupling biomass with solar heat); moreover gas emissions will be avoided at the final user's level. The use of convective heat transfer in place of conventional radiant furnaces, by means of a non-pressurized heat transfer fluid like MS operating at about 550 °C, reduces the material concerns (use of special steel alloys) and the overall plant volume.

Acknowledgements

Besides the authors, the following scientists and laboratory assistants have appreciably contributed to this work: Gianfranco Canti, Fabrizio Fabrizi, Pietro Tarquini, Marcello De Falco (University "La Sapienza", Rome), Luigi Marrelli (University "La Sapienza", Rome).

References

[1] Rostrup-Nielsen J.R., Sehested J., Norskov J.K.: “Hydrogen and Synthesis Gas by Steam- and CO_2 Reforming”, Adv. Catal. 2002, vol. 47, p.65-139.

[2] Moeller S., Kaucic D., Sattler C.: “Hydrogen production by solar reforming of natural gas: a comparison study of two possible process configurations”. ASME J. Sol. Energy Eng. 2006, vol.128, p16–23.

[3] Giaconia A., Grena R., Lanchi M., Liberatore R., Tarquini P.: “Hydrogen/methanol production by sulfur-iodine thermochemical cycle powered by combined solar/fossil energy”; Int. J. Hydrogen Energy, 2007, vol.32, p.469-481.

[4] Giaconia A., De Falco M., Caputo G., Grena R., Tarquini P., Marelli L.: “Solar Steam Reforming of Natural gas for Hydrogen Production using Molten Salt Heat Carriers”, AIChE J. 2008, vol. 54, p.1932-1944.

[5] De Falco M., Giaconia A., Marrelli L., Tarquini P., Grena R., Caputo G.: “Enriched methane production using solar energy: an assessment of plant performance”; Int. J. Hydrogen Energy, 2009, vol.34, p.98-109.

[6] De Falco M., Marrelli L., Basile A., Gallucci F., Giaconia A., Di Paola L. : “Design of an Industrial Methane Membrane Steam Reformer: Study of Efficiency Improvement”. 2nd International Hydrogen Energy Congress and Exhibition IHEC 2007, Istanbul (Turkey), 13-15 July 2007.

Ordered Mesoporous Carbons as Catalysts with Remarkable Activity and Stability for Hydrogen Production without CO_2 Emissions by CH_4 Decomposition

J.A. Botas, Department of Chemical and Energy Technology, ESCET, Rey Juan Carlos University, Móstoles, Spain
D.P. Serrano, Department of Chemical and Energy Technology, ESCET, Rey Juan Carlos University, Móstoles, Spain and IMDEA Energía, Móstoles, Spain
P. Pizarro, **G. Gómez**, Department of Chemical and Energy Technology, ESCET, Rey Juan Carlos University, Móstoles, Spain

1 Introduction

Hydrogen is currently regarded in the mid-term as a promising energy vector in both transport and power generation sectors. However, hydrogen is not a primary energy source, since it cannot be found free in our planet and it must be produced from other compounds. Conventional H_2 production is carried out by steam reforming of methane (SMR), which is accompanied by CO_2 generation [1]. Thermocatalytic decomposition of methane has become an attractive alternative for hydrogen production. In this process, methane is transformed into solid carbon and hydrogen, which implies that the latter is free of CO/CO_2 emissions, while moderate energy consumptions are required [2]. Although metal catalysts exhibit high activities, they are rapidly deactivated by carbon depositions [3]. Furthermore, regeneration of metal catalysts by burning those carbon deposits is not a valid option since it would lead to undesirable CO_2 emissions. Alternatively, the use of carbonaceous materials as catalysts for methane decomposition is being extensively explored. The most remarkable advantages of carbon catalysts are: a) high thermal stability; b) regeneration step is not needed; c) the reaction could be catalytically self-provided and d) the carbon produced may have different commercial applications [4]. Numerous types of carbonaceous catalysts have been tested for decomposition of methane [4, 5]. In recent works, we have reported the use of ordered mesoporous carbons (CMK type) in this reaction. The best results were obtained over CMK-5 carbon, characterized by having amorphous pore walls, high surface area and a double mesopore system [6, 7].

In this work, long term catalytic activity and stability of CMK-type carbons, two commercial carbon blacks and one activated carbon were compared when they were used as catalysts under different isothermal conditions in the methane decomposition for hydrogen production.

2 Experimental

2.1 Carbon catalyst preparation

CMK-3 and CMK-5 carbons were synthesized using a nanocasting pathway with pure silica SBA-15 as hard template. The preparation procedure has been earlier reported [7], being based on the method described by Ryoo and col [8].

For the SBA-15 preparation, tetraethylorthosilicate (TEOS, Aldrich) and non-inonic triblock copolymer (Pluronic P-123, Aldrich) were used as silica source and as structure directing agent, respectively.

For the synthesis of CMK carbons, furfuryl alcohol (FA, Acros Organics) was used as carbon precursor, oxalic acid (OA, Acros Organics) as polymerization catalyst and trimethylbenzene (TMB, Aldrich) as solvent. The synthesis steps were as follows: a) infiltration of a solution containing 0.012 g OA / 3 mL FA in TMB into the SBA-15 pores by the wetness impregnation technique; b) polimerization at 90 ºC, and c) calcination under inert atmosphere at 850 ºC; d) silica termplate removal by dissolution with an ethanol-water mixture containing 1M NaOH; e) filtration and washing of the black powders, and f) drying at 90 ºC overnight. Two CMK type samples were so obtained by using volumetric FA/TMB proportions of 100 % (CMK-3) and 60 % (CMK-5), respectively.

For comparison purposes, three commercial carbons were used as reference materials: mesoporous activated carbon (AC-mes, Darko) and two carbon blacks from Cabot Corp (black pearls 2000, CB-bp, and vulcan XC72, CB-v).

2.2 Carbon catalyst characterization

Textural properties of the catalysts were measured by N_2 physisorption analyses (77 K) using a Micrometrics Tristar 3000 instrument. Samples were previously degassed at 200 ºC under nitrogen flow. The surface area was calculated by applying the Brunauer–Emmet–Teller (BET) equation. Pore size distribution of mesoporous carbons was calculated using the Barret–Joyner–Halenda (BJH) model and with the application of the t-plot methods the micro and mesopores contribution in carbon catalysts were determined.

2.3 Methane decomposition reactions

Methane decomposition reactions were performed on a simultaneous DSC-TGA thermobalance (TGA-DCS1, Mettler Toledo). A flow of 200 ml·min^{-1} of 10 % CH_4 in Ar was employed as reactive gas. Reactions were operated under isothermal conditions using different temperatures in the range 890-990 ºC. Previous to the reaction, carbon catalysts were dried at 250 ºC with nitrogen. Hydrogen production was indirectly measured through the weight increase of the catalysts during the reaction due to solid carbon deposition, according to the following reaction scheme:

$$CH_4\ (g) \rightarrow 2\ H_2\ (g) + C\ (s) \qquad (1)$$

3 Results and Discussion

Figure 1.A. shows the N_2 (77 K) adsorption-desorption isotherms of all samples and Figure 1.B the BJH pore size distribution of mesoporous carbons. The samples AC-mes and CB-bp present a type II isotherm, according to IUPAC classification; they show an important adsorption at low values of relative pressures, indicating the presence of micropores together with a significant adsorption at intermediate relative pressures due to the mesoporous feature of the catalyst. On the other hand, CB-v sample exhibits the lowest porosity, which is consistent with being formed mainly by non-porous nanoparticles. In the case of CMK carbons, both samples exhibit type IV isotherms, clearly denoting the presence of mesoporosity. CMK-3 shows a single adsorption step, which indicates that this material is formed by just one type of mesopores (3 nm). In contrast, two steps can be observed for the CMK-5 sample (3 and 5.8 nm). Consequently both CMK samples have in common a pore system of 3 nm diameter size. These mesopores are generated by the removal of the silica walls in SBA-15, while the second type of mesoporosity is due to the partial filling of the SBA-15 pores with the carbon precursor during the CMK-5 preparation.

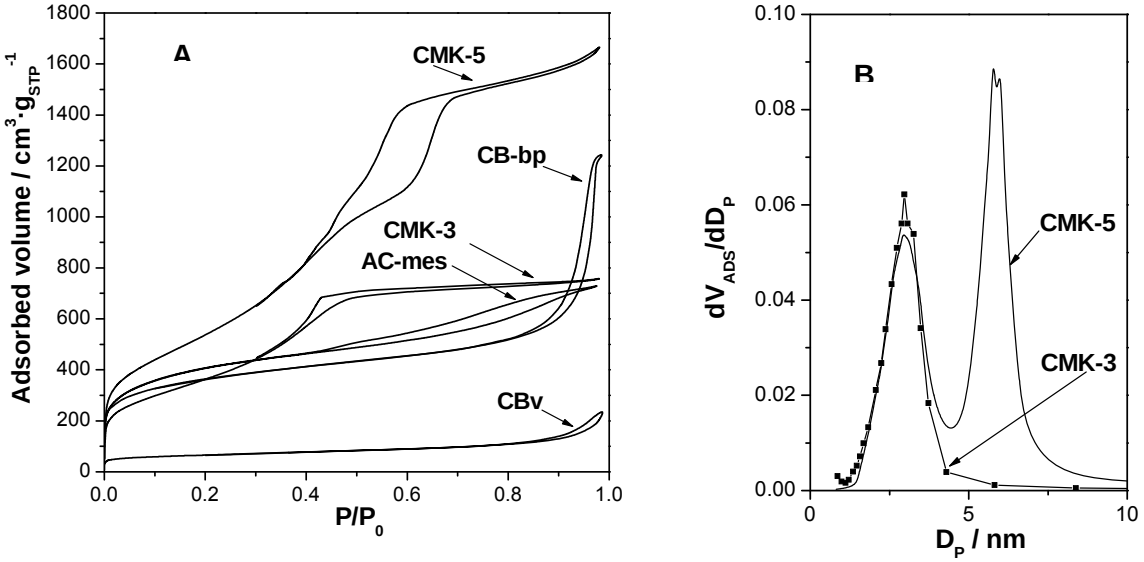

Figure 1: A. N_2 adsorption-desorption isotherms (77 K) of the catalysts, and B. BJH pore size distributions of mesostructured CMK-3 and CMK-5 carbons.

Table 1 summarizes the textural properties of the different carbons determined from the nitrogen adsorption isotherms. Except for CB-v carbon, all the samples exhibit large BET surfaces with values higher than 1000 $m^2 \cdot g^{-1}$. In the case of commercial carbons the largest contribution of micropores to the overall surface is observed. In contrast, no microporosity is observed in the case of CMK carbons in agreement with their purely mesoporous nature.

Table 1: Textural properties of carbon catalysts.

	S_{BET} / m^2 g^{-1}	S_{MICRO} / m^2 g^{-1}	V_{PORE} / cm^3 g^{-1}
CMK-5	1940	0	2.37
CMK-3	1323	0	1.08
CB-bp	1285	988	1.93
CB-v	231	134	0.31
AC-mes	1465	542	1.13

The catalytic activity of CMK-5, CMK-3 and commercial carbons towards hydrogen production via methane decomposition was evaluated through thermogravimetric measurements using the installation and conditions described in the experimental section. Figure 2 compares the activity evolution of these carbon catalysts along the reaction time under different isothermal conditions, expressed as catalyst weight increase caused by deposition of the carbonaceous co-products. It can be observed that the AC-mes sample presents the lowest catalytic activity of all samples. In the case of CB-bp carbon, except for 890 ºC, short reaction times are enough to achieve high values of activity, however, the deactivation is faster with increasing temperature at higher reaction times. CB-v carbon presents the highest initial catalytic activity at all temperatures studied, but as reaction times increases hydrogen production rate begins to decrease (acquiring the typical form of a deactivation process). This effect is more pronounced with increasing temperature. For the CMK samples, after a sharp initial change in the slope that takes place at short reaction times, the carbon deposition rate remains almost constant, indicating that these materials exhibit a high resistance to deactivation, being more relevant in the case of CMK-5. This better behaviour of CMK-5 is attributed to their textural properties consisting in a BET surface area close to 2000 m2·g-1 together with a double system of mesopores, which favours a rapid access of the methane molecules to the active sites and prevents the catalyst deactivation by the carbon formed from methane. In these tests, the amount of carbon deposited per gram of catalyst is quite superior to that corresponding to the complete filling of the CMK-5 and CMK-3 pores. Consequently, it must be concluded that the carbon produced from methane decomposition may leave the CMK pores, growing towards the outside part of the catalyst particles.

Furthermore, when the reaction at 990 ºC was extended up to 48 hours CMK-5 is the sample with the greater activity and stability, confirming its potential use as catalyst for hydrogen production by methane decomposition. After 72 hours of reaction time at 990 ºC about 15 and 31 grams of carbon deposits per gram of raw catalysts were formed using CMK-3 and CMK-5 catalysts, respectively.

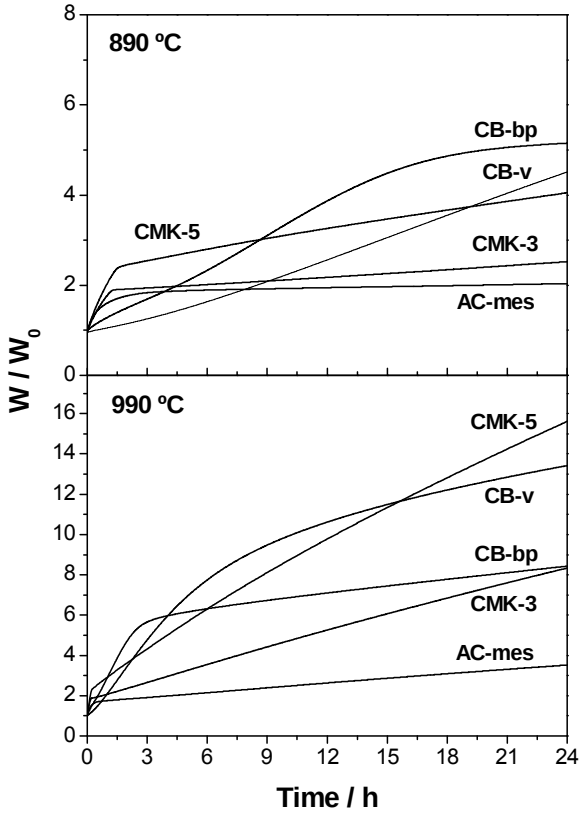

Figure 2: Catalytic methane decomposition tests. Evolution of weight for different carbon catalysts at different isothermal conditions.

4 Conclusions

Ordered mesoporous carbons, designated as CMK-3 and CMK-5, have shown to be excellent catalysts for the hydrogen production by methane decomposition. The combination of high textural properties, arising from the structure replication of SBA-15, and the essentially amorphous nature of the pore walls, accounts for their exceptional catalytic activity. Moreover, the presence of uniform mesopores and high surface area in these materials explain their strong resistance to deactivation by the formation of carbon deposits.

Acknowledgements

The authors thank to Spanish “Ministerio de Educación y Ciencia” for supporting this work through the Project ENE2008-05471/ALT.

References

[1] W.H. Scholz. Processes for industrial production of hydrogen and associated environmental effects. Gas. Sep. Purif. 7 (1993) 131-139.

[2] M. Steinberg. The Hy-C process (thermal decomposition of natural gas) potentially the lowest cost source of hydrogen with least CO2 emissions. Energy Convers. Mgmt. 36 (1995) 791-796.

[3] N.Z. Muradov, T.N. Veziroglu. From hydrocarbon to hydrogen-carbon to hydrogen economy. Int. J. Hydrogen Energy 30 (2005) 225-237.

[4] N. Muradov, F. Smith, A.T. Raissi. Catalytic activity of carbons for methane decomposition reaction. Catal. Today 102-103 (2005) 225-233.

[5] I. Suelves, M.J. Lázaro, R. Moliner, J.L. Pinilla, H. Cubero. Hydrogen production by methane decarbonization: carbonaceous catalysts. Int. J. Hydrogen Energy 32 (2007) 3320-3326.

[6] D.P. Serrano, J.A. Botas, P. Pizarro, R. Guil-López, G. Gómez. Ordered mesoporous carbons as highly active catalysts for hydrogen production by CH4 decomposition. Chem. Commun. (2008) 6585-6587.

[7] J.A. Botas, D.P. Serrano, P. Pizarro, R. Guil-López, G. Gómez. Methane catalytic decomposition over ordered mesoporous carbons: a promising route for hydrogen production. Int. J. Hydrogen Energy (2009), doi: 10.1016/ijhyener.2009.10.031.

[8] R. Ryoo, S.H. Joo, S. Jun, T. Tsubakiyama, O. Terasaki. Ordered mesoporous carbon molecular, sieves by templated synthesis: the structural varieties. Stud. Surf. Sci. Catal. 135 (2001) 150.

A Redox Cycle Approach for the Production of H_2 by Two-step Methanol Reforming

Stefano Cocchi, **Fabrizio Cavani**, **Sauro Passeri**, **Marziale Comito**, University of Bologna, Italy

1 Introduction

During recent years, many processes for the production of hydrogen from renewable sources have been proposed, comprising thermal, catalytic, electrolytic and photolytic processes [1]. Catalytic steam-reforming (coupled with the WGS reaction), currently the most used process for the production of hydrogen from natural gas, is also an option that can be used for the transformation of renewables, e.g., bioalcohols, into hydrogen. However, SR+WGS has the drawback that due to thermodynamic reasons CO impurities cannot be avoided, and further downstream technologies (e.g., CO/H_2 separation with membranes or CO-PrOx reaction) have to be used in order to obtain high purity hydrogen streams, to be used, e.g., as the feed for fuel-cell devices. Due to this reason, and also because of the fascinating challenge of obtaining an inherent separation of hydrogen from the C-containing products, during last years various alternative approaches have been proposed, in which the SR reaction is decoupled into two spatially and temporarily separated steps [2]. In the chemical-loop approach, during the first step a reductant (usually methane) is first contacted with a metal oxide, which oxidizes the former into carbon oxides and water. The reduced metal oxide is then reoxidized with water, to produce hydrogen and restore the original oxidation state and the O^{2-} content of the metal oxide (Scheme 1).

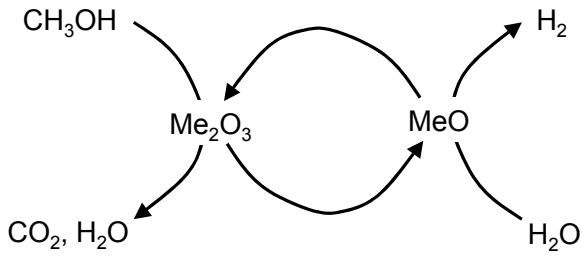

Scheme 1: Chemical-loop approach for methanol SR.

An example is the process recently developed by ENI, in which Fe_2O_3 is used as the electrons/O^{2-} carrier for the production of hydrogen from natural gas [3]. Worth of note, similar redox-decoupled approaches have also been proposed for the catalytic selective oxidation of organic substrates with molecular oxygen, that use metal oxides-based catalysts (Mars-van Krevelen redox mechanism) [4].

Materials employed for the cycle SR are similar to those used for thermochemical water splitting [5]. Amongst the most interesting systems described in the literature, ferrite-type spinel mixed oxides of general composition $Me^{II}_xFe^{II}_{1-x}Fe^{III}_2O_4$ (where Me = Co, Ni, Zn) offer

the possibility to modulate their redox properties by means of changing the divalent metal type and content.

In the present work, we report about a study on the feasibility of a two-step cycle approach for the catalytic production of hydrogen from methanol and water, using the spinel-type oxide $CoFe_2O_4$ as the electrons carrier.

2 Experimental

The spinel oxide $CoFe_2O_4$ was prepared by co-precipitation, via drop wise addition of an aqueous solution containing Fe(III) and Co(II) nitrates (total nitrates concentration 1.5M) into a NaOH 2M solution, at 50 °C, while maintaining the pH at 12. The precipitate was then separated under vacuum filtration, washed with abundant water, dried at 120 °C for 4 h and finally calcined at either 450 or 750 °C, for 8 h. The ferrite formation occurred already after digestion of the precipitate at 40 °C. The materials (both after thermal treatment and after reduction with methanol) were characterized by means of XRD. Calcined catalysts were also characterized by means of surface area measurement (BET) and Thermal-Programmed-Reduction analysis.

Reactivity experiments were carried out at atmospheric pressure, using a glass-made tubular flow reactor, loaded with 0.4 g catalyst. The reduction step was carried out using an inlet feed containing 15.6 vol% methanol in N_2 carrier; residence time was equal to 0.21-0.26 s, and reactor temperature was varied between 300 and 450 °C. The oxidation step was carried out using an inlet stream containing 29.3 vol% water in N_2 carrier; residence time was 0.20 s. The reactor outlet flow was kept at 200 °C and fed to an automatic sampling device for GC (microGC Agilent 3000A) analysis of unconverted methanol and of reaction products. Due to the presence of condensable products like water or methanol, the overall outlet volumetric flow (V_{out}), could not be directly estimated. Therefore, conversion and product yields were calculated using an iterative procedure on concentrations analytically determined, using an indirect estimation of V_{out}. Hydrogen was taken as the basis for calculation, because it was the only element for which an inlet-outlet atomic balance has to be 100 %. In fact, during methanol oxidation, the instantaneous C balance was less than 100 % because of coke accumulation on the ferrite, and O balance was higher than 100 % during the initial period, because of the O deriving from the reduction of the ferrite mixed oxide. On the other hand, the H balance was used to estimate the carbon deposition and the contribution to products formation deriving from ferrite bulk oxygen. For the reoxidation step, the change of flow was neglected, because the main reaction (reoxidation of the reduced oxide with water) did not imply a variation of the number of moles with respect to the fed ones.

3 Results and Discussion

3.1 Characterization of materials

During these specify experiments aimed at the characterization of reduced samples, residence time of 1s (higher than that used for reactivity tests) was used. Table 1 compiles the main characteristics of two samples calcined at 450 (CF-450) and 750 °C (CF-750). In both cases, XRD patterns evidenced the formation of the inverse spinel structure, but CF-450 was less crystalline than CF-750. X-ray diffraction patterns and Raman spectroscopy

confirmed the different morphology of the two samples. TPR measurements evidenced the presence of more reactive surface sites in CF-450 sample; a model was proposed in which smaller crystallites expose predominately (111) facets, preferentially terminated in tetrahedral Fe^{3+} surface sites, while sintering favours (110) and (100) facets and Co/Fe surface compositions is closer to the bulk inverse spinel phase [6]. The crystallinity of the samples greatly affected the rate of solid reduction and hence the reactivity behaviour.

X-ray diffraction pattern of samples were recorded after different times of exposure to the methanol stream (Figure 1).

Table 1: Main characteristics of samples prepared, both calcined and after reduction with methanol.

Sample	Treatment	Crystallite size, nm	Surface area, m^2/g
CF-450	After calcination	13	55
CF-450	After reduction with methanol (30 min) and reoxidation with steam	32	14
CF-750	After calcination	32	10
CF-750	After reduction with methanol (30 min) and reoxidation with steam	33	10

Contacting the CF-450 sample with methanol at T> 300 °C led to the progressive reduction of the spinel, with development of a metallic Co-Fe phase. At high temperature, the formation of metal carbide was also observed. With the more crystalline CF-750 sample, instead, no bulk reduction of the spinel was observed at 300 and 360 °C within 2 h reaction time. With both samples, the reoxidation of the reduced spinel with water led to the formation of $CoFe_2O_4$; however, some residual CoFe alloy hinted for an incomplete bulk oxidation of the material by steam. Moreover, the reoxidized CF-450 showed a remarkable increase of crystallinity with respect to the fresh sample, morphological and structural parameters finally being similar to those of fresh CF-750 (Table 1); sintering of the less crystalline material was due to the strongly exothermal oxidation process.

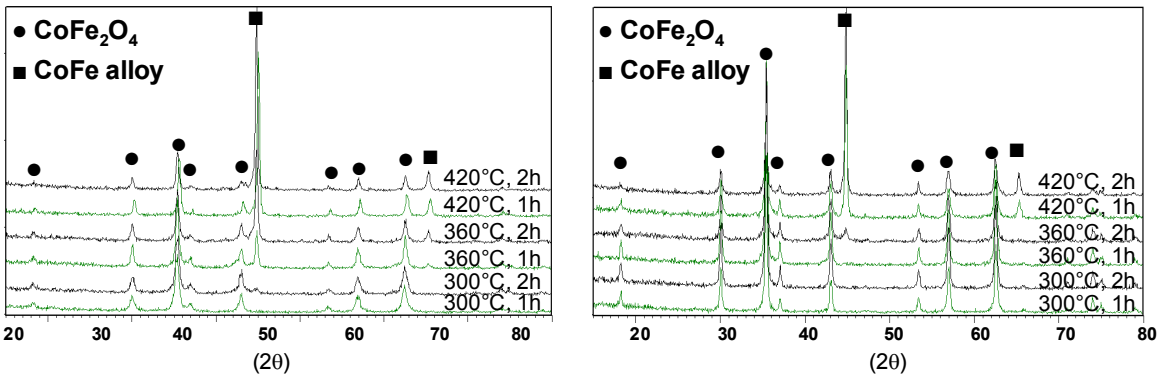

Figure 1: XRD patterns of CF-450 (left) and CF-750 recorded after different times of exposure to the diluted methanol stream, at various temperatures. (Residence time = 1s).

3.2 Reactivity tests

An example of the results obtained with sample CF-450 during the first step of the cycle, at 420 °C, is shown in Figure 2. The figure reports the instantaneous methanol conversion, and yields to CO, CO_2, CH_4, H_2O, H_2 and coke. The unsteady-state behaviour was due to the progressive reduction of the spinel oxide. The conversion of methanol was total during the entire experiment time. The ferrite catalysed the combustion of methanol to CO_2 and H_2O, but also the decomposition of methanol into CO and H_2; in fact, the yield to H_2 was relatively high even with the fully oxidized catalyst. Moreover, the yield to H_2 was much greater than that to CO, suggesting that additional reactions producing hydrogen were coke formation and methanol reforming, the latter using the in-situ produced H_2O. A contribution deriving from WGS can be excluded, due to high concentration of CO_2 from combustion. A reaction also contributing to CO_2 formation, a compound that was produced even with the strongly reduced material, was the Boudard reaction (disproportion of CO to CO_2 and coke). Methane formed by hydrogenation of CO, but possibly also by decomposition of methylformate, the latter being formed by the Tishchenko dimerization of formaldehyde.

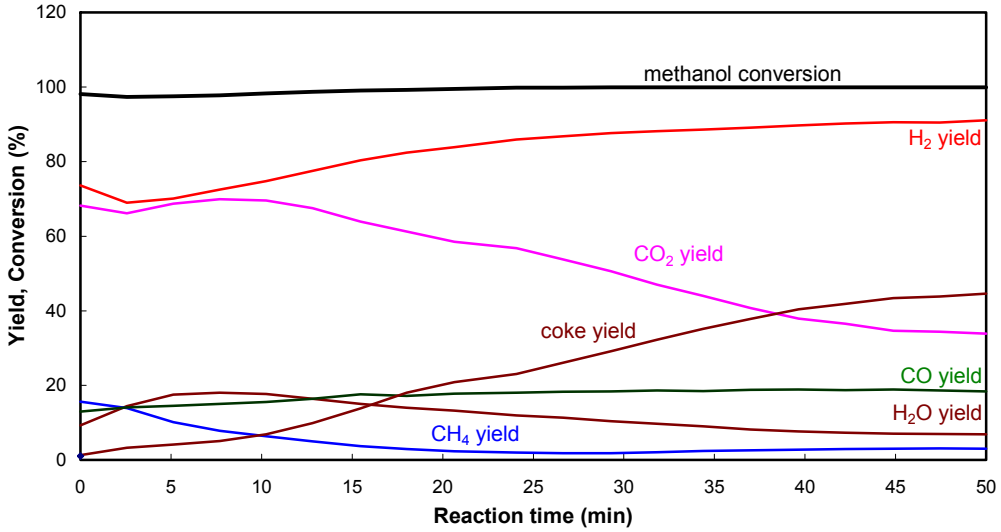

Figure 2: Instantaneous yields to products in methanol oxidation over CF-450 spinel in function of the reaction time (T=420 °C).

When the first step was carried out at low temperature, e.g., at 360 °C or 300 °C, the relative amount of the various products changed, and also the variation of yield observed during time for each product, was considerably modified with respect to the case of the reduction done at 420 °C. A critical point of this step was the accumulation of coke, which however formed with a lower rate when temperatures less than 400 °C were used (but with the drawback of an incomplete conversion of methanol).

Figure 3 shows the effect of reaction time during the reoxidation of the pre-reduced spinel with water, carried out at 420 °C after the reduction at 300 °C.

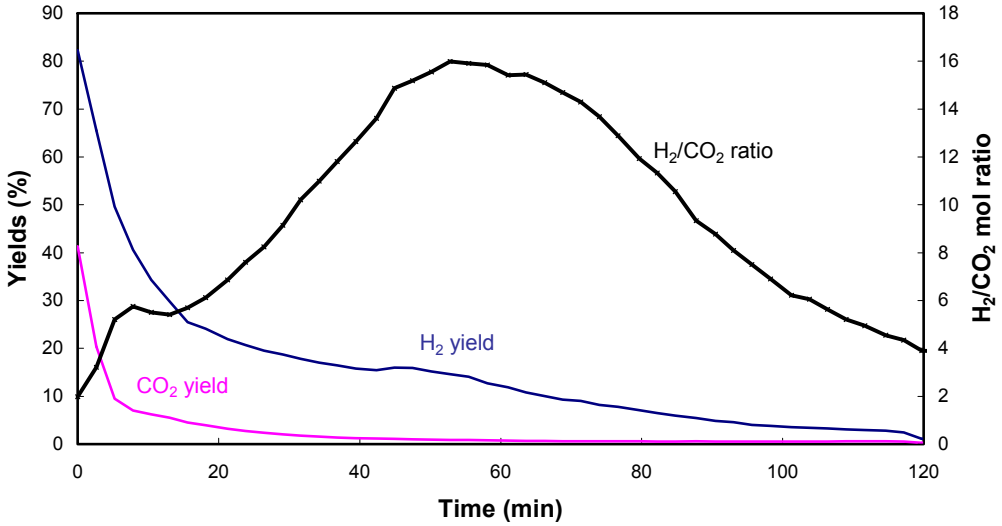

Figure 3: Instantaneous yields to products during reoxidation of the pre-reduced CF-450 spinel with water, at 420 °C, in function of the reaction time.

Carbon dioxide formed by coke gasification; the H_2/CO_2 molar ratio was low at the beginning of the reoxidation step, then increased reaching a maximum value after approximately one hour. The maximum did correspond to the zone at which the gasification of coke had been completed, and hence the production of CO_2 was minimal.

The reduction step was repeated three times after the corresponding reoxidation step; results obtained were very similar to those obtained during the first cycle. This indicates the feasibility of the chemical-loop approach with the $CoFe_2O_4$ spinel.

4 Conclusions

The chemistry of the two-step reforming (chemical-loop) reforming of methanol has been investigated using $CoFe_2O_4$ as the electrons/oxygen carrier. The main chemical-physical features of the ferrite were greatly affected by the temperature used for the thermal treatment of the mixed oxide. Reduction-reoxidation cycles were repeated, confirming the complete reversibility of the redox process. The major drawback was the accumulation of coke during the reduction step; however, the amount of coke was a function of the main reduction parameters, i.e., temperature and reaction time.

References

[1] D. Guin, B. Baruwati, S.V. Panorama, J. Mol. Catal. A 242 (2005) 26

[2] S. Takenaka, M. Serizawa, K. Otsuka, J. Catal. 222 (2004) 520

[3] M. Gemmi, M. Merlini, U. Cornaro, D. Ghisletti, G. Artioli, J. Appl. Cryst. 38 (2005) 353

[4] F. Cavani, N. Ballarini, S. Luciani, Topics Catal. 52 (2009) 935

[5] T. Kodama, N. Gokon, Chem. Rev. 107 (2007) 4048

[6] N. Ballarini, F. Cavani, S. Passeri, L. Pesaresi, A.F. Lee, K. Wilson, Appl. Catal. A, 366 (2009) 18

Hydrogen Production from Coal and Biomass Co-gasification Process with Carbon Capture and Storage

Calin-Cristian Cormos, **Serban Agachi**, Babes-Bolyai University, Faculty of Chemistry and Chemical Engineering, Cluj-Napoca, Romania

1 Introduction

Introduction of hydrogen in energy system as a new energy carrier complementary to electricity and conventional fuels (e.g. natural gas, oil derived products, coal etc.) is raising much interest, as this offers significant advantages including reduction of greenhouse gas emissions at the point of end use, enhancement of the security of energy supply and improvement of economic competitiveness. Hydrogen is used in chemical industry for various processes, e.g. ammonia and methanol synthesis, hydrogenation, hydro-cracking and hydro-desulphurization processes and it is currently produced from natural gas, oil derived products and coal. Among these feedstock types, solid fuels (fossil sources like coal and lignite but also renewable energy sources like biomass) are likely to play a key role using gasification-based processes for large-scale hydrogen production, as required for the development of the hydrogen economy.

By gasification process, a solid feedstock is partially oxidized with oxygen and steam to produce syngas which can be used for conversion into different valuable compounds (e.g. hydrogen, ammonia, synthetic fuels) or to generate power in a combined cycle gas turbine. Integrated Gasification Combined Cycle (IGCC) is one of energy conversion processes having the highest potential for carbon capture with low penalties in term of efficiency and cost. In a modified IGCC scheme designed for carbon capture and storage, the syngas is catalytically shifted to maximize hydrogen level and to concentrate carbon species in form of carbon dioxide that can be later capture in a pre-combustion arrangement. After CO_2 and H_2S capture in a double stage Acid Gas Removal (AGR) system, hydrogen-rich gas is used in a combined cycle gas turbine (CCGT) for power generation and/or for production of purified hydrogen stream which can be used in (petro)chemical industry or for transport sector in hydrogen-fuelled fuel cells (PEM).

The paper assesses from technical point of view the hydrogen production through co-gasification process of coal and biomass (e.g. sawdust, agricultural wastes, meat and bone meal) simultaneous with carbon capture and storage (more than 90 % feedstock carbon capture rate). The main aim of the paper is to describe the methodology to design and evaluate the plant performances using critical factors like: fuel selection criteria, choice of gasification reactor, heat and power integration, carbon capture and storage (CCS) technologies, ancillary power generation, plant flexibility, methods to increase the plant energy efficiency, hydrogen and carbon dioxide quality specifications considering the use of hydrogen in transport sector (PEM fuel cells) and carbon dioxide storage in geological formation or using for Enhanced Oil Recovery (EOR). The case studies were investigated in

detail by process flow modelling (using ChemCAD software package) and the most promising plant concepts identified.

2 Plant Configuration of Hydrogen Production Based on Coal and Biomass Co-gasification with CCS

A conventional Integrated Gasification Combined Cycle (IGCC) without carbon capture uses syngas resulted from gasification (after removing ash and hydrogen sulphide) for power production by burning in a gas turbine. The hot flue gases coming from gas turbine are used to raise steam in Heat Recovery Steam Generator (HRSG), which by expansion in a steam turbine generates extra electricity in addition to the one generates by the gas turbine. The case studies investigated in this paper are producing only hydrogen, the electricity generated by the gas and the steam turbines are used only to cover the plant ancillary demand.

Compared with conventional IGCC concept which is designed for power production only, design modifications for hydrogen generation as well as introduction of carbon capture stage using pre-combustion method like gas – liquid absorption (e.g. chemical or physical solvents) involve some critical changes in the plant configuration. The conceptual layout of a modified IGCC scheme for hydrogen production with simultaneous carbon capture is presented in Figure 1 (as exemplification, a dry-feed gasifier with water quench was used e.g. Siemens gasifier) [1].

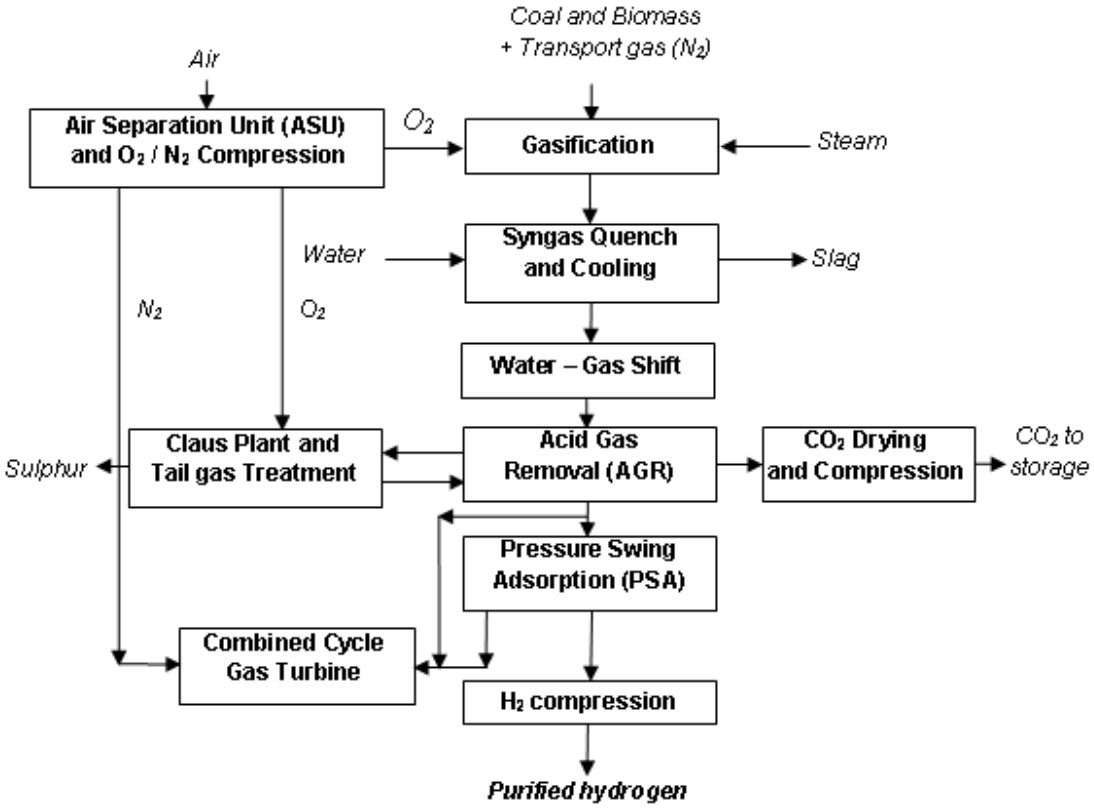

Figure: Layout of IGCC scheme for hydrogen production with carbon capture and storage (CCS).

Main differences of this scheme compared with conventional IGCC scheme without carbon capture are the following: introduction of catalytically conversion stage of CO (also called water gas shift – WGS); a modified Acid Gas Removal (AGR) system which captures, in addition of H_2S as in the conventional technology, also CO_2; the hydrogen purification stage by Pressure Swing Absorption (PSA) for the stream to be delivered to external customers (H_2 purity for export was set at 99.95 % vol. to be compatible with PEM fuel cells) and a combined cycle gas turbine (CCGT) running on hydrogen-rich gas.

Hydrogen produced is intended to be used in PEM fuel cells for transport sector which imply very strict quality specification (>99.95 % H_2 and virtually no CO and H_2S due to the possibility of fuel cells poisoning) [2]. Also, a major factor which influences the ancillary power consumption of the plant is the compression of captured carbon dioxide stream to more than 100 bar before being sent to geological storage or utilized for Enhanced Oil Recovery (EOR). This additional step gives a significant difference compared with conventional IGCC scheme. The compression of carbon dioxide stream is requiring a significant amount of energy which in the end will imply an energy penalty of the carbon capture design. The captured CO_2 stream will have to have very low concentration of water (<500 ppm) and hydrogen sulphide (<100 ppm) as these components could give corrosion problems along the pipeline network [3].

3 Modeling and Simulation of Hydrogen Production Scheme

In conventional IGCC process, a wide range of gasification reactors were and continue to be used to convert coal or lignite into syngas with good energy efficiency. But for hydrogen production with carbon capture, gasifier options are much more restricted because of this design particularity. For instance, air-blown gasifiers are unsuitable, mainly because of the nitrogen dilution which negatively influences the overall thermal balance of the plant and hydrogen purification step. Considering all the criteria (described in literature [4]) to be taken into account when choosing a gasifier for hydrogen production with carbon capture, it appears that entrained-flow gasifiers are the most promising reactors for this plant concept. Having that in mind, in the following paragraphs, the evaluation is geared mainly towards this type of reactors. The commercial gasification reactors of this type include: Shell, Siemens, GE Texaco, E-Gas etc.

As gasification reactor considered in modelling, as mentioned before the option was in favor of entrained-flow type operating at high temperature (slagging conditions) which give a high fuel conversion (~99 %). From different commercial gasification technologies available on the market, Siemens gasifier (formerly known Future Energy) was chosen, the main factors for consideration being dry feed design (which increases the energy efficiency compared with slurry feed type) and water quench which ensures the optimal condition for shift conversion (pre-condition for CO_2 capture).

When discussing the fuel selection for IGCC plant, the approach used for conventional power plants (steam plants) has to be changed radically. The coal used in steam plants is advised to have low content of ash and sulphur (to reduce corrosion and SOx emissions), but most important is that the ash has to have a relatively high melting point to prevent ash build up on the boiler heat transfer area. When analyzing IGCC concept, one of the advantages of this

technology over the conventional power plant is the ability to use lower grade coals or alternative fuels (e.g. biomass and solid wastes) most of them unable to be processes in a conventional power plant because of high ash, sulphur and chlorine content and low ash melting point. Processing lower grade coals or renewable energy sources has also an important economic benefit because these fuels are presumed to be cheaper. This paper investigates the possibility to blend the coal with various sources of biomass (e.g. sawdust, agricultural waste) for hydrogen production based on an IGCC scheme. Table 1 presents the composition and thermal characteristics of evaluated fuels.

Table 1: Feedstock composition and thermal properties.

Parameter	Coal	Sawdust	Wheat straw	Corn stalks	MBM
Proximate analysis (% wt.)					
Moisture (a.r.)	8.10	10.00	10.00	8.00	1.90
Volatile matter (dry)	28.51	80.05	69.94	73.40	73.40
Ultimate analysis (% wt. dry)					
Carbon	72.04	49.20	41.11	44.80	46.20
Hydrogen	4.08	5.99	5.20	5.39	6.70
Nitrogen	1.67	0.82	1.01	0.85	9.70
Oxygen	7.36	42.98	37.36	41.75	17.07
Sulphur	0.65	0.03	0.24	0.21	0.65
Chlorine	0.01	0.00	0.60	0.00	0.88
Ash	14.19	0.98	14.48	7.00	18.80
Calorific value (kJ/kg dry)					
Gross (HHV)	28 704.40	19 436.40	16 091.57	17 206.46	21 163.74
Net (LHV)	27 803.29	18 113.45	14 943.10	16 016.02	19 683.98
Ash composition (% wt.)					
SiO_2	52.20	9.44	54.64	63.30	0.00
Al_2O_3	27.30	1.56	5.73	0.00	0.00
Fe_2O_3	5.10	1.88	6.16	4.70	2.90
CaO	6.40	62.00	5.02	0.60	66.28
MgO	2.10	2.18	2.45	4.80	0.00
TiO_2	1.50	0.10	0.23	0.00	0.00
K_2O	1.00	15.00	14.09	8.40	13.00
Na_2O	0.30	0.61	2.16	0.50	17.82
SO_3	2.40	2.72	3.03	7.20	0.00
P_2O_5	1.30	1.23	2.43	2.10	0.00
SrO	0.00	0.15	0.00	0.00	0.00

It can be noticed from Table 1 that all alternative fuels investigated in the present paper (sawdust, agricultural wastes and meat and bone meal - MBM) have significant increased

content of modifier oxides (calcium, magnesium, sodium and potassium oxides) and lower silica and alumina content which means low slag viscosity temperatures [5]. These alternative fuels could be added to the coal to reduce the slag viscosity in a blending ratio (up to 20 – 30 % wt. alternative fuels) which does not change significantly reactor characteristics and performances compared with operating only on coal. At the same time, blending coal with these alternative fuels offers good option to find a useful way of recover the energy content of these materials in condition of reducing consumption of non-renewable energy sources (coal).

The plant concepts for hydrogen production with carbon capture and storage based on coal with or without addition of sawdust, wheat straw (WS), corn stalks (CS) and meat and bone meal (MBM) were modeled and simulated to quantify the overall plant performance indicators. Five case studies were investigated thoroughly in this paper (for all five cases, the feedstock thermal energy was 1000 MW):

- Case 1 – Coal only as feedstock;
- Case 2 – Coal with addition of sawdust (80 / 20 % wt. blending ratio);
- Case 3 – Coal with addition of wheat straw (80 / 20 % wt. blending ratio);
- Case 4 – Coal with addition of corn stalks (80 / 20 % wt. blending ratio);
- Case 5 – Coal with addition of meat and bone meal (80 / 20 % wt. blending ratio).

4 Results and Discussions

Hydrogen and electricity co-production schemes were modeled and simulated using process flow modelling software (ChemCAD). As thermodynamic package used in all simulations, Soave-Redlich-Kwong (SRK) model was chosen considering the chemical species present and process operating conditions (pressure, temperature etc.). Simulation of plant configurations yields all necessary process data (mass and molar flows, composition, temperatures, pressures, power generated and consumed) that are needed to assess the overall performance of the processes.

In all cases, the plant models were optimized by performing heat and power integration analysis (using pinch technique) of the combined cycle block (CCGT) for maximization of energy efficiency. Steam generated in gasification island (HP steam from gasifier cooling wall) and syngas conditioning line (HP and LP steam) was integrated in the steam cycle of the combined cycle gas turbine. After process optimization by heat and power integration studies, the overall plant performance indicators were calculated.

An overview of the main plant indicators for all four investigated case studies is presented in Table 2 (the electricity production was limited only to cover the plant ancillary demand).

Table 2: Overall plant performance indicators.

Main Plant Data	Units	Case 1	Case 2	Case 3	Case 4	Case 5
Solid fuel flowrate (a.r.)	kg/h	141994	153230	157044	155235	149159
Coal / Sawdust / WS / CS / MBM LHV (a.r)	MJ/kg	25.353 / 16.057 / 13.204 / 14.539 / 19.263				
Feedstock thermal energy – LHV (A)	MW_{th}	1000.00	1000.00	1000.00	1000.00	1000.00
Thermal energy of the syngas (B)	MW_{th}	801.00	793.30	788.04	795.00	825.20
Cold gas efficiency (B/A * 100)	%	80.10	79.33	78.80	79.50	82.52
Thermal energy of syngas exit AGR (C)	MW_{th}	711.83	706.43	700.39	706.79	736.73
Syngas treatment efficiency (C/B *100)	%	88.86	89.05	88.87	88.91	89.28
Gas turbine output	MW_e	56.42	56.12	56.66	56.17	57.81
Steam turbine output	MW_e	33.28	33.62	34.43	34.12	33.91
Gross electric power output (D)	MW_e	86.70	89.74	91.09	90.29	91.72
Hydrogen output – LHV (E)	MW_{th}	571.24	566.83	559.84	567.00	592.97
ASU consumption + O_2 compression	MW_e	38.32	38.32	39.05	38.45	36.77
Gasification island power consumption	MW_e	6.92	7.02	7.02	6.97	7.18
AGR + CO_2 drying & compression	MW_e	34.35	34.42	35.05	34.94	37.27
H_2 compression	MW_e	7.69	7.60	7.56	7.57	7.97
Power island power consumption	MW_e	2.42	2.38	2.41	2.36	2.53
Total ancillary power consumption (F)	MW_e	89.70	89.74	91.09	90.29	91.72
Net electric power output (G = D - F)	MW_e	0.00	0.00	0.00	0.00	0.00
Hydrogen efficiency (E/A * 100)	%	57.12	56.68	55.98	56.70	59.29
Carbon capture rate	%	92.35	92.83	93.64	93.25	92.24
CO_2 specific emissions (fossil+renewable)	kg/MWh	45.63	44.99	42.19	43.99	45.34
CO_2 specific emissions (fossil)	kg/MWh	45.63	38.54	37.01	38.06	38.71

As can be noticed from Table 2, in term of hydrogen production all case studies produce about 560 - 590 MW_{th} (based on hydrogen LHV) with an efficiency in range of 56 – 59 %.

Regarding the plant overall hydrogen efficiency, for cases 2 to 4 there is little to be differentiated among them (less than 0.7 % in term of overall hydrogen efficiency of the plant) and they are comparable with case 1 (coal only). Case 5 (coal blended with MBM) is more efficient with about 2.15 – 3.3 % compared with rest of the cases. This increase of plant efficiency can be explained by the cumulative effect of optimizing gasifier performances (lowering slag viscosity comparing with case 1 – coal only) and improved calorific value of alternative fuel used to be blended with coal, in this case MBM (comparing with cases 2 to 4).

Also, it can be noticed the fact that coal to alternative fuels blending ratio does not influence significantly the plant performance (comparing case 1 vs. cases 2 to 5). Specific CO_2 emissions (fossil and renewable) are in the range of 42 – 45 kg/MWh with about 92 – 93 % carbon capture rate. When counting only the fossil specific CO_2 emissions, the cases 2 to 5 are performing better than case 1 (only fossil). IGCC technology has also other benefits from environmental point of view: very low SOx and NOx emissions, possibility to process lower grade coals or other types of solid fuels (as evaluated in this paper) which are difficult to handle by conventional energy conversion process (e.g. steam plant).

5 Conclusions

The paper assesses the technical aspects of hydrogen production scheme with carbon capture based on a modified IGCC plant design. The aim was to develop a set of criteria that can be used to select the most appropriate gasification concepts for hydrogen and electricity co-production plant with carbon capture and storage and then to quantify the overall energy efficiency of the plant. A particular attention was devoted to the fuel selection (e.g. fuel blending) for both optimization of the gasifier performance and promote the usage of non-fossil fuels (various biomass sorts).

The most promising plant concepts for hydrogen production with carbon capture are all based on entrained-flow gasifiers. For one case of entrained-flow gasifier reactor (Siemens) with various feedstock (coal only or coal blended with various biomass sorts) different case studies were presented in detail for assessing the main plant performance indicators (e.g. hydrogen output; plant ancillary demand; hydrogen efficiency, specific CO_2 emissions etc.).

Acknowledgements

This work was supported by Romanian National University Research Council (CNCSIS-UEFISCSU), project number PNII – IDEI code 2455: “Innovative systems for poly-generation of energy vectors with carbon dioxide capture and storage based on co-gasification processes of coal and renewable energy sources (biomass) or solid waste”.

References

[1] Cormos, C.C., Starr, F., Tzimas, E., Peteves, S., 2008. Innovative concepts for hydrogen production processes based on coal gasification with CO_2 capture. Int. J. Hydrogen Energy 33, 1284-1294

[2] Besancon, B. M., Hasanov, V., Imbault-Lastapis, R., Benesch, R., Barrio, M., Mølnvik, M. J., 2009. Hydrogen quality from decarbonized fossil fuels to fuel cells. Int. J. Hydrogen Energy 34, 2350-2360

[3] De Visser, E., Hendriks, C., Barrio, M., Mølnvik, M.J., De Koeijer, G., Liljemark, S., Le Gallo, Y., 2008. Dynamis CO_2 quality recommendations. Int. J. Greenhouse Gas Control 2, 478-484

[4] Cormos, C.C., Starr, F., Tzimas, E., Peteves, S., Brown, A., 2007. Gasifier concepts for hydrogen and electricity co-production with CO_2 capture. 3-rd International Conference on Clean Coal Technologies, Italy

[5] Cormos, C.C., 2009. Assessment of hydrogen and electricity co-production schemes based on gasification process with carbon capture and storage. Int. J. Hydrogen Energy 34, 6065-6077

Water Gas Shift Reaction over Magnetite-based Catalysts in Membrane Reactor Conditions

J. Dufour, **C. Martos**, **A. Ruiz**, Department of Chemical and Energy Technology, ESCET, Universidad Rey Juan Carlos, Spain

1 Introduction

The water gas shift (WGS) reaction is used in many industrial processes for hydrogen production to enhance the hydrogen generation and to reduce the carbon monoxide content to the appropriate value for fuel cell applications. This is a reversible and exothermic reaction and it is usually carried out in two stages to maximize CO conversion. The first step is performed at high temperatures (320-420 ºC) under favorable kinetic conditions, using a Fe_3O_4-Cr_2O_3 based catalyst. The second one takes place at low temperatures (200-250 ºC) to favor thermodynamic conditions with a catalysts based on Cu/ZnO/Al_2O_3 [1]. An alternative to this process is the use of a hydrogen permeable membrane in the reactor that allows carrying out the reaction in a single stage. In this type of reactor, an equilibrium shift is produced by the removal of hydrogen from the reaction mixture leading to an increase of the CO conversion. This allows operating at lower H_2O/CO ratios without suffering thermodynamic constraints. The catalytic systems used for palladium membrane reactors are those for high temperature WGS since temperatures lower than 300 ºC leads to membrane degradation. However, CO_2 concentration will reach high levels into the reactor due to permeation of the H_2 through the membrane, producing the inhibition of the reaction rate over conventional catalysts. For this reason, they should be modified to operate in the extreme conditions imposed by membrane reactors [2].

The high temperature WGS catalysts contain iron oxide structurally promoted with chromium oxide (8-14 wt %). The active phase of the catalysts is magnetite (Fe_3O_4). This iron oxide forms an inverse spinel cubic structure with tetrahedral positions occupied by Fe^{3+} and the octahedral ones by equal amounts of Fe^{3+} and Fe^{2+}. The activity of magnetite in WGS reaction is related to the rapid electron hopping between $Fe^{3+}\leftrightarrow Fe^{2+}$ redox couple. The active phase loses activity under reaction conditions due to the reduction in surface area by thermal sintering [3-4]. Therefore, chromium oxide is usually added to magnetite as structural stabilizer. The conventional catalysts based on Fe-Cr have environmental and safety concerns since they can contain about 2 % wt. of toxic Cr^{6+} compounds. For this reason, the replacement of chromium by other promoters such as V, Th, Ga, Al, Mo and Mn has been recently studied [5-7].

Additionally, several authors have been developing new catalysts formulations to improve their performance in membrane reactors. Lund suggested that the inhibition of the catalysts by carbon dioxide could be reduced by decreasing the magnetite surface oxygen bond strength. Promotion of magnetite based catalysts with metals such as Cu or Ce could produce a decrease of the reduction temperatures of the material which is indicative of the weakening of surface oxygen bonds [8]. In this context the aim of this work is to prepare new

formulations of magnetite-based catalysts doped with different metals. The replacement of Cr by Mo was studied and the role of Cu and Ce as promoters in membrane reactor conditions was evaluated.

2 Experimental

Oxidation-precipitation method was used to prepare the catalysts, obtaining four different formulations: FeCrCu, FeMoCu, FeCrCe and FeMoCe. Additionally, FeCr and FeMo catalysts were prepared to compare them with the promoted materials. Initially, an aqueous solution of metal salts was prepared with Fe/Cr or Fe/Mo ratios of 12.2 (wt.) and with an appropriate Fe/promoter ratio to obtain solids with 2 % (wt.) of Cu or 1 % (wt.) of Ce. $FeCl_2$, $CrCl_3$, $(NH_4)_6Mo_7O_{24}$, $CuCl_2$ and $CeCl_3$ were the precursors used to prepare the catalysts. The solution was heated up to 70 ºC and stirred at 300 r.p.m. Next, ferrous ions were oxidized bubbling air into the system. Simultaneously, alkali was added drop-wise adjusting pH to 7 until the end of reaction. The solid was recovered by filtration and washed out with water to remove ions. Finally, the samples were dried at 70 ºC overnight.

X-ray powder diffraction (XRD) patterns of the catalysts were obtained on a Philips X-Pert diffractometer using CuKα radiation. The data were recorded in the 2θ range from 10º to 70º. Average crystallite sizes were calculated by applying the Scherrer equation. X-ray fluorescence (XRF) spectrometer Philips MagiX was used to determine Fe/promoter ratios. Temperature programmed reduction (TPR) was performed in a Micromeritics Autochem 2910 instrument. The sample (50 mg) was heated up from 323 to 1173 K (heating rate 10 K/min) under a hydrogen–argon mixture (10 % H_2) with a flowrate of 40 ml/min. Specific surface areas of samples were calculated from N_2 adsorption–desorption isotherms at 77 K that were measured on a Quantachrome NOVA 4000 instrument. Transmission electron microscopy (TEM) micrographs were obtained on a Philips Tecnai-20 electron microscope operating at 200 kV and equipped with an energy dispersive X-ray (EDX) spectrometer.

The performance of catalysts was tested in a fixed bed stainless steel reactor (i. d. = 9 mm) under isothermal conditions (380 ºC), 10 bar and GHSV = 10000 h^{-1}. All experiments were carried out using 1 g of catalysts. A feeding gas composition of 68.7 % N_2, 18.8 % CO and 12.5 % CO_2 was used and a low steam/CO molar ratio (H_2O/CO = 2) was introduced into the reactor to simulate the membrane reactor conditions. The product stream was analyzed by gas chromatography in a Varian CP-4900 Micro GC.

3 Results and Discussion

Table 1 shows Fe/promoters ratios of the synthesized catalyst measured by XRF. Metal contents for all the samples were near to the theoretical ones. A lower incorporation of Mo was detected as compared to FeCr materials. This fact could be explained by the value of pH used during the synthesis procedure. In the case of Cr^{3+}, chromium hydroxide precipitation occurs at pH 5. However, the precipitation of the solid phase in the case of Mo^{6+} happens at low pH (pH <5) and soluble species are predominant in the solution at pH 7. Comparing Cu with Ce, a lower content of the last metal was detected because its precipitation takes places at pH 8.

Table 1: XRF results of the catalysts prepared.

	XRF (wt.)			
Sample	Fe/Cr	Fe/Mo	Fe/Cu	Fe/Ce
FeCrCu	12.8	--	39.3	--
FeMoCu	--	14.6	38.8	--
FeCrCe	12.4	--	--	78.3
FeMoCe	--	15.0	--	60.7

XRD analyses were performed to study the iron oxide phases present in the catalysts. Figure 1 shows the results obtained by this technique. Magnetite was the only crystalline phase detected for all the samples. Cr, Mo, Cu or Ce separate phases did not appear in the diffractograms.

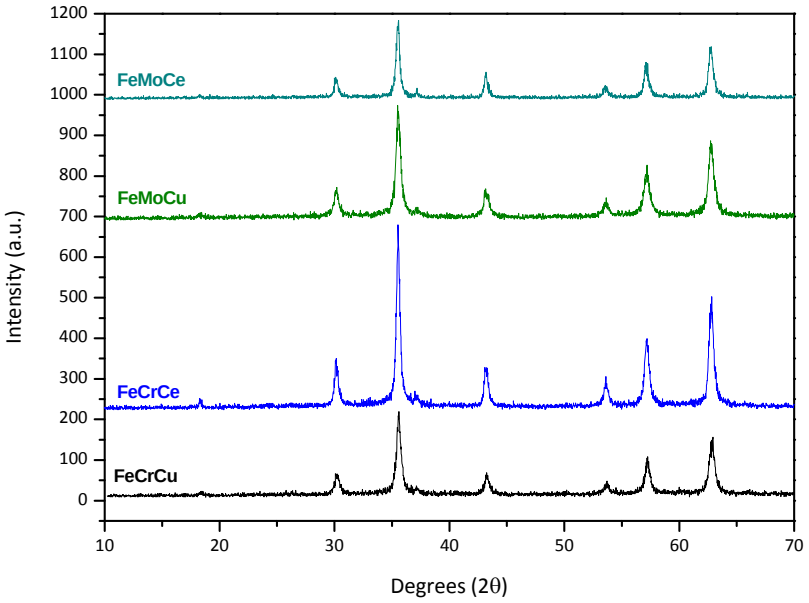

Figure 1: XRD patterns of the catalysts prepared.

Lattice parameters (a_o) were calculated from the highest intensity lines to study the incorporation of promoters into the magnetite lattice. These results are shown in Table 2. All the samples exhibited values slightly lower than that theoretical for magnetite (0.8397 nm). This fact could be explained by the existence of small amounts of maghemite (γ-Fe_2O_3), especially on the surface of the particles. The addition of Cr to the catalysts did not produce any variation of the lattice parameter, compared to a magnetite prepared by the oxidation-precipitation method (a_o = 0.8365 nm). In the case of Mo, a contraction of the lattice parameter was detected for FeMo sample. Addition of Cu to FeCr materials did not affect the lattice parameter but in the case of FeMo materials this metal produced an expansion of the unit cell. Finally, promotion with Ce did not change the lattice parameters on a large extent. These results suggested that for the catalysts based on FeCr, promoters were not

incorporated into magnetite lattice. In the case of catalysts based on FeMo, Mo and Cu were incorporated in the lattice of the iron oxide.

Table 2: Characterization results of the samples prepared.

	XRD		Ads.-Des. N_2	TPR		
Sample	a0 (nm)	Dc (nm)	SBET (m^2/g)	TPR1	TPR2	TPR3
FeCr	0.8368	22	107	301	565	614
FeCrCu	0.8370	19	109	223	485	618
FeCrCe	0.8374	29	121	306	528	626
FeMo	0.8357	28	32	373	603	763
FeMoCu	0.8377	19	74	220	513	663
FeMoCe	0.8362	25	46	332	578	727

The results obtained in this study were confirmed by TEM analysis. Figure 2 shows TEM micrographs obtained for the promoted samples. The materials were composed of spherical particles with sizes in the range of 20-100 nm. The results obtained by energy dispersive X-ray indicated that FeCr materials were composed of magnetite crystals surrounded by smaller high chromium and copper or cerium containing particles. However, this fine phase was not detected in the case of FeMo catalysts and EDX analysis showed that there was not a considerable variation in the metal contents in different crystals. This suggested that in these catalysts Mo and Cu were incorporated into the magnetite lattice.

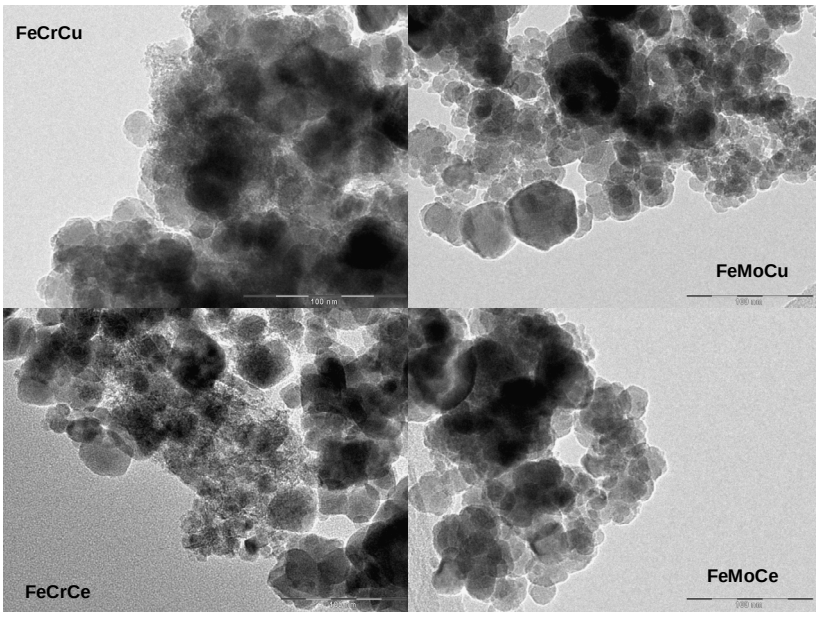

Figure 2: TEM micrographs obtained from promoted samples.

Crystallite sizes and BET surface areas obtained from N_2 adsorption-desorption isotherms are also shown in Table 2. The replacement of Cr by Mo produced a decrease in the BET surface area as a consequence of the larger crystallite size of FeMo sample and the absence

of small particles around magnetite crystals. Addition of copper did not modify BET surface area for FeCr material but produced an increase of this parameter in the case of FeMo catalysts. This could be related to the differences in copper incorporation for both samples. When the catalysts were doped with Ce a slightly increase in the BET surface areas was detected. In the case of FeCr materials, the addition of Ce produced larger crystallite size that could be explained by the deposition of cerium compounds over the magnetite crystals.

Redox properties of the catalyst were evaluated by TPR. The reduction temperatures obtained from these analyses are shown in Table 2. There were three main reduction peaks in the samples analyzed. The lower temperature peak (TPR1) was attributed to the reduction of Fe^{3+} species to Fe_3O_4. When the catalyst contained Cr^{6+} or Cu^{2+}, the reduction of these metals also happened at this temperature. The second peak (TPR2) corresponded to the reduction of Fe_3O_4 to FeO and to the partial reduction of Mo^{6+}. The last peak (TPR3) was due to the reduction of FeO to metallic iron, CeO_2 to CeO_{2-x} and MoO_{3-x} to Mo. Replacement of Cr by Mo produced an increase of the reduction temperatures probably because of the lower BET surface areas and the larger crystallite sizes of FeMo materials. Addition of Cu t o FeCr and FeMo catalysts improved the reducibility of the samples. This decrease of the reduction temperatures could indicate the weakening of surface oxygen bonds in magnetite that could lead to a lower inhibition by carbon dioxide. Promotion with Ce did not change the reduction temperatures of the samples on a large extent, probably because that metal was not incorporated into magnetite lattice. These results suggested that Ce would not improve the performance of the catalysts in membrane reaction conditions.

Figure 3 shows the results obtained from the catalytic tests. A decrease of the catalytic activity was detected for non-promoted samples when Cr was replaced by Mo. This could be explained by the lower specific surface area of FeMo material. As expected by TPR results, addition of copper produced an increase of the CO conversion for FeCr and FeMo catalysts. This increase of the activity was higher for FeMo materials, probably because copper was incorporated into magnetite lattice for that sample, modifying the degree of covalency of $Fe^{3+}\leftrightarrow Fe^{2+}$ redox couple. This activity of FeMoCu sample is higher than that obtained for FeCrCu material. When Ce was added to the materials, an increase of the catalytic activity was not observed but higher hydrogen selectivity was obtained for the samples. These results agree with those obtained by TPR analysis, confirming that there is a relationship between the reducibility and the catalytic activity.

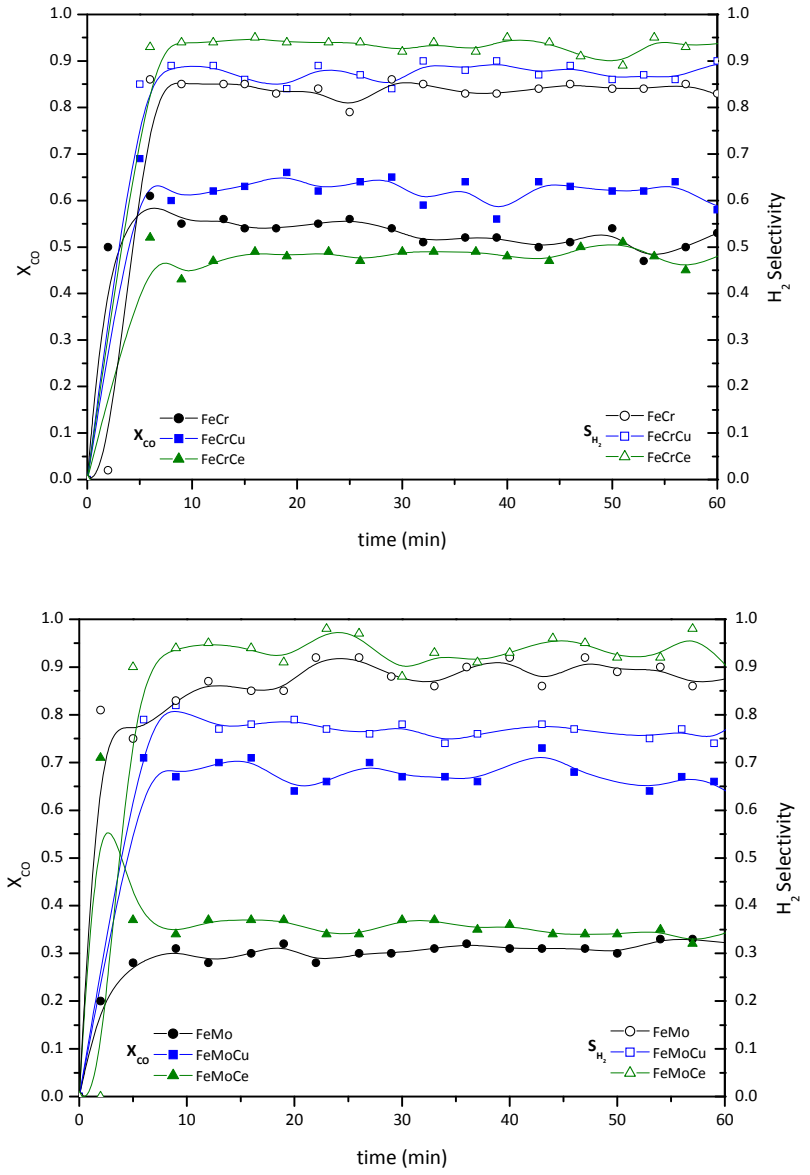

Figure 3: Catalytic activity results in WGS reaction.

4 Conclusions

Replacement of Cr by Mo in high temperature WGS catalysts decreased the reducibility and the catalytic activity of the samples. Addition of Cu to FeMo catalysts increased the reducibility and the CO conversion, suggesting the weakening of surface oxygen bonds in magnetite that improved the catalytic performance in membrane reactor conditions. Promoting with Ce did not change the redox properties and the catalytic activity of the material although higher hydrogen selectivity was obtained.

Acknowledgements

The authors acknowledge to the Ministry of Education and Science, the Ministry of Science and Innovation of Spain, Comunidad de Madrid and Universidad Rey Juan Carlos for funding through projects ENE2007-66959, CTQ2009-11934 and P2009/ENE-1743.

References

[1] Ladebeck, J.R.; Wagner, J.P. Handbook of fuel Cells-Fundamentals, Technology and Applications, Vol. 3, Part 2 (2003), 190-201.

[2] Ma, D.; Lund, C. R. F. Ind. Eng. Chem. Res., 42 (2003), 711-717.

[3] Rhodes, C.; Williams, B. P.; King, F.; Hutchings, G .J. Catal. Commun., 3 (2002) 381-384.

[4] Khan, A.; Chen, P.; Boolchand, P.; Smirniotis, P. G. Journal of Catalysis, 253(1) (2008), 91-104.

[5] Carneiro de Araújo, G.; Rangel, M. C. Catalysis Today, 62 (2000), 201-207.

[6] Li, K.; Luo, L. T.; Li, F. Y.; Le, Z. P.; Liu, C. H. Journal of Natural Gas Chemistry, 6 (1) (1997), 68-75.

[7] Júnior, I. L.; Millet, J. M. M.; Aouine, M.; Rangel, M. C. Applied Catalysis A: General, 283 (1-2) (2005), 91-98.

[8] Lund, C. R. F. Water-gas shift kinetics over iron oxide catalysts at membrane reactor conditions. Final report to the U.S. Department of Energy, August, 2002.

Carriers Selective Methanation of CO in CO_2–rich feed Gases on Supported Ru Catalysts

Stephan Eckle, Institute of Surface Science and Catalysis, Ulm University, Ulm, Germany
H. G. Anfang, Süd-Chemie A.G., Bruckmühl, Germany
R.J. Behm, Institute of Surface Science and Catalysis, Ulm University, Ulm, Germany

1 Objective

Economically and ecologically efficient techniques for the production of sufficiently pure H_2 are a prerequisite for the introduction of H_2 based energy technologies [1]. Today, H_2 is mainly produced by steam reforming / partial oxidation of fossil fuels [2][3], which, among other components, leaves CO (1-8 %) and substantial amounts of CO_2 (up to 20 %) in the resulting H_2-rich gas mixture ('reformate'). For the operation of low-temperature Polymer Electrolyte Fuel Cells (PEFCs), the resulting H_2-rich gas should be free of (anode) catalyst poisons, in particular the CO content has to be reduced to $\leq$10 ppm [4], which is most commonly achieved catalytically, by a combination of the Water Gas Shift (WGS) reaction and the Preferential Oxidation of CO (PROX) [5]. In cost sensitive, small scale applications, however, methanation of the CO may be a more attractive alternative for CO removal compared to the PROX reaction, since it uses the H_2 present in the feed gas and avoids the need for an additional dosing unit for O_2 dosing [6]. The losses of H_2 are tolerable, as long as the initial CO contents, after the WGS reaction, are low (0.5 %). Precondition for this concept, however, is that the reaction is highly selective for the oxidation of CO and that CO_2 methanation is essentially inhibited, otherwise the losses of hydrogen would become intolerable [6].

The selectivity for CO methanation in the selective methanation in CO_2-rich gas mixtures is generally attributed to a surface blocking by adsorbed CO, which is driven by the much higher adsorption energy of CO compared to CO_2. In this model CO_{ad} blocks the surface for (dissociative) adsorption of CO_2 and subsequent methanation reaction [7][8]. In that case, CO_2 methanation will be inhibited, as long as the CO partial pressure and hence the CO_{ad} coverage on the catalyst are sufficiently high [9][10][11]. However, most of the previous studies were conducted under conditions, where only little mechanistic insight on the reaction could be gained. Increasing the selectivity of Ru supported catalysts was also already tried in many different ways, including the use of different support materials such as TiO_2, Al_2O_3, SiO_2 [12] or of dopants [13], or varying the Ru particle size [14]. Also the use of zeolite supports was proposed as a promising alternative to standard supports such as TiO_2 or Al_2O_3, and the catalysts showed indeed a higher selectivity for the selective methanation of CO compared to Ru/Al_2O_3 or Ru/SiO_2 catalysts [15]. However, the physical origin, for improvement of the selectivity remained still unclear.

On the other hand the exact mechanism of the selective methanation of CO is still not solved yet. A large number of studies, mostly performed in the 1980's, state active carbon species as reactive intermediate [16]. In this concept, adsorbed CO_{ad} surface species dissociate to C_{ad}, which subsequently hydrogenates to CH_{ad}, $CH_{2,ad}$ $CH_{3,\,ad}$ and CH_4. In that case, care has to be taken that the steady-state carbon coverage is not too high to avoid deactivation of the catalyst [16]. Another mechanistic suggestion involves a hydrogen-assisted CO dissociation step [16]. Here, adsorbed H reacts with CO to an "HCO" formyl type species, which will dissociate either to CH_{ad} or react with another H atom to H_2CO. This is followed by subsequent CO bond scission to yield $CH_{2,ad}$. The produced $CH_{x,ad}$ surface species are hydrogenated to CH_4 afterwards. This „HCO" species, however, has not been observed spectroscopically so far.

In this contribution we report on the results of realistic field experiments and combined kinetic and *in situ* IR (DRIFTS) measurements under differential reaction conditions on Ru/supported catalysts, a Ru/zeolite catalyst and a Ru/Al_2O_3 catalyst. Measurements under realistic field conditions over the Ru/zeolite catalyst showed a high stability (100 % CO conversion) and CO selectivity (85 %) for over 1000 h. The latter measurements aimed at gaining more insight on the physical origin of the high selectivity for CO methanation and on the mechanism of the selective CO methanation reaction.

The combined kinetic and *in situ* DRIFTS measurements allowed us to not only determine the steady-state CO_{ad} coverages in different reaction atmospheres, but also to qualitatively assess the contribution from CO_2 decomposition to the CO_{ad} signal in the experiments performed under semi-realistic conditions. They were supported by additional experiments in a CO-free atmosphere (only CO_2 present).

SSITKA-type (*steady state isotope transient kinetic analysis*) DRIFTS transients, where one reactant is exchanged under steady-state conditions by its labelled isotopomer ($^{12}CO \rightarrow {}^{13}CO$) show a direct correlation between a possible formyl-type species with CO exchange and CH_4 production. The HCO species is likely to be the reaction intermediate of the selective CO methanation.

2 Experimental

The kinetic measurements were conducted at 190 °C under differential conditions in semi-realistic and idealized (CO_2 free) atmosphere (x kPa CO, 3 kPa N_2, 15.5 kPa CO_2, rest H_2) with varying CO concentration (6000 ppm, 3000 ppm, 1000 ppm, 100 ppm) and a gas flow of 41.6 Nml/min. The catalysts were diluted with SiO_2, which is inactive for the reaction under present reaction conditions. First they were heated in N_2 to 150 °C, subsequently the temperature was increased to 190 °C in reactive atmosphere. In-situ IR measurements were conducted in the same manner as described above. Background spectra were taken at 150 °C und N_2 atmosphere. SSITKA type measurements were conducted after 1000 min under idealized conditions to obtain a steady-state situation, before switching to the reactants isotopomer (i.e. $^{12}CO \rightarrow {}^{13}CO$).

3 Results

The Ru/zeolite showed a very high stability and selectivity over 1000 h time on stream in field experiments.

3.1 Mechanism for CO methanation

DRIFTS experiments on the Ru supported catalysts showed the typical CO_{ad} surface species with bands in the range of 2200 – 1900 cm^{-1}. Their coverage was correlated with the temporal evolution of the activity, indicating that these species or at least the related adsorption sites are directly involved in the CO methanation reaction. On the Ru/Al_2O_3 oxide catalyst, we also identified a surface species with a characteristic band at 1740 cm^{-1}, which we attribute to a formyl (HCO) molecule, as seen by formaldehyde adsorption on the catalyst. In transient experiments (exchange of ^{12}CO by ^{13}CO), the build-up and decay of this surface species was found to correlate with the build-up and decay of linearly adsorbed CO_{ad} and with the CH_4 formation as shown in Fig. 1.

On the Ru/zeolite catalyst, we could not identify such adsorbed formyl species under reaction conditions. However, due to the much higher activity of the latter catalyst compared to the Ru/Al_2O_3 catalyst, the steady-state coverage of the "HCO_{ad}" molecule may be too low for its detection. Nevertheless, we favor a similar reaction pathway and mechanism on both catalysts, with a similar activated complex, since the activation energies are similar in both cases [17].

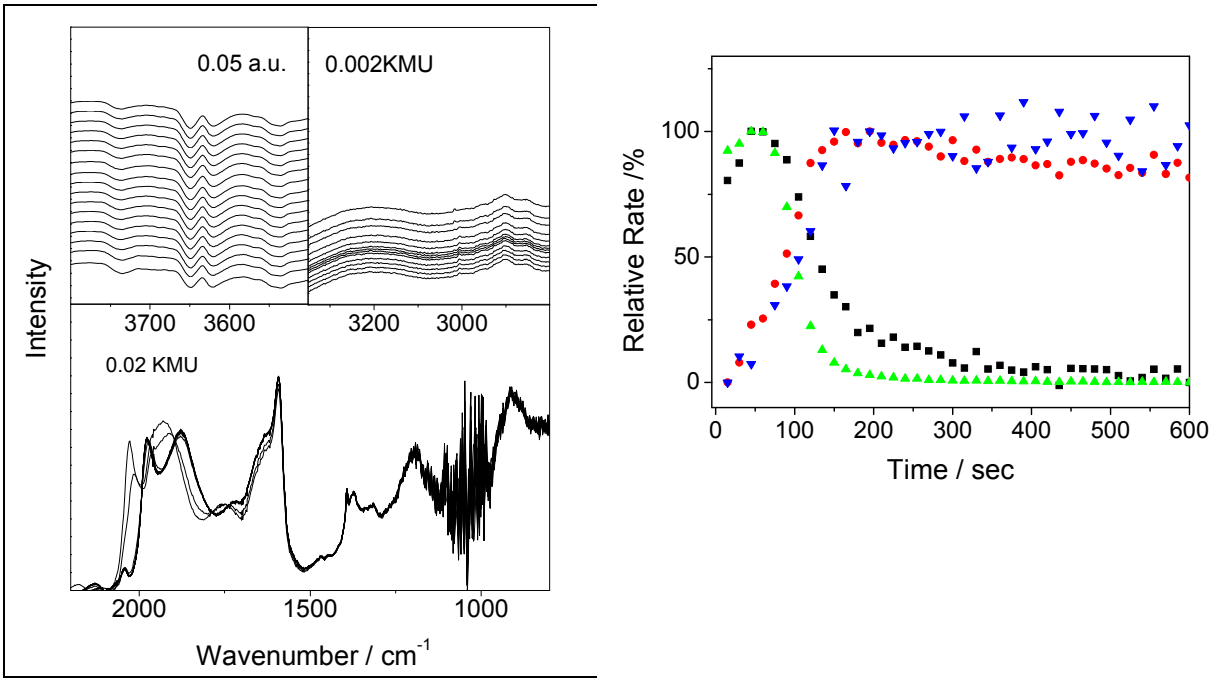

Figure 1: **<u>left:</u> DRIFTS transients after 1000 min reaction under idealized conditions and subsequent switch from ^{12}CO to ^{13}CO. <u>right:</u> signal intensities of respective peaks: (■) ^{12}CO, (▲) ^{12}CHO, (▼) $^{13}CH4$, (,) ^{13}CHO**

3.2 Selectivity for CO methanation

In the kinetic and *in situ* spectroscopy studies it was found, that at low CO concentrations (100 ppm) the CO_{ad} coverage is very low, also in the presence of 15.5 kPa CO_2, while on the Ru/Al_2O_3 catalyst, the CO_{ad} coverage is much higher. The resulting value of the CO_{ad} band intensity on that catalyst is the same as that in a "normal" reaction gas mixture with 0.6 kPa CO, where full coverage can be assumed. Hence, on the Ru/Al_2O_3 catalyst, dissociation of adsorbing CO_2 provides another channel for the formation of CO_{ad}, in addition to CO adsorption. Facile decomposition of CO_2 to CO_{ad} on this catalyst is supported by the fact that also in (CO-free) CO_2 reformate CO_{ad} saturation coverage is reached. In the kinetic experiment, the CO selectivity reached a value of 100%. In total, the CO_{ad} band intensity correlates with the selectivity value, therefore CO_{ad} blocking of active sites is held responsible for the prevention of CO_2 methanation.

In contrast, on the Ru/zeolite catalyst, such correlation was not observed. At very low CO concentration (100 ppm) and in the absence of CO_2, the CO_{ad} band intensity is only 6 % of the saturation value obtained under normal reaction conditions (0.6 kPa CO, rest H_2). The same CO_{ad} band intensity and hence the same CO_{ad} coverage was obtained also in the presence of CO_2 (15.5 kPa CO_2). In this case, the blocking mechanism can not explain the experimental finding of a very high selectivity for CO methanation. Instead, the high selectivity is attributed to an inherently low activity of the Ru/zeolite catalyst for CO_2 methanation, which was tentatively attributed to the very small size of the Ru nanoparticles on the catalyst [18].

The proposed mechanism fully explains the high selectivity of the Ru/zeolite in practical applications, where the Ru/zeolite catalyst shows complete CO removal (<10 ppm) with negligible CO_2 methanation, whereas for the Ru/Al_2O_3 catalyst CO_2 methanation will start to contribute as soon as the CO partial pressure / coverage drops below a critical value.

References

[1] W. Lubitz, W. Tumas, Chem.Rev. 2007, 107 3900-3903.

[2] S. Kawatsu, J.Power Sources 1998, 71 150-155.

[3] D. R. Palo, R. A. Dagle, J. D. Holladay, Chem.Rev. 2007, 107 3992-4021.

[4] W. Vielstich, in Encyclopedia of Electrochemistry - Interfacial Kinetics and Mass Transport ,Vol. 2, (Eds.: A. J. Bard, M. Stratmann, E. J. Calvo), VCH, Weinheim 2003.

[5] J. R. Ladebeck, J. P. Wagner, in Handbook of Fuel Cells - Fundamentals Technology and Applications ,Vol. 3, (Eds.: W. Vielstich, A. Lamm, H. A. Gasteiger), Wiley, Chichester 2003, p. pp. 190-201.

[6] J. R. Rostrup-Nielsen, K. Aasberg-Petersen, in Fuel Cell technology and applications ,Vol. 3, (Eds.: W. Vielstich, H. A. Gasteiger, A. Lamm), Wiley, Chichester 2003, p. pp. 159-176.

[7] T. Inui, M. Funabiki, Y. Takegami, Ind.Eng.Chem.Prod.Res.Dev. 1980, 19 385-388.

[8] M. B. I. Choudhury, S. Ahmed, M. A. Shalabi, Appl.Catal.A 2006, 314 47-53.

[9] A. Rehmat, S. S. Randhava, Ind.Eng.Chem.Prod.Res.Dev. 1970, 9 512-515.

[10] M. Echigo, T. Tabata, J.Chem.Eng.Japan 2004, 37 75-81.

[11] M. Krämer, M. Duisberg, K. Stöwe, WF. Maier, J.Catal. 2007, 251 410-422.

[12] P. Panagiotopoulou, D. I. Kondarides, X. E. Verykios, Appl.Catal.B 2009, 88 470-478.

[13] M. Krämer, K. Stöwe, M. Duisberg, F. Müller, M. Reiser, S. Sticher, WF. Maier, Appl.Catal.A 2009, 369 42-52.

[14] A. R. Dagle, Y. Wang, G.-G. Xia, J. J. Strohm, J. Holladay, D. R. Palo, Appl.Catal.A 2007, 326 213-218.

[15] S. Scirè, C. Crisafulli, R. Maggiore, S. Minico, S. Galvagno, Catal.Lett. 1998, 51 41-45.

[16] G. A. Mills, F. W. Steffgen, Catal.Rev.Sci.Eng. 1974, 8 159-210.

[17] S. Eckle, Y. Denkwitz, R. J. Behm, J.Catal. 2010, 269 255-268.

[18] Eckle, S., Anfang, H.-G., and Behm, R. J. What drives the selectivity for CO methanation in the methanation of CO_2-rich reformate gases on supported Ru catalysts? Applied Catalysis A: General . 2010., submitted

Hydrogen Production from Reformate Gas by a Cyclic Water Gas Shift Reactor

C. Hertel, **P. Heidebrecht**, **L. Rihko-Struckmann**, Max-Planck-Institute for Dynamics of Complex Technical Systems, Magdeburg, Germany
K. Sundmacher, Max-Planck-Institute for Dynamics of Complex Technical Systems, Magdeburg, Germany and Process Systems Engineering, Otto-von-Guericke University, Magdeburg, Germany

1 Introduction

Hydrogen plays an important role in today's chemical industry. Also, in many scenarios of future energy supply systems, hydrogen is considered as a main energy carrier. The main path for hydrogen generation is the steam reforming process, based on fossil fuels or on renewable biomass. Applications such as fuel cells, but also some chemical processes, require very pure hydrogen, especially with respect to carbon monoxide. In the classical process scheme, a series of two water gas-shift reactors together with a deep-removal reactor (preferential oxidation, palladium membranes, pressure swing adsorption or methanisation) is used to decrease the concentration of carbon monoxide in the reformate gas to sufficiently low levels. While the reforming process operates at temperatures above 700 °C, this cleaning sequence requires the temperature to be lowered to less than 100 °C. Thus, two drawbacks of this process become obvious: the sequence of three reactors with intermediate heat exchangers and the energy loss due to the necessary cooling of the gas.

The cyclic water gas-shift reactor (CWGSR, Fig. 1) (Messerschmitt, 1911) is an alternative to the classical water gas-shift process. It works at temperatures similar to those used in steam reforming (650-850 °C). Each process cycle is divided into two phases: during the first phase, reformate gas (hydrogen contaminated with carbon monoxide) is fed into a fixed bed of metal oxide. The metal oxide, usually iron oxide, is reduced and the gases are oxidised (Eqs. 1 and 2, forward reaction). After sufficient time, feeds are switched and steam is fed into the reactor. During this second phase, the metal is oxidised again (Eqs. 1 and 2, backward direction), producing a mixture of hydrogen and water which is free of carbon monoxide.

$$Fe_3O_4 + H_2/CO \leftrightarrow 3\ FeO + H_2O/CO_2 \quad (1)$$

$$FeO + H_2/CO \leftrightarrow FeO + H_2O/CO_2 \quad (2)$$

The CWGSR produces pure hydrogen from reformate gases in a single unit.

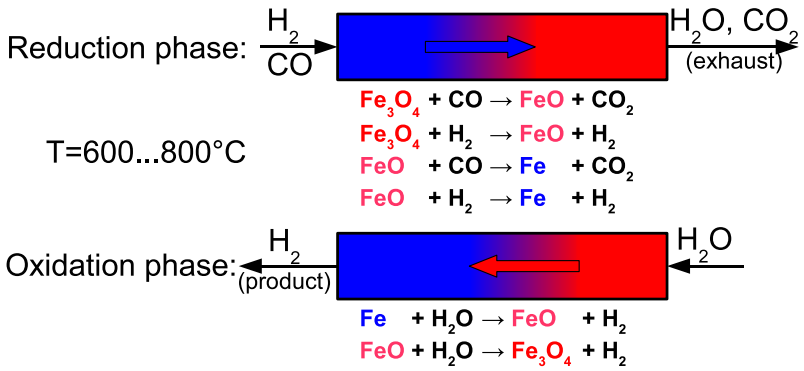

Figure 1: CWGSR working principle.

2 Objectives

The project focuses on the analysis, design and the practical realisation of this reactor. To obtain this goal, the following objectives are pursued:

- Development of a cheap, suitable and stable fixed bed material based on iron oxide.
- Evaluation of reaction kinetics and oxygen capacity.
- Model based analysis, design and control.
- Validation in a pilot plant.

3 Material Development

Pure iron oxide suffers from deactivation in regular CWGSR operations very quickly due to loss of active surface by sintering. Experiments show that additions of $CeZrO_2$ improve the activity and stability of the material (see Fig. 2). This finding is supported by REM images of new and used material (see Fig. 3) (Galvita et al. 2008).

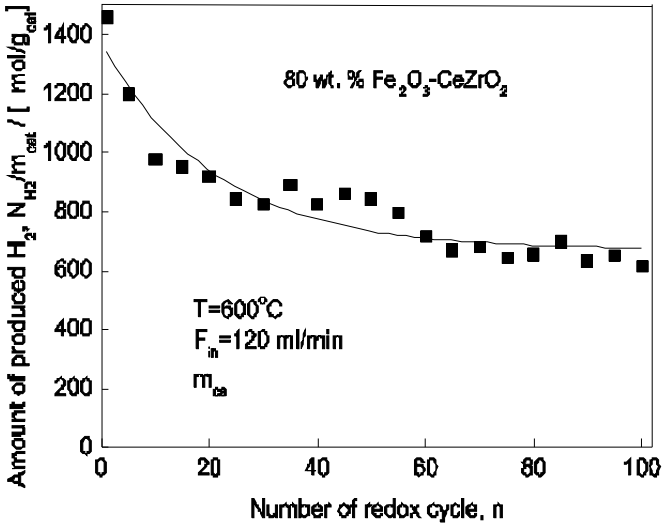

Figure 2: Material activity over 100 cycles.

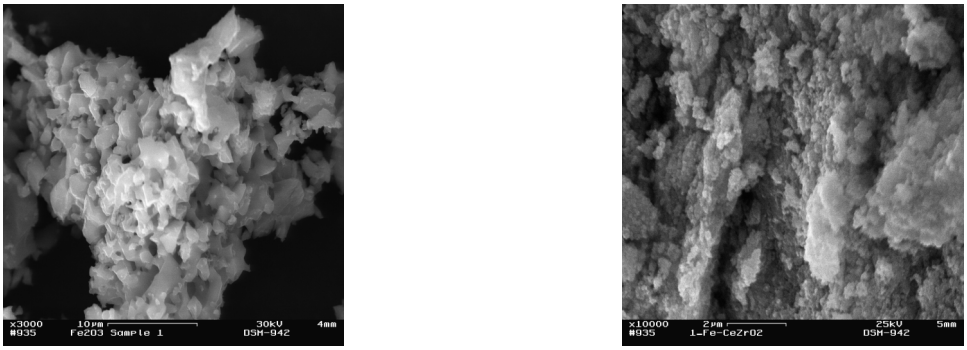

Figure 3: REM pictures of Fe_2O_3 (left) and 80-Fe_2O_3-$CeZrO_4$ (right) after 4 cycles.

4 Reaction Kinetics

Reaction kinetics were determined by thermo-gravimetric analysis (TGA) under different atmospheres of CO/CO_2. By properly choosing the ratio of CO and CO_2 in the reactant gas, the different reduction/oxidation reactions could be investigated separately. Fig. 4a shows the equilibrium diagram of the iron/iron oxide system in an atmosphere of CO and CO_2. The arrows indicate which gas compositions may be applied in order to obtain reduction of the bed material to a certain oxide species. Fig. 4b shows an exemplary TGA result of a sequence of reduction steps. The final weight reduction corresponds very well with the stoichiometric value, showing that the material can be completely reduced within reasonable time.

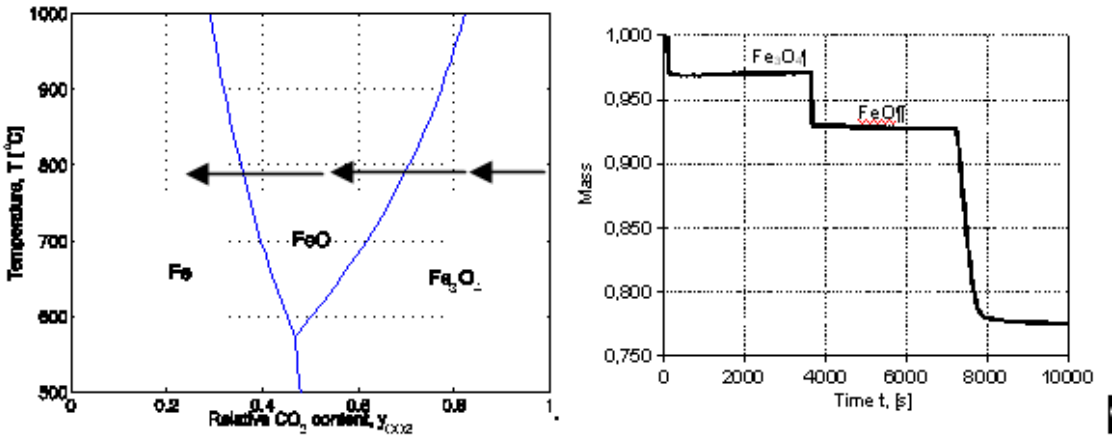

Figure 4a: left: Equilibrium lines of the system Fe/Fe_xO_y + CO/CO_2.
right: TGA measurement curve during stepwise reduction experiment.

The reaction rates were described by a modified Avrami-Erofeyev kinetic, which accounts for temperature, gas partial pressures and the thermodynamic equilibria (see Fig. 5). Typical reaction orders are approximately 1.8 with regard to the gas phase and 0.2 w.r.t. to the solid,

which can be interpreted as 1...2 dimensional product growth from already present nuclei at reaction start.

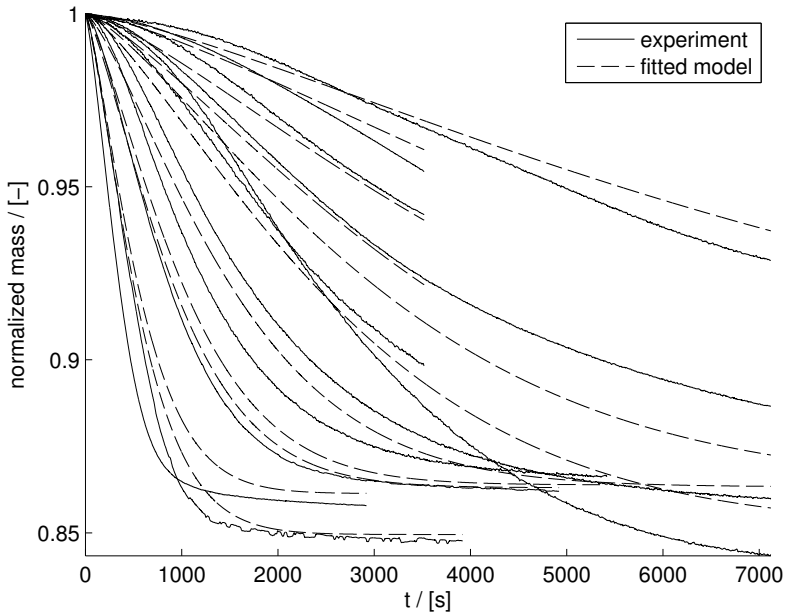

Figure 5: Measured and simulated TGA curves for the reaction FeO + CO → Fe + CO_2 subject to different temperatures and partial pressures of CO and CO_2.

5 Model Based Analysis

First simulations showed a significant advantage of the counter-current flow operation as shown in Fig. 1, as opposed to the straightforward co-flow operation (Heidebrecht et al. 2007). By switching the inlet and outlet ports, the fixed bed's oxidation gradient can maintain its orientation, which leads to less gas loss during phase switching, and higher fuel gas utilisation. Furthermore, regenerative heat exchange can be utilized to ease thermal integration of the reactor.

For a thermodynamic analysis, a mathematical model was used where equilibrium between gas and solid was assumed. Reaction zones then move as fronts through the reactor which then rest, on average, at one of the reactor ends (Heidebrecht et al. 2009). The positions depend on the relative duration of the reduction phase, S^l, and temperature, T. This leads to the formation of different operating regimes (see Fig. 6), which differ in fuel gas utilisation η_{fuel} and product concentration $x_{H2,out}$. For example long reduction phases at high temperatures cause both reaction fronts to be located at the right end of the reactor, leading to low efficiencies but high hydrogen concentrations (see Fig. 7).

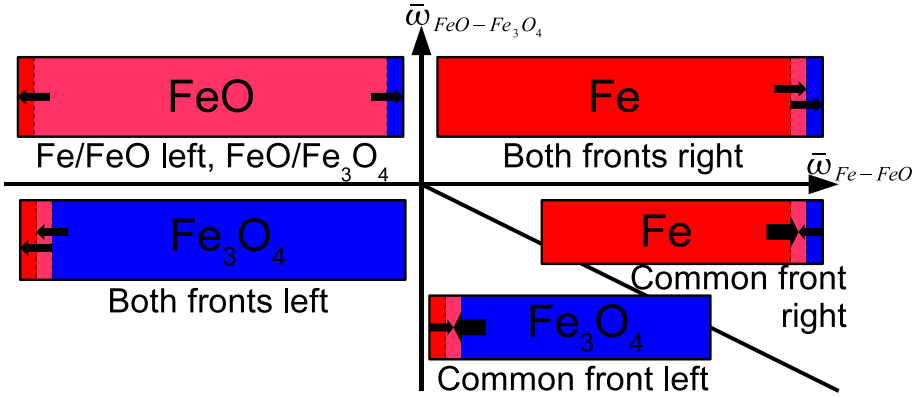

Figure 6: CWGSR operating regimes in reverse-flow mode.

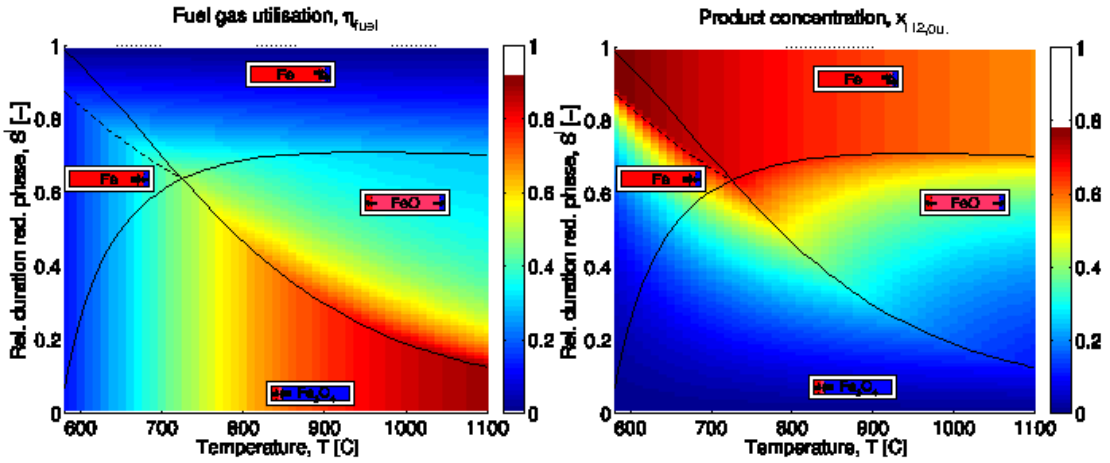

Figure 7: Fuel gas utilisation and H_2 product concentration in different regimes, depending on temperature and relative reduction phase duration.

Other, more complex models are currently under development. They will be applied to optimise design and operating parameters.

6 Pilot Plant

A pilot plant with a CWGSR bed length of 70 cm, inner diameter of 20 mm and bed mass of 200 g has been built (see Fig. 8a). Typical flow rates are several Nl/min.

In Fig 8b, a first proof of concept is shown: The exhaust gas compositions during several reduction phases (CO, CO_2) and the product concentration (H_2) during the oxidation phase.

The plant will be used to validate the developed models and support derived results.

Figure 8a: Pilot Plant with a 70 cm · Ø 20 mm fixed bed, several Nl/min flow.

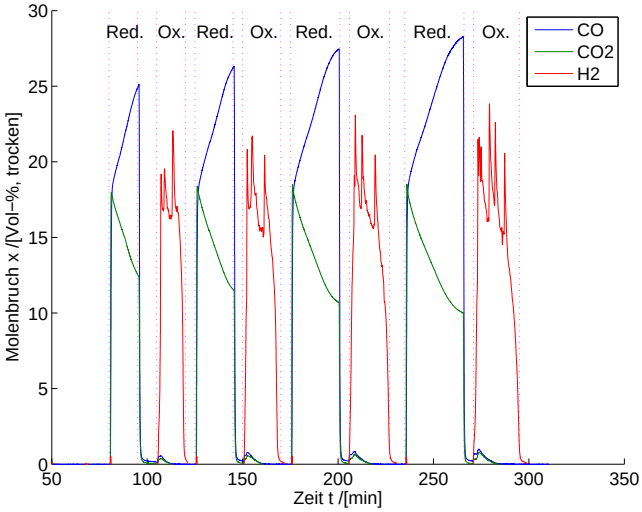

Figure 8b: Outlet measurements: CO, CO_2 and H_2 concentrations during repeated reduction and oxidation steps.

References

[1] Messerschmitt, 1911, German Patent 266863

[2] Galvita, V., Hempel, T., Lorenz, H., Rihko-Struckmann, L., Sundmacher, K., Ind. Eng. Chem. Res. 47, 2008, 303-310

[3] Heidebrecht, P., Hertel, C., Sundmacher, K., Int. J. Chem. Reac. Eng. 6, 2008, A19

[4] Heidebrecht, P., Sundmacher K., Chem. Eng. Sci., 64, 2009, 5057-5065

Investigations on Steam Reforming Catalysts for Diesel Fuel

M. Maximini, **T. Huck**, **R. Wruck**, **K. Lucka**, OWI Oel-Waerme-Institut GmbH, Germany

Abstract

Fuel cells can be applied as highly efficient auxiliary power units when being supplied with hydrogen. Since there is no adequate hydrogen infrastructure available yet, liquid fuels like Diesel can serve as a hydrogen source when it is converted into a hydrogen-rich gas in a reforming process fuel conversion by steam reforming (SR) promises the highest hydrogen yield in comparison to autothermal reforming (ATR) or catalytic partial oxidation (CPO). In the presented work several SR catalysts were tested at 750 °C and a steam to carbon ratio of 4, using a Diesel reference fuel with a sulphur content of ξ_s<10 ppm. Steam reforming was studied for varying Gas Hourly Space Velocities (GHSV) with respect to the hydrogen yield. In addition, studies of catalyst deactivation in the presence of sulphur and the catalysts' ability to regenerate by carbon combustion with air were completed. Some catalysts show promising results, while we identify one catalyst that has a high potential for a continuous Diesel SR application. Closing the presentation, we discuss the reproducibility of the results, and we give recommendations for further investigations.

1 Introduction

Fuel cells (FC) are highly efficient energy converters that can be applied as stationary or mobile auxiliary power units (APU) when being supplied with hydrogen. The fact that there is no adequate hydrogen infrastructure available yet drives alternative approaches to supply FC. In order to facilitate a breakthrough of the technology, a promising approach is the use of hydrocarbons as a hydrogen source. In particular for mobile applications, liquid fossil fuels like Diesel are suitable due to their high energy density, their easy storage and their already existing distribution infrastructure.

To generate hydrogen from Diesel, reforming processes like steam reforming (SR), autothermal reforming (ATR) or catalytic partial oxidiation (CPO) have to be applied. In comparison to ATR and CPO, SR promises a higher hydrogen yield generating hydrogen from hydrocarbons and steam, based on catalytic reactions. However, steam reforming Diesel is challenging because of its complex composition of aromatic and aliphatic hydrocarbons and its sulphur content. Sulphur is a catalyst poison blocking the catalyst's active surface. In the same way the catalyst is deactivated by carbon deposits, formed during the reforming process. To overcome catalyst deactivation and to achieve long-term durability for Diesel SR, suitable catalysts have to be found.

In recent years, there have been efforts to develop sulphur-tolerant catalysts that are capable to convert Diesel and fossil fuels of similar compositions at high conversion rates. Kataria et al. performed investigations on steam reforming of jet fuel with sulphur contents of 100 ppm.

They observed a dramatic decrease in catalyst activity with time in comparison to processing a sulphur free fuel. They also found that the sulphur content promoted carbon formation [3]. Steam reformer for light fuel oil and Diesel were investigated by several authors [1, 4, 6]. Reformer tests were conducted with a sulphur free reference fuel and desulphurised Diesel. The results show that lower temperatures as well as increased flow rates result in lower conversion rates [1, 2]. The reforming of desulphurised Diesel with sulphur contents <1 ppm already shows a noticeable catalyst deactivation [5]. Thormann carried out steam reforming experiments on synthetic Diesel and conventional Diesel with sulphur contents <10 ppm using rhodium catalysts. He found that catalyst deactivation is significant but reversible [4].

The results of prior research show the necessity to further develop SR catalysts for sulphur containing liquid fuels. In order to use liquid fuels as a hydrogen source for FC, new catalysts have to be found that offer high fuel conversion rates, low deactivation tendency and the ability to regenerate from deactivation.

The presented work describes the tests of 9 noble metal catalyst samples of different formulations for Diesel SR. Diesel reference fuel with a sulphur content of 6 ppm was reformed in order to study the catalyst performance at different Gas Hourly Space Velocities (GHSV) and the catalyst deactivation. Considering long-term durability, the regeneration ability was investigated, observing the product gas concentrations after the combustion of carbon deposits with air.

2 Materials and Methods

For the catalyst tests, Diesel reference fuel and de-ionised water with a conductivity lower 10 µS/cm were used. The fuel composition was determined to comprise of the fractions as described in Table 1.

Table 1: Fractions of the used Diesel reference fuel.

Content	Test method	Value	Unit
Alkane, Naphthene		72,5	% by weight
Polycyclic aromatic hydrocarbons	DIN EN 12916	3,3	% by weight
Mono-aromatic		20,9	% by weight
Di-aromatic		3,2	% by weight
Tri-aromatic		0,1	% by weight
sulphur	DIN EN ISO 20884	6	mg/kg

The catalyst tests were completed on the test rig as shown in Figure 1. The rig comprised of the five main sections: dosing, mixture preparation, mixture conditioning, steam reforming and analysis.

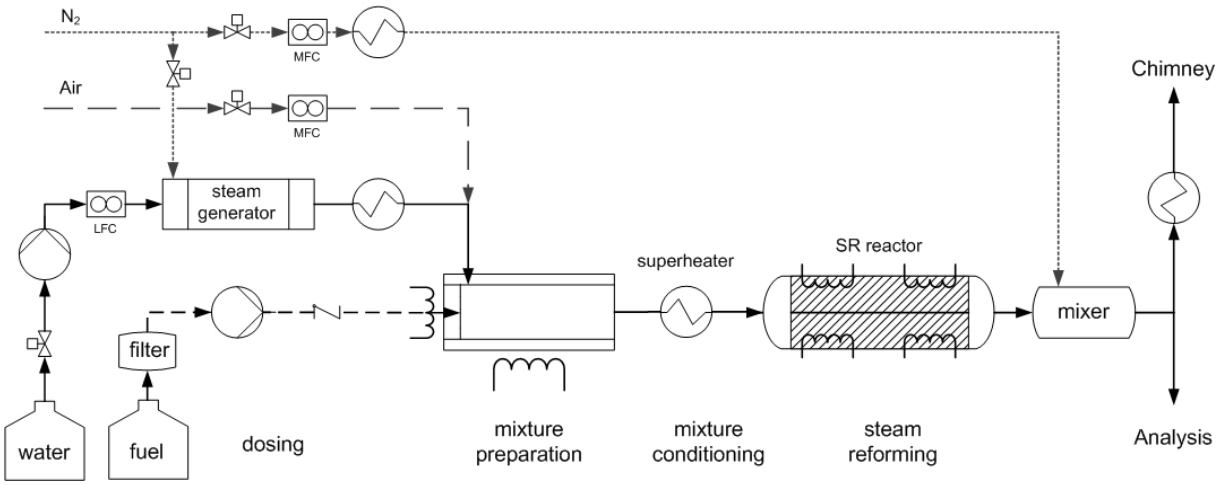

Figure 1: Test rig for steam reforming studies.

For dosing Diesel a dosing pump was employed, pumping the fuel into the mixture preparation device to vaporise on a heated porous surface. Water was dosed and vaporised in a controlled steam generator. The generated steam was superheated and led into the mixture preparation device to mix with the Diesel vapour at a temperature of approximately 450 °C. In the mixture conditioning zone the Diesel-steam-mixture heated up to provide consistent inlet temperatures of 750 °C for the SR reactor. The reactor consisted of a single channel of catalytically coated plates embedded into a heated body to achieve isothermal conditions for the reforming reactions.

Steam reforming was studied at 750 °C, and a steam to carbon ratio (S/C) of 4 was applied. Starting with an initial fuel feed corresponding to a thermal power input of 0.75 kW_{th}, the power input was increased stepwise to 1.00 kW_{th} and 1.25 kW_{th}.

The resulting educt flows corresponded to the GHSVs of 45,000 h^{-1}, 60,000 h^{-1} and 75,000 h^{-1}, relating the GHSV to the channel volume. The product gas was continuously analysed over the test period, measuring hydrogen (H_2), carbon monoxide (CO), carbon dioxide (CO_2) and methane (CH_4) concentrations with a Rosemount NGA 2000 analyser. Unconverted hydrocarbons were analysed with a Rosemount Thermo-FID to determine the fuel conversion rate. Due to technical FID limitations, the product gas was diluted to H_2 concentrations lower 10 % V/V with nitrogen. FID measurements were taken in five reading points over a test period (cp. Figure 2) when steady-state reactor temperatures were reached. Steady-state was considered when temperature deviation from set temperatures was lower 5 K at the reactor inlet and outlet. After reading point 3, the process was run at a constant fuel feed equivalent to 1.25 kW_{th} to observe the deactivation of the catalyst. Then, the reactor was flushed with nitrogen to initiate the regeneration process, using air for the combustion of carbon deposits. To evaluate the regeneration ability of the catalyst the initial fuel feed was set for another measurement.

3 Results and Discussion

In our study 9 noble metal catalyst samples (A1 to A9) were investigated. in order to show reproducibility of the results, catalyst A4 was of the same formulation as A3 and A6 was of

the same formulation as A5. As an example, Figure 2 shows the results of the test with catalyst A7. We obtain an initial H_2 concentration of more than 68 % before it falls due to the fuel feed increase resulting in higher GHSVs and therefore lower conversion rate. The increased GHSV also causes dropping CO_2 concentrations and rising CO concentrations revealing a reduction of the shift reaction. In the beginning of the degradation study (cp. Figure 2: reading point 3 to 4) we still find 63 % H_2 in the product gas. The catalyst activity steadily drops within the 3 hour study duration, but can partially be recovered after the regeneration with air. The CO_2 peak in the regeneration indicates the combustion of carbon deposits, and therefore suggests that deactivation from carbon formation is reversible. Evidently, we obtain a significant higher H_2 yield after the regeneration. This result is consistent to prior studies that suggest that deactivation is primarily from carbon formation [2]. The H_2 yield, however, does not reach the initial value, suggesting that the regeneration duration is insufficient to regenerate the catalyst from sulphur deactivation.

Figure 3 describes the catalyst performances for three fuel feeds in terms of the achieved H_2 yields. At the the initial fuel feed of 0.75 kW, accordant to a GHSV of 45,000 h^{-1}, the hydrogen yields are in a close range of a minimum of 64 % (A3) and a maximum of 68 % (A2). However, the catalysts respond differently to increased fuel feeds and thereby higher GHSVs. The performances of catalysts A4 and A6 significantly drop for a fuel feed of 1.25 kW accordant to a GHSV of 75,000 h^{-1}. Catalyst A7, in contrast, is the least sensitive to higher GHSVs. The best hydrogen yield at the highest fuel feed is obtained with catalyst A2.

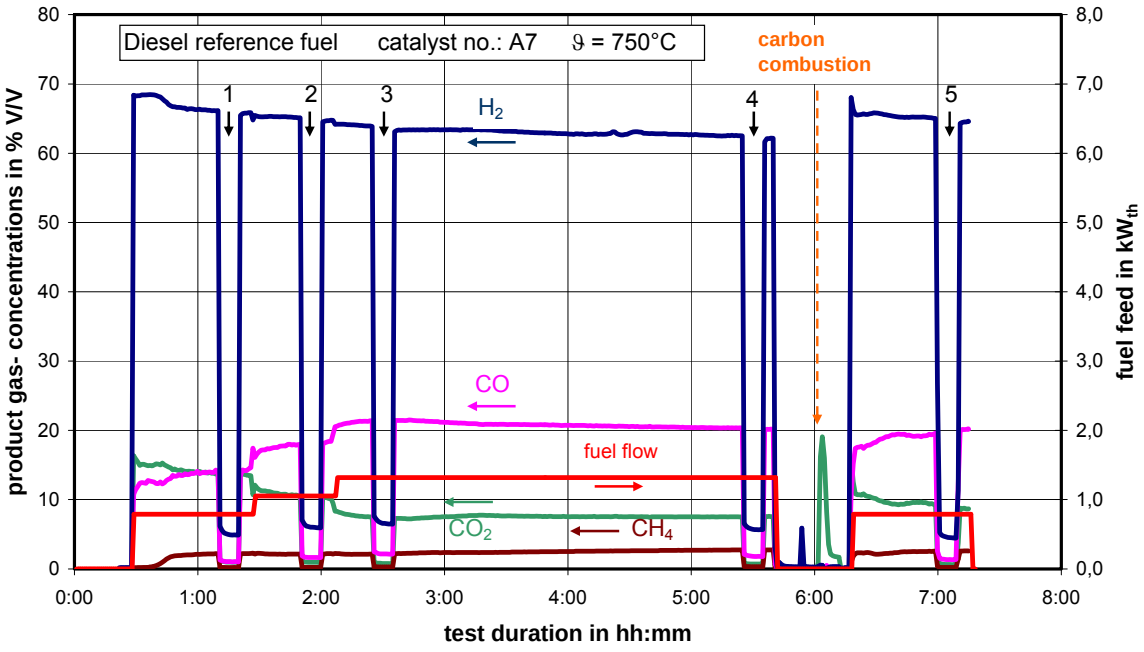

Figure 2: Product gas-concentrations achieved with catalyst A7.

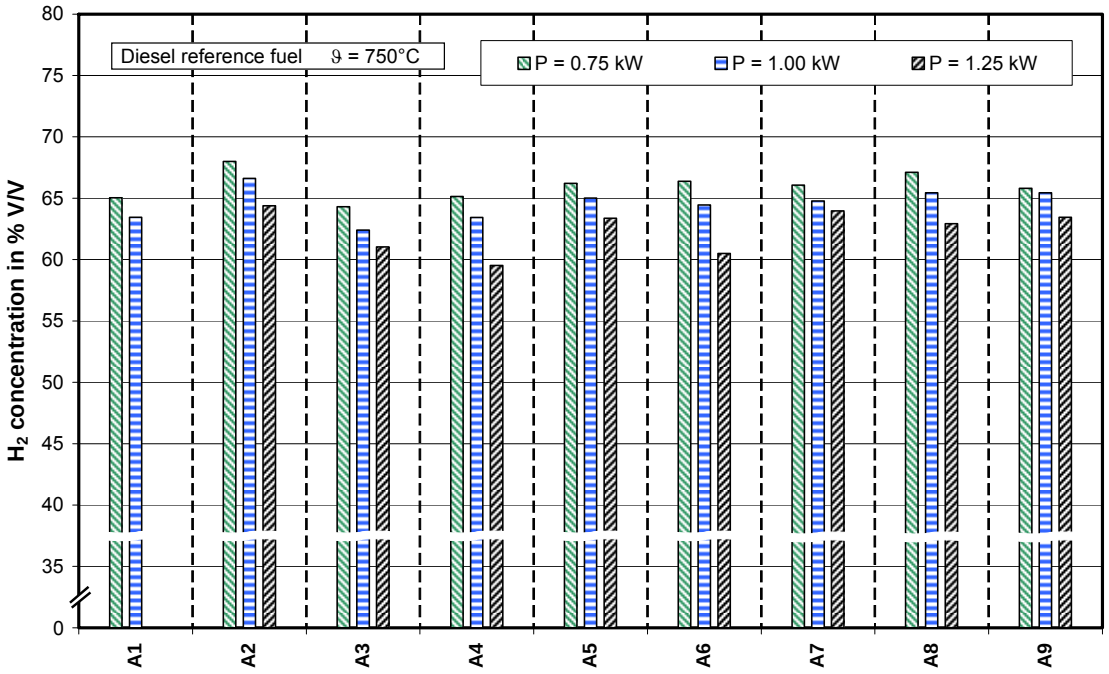

Figure 3: H2 yield of all catalysts for the investigated fuel feeds.

The results of the catalyst deactivation study are shown in Figure 4 by means of the degradation rate D. The degradation rate is calculated from the concentrations measured at reading points 3 and 4, the GHSV and the time between the reading points.

$$D = \frac{c_3 - c_4}{c_3 \quad \Delta t_{3,4} \quad GHSV}$$

The degradation rate is described for fuel conversion, H_2 concentration, CO_2 concentration and CO concentration within which the main focus has to be on the degradation of fuel conversion due to the applicability for Diesel reformers. We find that degradation characteristics in fuel conversion vary significantly among the catalysts. However, as a result of the necessary dilution for the FID measurement, the value for fuel conversion is the most sensitive to measurement errors. We, therefore, concentrate on degradation of H_2 concentrations to evaluate the catalysts.

Catalysts A1, A3 and A9 show good degradation characteristics for all gas concentrations while catalyst A7 seems to be exceptionally suitable for Diesel SR. Catalysts A2 and A5 can be considered unsuitable for a Diesel reformer due to their high degradation rates. High degradation in CO_2 concentrations along with a considerable low degradation for CO indicates that the shift reaction is being constrained due to the catalyst deactivation, as can be observed for A3. In contrast, the shift reaction seems to be enhanced for catalyst A8.

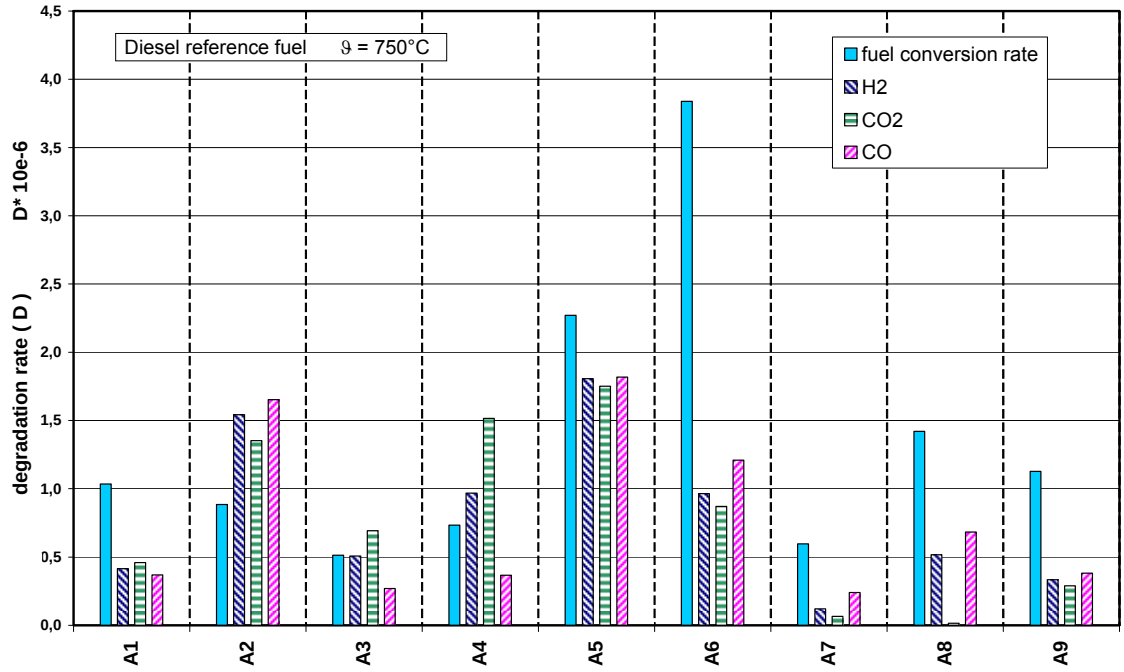

Figure 4: Results of the deactivation study.

The regeneration ability of the catalysts, described in Figure 5, is evaluated by the comparison of initial product gas concentrations and final concentrations after regeneration. For catalysts A6 and A9 we find nearly initial gas concentrations indicating that quasi full regeneration of the catalysts is possible. However, in reproducing the test results of catalyst A5 with A6, we had to stop the degradation study due to dramatic catalyst deactivation. Hence, there was less time for sulphur to deactivate the catalyst.

For the rest of the catalysts no satisfying regeneration was achieved. Additionally, we observe a decreased shifting ability for catalysts A5, A7 and A8, revealed by higher CO concentrations along with lower CO_2 concentrations.

In reproducing the test results, we find good reproducibility for catalyst A3 (cp. catalyst A4). Comparing the results for A5 and A6 we observe major discrepancies. We suppose that they may occur due to varying test durations and varying times for the reading points. Steady-state temperatures, being the precondition for measurements, were reached at different times. Furthermore, we had to advance regeneration due to the high catalyst deactivation. We recommend that further investigations are being conducted using an automated testing procedure with consistent test durations.

Summarising the results, we find that no catalyst in particular comprehends optimum characteristics in every aspect. Catalyst A7, however, shows the highest potential for an application in a continuous Diesel steam reforming process.

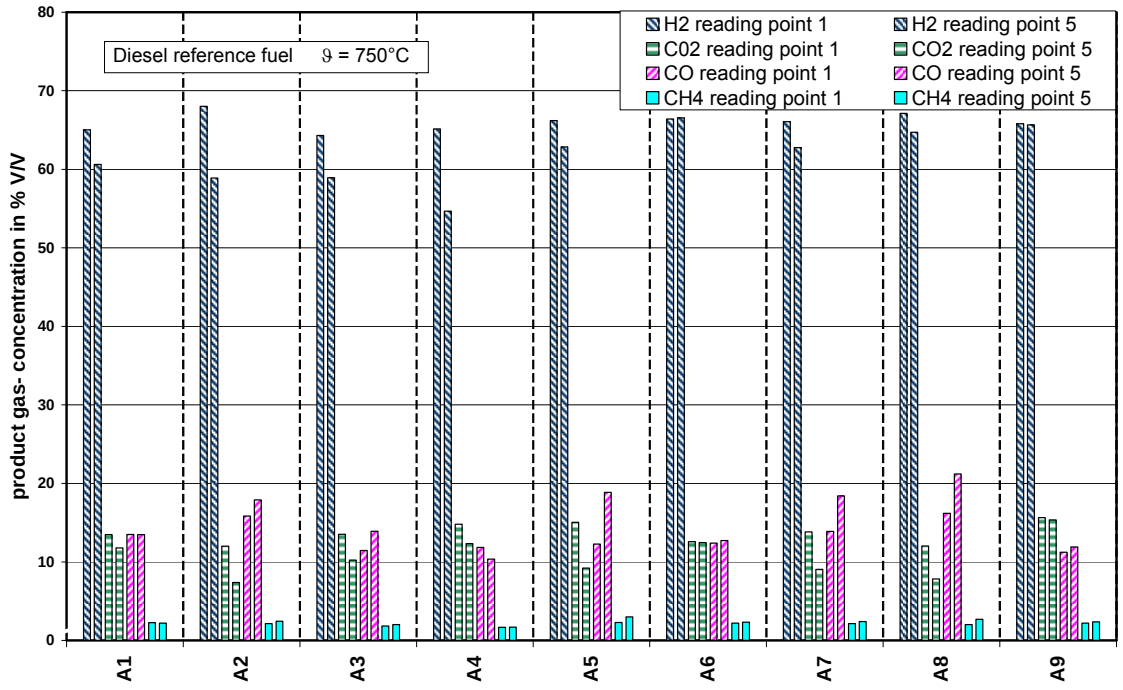

Figure 5: Regeneration ability of the catalysts.

4 Significance

Due to their high efficiencies, fuel cell systems are very attractive alternative to existing electric power generators applied as APUs. In particular for mobile applications, FC systems based on liquid fuels are promising since there are no storage or handling issues in contrast to the usage of pure hydrogen. Diesel is a liquid fuel that is already in use for heavy-duty and conventional vehicles, and hence has an existing distribution infrastructure. Steam reforming Diesel in order to supply FC with hydrogen, however, is challenging because of its sulphur content that deactivates the SR catalyst. Several SR catalyst were identified that showed promising characteristics in the presence of sulphur. One catalyst in particular showed high potential for a Diesel steam reformer. To verify the results and to improve reproducibility, an automated test procedure has to be applied in further studies.

References

[1] Wruck, R., et al.: Investigations on the operation of a steam Reformer for gasoil integrated in a PEFC-system for stationary applications, European Fuel Cell Forum 29.06. - 03.07.2009, Lucerne

[2] Wruck, R., et al.: Compact steam reformer with integrated catalytic burner for PEM fuel cell applications, H2 EXPO, Hamburg, 2006

[3] Kataria, A.; Ayyappan, P.; Abraham, M.; Development of Sulfur Tolerant Catalyst for Jet Fuel Steam Reforming; North American Catalysis Society; 20th North American Meeting, Houston, Texas; 2007

[4] Thormann, J.: Diesel-Dampfreformierung in Mikrostrukturreaktoren, Forschungszentrum Karlsruhe, Wissenschaftliche Berichte, FZKA 7471, 2009

[5] Mengel, C., et al.: Diesel steam reforming for PEM Fuel Cells, Journal of fuel cell science and technology, 2008, vol. 5, n°2, ISSN 1550-624X

[6] Kolb, G., et al.: Microstructured reactors for diesel steam reforming, water-gas shift and preferential oxidation in the kilowatt power range, Catalysis today, 147S (2009) 180

Catalytic Gasification of Glycerol in Supercritical Water for Hydrogen Production

Daniel Montané, Catalonia Institute for Energy Research (IREC). Bioenergy and Biofuels Division. Av. Països Catalans, 16. 43007, Tarragona, Spain
Anna May, **Joan Salvadó**, Universitat Rovira i Virgili. Departament d'Enginyería Química. Av. Països Catalans, 26. 43007, Tarragona, Spain

1 Introduction

Glycerol is a polyalcohol with several commercial applications in food and cosmetics, but nowadays massive amounts of low-purity glycerol are being obtained as byproduct in the manufacture of fatty acids and biodiesel. The surplus amount generated from biodiesel is so large – more than 600 000 tonnes in Europe in 2006 [1] – that glycerol market price has decreased to less that 0.05 €/kg [2,3]. Due to its low purity, crude glycerol from biodiesel cannot be used in cosmetics or food unless a costly refining process is undertaken, but its wide availability and cheap price offer new opportunities for chemistry and energy [4]. Among those, the production of hydrogen by supercritical water processing of concentrated glycerol solutions is an option that is being studied nowadays.

Non-catalytic glycerol decomposition in SCW proceeds through a complex reaction mechanism that is summarized in two competing pathways, ionic and free-radical, whose predominance depends on water density and acidity [5, 6]. At low temperature and high pressure (i.e., high water density) a set of ionic reactions forms acetaldehyde, formaldehyde and acrolein as main products. At low water density a free-radical pathway leads to the preferential formation of allyl alcohol and methanol. Gases are typical products of the free-radical reactions, and their yield is favored by low water density. Complete gasification is achieved only above 700 °C, but hydrogen is not favored as the main product. Gasification efficiency is high with diluted glycerol solutions, but it decreases dramatically when the substrate concentration is above 20 wt%. This is because of the dominance of condensation reactions between glycerol decomposition products that lead to the formation of tarry materials and char [7,8].

Several heterogeneous catalysts have been studied to promote hydrogen yield and reduce the formation of tars and char [7]. Among those, Ruthenium-based catalysts have been shown to offer the best results for SCW gasification of biomass feedstocks [9,10], but still temperatures above 700°C are required to have a high selectivity towards hydrogen [11]. In fact, no catalyst capable of reaching complete conversion of glycerol and a hydrogen yield close to the stoichiometric value at a temperature below 550°C has been found yet, partially because of the formation of methane as competing final product.

In this work we focused on the SCW gasification of glycerol over a Ru/ZrO_2 catalyst in the low temperature range. Experiments at incomplete conversion of glycerol were performed and the reaction products were determined and quantified at increasing residence time. The influence of the catalyst on the pathways of glycerol conversion is discussed.

2 Experimental

A shell-type catalyst with an average content of 1% Ru, was prepared by incipient wetness impregnation following literature procedures [12-14]. The support (ZrO_2 with a particle diameter between 100 and 200 μm and a surface area of 0.1 m^2/g) was impregnated with the adequate amount of an aqueous solution of precursor ($RuCl_2$) and dried at 110°C for 24 h. Then the sample was crushed and oxidized at 500°C for 4 h, reduced with hydrogen at 400 °C for 5 h, cooled to room temperature under nitrogen and stored in caped vials until use. The catalyst was characterized by x-ray diffraction, surface area, SEM and ESEM. Activity of the catalyst was measured in a fixed-bed reactor with the catalyst (1 to 3 g) diluted with ZrO_2 particles (5 to 8 g) of the same size distribution to improve heat transfer and temperature homogeneity. Gaseous products were quantified by an on-line gas chromatograph (Agilent microGC 3000A), and condensable products by HPLC (Agilent 1100 series).

3 Results

Experiments were performed at 510 and 550°C using a glycerol feed concentration of 5% wt, and nominal residence times below 9s. The conversion of glycerol, X (equation 1), the yield of the identified reaction products, Y_j (equation 2), the carbon balance CB, (equation 3), and the hydrogen yield potential HYP, (equation 4) were calculated for each experiment. $F_{Gly\text{-}0}$ and F_{Gly} are the molar flow rates of glycerol at the reactor inlet and outlet, respectively, F_j the molar flow rate of any specie at the reactor outlet, nC_j is the number of carbons in compound j, and $n_{H2,j}$ denotes the moles of hydrogen gas that would be formed if species j were completely converted into H_2 and CO_2 following the stoichiometric equation 5.

$$X[\%] = 100 \cdot \left(\frac{F_{Gly-0} - F_{Gly}}{F_{Gly-0}} \right) \tag{1}$$

$$Y_j \left[\frac{mol}{mol_{Glycerol}} \right] = \frac{F_j}{F_{Gly-0}} \tag{2}$$

$$CB[\%] = 100 \cdot \left(\frac{3 \cdot F_{Gly} + \sum_{j=1}^{m} n_{C\,j} \cdot F_j}{3 \cdot F_{Gly-0}} \right) \tag{3}$$

$$HYP = \sum_{j=1}^{m} n_{H_2,j} \cdot F_j \tag{4}$$

$$C_x H_y O_z + (2x - z) \cdot H_2O \rightarrow \left(2x - z + \frac{y}{2} \right) \cdot H_2 + x \cdot CO_2 \tag{5}$$

$$\tau[s] = \frac{V_R \cdot \phi \cdot \rho_{m,R}}{m_0} \tag{6}$$

The residence time of the reacting mixture inside the reactor, τ, was estimated with equation 6, assuming that the density of the reacting mixture approached that of pure water at the temperature and pressure of the experiment. This is a coarse approximation in our case since glycerol concentration was relatively high (5 wt% in the feed), and therefore density of the reaction mixture should be calculated accounting for the change of composition due to the conversion of glycerol and the formation of products. However, this calculation is not straightforward at supercritical conditions and we used this simplified procedure to have an approximate estimation of the residence time. In equation 6, V_R is the volume of the catalyst bed, φ is the void fraction of the bed, m_0 the mass flow rate of water and glycerol fed to the reactor, and $\rho_{m,R}$ is the density of pure water at the reactor conditions of P and T. The latter was calculated according to Wagner and Kruse [15].

Preliminary experiments were developed to assess the stability of the catalyst. Glycerol conversion and the composition of the gas products were monitored for extended periods to determine changes in the activity of the catalyst and product selectivity. In general the catalyst had an initial period in which significant changes in gas composition were observed, but its activity reached stable conditions after 4h of operation. Figure 1 shows glycerol conversion and gas composition for an extended experiment at 350 bar and 550°C. The first section corresponded to a residence time of around 7.5 s, in which complete glycerol conversion was achieved. After 1100 min of operation the feed flow was increased to reduce the residence time to 2.0 s, which resulted on an average conversion of 0.91 when the system did reach a new steady state. Again, around 4 h were required for stabilization. Therefore, all experiments were performed after the catalyst was stabilized for at least 5 h at the intended operation conditions.

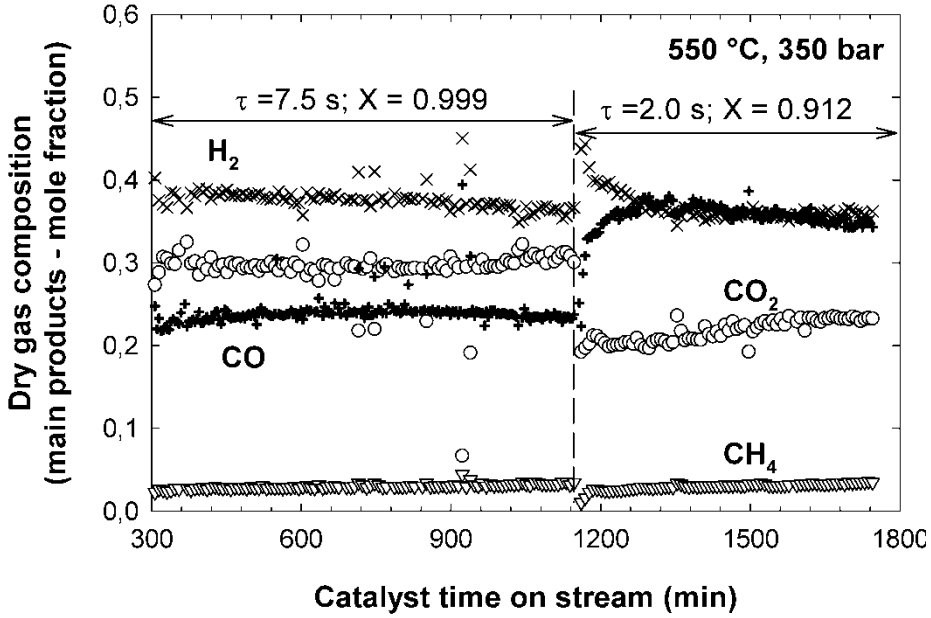

Figure 1: Catalyst stability. Dry gas composition for an extended experiment at 550°C and 350 bar at two different residence times.

Figure 2 shows the conversion of glycerol at 510 °C and 350 bar, for non-catalyzed experiments using a bed of ZrO_2 particles and for experiments with the Ru/ZrO_2 catalyst. Conversion reached 22% at a residence time of 8.2 s in the non-catalyzed experiment, and it was increased to 98% at the same residence time. The overall pseudo-first rate constant for the non-catalytic gasification of glycerol was 0.034 s^{-1}, in agreement with the values reported in other studies [5], and 0.377 s^{-1} for the catalyzed reaction. Figure 2 also shows the effect of increasing reaction temperature to 550°C. Glycerol conversion was 99.9% at 7.5 s, with a reaction rate constant of 0.992 s^{-1}.

The yields of the main reaction product, which were expressed as mole of product formed per mole of glycerol fed to the reactor (equation 6), are reported in Figures 2 and 3. For the hydrothermal processing at 510°C the main condensable reaction products were acetaldehyde, hydroxyacetone and acetic acid, and gaseous products comprised hydrogen, carbon oxides and methane. Minor amounts of allyl alcohol, propionaldehyde and acrolein, and trace amounts of acrylic acid and ethylene were also detected. This wide variety of products reflects the complexity of the reaction mechanisms involved in the hydrothermal decomposition of glycerol, which can be summarized into the coexistence of competing ionic and free radical pathways [5].

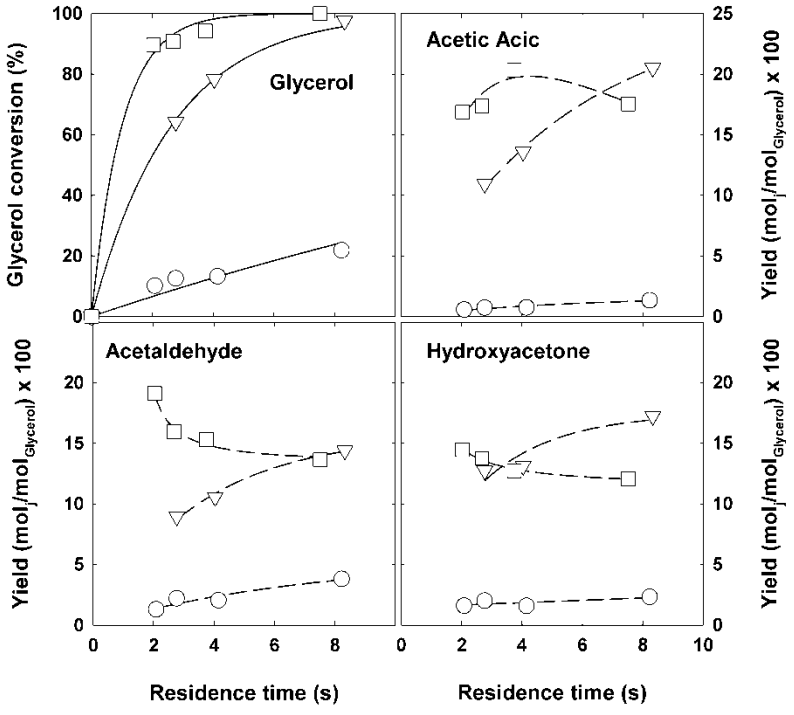

Figure 2: Glycerol conversion at 350 bar and main condensable products for the non-catalytic reaction at 510°C (○) and the catalyzed reaction at 510°C (▽) and 550°C (□).

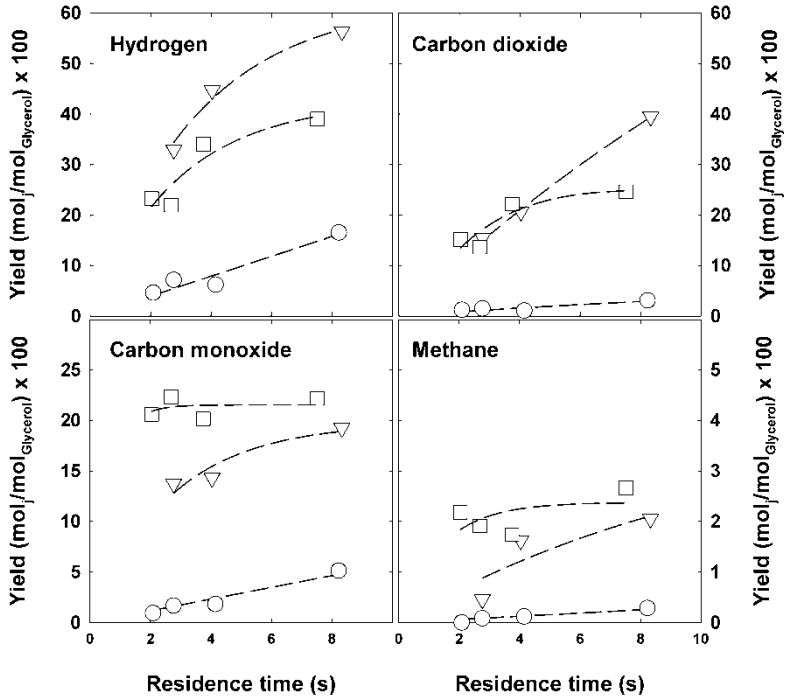

Figure 3: Main gaseous products for the non-catalytic reaction at 350 bar and 510°C (○) and the catalyzed reaction at 510°C (▽) and 550°C (□).

The ionic path dominates at high-water density – low temperature and high pressure – a situation in which the ion product of water is high enough to allow the existence of free protons and hydroxyl ions that may catalyze ionic reactions, and the static dielectric constant of water is high enough to stabilize ionic species and reaction intermediates. The free radical decomposition route dominates at low water density – high temperature and low pressure – where ionic chemistry is not favored due to the low dielectric constant of the media and low water ion product. Table I shows relevant properties for the conditions we have covered in our study, which were calculated according to Wagner and Kruse [33]. At 510°C and 350 bar the ion product of water is six orders of magnitude lower than for water at room temperature and the dielectric constant is close to that of steam, which indicates that the ionic route will play a minor role in our case and that the free-radical pathway should dominate.

The catalyst had a significant influence on the selectivity of the different reaction products. Acetic acid became the main condensable product instead of acetaldehyde. For instance, at 510°C and 8.5 s residence time – complete glycerol conversion – the yield of acetic acid grew from 0.015 mol/mol$_{Gly}$ in the non-catalyzed experiments to 0.25 mol/mol$_{Gly}$, while that of acetaldehyde only went from 0.045 to 0.15 mol/mol$_{Gly}$. The yield of hydroxyacetone grew from 0.025 to 0.18 mol/mol$_{Gly}$, also below the yield of acetic acid. Permanent gases – shown in Figure 3 – were the major products, and the yields of hydrogen, carbon oxides and methane all increased when the catalyst was used. The catalyst favored both C-C cleavage reactions that formed acetic acid and acetaldehyde, and dehydration reactions that formed C3 products, mainly hydroxyacetone. The catalyst also promoted reforming to form hydrogen, carbon oxides and methane (secondary products), although glycerol was preferentially converted into primary products (i.e. acetic acid, acetaldehyde and

hydroxyacetone), which were then converted into gases at a slower rate. This may be observed in the experiment at 550°C. A glycerol conversion above 95% was reached in 4 s, when a maximum in acetic acid yield was attained. Notably, the yields of acetaldehyde, hydroxyacetone, and other condensable primary products decreased with residence time in the entire interval covered by the experiment, showing that they were converted into secondary products. The yield of hydrogen was lower than at 510°C because more carbon monoxide and methane were formed, thus reducing hydrogen yield. However, gases were not the sole secondary products. Figure 4 shows the carbon balances for the non-catalyzed and catalyzed experiments. At 510°C the carbon balance closure in the non-catalyzed experiments was better than 90%, and it was between 70 and 85% at 550°C. The carbon unaccounted for was mostly attributed to formaldehyde and methanol – which were not properly recovered nor quantified in our experimental setup – since no carbon formation on the surface of the bed particles could be observed. On the contrary, the catalyzed experiments had carbon balance closures between 80 and 60%, decreasing continuously as the residence time was increased. Although the formation of methanol and formaldehyde represented a fraction of the carbon unaccounted for, the main reason for the poor carbon balance closure was the formation of carbon deposits on the bed. In fact carbon deposits were not observed on the particles of Ru/ZrO_2 catalyst but on the inert ZrO_2 particles that were used to dilute the catalyst bed, and eventually caused partial plugging of the bed and pressure build-up during extended experiments when temperature was below 510°C. This implies that carbon deposits evolved from the primary reaction products through condensation reactions in the aqueous phase that formed tar-like carbon precursors. The formation of tar at temperatures below 600°C has been reported for the hydrothermal gasification of glucose. In our case a proton-catalyzed ionic reaction pathway may be considered due to the relative high concentration of acetic acid and other acidic species. However, the low ion product (kW) and static dielectric constant (ε) of water at the reaction conditions we used – for instance, kW and ε were 1.67×10^{-20} $(mol/kg)^2$ and 1.984 at 510°C and 350 bar, respectively [33] – point to a more likely free-radical pathway as dominant.

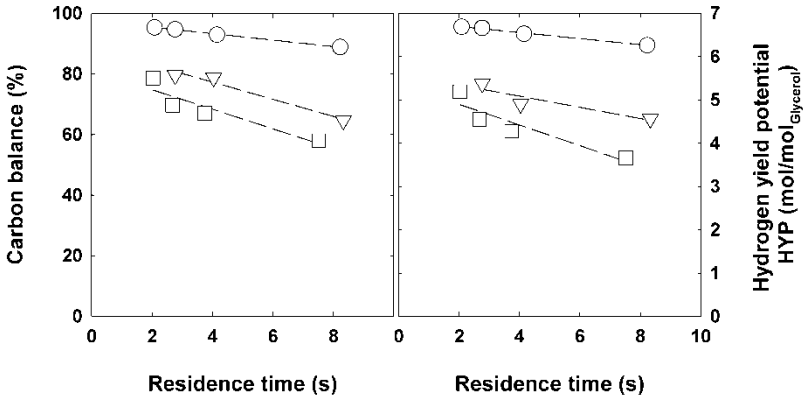

Figure 4: Carbon balance and hydrogen potential yields for glycerol conversion at 350 bar: 510°C non-catalyzed (○) and catalyzed at 510°C (▽) and 550°C (□).

4 Conclusions

The hydrothermal and catalytic conversion of glycerol has been studied in supercritical water at 350 bar and intermediate temperatures (510 and 550°C), covering an interval of residence time that gave incomplete conversion of glycerol. The catalyst – 1% Ru on CaO-stabilized ZrO^2 – augmented the rate of glycerol conversion and favored carbon-carbon scission reactions to form acetic acid and acetaldehyde as the main primary products. The catalyst also converted the primary products into gases through reforming, although the rate of reforming was slower than that of the formation of primary products. When the catalyst was used, the higher concentration of acidic species in the fluid prompted the formation of tar-like adducts that lead to the deposition of carbon on the bed – particularly on the surface of the inert particles of ZrO_2 that were used to dilute the catalyst particles – and a poor carbon balance. In conclusion, although the Ru/ZrO_2 catalyst presented good stability and overall activity, its selectivity towards reforming reactions was not high enough in the intermediate temperature range we studied. From a practical standpoint, low temperature and pressure are desirable in the hydrothermal processing of biomass in supercritical water to reduce the requirements of construction materials and operation costs. Optimization of the properties of the catalyst to enhance the reforming activity at low temperature and the selectivity towards gas products, and the capacity for processing high concentrations of biomass, are key aspects that need to be solved for the implementation of technology of supercritical water gasification.

Acknowledgments

This research was supported by the Ministry of Science and Innovation of the Spanish Government (project CTQ2008-02491/PPQ), and the Catalan Regional Government (2009SGR-00237).

References

[1] M. Pagliaro, M. Rossi, The Future of Glycerol. New Usages for a Versatile Raw Material, RSC Publishing, Cambridge, UK, 2008.

[2] D.T. Johnson, K.A. Taconi. Environ. Prog. 26 (2007) 338-348.

[3] Miller-Klein Associates, Impact of Biodiesel Production on the Glycerol Market (2006). http://www.hgca.com/document.aspx?fn=load&media_id=3605&publicationId=2363

[4] M. Pagliaro, R. Ciriminna, H. Kimura, M. Rossi, C. Della Pina. Angew. Chem. Int. Ed. 46 (2007) 4434-4440.

[5] W. Bühler, E. Dinjus, H.J. Ederer, A. Kruse, C. Mas. J. Supercrit. Fluid. 22 (2002) 37-53.

[6] M.J. Antal, W.S.L. Mok, J.C. Roy, A.T. Raissi. J. Anal. Appl. Pyrol. 8 (1985) 291-303.

[7] L. Kong, G. Li, B. Zhang, W. He, H. Wang. Energ. Source. Part A 30 (2008) 1166-1178.

[8] X. Xu, Y. Matsumura, J. Stenberg, M.J. Antal Jr. Ind. Eng. Chem. Res. 35 (1996) 2522-2530.

[9] M. Osada , T. Sato, M. Watanabe, T. Adshiri, K. Arai. Energ. Fuel. 18 (2004) 327-333.

[10] X. Hao, L. Guo, X. Zhang, Y. Guan. Chem. Eng. J. 110 (2005) 57-65.

[11] A.J. Byrd, K.K. Pant, R.B. Gupta. Fuel 87(2008) 2956-2960.
[12] Y. Boucouvalas, Z. Zhang, X.E. Verykios. Catal. Lett. 40(1996) 189-195.
[13] D.C. Elliott, T.R. Hart, G.G. Neuenschwander. Ind. Eng. Chem. Res. 45(2006) 3776-3781.
[14] D. Li, N. Ichikuni, S. Shimazu, T. Uematsu. Appl. Catal. A-Gen. 180 (1999) 227-235.
[15] W. Wagner, A. Kruse, Properties of Water and Steam. Springer-Verlag, Berlin, 1998.

Reforming of Diesel Fuel for Hydrogen Production over Catalysts Derived from $LaCo_{0.8}M_{0.2}O_3$ (M = Ni, Ru, Fe, Ga)

N. Mota[*], **M.C. Álvarez-Galván,** Instituto de Catálisis y Petroleoquímica (CSIC), Madrid, Spain
F. Rosa, Centro de Experimentación "El Arenosillo" (INTA), Huelva, Spain
J.L.G. Fierro, **R.M. Navarro**, Instituto de Catálisis y Petroleoquímica (CSIC), Madrid, Spain

1 Introduction

In recent years, the need to reduce pollutant emissions to atmosphere has favored the development of new technologies for the production of energy. The use of hydrogen is a feasible choice for energy production, being less contaminant and more efficient than internal combustion engines, especially when it is associated to fuel cells [0,0]. One of the main ways to produce hydrogen is by catalytic reforming of fossil fuels. Nowadays, there is an increasing interest in the development of technologies for the conversion of liquid hydrocarbons in hydrogen rich gas mixtures as a way to overcome the current technical limitations in hydrogen supply and storage. The use of diesel as a source of hydrogen offers advantages such as its high volumetric hydrogen density and well-established delivery infrastructure; however, the reforming of this fuel needs very active catalysts for the reforming of hydrocarbons of different nature and resistant to high temperatures, to sulphur poisoning and also, to coke formation [0]. An alternative to traditional catalysts based on transition metals supported over oxides doped with rare earths are perovskites (ABO_3), that present high resistance at elevated temperatures and to sulphur poisoning and produce, under reaction, a highly dispersed transition metal (B^0) over the oxide (A_2O_3). Previous works have point to $LaCoO_3$ as a very promising catalyst precursor for hydrogen production by hydrocarbons reforming, where lanthanum oxycarbonates, formed under reaction, have a role in catalyst stability favoring coke gasification [0,0,0]. In the present work, oxidative reforming of diesel fuel was studied over catalysts derived from perovskite $LaCo_{0.8}M_{0.2}O_3$ (M = Ni, Ru, Fe, Ga) precursors. It has been analyzed the influence of the partial substitution of Co by the above cations over modifications in cell parameters, average crystallite size, surface area, reducibility, morphology and surface composition, establishing a relationship of those physicochemical characteristics with catalytic activity and stability.

2 Experimental

Perovskite precursors were synthesized by a modified citrate sol-gel method [0]. Aqueous nitrate solutions containing the precursors cations were added to a solution of citric acid and ethylenglycol (molar ratio 1:1 and citric acid/A+B= 2.5). The mixture was stirred and heated

[*] Corresponding author, email: noelia.mota@icp.csic.es

at 343 K for 5 h. The obtained resin was charred at 573 K for 2 h and calcined at 1023 K during 4 h.

Fresh, pretreated and used samples (after 24 h of reaction) were characterized by means of different techniques. The BET surface area of fresh and pretreated catalysts was calculated from the nitrogen adsorption-desorption isotherms at 77 K, measurements performed with a Micromeritics ASAP 2100 apparatus. Photoelectron Spectroscopy analyses were recorded using a Escalab 200R spectrometer equipped with a hemispherical electron analyzer using monochromatic Al Kα (1486.6 eV). XRD patterns were recorded using a Seifert 3000P vertical diffractometer and nickel-filtered Cu Kα radiation. Hydrogen temperature-programmed reductions (H_2-TPR) were conducted using a Micromeritics 2900 instrument by heating the sample under a 10 % H_2/Ar flow (50 mL/min) up to 973 K at a linearly programmed rate of 10 K/min.

Perovskite samples were activated, before diesel oxidative reforming reaction, with a reductive stream (H_2(10%)/N_2) at 973 K for 1 h. Afterwards, activity tests were performed in a fixed-bed reactor at 1023 K, to avoid complete conversion. Reactants were fed at a molar ratio of $H_2O/O_2/C$ equal to 3/0.5/1. The gas flow rate was kept at 75 mlN/min (GHSV = 20,000 h^{-1}).

3 Results and Discussion

XRD analyses indicated that all the prepared materials showed a perovskite structure with rhombohedral symmetry. However, it was found that the substitution of Co by Ni, Ru, Fe and Ga produced structural modifications in lattice parameters and mean crystallite size (table 1), that are more evident for the sample with Ru. XRD pattern of $LaCo_{0.8}Ru_{0.2}O_3$ also support these results, since it shows a shift in the diffraction lines and a disappearance of the typical doublet around 33º associated to above symmetry. These facts are attributed to the greater size of Ru^{3+} cation, that difficult its introduction in the perovskite lattice [0]. Partial substitution of Co by above elements also produces some increase in surface area (table 1).

The activation process produces a complete transformation of the perovskite structure which derives in a well dispersed phase of Co^0 and most likely of M^0 particles - although these last ones haven´t been detected by XRD, probably due to their small size - over a matrix of La_2O_3. The absence of diffraction lines of Co^0 in the Ru-containing activated sample is explained by the small mean size of these particles. It has been also found a greater size of Co^0 and La_2O_3 crystallites in activated systems with Ni and Ga (table 2), which could give to a lesser development of Co-Ni-La and Co-Ga-La interactions that have an important role in the reaction [0,0] and that may be the cause of the low conversion values observed in these samples (figure 1).

Table 1: Lattice parameters, particle size and surface area of perovskite precursors.

Perovskite precursors	Lattice Parameters (A)		Particle size (nm)	BET surface area (m^2/g)
	a = b	c		
$LaCoO_3$	5.46	13.07	54	1.1
$LaCo_{0.8}Ni_{0.2}O_3$	5.45	13.12	43	2.7
$LaCo_{0.8}Ru_{0.2}O_3$	5.24	5.24	20	2.9
$LaCo_{0.8}Fe_{0.2}O_3$	5.46	13.06	34	6.0
$LaCo_{0.8}Ga_{0.2}O_3$	5.51	13.08	52	2.0

XPS results derived from activated samples indicates a low Co+M/La surface ratio in the Ru-containing sample; however binding energies indicate a greater reduction degree of these phases that are in accordance with TPR profiles. The better surface reduction together with the higher proportion of La_2O_3, M^0 (Ru^0) and Co^0 in the surface will explain the better performance of this system at the beginning of the reaction.

XPS surface analyses of the activated samples also indicate that the proportion of cobalt species increases when cobalt is partially substituted by the different M cations, with the exception of the sample with Ru (Table 2). It is worth mentioning that a surface enrichment of the modifiers elements is produced in samples with Fe, Ru and Ga, especially in the sample containing Ga (Table 2).

Table 2: Particle size and surface Co/La, M/La (XPS) for the perovskite elements reduced and after reaction.

Precursor perovskites	Reduced				After reaction			
	XRD		XPS		XRD		XPS	
	Particle size La_2O_3 (nm)	Particle size Co^0 (nm)	Co/La	M/La	Particle size $La_2O_2CO_3$ (nm)	Particle size Co^0 (nm)	Co/La	M/La
$LaCoO_3$	23	20	0.27 (1)	-	33	19	0.43 (1)	-
$LaCo_{0.8}Ni_{0.2}O_3$	28	27	0.42 (0.8)	0.19 (0.2)	38	24	0.85 (0.8)	n.d.
$LaCo_{0.8}Ru_{0.2}O_3$	18	n.d.	0.08 (0.8)	0.26 (0.2)	29	14	0.56 (0.8)	0.34 (0.2)
$LaCo_{0.8}Fe_{0.2}O_3$	18	15	0.36 (0.8)	0.34 (0.2)	22	17	0.64 (0.8)	0.44 (0.2)
$LaCo_{0.8}Ga_{0.2}O_3$	31	22	0.37 (0.2)	0.59 (0.2)	30	18	0.24 (0.8)	0.12 (0.2)

M: Ni, Ru, Fe or Ga; n.d.: not detected; (…): nominal values

From the activity results, presented in figure 1 and related to mean conversions and products distributions values after 24 hours of reaction, could be derived that the lowest hydrogen yield and the greater selectivity to combustion, is shown by the catalyst with Ga, which is

explained by the lesser surface exposition of cobalt and gallium observed in this sample (table 2).

By the contrary, the relatively small size of lanthanum oxycarbonate and metallic cobalt, and the high surface proportion of both phases (table 2) in Fe and Ru-containing systems would increase the contact between them, increasing its activity and stability, thus inhibiting the formation of coke. The formation of these smaller crystallites should be a consequence of a deeper modification of the original $LaCoO_3$ perovskite structure, in the partial substitution of cobalt by the above elements, whose ionic size is more dissimilar with respect to cobalt ion. This fact together with the high intrinsic activity of Ru for reforming/partial oxidation reactions are key factors that make Co^0-Ru^0/La_2O_3 catalyst derived from the $LaCo_{0.8}Ru_{0.2}O_3$ precursor a good candidate for hydrogen production by oxidative reforming of heavy hydrocarbons.

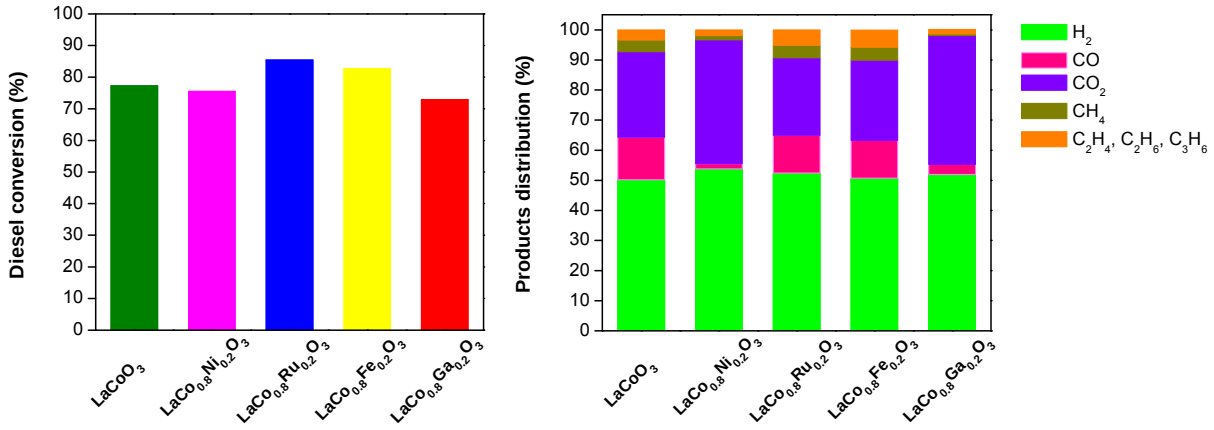

Figure 1: Diesel conversion and products distribution during oxidative reforming of diesel over $LaCoO_3$, $LaCo_{0.8}Ni_{0.2}O_3$, $LaCo_{0.8}Ru_{0.2}O_3$, $LaCo_{0.8}Fe_{0.2}O_3$ and $LaCo_{0.8}Ga_{0.2}O_3$ derived catalysts (1023 K, 20,000 h^{-1}, $H_2O/O_2/C=3/0.5/1$).

4 Conclusions

Physicochemical characterization of samples revealed that the substitution of Co by Ni, Ru, Fe and Ga produced modifications in cell parameters, average crystallite size, surface area and reducibility. These changes lead to different surface expositions of Co M, and La_2O_3 phases on catalysts derived from the reduction of perovskite precursors. The catalyst derived from $LaCo_{0.8}Ru_{0.2}O_3$ was the most active and stable for the production of hydrogen due to the high exposition of Co^0, the intrinsic activity of Ru and the small crystallite size of La_2O_3 which improves the contact between this phase and Co-Ru, favouring the gasification of coke deposits. In the other extreme, the catalyst with Ga presents the lowest reforming activity as consequence of its high selectivity towards combustion.

Acknowledgements

This work was carried out within the framework of the Project “Development of a Diesel fuel processor” carried out by INTA, CIDAUT, AICIA and Instituto de Catálisis y Petroleoquímica

(CSIC). NM and MCAG acknowledge financial support from the MCYT in JAE program and in the Ramon y Cajal research program, respectively.

References

[1] A.F. Ghenciu Current Opinion in Solid State and Mat. Sci. 6 (2002) 389

[2] R.M. Navarro, M.A. Peña, J.L.G. Fierro, Chem. Rev., 107 (2007) 3952

[3] J.C. Amphlett**,** R.F. Mann, B.A. Peppley, P.R. Roberge, A. Rodrigues, J.P. Salvador *J. Power Sources* 71(1998) 179.

[4] R.M. Navarro, M.C. Álvarez-Galván, J.A. Villoria, I.D. González, F. Rosa, J.L.G. Fierro, Appl. Catal. B Environ. 73 (2007) 247

[5] N. Mota, M.C. Álvarez-Galván, J.A. Villoria, F. Rosa, J.L.G. Fierro, R.M. Navarro, Topics Catal. 52 (2009) 1995

[6] J. Guo, H. Lou, Y. Zhu, X. Zhen, *Materials Lett.* 57 (2003) 4450

[7] M.P. Pechini, United States Patent Office, 3, 330, 673 (1967)

[8] G. Sierra Galleg, C. Batiot-Dupeyra, J. Barrault, E. Florez, F. Mondragon, Appl. Catal. A: Gen. 334 (2008) 251

[9] M.A. Peña, J.L.G. Fierro, Chem. Rev. 101 (2001) 1981

Catalytic Processing of High-Sulfur Fuels for Distributed Hydrogen Production

Nazim Muradov, **Karthik Ramasamy**, **Cunping Huang**, **Ali T-Raissi**, University of Central Florida, USA

Abstract

In this work, the development of a new on-demand hydrogen production technology is reported. In this process, a liquid hydrocarbon fuel (e.g., high-S diesel) is first catalytically pre-reformed to shorter chain gaseous hydrocarbons (predominantly, C_1-C_3) before being directed to the steam reformer, where it is converted to syngas and then to high-purity hydrogen. In the pre-reformer, most sulfurous species present in the fuel are catalytically converted to H_2S. In the desulfurization unit, H_2S is scrubbed and converted to H_2 and elemental sulfur. Desulfurization of the pre-reformate gas is carried out in a special regenerative redox system, which includes Fe(II)/Fe(III)-containing aqueous phase scrubber coupled with an electrolyzer. The integrated pre-reformer/scrubber/electrolyzer unit operated successfully on high-S diesel fuel for more than 100 hours meeting the required desulfurization target of >95% sulfur removal.

1 Introduction

A major challenge facing future Hydrogen Economy is the issue of hydrogen fuel delivery to end-users. Due to an enormous cost of building a new hydrogen delivery infrastructure, in the interim, it might be economically feasible to deliver high-energy density hydrocarbon fuels (e.g., diesel fuel) and reform them to H_2 on-site. The advantages are three fold: (1) an existing fuel delivery infrastructure can be utilized, (2) more energy can be delivered per trip when the tanker is filled with diesel instead of liquid or compressed hydrogen, and (3) the fuel dispensing station would be able to service both internal combustion and fuel cell powered vehicles at the same time.

Reforming high-sulfur (high-S) hydrocarbon fuels is particularly challenging due to rapid deactivation of conventional reforming catalysts by sulfurous compounds, and it has been a focus of intensive worldwide R&D efforts with a particular emphasis on vehicular (on-board) applications (e.g., [1-4]). Moreover, if sulfurous compounds (mostly, H_2S) are not removed from the reformate gas, they could poison the catalysts in the anode compartment of FC substantially decreasing its performance or permanently damaging it [5]. Florida Solar Energy Center (FSEC), in collaboration with the Chevron Technology Ventures (CTV), has developed a new on-demand hydrogen production technology for distributed applications. The objective of this work is to catalytically convert high-S liquid hydrocarbon fuels to an essentially sulfur-free gaseous feedstock for steam reformation, while consuming only a fraction of hydrogen product. The experimental results on the development and performance testing of the catalytic pre-reformer and desulfurization systems are presented in this paper.

2 Experimental

Hexadecane (98% purity) was obtained from Fisher and used without further purification. Thiophene (99%) was obtained from Alpha Aesar and used as received. Commercial diesel fuel was purchased from a local Chevron gas station. Since commercial diesel fuel contains low levels of sulfur (approximately 5.5 ppmw), the fuel was supplemented with thiophene (C_4H_8S) to elevate the sulfur content to 3180-5240 ppmw level. This thiophene-spiked diesel was then used in all experiments as a surrogate high-S fuel. The same was carried out with hexadecane. Alumina-supported Ni-Mo hydroprocessing catalyst in the form of 1 mm by 5 mm extruded pellets was provided by Haldor Topsoe. The composition of the Ni-Mo catalyst was (%w/w): NiO (2-5), MoO_3 (12-18), Al_2O_3 (68-80), $AlPO_4$ (5-11). Analysis of the products of pre-reforming was performed by means of gas chromatography (GC) as follows: Shimadzu GC-14B (flame ionization detector, helium carrier gas, capillary column). Analysis of sulfurous compounds (H_2S, thiophene, methyl-mercaptan) was conducted using Perkin Elmer GC (flame photometric detector, capillary column).

3 Results and Discussion

Description of the concept. Fig. 1 depicts a simplified block-diagram of the process for conversion of a high-S fuel to hydrogen. A high-S liquid hydrocarbon fuel (e.g., diesel fuel) is first catalytically processed in a pre-reformer (or hydro-reformer) to shorter chain hydrocarbons (C_1-C_3) in the presence of hydrogen (this process is similar to a hydrocracking process, therefore, hereafter we will also refer to this process “hydro-reforming”). In the pre-reformer, most sulfurous species present in the fuel are catalytically converted to hydrogen sulfide (H_2S).

Desulfurization of the pre-reformate gas is carried out in a special regenerative redox system, which includes a Fe-based scrubber coupled with an electrolyzer. Ferrous/ferric (Fe^{2+}/Fe^{3+}) redox couple is used for scrubbing and splitting H_2S to sulfur and hydrogen:

$$2Fe^{3+}_{(aq)} + H_2S_{(g)} \rightarrow 2Fe^{2+}_{(aq)} + S_{(s)} + 2H^{+}_{(aq)} \quad (1)$$

$$2Fe^{2+}_{(aq)} + 2H^{+}_{(aq)} \rightarrow 2Fe^{3+}_{(aq)} + H_{2(g)} \quad \text{(electrolysis)} \quad (2)$$

$$\text{Overall: } H_2S_{(g)} \rightarrow H_{2(g)} + S_{(s)} \quad (3)$$

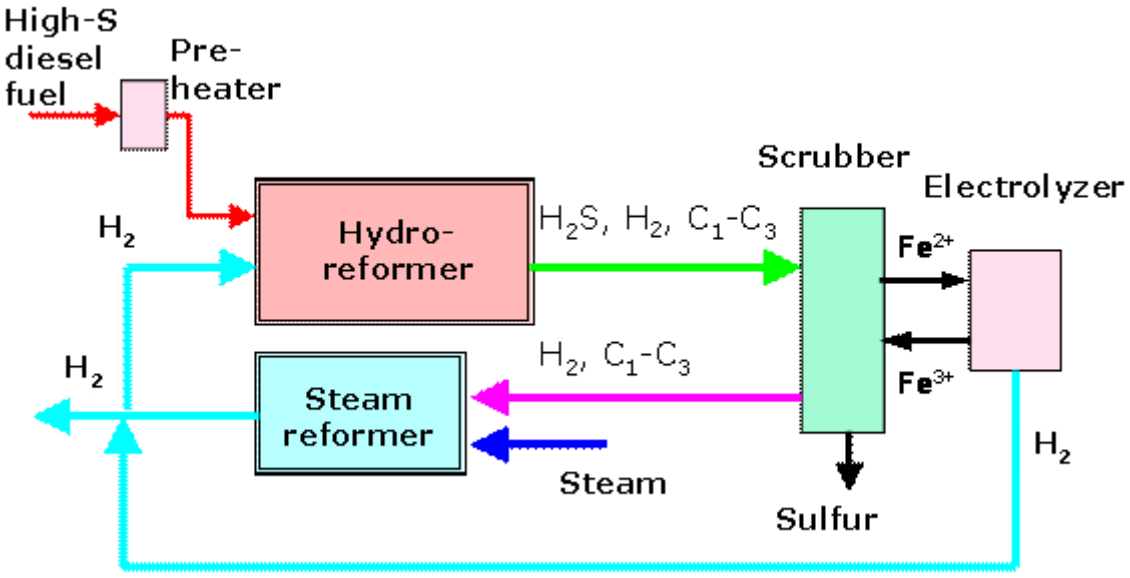

Figure 1: Block diagram of the proposed process for for conversion of high-S fuel to hydrogen.

Desulfurized pre-reformate gas is fed to the steam reformer, where it is mixed with steam and processed over Ni-catalyst to syngas. The syngas is further conditioned (or shifted) and purified (via pressure swing adsorption process) to high-purity H_2 according to a conventional steam methane reforming (SMR) process. A fraction of the output hydrogen product is recycled to the pre-reformer and used to conduct hydro-reforming of the high-S feedstock. It was estimated that the fraction of hydrogen product needed in the pre-reforming stage is in the range of 13-16%.

Hydro-reforming of high-S hexadecane and diesel fuel. Gas chromatogram of the effluent gas from high-sulfur (5240 ppm) hexadecane and diesel hydro-reforming over mixed Ni-Mo/Al_2O_3 - zeolite catalyst (1:2 ratio) at T=450 ^oC and P=14 atm is depicted in Figure 2, A and B, respectively.

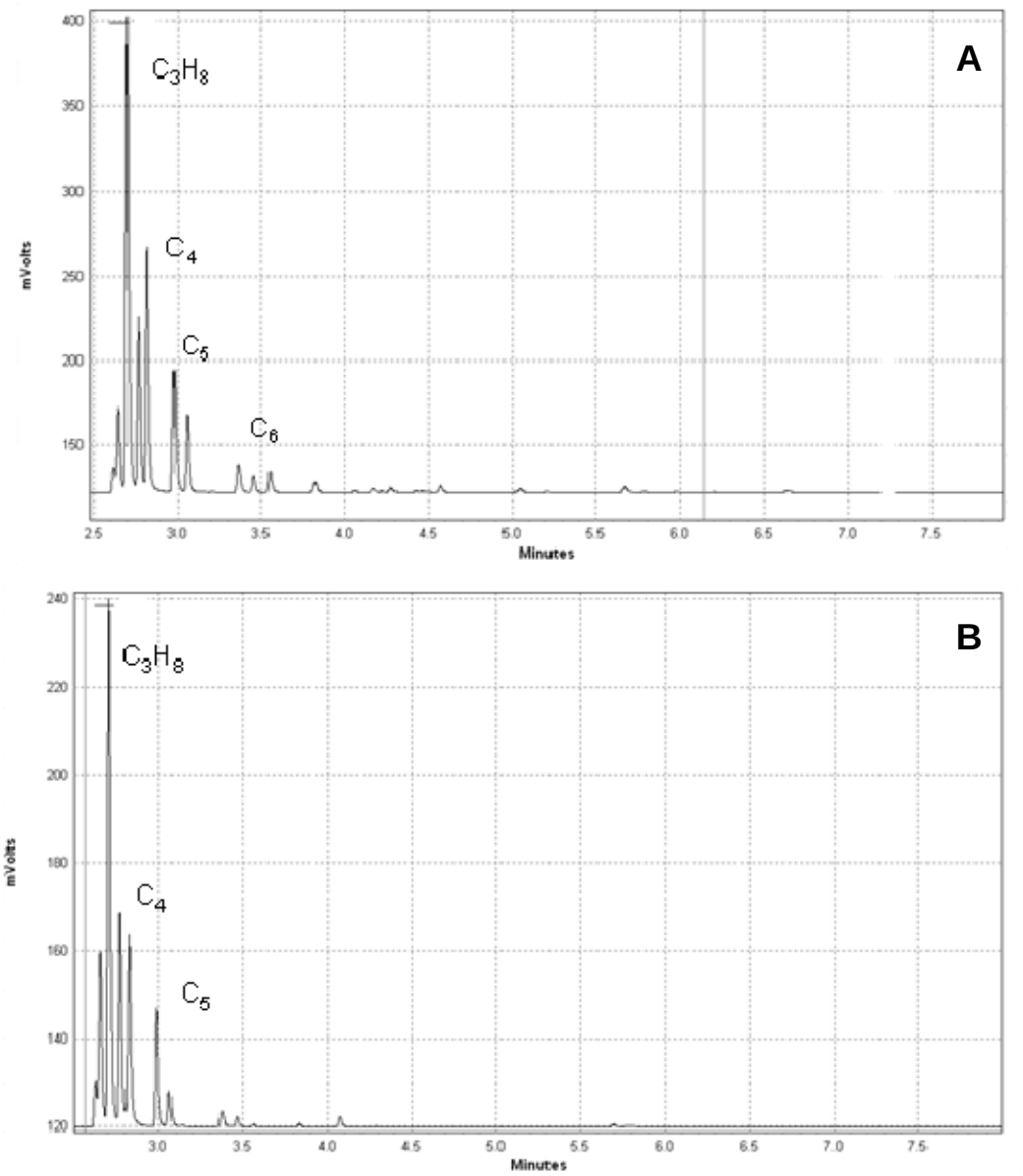

Figure 2: Gas chromotograms of the effluent gas from high-S hexadecane (A) and diesel fuel (B) hydro-reforming over mixed Ni-Mo/Al_2O_3 - zeolite catalyst (1:2 ratio). Thiophene content of the fuels: 5240 ppm. T=450 ^oC, P=14 atm.

The results revealed that the composition of the pre-reformate gas obtained from hexadecane and diesel fule are quite similar. After about 50 h a steady state regime is reached characterized by production of the pre-reformate gas consisting of C_1-C_5 hydrocarbons with propane being a predominant component of the product gas. There are practically no hydrocarbons higher than C_5 in the effluent gases. Overall, the experiment was run for about 100 h, with the average conversion of hexadecane and diesel fuel to gaseous products of 98% for and 95-97%, respectively.

Desulfurization of pre-reformate gas. Figure 3 provides a schematic diagram of the desulfurization sub-unit for the continuous removal of hydrogen sulfide from the pre-reformate gas and its splitting to hydrogen and sulfur.

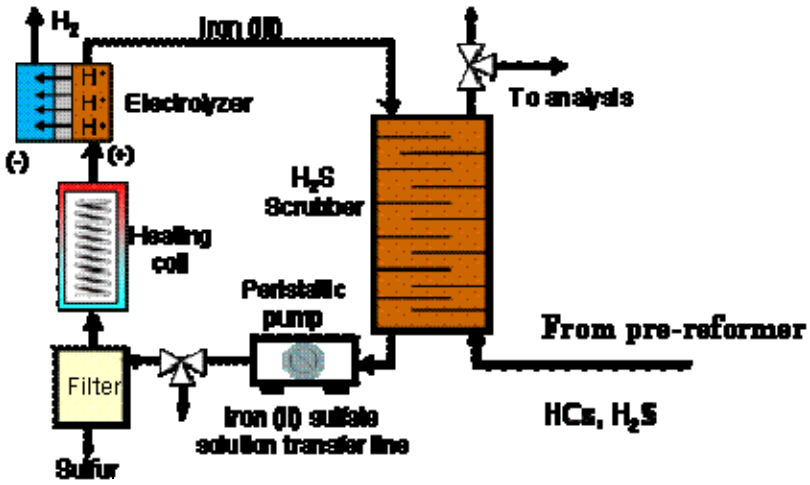

Figure 3: Schematic diagram of the desulfurization sub-unit for the continuous removal of hydrogen sulfide from the pre-reformate gas.

A gaseous mixture from the pre-reformer is directed to a scrubbing unit, which includes an absorption column filled with aqueous ferric sulfate solution, $Fe_2(SO_4)_{3(aq)}$ (total volume of solution 2.3 L). H_2S when dissolved in the aqueous solution is oxidized by ferric ion (Fe^{3+}) to elemental sulfur, and simultaneously ferric sulfate is reduced into ferrous sulfate, $FeSO_4$ (see Equation 1). Elemental sulfur is removed from the system by a filter, and the remaining ferrous sulfate solution is fed to an electrolyzer, where ferrous sulfate is oxidized back to ferric sulfate, and protons are reduced to hydrogen gas at the cathode. The regenerated ferric sulfate solution is then fed back to the absorption column of the scrubber for scrubbing hydrogen sulfide, forming a closed cycle with the net reaction being hydrogen sulfide decomposition to elemental sulfur and hydrogen gas. Electrolysis of acidic $FeSO_4$ aqueous solutions was carried out using a modified proton exchange membrane (PEM) electrolyzer. An electrolyzer potential of 0.80 to 1.03 volts was necessary for the electrochemical process to regenerate the scrubber solution at a rate sufficient to match the H_2S flow rate into the scrubber. The electrolytic system can be operated at the range of temperatures from ambient to 90 °C. In our experiments, desulfurization of the pre-reformate gas occurred optimally at the following process conditions: iron sulfate (total) concentration of 0.1 M, pH of 1.7-1.8, and electrolyte temperature of 50 °C.

In the combined diesel pre-reforming/desulfurization experiment, diesel fuel with 3180 ppmw of thiophene produced a pre-reformate gas with H_2S content of 185 ppmv, which was fed to the desulfurization unit. On average, about 3 ppmv of H_2S was detected exiting the ferric sulfate scrubber during the experiment. Based on the collected data from high-S diesel and hexadecane pre-reforming-desulfurization experiments, the fuel desulfurization yields were determined to be higher than 95%.

4 Conclusions

A novel process for converting high-sulfur diesel to hydrogen that employs a catalytic pre-reformer coupled with an efficient sulfur-scrubbing unit suitable for distributed hydrogen production applications has been developed. The integrated pre-reformer and sulfur-

scrubbing unit operated successfully for 100 hours, while achieving the desulfurization efficiencies of higher than 95%.

Acknowledgements

Financial support for this work was provided by the Florida Hydrogen Initiative (FHI) and Chevron Technology Ventures (CTV). Authors thank Haldor Topsoe and CTV for providing the samples of catalysts used in the experiments.

References

[1] C. Thomas, B. James, F. Lomax, I. Kuhn, Fuel options for the fuel cell vehicle: hydrogen, methanol or gasoline, Int. J. Hydrogen Energy 25 (2000) 551-567.

[2] A. Avchi, I. Onsan, D. Trimm, On-board fuel conversion for hydrogen fuel cells: comparison of different fuels by computer simulations, Appl. Catal. A: General 216 (2001) 243-256.

[3] L. Pettersson, R. Westerholm, State of the art of multi-fuel reformers for fuel cell vehicles: problem identification and research needs, Int. J. Hydrogen Energy 26 (2001) 243-264.

[4] Y. Jamal, M. Wyszinski, On-board generation of hydrogen-rich gaseous fuels – A review, Int. J. Hydrogen Energy 19 (1994) 557-572.

[5] J. Hirschenhofer, D. Stauffer, R. Engleman, M. Klett, Fuel Cell Handbook, U.S. DOE Technical Report DOE/FETC-99/1076, Morgantown, WV, 1999.

Obtaining Pure Hydrogen from Natural Gas Pyrolysis by Redox Processes

J.A. Peña, V. Ferreira, A. Marin, P. Duran, E. Romero, J. Herguido, Aragón Institute of Engineering Research (i3A), Universidad de Zaragoza, Spain

1 Introduction

"Steam Iron" is an old process devoted to "chemically" store and release pure hydrogen [1] which experienced its golden age in the early twentieth century. It needs a solid, usually iron oxide, which changes its oxidation state easily and reversibly. The method roughly consists in a first step where a hydrogen-containing gas reduces the oxide. In a second step, the reduced oxide replenishes its oxygen taking it from a steam stream, releasing hydrogen.

$$3\ Fe_2O_3 + H_2 \rightarrow 2\ Fe_3O_4 + H_2O \quad \text{(r.1)}$$

$$Fe_3O_4 + 4\ H_2 \leftrightarrows 3\ Fe + 4\ H_2O \quad \text{(r.2)}$$

The reduced material could be maintained for some time at open air and ambient conditions, offering the possibility of hydrogen "virtual" storing. With pure hydrogen feed, the method then only serves as "gas storage". With gas mixtures, appropriate conditions are needed to avoid the other compounds to adsorb or react with the solid.

An interesting way of obtaining hydrogen from natural gas without CO_2 releasing is the catalytic pyrolysis, where H_2 and C are the only products [1, 2]. As leaving gas also contains unreacted methane, a further hydrogen separation is mandatory. Thus the "steam-iron" process could suit well the needs of hydrogen purification if hydrogen reacts with the oxide and the other gaseous component remains unaltered. Nevertheless, the appropriate conditions must be carefully chosen, otherwise, carbon deposits could be formed on the solid (oxidized or reduced state) so that the subsequent hydrogen release would contain carbon species as unaccepted impurities (e.g. CO in PEMFC applications [3]). Possible reactions from methane are:

$$CH_4 \leftrightarrows C + 2\ H_2 \quad \text{(r.3)}$$

$$6\ Fe_2O_3 + CH_4 \leftrightarrows CO_2 + 4\ Fe_3O_4 + 2\ H_2 \quad \text{(r.4)}$$

$$Fe_3O_4 + 2\ CH_4 \leftrightarrows 2\ CO_2 + 3\ Fe + 4\ H_2 \quad \text{(r.5)}$$

In previous works, our research group has improved the iron oxide behavior by adding some other additives as aluminum and cerium oxides in small amounts [4]. This only fact rendered a considerable increase in the stability of the solid, since pure iron oxide loses its redox capacity quickly (in few cycles) [5]. Due to its low cost an iron oxide ore was also considered as testing material.

In this work these solids have used for carrying out the "steam-iron" process with a simulated gas coming from catalytic pyrolysis of natural gas. Hydrogen/methane ratio and temperature

have been varied to determine the conditions to avoid the methane decomposition during the reduction stage.

2 Experimental

The ternary oxide (98 mol% Fe_2O_3–1.5 % Al_2O_3–0.5 % CeO_2) was prepared in laboratory using the citrate method [6]. The ore contains 81 wt% Fe_2O_3, with SiO_2 (6 %), Al_2O_3 (2.5 %) and CaO (2.5 %) as main impurities. The experiments have been carried out in a quartz fixed bed reactor (45 mm length and 13 mm inner diameter). The concentration and temperature radial profiles can be considered neglected. The solid samples consisted of 3.75 g of Fe_2O_3 regardless of the hematite content of the samples. This ensures that the quantity of active species keeps constant allowing a better comparison. In all cases, this mass conformed 75 wt% of the solid sample and was complemented with another 25 wt% of crushed quartz acting as solid diluent. The particle diameter ranged from 160 to 250 μm.

In the reduction stage, a mixture (50 mol%) of hydrogen and methane (with 40/10, 30/20, 15/35 and 10/40 ratios) and argon (50 mol%) was fed with a flow rate of 250 Nml/min (ensuring no external diffusional limitations). The temperatures chosen for testing were 500, 525, 550 and 575 ºC. Given the dimensions of the reacting zone, an isothermal behaviour could be expected. It was also experimentally confirmed. Oxidation stages were performed with diluted steam in argon (25:75 by vol.) at the same experimental conditions than in the reduction process. Gas analysis was performed by GC.

A thermodynamic study was carried out to determine if methane reactions can take place and to obtain the threshold condition for methane decomposition, depending on temperature and H_2/CH_4 partial pressure ratio in the feed.

3 Results

Detection limits for measurement of CO and CO_2 at GC were determined to be 60 vppm. During reduction step no CO_2 was observed under any condition, so the reactions (r.4) and (r.5) could be considered neglected. In fact, reaction 5 has $\Delta G>0$, so is not thermodynamically favored. However, reaction (r.4) shows $\Delta G<0$ above 200 ºC. Hematite reduction is more rapid than magnetite reduction, but we must effectively consider that kinetics of reaction 4 probably result in a very slow process. However, under some experimental conditions, CO and/or CO_2 formation during oxidation steps were observed (Table 1). It evidences previous decomposition of methane (r.3) during reduction. This effect is boosted at low H_2/CH_4 ratios and high temperatures, as expected. Thus, at 500 ºC, the 20/30 ratio does not cause coke deposition while the 15/35 exhibits coke formation and methane conversion during reduction, and CO and CO_2 formation under the subsequent oxidation.

Thermodynamic calculations determine that the decomposition of methane is favored above 590 ºC. However, experimental results show (Table 1) that at lower temperatures methane reacts, as CO_x is detected in oxidation step. The reason can be found in the fact that during oxide reduction, metallic iron is formed. This metal can catalyze the decomposition of methane [7], lowering the reaction temperature from thermodynamic (thermal decomposition) value. This is valid as some hydrogen is present at feed, since hydrogen reduces the solid at

these temperatures. In the event of CH_4/Ar feeds (no hydrogen present), methane does not react up to higher temperatures.

Table 1: Results of CO_x formation during oxidation step with different temperatures and reduction feed ratios.

Feed mol% H_2/CH_4/Ar	10/40/50	15/35/50	20/30/50	30/20/50	40/10/50
Temperature	500 ºC	500 ºC	500 ºC	500 ºC	500 ºC
Ternary	CO: yes CO_2: yes	CO: yes CO_2: yes	CO: no CO_2: no	CO: no CO_2: no	CO: no CO_2: no
Ore	CO: yes CO_2: yes	CO: yes CO_2: yes	CO: no CO_2: no	CO: no CO_2: no	CO: no CO_2: no
Feed mol% H_2/CH_4/Ar	40/10/50	40/10/50	40/10/50	40/10/50	-
Temperature	500 ºC	525 ºC	550 ºC	575 ºC	-
Ternary	CO: no CO_2: no	CO: no CO_2: no	CO: no CO_2: no	CO: no CO_2: no	-
Ore	CO: no CO_2: no	CO: no CO_2: no	CO: no CO_2: no	CO: no CO_2: no	-
Feed mol% H_2/CH_4/Ar	30/20/50	30/20/50	30/20/50	30/20/50	-
Temperature	500 ºC	525 ºC	550 ºC	575 ºC	-
Ternary	CO: no CO_2: no	CO: no CO_2: no	CO: yes CO_2: yes	CO: yes CO_2: yes	-
Ore	CO: no CO_2: no	CO: traces CO_2: no	CO: yes CO_2: no	CO: yes CO_2: yes	-

The equilibrium constant (Figure 1) determines @ 500 ºC a H_2/CH_4 pressure ratio of 44/56. Ratios below it mean coke formation. Experimental results (ratio < 40/60) agree well with these calculations.

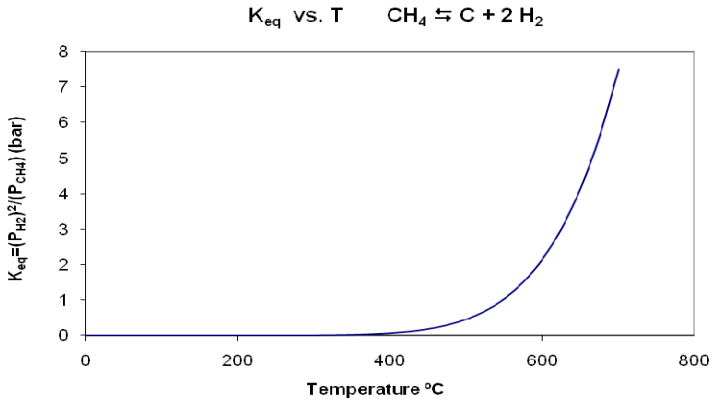

Figure 1: Equilibrium constant vs. temperature for the methane decomposition (r.3).

4 Conclusions

Gas from catalytic pyrolysis of natural gas (methane) has been proved to be suitable for use in the “steam-iron” process. This last can deal with hydrogen separation and purification (99.994 % in H_2 experimentally achieved along this work).

This is valid only under some feed and operating conditions. At 500 ºC, H_2/CH_4 ratios of 40/60 and above ensure no methane decomposition and hence hydrogen purification. Higher temperatures imply that this ratio must be also higher.

Typical streams from natural gas pyrolisis have a H_2/CH_4 ratio around 80/20 [2]. Therefore, operation temperatures up to 575 ºC are able to be used to purify hydrogen. This favors kinetics and shorter reaction times.

Small differences are found among the solids under study in separation/methane decomposition behavior. Both are useful for the pyrolysis gas streams.

References

[1] Otsuka, K., Mito, A., Takenaka, S., Yamanaka, I., Int. J. Hydrogen Energy, 26 (2001) 191-194.

[2] Muradov, M., Smith, F., Huang, C., T-Raissi, A., Catal. Today, 116 (2006) 281-288.

[3] Fuel Cells Handbook (Sixth Edition), EG&G Technical Services, Inc. to US Department of Energy (2002).

[4] Duran, P., Romero, E., Herguido, J., Peña, J.A., proc. I Simposium Iberico de hidrogeno, pilas de combustible y baterias avanzadas (HYCELTECH), Bilbao (Spain), 2008.

[5] Lorente, E., Peña, J.A., Herguido, J., Int. J. Hydrogen Energy, 33 (2008) 615-626.

[6] Kirchnerova, J., Alifanti, M., Delmon, B., Appl. Catal. A, 231 (2002) 65-80.

[7] Takenaka, S., Serizawa, M., Otsuka, K., J. Catal., 222 (2004) 520-531.

Low Temperature Hydrogen Production from Ethanol over Cerium and Cickel Based Oxyhydrides

Cyril Pirez, **L. Jalowiecki-Duhamel**, **M. Capron**, **F. Dumeignil**, UCCS Unité de Catalyse et de Chimie du Solide, Université des Sciences et Technologies de Lille, France

1 Introduction

In theory, hydrogen production from biomass or biomass derived liquids can be a carbon-emission free process since all carbon dioxide produced can be recycled back to plants using solar energy. Besides, ethanol is also safe, simple to handle, transport and store, so ethanol lends itself very well to a distributed-production strategy. A very interesting use of hydrogen is based on its conversion into power in fuel cell systems. The wide-spread application of fuel cells becomes closer to reality, so increased attention is focused on hydrogen production technology. Solid oxide fuel cells (SOFCs) are under development as energy production devices, they allow the use of carbon-monoxide resistant nickel anodes and the use of fuels different from hydrogen at the anode, in the so-called direct internal reforming SOFC. However the high operating temperatures undergo catalytic deactivation due to sintering of nickel crystallites and carbon deposition. Hence, worldwide efforts are in progress to discover novel, more active and more stable catalysts. Performing the reaction at lower temperature than 600 °C is a challenging goal.

$$C_2H_5OH + 3\ H_2O \rightarrow 2\ CO_2 + 6\ H_2 \quad (1)$$

Hydrogen production from ethanol steam reforming ($H_2O/C_2H_5OH = 3$) was investigated over cerium nickel $CeNi_XO_Y$ and ($0 < x \leq 5$) mixed oxide catalysts. The influence of different parameters was analysed, such as reaction temperature, Ni content and in-situ pre-treatment in H_2. While an ethanol conversion of 100 % is reached at 400 °C, a stable activity i.e. ethanol conversion, and H_2 selectivity can be obtained at very low temperature (200 °C) when the solid is previously in-situ treated in H_2 in a temperature range between 200 °C and 300 °C. In the present study, we report on H_2 formation activity over $CeNi_XO_Y$ catalysts for reforming of ethanol. The aim of this work was to develop a highly active, selective, stable and cost effective catalyst at relatively low temperature which should avoid carbon formation and also allow an application to fuel cells.

2 Experimental Methods

Catalytic performances were conducted at atmospheric pressure with a quartz fixed-bed reactor (inner diameter 10 mm) fitted in a programmable oven, in the temperature range of 50-480 °C. When noted, the catalyst was previously in situ treated in H_2 at 200 °C for 10 h. The water:ethanol mixture (molar ratio 3:1) is pumped into a heated chamber and vaporized. The water-ethanol gas (N_2) stream (total flow: 60 mL/min) is then fed to the reactor

containing 0.2 g of catalyst. The gases at the outlet of the reactor were taken out intermittently with the aid of a sampler directly connected to the system and analyzed on-line by FID and TCD gas chromatography. Reaction data were collected as a function of time and reported after about 5 h when the steady state was obtained for each temperature. Carbon is also formed but the quantity was not analyzed.

X-ray powder diffraction (XRD) analysis was carried out with a D 5000 Siemens diffractometer using a copper target and a secondary beam monochromator. The XRD patterns were registered in the 2θ domain (15-80 °) with a measured step of 0.02 ° and the time of integration was fixed to 12 seconds. The crystallites size was calculated using the Scherrer equation, from the most intense reflections observed for the NiO and CeO_2 crystallographic structures: (111), (200), (220).

Temperature-programmed reduction (TPR) was performed on a Micromeritics Autochem 2920 analyser, and hydrogen consumption was measured by a TCD detector: 25 mg of the sample was treated in the 5% H_2 – 95 % Ar gas mixture (2 l/h). The temperature was increased to 800 °C at a heating rate of 10 °C/min.

3 Results and Discussion

3.1 Characterization

Fig. 1 reports the diffraction patterns obtained with different $CeNi_XO_Y$ solids. A ceria like phase is apparent in every solid analyzed (*34-0394 JCPDS file*) while crystallized NiO (*4-0835 JCPDS file*) appears when $x \geq 0.4$. As already reported in previous studies for $CeNi_XO_Y$ compounds, a careful examination of the patterns shows that the addition of nickel affects not only the broadness of the ceria peaks, but also their position, attributed to the substitution of Ce^{4+} cations by Ni^{2+} cations inside the CeO_2 lattice and interpreted by the formation of a cerium-nickel solid solution. As a matter of fact, the nickel ionic radius (Ni^{2+}: 0.07 nm), is smaller than the cerium ionic radius (Ce^{4+}: 0.09 nm). It was reported that the highest proportion of solid solution is obtained for the $CeNi_{0.5}O_Y$ compound, as also observed here, when the molar ratio $Ni/M_T = 0.33$ (M_T = Ni + Ce, $Ni/M_T = x/(1+x)$). The studied $CeNi_XO_Y$ mixed oxides with $x < 0.4$ correspond to a solid solution with the substitution of Ni^{2+} ions in the CeO_2 lattice, to compounds in which crystallized NiO and solid solution coexist when $0.4 \leq x < 1$, and to a mixture of CeO_2 and NiO when $x > 1$.

The Temperature-Programmed Reduction (TPR) profiles in H_2 of the catalysts are shown in Fig. 2. A first temperature reduction peak at bout 270 °C is more intense for a low Ni content, when x = 0.1. When x increases from 0.1 up to 0.4 a second peak at about 370 °C increases. For higher Ni contents, the first peak decreases while the second peak shifts to higher temperatures (390 °C). It was already observed that a shoulder at 440 °C is emerging in the shape of the curve obtained for higher Ni contents. The reduction peak obtained at about 400 °C increases with the Ni content. For temperatures lower than 600 °C, a linear relationship is obtained between the total hydrogen consumed during TPR with the Ni content of the $CeNi_XO_Y$ compounds (Fig. 5), showing that H_2 is consumed in majority to reduce nickel species in this range of temperatures. The low temperature peak can be attributed to nickel species: i) belonging to the solid solution and/or to ii) small NiO particles, easily reducible, but with the simultaneous reoxidation of a part of these species by reduction

of the Ce^{4+} ions in their vicinity into Ce^{3+} species as the existence of a redox system was established (equations 2 and 3), then larger NiO crystallites are reduced when increasing temperature.

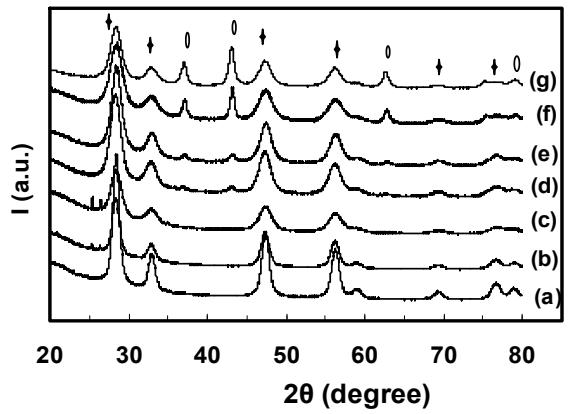

Figure 1: XRD patterns of CeNiXOY compounds. x = a) 0 b) 0.01 c) 0.2 d) 0.4 e) 0.5 f) 0.9 and g) 2.3. CeO2 (✦), NiO (O).

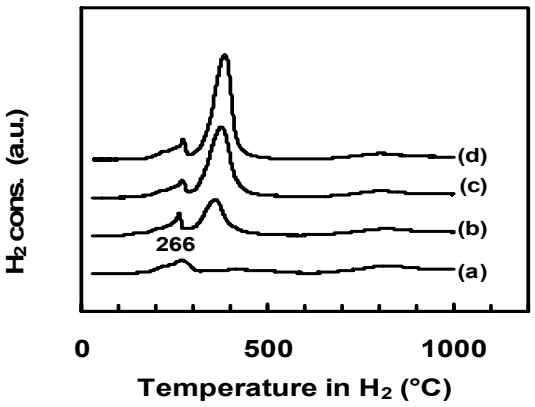

Figure 2: TPR of CeNiXOY compounds. x = a) 0.2, b) 0.4, c) 0.7 and d) 0.9.

3.2 Ethanol steam reforming

Ethanol transformation in presence of water was studied as a function of reaction temperature, activation treatment in H_2 and metal loading of $CeNi_XO_Y$ catalysts. Fig. 3 and 4 show, as examples, the results obtained over the fresh and treated in H_2 $CeNi_{0.5}O_Y$ catalyst versus reaction temperature. Over the fresh catalyst, an ethanol conversion is observed at temperatures higher than 300 °C, as expected it increases with temperature, and reaches 100 % at 480 °C (Fig. 3). When the $CeNi_{0.5}O_Y$ catalyst is previously in-situ treated in H_2 at 200 °C during 10 h, there is globally an increase versus temperature but with the existence of an optimum at about 30 % of conversion for a reaction temperature of 250 °C. Finally, total ethanol conversion is obtained at 480 °C and 400 °C over, respectively, the fresh and H_2 treated catalyst with about 50 % of H_2. So total ethanol conversion with about the same H_2 yield are obtained at 80 °C lower with an adequate pre-treatment of the catalyst in H_2.

Over the treated in H_2 $CeNi_{0.5}O_Y$ catalyst, the other products obtained are acetaldehyde, CO, CH_4 and CO_2 (Fig. 4). Whatever the temperature, ethylacetate and acetone formations are lower than 0.5 %. Acetaldehyde decreases with temperature and disappears at 400 °C. CO and CH_4 present optima at 250 °C following conversion (eq. 5), for temperatures higher than 300 °C CH_4 increases while CO remains at about 10 %. Concentration of CO_2 is lower than 1 % at 200 °C so as expected, the steam reforming of ethanol is negligible at these low temperatures, and it increases for higher temperatures.

Over the fresh $CeNi_{0.5}O_Y$ catalyst, between 200 °C and 300 °C the products observed are acetaldehyde and ethylacetate , typical of dehydrogenation reaction (with a very low ethanol conversion ~ 1%), and at 300 °C, H_2 is observed at about 70 %. Ethylacetate, acetaldehyde,

and acetone are found in concentration range between 5 and 10%, depending on the reaction temperature. For temperatures higher than 300 °C ethylacetate disappears, while acetone appears at 300 °C and presents an optimum of 10% at about 400 °C. CO_2 appears at temperatures higher than 250 °C and increases with temperature, while CO and CH_4 are formed at temperatures higher than 400 °C.

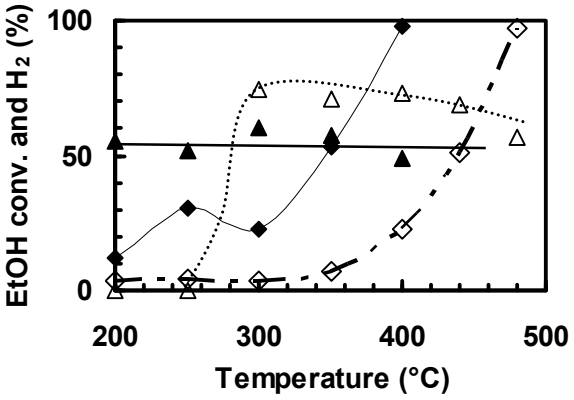

Figure 3: Ethanol conversion (◆,◇) and H_2 (▲,△) formation over fresh (white) and treated in H_2 at 200 °C (black) $CeNi_{0.5}O_Y$ catalyst.

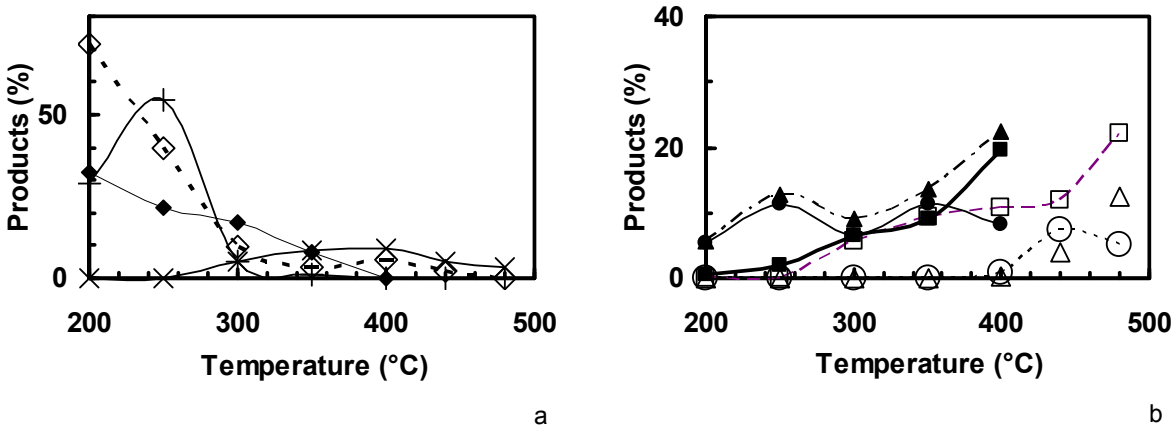

Figure 4: Products distribution obtained over fresh (white) and treated in H_2 at 200 °C (black) $CeNi_{0.5}O_Y$ catalyst. a) Acetaldehyde (◆,◇), ethylacetate (+) and acetone (x). b) CO_2 (□,■), CO (○,●) and CH_4 (▲,△). No ethylacetate, no acetone over treated in H_2 catalyst.

As the treatment in H_2 at 200 °C leads to a dramatic effect on H_2 formation at low temperatures (≤ 250 °C), the influence of the treatment temperature in H_2 was studied over the $CeNi_{0.7}O_Y$ chosen catalyst. As shown in Fig.5, ethanol conversion at 250 °C presents an optimum for a treatment temperature T_T in H_2 of 275 °C, following in a quite interesting way the first reduction peak seen by TPR. Moreover, the products distribution in the outlet gas stream depends also on the treatment temperature applied. H_2 is formed with treatment

temperatures in H_2 higher than 100 °C. For treatment temperatures T_T in H_2 lower than 200 °C, ethylacetate is the main product obtained with acetaldehyde as by-product. Formation of H_2 is optimum over a treated in H_2 at 200 °C catalyst, but for higher treatment temperatures it remains relatively stable. CH_4 and CO concentrations follow same evolutions; they present optima for $T_T \cong 275$ °C like conversion, and when acetaldehyde concentration presents a minimum.

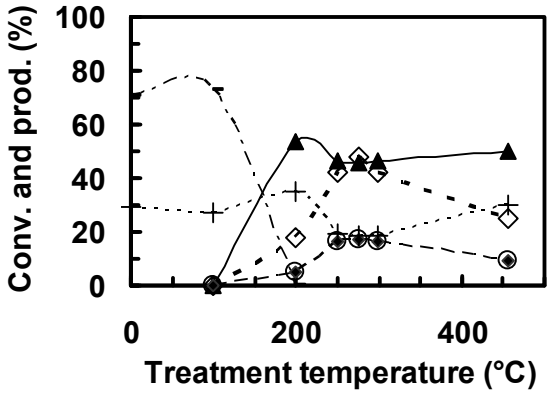

Figure 5: Ethanol conversion (◇) and products obtained at 250 °C over $CeNi_{0.7}O_Y$ catalyst versus treatment temperature in H_2. H_2 (▲) CH_3CHO (+), ethylacetate (-), CH_4 (◆), and CO (○). CO_2 (< 1%).

It is well known that physicochemical properties of a catalyst play an important role in the evolution of surface reactions. In ethanol transformation both dehydrogenation to acetaldehyde or dehydration to ethylene can occur upon the nature of the catalyst. Clearly, $CeNi_XO_Y$ catalysts possess good dehydrogenation properties, accentuated once treated in H_2 at 275 °C corresponding to the first TPR peak.

Besides, after an in-situ treatment in H_2 in particular between 200 °C and 300 °C, it was shown that the $CeNi_XO_Y$ solids studied become hydrogen reservoirs. During the activation treatment in H_2 in temperature, the anionic vacancies created are able to accept hydride species and the solids were called oxyhydrides.

Therefore, H_2 production from ethanol transformation certainly involves particular Ni species in strong interaction with Ce species. These Ni species are easily reducible and reoxidable by the presence of Ce in close vicinity (redox system). Clearly, the treatment in H_2 between 200 °C and 300 °C leads to a beneficial effect on H_2 production. It was shown that this treatment allows the $CeNi_XO_Y$ mixed oxides to accept large quantities of hydrogen by the presence of anionic vacancies. Therefore, over the fresh catalyst, up to 300 °C acetaldehyde and ethylacetate are observed and H_2 produced from ethanol is certainly consumed by the solid leading to a partially reduced compound. Taking into account that dehydrogenation step requires abstraction of hydrogen species from alcohol, the ability of the solid to accept hydrogen can be a prerequisite condition and “filling” the solid with hydrogen (during the pre-treatment in H_2) allows its formation from alcohol at low temperatures.

4 Conclusion

Ethanol transformation in presence of water was studied over $CeNi_XO_Y$ ($0 < x \leq 5$) catalysts. The cerium-nickel solid solution and/or small NiO particles (nanoparticles) involve Ni species presenting the characteristic of being able to be reduced and reoxidized easily and reversibly. The active nickel species belongs to the NiO particles and/or to the cerium nickel solid solution where Ni species are in strong interaction with Ce species. Hydrogen can be produced at low temperature $\leq$ 250 °C once the $CeNi_XO_Y$ mixed oxides are previously in-situ treated in H_2 at about 250 °C leading to the formation of oxyhydrides. Finally, an active site is proposed based on the presence of anionic vacancies able to abstract hydride species from ethanol.

Optimum Temperature Policy for Sorption Enhanced Steam Methane Reforming Process for Hydrogen Production

Rajasree Retnamma[*], Energy Systems Modeling and Optimization Unit (UMOSE), National Laboratory of Energy and Geology (LNEG), Lisbon, Portugal
V. Ravi Kumar, **B.D. Kulkarni**, Chemical Engineering and Process Development Division, National Chemical Laboratory, Pune, India

Abstract

Sorption enhanced steam methane reforming (SE-SMR) process offers high potential for producing H_2 in fuel cell applications compared to conventional catalytic steam methane reforming (SMR) process. The reactor temperature can significantly affect the performance of the SE-SMR reaction and simultaneous adsorption behavior of CO_2. Determination of an optimal temperature policy in SE-SMR reactor is therefore an important optimization issue. Multi-stage operation is a possible way to implement optimum temperature policies. In the present work, simulation study has been carried out for multi-stage operation using a mathematical model incorporating basic mechanisms operating in a fixed bed reactor with nonlinear reaction kinetic features of an SE-SMR process. Three cases were considered for implementing the multi-stage concept and the results show that increase in temperature based on a policy leads to considerable improvement in the process performance.

1 Introduction

Sorption enhanced steam methane reforming (SE-SMR) process couples reaction and separation in a single unit and is attractive for producing H_2 in fuel cell applications. SE-SMR process uses a fixed packed column of an admixture of a SMR catalyst and an adsorbent. The adsorbent selectively removes carbon dioxide from the reaction zone and this enhances the conversion of CH_4 to H_2. The adsorbent is cyclically regenerated by using the principles of pressure swing adsorption. The reaction is highly endothermic and the determination of an optimal temperature profile is required for reducing the costs and improving the overall efficiency of operation. Coupled with multi-stage operation, it may be attractive for implementing an optimum temperature policy.

In the present work, a simulation study has been carried out on multi-stage SE-SMR process to predict optimum temperature policies for sorption enhanced steam methane reforming (SE-SMR) process. A dynamic model based on multi-component and overall mass balance, pressure distribution in the packed bed, energy balance for the bed-volume element, and non-linear Langmuir adsorption equilibrium isotherm coupled with a general reaction kinetic model was considered to predict the performance of the SE-SMR process. The linear driving force (LDF) model was used to describe the mass-transfer limited adsorption kinetics. Investigations were carried out (i) keeping inlet temperature constant for all stages (ii) step

[*] Corresponding author, email: rajasree.nair@ineti.pt

wise increase of temperature in stages to achieve maximum temperature in the last stage and (iii) increase of temperature based on a policy. The results show that increase of temperature based on a policy leads to considerable improvement in the process performance.

1.1 Mathematical model

The key chemical reactions of the SE-SMR process are given by:

$$CH_4 + H_2O \Leftrightarrow CO + 3H_2, \quad \Delta H_{298} = 206.2\ \text{kJ/mol} \tag{1}$$

$$CH_4 + 2H_2O \Leftrightarrow CO_2 + 4H_2, \quad \Delta H_{298} = 164.9\ \text{kJ/mol} \tag{2}$$

$$CO + H_2O \Leftrightarrow CO_2 + H_2, \quad \Delta H_{298} = -41.1\ \text{kJ/mol} \tag{3}$$

The mathematical model used to describe the SE-SMR process is a dynamic model and considers the non-isothermal, non-adiabatic, and non-isobaric nature of operation. The model assumptions used are:

- Axial dispersed plug flow prevails in the bed.
- Mass dispersion in the axial direction is considered.
- Mass dispersion in the radial direction is assumed to be negligible.
- The system is non-isothermal. Thermal dispersion in the axial direction is considered.
- The reaction kinetic model employed is that proposed by Xu and Froment (1989).
- Volumetric change of flow due to adsorption and reaction is taken into account in the overall material balance.
- The gas is assumed to be an ideal gas.
- The adsorbent and catalyst particles are the same size and spherical in shape.
- The pressure distribution in the packed bed adsorptive reactor is described by Ergun equation.
- The gas phase and the catalyst/adsorbent particles are assumed to be in local mass/thermal equilibrium at all times.
- The non-linear Langmuir model is used to describe the multi-component adsorption equilibrium isotherm.
- Linear driving force (LDF) model is used to represent the adsorption rate mechanism.

For the above assumptions, the reaction kinetic model, governing equations, and initial and boundary conditions are summarized below.

1. The reaction kinetic model:

   The reaction kinetic model proposed by Xu and Froment (1989) are:

$$R_I = \frac{1}{\alpha^2}\frac{k_1}{P_{H_2}^{2.5}}\left(P_{CH_4}P_{H_2O} - \frac{P_{H_2}^3 P_{CO}}{K_I}\right) \quad (4\text{ a})$$

$$R_{II} = \frac{1}{\alpha^2}\frac{k_2}{P_{H_2}^{3.5}}\left(P_{CH_4}P_{H_2O}^2 - \frac{P_{H_2}^4 P_{CO_2}}{K_{II}}\right) \quad (4\text{ b})$$

$$R_{III} = \frac{1}{\alpha^2}\frac{k_3}{P_{H_2}}\left(P_{CO}P_{H_2O} - \frac{P_{H_2} P_{CO_2}}{K_{III}}\right) \quad (4\text{ c})$$

$$\alpha = 1 + K_{CO}P_{CO} + K_{H_2}P_{H_2} + K_{CH_4}P_{CH_4} + \frac{K_{H_2O}P_{H_2O}}{P_{H_2}} \quad (4\text{ d})$$

   The formation or consumption rate r_i is then calculated by

$$r_i = \sum_{j=I}^{III} \eta_j \upsilon_{ij} R_j \quad (i = \mathrm{CH_4}, \mathrm{H_2O}, \mathrm{H_2}, \mathrm{CO_2}, \mathrm{CO}) \quad (5)$$

2. The overall mass balance equation:

$$\varepsilon_t \frac{\partial C}{\partial t} + \frac{\partial (uC)}{\partial z} + \rho_{ad} \sum_{i=1}^{n} \frac{\partial \bar{q}_i}{\partial t} - \rho_{cat} \sum_{i=1}^{n} \sum_{j=I}^{III} \upsilon_{ij} \eta_j R_j = 0 \quad (6)$$

3. The component mass balance for component i in the gas phase:

$$\varepsilon_t \frac{\partial C_i}{\partial t} + \frac{\partial (uC_i)}{\partial z} + \rho_{ad} \frac{\partial \bar{q}_i}{\partial t} - \rho_{cat} \sum_{j=I}^{III} \upsilon_{ij} \eta_j R_j = \varepsilon_b \frac{\partial}{\partial z}\left(D_L \frac{\partial C_i}{\partial z}\right) \quad (7)$$

   where, DL, the axial dispersion coefficient is evaluated by the correlation given by Edwards and Richardson (1968).

4. Pressure distribution:

   The pressure distribution in the reactor is described by Ergun equation (Ergun, 1952)

$$\frac{\partial P}{\partial z} = -K_D u - K_V u^2 \quad (8)$$

5. Adsorption Equilibrium:

   The multi-component Langmuir adsorption isotherm used to describe the adsorption equilibrium is

$$q_i^* = \frac{m_i b_i P_i}{1 + \sum_{j=1}^{n} b_i P_i} \quad (9)$$

6. Mass transfer rate:

   The Linear Driving Force (LDF) model used to describe the mass transfer of the adsorbate to the adsorbent is

$$\frac{\partial \bar{q}_i}{\partial t} = k_{fi}\left(q_i^{*} - \bar{q}_i\right) \tag{10}$$

   The Langmuir and LDF parameters used were as reported by Ding and Alpay (2000 a).

7. The energy balance for the bed-volume element:

$$\left[\varepsilon_t CC_{vg} + \left(\rho_{ad} + \rho_{cat}\right)C_{ps}\right]\frac{\partial T}{\partial t} + CC_{pg}u\frac{\partial T}{\partial z} - \rho_{ad}\sum_{i=1}^{n}\left(-\Delta H_{ad_i}\frac{\partial \bar{q}_i}{\partial t}\right) - \frac{2U}{R_0}\left(T_W - T\right) - \rho_{cat}\sum_{i=1}^{n}\sum_{j=I}^{III}\upsilon_{ij}\eta_j R_j \Delta H_{Rj} = \frac{\partial}{\partial z}\left(k_z\frac{\partial T}{\partial z}\right) \tag{11}$$

   where, k_z is the bed effective conductivity and is calculated using the correlation given by Yagi et al., (1960). The correlation proposed by Li and Finalyson (1977) and De Wasch and Froment (1972) is considered for calculating the wall-bed heat transfer coefficient U.

8. Initial Conditions:

   The initial conditions (at t = 0) used in the present study are as follows:

$$T = T_f,\ P_{H_2} = P_f,\ \bar{q}_i = 0$$

$$C_{H_2} = \frac{P_{H_2}}{RT_f},\ C_i = 0,\ (i = CH_4, H_2O, CO, CO_2). \tag{12}$$

   where T_f and P_f are feed gas temperature and pressure, respectively.

9. Boundary conditions:

   The following boundary conditions are used in the simulations

   (i) Reactor inlet ($z = 0$)

$$-\varepsilon_b D_L\left(\frac{\partial C_i}{\partial z}\right) = u_f\left(C_{fi} - C_i\right) \tag{13 a}$$

$$-k_z\left(\frac{\partial T}{\partial z}\right) = u_f CC_{pg}\left(T_f - T\right) \tag{13 b}$$

$$u = u_f,\ P = P_h \tag{13 c}$$

   (ii) Reactor outlet ($z = L$)

$$\frac{\partial C_i}{\partial z} = 0, \quad \frac{\partial T}{\partial z} = 0 \tag{13 d}$$

$$\frac{\partial u}{\partial z} = 0, \quad \frac{\partial p}{\partial z} = 0 \tag{13 e}$$

This is a complex system involving both reaction and separation. The reaction equilibrium constants and reaction rate constants are temperature-dependent. The adsorption

equilibrium isotherm is non-linear in nature and the equilibrium isotherm constants depend on temperature, pressure and vary with wet and dry feed conditions. Also, the above equations are coupled and cause steep composition gradient in the reactor. Equations 4-11 with appropriate initial and boundary conditions (equations 12-13) were numerically solved by finite difference method for predicting the H_2 production in the SE-SMR process. In this simulation 40 grid points along the reactor were used to obtain stable numerical solutions.

1.2 Results and discussion

Simulated results for the breakthrough curves and single stage operation were validated with experimental data given by Ding and Alpay (2000a, 2000b) for testing the accuracy of the numerical method. Three cases are considered for implementing the multi-stage concept and the results obtained are discussed below. The parameters used were as reported by Alpay (2000 b), except the column length is 0.44 m instead of 0.22 m. The maximum allowable temperature is 843 K for all three cases.

1.2.1 Case 1: Inlet temperature is kept constant at maximum feed temperature for all stages

In this case, inlet temperature of all stages is maintained at 843 K. The temperature profiles and H_2 profiles for single stage and multi-stage (2 and 3 stages) under steady state (obtained by solving the dynamic model) is plotted in figures 1-2 respectively. It is clear from figure 2 that there is not significant improvement in the process between single stage and multi-stage operation (2 and 3).

1.2.2 Case 2: Step wise increase of temperature in each stage to attain maximum feed temperature in the last stage

In this operation, maximum temperature is attained in the reactor by step wise increase of temperature in each stage, which depends on the number of stages, maximum allowable temperature and the temperature of the first stage. i.e., if there are N stages and T_{max} is the maximum allowable temperature, then temperature at the inlet of N^{th} stages is given by

$T_N = T_{N-1}+\Delta T$, where $\Delta T = (T_{max}-T_1)/N-1$ for $N > 1$.

Where, T_1 is the temperature of stage 1. The temperature profiles and H_2 profiles for single stage and multi-stage (2 - 6 stages) under steady state (obtained by solving the dynamic model) along the reactor is plotted in figures 3-4. It is evident from figure 4 that H_2 mole fraction along the reactor decreases with number stages.

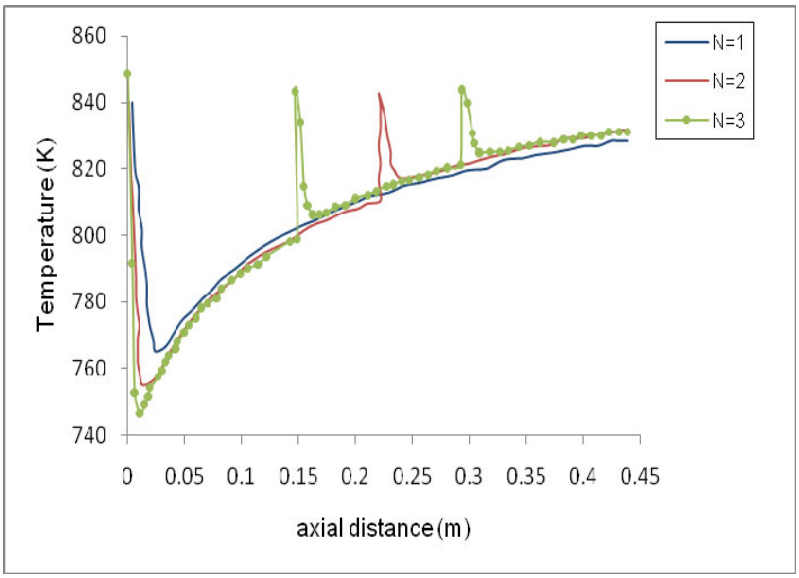

Figure 1: Temperature profiles with number of stages: Case 1.

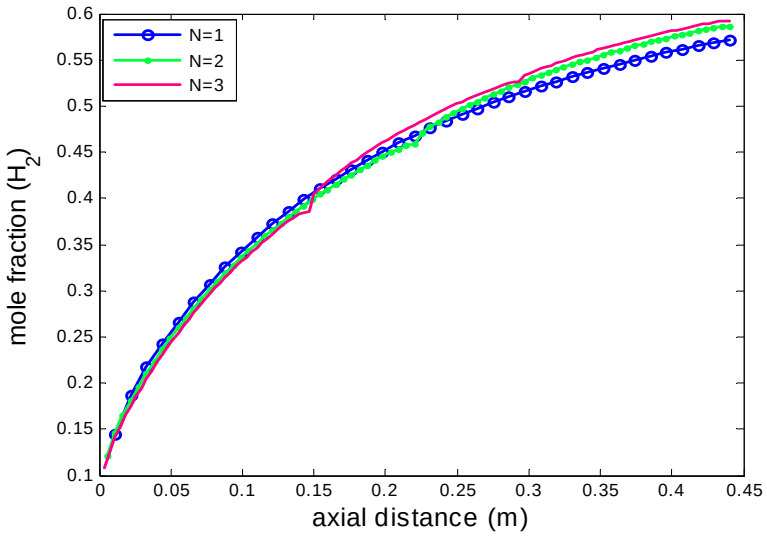

Figure 2: Concentration profiles of H_2: Case 1.

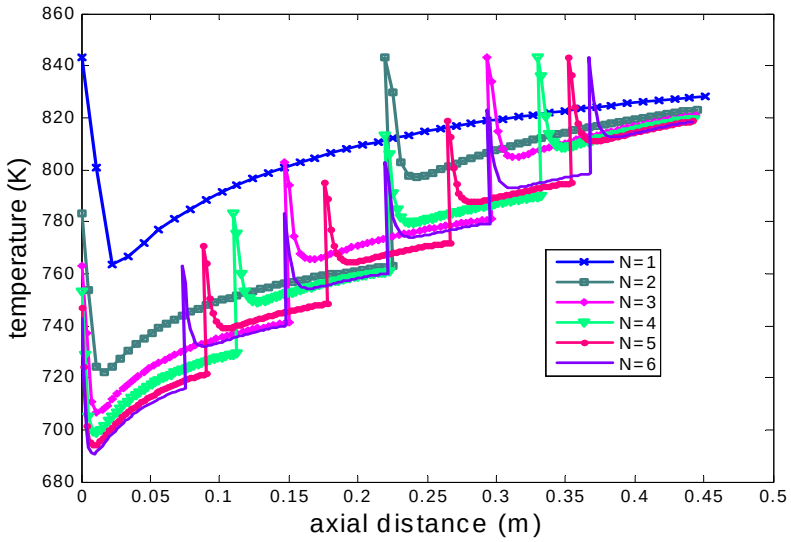

Figure 3: Temperature profiles with number of stages: Case 2.

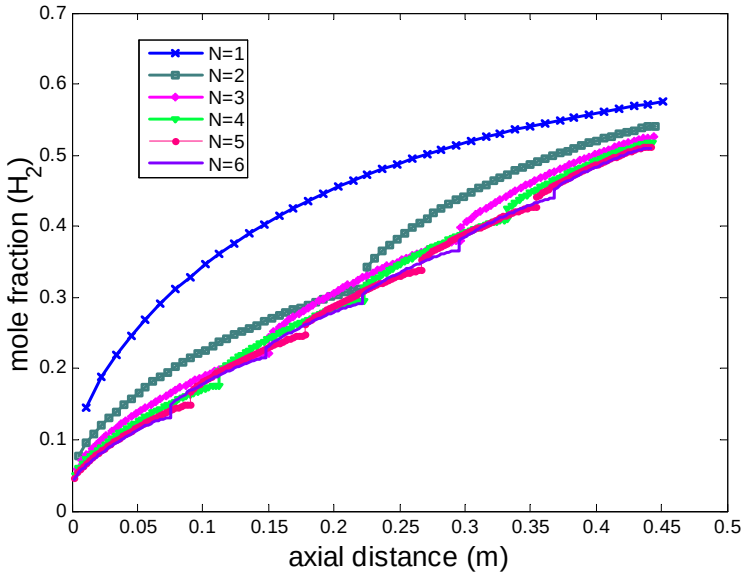

Figure 4: Concentration profiles of H_2: Case 2.

1.2.3 Case 3: Increase of temperature in each stage based on a policy

In this case, the inlet temperature of each stage is increased based on a policy with an aim to obtain an optimum temperature policy. An initial study with the temperature of the first stage is kept at 743 K and is increased by 20 K in the subsequent stages till the inlet temperature of a stage reaches 843 K was carried out to compare the results with the cases mentioned earlier. The temperature profiles and H_2 profiles for single stage and multi-stage (2 -6 stages) under steady state (obtained by solving the dynamic model) along the reactor is given in figure in figures 5-6. It is clear from figure 6 that there is a significant improvement in the process with multi-stage operation compared to a single stage.

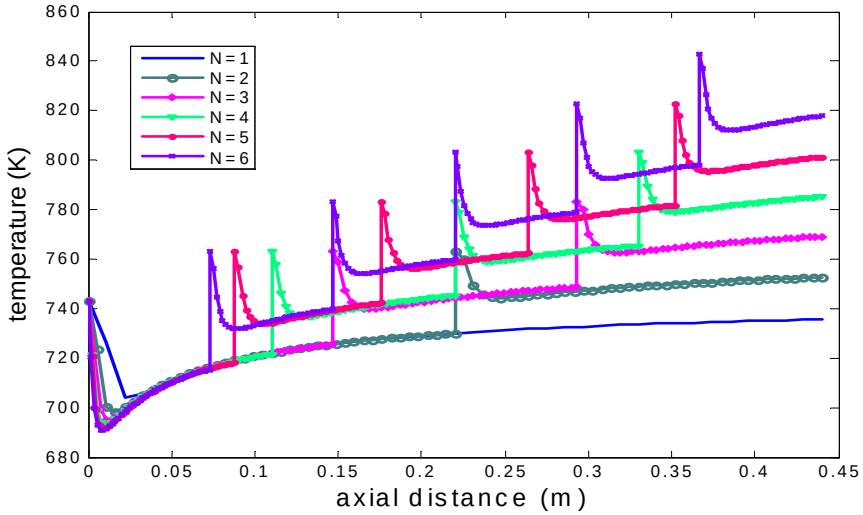

Figure 5: Temperature profiles with number of stages: Case 2.

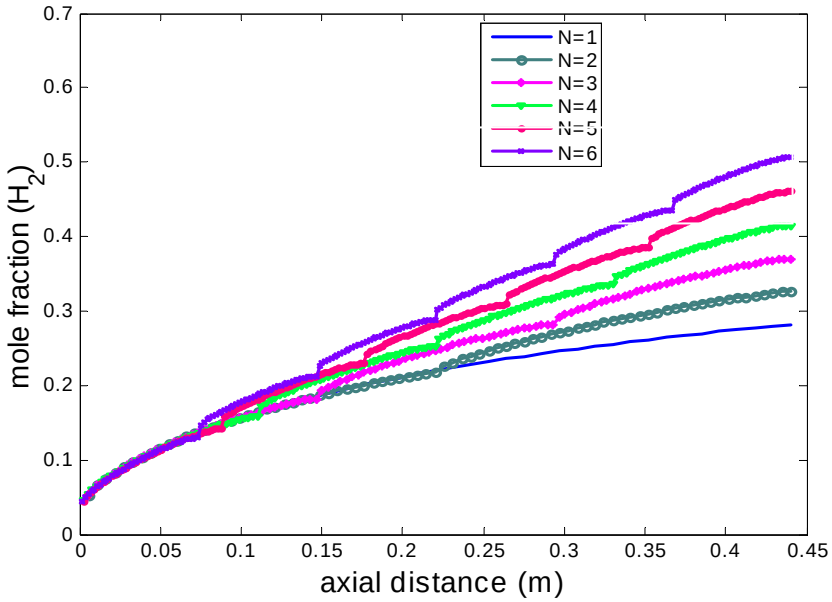

Figure 6: Concentration profiles of H_2: Case 3.

2 Conclusions

Simulation studies have been carried out for multi-stage operation of sorption enhanced steam methane reforming process for producing H_2 in fuel cell applications. Investigations on the influence of multi-stage operations led to the following conclusions: (1) there is not significant improvement in the performance of the process if the inlet temperatures of all stages are constant, (ii) step wise increase of temperature in stages to achieve maximum temperature in the last stage adversely affects the process performance, and (iii) increase of temperature based on a policy leads to considerable improvement in the process performance. The above simulation studies on multi-stage operation give insights for an

optimal temperature policy implementation in SE-SMR process for improved reactor performance.

Acknowledgement

R.R. acknowledges the Council of Scientific and Industrial Research (CSIR), New Delhi, for financial support.

Nomenclature

b_i Langmuir constant for component *i*, Pa^{-1}

c Total molar concentration in the bulk phase, mol/m^3

$c_{f\,I}$ Molar concentration of component i in the feed, mol/m^3

c_i Molar concentration of component *i*, mol/m^3

c_{pg} Gas-phase heat capacity, J/mol. K

c_{ps} Solid-phase heat capacity, J/kg. K

D_L Axial dispersion coefficient, m^2/s

$k_{f\,i}$ LDF mass-transfer coefficient of component *i*, s^{-1}

k_i Rate constant of reaction *i*, *i* = 1, 2; mol $Pa^{0.5}$/kg-cat. s, *i* = 3; mol/kg-cat. s. Pa

k_z Effective thermal conductivity, J/m.s.K

K_D Ergun equation coefficient, $N.s/m^4$

K_i Equilibrium constant of reactions (1)-(3), *i* = I, II; Pa^2, *i* = III; dimensionless

K_V Ergun equation coefficient, $N.s^2/m^5$

K_j Adsorption coefficient for component *j* (on catalyst surface), *j* = CO, H_2, CH_4; Pa, *j* = H_2O; dimensionless

k_z Effective thermal conductivity, J/m.s.K

L Reactor length, m

m_i Langmuir model constant for component *i*, mol/kg

P Local total pressure, Pa

P_h Feed pressure, Pa

P_i Partial pressure of gas-phase component *i*, Pa

$\bar{q}_i$ Solid phase concentration for component *i* (averaged over an adsorbent particle), mol/kg

q_i^* Equilibrium solid concentration, mol/kg

r_i Formation or consumption rate of component *i*, mol/kg-cat. s

R Universal gas constant, J/mol. K

R_0 Inner radius of the reactor, m

R_j Rate of reaction *j* (*j* = 1-3), mol/kg-cat.s

T time, s

T Temperature in bulk gas-phase, K

T_f Feed gas temperature, K

T_0 Initial bed temperature, K

T_w Wall temperature, K

u Superficial velocity, m/s

u_f Initial superficial velocity, m/s

U Overall bed-wall heat-transfer coefficient, J/m^2 . K

z Axial coordinate in the reactor, m

Greek letters

ε_b Bed porosity, dimensionless

ε_t Total bed porosity, dimensionless

η_i Catalyst effectiveness factor, dimensionless

ρ_{ad} Mass of adsorbent per bed volume, kg/m^3

ρ_{cat} Mass of catalyst per bed volume, kg/m^3

υ_{ij} Stoichiometric coefficient of component *i* in reaction *j*, dimensionless

$-\Delta H_{adi}$ Adsorption heat of component *i*, J/mol

ΔH_{Ri} Reaction heat of reaction *i*, J/mol

References

[1] A.P. De Wash, G.F. Froment, Chem. Engg. Sci. 27 (1972) 567.

[2] Y. Ding, E. Alpay, Chem. Engg. Sci., 55 (2000 a) 3461.

[3] Y. Ding, E. Alpay, Chem. Engg. Sci., 55, (2000 b) 3929.

[4] M.H. Edwards, J.F. Richardson, Chem. Engg. Sci. 23, (1968) 109.

[5] S. Ergun, Chem. Engg. Sci. 48 (1952) 89.

[6] C-H. Li, B.A. Finalayson, Chem. Engg. Sci. 32 (1977) 1055.

[7] J. Xu, G.F. Froment, N. Wakao, AIChE J. 35 (1989) 88.

[8] S.Yagi, D. Kunii, AIChE J., 35 (1989) 97.

Hydrogen Production from Natural Gas Thermal Cracking: Design and Test of a Pilot-scale Solar Chemical Reactor

Sylvain Rodat, **Stéphane Abanades**, **Gilles Flamant**, Processes, Materials, and Solar Energy Laboratory, CNRS-PROMES, Font-Romeu, France

Solar methane dissociation offers the possibility for the clean co-production of hydrogen and carbon black [1-2]. It appears as an alternative to the steam methane reforming and the furnace process [3] dedicated to the conventional production of hydrogen and carbon black, respectively. The solar process avoids both CO_2 emissions from fossil fuel combustion required to carry out the endothermic reaction and from the reaction of steam reforming. Indeed, the energy supplied by fossil fuel combustion is replaced by concentrated solar energy and methane cracking results in solid carbon and hydrogen only.

Maag et al. [4] developed a direct heating solar reactor seeded with particles. Direct solar heating was also experienced by Kogan et al. [5] with a tornado flow configuration. Indirect heating reactors based on tubular designs were proposed by Dahl et al. [6] and Rodat et al. [7]. The investigation of reaction kinetics was also addressed [8-10]. Nevertheless, the previous developed reactors did not exceed 10 kW scale. In order to acquire more experience towards a potential industrial application, a 50 kW multi-tubular solar reactor was constructed, tested, and simulated. This paper presents the experimental results related to the performances of this pilot-scale solar reactor.

1 Experimental Set-up

The reactor was designed for a nominal power of 50 kW of incident solar power (Figure 1). The reactor body is made of an aluminium shell (800x780x505 mm) and a water-cooled front face with a 13 cm-diameter aperture to let concentrated solar radiation entering within the reactor cavity. The radiations are absorbed by the graphite cavity (360x400x300 mm) that approaches a black body behaviour. To avoid contact of graphite with the oxidizing atmosphere, the opening is protected by a domed quartz window (outer diameter of 360 mm) swept by a nitrogen flow to avoid overheating. The space between the graphite cavity and the aluminium shell is filled with three different insulating layers to limit conduction losses. Seven graphite tubes (800 mm length, 26 mm OD, 18 mm ID) cross the graphite cavity horizontally and they are heated both by direct solar radiation and by IR-radiation from the hot graphite cavity walls. Each tube is fed with a mixture of argon and methane thanks to 2 mass-flow controllers dedicated to each tube (total of 14 mass-flow controllers). Each tube entrance is equipped with an absolute pressure sensor. At the exit, the products (particles and gases) from the tubes are collected and cooled down and then, they are directed towards a filter composed of 6 bags enabling the separation of the carbon black from the gaseous phase that is evacuated to the vent. Before this filter, a sampling pump is used to bypass a part of the products towards a secondary filter for gas analysis. The gas analysis system is composed of an online analyser for measuring hydrogen and methane concentrations (NGA 2000 MLT3) as well as a gas chromatograph (micro GC Varian CP

4900) for quantifying the gas species in the course of the experiment. The temperatures in the reactor are measured by five thermocouples and by one solar blind optical pyrometer (wavelength: 5.14 µm). Two type B thermocouples are set in contact with the graphite cavity, one at the top (B_top), another at the back (B_back). At about the same location, K-thermocouples (K_top and K-back) measure the temperature at a depth of 5 cm (from the aluminium shell surface) in the insulated zone. In addition, a type B thermocouple is inserted 24 cm inside the lowest graphite tube on which the optical pyrometer is also pointing, thus giving a redundant measurement of the reaction zone by two different means.

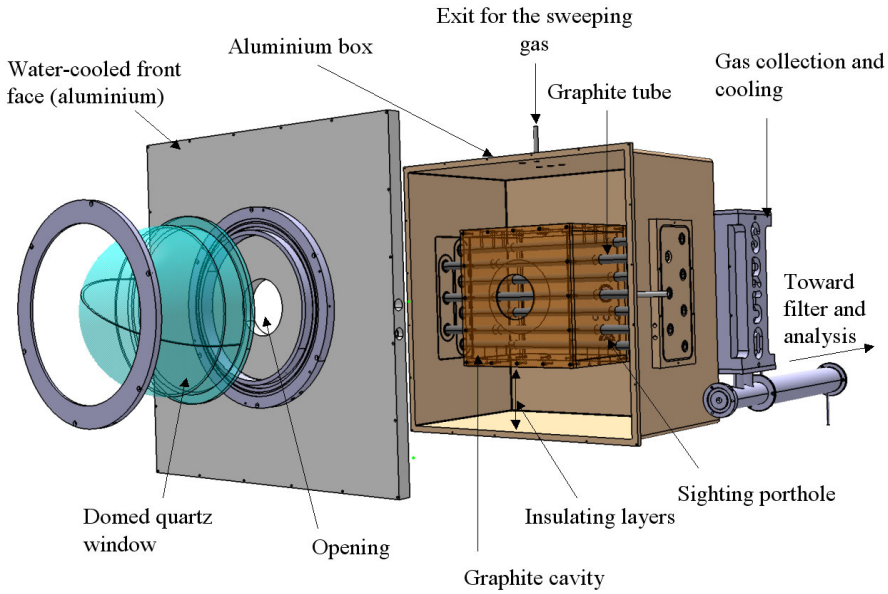

Figure 1: Scheme of the pilot-scale solar reactor.

An experimental run is composed of two steps. The first step is the heating of the reactor under concentrated solar irradiation coming from the 1 MW solar furnace of CNRS-PROMES. During this period, the tubes are fed with pure argon till the targeted temperature is reached. Then, a mixture of argon and methane is injected once the temperature is stabilized and the operating conditions are maintained during about an hour to produce significant amounts of carbon black for further analysis.

2 Experimental Conditions

The experimental conditions are listed in Table 1. Two series were carried out: the first one with 10.5 NL/min of CH_4 and 31.5 NL/min of Ar for temperatures between 1608 K and 1928 K (runs 1 to 5) and the second one with 21 NL/min of CH_4 and 49 NL/min of Ar for temperatures ranging from 1698 K to 1808 K (runs 6 to 8). In the first series, one experimental condition was repeated twice to check the results reproducibility (runs 3 and 4). In the second series, run 7 was repeated with only 21 NL/min of argon dilution (50 % of CH_4 in the feed) instead of 49 NL/min (run 8). After each experimental run at given operating conditions, the carbon was recovered in the filter so that carbon black samples were

representative of specific conditions. About 100 g of sample was recovered for each run and was available for analysis and characterization.

Table 1: Summary of the experimental conditions tested.

Run	Ar (NL/min)	CH_4 (NL/min)	CH_4 mole fraction	Pressure (Pa)	Tpyrometer (K)	Residence time (s)
1	31.5	10.5	0.25	43000	1608	0.070
2	31.5	10.5	0.25	46000	1693	0.071
3	31.5	10.5	0.25	43000	1778	0.063
4	31.5	10.5	0.25	42000	1793	0.061
5	31.5	10.5	0.25	42000	1928	0.057
6	49	21	0.3	47000	1698	0.043
7	49	21	0.3	43000	1808	0.037
8	21	21	0.5	41000	1798	0.059
9	49	21	0.3	45000	1873	0.038

3 Experimental results

Figure 2 shows typical measurements of temperatures, H_2 and CH_4 off-gas mole fractions, DNI (Direct Normal Irradiation) recorded for the experimental run 2. It can be decomposed in three experimental stages: heating of the reactor in Ar, cracking period (methane injection), and passive cooling of the reactor (no solar irradiation).

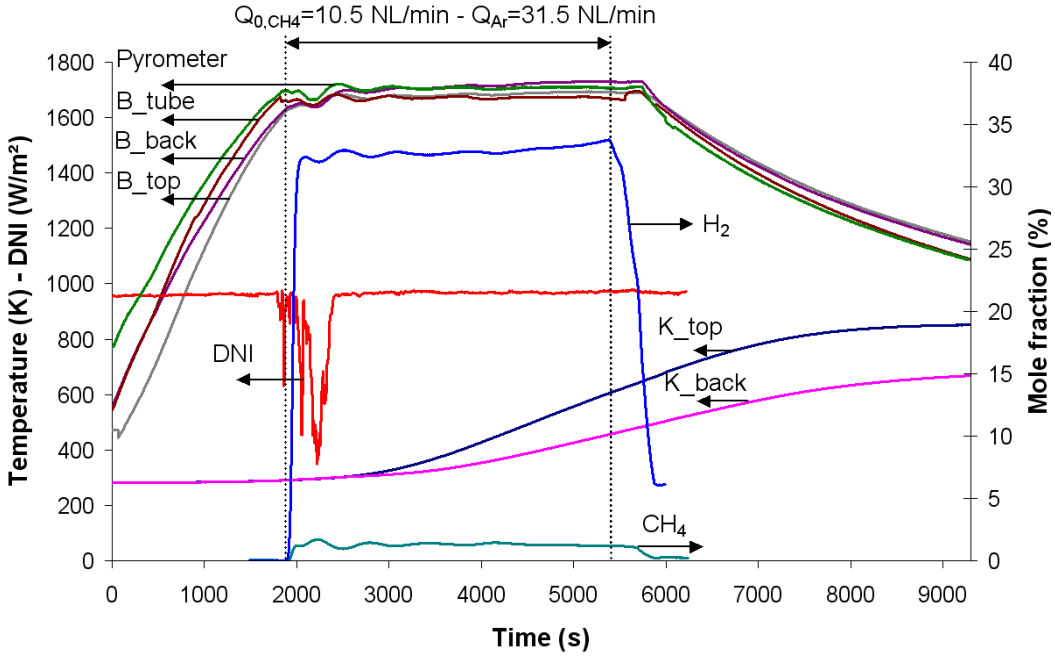

Figure 2: Online monitoring of temperatures, DNI, H_2 and CH_4 off-gas mole fractions.

After a heating period of about 40 min under an argon flow in the tubes, the temperature of the reactor reaches 1700 K. All the temperature sensors tend to a similar measured temperature ranging between 1670 K and 1720 K. The highest temperature is given by the pyrometer that points directly on the outer wall of a tube. It can be stated that the temperature is homogeneous around the cavity during the methane splitting period. When the targeted temperature is reached and stabilized, 31.5 NL/min of argon and 10.5 NL/min of methane are injected. H_2 is rapidly detected at the exit along with residual CH_4 (not dissociated). After 2400 s of isothermal experiment, the H_2 mole fraction in the off-gas increases slightly as a result of tubes clogging. Carbon deposit in the tubes causes a pressure increase and thereby a residence time increase that favours better CH_4 and C_2H_2 dissociation. After about one hour of isothermal experiment, the tubes are successively stopped because of their progressive blocking.

The reactor performances are given in terms of methane conversion, hydrogen yield, and carbon yield:

$$X_{CH_4}=\frac{F_{0,CH_4}-F.y_{CH_4}}{F_{0,CH_4}};\quad Y_{H_2}=\frac{F.y_{H_2}}{2.F_{0,CH_4}};\quad Y_C=\frac{F_{0,CH_4}-(F.y_{CH_4}+2.F.y_{C_2H_2}+2.F.y_{C_2H_4}+2.F.y_{C_2H_6})}{F_{0,CH_4}}$$

where $F_{0,CH4}$ is the inlet molar flow-rate of CH_4, y_i is the mole fraction of species i, and F is the total outlet flow-rate (including argon as buffer gas) obtained from:

$F = F_{Ar}/(1-\Sigma y_i)$ (F_{Ar} is the molar flow-rate of Ar)

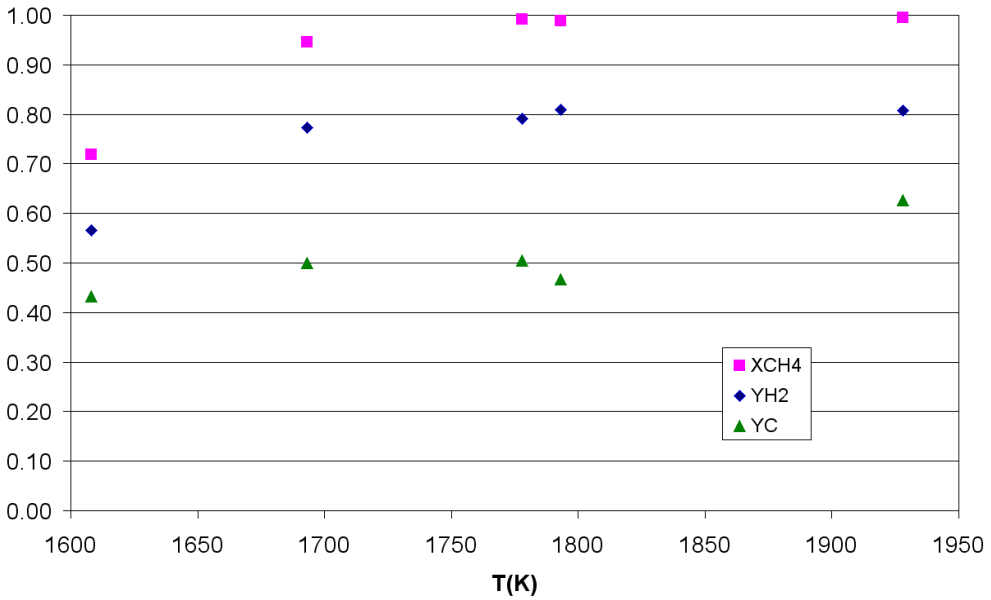

Figure 3: CH_4 conversion, H_2 yield, and C yield versus temperature for the first experimental series (Ar: 31.5 NL/min, CH_4: 10.5 NL/min).

Figure 3 shows the results concerning the first experimental series (Ar: 31.5 NL/min, CH_4: 10.5 NL/min) in terms of methane conversion, hydrogen yield, and carbon yield with increasing temperatures (1608 K-1928 K). The higher the temperature, the better the chemical performance. Moreover, the CH_4 conversion is always higher than the H_2 yield and

the C yield. Since the conversion of CH_4 into C_2H_2 leads to the production of 1.5 mole of H_2 per mole of CH_4 without carbon production, the H_2 yield is higher than the C yield. The intermediate C_2H_2 mainly affects the carbon yield. For temperatures above 1778 K, complete methane conversion is achieved.

Figure 4 shows the results related to the second experimental series (Ar: 49 NL/min, CH_4: 21 NL/min) in the temperature range 1698 K-1873 K. Similar trends are observed for the temperature influence but the CH_4 conversion never reaches completion even for temperatures up to 1873 K as a result of higher flow-rates than the first series. For the run #8 (50 % of CH_4 in the feed), better chemical performances are obtained due to a higher residence time as a result of the lower argon dilution (Ar: 21 NL/min instead of 49 NL/min). The comparison between the results of the first and second series shows enhanced performances for the first series, which points out again the strong influence of the residence time. Residence time and temperature thus appear as the most critical parameters.

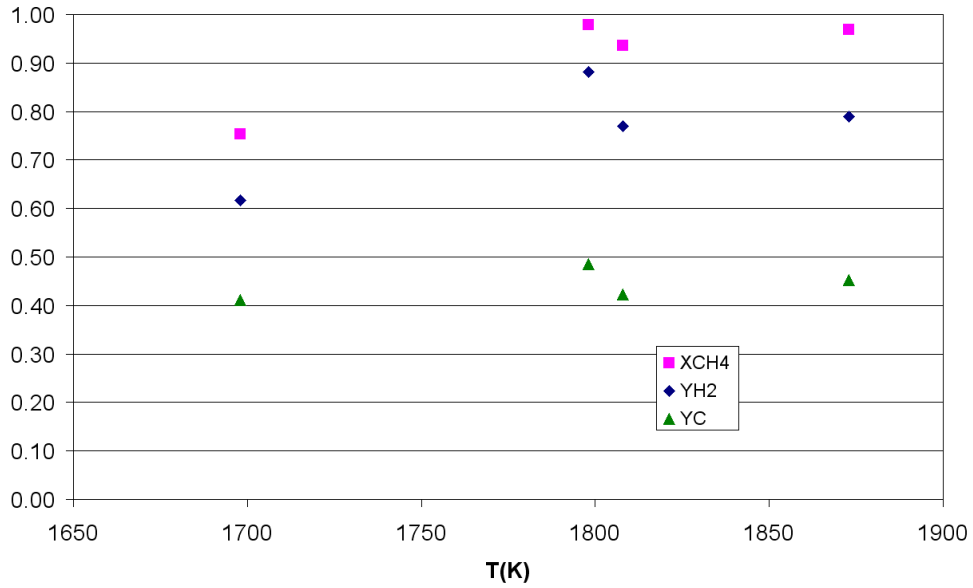

Figure 4: CH_4 conversion, H_2 yield, and C yield versus temperature for the second experimental series (CH_4: 21NL/min).

Acknowledgements

This study was funded by the European Project SOLHYCARB (2006-2010, Contract SES-CT2006-19770). The authors wish to thank O. Prévost, M. Garrabos, and J.L. Sans for their technical support during the solar reactor manufacturing and operation.

References

[1] P.L. Spath, W.A. Amos, Using a concentrating solar reactor to produce hydrogen and carbon black via thermal decomposition of natural gas: feasibility and economics, Journal of Solar Energy Engineering, 125(2), 2003, 159-164.

[2] T. Pregger, D. Graf, W. Krewitt, C. Sattler, M. Roeb, S. Möller, Prospects of solar thermal hydrogen production processes, International Journal of Hydrogen Energy, 34(10), 2009, 4256-4267.

[3] F.C. Lockwood, J.E. Van Niekerk, Parametric Study of a Carbon Black Oil Furnace, Combustion and Flame, 103(1-2), 1995, 76-90.

[4] G. Maag, G. Zanganeh, A. Steinfeld, Solar thermal cracking of methane in a particle-flow reactor for the co-production of hydrogen and carbon, International Journal of Hydrogen Energy, 34, 2009, 7676-7685.

[5] M. Kogan and A. Kogan, Production of hydrogen and carbon by solar thermal methane splitting. I. The unseeded reactor, International Journal of Hydrogen Energy, 28(11), 2003,1187-1198

[6] J. K. Dahl, K. J. Buechler, A. W. Weimer, A.Lewandowski and C. Bingham, Solar-thermal dissociation of methane in a fluid-wall aerosol flow reactor, International Journal of Hydrogen Energy, 29(7), 2004, 725-736.

[7] S. Rodat, S. Abanades, G. Flamant, High-Temperature Solar Methane Dissociation in a Multitubular Cavity-Type Reactor in the Temperature Range 1823-2073 K, Energy & Fuels, 23, 2009, 2666-2674.

[8] J.K. Dahl, V.H. Barocas, D.E. Clough, A.W. Weimer, Intrinsic kinetics for rapid decomposition of methane in an aerosol flow reactor, International Journal of Hydrogen Energy, 27(4), 2002, 377-386.

[9] S. Rodat, S. Abanades, J. Coulié, G. Flamant, Kinetic modelling of methane decomposition in a tubular solar reactor, Chemical Engineering Journal, 146(1), 2009, 120-127.

[10] M. Younessi-Sinaki, E.A. Matida, F. Hamdullahpur, Kinetic model of homogeneous thermal decomposition of methane and ethane, International Journal of Hydrogen Energy, 34(9), 2009, 3710-3716.

FLOX® Reformer – Hydrogen for Fuel Cells

Hans-Peter Schmid, WS Reformer GmbH, Renningen, Germany

1 Introduction

Hydrogen supply and infrastructure is one of the key success factors for a broad market penetration of fuel cells. Apart from this, the limited energy density of available hydrogen storage technologies reforming of commercial fuels is required for applications which need significant operation times (hours/day) and/or power output (< 1 kW). Further on, reforming enables manufacturers to independently develop the market, thus avoiding the risk in the progress of a area-wide hydrogen infrastructure.

However, in general the fuel cell system gets more complex and costly, which puts challenging technical requirements on the reforming components. These are:

- Hydrogen generation efficiency compared or even higher than centralized production. 75-80 % is state of the art and allows electric efficiency of 30-35 % of the system.
- Cost effectiveness. In mass production determined by weight, materials and compactness.
- Minimized complexity. A simple and stable control strategy as well as a minimum number of BOP-components (valves, blowers, pumps, etc.) is desirable.
- Low noise and efficient BOP-components. Hydrogen fuel cells are a priori zero emissive and noiseless.
- Gas processing should meet the lowest emission standards and must not overcome fundamental fuel cell benefits.

2 The Product Line FLOX® Reformer compact

WS Reformer adresses these challenges and offers reformer solutions for various hydrogen capacities and fuel cell technologies in the range 1-5 kW.

Table 1: Technical Data of FLOX® reformer compact types.

Product Name	FPM-C1	C1	C4	C6-HT
	Fuel processing module 	Reformer 	Reformer 	Reformer 
Feed	Natural Gas, LPG	Natural Gas, LPG DI-water, 5 bar	Natural Gas, LPG DI-water, 5 bar	Natural Gas, LPG Wet steam, 5 bar
Hydrogen capacity	1,2-2 Nm³/h	1,2-2 Nm³/h	4 Nm³/h	5 Nm³/h
Hydrogen purity	75 % in reformate HT-PEM: CO<1 % LT-PEM: <20ppm	75 % in reformate HT-PEM: CO<1 % LT-PEM: <20 ppm	75 % in reformate HT-PEM: CO<1% LT-PEM: <20 ppm	75 % in reformate HT-PEM:CO<1%
Efficiency**	75-80 %	75-80 %	78 %	85 %
Weight	30 kg	20 kg	45 kg	45 g
Size dxh	290x360x280 mm	250 x 420 mm	350 x 700 mm	350 x 800 mm

Table 1 highlights the basic technical data. All types include FLOX® combustion technology, which allows a compact design, high heat transfer rates, low emissions and highest efficiency. The patented FLOX® reforming process comprises high pressure steam cooling of the single, integrated CO-shift stage and an internal pressure hub of the reformate in the reformer, without the use of an extra feed-gas compressor. Since the heat management separates combustion air/exhaust and product/feed heat exchange, fast load following can be realized by one single temperature control loop, which is lead simply by heat demand.

Estimations of material usage and BOP requirements reveal, that the cost targets even at mid-size series production (1000-10.000 units/a) will be met.

3 Benefits of FLOX® Combustion in Steam Reformers

Core technology is the flameless oxidation (FLOX®) burner, which allows a very compact, cost-effective design along with high combustion densities and heat transfer rates by avoiding hot spots in the combustion chamber. FLOX® reveals further benefits in anode-off gas combustion, because sophisticated stabilizing and monitoring of low calorific hydrogen gas flames is inherently avoided. Further on, FLOX® makes extreme air-preheating at ultra

low NOx emissions possible. This is of greatest significance for the design of highly efficient HT-PEM systems.

4 Efficient High-Temperature PEM Systems

Latest developments and progress in durability [1] make HT-PEM fuel cells a serious commercialisation candidate for small, low-noise power-generators as well as for CHP-applications.

Considering the whole reformate fuel cell system, the advantages of HT-PEM compared to LT-PEM systems are obvious: cathode air humidification and CO-fine cleaning (<10 ppm) can be removed and the operation temperature of some 160 °C promise a more “valuable” heat level for heating purposes. Main disadvantages or problems occur by the reduced current density and cooling issues, particularly at larger stacks. The latter gets particularly important at CHP applications. Air cooling is no option, but cooling by generation of process steam in the stack as described in [2,3] is an elegant and advantageous solution. How this can be technologically realized at low cost shall not be discussed here. However, the implications for the reformer system will be emphasized and solutions will be presented.

Firstly, external steam generation (heat of vaporization, Δdhv=0,556 kWh/l) increases the reformer efficiency. It has been shown [4] that the increase lies in the range of 5 % and therefore has got the potential to compensate the efficiency drawback of the HT-PEM fuel cell. That means, also HT-PEM Systems can be operated at an overall electric efficiency over 35 %.

However, this has got significant impact on the reformer design, it’s internal heat management and combustion technology. In the following we summarize the findings of an extended pitch-point analysis of the reforming process based on reforming of 1 Nm³/h natural gas (10 kW) at 750 °C and S/C=3. Product gas has got a temperature of 200 °C (CO-Shift level) and the exhaust gas of the burner is assumed to be 250 °C. Fig. 1 shows the relevant heat fluxes and streams. The feed (natural gas/water) has to be heated up from 20 °C to 750 °C, the product gas has then to be cooled down to CO-Shift inlet (200 °C). Biggest heat sinks are reforming (1) and vaporization of water (4). The CO-Shift reaction releases heat (6). On the combustion side one has to account for preheating air and fuel (8) up to combustion temperature and subsequently cooling down the exhaust gas (7). For completion, wall heat and gas flow losses (3) are also shown. The overall energy balance is then closed by the fuel demand (not shown).

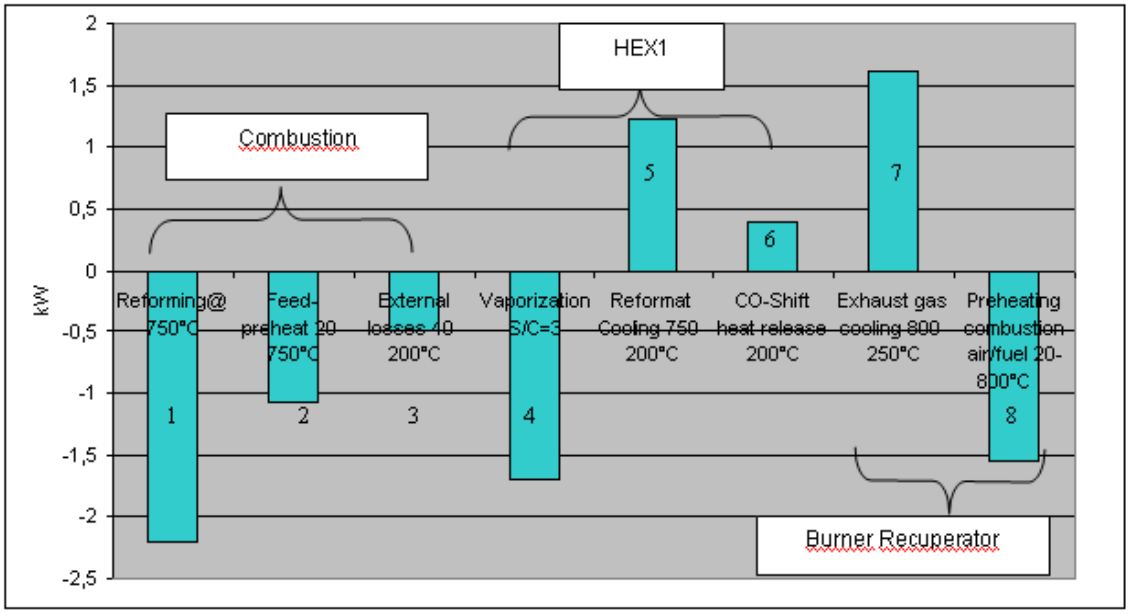

Figure 1: Heat flux and balancing in FLOX® reformers at 1 Nm³/h natural gas feed (methane).

In the productline FLOX® reformers compact C1 and C4 vaporization (4) balances reformat cooling (5) and CO-heat release (6) (HEX1). The combustion air and fuel (anode-off gas + NG fuel) is preheated (8) in the recuperator of the FLOX® burner by cooling down the exhaust gas (7). Preheating of feed (2) and reforming (1) takes place in the actual reforming reactor and is supplied by combusting the fuel. The advantages of this process are described in detail in [4].

Competitive concepts usually use exhaust gas heat (7) for vaporization (4). Feed preheating (2) can then be realized by reformate cooling (5). External air/fuel preheating is not necessary and takes place in the actual combustion chamber. The overall balance and efficiency of both concepts is equal as long as the temperatures of product- and exhaust gas as well as wall losses are identical.

However, considering the high efficient HT-PEM system, the heat sink “vaporization” is omitted within the reformer. That means, in order to balance the system the only remaining “heat sink” air/fuel preheating (8) is mandatory. This has tremendous influence on the combustion technology, because in classical flames external air preheating (600-700 K) leads to exponentially increased NOx emissions. For this reason, the author does not see an alternative to FLOX® combustion for high-end HT-PEM systems.

5 Efficient Solutions in the 5-kW class: FLOX® reformer compact C4/C6-HT

According to the requirements of the application, WS Reformer offers two solutions in the 5 kW class.

The C4 has got an internal steam generator and has to be fed with demineralized water, which usually is recycled in a condenser from the cathode air and the exhaust gas. The only additional BOP components are a water pump (e.g. membrane type, p=5 bar) and the air blower for the burner (60 mbar). Gas processing sub-system and fuel cell sub-system are

fairly decoupled. Once the combustion air (60 mbar) is supplied by the cathode air blower of the stack, the integration can be increased. The overall electric efficiency of the system then lies for LT-PEM system between 30 and 35 %, combined with HT-PEM stacks at state-of-the-art, 27-30 % seems to be achievable [5].

With the C6-HT, the integration between gas-processing and fuel cell is enhanced. The reformer needs wet steam as feed input, which preferably is generated by the stack heat directly in the HT-PEM fuel cell or in a secondary cooling circuit. The FLOX® burner including the air/exhaust gas recuperator and the reformer reactor remain the same as in the C4. In contrast to the C4, feed preheating (2) balances reformate cooling (5). The achievable overall electric efficiency for the concept is between 35 and 40 %. Although there are some challenges and restrictions with regard to tolerances in steam quality, the concept promises further simplification of the process, leading to dramatic cost savings and stable operation without sophisticated control strategies.

References

[1] T.J. Schmidt and J. Baurmeister, J. Power Sources, 176, 428 (2008).

[2] Carl A. Reiser, United States Patent No. 3,964,930

[3] R.D.Breault; Stack materials and stack design, pp.797—810, in Handbook of Fuel Cells – Fundamentals, Technology and Applicatons, Ed. Vielstich, Gasteiger, Lamm, Volume 4, 2003 John Wiley&Sons, Ltd.

[4] Schmid, H.P., Wünning, J.A.; FLOX Steam Reforming for PEM Fuel Cell Systems, Fuel Cells 2004,4,No.4 Wiley-VCH Verlag

[5] Schmid, H.P., “ FLOX® Dampfreformierung - Wasserstoff für die Brennstoffzelle“, VDI-Berichte, No2036, VDI-Verlag GmbH, Düsseldorf 2008

Design and Development of a 25 kW Diesel Fuel Processor

Daniel Sopeña, **Luis Aldea**, CIDAUT, Spain
Rufino Navarro, Institute of Catalysis, CSIC, Spain
Felipe Rosa, INTA/University of Seville, Spain

1 Introduction

Reforming processes consist of the chemical transformation of hydrocarbons to produce hydrogen by means of thermocatalytic reactions [1]. Although using diesel fuel for hydrogen production implies lower performances in the whole process, respect to gaseous fuels, it has the advantage of a higher energetic density, which favours storage in reduced volumes and it also has a distribution infrastructure all over the world.

INTA, CIDAUT, ICP_CSIC and AICIA are collaborating in a pre-commercial system of a hydrogen production diesel Oxidative Steam Reformer coupled to a 25 kW PEMFC, evolution of a previously 5kW prototype [2]. This system had a flexible design, which allowed the characterization of each reactor separately and jointly, without taking into consideration maximum efficiency. In the last years, a 25 kW fuel processor has been developed and tested. This system is autonomous, has a high level of thermal integration, reduces slightly start-up, stop and transitory times; and improves hydrogen concentration. CIDAUT has the responsibility of plant development and reactors design, whereas ICP-CSIC develops the different catalysts and AICIA will integrate the 25 kW PEM Fuel Cell next year.

2 Experimental

The fuel processor is composed by a set of reactors, a series of auxiliaries and instrument and control equipments. The auxiliaries guaranteed the adequate feeding currents to the reformer, the heat of the system, the cool reforming of gas outlets, maximise the thermal efficiency of the fuel processor, and includes secondary processes for increasing the useful life of the catalyst as inertization, catalyst cleaning, or system cooling.

The set of reactors is formed by:

- An OSR (Oxidative Steam Reforming) reactor, where the primary hydrogen production from diesel takes place. Air and water are also introduced as reactants. In this reactor diesel reacts with air and water following the reaction:

  $C_nH_m + a{\bullet}n\ (O_2{+}3.76N_2) + b{\bullet}n\ H_2O \Rightarrow p\ CO + q\ CO_2 + r\ H_2 + s\ H_2O + a{\bullet}n{\bullet}3.76\ N_2$

  where ‘a’ is the oxygen to carbon ratio and ‘b’ is the water to carbon ratio. The target values for O2/C ratio range from 0.45 to 0.5 with a H2O/C ratio next to 3. The homogeneous mixture of the reactives and the vaporisation of the diesel fuel take place by means of a swirl effect inside the mixing chamber, and using also pre-combustion reactions that occurs around 400 – 500 ºC denominated cold flame [3]. The OSR reactor operates at temperature higher than 800 ºC to avoid ethylene

formation. The catalyst formulation used in this reactor is a cobalt based catalyst derived from perovskites precursors with improved thermal and coke resistance.

- A Desulphuriser working around 300 ºC and with the goal of sulphur removal from the reforming gas outlet by means of adsorption of the formed H_2S.
- A WGS (Water Gas Shift) Reactor, which is in charge of the CO selective conversion via its oxidative reaction with water to obtain CO_2 and H_2. The used catalyst is based on Pt deposited on mixed CeO_2–TiO_2, operating at 275 ºC.
- A Prox (Preferential Oxidation) Reactor performs the selective removal of CO by direct oxidation with air. The catalyst is a monolith that contains highly dispersed Pt on alumina, working between 150 - 175 ºC with an O_2/CO ratio ranging from 1.3 to 1.

Table 1: Typical approximate compositions on dry basis at the outlet of each reactor.

	H_2	N_2	CO_2	CO	CH_4	C_2H_4
OSR Reactor	30 %	49 %	14 %	7 %	1 %	<500 ppm
WGS Reactor	36 %	Balance	21 %	0.3 %	1 %	<500 ppm
PrOx Reactor	36 %	Balance	21 %	<50 ppm	1 %	<500 ppm

The scheme in Figure 1 presents the input of reactive currents (diesel, air and water) inside the mixing chamber and from there to the OSR Reactor and the rest of reactors. Air could be preheated with a heat exchanger that cools the gas reforming at the output of the WGS reactor. Water is preheated basically by two heat exchangers: a first one cools the gas reforming stream at the output of the OSR Reactor, while the second one cools the combustion gases produced in the burner for adapting them to the Desulphuriser temperature. A second air flow is added to the PrOx Reactor, which by means of the O_2/CO ratio at the input, controls the CO composition in ppm's of the reforming gas at the outlet of this reactor. A diesel burner (which can also run on reforming gas) is entrusted to supply heat for the system starting-up and to control the temperatures of the reactors.

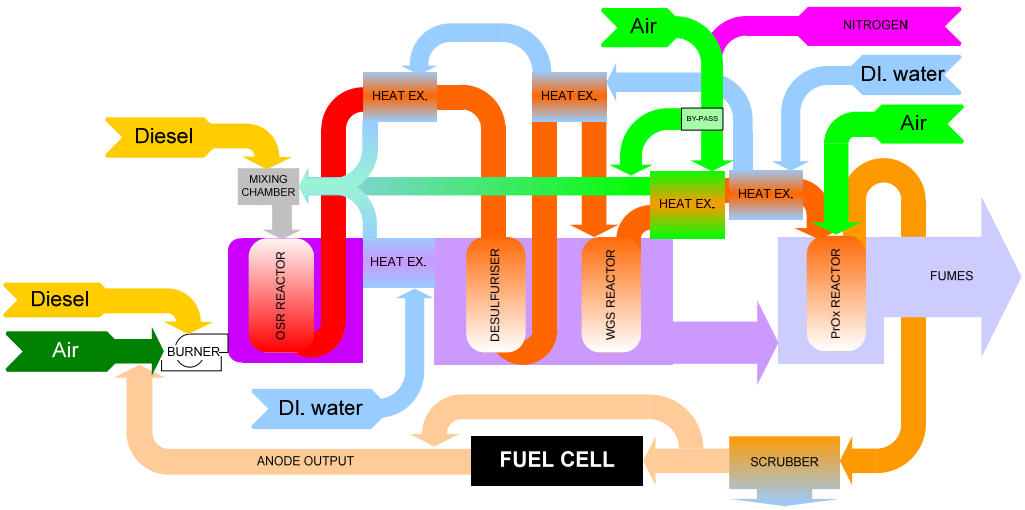

Figure 1: Working scheme of the 25 kW fuel processor.

After the PrOx Reactor, the reforming gas is cooled by means of a scrubber and a coalescent filter, with the aim of condensing and recovering the excess of water contained in this flow [4]. Afterwards, if it fulfils temperature, humidity and gas composition conditions set by the PEMFC manufacturer, the reforming gas is conducted to the fuel cell. If it does not, it can be expelled to the environment (burned by a flare), or fed to the boiler's burner that heats the system. Moreover, the outlet of the fuel cell anode could be introduced in the air current that feeds the diesel burner for increasing the global efficiency of the system.

One of the design critical issues was the burner design and the study of heat transfer in the OSR reactor. For solving that, a fluid-mechanical model of the reactor-burner set was accomplished, taking into account not only mass and energy transport but also reaction kinetics of the reactor. The whole model was fit and validated through a series of experimental tests in the 5 kW facility [5]. Figure 2 presents results from this simulation. Figure 2.a shows temperature profile inside the OSR reactor and Figure 2.b includes also the flow lines and temperature of the fumes.

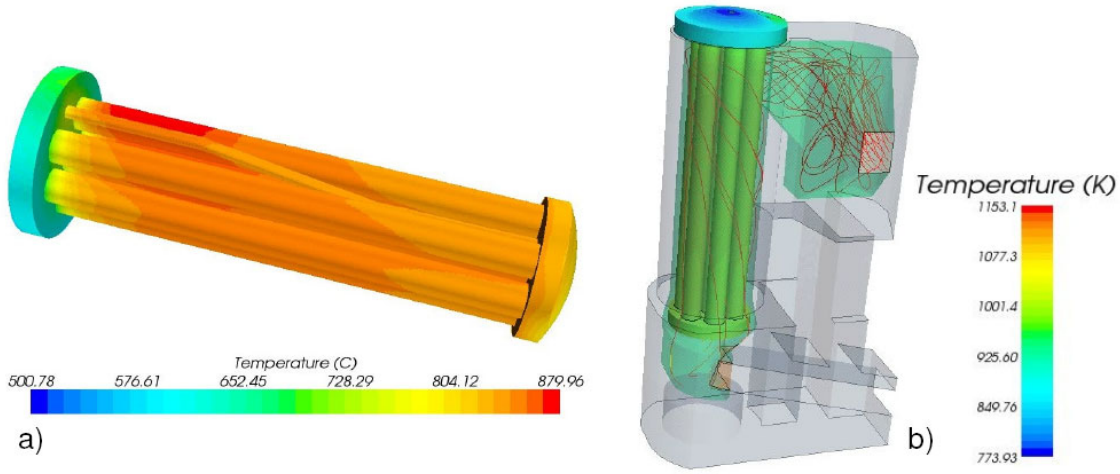

Figure 2: CFD simulation results; a) OSR temperature profile, b) General view of the simulation, including flow lines and temperature of combustion gases.

Another critical point was the physical design of the set of reactors and the PrOx Reactor. A 3D design tool and a tensile and materials study were used for this issue (Figure 3).

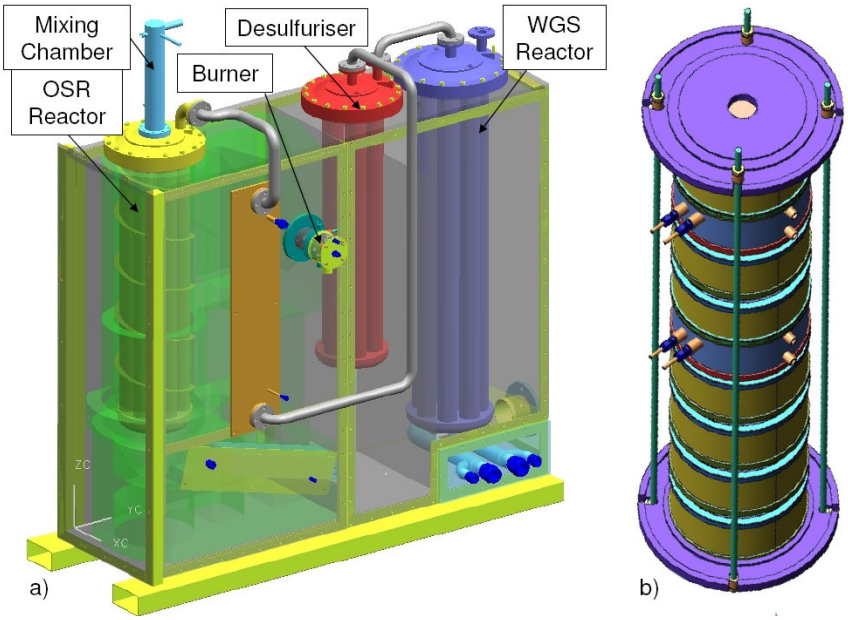

Figure 3: 3D views of a) reactor set, and b) PrOx reactor.

Figure 4 shows several photographs of the whole facility and of the set of reactors.

Figure 4: Fuel processor facility; a) Exterior view of the cabinet, b) Instrumentation of feeding lines and cooling of the reformer, c) set of reactors and scrubber, d) Gas measurement systems and water line, e) electric enclosure and control system.

3 Results

Figure 5 shows results from a typical test, working the facility at 12 kW. Horizontal axis of each graph represents time in seconds. Figures 5.a and 5.c show temperature profiles of each reactor of the fuel processor. As it can be observed, OSR reactor temperatures lie inside the 800 – 900 ºC range, except T_OSR3 and T_OSR3' (placed in the lower part of the reactor) that, due to thermal inertia, need more time to reach the optimum. WGS reactor and desulphuriser temperatures are inside their working zone, while PrOx reactor temperatures are slightly lower than 150 ºC. In this condition, the PROX reactor is able to decrease the CO concentration below 50 ppm. Graphs 5.b and 5.d present the evolution of the gas reforming compositions throughout the fuel processor and some significant data as water, air and diesel flows, O_2/C and H_2/C ratios, and system pressure. It can be seen in these graphs that hydrogen composition decreases when O_2/C ratio increases, with CO concentration around 5 %.

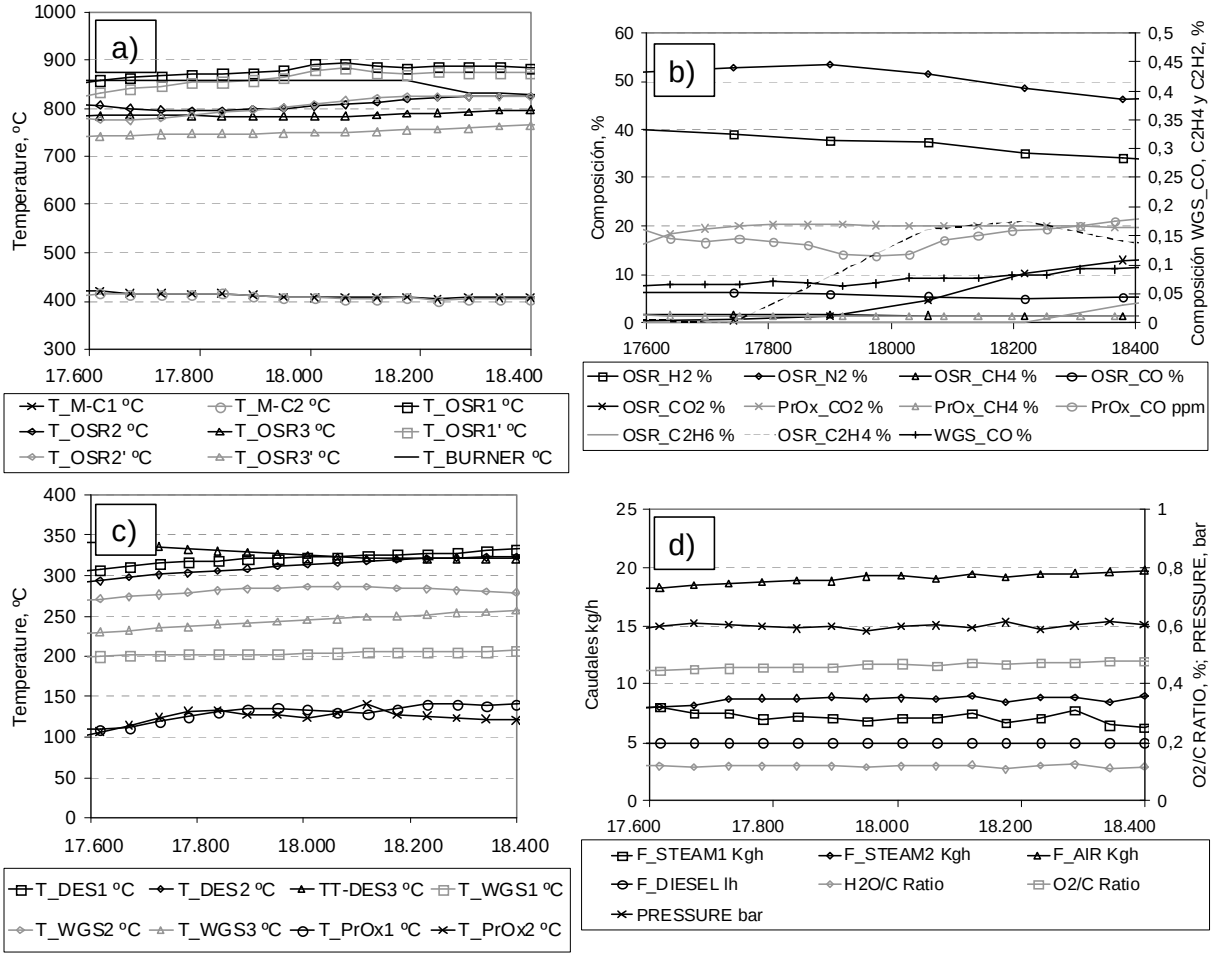

Figure 5: a) Temperature profile in Mixing Chamber (M-C) and OSR Reactor; b) Temperature profile in Desulphuriser and WGS and PrOx Reactors; c) Gas composition in several points; d) several physical variables evolution.

4 Conclusions and Future Works

A fuel processor able to process diesel, and producing a gas stream to be used in 25 kW PEMFC has been developed. Tests for tuning the facility and design validation of each reactor have been carried out.

The fuel processor will be moved to INTA facilities in May, when a test plan for different working conditions will start to be accomplished.

References

[1] C. Pereira, J-M Bae, S. Ahmed, and M. Krumpelt. *"Liquid Fuel Reformer Development: Autothermal Reforming of Diesel Fuel"*. Hydrogen Program Technical Review. California, 2000.

[2] D. Sopeña, A. Melgar, Y. Briceño, R. Navarro, C. Alvarez, F. Rosa Iglesias. *"Diesel Fuel Processor for Hydrogen Production for 5 Kw Fuel Cell Application".* International Journal of Hydrogen Energy . Vol. 32. No. 10-11. 2007. Pag. 1429-1436

[3] Hartmann L, Lucka K, Köhne H. *"Mixture preparation by cool flames for diesel-reforming technologies".* J Power Sources 2003;118:286–97.

[4] D. C. Kincaid, T. S. Langley. *"A Water Droplet Evaporation and Temperature Model"* ASAE (Vol. 32, No.2, pp. 457-463, 1979).

[5] Liu DJ, Kaun TD, Liao HK, Ahmed S. Characterization of kilowattscale autothermal reformer for production of hydrogen from heavy hydrocarbons. Int J. Hydrogen Energy 2004;29:1035–46.

Development of Hydrogen Production Catalysts from Dimethyl Ether

Kaoru Takeishi, Department of Materials Science and Chemical Engineering, Shizuoka University, Shizuoka, Japan

Abstract

Dimethyl ether (DME) is expected as one of clean fuels. We have been studying on DME steam reforming for hydrogen production. Copper alumina catalysts prepared by the sol-gel method produced large quantities of H_2 with DME steam reforming. Aiming at practical use of the catalysts, some experiments were carried out such as catalyst life time tests (durability test) and fixation of the catalysts on commercial catalysts in order to reduce the pressure loss and in order to make the catalysts inexpensive. In the case of the 240-h accelerated durability test, there is no deactivation, so that the sol-gel Cu-Zn/Al_2O_3 catalysts have long durability. The catalysts are easy to fix on the spherical aluminas, and the fixing (coating) makes less the amount of the sol-gel catalysts in the whole catalysts including the alumina. In case of coated spherical alumina (1-2 mm diameter) catalyst, the amount of the sol-gel Cu-Zn/Al_2O_3 catalyst was cut down into 1/5 times comparing with the sol-gel powder catalyst. This fixation on commercial spherical alumina will make the price of the catalyst inexpensive, and the pressure loss will be able to decrease. The further development is still need, but the catalysts have enough capability for practical use.

1 Introduction

It is expected that fuel cell is one of the methods for restraint of the global green effect. Steam reforming of fossil fuels is actively researched and developed as hydrogen supply methods for the fuel cells. Dimethyl ether (DME) does not contain the poisonous substances, and it burns without particulate matters (PM), without sulfur oxide (SOx), and with less nitrogen oxide (NOx). DME is expected as a clean fuel for the 21st century [1, 2]. DME has also recently become a potential fuel for hydrogen production to be used in fuel cells. DME is able to take the place of light oil and liquefied petroleum gas (LPG), and its physical properties are similar to those of LPG. There is possibility that DME infrastructures will be settled more rapidly than those of hydrogen, because LPG infrastructures existing are able to be used for DME.

I have been studying on steam reforming of DME for the hydrogen production. The new type catalysts prepared by a sol-gel method have been developed [3-5]. These catalysts produce hydrogen more effectively at lower reaction temperature than mixed catalysts with DME hydrolysis catalysts and methanol steam reforming catalysts. Cu-Zn (29-1wt. %)/Al_2O_3 is the most effective catalyst for hydrogen production in my recent study.

Aiming at practical use of the catalysts, catalyst life time tests (durability tests) were carried out. In order to reduce the pressure loss and in order to make the catalysts inexpensive,

fixation of the catalysts on commercial aluminas was examined. In this paper, the details are commentated.

2 Experimental

Cu-Zn(29-1wt.%)/Al_2O_3 powder catalyst prepared by the sol-gel method [3-5] was used for this study. The preparation method is mentioned in previous papers, and some catalysts were ground by an agate mortar to less than 150 μm diameters [3-5]. The other catalysts were fixed on commercial spherical aluminas (KHO-12S (diameter 1-2 mm) and KHO-24S (diameter 2-4 mm) manufactured by Sumitomo Chemical Co., Ltd.). The spherical aluminas were immersed in the sol condition precursor of the sol-gel Cu-Zn/ Al_2O_3 catalyst. The immersed catalysts were dried using a rotary evaporator. The dried catalyst was calcined at 500 ^oC for 5 h and was reduced by flowing H_2 at 450 ^oC for 10 h. This severe pretreatment was particularly performed for reactive comparison to avoid the catalytic deterioration with sintering of the catalyst by the reaction heat on continuous experiments with the same catalyst. For the durability test, the catalyst reduced at 350 ^oC for 5 h. Usually DME steam reforming is carried out under atmospheric pressure, but reaction pressure was 0.3 MPa for the accelerated durability test. Therefore, atmospheric pressure and pressurized reactors were used for the DME steam reforming, respectively. The supply of the reaction gas to the catalyst layer was adjusted to several space velocity by the flow speed and concentration of reactant (Ar with DME/steam = 1/3), except of DME/steam = 1/4 for the durability test. The reaction gas and products were analyzed by gas chromatographs (TCD, FID, and methanizer). The atmospheric pressure reactor was part of a closed circulation system. Before the reaction, the BET specific surface area of the catalyst in the reactor without the exposure to the air was measured using N_2 gas at −196 ^oC. After the evacuation of N_2 gas at room temperature for 30 min, the amount of CO it adsorbed in the same reactor without the exposure of the air was analyzed using CO gas at 0 ^oC. After the evacuation of CO gas at 300 ^oC for 1 h, steam reforming of DME over the same catalyst was performed in the same reactor without the exposure of the air.

The surface of the spherical alumina catalyst coated by the sol-gel Cu-Zn/Al_2O_3 catalysts prepared by the sol-gel was analyzed using a scanning electro-microscope (SEM, KEYENCE VE-9800).

3 Results and Discussion

3.1 Observation of catalysts

The photos of the catalysts prepared by the sol-gel method are shown in Figure 1. Figure 1(a) is the photo of the powder catalysts prepared by the sol-gel method. Usually Cu-Zn/ Al_2O_3 catalysts prepared by the sol-gel method were ground to less than 150 μm diameters, and these catalysts were used in the previous research [3-5]. Figure 1(b) is the SEM photo of the developed catalyst for this study on this paper. The sol-gel Cu-Zn/ Al_2O_3 catalyst was coated on the spherical alumina by immersing in the sol condition precursor of the sol-gel Cu-Zn/ Al_2O_3 catalysts. For practical use, pressure loss should be reduced. Therefore, spherical aluminas (KHO-12S & KHO-24S) were used as the supports of the catalysts. Figure 1(b) shows the catalysts that spherical alumina (KHO-12, 1-2 mm diameter)

was coated with the sol-gel Cu-Zn/ Al_2O_3 catalyst, and the sol-gel Cu-Zn/ Al_2O_3 catalyst looks well coated on the spherical alumina.

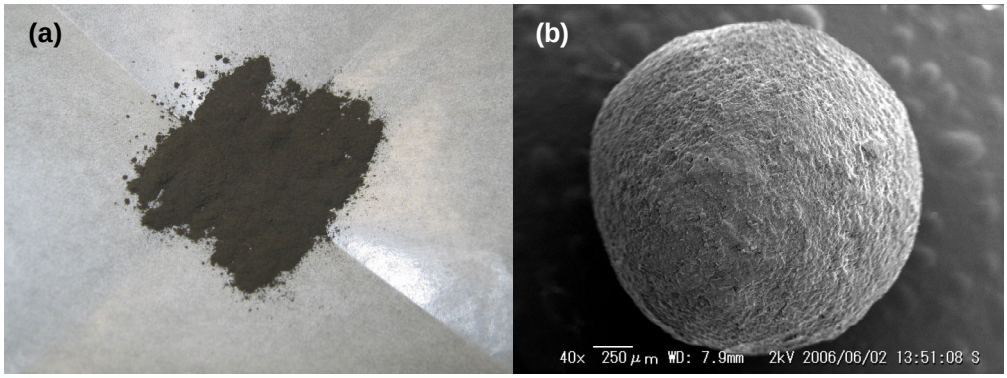

Figure 1: Photos of used catalysts in this research.
(a) Powder catalysts (sol-gel Cu-Zn/Al_2O_3, diameter < 150 μm) after the calcinations
(b) SEM photo of the spherical alumina (1-2 mm diameter) coated Cu-Zn/Al_2O_3 (sol-gel) catalyst

3.2 Physical properties of these catalysts

Coating percent was estimated from the increased amount of the catalysts by the fixation of sol-gel Cu-Zn/ Al_2O_3 catalyst. As shown in Table 1, KHO-12S (1-2 mm diameters) was coated in higher amount of 5.96 % than that of KHO-24S (3.56 %). Values of the BET specific surface area were decreased with the increase of the percent of sol-gel Cu-Zn/ Al_2O_3 catalyst coating. Amount of CO adsorbed is related to amount of active sites, dispersion of metal, and so on. Amounts of CO adsorbed were increased with the increase of the coating percent of sol-gel catalyst.

Table 1: Physical data of the Cu-Zn/Al_2O_3 powder catalyst and the coated catalysts on the spherical aluminas.

Catalyst	Coating percent (%)	BET surface area ($m^3\ g^{-1}$)	CO adsorbed ($\mu mol\ g^{-1}$)
Cu-Zn/Al_2O_3 (Powder)	-	215	20
Cu-Zn/Al_2O_3/spherical Al_2O_3 (KHO-24S, 2-4 mm)	3.56	200	46
Cu-Zn/Al_2O_3/spherical Al_2O_3 (KHO-12S, 1-2 mm)	5.96	160	76

3.3 DME Steam reforming over these catalysts

The three catalysts were used for DME steam reforming. The used each catalyst whole weight (including spherical alumina and coated sol-gel Cu-Zn/ Al_2O_3 catalyst), sol-gel Cu-Zn/ Al_2O_3 catalyst weight, and DME conversion over each catalyst are shown in Table 2. Main

products were H_2 and CO_2. The catalyst whole weight was increased for high conversion as shown in Table 2. The DME conversion of the sol-gel Cu-Zn/ Al_2O_3 powder catalyst and Cu-Zn/ Al_2O_3/spherical Al_2O_3 (KHO-24S) was around 95 %, even if the reforming temperature was 275 ^oC. Cu-Zn/ Al_2O_3/spherical Al_2O_3 (KHO-12S) should have been slightly more weight for around 95 % DME conversion at 275 ^oC of the reaction temperature. However, the DME conversion of the all catalysts at 300 ^oC was almost 100 %, respectively. Therefore, the fixation of sol-gel catalyst on commercial spherical alumina made the weight of the sol-gel Cu-Zn/ Al_2O_3 catalyst reduced. In case of coated spherical alumina (1-2 mm diameter) catalyst, the amount of the sol-gel Cu-Zn/ Al_2O_3 catalyst was cut down into 1/5 times comparing with the sol-gel powder catalyst. This fixation on commercial spherical alumina will make the price of the catalyst inexpensive, and the pressure loss will be able to decrease.

Table 2: Comparison of DME conversion over the Cu-Zn/Al_2O_3 catalyst and the Cu-Zn/Al_2O_3 coated spherical alumina catalysts.

Catalyst	Weight of catalyst (g)	Weight of sol-gel catalyst (g)	DME conversion at 275 ^oC (%)	DME conversion at 300 ^oC (%)
Cu-Zn/Al_2O_3 (Powder)	0.10	0.10	95	100
Cu-Zn/Al_2O_3 /spherical Al_2O_3 (KHO-24S, 2-4 mm)	1.42	0.050	99	100
Cu-Zn/Al_2O_3 /spherical Al_2O_3 (KHO-12S, 1-2 mm)	0.30	0.018	87	98

3.4 Accelerated durability test of the DME steam reforming catalysts

Usually DME steam reforming is carried out under atmospheric pressure, but as the accelerated durability test the reaction pressure was 0.3 MPa and the reaction temperature was 320 ^oC. The Cu-Zn/ Al_2O_3 powder catalyst and the Cu-Zn/ Al_2O_3 coated KHO-12S alumina catalyst were used for this test. The part of the results on the Cu-Zn/ Al_2O_3 (sol-gel) powder catalyst is shown in Figure 2. There was no big deactivation. Cu-Zn/ Al_2O_3 (sol-gel) is sufficiently durable catalyst. This catalyst will be used in practical. However, in case of the Cu-Zn/ Al_2O_3 (sol-gel) coated alumina catalyst DME conversion and the activity slightly decreased. After this durability test, the sol-gel catalyst was peeled off from the spherical alumina. In this time, the fixed catalyst was made by soaking the alumina into the sol condition of Cu-Zn/ Al_2O_3. It was suggested that the improvement of the fixation method is necessary.

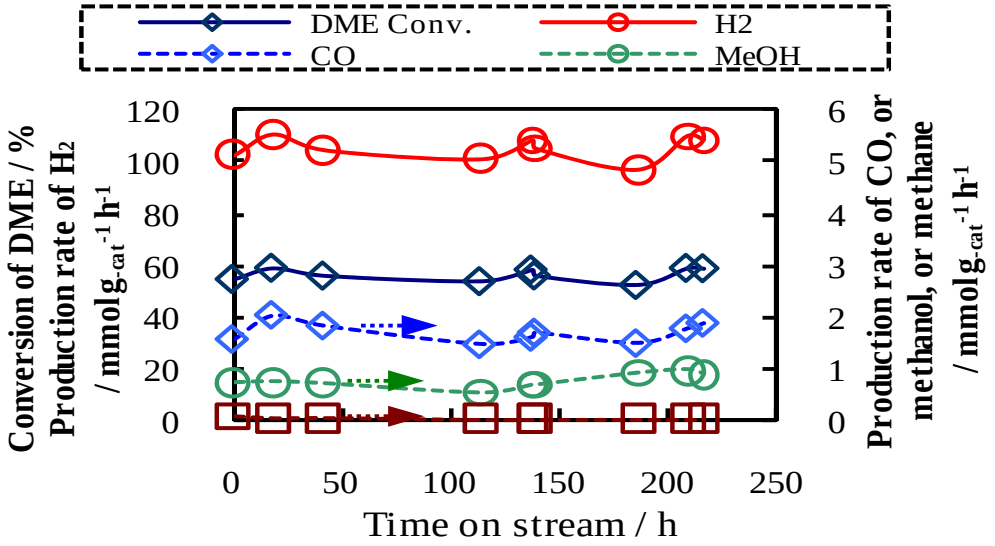

Figure 2: **Time course of DME conversion and production rates on DME steam reforming at 320 °C and under 0.3 MPa over Cu-Zn/Al_2O_3 powder catalyst prepared by the sol-gel method. Reaction temp.: 320 °C, reaction material SV: 2.0x103 h-1, DME/H_2O = 1.0/4.0.**

4 Conclusion

The sol-gel Cu-Zn/ Al_2O_3 catalysts have long durability, and the catalysts are easy to fix on the spherical aluminas. The further development is still needed, but the catalysts have enough capability for practical use.

References

[1] T. H. Fleisch, A. Basu, M. J. Gradassi, J. G. Masin, Dimethyl ether: A fuel for the 21st century, Studies in Surface Science and Catalysis, 107, 117-125 (1997).

[2] K. Takeishi, Dimethyl ether and catalyst development for production from syngas, Biofuels, 1 (1), 217–226 (2010).

[3] K. Takeishi, H. Suzuki, Steam reforming of dimethyl ether, Applied Catalysis A: General, Vol. 260, 2004, pp. 111-117.

[4] K. Takeishi, K. Yamamoto, Catalysts for hydrogen production from dimethyl ether, Japan Patent, No. 3951127; US Patent, No. 7,241,718; etc.

[5] K. Takeishi, Hydrogen production by steam reforming of dimethyl ether over single type copper alumina catalysts, 17th World Hydrogen Energy Conference (WHEC2008), Proceedings, No.114 (2008).

A Novel Technique for Hydrogen Production from Hog-Manure in Supercritical Partial Oxidation (SCWPO)

Emhemmed A Youssef, **Paul Charpentier**, Department of Chemical and Biochemical Engineering, the University of Western Ontario, London, Ontario, Canada
George Nakhla, Department of Chemical and Biochemical Engineering, Department of Civil and Environmental Engineering, the University of Western Ontario, London, Ontario, Canada
Elsayed Elbeshbishy, **Hisham Hafez**, Department of Civil and Environmental Engineering, the University of Western Ontario, London, Ontario, Canada

Abstract
In this study, the catalytic hydrogen production from hog manure using supercritical water partial oxidation was investigated in a batch reactor at a temperature of 500 °C, and pressure of 28 MPa using several metallic catalysts. Hog manure was characterized by a total and soluble chemical oxygen demand (TCOD, SCOD) of 57000 and 28000 mg/L, total and volatile suspended solids (TSS, VSS) of 25000, 19000, and ammonia of 2400 mg/L, respectively. The order of H_2 production was the following: Pd/AC > Ru/Al_2O_3 > Ru/AC > AC > NaOH. The order of COD reduction efficiency was as follows: NaOH > Ru/AC > AC > Ru/Al_2O_3 > Pd/AC. The behaviour of the volatile fatty acids (VFA's), ethanol, methanol, ammonia, H_2S, and Sulfate was investigated experimentally and discussed. A 35 % reduction in the H_2 and CH_4 yields was observed in the sequential gasification partial oxidation (oxidant at an 80 % of theoretical requirement) experiments compared to the gasification experiments (catalyst only). Moreover, this reduction in gas yields was coincided with a 45 % reduction in the liquid effluent chemical oxygen demand (COD), 60 % reduction of the ammonia concentration in the liquid effluent, and 20 % reduction in the H_2S concentration in the effluent gas.

1 Introduction

Conversion of waste biomass to energy is of great interest due to simultaneous resource recovery and pollution abatement. Hog manure contains major plant nutrients and organic matter that can be utilized as a potential to produce hydrogen-rich gaseous fuel. Thus, hydrogen production from hog manure may be a solution for cleaner fuel as well as disposal problems. However, hog manure usually contains water and a dry feedstock is required for conventional gasification, and because the drying process is an energy-intensive operation, supercritical water is a promising technology for gasifying waste biomass with high moisture content. Supercritical water (SCW) is an emerging technology that has been developed to treat hazardous waste streams as well as producing green gases such as hydrogen [9, 18, and 28]. Supercritical water can dissolve most organic substances and gases and has low viscosity and strong transport ability. Above water supercritical conditions (T>374 °C,

P>22.1 MPa), the density, dielectric constant, and ionic product of water decrease, and the SCW acts as a non-polar solvent with high diffusivity and excellent transport properties [9, 11, 15, and 19]. This facilitates the dissolution of many non-polar organic compounds and gases in water. The SCW high diffusivity coupled with high solubility of both gases and organic materials provide high mass transfer fluxes which accelerate reactions [22]. Thus, SCWO is considered useful to eliminate a wide range of problematic wastes from abroad variety of industries [19].

The fact that manure has a very high water content (>95 % on a wet basis), makes it more suitable for the SCW process than other conventional treatment processes. Furthermore, hog manure due to its high water, solids, and ash content is not amenable to treatment in conventional fossil-type furnaces such as incinerators and gasifiers [35] due to high energy consumption and plugging. Moreover, sulfur in the waste is converted to sulfur dioxide and trioxides [35] which increases corrosiveness. Biological treatment of hog manure, although technically feasible, requires extremely long hydraulic retention time (HRTs) of the order of days, high energy input, has a potential for odor generation, and a poor response to dynamic loading conditions as well as exhibits sensitivity to toxins [36]. Each of these treatment methods has shortcomings and therefore may not be the best option for treating organic and toxic wastes [30]. Thus, employing SCW to produce green energy from waste streams such as hog manure has many advantages. Indeed, using SCW as a reaction medium avoids the expensive step of drying. In fact, estimated feedstocks of 30 % or higher moisture content are preferable and more economical in SCW [32]. Moreover, the ability of SCWG to achieve higher conversion (over 99 %) of the solid particles and high hydrogen production coincident with suppression of char and tar formation [23] renders them very attractive.

Several studies have been reported in literature on biomass or biomass model compounds gasification for H_2 production using SCW [2, 3, 5, 7, 9, 10, and 28]. These studies employed both heterogeneous and homogeneous catalysts (such as NaOH, KOH, activated carbon, metallic catalysts). Osada et al. [1, 2, and 3] reported that supported ruthenium, rhodium, platinum, palladium, and nickel catalysts are active in decomposition of aromatic compounds. The aforementioned authors pointed out that lignin is first converted to alkylphenols and formaldehyde through hydrolysis in supercritical water; the alkylphenols and formaldehyde decompose to gases over the above mentioned catalysts. Osada et al [1] who conducted gasification experiments of biomass, coal and waste plastics in an autoclave at 450 °C, 44 MPa, and 120 minutes reported that Ruthenium (Ru) metal particles aggregated during the first run because the surface area of the $A_{l2}O_3$ support drastically decreased due to its crystal structure change from γ-Al_2O_3 to α-Al_2O_3.

In a recent study, Zhang et al. [8], conducted partial oxidative gasification of municipal sludge (5 wt%) with NaOH catalyst, using a batch type reactor at a temperature ranging of 350-500 °C, pressure range 23-28 MPa and residence time from 5 to 40 min. The aforementioned authors reported that municipal sludge can be gasified in supercritical water with no char and tar at a relatively lower temperature of 500 °C than the 700 °C required for biomass. Their experimental results on hydrogen production from municipal sludge showed that addition of base catalyst (NaOH) coupled with partial oxidation enhanced the hydrogen mole fraction yield from 20 % to 40 %. The addition of NaOH lowered the decomposition temperature of sludge and promoted the water-gas shift reaction.

Osada et al. [4] who studied the effect of both base (NaOH) and metal zirconium oxide (ZrO_2) catalysts on the partial oxidative gasification of *n*-hexadecane and lignin in SCW reported a doubling of the hydrogen yield from lignin by adding zirconia catalyst at an oxygen-to-carbon ratio of 1.0, and four times higher hydrogen yield upon addition of sodium hydroxide (NaOH). Yamaguchi et al [10] reported that ruthenium, rhodium, platinum, palladium, and nickel noble metal catalysts which supported on activated carbon showed higher hydrogen and carbon monoxide selectivity. According to Cortright et al. [21], H_2 selectivity is evaluated to know how many hydrogen atoms in an organic compound can be taken out as H_2 in the gas phase. The role of gasification is to promote the water-gas shift reaction whereas the thermal decomposition of intermediates is enhanced by the partial oxidation. This suggests that the hydrogenation of biomass by employing sequential gasification partial oxidation could enhance the H_2 production rate. Thus, the relevant processes could be approximated by the following general reactions:

Gasification:

$$C_mH_nO_pN_jS_{k\ \{Catalyst\}} \rightarrow CO+CO_2+H_2+CH_4+H_2S+\text{Intermediate products} \quad (1)$$

Partial oxidation:

$$[C_mH_nO_pN_jS_k]_{\{\%O2<1\}} + \text{Intermediate products} \rightarrow CO_2+CO+H_2+H_2S+\text{other components} \quad (2)$$

Water-gas shift reaction:

$$CO+H_2O \rightarrow \text{active hydrogenating species} \rightarrow CO_2+H_2 \quad (3)$$

Methanation reactions:

$$CO+3H_2 \rightarrow CH_4+H_2O \quad (4)$$
$$CO_2+4H_2 \rightarrow CH_4+2H_2O \quad (5)$$

Search of data bases such as SciFinder Scholar, Engineering Village, and Google using the key words of supercritical water gasification; catalysts; hydrogen; hydrogen generation; biomass; gasification; hog manure; wastewater; supported carbon catalyst; hydrogen production revealed that to the best of the authors knowledge no work has been reported on hydrogen production from hog manure in supercritical water despite the selected few aforementioned studies of municipal waste. The challenges of hog manure stem directly from the high solids content and the odorous compounds i.e. ammonia and sulfur. Furthermore, it is evident from the above literature that even studies on thermal hydrogen production from wastes have focused on the energy recovery aspect without due consideration of residual liquid quality and odorous compounds emissions. Thus, while the overall objective of this

study is to demonstrate the feasibility of hydrogen production from hog manure using SCW, the specific goals include:

- Parallel side-by-side assessment of the impact of sequential gasification and partial oxidation relative to the conventional gasification and partial oxidation solely on the fate of ammonia, and organics that has not been reported in literature.
- Evaluate the activity of different commercial heterogeneous and homogenous catalysts including supported activated carbon metallic on the gaseous products as well as the liquid effluent quality.

2 Materials and Methods

2.1 Materials

Hog manure was obtained from a facility in South Western Ontario used as the feed characterized by a total and soluble chemical oxygen demand, Volatile suspended solids, ammonia. 5 % ruthenium supported on alumina and 5 % ruthenium supported on carbon catalysts were purchased from Alfa Aesar (Ward Hill, MA, USA). Alkali NaOH reagent grade and 5 % palladium supported on carbon catalysts were obtained from Sigma-Aldrich Canada ltd (Oakville, Ontario, Canada). Activated carbon was purchased from Caledon Laboratories Ltd (Georgetown, Ontario, Canada).

2.2 Experimental setup

Experiments were performed in the main reactor body procured from Autoclave Engineers, (Erie, Penna, U.S.A). Figure 1 portrays a schematic diagram of the experimental system setup. The reactor was constructed of Hastelloy C-276 with a capacity of 600 ml, with a maximum pressure rating of 41.4 MPa and maximum temperature rating of 343 °C. From the pressure-temperature rating of the Hastelloy alloy published on the manufacturer's web site, the reactor operating conditions were modified to sustain higher temperature of maximum 500 °C at a lower pressure level of 36 MPa. This facilitated operation of the reactor above the critical conditions of water (374 °C, 22.13 MPa).The reactor was heated with a 1.5 kW electrical furnace that surrounded its main body supplied by Autoclave Engineers, (Erie, Penna, U.S.A). The reactor was a batch reactor, but allowed for sampling of gas and liquid samples throughout the experiments.

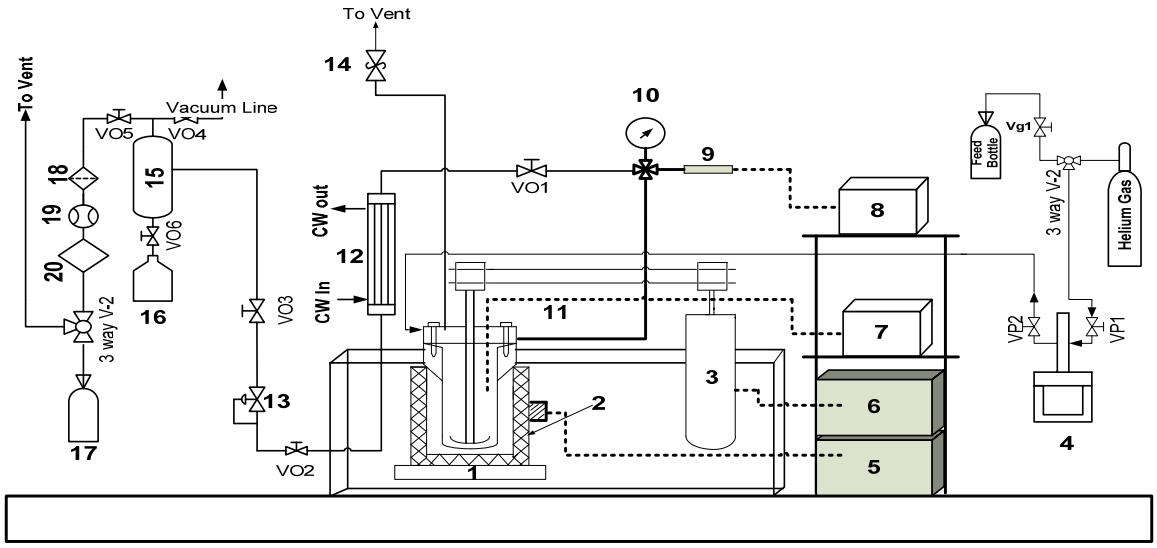

Figure 1: 1-Reactor, 2-Heater, 3-Motor, 4-Isco Syringe Pump, 5- Temperature controller, 6-Motor speed controller,7- Temperature reader,8- Pressure reader, 9-Pressure Transducer, 10- Pressure gauge, 11- Thermocouple, 12 Double pipe H/E, 13-Pressure Reducing Valve, 14-Relife Valve , 15- Gas/liquid Separator, 16- Liquid effluent tank, 17- Gas Bag, 18- Line Filter, 19- Mass flow meter, 20- H_2S logger.

2.3 Experimental procedure

The experimental procedure consisted of several steps starting by opening and washing the reactor thoroughly with (4:1) acetone-water mixture to collect any residual carbon from previous experiments. The catalyst and 100 ml of hog manure were added to the reactor after which it was closed and purged with helium gas at a constant pressure rate of 0.2 MPa for 20 minutes to drive away all the air and oxygen that may be presented in the system. After purging with helium, the outlet valve (VO1) was closed and the pressure in the reactor was increased to 0.7 MPa to prevent water evaporation through the heating phase. The reactor was heated to the desired temperature, and the pressure was increased accordingly to about 22.8 MPa. Reaction time was measured after the desired temperature was reached.

In the experiments where hydrogen peroxide was used as an oxygen source, a known amount of hydrogen peroxide solution was injected to the reactor against its pressure by employing an ISCO syringe pump (Model 100 DX, Lincoln NE, USA). Experiments with glucose as feed revealed that the H_2 yield was minimum at a reaction time of 15 minutes. Thus, the oxygen dose was injected after 15 minutes of reaction time i.e. (after 15 minutes of reaction time at 500 °C). At the completion of the reaction time of 30 minutes, the valve (VO1) was opened to allow for effluent gases to pass through condenser (double pipe heat exchanger manufactured locally) where it cooled and depressurized using a Swagelok piston-sensing high pressure reducing regulator (KHP series, Solon, OH, USA). The cooled depressurized effluent passed to a gas liquid separator (manufactured locally) where gases and liquid products were separated. The gaseous product left the separator to pass through an in-line filter to remove any moisture, and an OMEGA mass flow meter (FMA 1700/1800

series 0-2 L/min, Laval Quebec, Canada). The mass flow meter was equipped with a totalizer that utilizes a K-factor to relate the mass flow rate of nitrogen as an actual calibrated reference gas. The details of gas flow calculations are reported elsewhere [5]. The effluent gases were then collected in 3L Tedlar sampling bag. As soon as the gas bag filled, the flow of product gases was vented. Simultaneously, the liquid product was collected from the bottom of the gas liquid separator.

After each experiment, the reactor was left to cool down. The reactor was then opened and filled with (4:1) acetone-water mixture. The mixture was used to recover both the catalyst and the unconverted carbon. Two phases were observed in the recovered mixture, the catalyst at the bottom and the treated liquid containing the residual contaminant. The catalyst was then recovered by filtration using 0.45 μm sterile membrane filter (Catalog. No 7141104, Whatman Limited, Maidstone, England). Following the recovery of the solid catalyst, the acetone-water mixture containing the residual contaminant was allowed to evaporate at 105 °C for 12 hours in a furnace (Sheldon Manufacturing Inc, Model 1350GM, Cornelius, OR, USA).

After evaporation, the solid of acetone-water mixture was collected, weighed, and then analyzed using thermogravimetric analysis technique. The apparatus used for thermogravimetric analysis was acquired from THE M&P LAB Co (Model TA SDT Q600, NY, USA). Samples of approximately 20 milligrams were placed in 90μL alumina pans and placed in the apparatus. The samples were run using dual Sample Mode in a Nitrogen atmosphere (100mL/min) at a rate of 20 °C/min from room temperature to 800 °C. The resulting data was analyzed in the form of weight percent versus temperature. Since carbon burns at temperatures below the 800 °C used in the test, the weight of carbon in the sample i.e. the carbon left in the reactor excluding the catalyst and support (which was removed by filtration), was calculated as the initial weight less than the final residual after thermogravimetric analysis. Subsequently in order to assess the COD balance, the residual carbon was converted to COD using a factor of 2.7 gCOD/gcarbon.

2.4 Analytical procedures

Gaseous products were analyzed by gas chromatograph (Shimadzu, GC-2014) equipped with a thermal conductivity detector and 120/80 D Hayesep stainless steel nickel packed column (Grace Davidson, Columbia, MD,USA) with dimensions of 6.2 m length x 3.18 mm internal diameter. Helium was used as the carrier gas. The gas chromatograph was calibrated using a standard gas mixture of known composition obtained from Matheson Tri Gas Co (Coulombs, OH, USA). The analysis was performed manually using 1ml gas tight syringe (SGE, Model number 008100, Reno, NV USA) collected from the Tedlar gas sampling bag. For each analysis, at least three injections were performed and the results were averaged to minimize the analytical error.

The organic content of the process liquid effluent was examined using the following parameters i.e. total and soluble chemical oxygen demand (TCOD & SCOD), volatile fatty acids (VFAs), ethanol, methanol, ammonia, sulfate (PO^{2-}_4), alkalinity, nitrate, total phosphorous, and pH. Total and soluble chemical oxygen demand (TCOD, SCOD) were measured using HACH methods and test kits (HACH Odyssey DR/2500). Individual VFAs were analyzed by a gas chromatograph (Varian 8500) with a flame ionization detector (FID)

equipped with a fused silica column having dimensions of 30 m length x 0.32 mm internal diameter. Helium was used as a carrier gas at a flow rate of 5 ml/min. The temperatures of the column and detector were 110, 250 °C, respectively. For ethanol and methanol measurement, the same gas chromatograph (Varian 8500) with a refractive index detector (RID) was used. The pH was measured using portable pH meter (Oakton, Model WD-35615-22, IL, USA). All analyses were performed according to standard methods for the examination of water and wastewater (APHA and AWWA, 1992).

2.5 Data Interpretation

For the purpose of COD balance calculations, the reactor feed, and liquid effluent COD were measured. The gaseous product COD was also calculated. The product gas yield, gas composition, COD reduction efficiency, and COD balance are defined as follows:

$$\text{Gas composition (\%)} = (\text{mol gas product}) / (\text{sum of mol gas product}) \times 100 \quad (6)$$

$$\text{Product gas yield} = \text{gas volume produced (ml)} / \text{COD removed (g)} \quad (7)$$

$$\text{COD reduction efficiency (\%)} = \{[COD_{initial} - COD_{final}] / [COD_{initial}]\} \times 100 \quad (8)$$

$$\text{COD balance} = [COD_{\text{gas product}} + COD_{\text{liquid product}} + COD_{\text{reactor residual}}] / [COD_{in}] \quad (9)$$

The reactor residual carbon i.e. unconverted carbon was determined as described in section 2.3 to assess the COD reactor residual.

3 Results and Discussion

3.1 Effect of residence time and partial oxidation on gas yield from hog manure in SCW

We first investigated the effect of residence time on the gas yield at a temperature of 500 °C, pressure of 31 MPa, oxygen dose (OD) equals to 80 % of the theoretical COD required to oxidize all the initial COD, and residence times of 30, 60, and 90 min. The oxygen dose was optimized in a previous study and was adopted as a base line for catalysts evaluation [5]. Figure 2 shows H_2, CO, and CO_2 yields in the gas stream. As shown in Figure 2, the CO yield was always insignificant, the order of, CH_4, and CO_2 yield was as follows: 60>30>90 minutes.

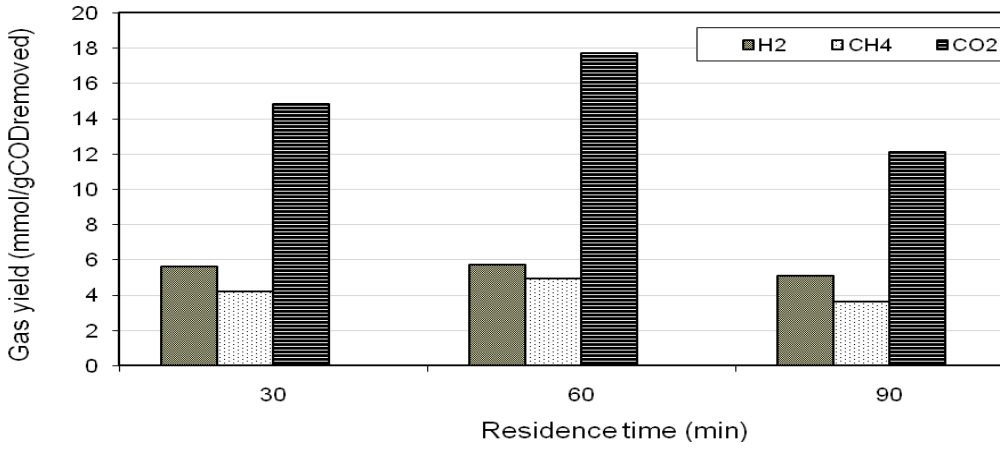

Figure 2: Gas yield distribution in partial oxidation experiment at different residence time.

The H_2 yield at a reaction time of 60 minutes of 5.7 mmol/gCOD removed was higher than the 30 minutes reaction time by an insignificant amount (0.1 mmol/gCOD removed). Thus, since all differences were not substationally significant, we selected the reaction time of 30 minutes as a base line for the subsequent experiments. However, the yield of methane increased from 4.2 mmol/gCOD removed at 30 minutes to 4.9 mmol/gCOD removed at 60 reaction time which implies acceleration of the methanation reactions as per equations 4 and 5. On the other hand, the absence of CO in the effluent gas in the three experiments means that water-gas shift reaction occurred and may be one of the reasons for the enhancement of H_2 production [9, 10]. However, the exact extent of the water-gas shift reaction was not evidently identified since CO_2 could be produced from other reactions or from the thermal decomposition of some intermediates. Another possible way of H_2 formation is the thermal decomposition of the intermediate compounds [8, 28, and 33]. In other words, the presence of oxygen as an oxidant probably contributed to the H_2 formation by oxidizing some of the organic intermediate compounds as reported in our previous study [5].

Table 1 summarizes the liquid effluent quality for the reaction times. It is apparent that residual ammonia at 90 minutes decreased by 20 % to 4180 mg/L relative to 30 and 60 minutes. A COD reduction of 83 %, 85 % and 81 % was achieved at residence times of 30 min, 60 min and 90 min, respectively, and the reduction in COD was found to be independent of the residence time. The lowest residual COD of 8775 mg/L was observed at the 60 minutes reaction time which was 18 % lower than the maximum COD at 90 minutes. This implies that after 60 minutes of reaction, some components were involved in intermediate reactions and formed other liquid components that eventually increased the TCOD and SCOD. The VFAs, ethanol and methanol combined constituted 33 %, 33 % and 24 % of the SCOD at residence times of 30, 60 and 90 minutes, respectively. In all experiments, and as reported in Table 2, the TSS and VSS concentrations were less than 300 mg/L which corresponds to destruction of > 98% of the initial values.

Table 1: Liquid effluent characterization in partial oxidation experiments.

Reaction time	30 min	60 min	90 min
OD	0.8	0.8	0.8
TSS	540	220	440
VSS	400	160	360
TCOD	9740	8775	10740
SCOD	6942	6480	8160
NH4	4950	5030	4180
PO4-	454	270	302
VFA	2323	2129	1964
Alkalinity	N/A	31030	28890
Nitrate	15	9	8
pH	9.23	9.3	9.21
COD reduction (%)	83	85	81
COD balance	85.3	85.6	87.4

3.2 Effect of catalysts on gas yield from hog manure in SCW

The effect of different catalysts on SCW gasification of hog manure was investigated by using 2.5 grams of catalyst in each experiment, and eliminating the oxygen addition. Figure 3 shows the product gas distribution for each catalyst. The major components of the product gas yield in all experiments were CO_2, H_2, and CH_4. However, trace amounts of CO was detected only in the case when NaOH was used as a catalyst. The negligible CO yield (almost 0 mmol/gCODremoved) during the Pd/AC, Ru/Al_2O_3, Ru/AC, and AC catalytic experiments was found to be in good agreement with the results obtained for AC catalyst by Antal and Xu [9, 29, and 29]. Furthermore, Elliott and Sealock [33] selected the rate of CO disappearance as a measure of the water-gas shift reaction rate in preference to the rate of CO_2 or H_2 increase. It was noticed that the H_2/CO_2 yield ratio equaled to 1.2 in the case when NaOH was used as a catalyst. Zhang et al [8] reported that alkali salts increase the reaction rate of the water-gas shift reaction, and ultimately the reaction of CO with water to produce H_2 and CO_2 as per equation 3.

The higher than unity H_2/CO_2 yield ratio implies that the CO_2 was not completely recovered since CO_2 tends to dissolve in alkaline solutions (NaOH in this case).

As apparent from Figure 3, the Pd/AC catalyst produced the highest H_2 yield followed by Ru/Al_2O_3. Yamaguchi et al. [10] reported that the selectivity and yield of H_2 was the highest with Pd/C catalyst whereas the Ru/C catalyst was the most active for lignin gasification. However, and as shown in Table 2, COD reduction efficiency with the Pd/AC catalyst was lower than with Ru/Al_2O_3 and Ru/AC catalysts since the Ruthenium metal surface is known to promote the methanation hydrogen-consuming reactions [10] as per equations (4 & 5).

Furthermore, the COD removal efficiency in the absence of oxygen was retarded in all the experiments to less than 70 %, except for the experiments where NaOH was used as a

catalyst where a COD removal efficiency of 81 % was achieved comparable to what was observed with partial oxidation. The Pd/AC catalyst affected the highest removal of ammonia as well as the lower H_2S concentration in the gas, which coupled with highest H_2 yield rationalizes the retention of Pd/AC for subsequent sequential gasification partial oxidation testing.

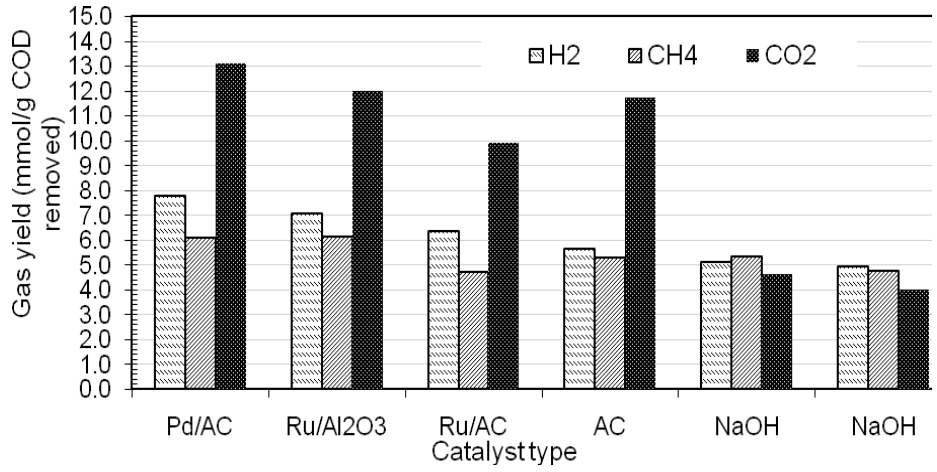

Figure 3: Gas yield distribution with different metal supported catalysts.

Table 2: Liquid effluent characterization in gasification experiments.

Catalyst	Pd/AC	Ru/Al_2O_3	Ru/AC	AC	NaOH	NaOH
Concentration (mg/L)						
TCOD	22000	20100	18660	19460	11140	10760
SCOD	21500	15200	16920	11720	9050	8940
TSS	900	840	1600	420	900	840
VSS	800	720	580	360	800	720
PO4-	519	387	513	309	427	453
Niterate	26	7	6	0	0	0
Alkalinity	23450	28160	35000	10130	27450	N/A
pH	9.37	9.27	9.46	9.57	9.88	9.83
COD reduction (%)	61	65	71	66	81	81
COD Balance	89	80.7	90.2	99.2	98.6	96

3.3 Effect of partial oxidation and catalyst on gas yield from hog manure in SCW

We studied the effect of two different oxygen dose (OD) of 60 % and 80 % of the theoretical COD required to destroy all the initial COD on the product gas yield in presence of Pd/AC catalyst. Figure 4 reports the product gas yield in mmol/gCOD removed. At an (OD) of 60 %, 3 mmol CH_4/gCOD removed and 3.5 mmol H_2/gCOD removed was produced comparing to 3 mmolCH_4/gCOD removed and 5 mmol/gCOD removed at an (OD) of 80 % was employed.

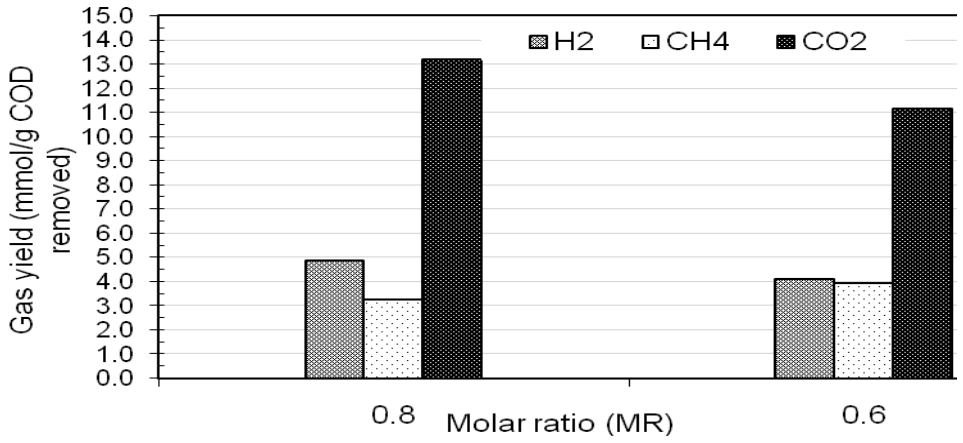

Figure 4: Gas yield distribution at gasification followed by partial oxidation experiments.

These results indicated that at an (OD) of 60 %, the methanation reaction proceeded and consumed part of the produced H_2 to form CH_4 which was also confirmed by the lower CO_2 yield of 11mmol/gCOD removed compared to the 14mmol/gCOD removed at an (OD) of 80 %, [7, 33]. The lower CO_2 yield at an (OD) of 60 %, could be also attributed to the lack of oxygen which affects the formation of CO_2 through direct oxidation of CO to CO_2. Furthermore, and according to Cortright et al [21], the H_2/CO_2 yield ratio of 1.0 at an (OD) of 60 % suggests that CO was consumed through water-gas shift reaction to form H_2 prior the introduction of hydrogen peroxide (H_2O_2) to the reactor as an oxygen source. This is also supported by Zhang et al [8], who reported that the improvement of H_2 yield in the presence of catalyst in the reactor is explained by the production of CO by partial oxidation followed by water-gas shift reaction.

On the other hand, Table 3, showing the main liquid products in the sequential gasification partial oxidation experiments, indicates that COD removal efficiencies at an (OD) of 60 % and 80 % were comparable at 79 % and 81% respectively whereas the COD balance closures were 94 % and 89 % respectively, with COD balance closure of 94 % and 89 %. In all experiments, the liquid effluent collected from the gas-liquid separator was characterized by a dark brown color with burnt smell.

Table 3: Liquid effluent characterization in sequential gasification and partial oxidation experiments.

OD	0.8	0.6
Catalyst	Pd/AC	Pd/AC
TCOD	11920	10800
SCOD	7400	8800
TSS	820	860
VSS	700	600
PO4-	489	504
VFA	1700	1891
Niterate	8	14
Alkalinity	10127	26050
pH	9.24	9.31
COD reduction (%)	79	81
COD Balance	94	89

4 Summary

Catalytic and non-catalytic hydrogen production from hog manure using supercritical water partial oxidation, gasification, and sequential gasification partial oxidation was investigated in a batch reactor at a temperature of 500 °C, and pressure of 28 MPa using several metallic catalysts. The feasibility of hydrogen and methane production was demonstrated using sequential gasification partial oxidation. The order of H_2 production in catalytic gasification was the following: Pd/AC > Ru/Al_2O_3 > Ru/AC > AC > NaOH. The order of COD reduction efficiency was as follows: NaOH > Ru/AC > AC > Ru/Al_2O_3 > Pd/AC. The following can be concluded:

- Sequential gasification and partial oxidation is better than each one individually from an environmental point of view as it produced the lowest ammonia concentration of 1534 mg/L, the lowest effluent COD concentration in liquid phase, and the lowest H_2S concentration of 130 ppm in the gas phase.
- Of all employed catalysts, Pd/AC was the best as it provided the highest H_2 yield as well as the lowest H_2S concentration in the gas phase.

In conclusion, future investigation into higher temperatures and catalyst deactivation is required.

Acknowledgements

The authors gratefully acknowledge support from Ontario Centers of Excellence (OCE), and the financial support in the form of Discovery Grant from the Natural Science and Engineering Research Council of Canada (NSERC). The Libyan Secretariat of High Education support in the form of student Scholarship for Emhemmed A Youssef is highly acknowledged.

References

[1] Osada M, Sato O, Watanabe M, Arai K, Shirai M. Stability of Supported Ruthenium Catalysts for Lignin Gasification in Supercritical Water. *Energy Fuels* 2006; 20: 930–935.

[2] Osada, M.; Sato, O.; Watanabe, M.; Arai, K.; Shirai, M. Catalytic Gasification of Wood Biomass in Subcritical and Supercritical Water. Combust Sci Technol 2006; 178: 537–552.

[3] Osada M, Sato O, Hiyoshi NM, Arai K, Shirai M. Effect of Sulfur on Catalytic Gasification of Lignin in Supercritical Water. Energy & Fuels 2007; 72:1854–1858.

[4] Osada M, Sato O, Hiyoshi NM, Arai K, Shirai M. Catalytic effects of NaOH and ZrO2 for partial oxidative gasification of n-hexadecane and lignin in supercritical water. Fuel 2003; 82:545–552.

[5] Youssef AE, Chowdhury BM, Nakhla G, Charpentier P. Effect of nickel loading on hydrogen production and chemical oxygen demand (COD) destruction from glucose oxidation and gasification in supercritical water. Int J Hydrogen Energy 2009; In press.

[6] Buhler W, Dinjus E, Ederer H, Kruse A, Mas C. Ionic reactions and pyrolysis of glycerol as competing reaction pathways in near-and supercritical water. J Supercrit Fluids 2002; 22(1): 37–46

[7] Sinag A, Kruse A, Schwarzkopf V. Key compounds of the hydropyrolysis of glucose in supercritical water in the presence of K2CO3. In. Eng Chem Res 2003; 42(15): 3516–3521.

[8] Zhang Q, Shuzhong W, Liang W, Donghai Xu. Catalytic Hydrogen Production from Municipal Sludge in Supercritical Water with Partial Oxidation. Proceeding in International Conference on Power Engineering October 23-27, 2007, Hangzhou, China

[9] Xu XD, Antal MJ Jr. Gasification of Sewage Sludge and other Biomass for Hydrogen Production in Supercritical Water. Environ Prog 1998; 17:215

[10] Yamaguchi A, Hiyoshi N, Sato O, Bando K, Osada M, Shirai M. Hydrogen Production from Woody Biomass over Supported Metal Catalysts in Supercritical Water. Catalysis Today 2009; 182:192–195

[11] Webley PA, Tester JW, Holgate HR. Oxidation Kinetics of Ammonia and Ammonia-Methanol Mixtures in Supercritical Water in the Temperature Range 530-700 °C at 246 bar. Ind Eng Chem Res 1991; 30:1745-1754.

[12] Killilea WR, Swallow KC, Hong GT. The Fate of Nitrogen in Supercritical-Water Oxidation. J Supercrit Fluids 1992; 5: 72-78.

[13] Takahashi Y. Water oxidation waste management system for CELSS- The state of art. boi. Sci in space 1989; 1: 45-54.

[14] Shanableh A, Gloyna EF. Supercritical Water Oxidations of Wastewater and Sludges. Water Sci Technol 1991; 23: 389.

[15] Cocero MJ, Alonso E, Torıo R, Vallelado D, Fdz-Polanco F. Supercritical Water Oxidation in a Pilot Plant of Nitrogenous Compounds: 2-Propanol Mixtures in the Temperature Range 500-750°C. Ind. Eng. Chem. Res. 2000, 39, 3707-3716.

[16] Shanableh A, Jomaa S. Production and transformation of volatile fatty acids from sludge subjected to hydrothermal treatment. Water Sci Technol 2001; 44, 10: 129-135.

[17] Shanableh A. Production of useful organic matter from sludge using hydrothermal treatment. Water Res 2000; 34, 3:945-951.

[18] Portela RJ, Nebot E, de la Ossa M. Generalized kinetic models for supercritical water oxidation of cutting oil wastes. J. Supercrit Fluids 2001; 21:135–145.

[19] Li L, Chen P, Gloyna EF. Kinetic model for wet oxidation of organic compounds in subcritical and supercritical water, in: Supercritical Fluid Engineering Science. ACS Symp 1993; Ser: 514.13.

[20] Meyer JC, Marrone AP, Tester WJ. Acetic Acid Oxidation and Hydrolysis in Supercritical Water. AIChE Journal 2004; 41 (9): 2108-2121.

[21] Cortright RD, Davda RR, Dumesic JA. Hydrogen from catalytic reforming of biomass-derived hydrocarbons in liquid water. Nature 2002; 418: 964-967.

[22] Akiya N, Savage PE. Roles of water for chemical reactions in high-temperature Water. Chem. Rev 2003; 102: 2725–2750.

[23] Calzavara Y, Dubien CJ, Boissonnet G, Sarrade S. Evaluation of biomass gasification in supercritical water process for hydrogen production. Energy Conversion and Management 2005; 46: 615-6731.

[24] Ploeger MJ, Mock AM, Tester JW. Cooxidation of ammonia and ethanol in supercritical water, part 1: Experimental results. AIChE Journal 2007; 53 (4): 941-947.

[25] Helling RK, Tester JW. Oxidation of simple compounds and mixtures in supercritical water: carbon monoxide, ammonia, and ethanol, Env. Sci. Technol 1998; 22: 1319–1324.

[26] Wang T, Zhu Xi. Sulfur transformations during supercritical water oxidation of a Chinese coal. Fuel 2003; 82: 2267–2272.

[27] Yanagida T, Minowa T, Nakamura A, Matsumura Y, Noda Y. Behavior of Inorganic Elements in Poultry Manure during Supercritical Water Gasification. Journal of the Japan Institute of Energy 2007; 86: 731-736.

[28] Xu XD, Aihara M, Antal MJ Jr. Hydrogen Production by Steam Reforming Glucose in Supercritical Water. Energy & Fuels 1993; 7: 514-577.

[29] Xu XD, Matsumura Y, Stenberg J, Antal MJ Jr. Carbon-Catalyzed Gasification of Organic Feedstocks in Supercritical Water. Ind. Eng. Chem. Res 1996; 35: 2522-2530.

[30] Gasafi E, Meyer L, Schebek L. Exergetic efficiency and options for improving sewage sludge gasification in supercritical water. Int. J. Energy Res 2007; 31:346–363

[31] Abraham AM, Aki NV. An economic evaluation of catalytic Supercritical Water Oxidation. Enviro Prog 1998; 17: No.4.

[32] Savage E P. A perspective on catalysis in sub- and supercritical water. J. Supercrit. Fluids 2009; 47: 407–414.

[33] Elliott CD, Sealock JL. Aqueous catalyst systems for the water-gas shift reaction. 1. Comparative catalyst studies. Ind. Eng. Chem. Res 1983; 22 (3): 426-431.

[34] Goto M, Shiramizu D, Kodama A, Hirose T. Kinetic Analysis for Ammonia Decomposition in Supercritical Water Oxidation of Sewage Sludge. Ind. Eng. Chem. Res 1999; 38: 4500-4503.

[35] Buckley J, Schwarz P. Renewable Energy from Gasification of Manure: An Innovative Technology in Search of Fertile Policy. Enviro Monit and Asses 2003; 84: 111–127.

[36] Bernet N, Beline F. Challenges and innovations on biological treatment of livestock effluents. Bioresource Technology 2009; 100(22): 5431-5436.

Reforming and Gasification – Biomass

Achim Schaadt, Siegfried W. Rapp, and Christopher Hebling

Abstract

Gasification is an efficient method to convert both wet and dry biomass into a gaseous product with a usable heating value. Recently, the technology for the gasification of dry biomass has approached commercialization for some applications. In addition, a variety of processes for different products are currently tested in pilot plants. In future, these processes could provide a significant contribution for the sustainable production of biomass-derived energy carriers which could be used for mobile and stationary applications (e.g., fuel cells). In contrast to conventional gasification, hydrothermal processes can efficiently convert biomass with its natural water content. However, hydrothermal gasification still requires further research and development before large-scale pilot plants can be built.

Industrial Scale Hydrogen Production from Biomass via CHOREN's Unique Carbo-V-process

Jochen Vogels, CHOREN Industries GmbH, Germany

1 Introduction

Worldwide fossil-fuel demand is increasing rapidly and known resources are diminishing. Energy sources such as oil and gas in Western Europe are almost depleted resulting in an even higher dependency from fuel imports in the near future. These aspects combined with climate-change concerns have increased demand for renewable, clean and sustainable energy whereas "green" hydrogen as energy carrier could take a major role in the future.

Already 10 years ago, Germany-based CHOREN Industries, a leading gasification technology company, started development and testing of its highly innovative Carbo-V gasification process converting all kinds of woody biomass into high-quality synthesis gas. In 2009, CHOREN in collaboration with Shell finished construction work for its 120 m€ semi-industrial BTL (Biomass To Liquids) production plant in Freiberg, Saxony, being the first of its kind in the world. From mid 2010, the 18 million litres/year BTL facility will produce second-generation synthetic transport fuels from forest residues and waste wood. After successful commissioning and start-up of this demonstration facility, CHOREN will scale up its technology towards large scale Syngas production plants (Sigma plants).

2 The Carbo-V Gasification Process

The Carbo-V gasification process developed by CHOREN presents an innovative and efficient way of converting biomass feedstock into clean, tar-free and low-methane synthesis gas. Thereby the three-stage Carbo-V gasification process combines the advantages of an entrained flow gasification originating from coal utilization with an innovative pre-conditioning of the solid biomass which is done by a thermal process (pyrolysis) called "Low Temperature Gasification" (LTG).

In a first process step (LTG), the wood chips are thermally cracked at temperatures between 400 °C and 500 °C. The products of this pyrolysis decomposition are charcoal and a pyrolysis gas containing the volatiles components of the wood diluted in the gasification agent. The necessary heat for this pyrolysis process is gained by oxidizing a small amount of the charcoal in the LTG. This oxidation is performed by a gasification agent gas which consists of a mixture of oxygen and saturated steam. This mixture is fed to the LTG through nozzles at the bottom of the reactor.

The char from each LTG is cooled, de-compressed to atmospheric pressure, screened, grinded, stored and then fed to the High Temperature Gasifier.

In the second process step, the pyrolysis gas as well as the recycled residual coke is further oxidized with pure oxygen in the combustion chamber of the HTG at temperatures above the melting point of the fuel ash. Thus the hydrocarbon-rich pyrolysis gas will be converted to a hydrocarbon-free process gas consisting only of CO, CO_2, H_2 and steam.

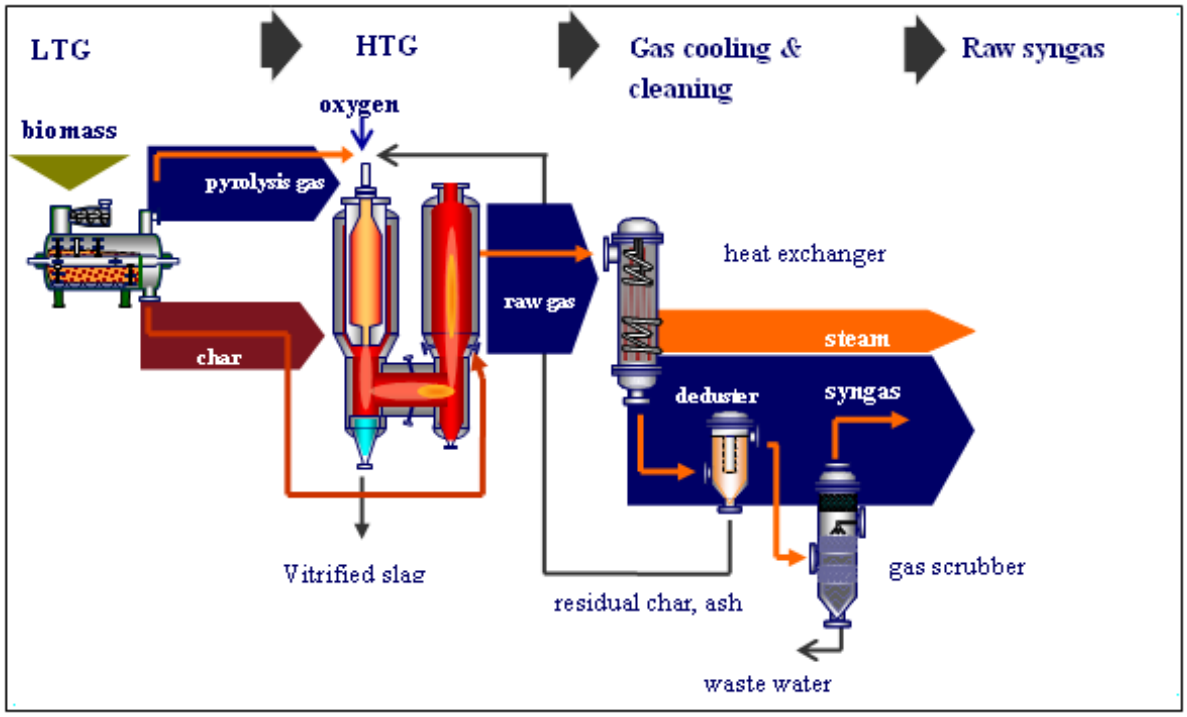

Figure 1: The Carbo-V gasification process.

In the third process step, char from the storage silo is fed to the endothermic part of the Carbo-V gasifier via a chamber sluice. The hot process gas from the burning chamber now reacts with the char in the gasification reactor of the HTG according to following basic reactions:

$C + CO_2 = 2\ CO$ $\Delta HR = +\ 172$ MJ/kmol

$C + H_2O = CO + H_2$ $\Delta HR = +\ 131$ MJ/kmol

As these reactions are strongly endothermic, the chemical reactions cool down the gas within the reaction vessel by more than 500 °C. This procedure is also called “chemical quenching” and is one of the major features of the Carbo-V gasification process. It allows keeping a high heating value of the product gas.

The crude syngas leaving the HTG is now further cooled down to below 200 °C via a special designed gas cooling system. The heat from the gas cooling system is used to produce high pressure steam (up to max. 90 bar).

Following the gas cooling system, the crude gas loaded with dust, residual carbon and the ash components of the feedstock has to be cleaned from solid particles. This occurs in a two-stage de-dusting system. The coarse particles are separated by a gas cyclone followed by a bag house filter system for the fine de-dusting. The residual coke is de-compressed over a chamber sluice and discharged from the system. After grinding of the residual coke to a suitable size, the solid fraction containing also the ash components is fed back to the burner of the high temperature gasifier by as a fluidized dense flow steam. A small portion of the

filter dust is removed from the process to prevent the enrichment of impurities in the residual coke circuit.

Due to the high gasification temperature in the burning chamber of the HTG, the ash components get melted. The melted ash forms a solid layer on the refractory material within the burning chamber which protects the refractory material from thermal stresses thus permitting long life times of the refractory material. The melted ash trickles down at the wall of the gasifier and is collected in a water basin below the gasifier. In the water basin the melted ash is rapidly cooled and converted to a slag granulate. The vitrified slag will be periodically discharged from the gasifier over a chamber sluice.

In CHOREN's demonstration plant in Freiberg, also called the Beta plant, the next process step within the gasification island consists of a four (4)-stage wet gas cleaning system: gas cooling (by Venturi washer), chlorine removal, sulphur removal and finally gas cooling to below 40 °C.

3 CHOREN's Beta Plant in Freiberg

The Beta plant in Freiberg will serve as a first of a kind demonstration plant for the production of synthetic bio-fuels (BTL) featuring CHOREN's Carbo-V gasification technology and Shell's Fischer-Tropsch and refinery technologies. The plant has been designed for a yearly production capacity of 15,000 tons of BTL products (diesel and naphtha). The corresponding feedstock consumption will be appox. 65,000 tons/year of dry wood. Excess heat derived from the gasification as well as from the Fischer-Tropsch process will be converted to steam and subsequently converted to electric power by a steam turbine. The syngas is produced by a 45 MW oxygen-blown Carbo-V gasification unit which is operated with 5 bar pressure.

Figure 2: View on CHOREN's BTL demonstration plant in Freiberg (Beta plant).

Typically, the dry syngas composition consists of 35-40 vol.-% H_2 and 35-40 vol.-% CO. The balance is for CO_2 and little amounts of N_2 und CH_4.

Construction work of Beta plant was completed by mid 2009, followed by a comprehensive testing and approval period. In January 2010, hot commissioning of the gasification island has been started. The first operational results were rather encouraging especially regarding gas composition and gas quality. On the other hand, some mechanical problems and deficiencies within the process control systems have caused some delays which in terms are rather normal when commissioning new technologies.

Until summer 2010, the hot commissioning and testing procedure for the gasification island will be finished. After a short revision of the gasification plant, the syngas production will start again and the hot commissioning of the downstream units will follow. “First product” is scheduled by 3rd quarter, 2010.

4 Application Universe for Syngas

With the multi-stage Carbo-V gasification process a high quality synthesis gas (containing mostly CO and H_2) will be produced offering a wide spectrum of industrial applications. Besides the production of Fischer-Tropsch liquids (diesel, naphtha, jet kerosene) and waxes, the syngas may be converted to heat and power, to alcohols such as methanol or ethanol or to green hydrogen. Currently, CHOREN undertakes a feasibility study for the implementation of a gasification based commercial hydrogen production facility in South America using 100 % of woody biomass as fuel input.

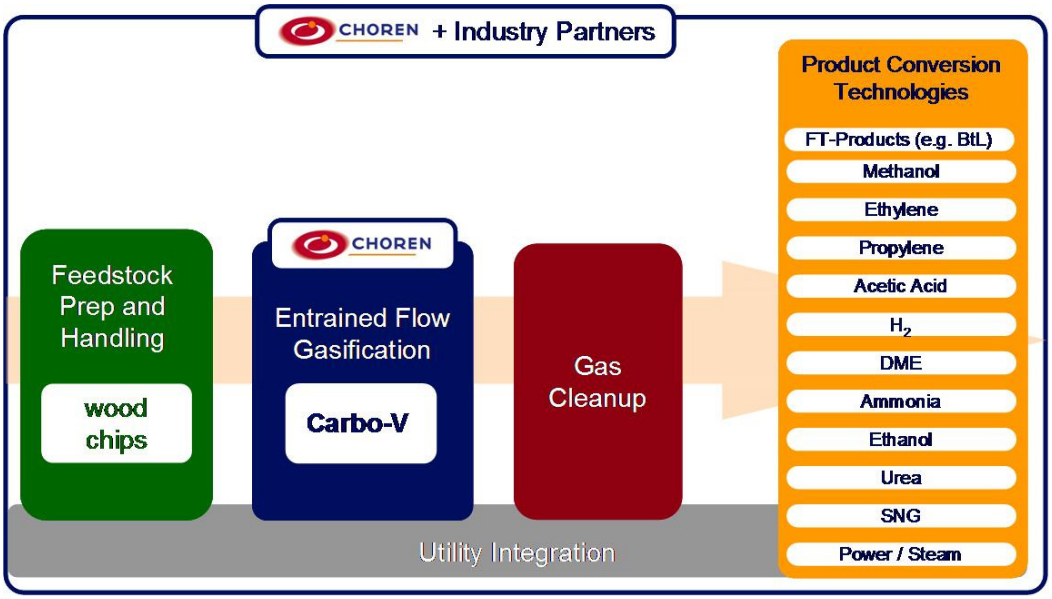

Figure 3: Application universe for syngas.

5 Large-scale Production of Hydrogen Derived from Biomass

Hydrogen does not exist alone in nature. Therefore, all hydrogen production processes are based on the separation of hydrogen from hydrogen-containing feedstock such as light

hydrocarbons, water or bio-mass. Essentially, there are two methods to separate hydrogen: thermal and electro-chemical. The most common method to commercially produce hydrogen is based on the so-called Steam Methane Reformation Process using natural gas as feedstock. This process consists of two steps: 1) reformation of natural gas with high temperature steam to syngas and 2) using a water-gas shift reaction to form hydrogen and carbon dioxide from the carbon monoxide produced in the first step.

Steam Methane Reformation

Step 1: $CH_4 + H_2O \rightarrow CO + 3\ H_2$

Step 2: $CO + H_2O \rightarrow CO_2 + H_2$

To a lesser degree, hydrogen is produced by an Electrolysis process whereas water is divided into hydrogen and oxygen by passing electricity through an ionic water bath. Thereby, the production costs of hydrogen strongly depend on the costs of the electricity. In the case this electricity is generated by renewable technologies such as solar-, hydro- or wind power, hydrogen can be produced with almost zero greenhouse gas emissions. On the other hand, this production route is in most cases not attractive from an economic point of view.

The use of biomass as feedstock for hydrogen production has potential to combine the benefits of the electrolysis regarding environment with the benefits of the Steam Methane Reformation regarding productivity and economics. In principle, the gasification of biomass replaces the Steam Methane Reformer, whereas the subsequent downstream process will stay the same.

The overall process design of a biomass derived hydrogen production plant is illustrated in the following simplified block flow diagram.

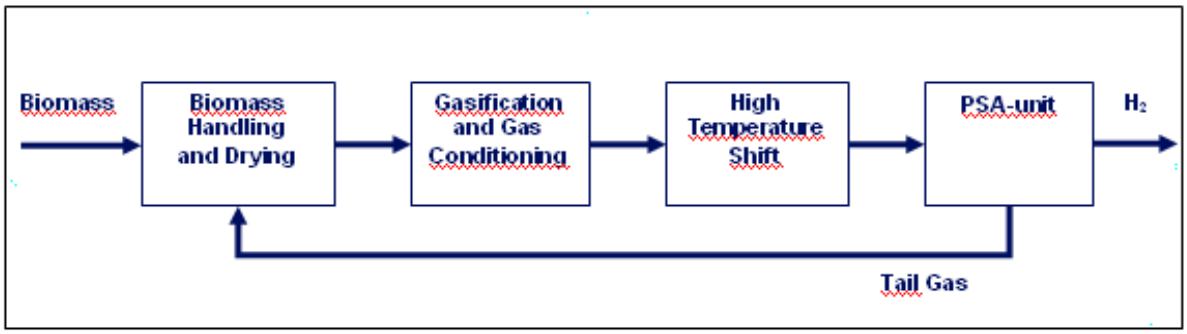

Figure 4: Hydrogen production via biomass gasification.

In a process study carried out by CHOREN, a 160 MW oxygen-blown and pressurized Carbo-V gasification unit has been selected to produce high quality syngas (CO plus H_2). Leaving the gasification unit, the syngas passes through a shift reactor where carbon monoxide reacts with steam to hydrogen and carbon dioxide. Leaving the shift reactor, the gas contains approx. 75 vol.-% hydrogen. The balance is for carbon dioxide and some

unconverted carbon monoxide as well as very low amounts of methane and nitrogen. For the hydrogen purification, a pressure swing adsorption unit (PSA) is used to separate the hydrogen from the other gas components in the shifted gas stream. The PSA system adsorbs the CO, CO_2 and other impurities in a multi-stage fixed bed adsorber. The impurities desorb from the bed upon “swinging” the adsorber from the feed (high) to the tail gas (low) pressure and by using a high-purity hydrogen purge. A hydrogen recovery rate of up to 90 % is possible with a product purity of 99.999 vol. %. Beside the pure hydrogen product, the PSA system produces a low-pressure tail gas which contains also some hydrogen used for the regeneration of the adsorbent. This tail gas has a low heating value and can for example be used as fuel gas for the feedstock dryer.

With such a plant configuration, approx. 33,300 Nm^3/h respectively 3,000 kg/h of pure hydrogen can be produced using 32 tons/h of bone dry woody biomass. The production costs of the bio-hydrogen have been calculated with 60 to 90 Euros per MWh depending mainly on the variety of costs for biomass and electricity. The production cost of hydrogen via Steam Methane Reforming process usually is between 40 and 60 Euros per MWh based upon typical average market prices in Western Europe for natural gas.

6 Conclusion

From the results of our study work it can be concluded that green hydrogen (with low emissions) can be produced via biomass gasification economically in regions where natural gas prices are high or where cheap renewable electricity is not available. This applies all the more for regions where abundant biomass is available at low prices.

Alkali-promoted Hydrothermal Gasification of Biomass for High Yield/ High Purity Hydrogen Gas (and Methane) Production

Jude Onwudili, Paul T. Williams, Energy & Resources Research Institute, University of Leeds, UK

1 Introduction

A significant amount of research has been carried out over the last two decades in the area of hydrothermal biomass gasification. A search of publications from this field in *ScienceDirect* with the topic - '*hydrothermal gasification of biomass'* - produced 439 related journal articles. Of this number, almost 400 articles were published within the last 10 years. Infact, 24 % of the total publications occurred in 2009 alone, with 65 furthers articles already published, less than 3 months into 2010. This simple analysis demonstrates the high volume of activities involved in this developing technology. Much of the research in hydrothermal gasification of biomass involves the use of catalysts and additives that can positively influence the predominant reactions with the aim of lowering the production cost of high calorific value gases produced from the process. Hydrogen and methane production from this process have been well demonstrated in research. Attempts have been made regarding a deeper understanding of the mechanisms of the gasification process [1, 2]. While the need of catalysts may not be very significant for gasification in supercritical water, certainly, they are required under subcritical and near-critical water conditions [3]. Several catalysts and additives have found use in the promotion of hydrothermal biomass gasification for hydrogen production. Different nickel catalysts, activated carbon, metal oxides and alkali-metal compounds have been reported to significantly influence the production of gases from biomass under hydrothermal conditions. It appears, however, that the alkali-type additives or catalysts have become very attractive for high hydrogen yields as they have been shown to catalyze the water-gas shift reaction – a predominant reaction in hydrogen production. In the literature, the alkali additives commonly used include NaOH, KOH, LiOH, Na_2CO_3, K_2CO_3 and $Ca(OH)_2$. Beyond that, some researchers [1, 2, 3] have shown that alkali catalysts play significant roles in the hydrothermal biomass degradation mechanism. It has been found that the composition of products from the gasification process depended on the formation of gasifiable intermediate compounds such as formic acid (as alkali-metal formate e.g. sodium formate) and acetic acid (as alkali-metal acetate e.g. sodium acetate). Many researchers have corroborated these findings regarding the effects of alkali additives, which include increased gasification efficiency and suppression of oil/tar and char formation [4]. In related studies, Jin et al [5, 6], isolated and quantified similar compounds obtained during the hydrothermal decomposition of different biomass and biomass model compounds at temperatures ranging from 250 – 300 °C, in the presence of hydrogen peroxide and alkali. Kruse et al [7] suggested a mechanism involving the formation of intermediate alkali metal

formates prior to hydrogen production. Hence, the role of alkalis in hydrothermal biomass conversions has been found to be highly significant.

In this paper, a parametric study of the decomposition of sodium formate and sodium acetate was investigated in relation to reaction temperature. All experiments were carried out in the absence of oxygen or oxygen source. The behaviour of these compounds which are regarded as the intermediate compounds of hydrothermal biomass gasification would provide more understanding of the reaction mechanisms. Furthermore, the influence of reaction temperature on the composition of gasification products of some biomass samples was investigated. The biomass samples included glucose, cellulose, starch, rice husk, rice straw and potato. The gasification experiments have been carried out in the presence of sodium hydroxide as promoter or additive.

2 Materials and Experimental Procedure

Glucose, microcrystalline cellulose and starch were obtained from Alfa Aesar, UK. Rice husk, rice straw, and potato were sourced as real-world biomass samples. The biomass samples have been characterized and reported elsewhere [2]. Analytical grade sodium hydroxide in the form of pellets, sodium formate and anhydrous sodium acetate were purchased from Sigma-Aldrich, UK.

The hydrothermal reactions of the samples were investigated in a Hastelloy-C batch reactor obtained from the Parr Instrument Co., Inc. USA. The reactor has 75 ml of volume capacity and the maximum operating temperature and pressure are 600 °C and 45 MPa, respectively. The schematic and operational procedure of the reactor has been detailed in an earlier paper [2]. 1 g of each sample was weighed into the reactor and mixed with a known volume of liquid. The biomass samples were reacted in a known volume of 2M aqueous sodium hydroxide.

The reactor loading was carried out under nitrogen atmospheres to exclude air. The reactor was then sealed and placed in a ceramic heater to raise the reaction temperature at a rate of 12 °C/min. Since the reactor was a closed system, increasing the temperature led to increase in pressure, which was read off the gauge fitted. The reaction time started once the desired temperature was reached. The reaction time was designated as zero minute, when the reaction was stopped immediately the set temperature was reached. At the end of each experiment, the heating was stopped and the reactor was removed from the heater and rapidly cooled to room temperature by an air cooling system. After cooling, the final ambient temperature and pressure were noted, respectively. The gas outlet valve was then opened to collect the gas samples. After the gas sampling, the reactor was opened to sample the liquid sample and solid residues (if any).

3 Products Analyses

Analysis of the effluent gas mixtures was carried out with two gas chromatographs with packed columns for the separation of components of permanent gases and hydrocarbon (C1-C4) gases, respectively. The analytical procedures have been detailed in several earlier papers [2, 8]. The liquid effluent obtained from the reactor at the end of the experiment was analyzed to determine the presence of organic carbon (TOC), inorganic carbon (TIC) and

dissolved solids. These analyses were done for samples from the decomposition of sodium acetate and sodium formate. The instrument used was a Hach-Lange IL550 TOC-TN analyzer fitted with two NDIR held at 800 °C. The instrument was operated in the differential TOC determination mode, in which case the same sample was analyzed consecutively for TOC and TIC contents. The analyzer was set up to make four determinations (n = 4) on each sample and the average results used. Typical standard deviation of replicate determinations ranged from 0.2-2 %.

4 Results and Discussion

4.1 Hydrothermal decomposition of 'intermediate' compounds

In order to better understand the function of sodium hydroxide in the biomass gasification process, the 'intermediates' species suspected to be formed during the reaction were reacted under conditions similar to those used for the biomass samples. Sodium formate and sodium acetate were each individually studied as precursors to hydrogen and methane formation, respectively.

4.1.1 Sodium formate

Sodium formate was reacted within the temperature range of 250 °C to 450 °C, corresponding to running pressures of 4 MPa to 34 MPa. The reactions were used to monitor the effect of reaction temperature on sodium formate decomposition. Results showed that even at 250 °C, gas analysis results showed that hydrogen and CO, albeit, in very low concentrations were the only gases present. However, CO disappeared completely from the gas product beyond this temperature, such that at 300 °C, no CO was detected. Throughout the temperature range studied, in terms of the volume percent of gas, the proportion of hydrogen was consistently greater than carbon dioxide as shown in Fig. 1.

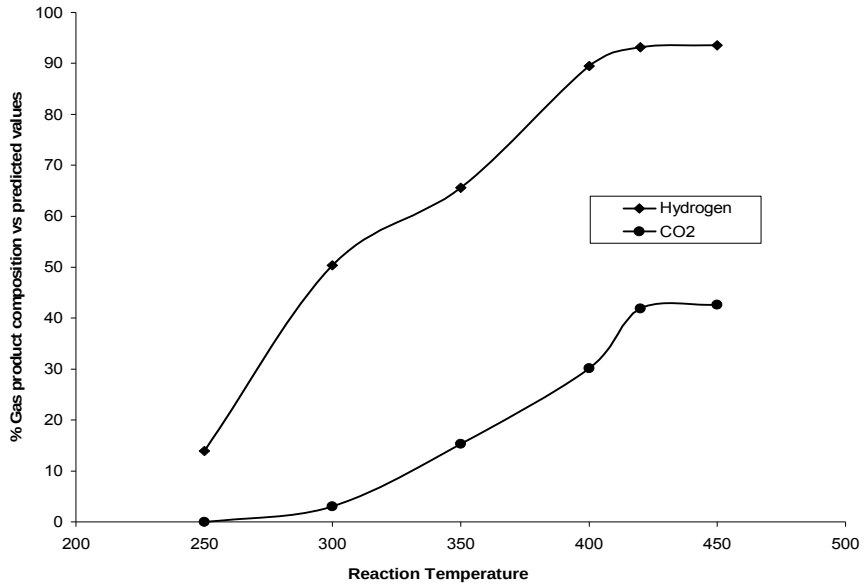

Figure 1: Hydrogen and carbon dioxide produced as percentage of predicted values.

Subsequently, the reaction equation for the hydrothermal decomposition of sodium formate was proposed as follows;

$$2HCOONa + H_2O \rightarrow 2H_2 + Na_2CO_3 + CO_2 \quad (1)$$

The presence of carbon dioxide in the gas stream underlies the requirement for a little excess of sodium hydroxide more than the biomass sample. For example in the production of sodium formate 1:1 mole ratio is required of formic acid and sodium hydroxide. Hence, its decomposition will also be in the same ratio pattern, providing no excess sodium ions to capture all the CO_2 during reactor cooling. Fig. 1 is therefore based on the comparison of the amounts of hydrogen and carbon dioxide produced during the reaction and those predicted by the equation. While hydrogen gas production agreed with the prediction at temperature around 400 °C and above, CO_2 values only achieved a maximum of 42 % of predicted value even at 450 °C. This could be as a result of the apparent solubility of CO_2 in a solution of sodium carbonate. It was observed that the liquid effluent released gas bubbles just by simple agitation. The lower values of both hydrogen and CO_2 temperature below 400 °C, was an indication of incomplete decomposition of sodium formate. This much is corroborated by the TOC and TIC values of the corresponding liquid effluents obtained. Increasing reaction temperature led to a gradual decrease in TOC values at first and then the rate of TOC removal increased sharply between 300 °C and 350 °C. At 420 °C and above the TOC values of the liquid effluents were less than 0.001 mg/L. The rate of increase of TIC formation was a mirror image of the trend in TOC removal, such that over 99 % of the organic carbon in the sodium formate was obtained as inorganic carbon at temperatures above 420 °C. Hence complete decomposition of sodium formate to mainly hydrogen gas occurred after reaching 420 °C and above.

4.1.2 Sodium acetate

Sodium acetate was reacted within the temperature range of 350 °C to 500 °C, corresponding to running pressures of 12 MPa to 43 MPa. The conditions at 500 °C were at the limits of the reactor capability. Results showed that methane formation only became measurably significant from 400 °C, indicating that sodium acetate required higher temperature to decompose than sodium formate. No significant amount of hydrogen was produced up to 400 °C. A small amount of carbon dioxide was detected all through the temperature range when methane was produced. Hence the predominant reaction equation was suggested to be as follows;

$$2CH_3COONa + H_2O \rightarrow 2CH_4 + Na_2CO_3 + CO_2 \quad (2)$$

The formation of methane according to equation (2), did not become significant until about 450 °C. The thermal decomposition of sodium acetate is known to occur around 450 °C, this research shows that in hydrothermal media, the decomposition actually started around the critical point of water (374 °C, 22.1 MPa). However, as shown in Fig. 2, the decomposition produced about 50 % of the predicted amount of methane at 480 °C, 38 MPa and was further

enhanced to just over 70 % at 500 °C, 43 MPa. The continuous increase in methane gas is an indication of the decomposition behaviour of sodium formate in hydrothermal conditions. However, as the temperature of reaction increased beyond 400 °C, there was a slight increase in hydrogen gas product while methane increased dramatically. The formation of hydrogen could have resulted from the supercritical water reforming of the formed methane to produce hydrogen and CO_2 according to the equation;

$$CH_4 + 2H_2O \rightarrow 4H_2 + CO_2 \quad (3)$$

The rate of formation of hydrogen and carbon dioxide was much slower than the predominant reaction leading to methane formation. As shown in Fig. 2, just about 1/10th of methane reforming efficiency was achieved against what equation (3) predicted. The maximum TOC removal from sodium acetate removal was nearly 73 %, for the reaction at 500 °C, 43 MPa, corresponding to the highest methane yield.

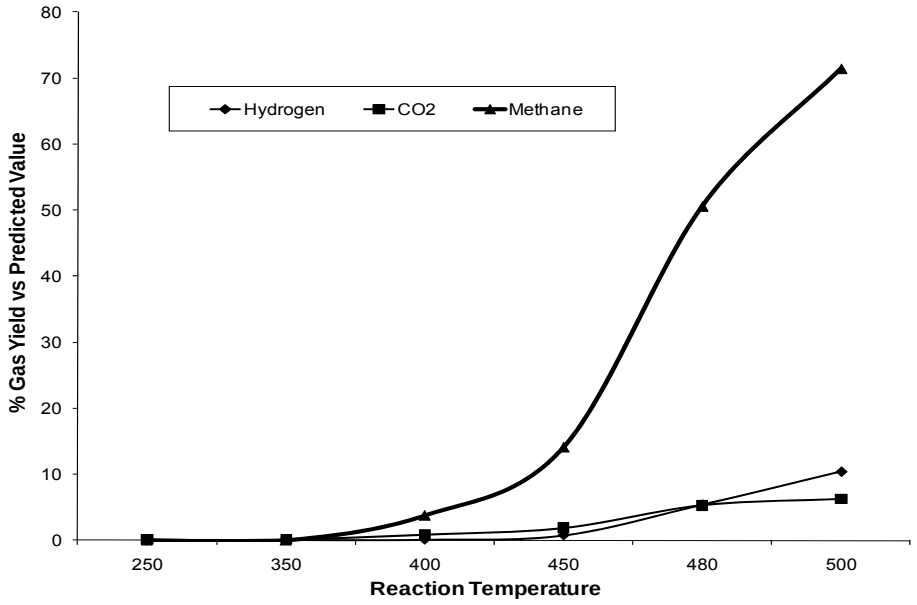

Figure 2: Evolution of gaseous products from CH_3COONa in relation to reaction temperature.

4.2 Gasification results from biomass samples

Earlier studies [2] attempted to outline a reaction scheme for the alkali promoted gasification of glucose as a model compound of biomass. The work showed that the major reaction occurring for glucose in the presence of alkali could be represented by the following;

$$C_6H_{12}O_6 + 6NaOH + 6H_2O \rightarrow 6NaHCO_3 + 12H_2 \quad (4)$$

This equation predicts that no carbon dioxide or carbon monoxide should be detected in the gas products from the reaction. However, sodium bicarbonate is not stable at high

temperatures, whereas sodium carbonate is stable. Hence, while the formation and stability of sodium carbonate is favoured under the reaction conditions, its formation signifies that carbon dioxide would still remain in the gas phase. Experiments did not show this, indicating that the formation of sodium bicarbonate may have occurred during or after reactor cooling as shown below;

$$Na_2CO_3 + CO_2 + H_2O \rightarrow 2NaHCO_3 \quad (5)$$

Hydrogen gas was the major gas product, with some methane of up to 15 % of the total gas formed. The ability sodium hydroxide to catalyze this gasification process is underscored by its ability to capture the CO_2 from the water-gas shift reaction, thereby driving the reaction in the forward reaction. The detailed discussion of this research can be found in Onwudili and Williams [2]. Fig. 3 shows that irrespective of the biomass type, hydrogen remained the predominant gas at 450 °C.

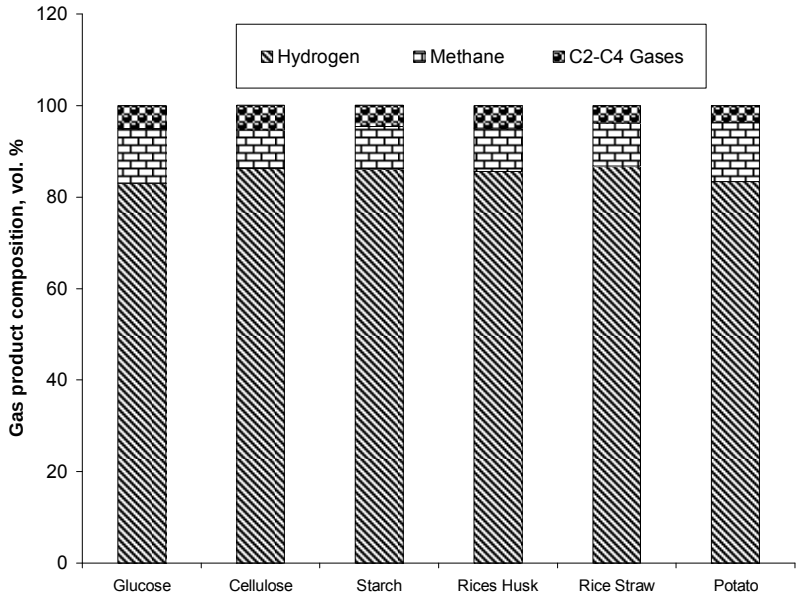

Figure 3: Gas product compositions in volume percent.

Moreover, it shows that similar amounts of the gases have been produced by the different biomass samples, indicating that the effect of sodium hydroxide was essentially similar for all the different types of biomass. This means that similar amounts of different carbonaceous materials of the type found in these biomass samples could react in a similar manner, generating similar intermediate compounds, which then undergo identical reactions, to produce similar gaseous compounds of fairly similar concentrations. It is therefore interesting to see that the function of sodium hydroxide in this hydrothermal gasification process was nearly specific. A careful examination of Fig.3 shows that glucose and potato produced a little bit less hydrogen and a little bit more methane than the other biomass samples. This

may indicate that these two sugar-type biomass samples are more likely to produce more sodium acetate than the others.

5 Conclusion

The process of hydrogen and methane formation during alkali-promoted hydrothermal biomass gasification has been investigated using sodium formate and sodium acetate as 'intermediate' decomposition products. Results confirmed that sodium formate may be responsible for almost all the hydrogen produced, while sodium acetate produced mainly methane. However, it is also possible to produce hydrogen gas from sodium acetate at much higher temperatures (450 -500 °C), possibly from supercritical water reforming of the initial methane produced. The hydrothermal gasification of several biomass samples showed that similar types and concentrations of hydrogen and methane could be produced from different biomass materials in the presence of sodium hydroxide. Experimental results show that hydrogen and methane can be obtained at significantly high purity from the process.

References

[1] Watanabe, M., Inomata, H., Osada, M., Sato, T., Adschiri, T., Arai, K.,. Fuel. 2003; 82: 545-552.

[2] Onwudili, J.A., and Williams, P.T. Int. Journal of Hydrogen Energy. 2009; 34: 5645-5656.

[3] Xu, D.H., Wang, S.Z., Hu, X., Chen, C., Zhang, Q.M., Modern Chem. Ind. 2007; 27 (suppl. 1): 88-92

[4] Sinag, A., Kruse, A. and Rathert, J., Ind. Eng. Chem. Res. 2004; 43(2): 502-508.

[5] Jin, F., Yun, J., Li, G., Kishita, A., Tohji, K., Enomoto, H., Green Chemistry, 2008: 10: 612-615.

[6] Jin, F., Zhou, Z., Kishita, A., Enomoto, H., J. Mater. Sci., 2006; 41: 1495-1500

[7] Kruse, A., Dinjus, E., Z. Phys. Chem., 2005; 219: 341-366

[8] Onwudili, J.A. and Williams, P.T., Fuel. 2010; 89(2): 501-509.

[9] Watanabe, M., Sato, T., Inomata, H., Smith, R.L., Arai, K., Kruse, A., Dinjus, E., Chem. Rev. 2004; 104: 5803-5821

Green Hydrogen and Natural Gas from Digester Gas of Wastewater Treatment Plants

Burkhard Teichgräber, **Angelika Kraft**, **Daniel Rossol**, Emschergenossenschaft, Germany
Markus Schröder, Tuttahs & Meyer Ingenieurgesellschaft, Germany

1 Introduction

Emschergenossenschaft and Lippeverband are in charge of the water management in the catchment areas of Emscher and Lippe, and among other things of the wastewater treatment of ca. 4 million inhabitants and ca. 3 million population equivalents (PE) from industry. For this purpose there are 58 wastewater treatment plants (WWTP) with a capacity from 500 – 2.4 million PE. The annual sludge amount adds up to 92.000 t dry solids.

Digester gas is produced during the anaerobic stabilisation of sewage sludge. It is a high-quality renewable energy source due to its high energy content. Since the 1920s, the digester gas is collected and used for energy generation at WWTPs, which reduces the costs for energy delivery [1].

Digester gas utilisation in combined heat and power plants (CHPs) is an established method of on-site power generation, at WWTPs with a population equivalent of more than 10,000, this method is regarded as state-of-the-art. Emschergenossenschaft and Lippeverband have 34 WWTPs with CHPs. The electrical power of the CHPs range from small modules with 13 kW to the large modules at WWTP Emschermündung with a total electrical power of 5.5 MW. The utilisation of the digester gas via heat-power-coupling allows for high energetic efficiency degrees: the mechanical efficiency degree amounts to 30 %-35 %, the thermal efficiency degree is 50 % [2].

By co-fermentation, that is the co-treatment of organic substances such as residues from the food industry or biological waste in the fermentation tank, the digester gas production and thus the on-site energy generation can be boosted significantly.

In the practical WWTP operation, digester gas utilisation has so far been employed for the classical paths boiler, CHP, or direct drive. The processing of digester gas into biomethane and hence to hydrogen is one way of satisfying the demand for green fuels. The owners of WWTPs can integrate these considerations into construction and operation. The processing of digester gas will particularly tap the area of mobile energy utilisation. The economically sound employment of the produced energy sources biomethane and hydrogen will be possible if the price for mobile energy carriers considerably exceeds that for electric energy from large WWTPs and pipeline-bound transport, or if extensive co-fermentation at WWTPs will lead to energy surpluses. The discharge will be particularly lucrative for the owners of WWTPs if the internal energy demand of the treatment plant can be covered completely [3].

2 Processing of Digester Gas into Natural Gas and Hydrogen

Digester gas consists mainly of methane and carbon dioxide, but also includes a wide range of minor components [4]. The digester gas quality depends on the composition of the effluent of the WWTP – many substances which are conveyed into the wastewater from industrial and domestic sources reappear in the digester gas. In regard to digester gas utilisation in CHPs, sulphur compounds and siloxane are especially harmful.

The procedural elimination efforts differ considerably for the various components [5]. The demands on the purity of the digester gas depend on the intended purpose: the conventional utilisation of digester gas in boiler or CHP generally necessitates only dust and moisture removal, sometimes desulphurisation. If the siloxane concentrations are high, these substances must also be removed from the digester gas, lest they cause damages through silicium fouling in the CHP.

For the processing into biomethane, however, the technical efforts are considerably higher: apart from the removal of minor components such as hydrosulphide and siloxane, the carbon dioxide must be removed as well. The following methods are suitable for this procedure:

- **Pressure swing adsorption**: reversible adsorption of CO_2 to carbon molecular sieves
- **Power water scrubbing**: reversible absorption of CO_2 in pressurised water
- **Physical adsorption with organic solvents**: absorption of CO_2 in pressurised solvents
- **Chemical absorption with organic solvents**: almost pressure-less absorption of CO_2 in solvents(e. g. mono-ethanol-amine or di-ethanolamine)
- **Membrane methods**: gas separation via membranes, so far only used in pilot plants
- **Cryogenic methods**: gas separation through liquefaction at high temperatures, for biogas processing so far only used in pilot plants

The next upgrading step to hydrogen corresponds to the industrial steam reformation of natural gas. It is also possible to produce hydrogen directly from digester gas without biomethane production, but so far it has not been realised in an industrial scale.

3 EuWaK Project – Natural Gas and Hydrogen from Wastewater Treatment Plants

The processing of digester gas into biomethane and hydrogen is currently being tested and developed further by the Emschergenossenschaft in a demonstration project at the WWTP Bottrop. The project has been funded by the federal land of North Rhine-Westphalia and the European Union. Project partners of the Emschergenossenschaft during the development and realisation of the project were engineering company for water and waste management Tuttahs & Meyer ltd. (T&M), the research institute for water and waste management of the RWTH Aachen (FiW), the engineering office Redlich and Partner GmbH (IBR), and the city of Bottrop.

In the pilot project, digester gas is processed into biomethane and hydrogen. In the course of the project, the complete local hydrogen infrastructure chain from the renewable energy source sewage sludge to the final hydrogen consumer was established for the first time. The target of the project is the production of highly pure hydrogen from sewage sludge and other

biomass which can then be used as fuel in fuel cell-driven vehicles. An intermediate step is the production of biomethane, in order to establish the WWTP as filling station location through the fuelling of natural gas vehicles with biomethane.

In the first processing stage, biomethane is produced from a component stream of the digester gas from the WWTP Bottrop via pressure swing adsorption (PSA). One component stream of the biomethane is discharged and delivered at a natural gas filling station to in-house vehicles running on natural gas. In a second step, the remaining biomethane is converted into hydrogen in a steam reformer with downstream upgrading (CO-shift and pressure swing adsorption). It was decided to consume the hydrogen not in a fuel cell, but in a combustion engine, as the hydrogen engine is less sensitive to changes in the hydrogen quality than fuel cells and thus more suitable for a pilot project the focus of which was not the development of fuel cell technology. Moreover, the investment costs for fuel cells are very high, and at the current technological status their service life is considerably shorter than that of the engines.

The hydrogen engine stands in a school which is about 1 km away from the WWTP and to which a swimming pool is attached. The engine serves for the supply of power and heat; the hydrogen production unit is connected to the school with a pipeline.

Communication and data exchange between the gas production unit and the consumers natural gas filling station and hydrogen CHP are steered by a superordinate control software.

After a two-year initial phase for planning, licensing, advertising, and awarding, the entire plant was built during 2007. The extensive start-up stage, test runs, and first optimisation stage stretched into 2008 and 2009. Currently, the operation of the EuWaK is being accompanied scientifically in a research project. Furthermore, in 2009/2010 a hydrogen filling station was built as another project module. It will be connected to the EuWaK plant, so that hydrogen-driven vehicles will in future be fuelled with „green“ hydrogen from digester gas.

4 Operation Results

During the start-up stage, the interfaces between the single components had to be fine-tuned to each other and the single aggregates be adjusted. The engine control of the hydrogen engine had to be adjusted to the high combustion speed of the hydrogen. Among other measures, the ignition point was optimised and the gas control path adjusted. The engine was constructed and built as a prototype especially for the EuWaK project. The necessary technical improvements and adjustments during the test runs were thus part of the research and development work of the project.

Through the tight interlacing of the plant components, which led to interconnections and occasional malfunction of single components, the start-up stage was characterised by intermittent downtimes in the operation, so that as yet relatively few measuring values and operation data from the start-up stage are available. The biomethane produced was of an excellent quality, with an average methane content of more than 97 % and a dew point of -65 °C and lower. The biomethane could so far be used without any problems by the vehicles fuelled therewith.

During the processing of the digester gas, the minor components turned out to be a major challenge, especially BTEX and longer-chain hydrocarbons. Because of the high ratio of

industrial dischargers, the digester gas of the WWTP Bottrop shows significant amounts of those compounds. An activated carbon filter had been planned for the removal of the minor components, but it proved to be incapable of dealing with the unexpectedly high concentrations, so that an additional filter had to be installed, which achieved very good elimination rates. The optimisation of the gas scrubbing and the testing of alternative procedures were a crucial part of the research stage, during which the online monitoring of the minor components was implemented as well. During the test runs, the possibilities of removing BTEX from the digester gas with chemical-physical methods combined with biological treatment will be examined.

Because of several interruptions of the operation, the availability of the entire plant during 2009 amounted to only 1,400 operation hours approximately. Downtimes were mainly due to maintenance work caused by BTEX loads and alleviation of disturbances. It can be assumed that the additionally implemented activated carbon filter system combined with the online monitoring will lead to a much better availability of the plant.

The natural gas amount which could be delivered to the vehicles in 2009 is equivalent to a mileage of ca. 42,000 km. The consumed digester gas mass amounts to about 1 % of the entire digester gas amount of the WWTP Bottrop in 2009.

Apart from the availability, the efficiency degrees must still be improved as well. The energetic efficiency degree of the biomethane production reached up to 90 %, the hydrogen production from biomethane had an average efficiency degree of 50 %. Because of the cold winter, much energy had to be used for heating, which had a negative effect on the overall efficiency degree of the process. During the research operation, the energetic balance of the entire process will be analysed to identify further optimisation potentials.

5 Evaluation and Outlook

In order to achieve the stable and efficient operation of the EuWaK plant, improvement potentials must be identified and realised during the research operation, with a particular emphasis on the following issues:

- **Research operation**: How can a disturbance-free operation with high availability and minimal starting and shutdown be achieved?
- **Consumption and production:** How can the primary gas and energy demand used for the generation of the product gas be controlled in an optimal way to achieve the best possible utilisation degree?
- **Digester gas composition and product gas quality**: How can the final product hydrogen and the by-product natural gas be produced from digester gas at a continuously high quality level? Which maximum quality can be reached with the processing plant?
- **Proof of efficiency of the entire plant and profitability considerations**: Which product yield is reached with entire plant and how high is the overall efficiency degree?
- **Determination of the costs for deliverable hydrogen:** Where is the economic optimum of this technological procedure between the necessary processing efforts

and the achievable quality, given that as yet there are no general quality standards for the intended hydrogen qualities?

- **Expansion potentials and transferability of insights:** Can the insights gained from the operation of the plant and the system integration be transferred to other wastewater treatment plants and hydrogen production locations (such as biogas plants)? Which further application areas can be opened up with the achieved product gas qualities?

The chosen concept of a two-stage processing is still justifiable today, as natural gas or biomethane have been incorporated as bridging technology, the advantage of which is that biomethane can be discharged as fuel and the WWTP can be used as filling station location. Unfavourable are the high energetic efforts. In the long run, hydrogen will thus be produced directly through steam reformation of digester gas.

In future, the mobile utilisation will be in the foreground. There will be a great demand for fuel produced from regenerative sources. Hydrogen from digester gas is a zero emission concept. As soon as the stable operation of the EuWaK plant has been achieved, with product gas of a continuously high quality being produced, the public utilisation of both the natural gas filling station and the hydrogen filling station can be set up as the next target.

References

[1] Loll, U. (2008): Historische Entwicklung der Biogastechnik in Deutschland. DWA-Energietage 2008 in Fulda

[2] Steinmetz, H. (2007): Ansätze für energieoptimierte Kläranlagen. In: Stuttgarter Berichte zur Siedlungswasserwirtschaft. Bd. 191: Innovative Konzepte für Kläranlagen; Oldenbourg Industrieverlag GmbH, 2007

[3] Grün, E., Teichgräber, B. (2010): Hydrogen Production as part of Sustainable Use of Energy in Wastewater Treatment Plants. Vortrag bei der Weltwasserstoffkonferenz 2010 in Essen.

[4] Hiller, R. Urban, W. (2005): Erfahrungen mit der Aufbereitung von Bio-, Klär- und Deponiegas für den Einsatz in einer Schmelzkarbonat-Brennstoffzelle. Vortrag beim Workshop „Brennstoffzellen für Biogas“am 28.04.2005 in Potsdam, Leibnitz-Institut für Agrartechnik Potsdam-Bornim e.V.

[5] DWA (2006): Einsatz von Brennstoffzellen auf Kläranlagen. Merkblatt M299, Ausgabe 06/2006

Delaminated Zeolites as Support of Active Metals for the Preparation of Highly Active and Selective Catalysts for Hydrogen Production: Steam Reforming of Bioethanol

Antonio Chica*, **Javier Francisco Da Costa-Serra, Salvador Sayas**, Instituto de Tecnología Química (UPV-CSIC), Valencia, Spain

1 Introduction

Hydrogen has attracted much attention as alternative fuel mainly due to environmental aspects. Furthermore, the reserves of fossil fuels on earth are finite and no matter how long they will last, a cleaned and renewable energy alternative independent of fossil fuels has to be developed for the future [1,2]. Currently, the most favourable route to produce hydrogen comes from non-renewable energy sources such as fossil fuels, which is associated with release of large quantities of greenhouse gases to the atmosphere, especially CO_2 and others harmful emissions [3,4]. Thus, a new eco-friendly reservoir of hydrogen is needed for a clean and sustainable production of energy. Biomass-derived compounds such as bioethanol could be this source since it is easy to produce, and is also safe to handle, transport and store [5,6]. Catalytic conversion of bioethanol to hydrogen through steam reforming reaction highly depends on the type of metal catalyst used, type of precursors, preparation methods, type of catalyst support, presence of additives, and operating conditions [6-11]. Among them support plays an important role in the reforming activity since it can help to improve the dispersion of metal catalyst enhancing the metal catalytic activity via metal-support interactions and avoiding the metal sinterization [12]. New delaminated zeolitic materials have been synthesized in our laboratories [13,14]. The singular structure of these delaminated zeolites, and particularly the very high and well-defined external surface area, makes these materials attractive to be used as supports for dispersing active metal phases. In the present work we have explored the activity and selectivity of Co metallic particles supported over two delaminated zeolites (ITQ-2 and ITQ-6) in the steam reforming of bioethanol. The characterization of these materials by DRX, BET area, and TPR has allowed to establish interesting relationships between their catalytic performance and physico-chemical properties.

2 Experimental

2.1 Catalysts preparation and characterization

Pure silica ITQ-2 and ITQ-6 zeolites were prepared as described in [13] and [14], respectively. The incorporation of Co was accomplished by incipient wetness impregnation with an aqueous solution containing the required amount of $Co(NO_3)_2$ $6H_2O$ to achieve a nominal concentration of 20 wt% of Co in the final catalysts. Supports containing Co were

* Corresponding author, email: achica@itq.upv.es

calcined in muffle oven at 873 K for 3 h before reaction. The cobalt content in the calcined samples was determined by atomic absorption spectrophotometry (AAS). Textural properties were obtained from the nitrogen adsorption isotherms determined at 77 K. X-ray diffraction was used to identify the nature of the crystalline cobalt phases.

The reduction properties of the supported oxidized cobalt phases were studied by temperature-programmed reduction (TPR). The degree of reduction was determined from TPR experiments comparing the total amount of hydrogen consumed by each catalyst and the amount of hydrogen theoretically necessary to complete the reduction of Co_3O_4 oxide species present in the catalyst. The metallic particle size was estimated from H_2 adsorption using the double isotherm method. The average Co particle sizes were estimated from the metal's surface area assuming a spherical geometry.

2.2 Catalytic test

Steam reforming experiments were carried out in a continuous fixed bed reactor at atmospheric pressure, H_2O/BioEtOH molar ratio of 13, GHSV 4700 h-1 and a range of temperatures between 673 K and 873 K. Before reaction the catalysts were reduced "in situ" in flow of H_2 at 873 K for 2 hours. The analysis of the compounds of reaction was carried out online using a gas chromatograph equipped with two columns (TRB-5 and CarboSieve SII) and two detectors, thermal conductivity (TCD) and flame ionization (FID). The bioethanol conversion and selectivity to the different reaction products were determined according to the equations (1) and (2), where $(F_{EtOH})_o$ is the flow of bioethanol fed to the reactor, $(F_{EtOH})_f$ the flow of bioethanol that comes from the reactor and F_j the flow of product j that comes from the reactor. Selectivity values were calculated as the molar percentage of the products obtained, excluding water.

$$X(\%, mol) = \frac{(F_{EtOH})_o - (F_{EtOH})_f}{(F_{EtOH})_o} \times 100 \quad (1)$$

$$S(\%, mol) = \frac{F_j}{(\Sigma F_j)_{products}} \times 100 \quad (2)$$

3 Results and Discussion

3.1 Characterization

X-ray diffraction patterns of calcined ITQ-2 (data not shown) does not show the 00l peaks with the 2.5 nm periodicity typical of the MWW topology, indicating a reduction of long-range order along the c axis. These structural changes are in agreement with the proposed structure in which the ITQ-2 material is mostly formed by single layers of the corresponding lamellar precursors. The XRD patterns of calcined ITQ-6 compared to the Ferrierite obtained after calcination of Ferrierite precursor at 853 K (data not shown) show that while the intensities of the reflections corresponding to planes (0kl) were basically unchanged, those corresponding to (h00) have strongly decreased in ITQ-6. This indicates a remarkable loss of

order along the a axis, which would be consistent with a delamination of the layered Ferrierite precursor.

Textural properties of the ITQ-2 and ITQ-6 pattern derived from the N_2 adsorption isotherms are summarized in Table 1. As observed, the original zeolites present a high BET surface area and total pore volume. A reduction of surface area and pore volume is noted in both samples after incorporation of Co. This lost of area can be explained if we assume that Co in calcined zeolites are present in the form of Co_3O_4 and that these phases does not contribute to the surface area [15,16]. Thus, the incorporation of high level of cobalt (20 wt.%) would lead to a dilution effect, which could explain the surface area reduction detected. Pore volume of the samples containing Co is also lower than in the pattern materials. This indicates that a partial plugging of the support pores could also be occurring after Co incorporation.

The X-ray diffractograms (not shown) of the oxidized Co samples (Co/ITQ-2 and Co/ITQ-6) exhibit the reflections characteristic of the spinel Co_3O_4 phase, as it is usually observed for siliceous materials impregnated with cobalt nitrate precursor [17,18]. For comparison purposes, it has been calculated the average diameters of the Co_3O_4 estimated from XRD patterns using the Scherrer equation [19], Table 1. Particle size of Co_3O_4 on Co/ITQ-2 material is found to be smaller than that supported on Co/ITQ-6.

Table 1: Metal content and textural properties of ITQ-2 and ITQ-6 supports and metal-containing catalysts determined by nitrogen adsorption.

Catalyst	Metal content (wt.%)	Surface area (BET) m^2/g	Pore volume (BJH) cm^3/g	Oxide particle size (XRD) (nm)	Metal particle size (H_2-Chemisorption) (nm)
ITQ-2		887	0.72		
ITQ-6		594	0.85		
Co/ITQ-2	20.1	487	0.31	15.9	9.6
CO/ITQ-6	19.5	377	0.42	21.6	14.8

The reduction behaviour of the supported cobalt oxide particles in the catalyst has been studied by temperature-programmed reduction (TPR). The corresponding reduction curves are shown in Figure 1. As observed, both samples present two main reduction features with maxima at about 575 K and 590 K, which correspond to the two-step reduction process in which Co_3O_4 is first reduced to CoO and then CoO is reduced to Co^o, as reported by different authors [18-21]. For Co/ITQ-2 sample the area of the second reduction peak is larger than that for the Co/ITQ-6. Additional broad diffuse hydrogen consumption between 600 K and 1000 K has been also observed both samples, suggesting the existence of several cobalt species reducing at approximately the same temperature, which can be ascribed to the reduction of cobalt silicates probably formed by reaction of highly dispersed CoO with the silica support during the reduction process [18, 22, 23]. The reduction temperature and peak area of this broad peak can be seen that is higher for the Co/ITQ-2 sample. The reduction temperature and the peak width are indications of the degree of reduction and the level of interaction between different species. Thus, TPR results seem to indicate that cobalt oxide

exhibit higher interaction with ITQ-2 support. In the case of Co/ITQ-2 the broad peak detected at higher temperatures suggests that a part of the Co species strongly interact with support resulting difficult their reduction. Taking into a count that the catalysts are reduced at 873 K before reaction it is possible that a part of the Co species in the ITQ-2 support remain in their oxidized form, thus, they could not participate in the bioethanol steam reforming reaction. The low particle-size determined by DRX for the cobalt oxide species supported on ITQ-2 material could also give explanation for the high reduction temperature displayed by part of the supported cobalt. The size of the Co metallic particles was determined by H_2-chemisorption. As it can be seen in Table 1 the smallest Co metallic particles are present in the ITQ-2 support, as it was expected from the lower particle size of the Co oxides detected by DRX for this sample.

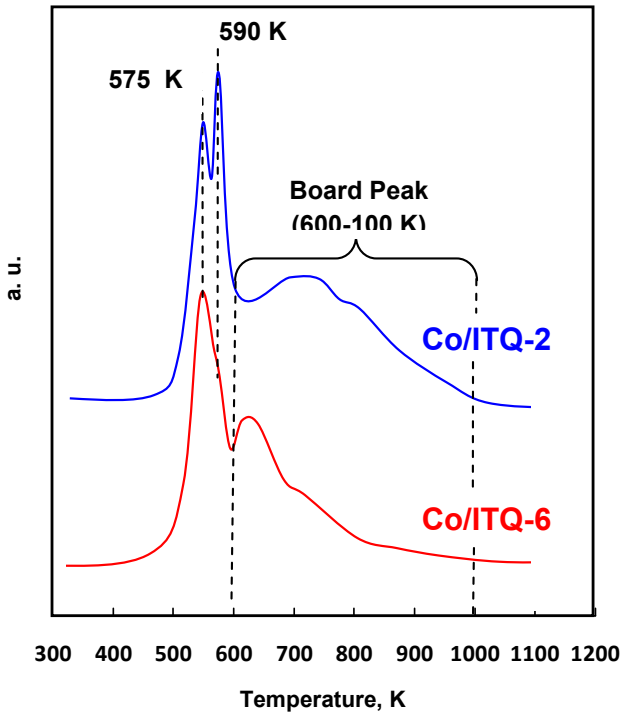

Figure 1: TPR profiles of Co-supported catalysts.

3.2 Catalytic activity

Figure 2 shows the bioethanol conversion as function of the reaction temperature. Co/ITQ-2 sample exhibited higher bioethanol steam reforming activity than Co/ITQ-6 material. Catalytic activity of the cobalt supported catalysts was also compared at 673 K, H_2O/EtOH of 13, GHSV of 4700 h^{-1} and atmospheric pressure. The global reaction rate determined as gram of bioethanol converted per gram of catalyst and per second for the Co/ITQ-2 sample was found to be 2 times higher than that in Co/ITQ-6 (1,8 10^{-2} and 0.9 10^{-2}, respectively). The higher activity of the Co/ITQ-2 sample can be attributed to the small metallic Co particles resulting in a greater density of active metallic surface where the reforming of bioethanol can be carried out. The hydrogen selectivity and catalyst stability are others important

parameters to be taken into account for the practical application of one catalyst. The hydrogen selectivity with reaction temperature is also shown in Figure 2.

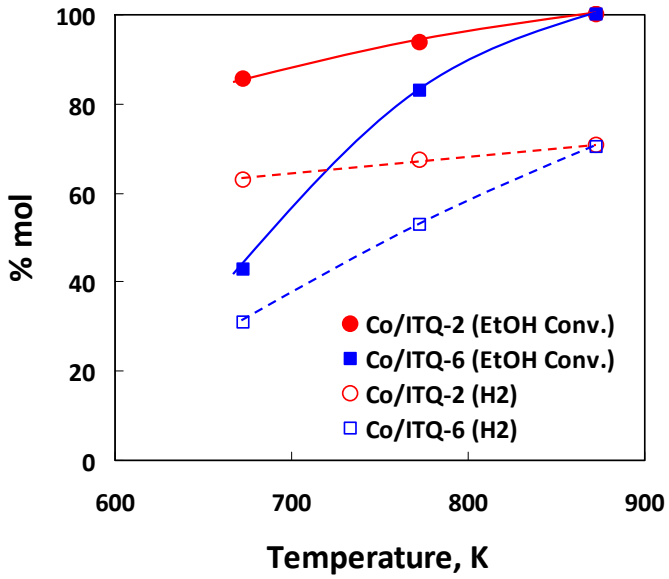

Figure 2: Bioethanol conversion and H_2 selectivity versus reaction temperature. Reaction conditions: H_2O/bioEtOH= 13, GHSV= 4700 h^{-1} and atmospheric pressure.

Both samples showed high hydrogen yields at high temperatures (873 K), however the Co/ITQ-2 was the most selective catalyst to hydrogen at low temperatures. The stability of these catalysts was also tested. It is well known that the stability of a steam reforming catalyst is strongly related to coke deposition and metal sintering. After 72 hour of reaction time at 773 K deactivation was only detected for Co/ITQ-6 catalyst. The elemental analysis of the catalysts after reaction shows the presence of coke in both catalysts. Percentage of carbon was slightly larger for Co/ITQ-6 sample. However, the amount of deposited carbon cannot explain by itself the deactivation exhibited by the Co/ITQ-6 material. Together to the coke deposition it is possible that others effects as metal sinterization could account for the detected deactivation. The best results obtained with the Co/ITQ-2 sample could be due to its particular structure formed by hexagonal array of “cups” (0.7×0.7 nm, see Figure 3), which would provide an excellent position for the stabilization of the Co metallic particles improving their dispersion, decreasing their size and avoiding their sinterization during reduction and reaction steps.

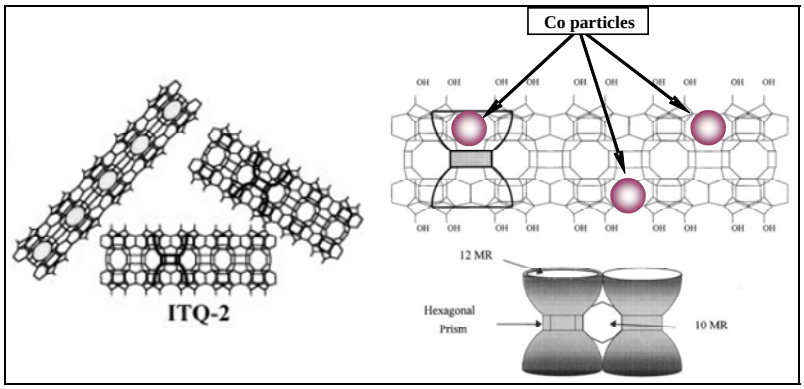

Figure 3: Schematic representation of the Co/ ITQ-2 structure.

The results here presented show that using pure silica delaminated ITQ-2 zeolite as support of Co can be prepared a good bioethanol steam reforming catalyst, with high activity, hydrogen selectivity, and stability, to produce hydrogen.

References

[1] G.W. Huber, A. Corma, *Angew. Chem. Int. Ed.* 46 (2007), pp. 7184.

[2] J. Kjärstad, F. Johnsson, *Energy Policy* 37 (2009), pp. 441–464.

[3] M. H. Kim, E. K. Lee, J. H. Jun, S. J. Kong, G. Y. Han, B. K. Lee, T.-J. Lee, K. J. Yoon, *Int. J. of Hydrogen Energy* 29 (2004), pp. 187–193.

[4] J.R. Rostrup-Nielsen, T. Rostrup-Nielsen, *CATTECH* 6-4 (AUG 2002), pp. 150-159.

[5] A. Midilli, I. Dincer, *Int. J. of Hydrogen Energy* 33 (2008), pp. 4209–4222.

[6] J. Llorca, P.R. de la Piscina, J.A. Dalmon, J. Sales, N. Homs, *Appl. Catal., B* 43 (2003), pp. 355.

[7] A. Birot, F. Epron, C. Descorme, D. Duprez, *Appl. Catal. B* 79 (2008), pp. 17.

[8] G.B. Sun, K. Hidajat, X.S. Wu, S. Kawi, *Appl. Catal. B* 81 (2008), pp. 303.

[9] V. Fierro, V. Klouz, O. Akdim, C. Mirodatos, *Catal. Today* 75 (2002), pp. 141.

[10] A.C. Bagasiannis, P. Panagiotopoulou, X.E. Verykios, *Top. Catal*. 51 (2008), pp. 1.

[11] S. Cavallaro, *Energy Fuels* 14 (2000), pp. 1195.

[12] P.D. Vaidya, A.E. Rodrigues, *Chem. Eng. J.* 117 (2006), pp. 39.

[13] A. Corma, V. Fornés, S.B. Pergher, patent EP 9605004 (1996) and WO 9717290 (1997).

[14] A. Corma, A. Chica, U. Díaz and V. Fornés, patent US6469226 B1 (2002), to BP-AMOCO.

[15] A. Chica, S. Sayas, *Catal. Today* 146 (2009), pp. 37–43.

[16] P. Concepción, C. Lopez, A. Martínez, V.F. Puntes, *J. Catal.* 228 (2004), pp. 321–332.

[17] A.Y. Khodakov, A. Griboval-Constant, R. Bechara, F. Villain, J. Phys. Chem. B 105 (2001) 9805.

[18] B. Ernst, S. Libs, P. Chaumette, A. Kiennermann, Appl. Catal. A 186 (1999) 145.

[19] B.D. Cullity, Elements of X-Ray Diffraction, Addison–Wesley, London, 1878.

[20] R. Riva, H.Miesner, R. Vitali, G. Del Piero, Appl. Catal. A 196 (2000) 111.

[21] D.G. Castner, P.R. Watson, I.Y. Chang, J. Phys. Chem. 94 (1990) 819.

[22] E. van Steen, G.S. Sewell, R.A. Makhothe, C. Micklethwaite, H. Manstein, M. de Lange, C.T. O´Connor, J. Catal. 162 (1996) 220.

[23] B. Sexton, A. Hughes, T. Turney, J. Catal. 97 (1986) 390.

Hydrogen Production from Glucose in Ionic Liquids

D. W. Assenbaum, **N. Taccardi**, **M.E.M. Berger**, **A. Bösmann**, **F. Enzenberger**, **R. Wölfel**, **P. Wasserscheid**, Lehrstuhl für chemische Reaktionstechnik, Universität Erlangen-Nürnberg, Germany

1 Introduction

Depletion of oil and gas reserves and growing global warming concerns have created a world-wide interest in new concepts for future sustainable energy supplies. The development of effective ways to produce hydrogen from biomass is expected to be one important contribution to such a goal [1]. Nowadays, three main processes are considered for future industrial application, namely: gasification of biomass [2], reforming in supercritical water [3] and aqueous phase reforming [4,5]. Other technologies such as enzymatic decomposition of sugars or steam reforming of bio-oils suffer from low hydrogen production rates and/or complex processing requirements and can probably not be considered for industrial applications in the closer future [6,7]. On the other hand, either the gasification of biomass, which is typically carried out at temperatures above 800 °C using Ni or Fe catalysts [8,9,10,11], or the reforming in supercritical water, which is typically carried out in presence of Ru catalyst at pressures of 300 bar and temperatures ranging from 500 to 700 °C [12], suffer of poor energetic efficiency as a lot of energy is required to run the reactions. More recently, an alternative to the two aforementioned high temperature processes has been proposed as “aqueous phase reforming” (APR) by Dumesic and coworkers [13,14,15,16,17]. They achieved the reforming of polyols (such as ethylene glycol, glycerol and sorbitol) using heterogeneous catalysts at temperatures between 200 and 250 °C and pressure typically between 15-50 bar. The temperature level of the reaction allows generating hydrogen with low amounts of CO in a single reactor. The process typically forms 35 % of hydrogen, 40 % of CO_2 and 25 % of combined alkanes. The high amount of formed alkanes originates eventually from CO hydrogenation and Fischer-Tropsch (F-T) reaction [18,19,20,21], those are thermodynamically favored in the above mentioned conditions. However, heterogeneously catalyzed APR technologies suffer from the fact that the overall reaction rates are often restricted by mass and heat transport problems. Lastly, there are severe limitations concerning the feedstock selection as for some important substrates, such as e.g. glucose, the process can only be operated in very diluted systems to avoid rapid tar formation [22,23,24].

In this contribution we describe for the first time a catalytic reaction system producing hydrogen from glucose in astonishingly high selectivities using a single reaction step under very mild conditions. The catalytic reaction system is characterized by its homogeneous nature and comprises a Ru-complex catalyst dissolved and stabilized in an ionic liquid medium. Ionic liquids are salts of melting points below 100 °C [25]. These liquid materials have attracted much interest in the last decade as solvents for catalytic reactions [26] and separation technologies (extraction, distillation) [27,28,29,30,31,32]. Besides, these liquids have found industrial applications as process fluids for mechanic [33] and electrochemical applications [34]. Finally, from the pioneering work of Rogers and co-workers, it is known that

ionic liquids are able to dissolve significant amounts of water-insoluble biopolymers (such as e.g. cellulose and chitin)[35] and even complex biopolymer mixtures, such as e.g. wood, have been completely dissolved in some ionic liquids [36].

In our specific application, the role of the ionic liquid is threefold: a) the ionic liquid dissolves the carbohydrate starting material thus expanding the range of applicable carbohydrate to water insoluble polymers; b) the ionic liquid provides a medium to dissolve and stabilize the catalyst; c) the ionic liquid dissolves hydrogen at a very low level, so inhibiting any possible collateral hydrogen-consuming process (detailed investigation of the hydrogen solubility in ionic liquids have been reported by e.g. Brennecke and coworkers [37]).

2 Results and Discussion

The process was carried out using a pressure-less glass reactor, purged with a stream of argon (200 ml/min) and connected to a hydrogen analyzer (heat conductivity based hydrogen analysis, EMERSON Hydros 100). This set-up encloses a series of washing bottles and cooling traps in order to remove all condensables and to provide a selective gaseous product analysis. The amount of evolved hydrogen was determined by integrating the detector signal *vs.* time. The obtained results are given in Table 1.

The ionic liquids listed in Table 1 were chosen on the base of previous reports on the dissolution of biopolymers and sugars in ionic liquids [38,39,40,41]. The $[(p\text{-cymene})RuCl_2]_2$/ TMEDA system was selected as catalyst, because of its remarkable long time stability at relatively high temperature, as reported by Beller and coworkers, in which this complex was applied for the dehydrogenation of isopropanol [42].

Table 1: Overview of glucose hydrate ($C_6H_{12}O_6*H_2O$) dehydrogenation experiments using different ionic liquids at 180°C and $[(p\text{-cymene})RuCl_2]_2$/TMEDA as the catalyst.

entry	ionic liquid	H_2 production 1h /ml (Yield / %)[a]	TON (1h)
1	[EMIM][$HP(OMe)O_2$]	56 (2.9)	35
2	[EMIM][$MeP(OMe)O_2$]	65 (2.5)	40
3	[EMIM][acetate]	49 (2.2)	31
4	[MMIM][Me_2PO_4]	18 (0.8)	11

Reaction conditions: $C_6H_{12}O_6{\cdot}H_2O$ 3.00g (15mmol), $[(p\text{-cymene})RuCl_2]_2$ 40mg, TMEDA 300mg, IL 50g, 180°C; [EMIM]= 1-ethyl-3-methylimidazolium, [MMIM]= 1,3- dimethyl-imidazolium. [a)] Evolved hydrogen determined through integrating the detector signal over the time; total hydrogen yields refer to the production of hydrogen from glucose, i.e. 100% yield corresponds to the formation of 6 mols H_2 from one mol of glucose; total hydrogen yield refers to the production of hydrogen from glucose, i.e. 100% yield corresponds to the formation of 6 mols H_2 from one mol of glucose.

Analysis of the gas phase showed no hints for CO, methane or other higher alkanes formation (below detection limit). Apart from hydrogen, the only detectable gas product was CO_2. Hydrogen and CO_2 were detected in a 1:1 ratio. The lack of CO and alkane is technically very interesting as a pure hydrogen/CO_2 mixture would greatly facilitate the downstream hydrogen purification processes or, in principle, could be direct used for feeding

fuel-cells. Another important outcome of these experiments was the fact that all the tested ionic liquid/glucose mixtures remained liquids and did not show any visible solid formation under the entire reaction time. This is remarkable, given the fact that the dehydration reaction with consequent solid tars formation has prevented so far the successful application of heterogeneous catalyzed APR approaches for glucose. Moreover, in aqueous systems, hydrogen consuming side reactions (formation of alkanes) have been observed if glucose is used as the feedstock. These limitations require the use of highly diluted feedstock solutions (usually < 1 % for glucose) and the processing of excessive amounts of water [43].

Aimed to improve hydrogen production, the reaction time was prolonged. With the only exception being the ionic liquid [EMIM][$CH_3P(OMe)O_2$], in all cases either decomposition of the cation ([EMIM][acetate]) or of the anion [EMIM][$HP(OMe)O_2$] was observed. However, no improvement of the hydrogen yield was achieved. Thus, the reason of the low yields was addressed. At first glance, it could be alleged the possible *in situ* N-heterocyclic carbene (NHC) complexes formation as reason for the low activity observed. It is well known [44] that the proton at carbon 2 of the imidazolium ring possesses enough acidity to be abstracted (even by relatively weak bases such as acetate) with consequent generation of a NHC, which coordinates the metal centre and blocks the coordination sites. Recently, such chemistry has also been observed for the protons in position 4 or 5 of the imidazolium ring (abnormal NHC) [45]. Therefore, we shifted from imidazolium to phosphonium salts. The ionic liquid tetrabutylphosphonium methylphosphonate ([Bu_4P][$CH_3P(OH)O_2$]) was prepared by simply reacting an aqueous solution of phosphonium hydroxide with a solution of methylphosphinic acid in the same solvent. After water evaporation, a waxy solid was obtained that was fully characterized. The results of the comparison between [EMIM][$CH_3P(OMe)O_2$] and [Bu_4P][$CH_3P(OH)O_2$] are presented in Table 2.

Table 2: Overview of [(p-cymene)$RuCl_2]_2$/TMEDA catalyzed dehydrogenation experiments using different methylphosphonate ionic liquids.

entry	ionic liquid	feedstock	H_2 produced in 1h / ml (Yield /%)[a]	TON (1h)
1	[EMIM][$MeP(OMe)O_2$]	$C_6H_{12}O_6 \cdot H_2O$	56 (2.5)	35
2	[EMIM][$MeP(OMe)O_2$][b]	$C_6H_{12}O_6 \cdot H_2O$	93 (4.2)	58
3			54 (2.9)	37
3.1			75 (3.6)	47
3.2			61 (3.0)	39
3.3			56 (2.7)	35
3.4			41 (2.0)	26
3.5	[Bu_4P][$CH_3P(OH)O_2$][c, d]	$C_6H_{12}O_6 \cdot H_2O$	44 (2.2)	28
4	[Bu_4P][$CH_3P(OH)O_2$][b, e]	$C_6H_{12}O_6 \cdot H_2O$	116 (5.2)	72

Reaction conditions: $C_6H_{12}O_6 \cdot H_2O$ 3.00g (15mmol), [(p-cymene)$RuCl_2]_2$ 40mg, TMEDA 300mg, IL 50g, 180°C; [EMIM]= 1-ethyl-3-methylimidazolium, [Bu_4P]= tetrabutylphosphonium; [a] Evolved hydrogen determined through integrating the detector signal over the time; total hydrogen yields refer to the production of hydrogen from glucose, i.e. 100% yield corresponds to the formation of 6 mols H_2 from one mol of glucose; [b] reaction at 150°C; [c] 3.00g aliquots of glucose were added to the system after hydrogen production ceased; [d] dry ionic liquid; [e] ionic liquid contained 5% of water.

The results obtained allowed us to exclude a possible intermediation of NHC-complexes (entries 1 and 3). On the other hand, it has to be highlighted that the catalytic system showed to be robust, as demonstrated by experiment in entry 3, where other 5 successive additions of glucose were made over 48 h at 180 °C (Figure 1). By the slope of the curves in Figure 1, it could be deduced that after the first addition a catalytic species formed in the system that was more active than the parental [(p-cymene)$RuCl_2]_2$/TMEDA system.

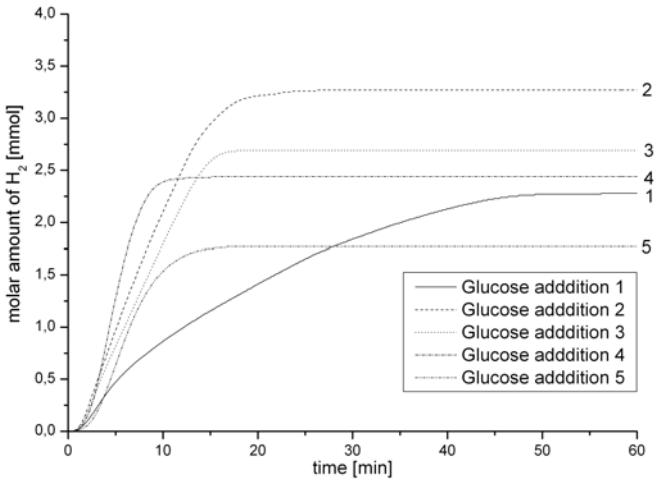

Figure 1: Hydrogen evolution vs. time for the different glucose additions in $[Bu_4P][CH_3P(OH)O_2]$ at 180 °C.

The system remained liquid along the whole experiment, as the formation of tarry solid seemed to be substantially suppressed in the ionic liquid. Interestingly, the presence of water seemed to play an important role on the process efficiency (entries 3 and 4). In particular, it could be seen that although the lower reaction temperature (the system could not reach the foreseen temperature of 180 °C due to the reflux of water), it was possible to get a slight improvement of yields.

The evidences collected so far, namely the nature of gaseous products and the effect of water suggested that this new catalytic system could not follow a common alcohol dehydrogenation mechanism [42 and references cited therein]. In order to elucidate this hypothesis, we investigated the system by means of ^{13}C-NMR spectroscopy using fully ^{13}C-labelled glucose (99 % ^{13}C). The fate of the ^{13}C-labeled substrate was investigated during two sets of experiments: in the first set, thermolysis at 150 °C of $^{13}C_6$-glucose was carried out in the ionic liquids without any Ru-catalyst. The second set of experiments was mimicking the catalytic process, with the thermolysis carried out in presence of [(p-cymene)$RuCl_2]_2$/TMEDA. In all the ionic liquid tested, complete disappearance with decomposition of glucose was observed within 90 min. By comparing the spectra of the Ru-free and the Ru-containing samples, only one pronounced difference could be noticed: an intense singlet in the region 170÷176 ppm appearing in the Ru-free samples that was missing in the respective Ru-containing systems (Figure 2). This singlet peak can be easily attributed to formic acid, which formed during the thermal degradation of glucose [46]. Obviously, this formic acid is

immediately transformed to hydrogen and CO_2 in the presence of the Ru-catalyst [47]. The above hypothesis was also supported by the observation of a 1:1 ratio H_2:CO_2 in the gas phase. The GC-MS analysis of gaseous product revealed an enrichment of $^{13}CO_2$ up to 90 % (the missing ^{13}C could be attributed either to experimental error or contamination during the gas handling with atmospheric CO_2).

In this view, the role of water could also be explained. In fact, it has been reported that the formation of formic acid from glucose proceeds trough a de-hydratation/re-hydratation sequence (scheme 1) [48].

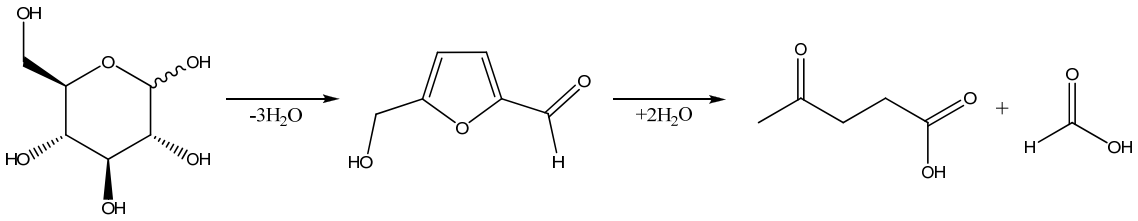

Scheme 1: Formation of formic acid via de-hydration/re-hydration of D-glucose [48].

As depicted in the scheme, the re-hydratation step is responsible for the formation of formic acid, thus the lower the water content in the system the slower its formation.

3 Conclusion

In conclusion we have demonstrated the feasibility of a new ionic liquid based catalytic system that allows the conversion of glucose to hydrogen. The issue of a suitable ionic liquid for such application was addressed and the new ionic liquid $[Bu_4P][CH_3P(OH)O_2]$ was synthesized and characterized. The ionic liquid/catalyst system showed to be robust and stable up to 48 h at 180 °C, allowing up to six consecutive glucose dehydrogenation reactions without formation of tarry solid materials. Isotopes labelling studies allowed us to gain new insights about the reaction mechanism and to identify a reasonable reaction scheme for the carbohydrate dehydrogenation. It was found that in ionic liquid glucose thermally decomposed yielding formic acid. The generated formic acid was quickly and selectively decomposed to CO_2 and hydrogen in a Ru-catalyzed process. The outcomes of this study are important as new scenarios for exploiting bio-feedstock are described. As a matter of fact, a catalytic IL based system was developed for the direct conversion of biomass to hydrogen and carbon dioxide in very high selectivity. This kind of hydrogen production could be potentially integrated into advanced bio-refinery concepts, as almost all existing bio-refinery schemes suffer from the lack of “non-fossil” hydrogen to balance the shortage of hydrogen in going from biogenic polyols to fuel components like alkanes or ethers. Clearly, the presented process is still in its infancy and its efficiency has to be improved for practical applications.

References

[1] G. W. Huber, J. A. Dumesic, Catalysis Today 111 (2006) 119–132

[2] R. Toonssen, N. Woudstra, A.H.M. Verkooijen, International Journal of Hydrogen Energy Volume 33, Issue 15, August 2008, Pages 4074-4082

[3] N. Boukis, V. Diem, U. Galla, P. D'Jesús, A. Kruse, H. Müller, E. Dinjus, ITC, NACHRICHTEN - Forschungszentrum Karlsruhe Jahrg. 37 3/2005 S. 116-123.

[4] R.D. Cortright, R.R. Davda and J.A. Dumesic, Nature 418 (2002), 964–967.

[5] R.R. Davda, J.W. Shabaker, G.W. Huber, R.D. Cortright, J.A. Dumesic, Applied Catalysis B: Environmental 56 (2005) 171-186.

[6] J. Woodward, M. Orr, K. Cordray, E. Greenbaum, Nature 405 (2000) 1014.

[7] L. Garcia, R. French, S. Czernik, E. Chornet, Appl. Catal. A Gen. 201 (2000) 225.

[8] E.G. Baker, L.K. Mudge, M.D. Brown, Ind. Eng. Chem. Res. 1987, 26, 1335–1349.

[9] P. De Filippis, C. Borgianni, M. Paolucci, F. Pochetti, Biomass and Bioenergy, 2004, 27, 247-252.

[10] T. Nordgreen, T. Liliedahl, K. Sjöström, Fuel, 2006, 85, 5-6, 689-694.

[11] S. Rapagnà, N. Jand, A. Kiennemann, P.U. Foscolo, Biomass and Bioenergy 19 (2000) 187-197.

[12] D.C. Elliott, Biofuels, Bioproducts and Biorefining 2 (2008), pp. 254–265.

[13] R. R. Davda, J.W. Shabaker, G.W. Huber, R.D. Cortright, J.A. Dumesic, Appl. Catal. B Environ. 43 (2002) 13.

[14] W. Shabaker, G.W. Huber, R.R. Davda, R.D. Cortright, J.A. Dumesic, J. Catal. 215 (2003) 344.

[15] W. Shabaker, G.W. Huber, R.R. Davda, R.D. Cortright, J.A. Dumesic, Catal. Lett. 88 (2003) 1.

[16] G. W. Huber, J.W. Shabaker, J.A. Dumesic, Science 300 (2003) 2075.

[17] R. R. Davda, J. W. Shabaker, G. W. Huber, R. D. Cortright, J. A. Dumesic, Applied Catalysis B: Environmental 56 (2005) 171–186.

[18] R. S. Dixit, L. L. Taviarides, Ind. Eng. Chem. Process. Des. Dev. 22 (1983) 1.

[19] E. Iglesia, S. L. Soled, R. A. Fiato, J. Catal. 137 (1992) 212.

[20] C. S. Kellner, A.T. Bell, J. Catal. 70 (1981) 418.

[21] M. A. Vannice, J. Catal. 50 (1977) 228.

[22] G. Eggleston, J.R. Vercellotti, J. Carbohydr. Chem. 19 (2000) 1305.

[23] M. Kabyemela, T. Adschiri, R.M. Malaluan, K. Arai, Ind. Eng. Chem. Res. 36 (1997) 1552.

[24] B.M. Kabyemela, T. Adschiri, R.M. Malaluan, K. Arai, Ind. Eng. Chem. Res. 38 (1999) 2888.

[25] P. Wasserscheid, W. Keim, Angew. Chem., Int. Ed. 2000, 3776-XXX.

[26] P. Wasserscheid, P. S. Schulz in P. Wasserscheid, T. Welton (eds.) „Ionic Liquids in Synthesis“, Wiley-VCH, 2nd edition, 2007, pp. XX-YY.

[27] J.G. Huddleston, H.D. Willauer, R.P. Swatloski, A.E. Visser, R,D. Rogers, Chem. Commun., 1998, 1765-1766.

[28] A.E. Visser, R.P. Swatloski, W.M. Reichert, J.H. Davis Jr., R.D. Rogers, R. Mayton, S. Sheff, A. Wierzbicki, Chem. Commun., 2001, 135 – 136.

[29] W. Arlt, M. Seiler, C. Jork, T. Schneider, German Patent DE 10114734, 2001.

[30] J. Gmehling, M. Krummen, German Patent DE 10154052, 2003.

[31] K.N. Marsh, J.A. Boxall and R. Lichtenthaler, Fluid Phase Equilibr. 219 (2004), 93–98.

[32] Y. Ge, L. Zhang, X. Yuan, W. Geng, J. Ji, J. Chem. Thermodyn., 2008, 40(8), 1248-1252.

[33] T. Predel, E. Schlücker, P. Wasserscheid, D. Gerhard, W. Arlt, Chem. Engin. & Technology 2007, 30(11), 1475-1480.

[34] Tetsuya Tsuda and Charles L. Hussey, Interface 2007, 42-49.

[35] Swatloski et al., J. Amer. Chem. Soc. 2002, 124, 4974

[36] D. A. Fort, R.C. Remsing, R.P. Swatloski, P. Moyna, G. Moyna, R.D. Rogers, Green Chem. 2007, 9, 63-69.

[37] J.L. Anthony, E.J. Maginn, J.F. Brennecke J. Phys. Chem. B, 2002, 106 (29), 7315–7320.

[38] R. P. Swatloski, R. D. Rogers and J. D. Holbrey, WO Pat. 03/029329, 2003.

[39] R.P. Swatloski, S.K. Spear, J.D. Holbrey, R.D. Rogers (2002). J. Amer. Chem. Soc. 124/18, 4974–4975.

[40] Y. Fukaya, K. Hayashi, M. Wada, H. Ohno, Green Chem. (2008), 10(1), 44-46.

[41] Balensiefer, Tim; Brodersen, Julia; D'Andola, Giovanni; Massonne, Klemens; Freyer, Stephan; Stegmann, Veit.WO 2008090155

[42] H. Junge, B. Loges, M. Beller, Chem. Commun., 2007, 522–524.

[43] B.M. Kabyemela, T. Adschiri, R.M. Malaluan, K. Arai, Ind. Eng. Chem. Res. 38 (1999) 2888.

[44] J. D.Scholten, G. Ebeling, J. Dupont, Dalton Transactions (2007), (47), 5554-5560 and references there in.

[45] C. E. Ellul, M. F.Mahon, O. Saker, M. K. Whittlesey, Angewandte Chemie, International Edition (2007), 46(33), 6343-6345.

[46] H. Sugisawa, Journal of Food Science (1966), 31(3), 381-5.

[47] C. Fellay, P. J. Dyson, G. Laurenczy Angew. Chem. Int. Ed. 47 (2008) 3966

[48] K. Lourvanij,G. L. Rorrer, J. Chem. T ech. Biotechnol. 1997, 69, 35-44

Hydrogen Production by Ethanol Steam Reforming on Ni/SiO_2 Catalysts: Effect of Ce and Zr Incorporation

J.A. Calles, A. Carrero, A.J. Vizcaíno, M. Lindo, Rey Juan Carlos University, Madrid, Spain

1 Introduction

Energy sustainability and CO_2 emissions are currently one of the major challenges and much effort has been done to diminish our dependence on fossil fuels and reduce greenhouse gas emissions. Hydrogen has been projected as a potentially very attractive energy carrier since its combustion and use in a fuel cell produce only water and energy [1]. The conventional methods for hydrogen production are based on gasoline or natural gas reforming, but the environmental goal of decreasing atmospheric CO_2 needs the use of renewable resources. In this sense, steam reforming of bio-ethanol is a very interesting alternative among the various processes proposed for hydrogen production, because ethanol is abundantly available from biomass, is easy to store and non-toxic [2, 3].

The steam reforming of ethanol has been widely investigated over several catalytic materials. Supported nickel catalysts provide good activity and high selectivity to H_2 and CO_x [2-8]. Besides Ni active phase, the nature of the support significantly affects the activity, selectivity and stability of catalysts [9]. In a previous work, we concluded that Ni supported on SiO_2 showed good catalytic performance, but coke formation was relatively high. On the other hand, although silica exhibits high surface area, when exposed to high temperature in the presence of steam, it may aggregate so silica-supported catalysts would decrease their surface area, probably leading to active metal sintering, loss of activity and promotion of coke formation. Several attempts have been done in order to reduce Ni supported catalyst deactivation. According to the literature, ceria has an excellent ability to store, release and transport oxygen, which may favor carbon oxidation/gasification [10-12]. Moreover, the ability of materials based on CeO_2 and/or ZrO_2 to resist carbon deposition has been described [14-16]. In fact, it was reported that the addition of zirconia to silica increased its steam resistance [13]. However, the main drawback of using ZrO_2 and CeO_2 as supporting materials is their low surface area.

The aim of the present work is to investigate steam reforming of ethanol over Ni/SiO_2 modified with 10 % Ce or Zr. The main objective was to study the effect of the support composition on the catalytic activity and products distribution.

2 Experimental

2.1 Catalysts preparation

In order to study the effect of Ce and Zr addition on Ni/SiO_2 catalysts used in ethanol steam reforming, a series of catalysts containing 10 wt% Ce or Zr and 7 wt% Ni have been prepared. The importance of Ni addition before or after Ce or Zr has also been studied. In both cases, metals were incorporated by incipient wetness impregnation using mixed

aqueous solutions of the metal precursors, $Ce(NO_3)_3 \cdot 6H_2O$, $ZrO(NO_3)_2 \cdot xH_2O$ and $Ni(NO_3)_2 \cdot 6H_2O$ (Scharlab), with the proper concentration to obtain the nominal contents in the final solid. After the incorporation of the first metal, the materials were air-dried overnight and calcined at 500 °C for 5 h with a heating rate of 1.8 °C/min. Then, addition of the second metal was performed following the same impregnation and calcination procedures described above. A Ni/SiO_2 catalyst was also prepared as the reference material.

Prior to the steam reforming reaction all the catalyst were reduced in the fixed-bed reactor used for catalytic tests under flowing pure hydrogen (30 NmL/min) at 550 °C for 4.5 h with a heating rate of 2 °C/min.

Catalysts have been denoted as $Y/X/SiO_2$, where X is the metal that is firstly incorporated and Y is added in the second place.

2.2 Catalysts characterization

Catalysts were characterized by Inductively Coupled Plasma Atomic Emission Spectroscopy (ICP-AES), Nitrogen Adsorption-Desorption at 77 K, X-ray Powder Diffraction (XRD), Ammonia Temperature Programmed Desorption (NH_3-TPD), Hydrogen Temperature Programmed Reduction (H_2-TPR) and Transmission Electron Microscopy (TEM).

ICP-AES technique was used to determine the actual cerium, zirconium and nickel content in the catalysts on a Varian VISTA-PRO AX CCD-Simultaneous ICP-AES spectrophotometer. Catalysts textural properties were measured in a Micromeritics TRISTAR 2050 sorptometer. Surface areas were calculated according to BET method. The acid properties of the supports were determined by NH_3-TPD in a Micromeritics AUTOCHEM 2910 equipment. Adsorbed NH_3 was determined by increasing temperature up to 550 °C with a heating rate of 15 °C/min, keeping this temperature constant for 30 min. H_2-TPR measurements were carried out with the same apparatus described for TPD. The samples were analyzed under 10 % H_2 in Ar flow (35 NmL/min) with a heating rate of 5 °C /min from 25 °C to 800 °C. TEM micrographs were acquired on a Phillips TECNAI 20 equipped with LaB_6 filament and an accelerating voltage of 200 kV.

2.3 Catalytic test

Catalysts were tested for ethanol steam reforming reaction on a MICROACTIVITY-PRO unit, as described elsewhere [17].

The catalyst (around 315 mg) was placed in the reactor and in situ reduced using the method described above. After the catalyst activation, the reaction temperature was fixed at 600 °C and catalytic test was carried out at atmospheric pressure under nitrogen-diluted conditions. A liquid water/ethanol reaction mixture with 3.7 molar ratio was introduced at a flow rate of 0.075 mL/min, vaporized at 150 °C and further eluted by N_2 (30 NmL/ min). WHSV defined as the ratio between the inlet feed (water + ethanol) mass flow rate and the mass of catalyst, was fixed at 12.7 h^{-1}.

The composition of the output gas stream was determined online by a gas chromatograph. Condensable vapours (ethanol, water and acetaldehyde) were trapped in the condenser and later analysed in the chromatograph.

Carbon deposited during reaction was evaluated from thermogravimetric analyses (TGA) on a TA instruments SDT 2960 thermobalance using an air flow of 100 mL/min and a heating rate of 5 °C/min up to 700 °C.

3 Results and Discussion

3.1 Catalysts characterization

The physicochemical properties of the prepared Ni catalysts are summarized in Table 1. ICP analysis revealed that silica support was loaded with the desired amounts of Ni and Ce or Zr. Regarding textural properties, all the catalysts present high surface area and pore volume. The incorporation of Ce and Zr slightly decreased the surface area and pore volume in comparison to the Ni/SiO_2 catalyst. Table 1 also shows that Zr incorporation into silica support results in the appearance of a little population of acid sites.

Table 1: Catalysts physicochemical properties.

	Ni[a] (wt %)	Ce[a] (wt %)	Zr[a] (wt %)	S_{BET} (m^2/g)	V_p[b] (cm^3/g)	Acidity[c] (meq NH_3/g)
Ni/SiO_2	7.81	-	-	263	1.07	-
$Ce/Ni/SiO_2$	6.70	8.74	-	228	0.95	-
$Ni/Ce/SiO_2$	6.73	9.22	-	204	0.93	-
$Zr/Ni/SiO_2$	6.74	-	9.43	236	0.88	0.144
$Ni/Zr/SiO_2$	6.77	-	8.87	211	0.87	0.133

[a] ICP-AES measurements
[b] Determined at $P/P_o = 0.98$
[c] Calculated from ammonia TPD measurements

Fig. 1.a. shows the XRD patterns of the reduced samples, together with Ni metal particles size calculated by means of the Scherrer equation. All samples presented diffraction peaks at 2θ = 44.4°, 51.8° and 76.3°, corresponding to cubic Ni (JCPDS 01-070-1849). For samples containing Ce peaks at 2θ = 28.5°, 33.0°, 47.4° and 56.3° were also observed, corresponding to cubic CeO_2 (JCPDS 00-034-0394). No diffraction peaks of Zr species can be seen, suggesting that the ZrO_2 crystallites are too small to be detected, which agrees with the results of Navarro et al. [18] in Zr/Al_2O_3, because for Zr loadings up to 6.6 μmol Zr/m^2 , Zr ions exists in atomic dispersion. The formation of relatively large Ni crystallites, around 20 nm, was found on all the catalysts, although they are slightly smaller on the Zr-modified catalysts. This indicates that the addition of ZrO_2 can promote the dispersion of the Ni species.

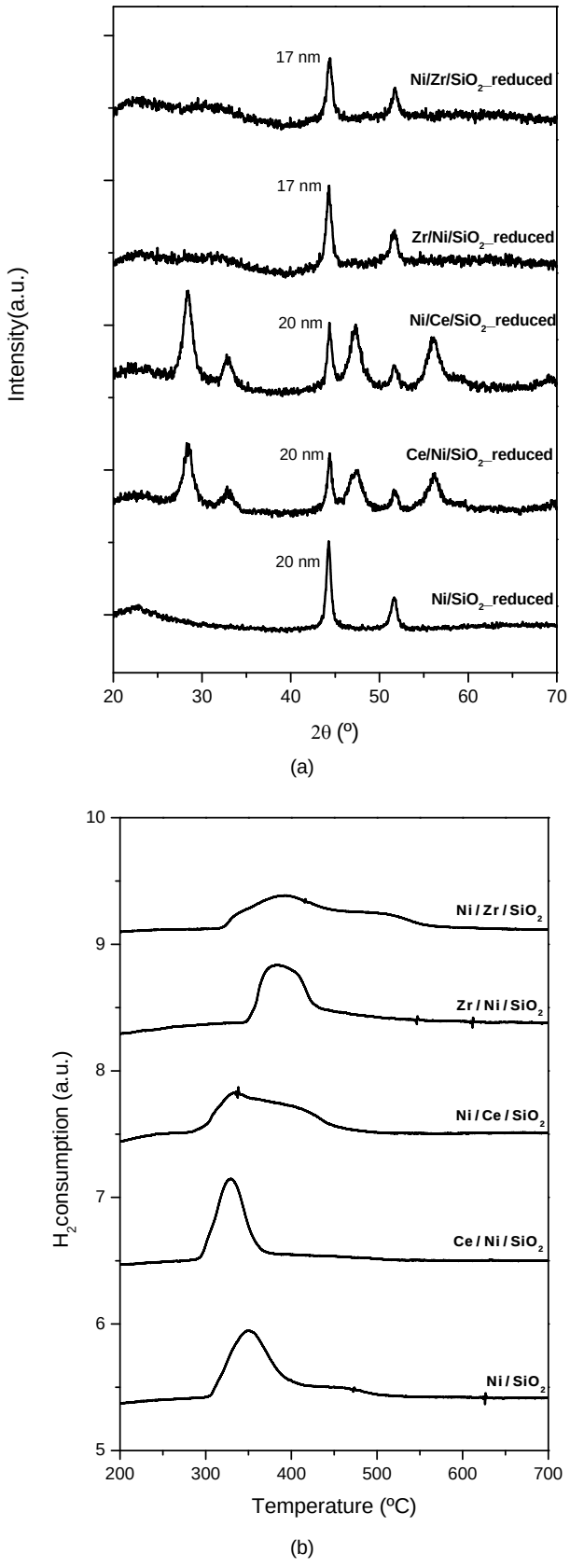

Figure 1: X-ray difractograms (a) and H_2-TPR profiles (b) of Ni-catalysts.

The reducibility of catalysts is determined by H_2-TPR experiments. Fig. 1.b. gives the reduction profiles of Ni catalysts. For the Ni/SiO_2 catalyst, one reduction peak appears around 350 °C, due to reduction of Ni^{2+} to Ni^{o}, as well as a broad small shoulder around 450 °C, which may be caused by a part of the Ni phase with stronger metal-support interaction.

After addition of Ce and Zr to Ni/SiO_2 catalysts similar profiles were obtained with a main peak and a broad shoulder. However, the reduction temperature shifts to lower value in the case of $Ce/Ni/SiO_2$ sample, indicating the promotion of Ni reducibility by CeO_2 incorporation to the silica supported Ni catalysts, effect typically found for lanthanide elements [12]. On the contrary, $Zr/Ni/SiO_2$ sample reduces at higher temperatures, which may be related with a higher NiO interaction with the support as a consequence of its smaller crystal size.

On the other hand, when Ni was impregnated after the Ce or Zr oxides incorporation, plateau-shaped profiles are obtained and reduction occurs in a broad temperature range. This indicates that several types of NiO phases differing in the metal-support interaction strength are present within each sample. Profile corresponding to the $Ni/Zr/SiO_2$ sample reaches higher temperatures probably due to easier contact of NiO with the ZrO_2 phase, which is well dispersed over the support, unlike the CeO_2 particles evidenced in the XRD patterns, found on the $Ni/Ce/SiO_2$ sample (Figure 1a).

3.2 Effect of Ce and Zr incorporation on catalytic performance

Table 2 shows the catalytic results obtained in ethanol steam reforming at 600 °C after 8 hours of reaction.

Ethanol conversion over all catalysts was total at the beginning of reaction, however for Ni/SiO_2 sample, slight deactivation can be observed with reaction time, while this is lower in the case of the $Ce/Ni/SiO_2$ sample and negligible for the rest of catalysts. Although hydrogen selectivity is similar for all the samples (around 80 mol%), some differences can be observed relating products selectivities. The presence of CeO_2 increases the CO_2/CO ratio, since it favours water-gas shift reaction [19, 20]. On the other hand, $Zr/Ni/SiO_2$ catalyst, gives small amounts of C_2H_4 and C_2H_6, considered as undesired products, due to the acidic nature of this catalyst. It is well-known that ethanol is dehydrated by the acid sites producing ethylene and ethane, the product of ethylene hydrogenation [21]. Although these products could no be detected on the $Ni/Zr/SiO_2$ sample, they were probably formed, but rapidly converted into another product, presumably coke.

Regarding the impregnation order of Ni and Ce/Zr, it can be observed that the incorporation of Ni after Ce or Zr leads to lower selectivity to intermediate products and, thus, higher selectivity towards the main products (H_2 and CO_2) after 8 hours on stream. This may be ascribed to higher nickel-support interaction detected by H_2-TPR (see Fig. 1), which would prevent nickel sintering under reaction conditions.

Results about coke formation are also shown in Table 2. Values indicate that coke formation occurs at much higher rate on Zr-modified catalysts. The amount of coke formed on these samples is a consequence of their acidity promoting the dehydration of ethanol to ethylene, which acts a hard precursor for the coke formation [21]. Although, the highest coke amount was found on the $Ni/Zr/SiO_2$ sample, no deactivation was observed, since carbon nanofibres

typically formed on this kind of catalysts do not embed metal particles and the high surface area of the supports can accommodate high amount of coke [22]. On the other hand, the presence of CeO_2 in Ni/SiO_2 catalyst diminishes coke formation, mainly if we consider that higher ethanol conversion was obtained over Ce-modified catalysts. This may be a consequence of enhancement of carbon gasification by CeO_2, mainly when added over Ni/SiO_2 [10-12].

Table 2: Catalytic results on ethanol steam reforming reaction.

	$X_{Ethanol}$ (mol %)	Selectivity (mol %)							Coke (g coke/ g cat h)
		H_2	CO_2	CO	CH_4	CH_3CHO	C_2H_4	C_2H_6	
Ni/SiO_2	97.1	82.6	50.9	33.7	13.9	1.5	0	0	0.37
$Ce/Ni/SiO_2$	98.5	82.0	49.6	29.9	19.5	1.0	0	0	0.23
$Ni/Ce/SiO_2$	100	84.4	55.9	25.6	18.5	0	0	0	0.37
$Zr/Ni/SiO_2$	100	79.2	43.5	29.1	21.2	0	4.9	1.3	0.57
$Ni/Zr/SiO_2$	100	82.5	62.8	27.1	10.1	0	0	0	0.62

4 Conclusions

Ethanol steam reforming reaction has been studied over Ni/SiO_2 catalysts modified by Ce and Zr. Regarding to catalysts characterization, the incorporation of ZrO_2 on silica or Ni/SiO_2 increases the interaction between Ni and the support, which may be a consequence of the lower Ni crystallites size obtained by XRD. Meanwhile, for Ce-modified catalysts, the presence of CeO_2 favors the reducibility of NiO.

In addition, all catalysts present high activity (hydrogen selectivity around 80 %) and stability (ethanol conversion close to 100 % along the 8 hours of time on stream). Cerium addition to silica or Ni/SiO_2 enhances WGS reaction and coke gasification leading to higher selectivity towards methane and carbon dioxide with lower coke deposition. However, coke generation is higher on Zr modified samples due to the formation of ethylene (a known coke precursor) on acid sites provided by ZrO_2. Concerning to impregnation order, the incorporation of Ce and Zr prior to nickel on silica support gives steam reforming catalysts with better performance.

References

[1] Vizcaíno AJ, Arena P, Baronetti G, Carrero A, Calles JA, Laborde M, et al. Ethanol steam reforming of LNG over Ni/Al_2O_3 catalysts: effect of Mg addition. Int J Hydrogen Energy 2008;33:3489-92.

[2] Fierro V, Akdim O, Provendier H, Mirodatos C. Ethanol steam reforming over Ni-based catalysts. J Power Sources 2005;145:659–66.

[3] Comas J, Mariño F, Laborde M, Amadeo N. Bio-ethanol steam reforming on Ni/Al_2O_3 catalysts. Chem Eng J 2004;98:61–8.

[4] Klouz V, Fierro V, Denton P, Katz, Lisse JP, Bouvot-Mauduit S,et al. Ethanol reforming for hydrogen production in a hybrid electric vehicle. Process optimisation. J Power Sources 2002;105:26–34.

[5] Fatsikostas AN, Kondarides DI, Verykios XE. Production of hydrogen for fuel cells by reformation of biomass-derived ethanol. Catal Today 2002;75:145–55.

[6] Frusteri F, Freni S, Chiodo V, Spadaro L, Di Blasi O, Bonura G,et al. Steam reforming of bio-ethanol on alkali-doped Ni/MgO catalysts:hydrogen production for MC fuel cell. Appl Catal A Gen 2004;270:1–7.

[7] Auprêtre F, Descorme C, Duprez D. Bio-ethanol catalytic steam reforming over supported metal catalysts. Catal Commun 2002;3:263–7.

[8] Pompeo F, Nichio NN, Feretti OA, Resasco D. Study of Ni catalysts on different supports to obtain synthesis gas. Int J Hydrogen Energy 2005;30:1399–405.

[9] De Lima SM, Da Silva AM, Da Costa LOO, Graham UM, Jacobs G, Davis BH, Mattos LV, Noronha FB. Study of catalyst deactivation and reaction mechanism of steam reforming partial oxidation, and oxidative steam reforming of ethanol over Co/CeO_2 catalysts. J Catal 2009;268:268-81.

[10] Bismas P, Kurizru D. Oxidative steam reforming of ethanol over Ni/CeO_2-ZrO_2 catalyst. Chem Eng J 2008;136:41-9.

[11] Pakulska MM, Grgicak CM, Giorgi JB. The effect of metal and support particle size on NiO/CeO_2 and NiO/ZrO_2 catalyst activity in complete methane oxidation. Appl Catal A 2007;332(1):124-9.

[12] Calles JA, Carrero A, Vizcaíno AJ. Ce and La modification of mesoporous Cu-Ni/SBA-15 catalysts for hydrogen production through etanol steam reforming. Micro meso materials 2009;119:200-7.

[13] Takahashi R, Sato S,Sodesawa T, Yoshida M, Tomiyama S. Addition of zirconia in Ni/SiO_2 catalyst for improvement of steam resistance. Appl Catal A 2004;273:211–5.

[14] Navarro RM, Álvarez-Galván MC, Rosa F, Fierro JLG. Production of hydrogen by oxidative reforming of etanol over Pt catalysts supported on Al_2O_3 modified with Ce and La. Appl Catal B 2005;55:229-41.

[15] Baocai Z, Weijie C, Yong L, Yide X, Wenjie S. Hydrogen production by steam reforming of ethanol over an Ir/CeO_2 catalyst: Reaction mechanism and stability of the catalyst. Int J Hydrogen 2008;33:4377-86.

[16] Ekaterini Ch. Vagia, Angeliki A. Lemonidou. Investigations on the propierties of ceria-zirconia-supported Ni and Rh catalysts and their performance in acetic acid steam reforming. J Catal 2010;269:388-96.

[17] Vizcaíno AJ, Carrero A, Calles JA. Hydrogen production by ethanol steam reforming over Cu–Ni supported catalysts. Int J Hydrogen Energy 2007;32:1450–61.

[18] Sánchez-Sánchez MC, Navarro RM, Fierro JLG. Ethanol steam reforming over Ni/MxOy-Al2O3 (M = Ce, La, Zr and Mg) catalysts: Influence of support on the hydrogen production. Int J Hydrogen Energy 2007;32:1462-71.

[19] Djinovic P, Batista J, Pintar A. WGS reaction over nanostructures CuO-CeO2 catalysts prepared by hard template method: Characterization, activity and deactivation. Catal Today 2009;147:191-7

[20] Andreeva D, Ivanov I, Ilieva L, Sobczak JW, Avdeev, Tabakova T. Nanosized gold catalysts supported on ceria and ceria-alumina for WGS reaction: Influence of preparation method. Appl Catal A 2007;333:153-60.

[21] Trim DL. Coke formation and minimisation during steam reforming reactions. Catal Today 1997;37:233–8.

[22] Carrero A, Calles JA, Vizcaíno AJ. Hydrogen production by ethanol steam reforming over Cu-Ni/SBA-15 supported catalysts prepared by direct synthesis and impregnation. Appl Catal A Gen 2007;327:82–94.

The Cycle Use Test of Pt Based Catalyst for the Steam Reforming of Naphthalene/ Benzene as Model Tar Compounds of Biomass Gasification

Takeshi Furusawa, Katsuhiko Saito, Masahide Sato, Noboru Suzuki, Utsunomiya University, Graduate School of Engineering, Japan

1 Introduction

Biomass gasification offers great potential for alleviating global environmental problems because biomass is a carbon neutral resource [1]. Gasification involves partial oxidation of raw material to obtain a mixture of hydrogen, carbon monoxide, water, and small amount of methane and higher hydrocarbons. The product gas also contains variable amounts of ash particles, volatile alkali metals and tar, which is a complex mixture of aromatics [2]. The condensable compounds in tar may cause problems in downstream equipment making catalytic hot gas cleaning a necessary step in gasification system [3-4]. Several research groups had already reported the excellent catalysts applied for removal of tar derived from biomass gasifier [3-6], while other research groups developed new catalyst for steam reforming of tar model compound such as benzene [7], toluene [8], phenol [9], and naphthalene [10-11]. If one considers about test reaction to find out new catalysts for tar removal, steam reforming of naphthalene/ benzene is most suitable test reaction because both benzene and naphthalene are most stable tar compounds and are difficult to decompose [10-11]. In this point of view, steam reforming of naphthalene under ideal reaction condition or simulated gas condition have been studied over Ni-Cr/Al_2O_3·MgO·La_2O_3 [10], pretreated olivine [12], Ni/WO_3/MgO-CaO [13], Nickel-activated candle filter [14], commercial nickel-based catalysts [11, 15], CaO+MgO [16], Ni/dolomite [17], Ni/olivine [18], Ni/$Ce_{0.75}Zr_{0.25}MnO_2$ [19] and Ni/MgO [20] to develop new catalyst for tar removal. According to these reported papers, the deposition of carbon species on the catalyst and irreversible adsorption of sulfur atoms on metal surface account for the catalyst deactivation, and several research groups tried to find out solutions for these problems. For example, Fujimoto *et al.* [13] had reported that the addition of WO_3 to Ni/MgO-CaO catalyst improved the resistance to sulfur poisoning and coking under simulated gas condition. Moreover, Li *et al.* [21] had reported that oxidation-decomposition-reduction regeneration process can effectively remove the sub-surface sulfur and completely regenrate the sulfur-poisoned Ni catalysts. However, it can be predicted that the improved catalyst also deactivated finally due to mainly carbon deposition when once catalyst used for tar removal. Therefore, we thought that the points for the regenerated method and catalytic performance of regenerated catalyst also should be considered. From this background, deactivated Ni/MgO catalyst was regenerated by mild oxidation treatment, and regenerated catalyst was used for steam reforming of naphthalene/ benzene under ideal reaction condition in our previous research [22]. It was found that Ni/MgO catalyst has tolerance toward only 3 cycle of steam reforming-oxidation treatment. The obtained results motivate us to find another catalyst which shows the excellent

performance for cycle test of steam reforming-regeneration treatment. In present study, Pt-based catalysts were prepared by impregnation method and used for cycle test of steam reforming of naphthalene/benzene - regeneration treatment. Moreover, either hydrogen treatment or mild oxidation treatment was selected as regeneration method, and the effect of regeneration method on the catalytic performances of Pt-based catalysts was also investigated.

2 Experimental

2.1 Preparation of catalyst

Pt-based catalyst was prepared by impregnating MgO (JRC-MGO-4 500A, 28-38 m^2/g) or Al_2O_3 (JRC-ALO-1, 200 m^2/g) with aqueous solution of $H_2PtCl_6 \cdot 6H_2O$ (Kanto Chemical Co.) followed by drying at 383 K overnight. The material was then calcined in air at 873 K for 8 h. The amount of Pt loading on the catalyst was controlled to be 1 wt.%. Naphthalene and benzene were purchased from Kanto Chemical Co., and used without further purification. Naphthalene/benzene solution was prepared to be 1:9 for molar ratio of naphthalene and benzene.

2.2 Characterization

The nitrogen adsorption isotherms of samples (0.1 g) before and after reaction were measured using a Nova 1200e (Yuasa Ionics Co.) to calculate the specific surface area based on the BET method. The samples were degassed at 573 K for 1 h before measurement and were conducted for nitrogen adsorption isotherms under N_2 at 77 K.

XRD measurements of samples before and after reaction were performed on a Rigaku powder diffractrometer with Cu-Kα radiation. The tube voltage was 40 kV, and the current was 40 mA. The XRD diffraction patterns were taken in the 2θ range of 10-80º at a scan speed of 2 º min^{-1}. XRF measurements of catalysts were performed using SEA2010 (SEIKO Instruments Inc.) to calculate the amount of Pt loading on the catalysts. The morphology and size of Pt particles on fresh reduced catalyst and used catalyst was observed by TEM (JEOL 2010). Average size of Pt particles on catalyst was calculated by estimating each size of 100 Pt particles corrected from TEM image.

The profile for the oxidation of carbon species on used catalyst was obtained by Temperature Programmed Oxidation with 10 % O_2/He. All deposited carbon species were oxidized to CO or CO_2, and the consumption of O_2 was detected by TCD. A 40 mL min^{-1} feed of 10 % O_2/He was used for oxidation and the temperature was firstly ramped at 10 K min^{-1} to 873 K. Until no peak was observed, the temperature of reactor kept at 873 K for a while and time needs for complete oxidation of deposited carbon species at 873 K was measured. The temperature was subsequently heated up at 10 K min^{-1} to 1273 K to check the existence of additional carbon species on the catalyst.

2.3 Catalytic tests

2.3.1 Steam reforming of naphthalene/benzene

Catalytic tests were conducted using the atmospheric flow experimental system. The catalyst was palletized, crushed and sieved to 0.35-0.5 mm before use and was reduced in H_2/Ar (50 vol%/50 vol%) mixture with heating rate at 10 K min^{-1} to 1173 K and held at 1173 K for 1 h. After reduction, the catalyst bed was cooled down to 973~1073 K under Ar flow and the feed gases were allowed to pass through the catalyst bed at a gaseous feed rate of 400 mL min^{-1}. Nitrogen was used to carry the naphthalene and benzene vapors into the reactor with heating all pipelines at 473 K; a flow rate of nitrogen was 40 mL min^{-1} carrying 0.36 g h^{-1} of naphthalene and 1.98 g h^{-1} of benzene. The water was pumped at a flow rate of 3.3~9.9 g h^{-1} in order to achieve a GHSV of 19200 h^{-1} (residence time; 0.18 s), based on the apparent bulk density of the catalyst bed (0.8 g cm^{-3}) for 1 g of catalyst. Water to carbon of naphthalene and benzene molar ratio is 1~3. The effluent gases from the reactor were fed through cotton filter set inside ice-cold trap and $CaCl_2$ column, connected in series. Un-reacted naphthalene, benzene and H_2O were recovered in the ice-cold trap. The non-condensible gases, which included C_1-C_3 hydrocarbons, carbon monoxide, carbon dioxide, hydrogen, and nitrogen were analyzed by gas chromatography (HP6890 equipped with a TCD detector, molecular sieve 5A column and porapak Q column). After the reaction, the reactants were switched with Ar at the reaction temperature; subsequently the catalyst was cooled down to room temperature and used for further characterization. The catalytic activity for the steam reforming was evaluated by calculating the carbon conversion to gas [%] using the equation described below;

$$\text{Carbon conversion to gas [\%]} = \frac{\text{Total molar of carbon atoms of gas products}}{\text{Total molar of carbon atoms of feed gases (naphthalene + benzene)}} \times 100\,[\%] \quad (1)$$

2.3.2 Cycle test of steam reforming and regeneration treatment

After the steam reforming of naphthalene/benzene at 1023~1073 K for 3 h with catalyst, used catalyst was cooled down to 873 K and was oxidized under 10 % O_2+Ar mixture or reduced under 10 % H_2+Ar mixture at same temperature for 40 min. Regenerated catalyst was heated up to 1023~1073 K again and then reactants fed to regenerated catalyst bed to evaluate the catalytic performance as 2nd run. This cycle for the steam reforming and regeneration treatment was defined as a 1 cycle in present paper. The cycle usage tests repeated until the deactivation of catalyst was observed.

3 Results and Discussion

3.1 The effect of reaction temperatures on the catalytic performances

Figure 1 shows the catalytic peformances of Pt/Al_2O_3 catalysts for the steam reforming of naphthalene/benzene at various reaction temperatures with S/C=3. The activity of Pt/Al_2O_3 catalyst was gradually decreased from 85 % to 75 % at 1023 K during 30 h reaction due to

carbon deposition which was confirmed by the result of TPO measurement, while this catalyst showed high and stable activity (carbon conv. to gas: 90 %) at 1073 K for 30 h. Moreover, the catalyst showed low catalytic activity at 973 K. From these obtained results, 1023 K was selected as reaction temperature for cycle test in the case of Pt/Al_2O_3.

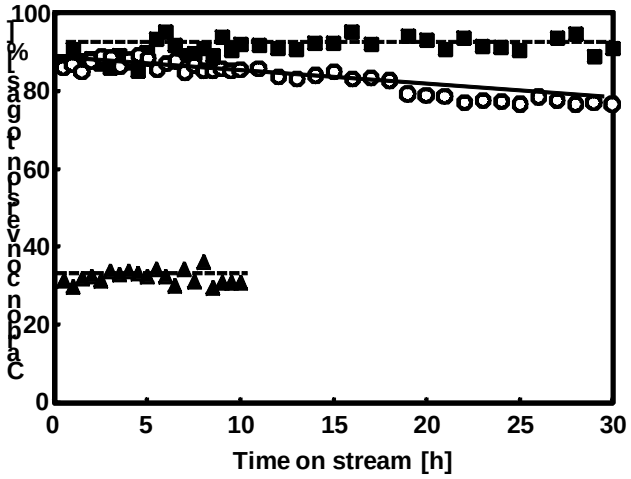

Figure 1: Catalytic performances of Pt/Al_2O_3 catalysts for the steam reforming of naphthalene/benzene at variuous reaction temperatures with S/C=3: ■ 1073 K, ○ 1023 K, ▲ 973 K.

In the case of Pt/MgO catalyst (not shown here), the activity of Pt/MgO catalyst was remarkably decreased from 80 % to 60 % during initial reaction period (8 h) at 1023 K, while this catalyst showed high and stable activity (carbon conversion to gas: 85 %) for 30 h at 1073 K. Judging from the results, 1023 K was selected as reaction temperature for cycle test with Pt/MgO catalyst as well.

3.2 Cycle tests of Pt-based catalysts

Figure 2 shows the result of cycle test (steam reforming – oxidation treatment) using Pt/Al_2O_3 catalyst at 1023 K with S/C=3. The activity was lost after 1st oxidation treatment, while catalyst showed stable activity during 1st steam reforming step. Since TPO result of oxidized catalyst after 1st oxidation treatment showed no carboneous species deposited on the catalyst, this observation could be related with changing catalyst structure such as Pt particle size, surface area and crystal structure of support. Among them, there are no differences between fresh catalyst and used catalyst in BET surface area (135 vs. 135 m^2/g) and crystal structure (XRD). On the contrary, TEM results indicated that average size of Pt particles on used catalyst significantly increased from less than 3 nm to 5.3 nm. This is probably the reason that Pt/Al_2O_3 catalyst lost its activity after 1st oxidation treatment.

To avoid the aggregation of Pt particles on catalyst, hydrogen treatment was selected as regeneration method instead of mild oxidation treatment. When used catalyst was reduced by hydrogen treatment, the activity of regenerated catalyst was recovered to initial activity of fresh catalyst, and Pt/Al_2O_3 catalyst had tolerance toward 5th cycle test of steam reforming-hydrogen treatment (not shown here). Judging from these results, hydrogen treatment was

suitable regeneration method in the case of Pt/Al_2O_3 catalyst. Moreover, Pt/MgO catalyst also lost its activity after 2nd oxidation treatment (not shown here) during cycle test of steam reforming-oxidation treatment. This result could be also explained by the sintering behavior of Pt particles during cycle test.

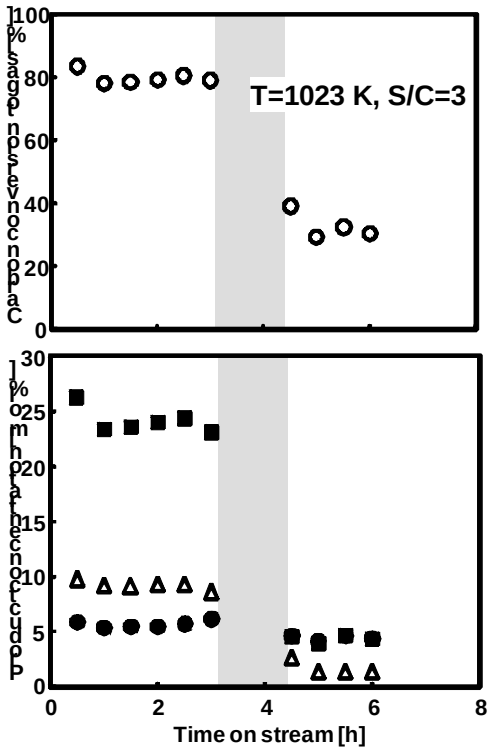

Figure 2: Cycle test of Pt/Al_2O_3 catalyst at 1023 K with S/C=3: ▭ period for mild oxidation treatment, ■ H_2, Δ CO_2, ● CO.

4 Summary

Although Pt/Al_2O_3 catalyst showed high and stable activity (carbon conversion to gas: 90 %) for steam reforming of naphthalene/benzene at 1073 K with S/C=3, this catalyst gradually lost its activity at 1023 K with S/C=3 due to deposition of carboneous species. Two kinds of regeneration treatment was conducted to enlong the life time of Pt/Al_2O_3 catalyst. Although regeneration treatment completely remove the carboneous species from catalyst, mild oxidation treatment led to decrease activity due to sintering of Pt particles. On the contrary, hydrogen treatment led to maintain activity until 5th cycle test. It was concluded from these obtained results that hydrogen treatment is suitable regeneration method during cycle test in the case of Pt/Al_2O_3 catalyst.

References

[1] A. V. Bridgewater, Appl. Catal. A, 116 (1994) 5.

[2] D. Sutton, B. Kelleher, J. R. H. Ross, Fuel Process. Technol., 73 (2001) 155.

[3] D. Dayton, NREL/TP-510-32815, 2002

[4] Z. Abu El-Rub, E. A. Bramer, G. Brem, Ind. Eng. Chem. Res., 43 (2004) 6911.
[5] J. M. Toledo, J. Corella, G. Molina, Ind. Eng. Chem. Res., 45 (2006) 1389.
[6] R. Zhang, R. C. Brown, A. Suby, Energy and Fuels, 18 (2004) 251.
[7] Hyun-Ju Park et al., Bioresource Technology, 101 (2009) S101.
[8] D. Swierczynski, S. Libs, C. Courson, A. Kiennemann, Appl. Catal. B, 74 (2007) 211.
[9] K. Polychronopoulou et al., J. Catalysis, 241 (2006) 132.
[10] D. N. Bangala, N. Abatzoglou, E. Chornet, AIChEJ., 44 (1998) 927.
[11] R. Coll, J. Salvadó, X. Farriol, D. Montané, Fuel Process. Technol., 74 (2001) 19.
[12] L. Devi, K. J. Ptasinski, F. J. J. G. Janssen, Fuel Process. Technol., 86 (2005) 707.
[13] K. Sato, K. Fujimoto, Catalysis Communications, 8 (2007) 1697.
[14] L. Ma, G. V. Baron, Powder Technology, 180 (2008) 21.
[15] C. Pfeifer, H. Hofbauer, Powder Technology, 180 (2008) 9.
[16] N. Alarcón et al., Appl. Catal. A, 267 (2004) 251.
[17] T. J. Wang et al., Biomass and Bioenergy, 28 (2005) 508.
[18] Z. Zhang et al., Appl. Catal. A, 363 (2009) 64.
[19] A. Bampenrat et al., Appl. Catal. A, 373 (2010) 154.
[20] T. Furusawa et al., Appl. Catal. A, 278 (2005) 205.
[21] L. Li et al., ACS, Division of Petroleum Chemistry, 54 (2009) 247.
[22] T. Furusawa et al., Catalysis Communications, 10 (2009) 552.

Hydrogen Production by Supercritical Water Gasification of Wastewater from Food Waste Treatment Processes

In-Gu Lee, Korea Institute of Energy Research, Korea

Abstract

Korean food wastes have high moisture content (more than 85 wt%) and their major treatment processes such as drying or biological fermentations generate concentrated organic wastewater (CODs of about 100,000 mgO_2/L). For obtaining both wastewater treatment and hydrogen production from renewable resources, supercritical water gasification (SCWG) of the organic wastewater was carried out in this work. The effect of catalyst, reaction temperature, and reactor residence time on COD destruction and composition of gas products was examined. As a result, a SCWG of the wastewater over Ni-Y/activated charcoal at 700 ^oC, 28 MPa yielded 99 % COD destruction and hydrogen-rich gas production (45 vol% H_2). A liquid-phase thermal pretreatment to destroy solid particles from the wastewater was proposed for more effective operation of the SCWG system.

1 Introduction

Million tons of food waste are generated annually in Korea. A unique feature of Korean food waste is the high moisture content (more than 85 wt%). Conventional methods to treat the food waste include anaerobic digestion (biomethanation) and dewatering combined with incineration or landfilling. Anaerobic digestion can produce combustible gas consisting exclusively of methane and carbon dioxide at relatively room temperature and pressure conditions. A critical disadvantage of the anaerobic digestion (biomethanation) is that this technology generates high organic content process water as a byproduct. The wastewater should be re-treated before it is released to nature. Dewatering is one of commercialized methods to treat food waste in Korea due to the process simplicity. However dewatering process also generates organic wastewater as byproduct, which has higher organic content (CODs of about 100,000 mgO_2/L) than the wastewater from biomethanation.

In this work, supercritical water gasification (SCWG) technology is examined to convert the organics in the wastewater from food waste treatment processes to hydrogen-rich gas. The SCWG technology is known to produce hydrogen-rich gas by complete gasification of aqueous organic wastes or wet biomass under appropriate reaction conditions. A wide range of whole organic wastes has been treated by the SCWG processes, including sewage sludge [1,2], agricultural wastes such as potato wastes [3], tannery wastes [4], alcohol distillery wastewater [5], and polyvinyl alcohol-contaminated wastewater [6]. Most efforts of those studies have been focused on obtaining optimal reaction conditions for complete destruction of organics in water and hydrogen production. More fundamental SCWG studies with model compounds as a reactant have also been carried out to understand the gasification chemistry [7-12].

2 Experimental Apparatus and Methods

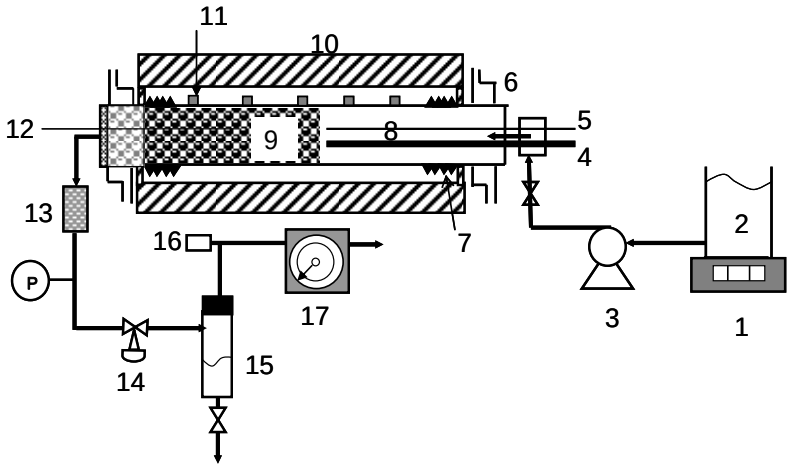

Figure 1: A schematic diagram of the SCWG system (1, digital balance; 2, feed reservoir; 3, high pressure pump; 4, rod heater; 5, annulus thermocouple; 6, heat exchanger; 7, coiled heater; 8, preheating zone of the reactor; 9, packed-bed of the reactor; 10, furnace; 11, thermocouple mounted on the reactor wall; 12, thermocouple inside the reactor; 13, filter; 14, back-pressure regulator; 15, gas-liquid separator; 16, gas sample outlet; 17, gas flow meter).

A schematic diagram of the apparatus used in this experiment is shown in Figure 1. The reactor was made of a Hastelloy C-276 tubing with 9.53 mm o.d., 6.22 mm i.d. and 293 mm total length. The reactor consisted of packed-bed of catalyst zone (5.6 cm^3) and reactant preheating zone (3.3 cm^3). The wastewater feeds were delivered into the reactor by a high pressure pump (Waters model 515) and quickly heated to the reaction temperature in the preheating zone by the combination of a coiled heater in the entrance region of the reactor and a rod heater present in the preheating zone of the reactor. Reactor was maintained at a desired temperature by a furnace and another coiled heater in the exit region of the reactor. Reaction temperature was measured by a type K thermocouple installed inside the packed-bed of catalyst. A back-pressure regulator (Tescom model 26-1762-24) was used to reduce the pressure of product flow from 28 MPa to atmospheric pressure. The reactor effluent was disengaged into gas and liquid products in a gas-liquid separator. The flow rate of gas effluent was measured by a wet test meter (Sinagawa model W-NK-0.5A). Liquid product was collected at the bottom of the separator to measure its flow rate. For the catalytic experiments, purified sand was first packed in the cold zone of the downstream of the reactor and then catalyst was consecutively packed in the heating section (about 5.6 cm^3) of the reactor.

Since the original wastewater obtained from the dewatering process of food waste contained significant amounts of solid particles, it was first sieved to less than 0.5 mm to remove big particles and then undertaken thermal treatment at 200 ^oC and 10 MPa to decompose the remaining solid to organic compounds dissolved in water. The product from the hydro-thermal treatment was quenched and its liquid-phase portion was separated to be used as a feed solution for SCWG process. This hydro-thermal treatment of the organic wastewater

generated gaseous product to a negligible extent and its amount was not measured in this work. Activated charcoal (Sigma C3014) in 0.42-0.83 mm size was used as a catalyst or a support for nickel catalyst. The activated charcoal contains about 6wt% ash and has a BET surface area of 920 m^2/g. A Ni-Y/AC catalyst was formulated by an incipient wetness method. The weight ratio between Ni and Y per 1g AC support was 0.25:0.0 for the Ni/AC and 0.25:0.10 for the Ni-Y/AC. Nickel(Ⅱ) nitrate hexahydrate (Aldrich No. 203874) and yttrium(Ⅲ) nitrate tetrahydrate (Aldrich No. 217239) were used as precursors. The catalyst was calcined in a nitrogen flow at 500 ^oC for 3 h, and reduced at 400 ^oC for more than 10 h under the flow of hydrogen gas.

Compositional analysis of the gaseous products were accomplished with a gas chromatograph (Donam Instruments model DS 6200) using a mixture of 8 % hydrogen in helium as a carrier gas. A thermal conductivity detector was employed for the detection of hydrogen, carbon monoxide, carbon dioxide, and methane, and a flame ionization detector for light hydrocarbons. An 80/100 mesh carbosphere molecular sieve packed column was used. Liquid effluent was analyzed for COD (by closed reflux titrimetric method), and pH (using a pH meter; Orion model 290A).

3 Results and Discussion

The COD value of the original wastewater obtained during dewatering food waste was about 100,000 mgO_2/L and reduced 40 wt% during the pretreatments (sieving and hydrothermal treatment). Figure 2 (a) shows gas production rate and COD destruction as a function of gasification time on stream during the SCWG of the pretreated feed solution at 700 ^oC, 28 MPa, and 12^{-1} LHSV with Ni-Y/AC catalyst. The gas production rate ranged from 400 to 500 L/h per reactor volume and COD destruction was 99 wt%. The feed solution has pH of 3.3 but the liquid effluent has pH over 7.0. The complete destruction of organic compounds to hydrogen-rich gas was believed to be caused by the catalytic role of the Ni-Y/AC and salts such as NaCl present in the feed solution. Figure 2 (b) shows the content of major constituents in the gaseous product.

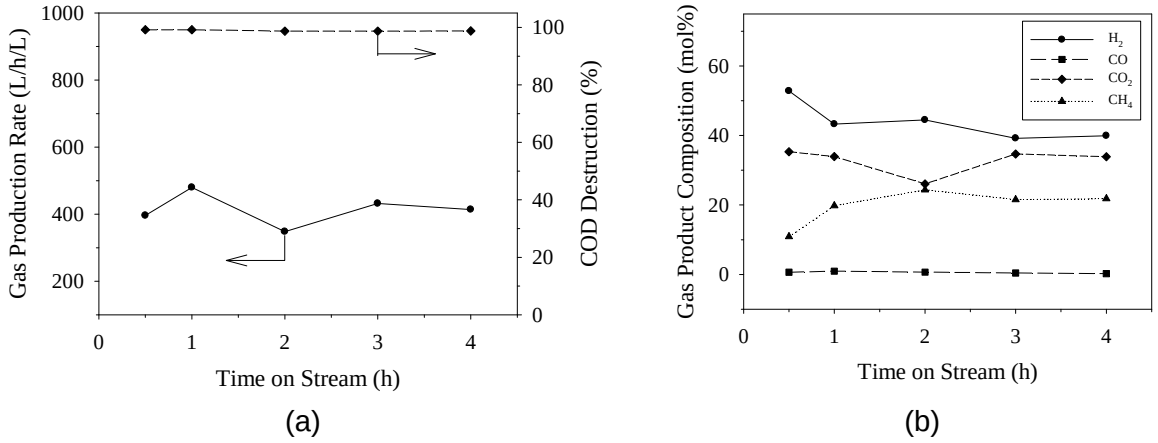

Figure 2: Gasification of pretreated wastewater from the dewatering of food waste in supercritical water at 700 ^oC, 28 MPa, and 12^{-1} LHSV with Ni-Y/AC catalyst.

The hydrogen content was initially 53 vol% and slightly decreased with time on stream. The methane showed quite different pattern. Carbon monoxide was produced in very small amount, indicating that the water-gas shift reaction was catalyzed in the reaction conditions.

Table 1 displays more experimental data obtained by the SCWGs of the wastewater from the food waste dewatering process. It is evident the presence of salts in the feed solution, which catalyzed the water-gas shift reaction. Activated charcoal (AC) significantly enhanced COD destruction but did not appear to catalyze the water-gas shift mechanism. The formulated Ni-Y/AC catalyst seems to activate hydrogen formation reactions. A bench-scale SCWG reactor (0.2L working volume) has been constructed for the study of system development at our laboratory. It is hoped to report more experimental results on the SCWG treatments of food waste deriven wastewater using the bench-scale reactor in the near future.

Table 1: Effect of temperature and catalyst on the SCWG of the wastewater from food waste processes at 28 MPa and 12^{-1} LHSV.

Reaction conditions				
Catalyst	no	no	AC	Ni-Y/AC
Temperature (^{o}C)	550	620	600	700
Feed solution				
COD (mgO_2/L)	54,840	54,840	57,600	59,520
TS (%)	3.2	3.2	3.0	<0.1
pH	3.3	3.3	3.7	3.1
Gaseous product				
Production rate (L/h/L)	349	434	523	420
HHV (kcal/Nm^3)	2,943	4,157	3,687	3,735
Composition (vol%)				
H_2	33.5	34.1	38.3	43.9
CO	1.5	0.8	1.3	0.6
CO_2	48.0	37.2	37.2	32.8
CH_4	13.9	22.3	19.8	19.7
Liquid effluent				
COD destruction (%)	77	90	99	99
pH	7.2	7.4	7.3	7.6

Acknowledgements

This work was supported by Ministry of Environment through KEITI, Republic of Korea.

References

[1] Xu, X.; Matsumura, Y.; Stenberg, J.; Antal, M. J. Jr. Carbon-catalyzed gasification of organic feedstocks in supercritical water. Ind. Eng. Chem. Res. 1996, 35, 2522-2530.

[2] Schmieder, H.; Abeln, J.; Boukis, N.; Dinjus, E.; Kruse, A.; Kluth, M.; Petrich, G.; Sadri, E.; Schacht, M. Hydrothermal gasification of biomass and organic wastes. Journal of Supercritical Fluids 2000, 17, 145-153.

[3] Antal, M. J. Jr.; Allen, S. G.; Schulman, D.; Xu, X. Biomass gasification in supercritical water. Ind. Eng. Chem. Res. 2000, 39, 4040-4053.

[4] Yanik, J.; Ebale, S.; Kruse, A.; Saglam, M.; Yüksel, M. Biomass gasification in supercritical water: II. Effect of catalyst. International Journal of Hydrogen Energy 2008, 33, 4520-4526.

[5] García Jarana, M. B.; Sánchez-Oneto, J.; Portela, J. R.; Sanz, E. N.; Martínex de la Ossa, E. J. Supercritical water gasfication of industrial organic wastes. The Journal of Supercritical Fluids 2008, 46, 329-334.

[6] Yan, B.; Wei, C. H.; Hu, C. S.; Xie, C.; Wu, J. Z. Hydrogen generation from polyvinyl alcohol-contaminated wastewater by a process of supercritical water gasification. Journal of Environmental Science 2007, 19, 1424-1429.

[7] Amin, S.; Reid, R. C.; Modell, M. Reforming and decomposition of glucose in an aqueous phase. The Intersociety Conference on Environmental Systems, San Francisco, CA, 1975; The American Society of Mechanical Engineers (ASME); New York, 1975; ASME Paper No. 75-ENAs-21, 1.

[8] Holgate, H. R.; Meyer, J. C.; Tester, J. W. Glucose hydrolysis and oxidation in supercritical water, AIChE Journal 1995, 41, 637-648.

[9] Kabyemela, B. M.; Adschiri, T.; Malaluan R. M.; Arai, K. Kinetics of glucose epimerization and decomposition in subcritical and supercritical water. Ind. Eng. Chem. Res. 1997, 36, 1552-1558.

[10] Lee, I. G.; Kim M. S.; Ihm S. K. Gasification of glucose in supercritical water. Ind. Eng. Chem. Res. 2002, 41, 1182-1188.

[11] Kruse, A.; Maniam, P.; Spieler, F. Influence of proteins on the hydrothermal gasification and liquefaction of biomass. 2. Model compounds. Ind. Eng. Chem. Res. 2007, 46, 87-96.

[12] Lee, I. G.; Kim M. S.; Ihm S. K. Catalytic gasification of glucose over Ni/activated charcoal in supercritical water. Ind. Eng. Chem. Res. 2009, 48, 1435-1442.

Hydrogen Production from Lignocellulosic Biomass by Two-Step Gasification Method

In-Gu Lee, Korea Institute of Energy Research, Korea

Abstract

Hydrogen can be produced from woody biomass by conventional gasification methods such as partial oxidation or steam gasification. Since these methods produce gas products with low content of hydrogen as well as high content of tar from gasification reactors, post-treatment processes including tar cracker and water-gas shift reaction process are usually necessary for obtaining clean hydrogen-rich gas from woody biomass. In this work, a two-step gasification method was experimentally studied as an alternative to the conventional methods. The first step of the gasification is the fast pyrolysis of biomass to obtain liquid-phase product (bio-oil) and the second step is to gasify the bio-oil to hydrogen-rich gas in supercritical water. The fast pyrolysis of woody biomass was carried out using a bench-scale fluidized-bed reactor. The gasification of bio-oil in supercritical water was performed using a continuous-flow reactor packed with catalyst. The effect of major reaction conditions such as temperature and catalyst on hydrogen yield will be discussed.

1 Introduction

In a conventional gasification, syngas is produced by partial oxidation of ligno-cellulosic biomass at high temperatures of about 800 ^{o}C. One of characteristics of the bio-syngas product is the low hydrogen content. It is required to employ hydrogen formation processes such as water-gas shift reaction system after the gasification reactor when the desired product is hydrogen. Two-step biomass gasification is an alternative technology to produce clean syngas rich in hydrogen, in which lingo-cellulosic biomass is first converted to liquid-phase bio-oil and then the bio-oil is subsequently gasified in water to clean combustible syngas. Two processes can be operated independently. Since bio-oil has much better storage and transportation characteristics than solid-phase biomass itself, it may be economical to convert biomass to bio-oil at the place where the biomass feedstock is collected, and then the bio-oil is transported to the syngas production facility.

In this work, woody biomass is first converted to bio-oil in a bubble fluidized-bed fast pyrolysis reactor at a bench-scale, and then the water-phase bio-oil is subsequently gasified in supercritical water to produce hydrogen-rich gas without contaminants such as tar or char. The SCWG technology is known to produce hydrogen-rich gas by complete gasification of aqueous organic wastes or wet biomass under appropriate reaction conditions. A wide range of whole biomass has been treated by the SCWG processes, including sewage sludge [1,2], agricultural wastes such as potato wastes [3], black liquor from pulp mill [4], and alcohol distillery wastewater [5]. More fundamental SCWG studies with model compounds as a reactant have also been carried out to understand the gasification chemistry [6-11].

2 Experimental Apparatus and Methods

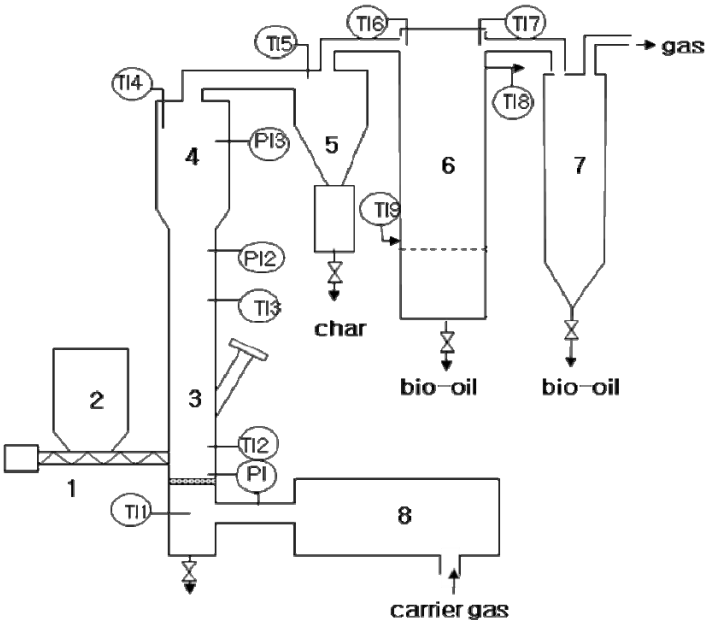

Figure 1: A schematic diagram of the fast pyrolysis reactor system for bio-oil production (1, screw feeder; 2, hopper; 3, reactor; 4, free-board; 5, cyclone; 6, condenser; 7, secondary separator; 8, carrier gas preheater).

The bio-oil production system consists of a sawdust feed hopper, a screw feeder, a bubbling fluidized-bed reactor, a cyclone, two heat exchangers, and a carrier gas preheater as shown in Figure 1. Sawdust from a saw mill was sieved to particle sizes less than 1.0 mm before used for the pyrolysis reaction. Sand with a particle size range of 0.4-0.8 mm was used as a fluidizing medium and nitrogen gas was used as a carrier gas. Pyrolysis reaction temperature was measured by a thermocouple (TI2 in Figure 1) employed inside the reactor. The capacity of the fast pyrolysis reactor was 4 kg/h of biomass on a design basis. Bio-oil product was obtained at the bottom of the quenching systems. The products were analyzed for their composition, heating value, and yield.

A schematic diagram of the apparatus used for bio-oil gasification is shown in Figure 2. The reactor was made of a Hastelloy C-276 tubing with 9.53 mm o.d., 6.22 mm i.d. and 293 mm total length. The reactor consisted of packed-bed of catalyst zone (5.6 cm^3) and reactant preheating zone (3.3 cm^3). The bio-oil feed was delivered into the reactor by a high pressure pump (Waters model 515). Reaction temperature was measured by a type K thermocouple installed inside the packed-bed of catalyst. A back-pressure regulator (Tescom model 26-1762-24) was used to reduce the pressure of product flow from 28 MPa to atmospheric pressure. The reactor effluent was disengaged into gas and liquid products in a gas-liquid separator. The flow rate of gas effluent was measured by a wet test meter (Sinagawa model W-NK-0.5A). Liquid product was collected at the bottom of the separator to measure its flow rate. For the catalytic experiments, purified sand was first packed in the cold zone of the downstream of the reactor and then catalyst was consecutively packed in the heating section (about 5.6 cm^3) of the reactor.

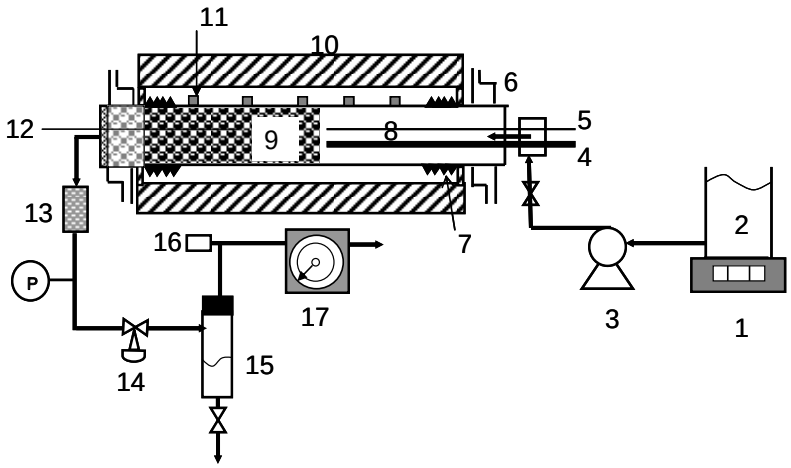

Figure 2: A schematic diagram of the SCWG system for the gasification of bio-oil (1, digital balance; 2, feed reservoir; 3, high pressure pump; 4, rod heater; 5, annulus thermocouple; 6, heat exchanger; 7, coiled heater; 8, preheating zone of the reactor; 9, packed-bed of the reactor; 10, furnace; 11, thermocouple mounted on the reactor wall; 12, thermocouple inside the reactor; 13, filter; 14, back-pressure regulator; 15, gas-liquid separator; 16, gas sample outlet; 17, gas flow meter).

The bio-oil obtained by the fast pyrolysis of sawdust consisted of two-phase; water-phase and tarry phase. The water-phase fraction of the bio-oil was separated and diluted with purified water to prepare for the feed solution for SCWG experiments. Activated charcoal (Sigma C3014) in 0.42-0.83 mm size was used as a catalyst or a support for nickel catalyst. The activated charcoal contains about 6 wt% ash and has a BET surface area of 920 m^2/g. A Ni-Y/AC catalyst was formulated by an incipient wetness method. The weight ratio between Ni and Y per 1g AC support was 0.25:0.0 for the Ni/AC and 0.25:0.10 for the Ni-Y/AC. Nickel(Ⅱ) nitrate hexahydrate (Aldrich No. 203874) and yttrium(Ⅲ) nitrate tetrahydrate (Aldrich No. 217239) were used as precursors. The catalyst was calcined in a nitrogen flow at 500 ^oC for 3 h, and reduced at 400 ^oC for more than 10 h under the flow of hydrogen gas.

3 Results and Discussion

Figure 3 (a) shows that the yield of total bio-oil slightly increased with pyrolysis temperature but the COD, as an indicator of organic content, decreased with pyrolysis temperature, which was more significant in water-phase fraction of the bio-oil product. The syngas product from the pyrolysis was about 20 wt% of the sawdust feed and its heating value was between 1,000-1,200 kcal/Nm^3. The seemingly low heating value of the syngas was due to the presence of high amounts of nitrogen gas which was used as a carrier gas. The hydrogen content of the syngas product was less than 8 vol% while the carbon monoxide content was over 12 vol%. A mass and energy balance analysis around the fast pyrolysis system indicated that the energy required by the pyrolysis reaction can be provided by the heat of combustion of the syngas product.

The water-phase fraction of the bio-oil product was separated and diluted to have COD values of about 100,000 mgO_2/L for the SCWG experiments. Table 1 displays the effect of

temperature and catalyst on the gasification results. The COD destruction of the bio-oil feed was less than 80 wt% without catalyst at the high temperature of 720 °C, but increased to 99 wt% when the AC catalsyt was employed. The hydrogen content of the gaseous product was not changed in the presence of the AC catalyst. These results indicate that the AC catalyst catalyzes gasification of organic compounds in bio-oil, but does not influence hydrogen formation mechanisms such as water-gas shift reaction. When the SCWG temperature reduced from 720 to 660 °C, the hydrogen content significantly drop from 33 to 17 vol% in the presence of the AC catalyst. However, the hydrogen content was relatively high and did not reduce much with decreasing temperature in the presence of the Ni-Y/AC. It can be said that the Ni-Y/AC activates hydrogen production reactions in the SCWG of bio-oil.

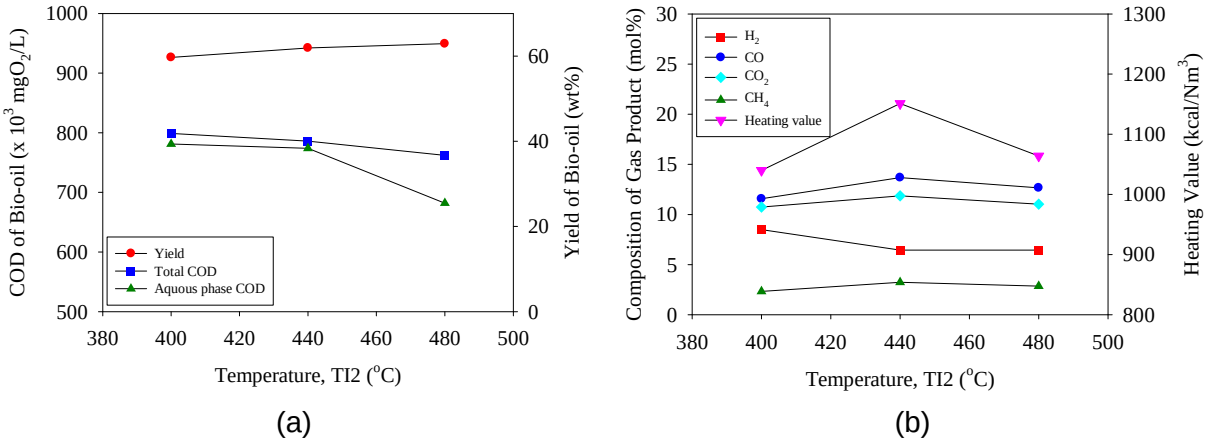

Figure 3: Effect of pyrolysis temperature on the product characteristics in the fast pyrolysis of sawdust.

Table 1: SCWG results of the water-phase bio-oil at 28 MPa and 12^{-1} LHSV.

Reaction conditions					
Catalyst	no	AC	AC	Ni-Y/AC	Ni-Y/AC
Temperature (°C)	720	720	660	720	660
Feed solution					
COD (mgO_2/L)	90,000	80,000	102,400	86,400	102,400
pH	2.2	2.4	2.0	2.5	2.1
Gaseous product					
HHV (kcal/Nm^3)	3,434	3,767	3,724	3,454	3,424
Composition (vol%)					
H_2	32.1	32.7	17.2	38.0	36.4
CO	12.2	3.3	7.3	1.9	1.1
CO_2	36.8	38.5	46.2	39.8	41.7
CH_4	15.2	22.0	21.7	16.6	17.4
Liquid effluent					
COD destruction (%)	79.1	99.2	92.0	97.8	96.9
pH	2.3	7.3	3.5	6.9	7.2

Acknowledgements

This work was supported by Ministry of Knowledge Economy through KETEP, Republic of Korea.

References

[1] Xu, X.; Matsumura, Y.; Stenberg, J.; Antal, M. J. Jr. Carbon-catalyzed gasification of organic feedstocks in supercritical water. Ind. Eng. Chem. Res. 1996, 35, 2522-2530.

[2)] Schmieder, H.; Abeln, J.; Boukis, N.; Dinjus, E.; Kruse, A.; Kluth, M.; Petrich, G.; Sadri, E.; Schacht, M. Hydrothermal gasification of biomass and organic wastes. Journal of Supercritical Fluids 2000, 17, 145-153.

[3] Antal, M. J. Jr.; Allen, S. G.; Schulman, D.; Xu, X. Biomass gasification in supercritical water. Ind. Eng. Chem. Res. 2000, 39, 4040-4053.

[4] Sricharoenchaikul, V. Assessment of black liquor gasification in supercritical water. Bioresource Technology 2009, 100, 638-643.

[5] García Jarana, M. B.; Sánchez-Oneto, J.; Portela, J. R.; Sanz, E. N.; Martínex de la Ossa, E. J. Supercritical water gasfication of industrial organic wastes. The Journal of Supercritical Fluids 2008, 46, 329-334.

[6] Amin, S.; Reid, R. C.; Modell, M. Reforming and decomposition of glucose in an aqueous phase. The Intersociety Conference on Environmental Systems, San Francisco, CA, 1975; The American Society of Mechanical Engineers (ASME); New York, 1975; ASME Paper No. 75-ENAs-21, 1.

[7] Holgate, H. R.; Meyer, J. C.; Tester, J. W. Glucose hydrolysis and oxidation in supercritical water, AIChE Journal 1995, 41, 637-648.

[8] Kabyemela, B. M.; Adschiri, T.; Malaluan R. M.; Arai, K. Kinetics of glucose epimerization and decomposition in subcritical and supercritical water. Ind. Eng. Chem. Res. 1997, 36, 1552-1558.

[9] Lee, I. G.; Kim M. S.; Ihm S. K. Gasification of glucose in supercritical water. Ind. Eng. Chem. Res. 2002, 41, 1182-1188.

[10] Kruse, A.; Maniam, P.; Spieler, F. Influence of proteins on the hydrothermal gasification and liquefaction of biomass. 2. Model compounds. Ind. Eng. Chem. Res. 2007, 46, 87-96.

[11] Lee, I. G.; Kim M. S.; Ihm S. K. Catalytic gasification of glucose over Ni/activated charcoal in supercritical water. Ind. Eng. Chem. Res. 2009, 48, 1435-1442.

Hydrogen Production by Steam Reforming of Bio-Oil Aqueous Fraction over Ni/CeO_2-ZrO_2 Catalyst

Chang-Feng Yan, Fei-Fei Cheng, Rong-Rong Hu, Guangzhou Institute of Energy Conversion, Chinese Academy of Sciences, Guangzhou, China

Abstract

Two kinds of Ni/CeO_2-ZrO_2 catalysts were prepared by impregnation method or by co-precipitation method. A laboratory scale fixed-bed reactor was employed to investigate the catalyst performance in hydrogen production by steam reforming bio-oil aqueous fraction. Effects of reaction temperature, and the different preparation methods of the catalyst on the hydrogen production performance of Ni/CeO_2-ZrO_2 catalysts were examined. The obtained results were compared with commercial nickel-based catalysts (Z417). Ni/CeO_2-ZrO_2 catalyst by co-precipitation method showed the best catalytic performances. At W/B=4.9, T=800 ºC, H_2 yield reaches the highest of 72.9 % and H_2 content of 70.0 % were obtained., these values were higher than Ni/CeO_2-ZrO_2 catalysts were prepared by impregnation method and commercial nickel-based catalysts (Z417).

1 Introduction

Hydrogen is an emerging new energy carrier with significantly environmental impact as its combustion is clean of pollutants. Most hydrogen now is generated from fossil fuels such as natural gas, naphtha, heavy oil and coal via catalytic reforming and partial oxidation processes [1]. Due to environmental pollution and the high dependence on fossil fuels, the world-wide interest in the energy area is focused on the production of hydrogen from alternative fuels. Biomass has been proposed as an alternative feedstock for hydrogen production not only because it is renewable but also because it is a CO_2 neutral energy supply [2]. Hydrogen can be generated from biomass mainly via two kinds of thermochemical processes, the gasification [3-4] or the flash pyrolysis [5-7] followed by steam reforming of the pyrolysis oil.

Recently, more attention has been paid to bio-oil aqueous fraction steam reforming and a few catalysts have been investigated, for example, UC G-90C [8-10], ICI 46-1[8,9], Ni-Al [11], Pt, Rh and Pt based catalyst [12] and so on. The aim of the present work is to investigate the catalyst Ni/CeO_2-ZrO_2 performance in hydrogen production by steam reforming bio-oil aqueous fraction and compare it with commercial nickel-based catalysts (Z417). Effects of reaction temperature and different preparation methods of the catalyst on the hydrogen yield and hydrogen selectivity is evaluated.

2 Experimental

2.1 Catalyst preparation

Two kinds of Ni/CeO_2-ZrO_2 catalysts were prepared impregnation method or co-precipitation method respectively. Firstly, The catalysts precursors were prepared by adding aqueous solution of $ZrOCl_2$ or aqueous mixture solution of metals, $ZrOCl_2$, $Ce(NO_3)_3$, which was depended on the catalyst component, to a vigorously stirred solution of NH_4OH at 50 °C. The resulted precipitate was filtered and washed with distilled water, then dried in air at 110 °C for 6 h. Finally, the support precursor was calcined in air at 600 °C for 6 h. Then, Ni/CeO_2-ZrO_2 catalysts were prepared by impregnating ZrO_2 (CeO_2-ZrO_2) powder with $Ni(NO_3)$ and $Ce(NO_3)_3$ ($Ni(NO_3)$),as Ni and Ce precursor, followed by drying at 110 °C for 12 h, calcinating at 800 °C for 6 h and natural cooling for testing.

2.2 Apparatus and steam reforming tests

The bio-oil aqueous fraction steam reforming experiments were carried out in a continuous flowing system using a fixed-bed reactor made of quartz under atmospheric pressure. The catalyst powder was placed in the middle of the quartz tube, which was heated by the furnace equipped with temperature controller. The calcined catalyst was reduced in situ in 5 % H_2/N_2 stream at 700 °C for 4 h prior to use. Bio-oil aqueous fraction was fed into the reactor at a constant rate by a peristaltic pump. The product gas exiting from the reactor was cooled and dried before entering gas chromatograph (GC522) for analysis. At the end of the catalytic tests, the catalyst was cooled under N_2 stream.

The bio-oil aqueous fraction steam reforming performance over a given catalyst was studied by measuring hydrogen yield efficiency and the content of product gas. Hydrogen yield efficiency was denoted as Y_{H_2}, the content of product gas (hydrogen, carbon dioxide, methane, carbon monoxide) was denoted as Vol%product. Since nitrogen was introduced as carrier gas, measured value of gas component was normalized. Hydrogen content was defined in terms of the moles of hydrogen in per mole of product gas:

$$V\%_{H_2} = \frac{H_2}{H_2 + CH_4 + CO + CO_2} \times 100\% \quad (4)$$

The calculated method of the content of other product gas was similar to that of H_2.

According to the reaction (3), the stoichiometric H_2 is calculated. Then hydrogen yield efficiency (Y_{H_2}) is calculated as follow:

$$Y_{H_2} = \frac{H_2 \text{ yield}}{\text{stoichiometric } H_2} \times 100\% \quad (5)$$

3 Results and discussion

3.1 Effects of reaction temperature

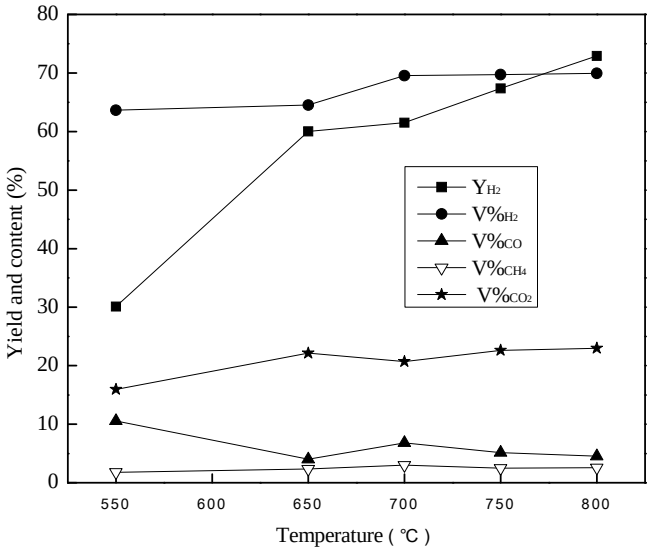

Figure1: Effects of reaction temperature on the hydrogen yield and the content of the product gas (Catalyst: Ni/CeO_2-ZrO_2 (12 wt% Ni, 7.5 wt% Ce) by co-precipitation method; W/B=7.7).

Fig. 1 presented the effects of reaction temperature on the reforming reaction under the reaction temperature ranging from 550 °C to 800 °C. It could be found that reaction temperature had significant effects on hydrogen yield and content of the product gas. The hydrogen yield increased obviously with the reaction temperature increasing. At 550 °C, the hydrogen yield was just 30.1 %, but it reached the highest of 72.9 % with the reaction temperature increase to 800 °C. In the shown reaction temperature range, CO content and CO_2 content presented on the contrary current, and CO content reached the maximum value of 10.6 %, but CO_2 content arrived at the minimum value of 16.0 % at 550 °C respectively. This may be attributed to the fact that the reverse water gas shift (RWGS) reaction occurred. Aupretre et al. [13] pointed out that CO was generated from RWGS reaction in the steam reforming ethanol as well. H2 content increased obviously as the reaction temperature increase, and reached the maximum value of 69.9 % at 800 °C. CH_4 content first increased and then decreased. At 700 °C, a maximum CH_4 content of 3.0 % was obtained, the cause of which might be that the side reaction of methanation of CO_2 took place in the steam reforming process at this condition. Vannice [14] pointed out that Ni showed high activity in the methanation of CO_2.

3.2 Comparison of two kinds of catalysts and commercial catalysts

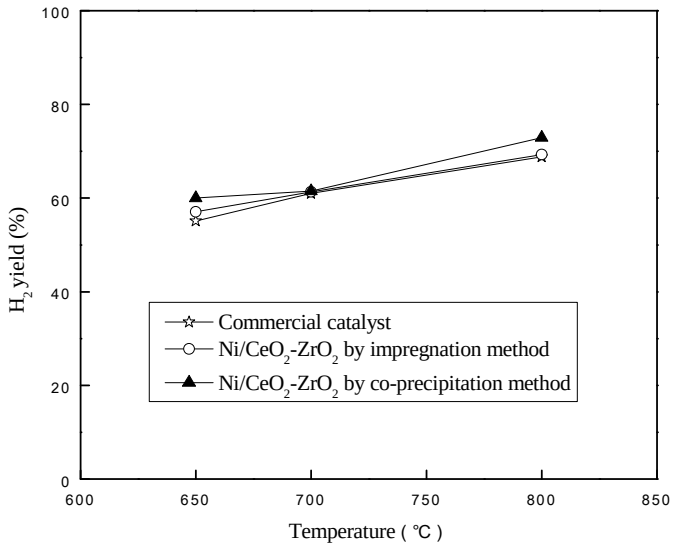

Figure 2: Comparison of H_2 yield between two kinds of self-prepared catalyst and commercial catalyst (Catalysts: Ni/CeO_2-ZrO_2 (12 wt% Ni, 7.5 wt% Ce); W/B=7.7).

Fig. 2 presented the hydrogen yield as a function of the reaction temperature for two kinds of self-prepared Ni/CeO_2-ZrO_2 catalyst and commercial nickel-based catalysts (Z417). As the reaction temperature increased from 650 °C to 800 °C, the hydrogen yields of three kinds of catalysts increased. In the given reaction temperature range, the hydrogen yields of self-prepared catalysts were higher than that of commercial catalysts, which indicated that self-prepared catalysts had better catalytic activities. Table 1 showed that the effects of three kinds of different catalysts on content of the product gas at the same conditions (T=650 °C, W/B=7.7). The H_2 and CO_2 contents got via catalyst by co-precipitation method was higher than the other catalysts, on contrast, the content of CO and CH_4 were lower. Hence, from hydrogen yield and content point of view, Ni/CeO_2-ZrO_2 catalyst by co-precipitation method had better catalytic performance than Ni/CeO_2-ZrO_2 catalyst by impregnation method and commercial nickel-based catalysts (Z417).

Table 1: Comparison of the content of the product gas between self-made catalyst and commercial catalyst.

Catalysts	$V\%_{H_2}$	$V\%_{CO}$	$V\%_{CH_4}$	$V\%_{CO_2}$
Commercial catalyst Z417	64.0	5.3	2.0	21.7
Ni/CeO_2-ZrO_2 by impregnation method	63.3	9.1	2.3	18.3
Ni/CeO_2-ZrO_2 by co-precipitation method	64.5	4.0	2.3	22.1

Catalysts: Ni/CeO_2-ZrO_2 (12 wt% Ni, 7.5 wt% Ce); W/B=4.9; T=650 °C

4 Conclusions

Based on the present results, we could find that Ni/CeO_2-ZrO_2 catalysts by co-precipitation method had higher catalytic activity for hydrogen production from the steam reforming of the bio-oil aqueous fraction. Reaction temperature had significant effects on hydrogen yield and content of the product gas. At T=800 °C and W/B=7.7, the hydrogen yield and content of the Ni/CeO_2-ZrO_2 catalyst by co-precipitation method reached the maximum value of 72.9 % and 70.0 % respectively in the range of experimental temperature, which were higher than those of Ni/CeO_2-ZrO_2 catalyst by impregnation method and commercial nickel-based catalysts (Z417). Thus, it was a promising catalyst for hydrogen production from bio-oil aqueous fraction steam reforming.

References

[1] M.A. Pefia, J.P. Gomez, J.L.G. Fierro, Appl. Catal. A: Gen. 144 (1996) 7-57.

[2] E.Ch. Vagia, A.A. Lemonidou, Appl. Catal. A: Gen. 351 (2008) 111-121.

[3] J. Schoeters, K. Maniatis, A. Buekens, Biomass 19 (1989) 129-143.

[4] D. Sutton, B. Kelleher, J.R.H. Ross, Fuel Proces. Technol. 73 (2001) 155-173.

[5] A.A. Lappas, M.C. Samolada, D.K. Latridis, S.S. Voutetakis, I.A. Vasalos, Fuel 81 (2002) 2087-2095.

[6] D. Mohan, C.U. Pittman Jr., P.H. Steele, Energy Fuels 20 (2006) 848-889.

[7] Z. Qi, C. Jie, W. Tiejun, X. Ying, Energy Cov. Manage. 48 (2007) 87-92.

[8] D. Wang, S. Czernik, D. Montane, M. Mann, E. Chornet, Ind. Eng. Chem. Res. 36 (1997)1507.

[9] M. Marquevich, S. Czernik, E. Chornet, D. Montane, Energy Fuels 13 (1999) 1160.

[10] D. Wang, D. Montane, E. Chornet, Appl. Catal. A: Gen. 143 (1996) 245.

[11] J. R. Galdamez, L. Garcia, R. Bilbao, Energy Fuels 19 (2005) 1133.

[12] C. Rioche, S. Kulkarni, F. C. Meunier, J. P. Breen, R. Burch, Appl. Catal. E: Environ. 61 (2005) 130.

[13] F. Aupretre, C. Descorme, D. Duprez, Catal. Commun. 3 (2002)263-267.

[14] M.A. Vannice, J. Catal. 50 (1977) 288-295.

State of the Art of Ceramic Membranes for Hydrogen Separation

Wilhelm-A. Meulenberg, Mariya E. Ivanova, Tim van Gestel, Martin Bram, Hans-Peter Buchkremer, Detlev Stöver, and José M. Serra

Abstract

Membrane technology can be integrated into many advanced system concepts for the production of liquid energy carriers and chemicals, for microfiltration, oxygen generation, low CO_2 emission power generation, hydrogen technology, and carbon dioxide capture. The separation of hydrogen by inorganic membranes for energy applications is a growing field with respect to the low efficiency losses of membrane-based processes. Inorganic hydrogen separation membranes find application in the separation of hydrogen from syngas in a fossil power plant and as an electrolyte in intermediate-temperature proton-conducting fuel cells or electrolyzers for hydrogen production. The separation can be performed by different membrane concepts. This chapter discusses the state of the art of (1) microporous ceramic membranes (amorphous and zeolitic) and (2) mixed proton-electron conducting ceramic membranes, focusing on their properties and current manufacturing and development status. The properties of each membrane type are discussed with respect to the foreseen range of applications. Finally, an outlook is given for R&D activities required in the next few years.

Development of a Compact Steam Reformer Using a Palladium Membrane for the Production of Hydrogen

R. Dittmeyer, **J. Thormann**, Institute for Micro Process Engineering, Karlsruhe Institute of Technology, Hermann-von-Helmholtz-Platz 1, 76344 Eggenstein-Leopoldshafen, Germany
M. Rüttinger, Plansee SE, Metallwerk Planseestrasse 71, A-6600 Reutte, Austria
B. Dittmar, **A. Behrens**, Linde AG, Engineering Division, Dr.-Carl-von-Linde-Strasse 6-14, D-82049 Pullach, Germany

1 Motivation

The Linde Group is a world leading gases and engineering company with almost 48,000 employees working in around 100 countries worldwide. Linde provides customers worldwide with all kinds of gases by cylinder, trailer, truck or even with dedicated production plants at the customers' site. The number of applications for hydrogen is rising mainly within users of small capacities (< 500 Nm^3/h H_2) compared to industrial consumption. Supply with hydrogen for this capacity involves delivery by truck. The shift of the supply to an onsite production is favoured for some cases due to economical, ecological and safety reasons. Scale-down of existing production technologies is economically not preferred. One reason is the high share of invest costs for the control and instrumentation of the pressure swing unit, which is costly even for smaller units.

Therefore a new development applying palladium membrane technology in a H_2 reformer unit (membrane reformer) was initiated for small scale applications, e.g. heat applications, glassware manufacture and hydrogen fuel stations for mobile applications. A compact design with fewer subunits compared to conventional reformers and improved economic characteristics can be achieved with the new technology. By applying a palladium membrane for the production of H_2, the equilibrium of the involved reactions can be shifted towards the product which will improve the efficiency of the process.

$$CH_4 + 3\,H_2O \leftrightarrow CO + 3\,H_2 \qquad \text{(Eq. 1)}$$

$$CO + H_2O \leftrightarrow CO_2 + H_2 \qquad \text{(Eq. 2)}$$

Membrane reformers have attracted a lot of interest over the last years, mostly in connection with fuel cell systems. But the concept of removing hydrogen from a reactor through an integrated membrane dates back to Gryaznov as early as 1969 [1]. Recently, research in the field of methane steam reformer including palladium (alloy) membranes was performed by several academic groups worldwide (reviews are given e.g. by Lukyanov et al. [2] or Dittmeyer and Caro [3]). The most advanced industrial application of a membrane reformer

for natural gas steam reforming was published by Mitsubishi Heavy Industries together with Tokyo Gas [4]. Their work is based on studies of Kikuchi, Uemiya and co-workers, see e.g. [5, 6]. The membrane reforming system integrates flat rectangular membrane elements and has a hydrogen production capacity of 40m_N^3/h, succeeded to produce 99.999% pure H_2 with an efficiency of 81.4% [7].

There are three options to apply the palladium membrane: thick self-supporting palladium or thin layers of palladium on a metal or a ceramic support. Preferred geometries for the membranes are tubular or plate shaped systems.

2 Project Scope & Partner

Following the demand for a small scale hydrogen production plant by the gas producing division Linde Gas, the R&D department of Linde Engineering division was commissioned to start an evaluation to identify existing technologies, their commercial and technical status as well as their availability. No technology was identified to match with Linde technologies.

A customized concept was developed to fit best with the Linde steam reformer technology. So the idea of combining a tubular membrane technology on a metal support with a conventional reformer from the Linde portfolio seemed promising.

The project has been set up and a cooperation team has been formed which covers industrial partners for the production and user side as well as an academic partner. In this joint development Linde, Plansee and KIT have set up an interdisciplinary team. Several work packages have been defined and assigned to the project partners (see Figure 1). Plansee as a world leading company in the fabrication of powder metallurgical components for high performance applications is responsible for the development and production of the membrane tubes, Linde as the producer of hydrogen and the group of Prof Dittmeyer at the Institute of Micro Process Engineering with long-time experience in heterogeneous gas-phase reactions in microstructured reactors as well as preparation and use of palladium composite membranes.

We are targeting an innovative small scale steam reformer for the production of hydrogen by using a palladium membrane for the separation of pure hydrogen.

The project aims at the demonstration of the new technology in a laboratory commercial scale pilot plant.

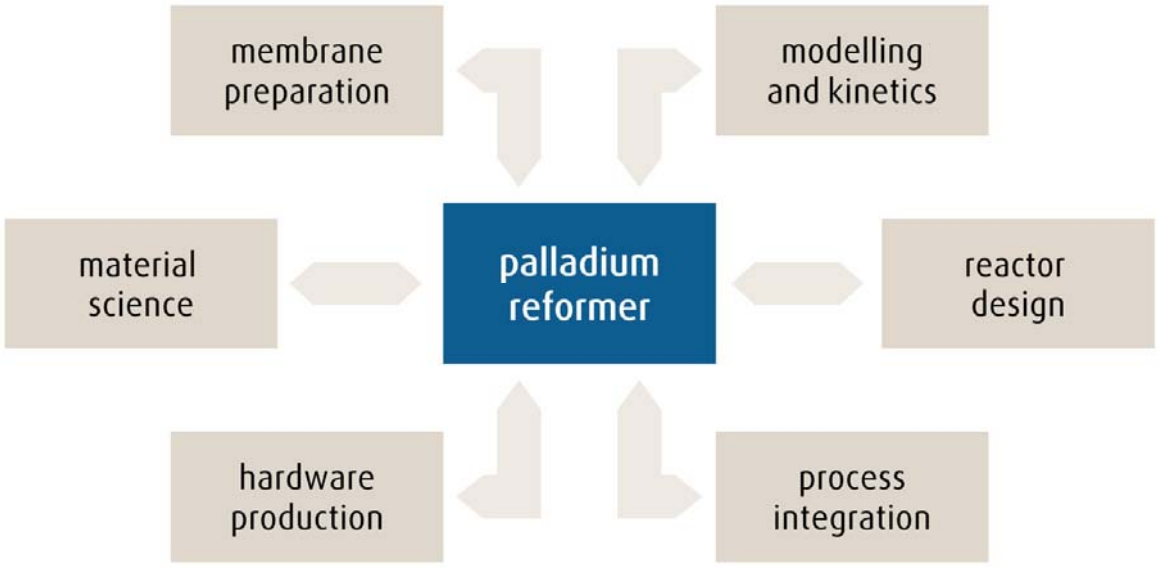

Figure 1: Interdisciplinary project cooperation.

Basis for the development of a membrane reformer is a stable and reliable membrane, so a metal supported membrane is the first choice. Therefore a diffusion barrier becomes necessary and helps to adjust the porosity of the layers. This diffusion barrier has to be adapted to the support and to the Pd membrane layer. A number of test samples are produced and these membranes are then evaluated in a new designed lab test rig, providing data about the performance of the membrane tubes, which can be used for the simulation. The next steps are the design and engineering of the reformer and adjustment of the additional units.

3 Development of Support Tubes and Diffusion Barrier

In order to maximize the hydrogen flux a thin-film composite membrane design is beneficial requiring a structural support. Metallic and ceramic substrates would be both applicable. However, metallic substrates offer a number of advantages, such as high strength, easy joining and similar thermal expansion coefficient to the selected Pd-membrane.

Plansee developed a ferritic alloy called ITM for new types of solid oxide fuel cells. As a result of fundamental development the oxide dispersion strengthened (ODS) alloy Fe26Cr (Mo, Ti, Y_2O_3) turned out to be most suitable for this application. New powder metallurgical (P/M) techniques for the fabrication of porous sheets and tubes of ITM were established. These substrates with high quality surfaces are used for fuel cells and high temperature membranes.

The metallic diffusion between the FeCr-matrix of the metallic substrate and the Pd-membrane must be prevented by a porous ceramic diffusion barrier layer (DBL), which is located directly at the substrate/membrane interface. Based on several years of experience in developing diffusion barrier layers for metal supported fuel cells Plansee adapted this

technology and was able to demonstrate the functionality. It shows a high open porosity which improves the gas diffusion towards the separating membrane.

4 Optimisation of the Pd-coating and Characterisation

The support tube of sintered ITM with the ceramic diffusion barrier layer on top is coated with a palladium layer by Electroless Plating (ELP) (see Figure 2). The Electroless Plating procedure is based on the reduction of a meta-stable palladium salt complex on a substrate surface activated by palladium seeds. The growing Pd grains form a film and the microstructure of this film has an important effect on the permeation properties. The Pd grain growth is determined by the ELP conditions, including the rate, duration, temperature, and supply of reactants. The basic procedure has been described already by Shu et al. in 1991 [8]. However, many researchers worldwide are still working on improvements of this technology as witnessed by approximately 5 research papers per year in the last decade. The optimisation of Pd-coating aims for the minimization of the palladium thickness while maintaining dense pore-free membrane characteristics. The minimization of the Pd membrane thickness reduces the costs for the precious metal palladium and enhances the hydrogen flow through the Pd membrane. But very thin Pd layers show an enhanced tendency for defects through which all gases can diffuse and consequently lead to impurities in the produced hydrogen flow. Thus, the Pd membrane is characterized by its hydrogen permeability and its selectivity (to separate hydrogen from other gases) as well as its long term stability.

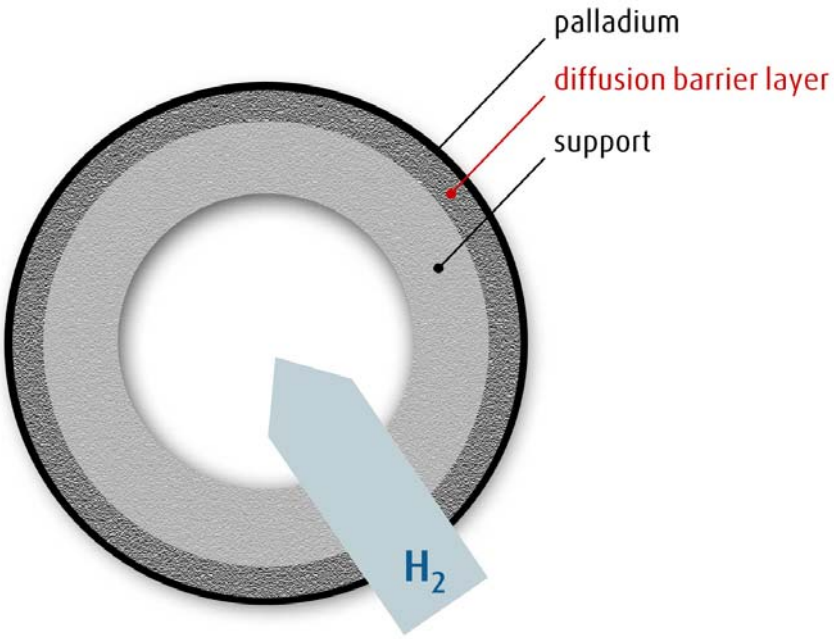

Figure 2: Cross-section of the membrane tube.

For achieving high hydrogen fluxes, high hydrogen selectivity and high long term stability the complete system of support material, diffusion layer and palladium membrane has to be optimized (see Figure 3). A large porosity of the metallic support and the ceramic diffusion

layer is needed for high hydrogen flows. The ceramic layer should provide a multitude of small pores by avoiding large pores and obtain a smooth surface with modest roughness for enabling the growth of a thin and well adhering Pd layer. The palladium coating procedure is optimized by adapting the ELP conditions to enable homogeneous Pd coating of the total DBL surface without any defects or impurities.

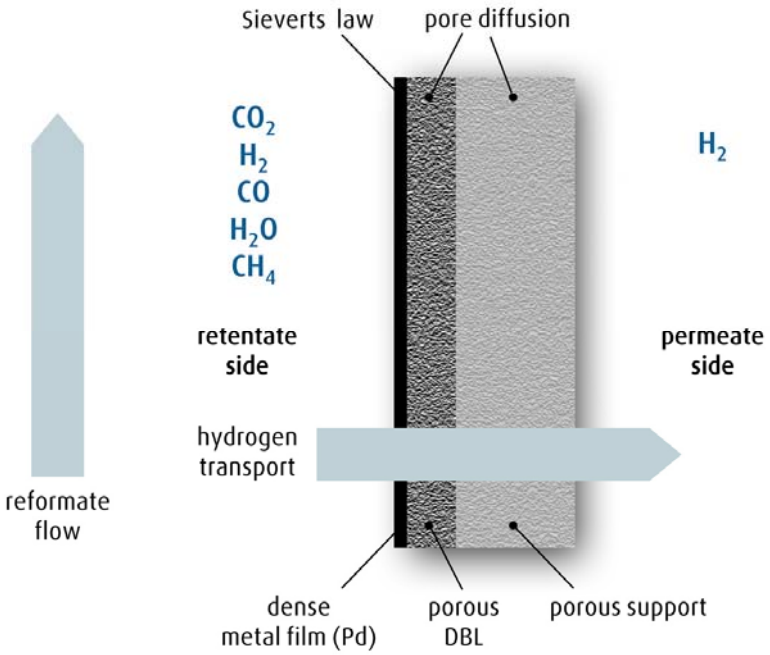

Figure 3: Membrane system consisting of metal support tube, ceramic diffusion barrier layer and dense palladium coating.

Palladium membranes show the feature of selective hydrogen transport. By placing the membrane directly into the steam reformer reactor, it is possible to withdraw pure hydrogen where it is generated. By doing so, shifting of the equilibrium of reforming and shift reactions towards the products is achieved, which improves the overall efficiency. By removing hydrogen through the membrane, the pure hydrogen product is obtained directly from the reformer tubes without further purification steps, e.g. pressure swing adsorption and CO-shift-converter which are necessary in the conventional reformer design (see Figure 4).

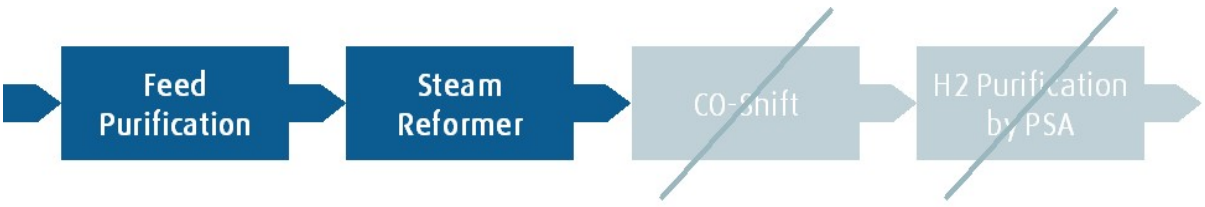

Figure 4: Units necessary for membrane reformer technology.

References

[1] Gryaznov, V.M.: Dokl. Akad. Nauk SSSR., 189, No. 4, (1969),pp 794-796

[2] Lukyanov, B.N.; Andreev, D.V.; Parmon, V.N.: Catalytic reactors with hydrogen membrane separation; Chem. Eng. J., 154 (2009), pp 258-266

[3] Dittmeyer, R.; Caro, J.: Catalytic Membrane Reactors in Handbook of Heterogeneous Catalysis, Edts. Ertl, G.; Knözinger, H.; Schüth, F.; Weitkamp, J.; , 2nd edition, 2008, Wiley-VCH Verlag, Weinheim, pp 2198-2248

[4] Yasuda, I.; Shirasaki, Y.: Development and Demonstration of Membrane Reformer System for Highly-efficient Hydrogen Production from Natural Gas; Materials Science Forum, Vols. 539-543 (2007,) pp 1403-1408

[5] Uemiya, S.; Sato, N.; Ando, T.; Matsuda, T.; Kikuchi, E.; Steam reforming of methane in a hydrogen-permeable membrane reactor , Journal of Applied Catalysis 67 (1990), pp 223-230

[6] Kikuchi, E.; Nemoto, Y.; Kajiwara, M. Uemiya, S.; Kojima, T.; Steam reforming of methane in membrane reactors: comparison of electroless-plating and CVD membranes and catalyst packing modes; Catalysis Today, 56 (2000), pp 75-81

[7] Green Car Congress: Tokyo Gas, Mitsubishi Heavy Improve Hydrogen Separation Membrane Reformer, 4 May 2008, http://www.greencarcongress.com/2008/05/tokyo-gas-mitsu.html

[8] Shu, J.; Greandjean, B.P.A.; Van Neste, A.; Kaliaguine S.: Catalytic palladium-based membrane reactors: A review Canadian Journal of Chemical Engineering, 69 (1991), pp 1036-1060

Demonstration of Highly-Efficient Distributed Hydrogen Production from Natural Gas with CO_2 Capture

Hideto Kurokawa, **Yoshinori Shirasaki**, **Isamu Yasuda**, Tokyo Gas Co., Ltd., Japan

1 Introduction

To reduce carbon dioxide (CO_2) emission in wide range of fields and industries, various efforts have been accelerated including research and development on hydrogen and fuel cell technologies. Hydrogen is expected to play a significant role as an energy carrier to mitigate CO_2 emission in the coming decades. Though hydrogen has no environmental impacts at the point of use, most of hydrogen is produced today from fossil fuel sources and used mainly in industries [1,2]. Further utilization of hydrogen requires key technology breakthroughs and device cost reduction in all domains over the hydrogen energy chain including fuel supply infrastructure. On-site hydrogen production from natural gas using the existing pipeline networks is one of the most promising pathways to produce and supply hydrogen to fuel cells and vehicles. Since hydrogen production from natural gas is a practical and reasonable way for early introduction of hydrogen energy into society, further CO_2 reduction must be considered in the future because carbon dioxide is released during hydrogen production. Carbon capture technologies are important at upstream of CCS (Carbon Capture and Sequestration) chain and lowering the energy penalty and capture cost is a key issue for practical application. Hydrogen separation membrane technology can be a solution to the issue and provide an efficient carbon capture in hydrogen production from natural gas.

A membrane reformer for hydrogen production is more compact and more highly-efficient than the conventional SMR (Steam Methane Reforming) with PSA (Pressure Swing Adsorption) system because steam reforming reaction of natural gas and hydrogen separation process proceed in a single reactor simultaneously without a separate shift converter and a purification system. A schematic diagram and principle of the membrane reformer is shown in Figure 1. In the membrane reformer, natural gas is reformed in the catalyst bed and only hydrogen can be separated from a reformed gas mixture by a hydrogen separation membrane. The reforming process with simultaneous hydrogen separation can be free from the limitation of chemical equilibrium [3] and provide higher energy efficiency than the conventional SMR technologies. Due to these advantages, the membrane reformer is expected to be applied to on-site hydrogen production including hydrogen refuelling stations for fuel cell vehicles. The membrane reformer offers another significant advantage of high CO_2 concentration of 70~90% in the reactor off-gas. Even under the rated operating condition where the CO_2 concentration of the reactor off-gas is the lowest, the CO_2 concentration is significantly higher than that of fossil fuel combustion systems, i.e., natural gas fired boiler: 7~10%, gas turbines: 3~4%, and coal fired boilers: 12~14% [4]. Due to the high CO_2 concentration of the off-gas, CO_2 purification is not required and CO_2 can be captured easily by only compression and liquefaction and the cost for carbon capture can be reduced significantly compared with the conventional reforming

systems. The membrane reformer is a very promising technology not only to achieve the highest efficiency in hydrogen production from natural gas but also to capture CO_2 efficiently. In the present study, we have demonstrated highly-efficient distributed hydrogen production with CO_2 capture using an advanced membrane reformer system.

2 Performance of 40 Nm^3/h-class Membrane Reformer System

Tokyo Gas has been working on an advanced membrane reformer system development for highly-efficient hydrogen production from natural gas for more than 15 years. We have successfully developed and operated a 40 Nm^3/h-class membrane reformer system (1st MRF) and demonstrated its high efficiency of 76.2% (HHV) and the product hydrogen was supplied to fuel cell vehicles in 2004 [5]. Hydrogen production efficiency from natural gas was defined by the following equation:

$$\text{Efficiency}(\%) = \frac{F_{H2} \times Q_{H2}}{F_{NG} \times Q_{NG} + W(\text{AUX})}$$

where F_{H2} is the flow rate of product hydrogen, F_{NG} is the flow rate of natural gas, Q_{H2} is the gross heating value of hydrogen, Q_{NG} is the gross heating value of natural gas, and W(AUX) is auxiliary power consumption. Electricity for hydrogen suction/compression unit was not included in the efficiency defined above. The development of the 1st MRF system also revealed that its compactness reduced the total volume of the system to 1/3 of the conventional reforming system based on SMR-PSA.

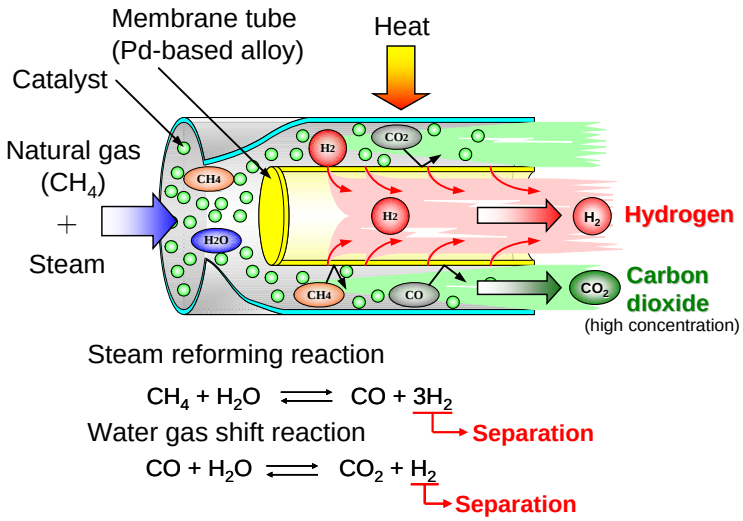

Figure 1: Principle of membrane.

We have achieved a significant milestone of over 80% efficiency with the improved version of the 40 Nm^3/h-class membrane reformer system (2nd MRF) in 2008. When the natural gas feed rate was 11.2 Nm^3/h, the hydrogen production rate was 40.5 Nm^3/h, and the improved system achieved a remarkable gain in hydrogen production efficiency up to 81.4% (HHV), which is about 5% higher than the previous system. The improved membrane reformer

system has achieved the world-highest efficiency in hydrogen production from natural gas and has been proved to give the highest efficiency among various competing technologies. These demonstrations proved that the hydrogen production efficiency of the membrane reformer system is about 10~15% higher than the conventional steam reforming technologies with PSA. Fig. 2 shows the off-gas composition of the membrane reformer systems. The concentration of CO_2 in the off gas increased significantly due to enhanced reaction by simultaneous hydrogen separation. When the natural gas feed rate was 3.2 Nm^3/h, the CO_2 concentration in the 1st MRF off-gas was as high as 90%. In the case of the 2nd MRF, the CO_2 concentration was 72% at minimum at the designed hydrogen production capacity of 40 Nm^3/h (natural gas feed rate = 11.2 Nm^3/h).

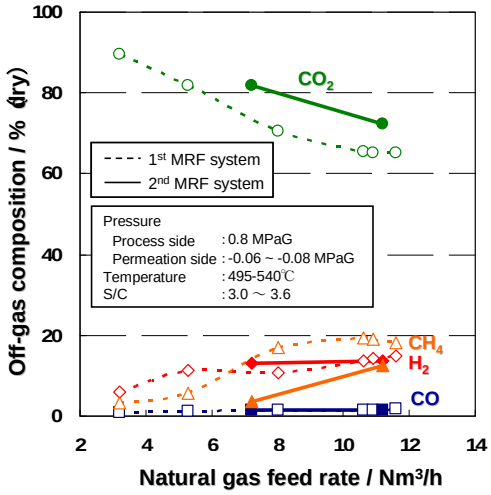

Figure 2: Natural gas feed rate dependence of off-gas composition.

3 Demonstration of Distributed Hydrogen Production with CO_2 Capture

The potential of the membrane reformer system to capture CO_2 was evaluated by calculation prior to the demonstration of distributed hydrogen production with CO_2 capture. CO_2 emission from each part and possible CO_2 reduction rate of the membrane reformer system were calculated by assuming that 100% CO_2 in the reactor off-gas can be captured by liquefaction process. The material balance of the 40 Nm^3/h-class membrane reformer system was calculated based on the actual operation data of the membrane reformer system. The CO_2 capture system is assumed to be composed of a water removal equipment, a compressor, a chiller and a gas-liquid separation unit. The off-gas from the membrane reformer system was assumed to be compressed up to 7.0 MPaG at over 29ºC, then cooled down to room temperature to liquefy and separate CO_2 in the gas-liquid separation unit. CO_2 emission from the electric power consumption was calculated from the average emission factor of the Tokyo area in 2008 (0.332 kg/kWh) [6]. The required electricity for the CO_2 capture system was also estimated with the theoretical power consumption of the compressor. The calculated CO_2 emission and possible reduction rate at the designed

capacity of the membrane reformer are shown in Figure 3. The amount of CO_2 emission from the reactor in the reformer system, which can be captured by liquefaction, was 56% at the designed capacity of 40 Nm^3/h. The estimation revealed that CO_2 emission in hydrogen production can be reduced significantly by capturing CO_2 from the off-gas.

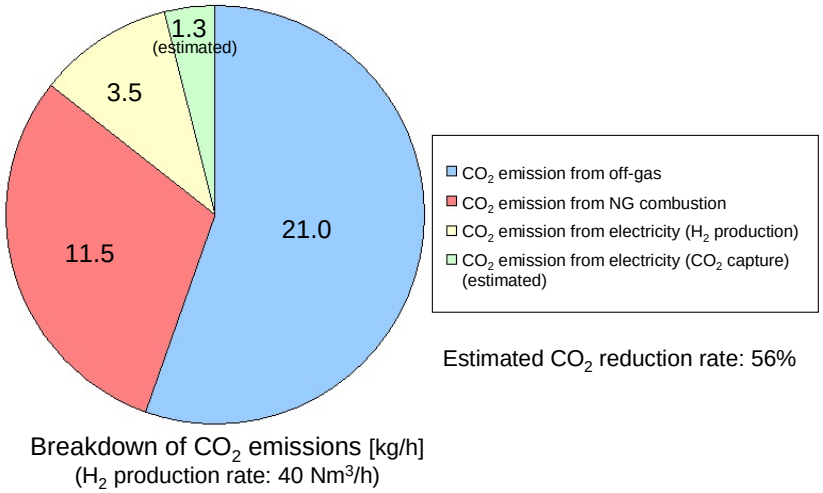

Figure 3: Estimated CO_2 emission and CO_2 reduction rate of the 40 Nm^3/h-class membrane reformer.

To confirm the CO_2 reduction potential of the membrane reformer system, a test equipment for CO_2 capture was developed for a demonstration test and attached to the 40 Nm^3/h-class membrane reformer system. Figure 4 shows the improved 40 Nm^3/h-class membrane reformer system and CO_2 liquefaction test equipment. Hydrogen production operation was carried out and part of the reactor off-gas was introduced into the test equipment to separate and capture CO_2. The obtained and calculated data from the demonstration at 75% of the designed capacity (hydrogen production rate = 30.6 Nm^3/h) are shown in Table 1. When the system was operated with CO_2 capture at 75% of the designed capacity, over 90% of CO_2 in the reactor off-gas was captured and CO_2 emission decreased from 25.1 to 12.6 kg/h, while electricity consumption was increased from 6.6 to 13.6 MJ/kg-H_2 by applying CO_2 capture. The total CO_2 emission of hydrogen production was decreased by 50% with only 3% energy loss. The total energy efficiency of hydrogen production was still as high as 78.6% (HHV) even with CO_2 capture, which is 5~10% higher than the conventional SMR + PSA technologies without CO_2 capture.

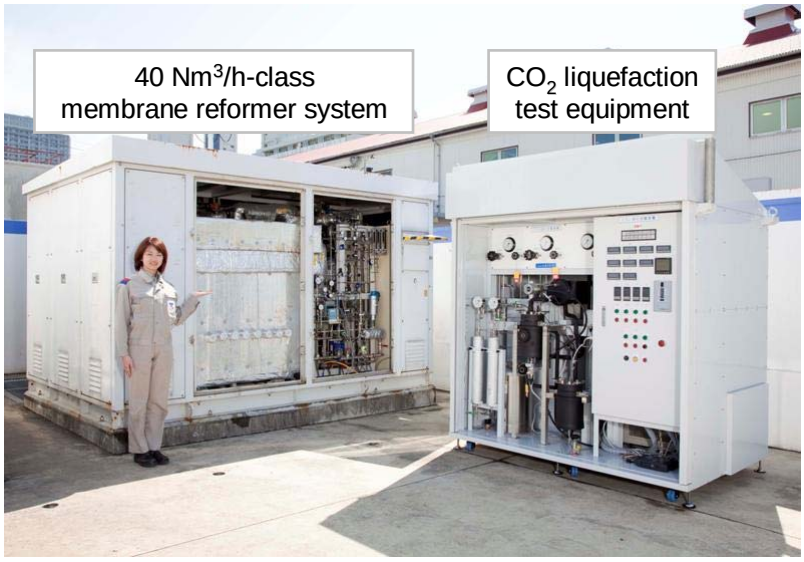

Figure 4: 40 Nm3/h-class membrane reformer system and CO_2 liquefaction test equipment.

Table 1: Energy efficiency of hydrogen production and CO_2 reduction rate.

		MRF 75% load (individual operation)	MRF 75% load + CO_2 capture (calculated from experimental data)
Input Energy ($MJ/kg\text{-}H_2$)	Natural gas	168.5	168.5
	Electricity	6.6	13.6
Hydrogen production rate (Nm^3/h)		30.6	30.6
Efficiency (%, HHV)		81.7	78.6
CO_2 emission (kg/h) [*1]		25.1	12.6
CO_2 reduction rate (%)		-	50

[*1] CO_2 emission from the electric power consumption was calculated from the average emission factor of the Tokyo area in 2008 (0.332 kg/kWh) [6]

4 Summary and Future Prospects

In the present study, distributed highly-efficient hydrogen production with CO_2 capture has been demonstrated with the 40 Nm^3/h-class membrane reformer system. The experiment was the first demonstration in the world in terms of small-scale on-site hydrogen production with CO_2 capture. The advanced membrane reformer system can reduce CO_2 emission to half with only 3% energy loss by applying the CO_2 capture system. CO_2 removal in on-site distributed hydrogen production used to be considered unrealistic with conventional technologies because of large energy loss, costly and space-consuming CO_2 purification and capture facilities. This study revealed that the advanced highly-efficient membrane reformer system has a potential to make it feasible to capture CO_2 efficiently even in on-site distributed hydrogen production and proved the possibility of feasible small scale CO_2 capture.

During the introduction period of hydrogen energy, local hydrogen network, which supplies hydrogen not only to fuel cell vehicles but also residential and stationary fuel cells, is expected to be a regional hydrogen supply model to facilitate the spread of hydrogen energy into the society. On-site hydrogen production is a key technology in the local hydrogen network and the advanced membrane reformer system with CO_2 capture is a promising technology to produce “low-carbon” hydrogen efficiently.

Acknowledgement

The development of the 40 Nm_3/h-class membrane reformer system was supported by the New Energy and Industrial Technology Development Organization (NEDO). The authors acknowledge their financial and technical supports.

References

[1] I*EA World energy outlook 2006*, International Energy Agency, Paris (2007).

[2] W.C. Lattin and V.P. Utgikar, *International Journal of Hydrogen Energy*, 32 (2007) 3230-3237.

[3] E. Kikuchi, S. Uemiya, T. Matsuda, *Studies in Surface Science and Catalysis*, 61 (1991) 509-515.

[4] B. Metz, O. Davidson, H. de Coninck, M. Loos, L. Meyer, *IPCC Special Report on Carbon Dioxide Capture and Storage*, Cambridge University Press, United Kingdom & New York, USA, (2005).

[5] Y. Shirasaki, T. Tsuneki, Y. Ota, I. Yasuda, S. Tachibana, H. Nakajima, K. Kobayashi, *International Journal of Hydrogen Energy*, 34 (2009) 4482-4487.

[6] TEPCO website, http://www.tepco.co.jp/en/challenge/csr/initiatives/CO2/index-e.html

Comparison of Composite Pd-Ag and Pd-Cu Membranes over PSS Supports for Hydrogen Separation

J.A. Calles, **R. Sanz**, **D. Alique**, Department of Chemical and Energy Technology, ESCET, University Rey Juan Carlos, Spain

1 Introduction

Nowadays, technologies to produce hydrogen are growing up due to it is considered a clean energy vector suitable for the substitution of actual fossil fuels based economy [1]. In particular, pure palladium based membranes and membrane reactors have been widely studied for hydrogen purification and its simultaneous production and purification due to its extremely high selectivity and good permeability [2]. However, the industrial application of these membranes retains some limitations, mainly the high cost of palladium and efficiency loss by hydrogen embrittlement [3]. For this reason, a growing attention has been focused to develop composite membranes with a thin active layer of precious metal over ceramic or metallic supports, achieving good mechanical stability and an important reduction in fabrication costs [4]. Moreover, it is possible to reduce and even eliminate the membrane embrittlement by preparing alloys of palladium with metals such as silver, copper or gold. In addition, some of these Pd based alloys can present high hydrogen permeability, better mechanical properties and sulfur resistance than those prepared with pure Pd [5]. Among a large number of preparation methods for composite membranes, a chemical process denoted as electroless plating (ELP) is the most widely used technique for the incorporation of Pd, Ag and Cu. This method is known for its simplicity of application, the possibility of achieving uniform deposition on supports with complex shapes, the easy of scale-up and the low cost of the process since electrical current is not required [6].

In this context, the present work is focused on the preparation and characterization of composed membranes of alloys of both Pd-Ag and Pd-Cu over porous stainless-steel supports. Both solutions used for the coating by ELP and the conditions of the thermal treatment carried out to obtain $Pd_{77}Ag_{23}$ and $Pd_{60}Cu_{40}$ alloys have been studied in detail.

2 Experimental

Tubular stainless steel supports with a porosity of ca. 20% and media grade of 0.2 μm (which means that 95% rejection of particles with a size greater than the grade is guaranteed) were provided by Mott Metallurgical. The supports have a thickness of 1.9 mm, external diameter of 12.9 mm and a length of 150 mm. Smaller PSS pieces were obtained by cutting the original substrates to 30 mm of length.

The preparation of alloys of Pd-Ag and Pd-Cu over PSS supports involves the next consecutive steps: chemical cleaning and surface activation of the support, metal deposition by ELP and obtaining the alloy by thermal treatment. Due to the presence of several contaminants on the surface of commercial supports such as oil, grease or dirt, it is necessary to carry out an appropriate cleaning. This process consists of consecutive

immersions in solutions of sodium hydroxide 0.1 M for 5 min, hydrochloric acid 0.1 M for 5 min and ethanol for 15 min. All washing steps were performed in an deionised water ultrasonic bath at 60 ºC with a rinsing between each immersion completing the process with a drying step at 110 ° C for 8 hours. After that, the activation of the PSS surface is necessary in order to initiate a homogeneous plating process with a relative low induction period. The process involves successive dip of the support in several acidic solutions of tin (1.0 g/L) and palladium (0.1 g/L) chlorides. Gentle rinsing with deionised water between both baths and one additional rising with dilute hydrochloric solution (0.01 M HCl) to prevent the hydrolysis of palladium ions fixed in the PSS supports were carried out. The immersions of PSS support in all baths were carried out at room temperature with a controlled vertical rotation (50 rpm) to ensure a suitable homogeneity. Moreover, the ends of the support were closed with Teflon tapes to keep out of solution at the internal surface of PSS support. The activation was repeated 6 times in order to achieve a homogeneous distribution of Pd nuclei. Next, metals were incorporated by electroless plating technique adding the reducing agent in several doses. The composition of the electroless plating baths and the deposition conditions are given in Table 1. The activated supports with the ends closed with Teflon tapes were immersed into 30 mL of the plating solution under vertical rotation at 60 ºC for Pd and Ag deposition and 25 ºC for Cu plating. Finally the membranes were rinsed with deionised water and dried at 110 ºC for 8 hours. The thickness and final composition for each alloy were controlled by using different number of inmersions in the plating solution of each metal. After that, the formation of the alloy occurs by thermal treatment under nitrogen atmosphere. Different procedures were carried out varying the temperature in the range 500-700ºC and the time of the process between 0-72 h.

Table 1: Composition of the electroless plating baths and the experimental procedure for Pd, Ag and Cu deposition.

Components of the different plating baths	Composition of pure Pd plating bath	Composition of pure Ag plating bath	Composition of Pd-Ag plating bath	Composition of pure Cu plating bath
$PdCl_2$ (g/L)	5.4	-	5.40	-
$AgNO_3$ (g/L)	-	5.17	1.52	-
$CuNO_3 \cdot 3H_2O$ (g/L)	-	-	-	9.67
NH_4OH 32% (mL/L)	390	390	390	-
NaOH (g/L)	-	-	-	8.65
Na_2EDTA (g/L)	70	70	70	29.78
N_2H_4 (mL/L)	10	10	10	-
HCHO (mL/L)	-	-	-	50
Temperature (ºC)	60	60	60	25
Time (min)	90	90	90	90
* $V_{solution}/S_{plating\ area}$ (cm^3/cm^2) =2.47				

All prepared membranes were characterized by SEM, XRD, gravimetric analysis and ICP-AES (inductively coupled plasma atomic emission spectroscopy) to determine the effectiveness of the different steps undertaken.

3 Results and Discussion

Two of the most critical factors that influence the preparation of palladium based alloys over PSS supports are the composition of the plating baths and the experimental conditions (temperature and time) of the thermal treatment of the alloy. As previously mentioned, in this work two different types of membranes, Pd-Ag and Pd-Cu, were prepared for avoiding some of the main drawbacks of Pd pure membranes, mainly the embrittlement in presence of hydrogen.

Pd-Ag alloy membranes can be prepared by sequential plating of individual metals or by co-deposition, followed in both cases by thermal diffusion treatment. Palladium and silver plating over activated PSS surface is performed by using similar bath compositions (shown in Table 1) with an efficiency around 35-45%. In both cases the low values for the efficiencies are due to the generation and precipitation of waste byproducts in bulk solution, maintaining the content of both metals in spent solutions lower than 1 mg/L (measured by ICP analysis). Moreover, previous studies have showed the possibility of making the metal deposition of Pd and Ag in any order without extraction of previously incorporated metal analyzing the spent solutions by ICP-AES. This fact lets to achieve a theoretical composition in the membrane near of the suitable value for high permeation fluxes ($Pd_{77}Ag_{23}$) by adjusting with the proper amount of metal plating. In this work this has been carried out by using three successive immersions on Pd plating bath and a further one in Ag plating bath. Furthermore, since Pd and Ag baths are very similar it has been possible to carry out the co-deposition of both metals for preparing the alloy. In this case, only one immersion of PSS support in the Pd-Ag plating bath was used. This method have the advantage of a theoretically easy homogenization in the thermal treatment process but it was found very difficult to adjust the composition in solution for obtaining an appropriate plating rate of each metal with a 77:23 ratio by the preferentially incorporation of Pd. Figure 1 shows the SEM images of modified PPS supports after each metal deposition. As can be seen, the covering is very homogeneous for Pd and Ag in any conditions.

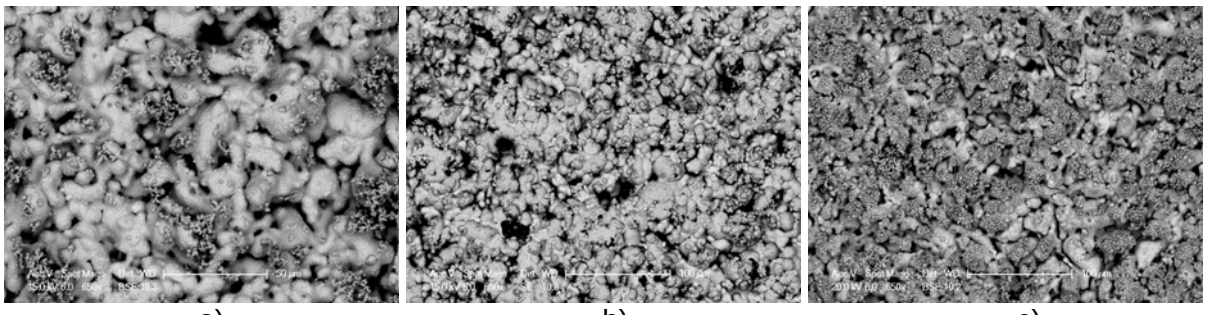

a) b) c)

Figure 1: SEM images of Pd-Ag composite membranes: a) Pd-Ag sequential plating, b) Ag-Pd sequential plating and c) co-deposition.

One of the most important factor which affects to the quality of the Pd-Ag alloy membranes is the conditions in which thermal treatment is carried out. In this work temperatures in the range 500-700 ºC under nitrogen atmosphere and times between 0 and 72 h have been employed. Figure 2 shows the XRD spectra for different temperatures and times of annealing over Pd-Ag membranes prepared by sequential and co-deposition plating. The figure shows the presence of typical metals diffraction peaks before annealing at 40º, 47º and 68º for Pd and 38º, 44º, 64º and 77º for Ag. As it can be seen, in the samples obtained by sequential step (Figure 2 a, b and c) thermal treatment of the samples provokes the presence of new signals between each diffraction peak of both metals due to the generation of a new phase: the Pd-Ag alloy (at 39º, 45º, 66º and 79º). Although the alloy was achieved for all cases, the behaviour of the Pd-Ag alloy is different depending on the temperature at which it is being treated. Thus, at 500ºC the peaks of the alloy are observed from 6 to 24 h of thermal treatment, but it disappeared at 48 h when and new peaks arose in the spectra. At 600ºC, peaks of the alloy appear from 6 h and remain up to 72 h, even growing strongly with time. And finally, at 700ºc it seems that alloy is achieved from 6 h of thermal treatment but at longer times peaks of Pd are also present. High temperature can increase the rate of intermetallic diffusion between the components of the PSS support and the membrane layer.

Moreover, the influence of preparing Pd-Ag membranes by sequential plating or co-deposition was evaluated. In Figure 2 are shown the results obtaining after thermal treatment at 600 ºC over these both membranes. As it can be clearly seen, in the XRD spectra of samples obtained by co-deposition method the alloy is not observed at any time, but also other several peaks different of Pd and Ag are shown. In these samples, other additional components (such as Na, Mg or Cl) are detected by EDX analysis, which are not detected in the sequential plating samples. The presence of additional components between Pd and Ag particles co-deposited may provoke unsuccessful annealing process with the appearance of unclear XRD spectra for the alloy. Moreover it is possible that both Pd and Ag can be deposited as isolated clusters in different areas with a reduced surface of contact between them. This fact can avoid the formation of a suitable alloy due to the difficulty for the homogeneous diffusion of both metals. According with all discussed results, 600ºC was selected for the thermal treatment of annealing on Pd-Ag membranes prepared by sequential plating.

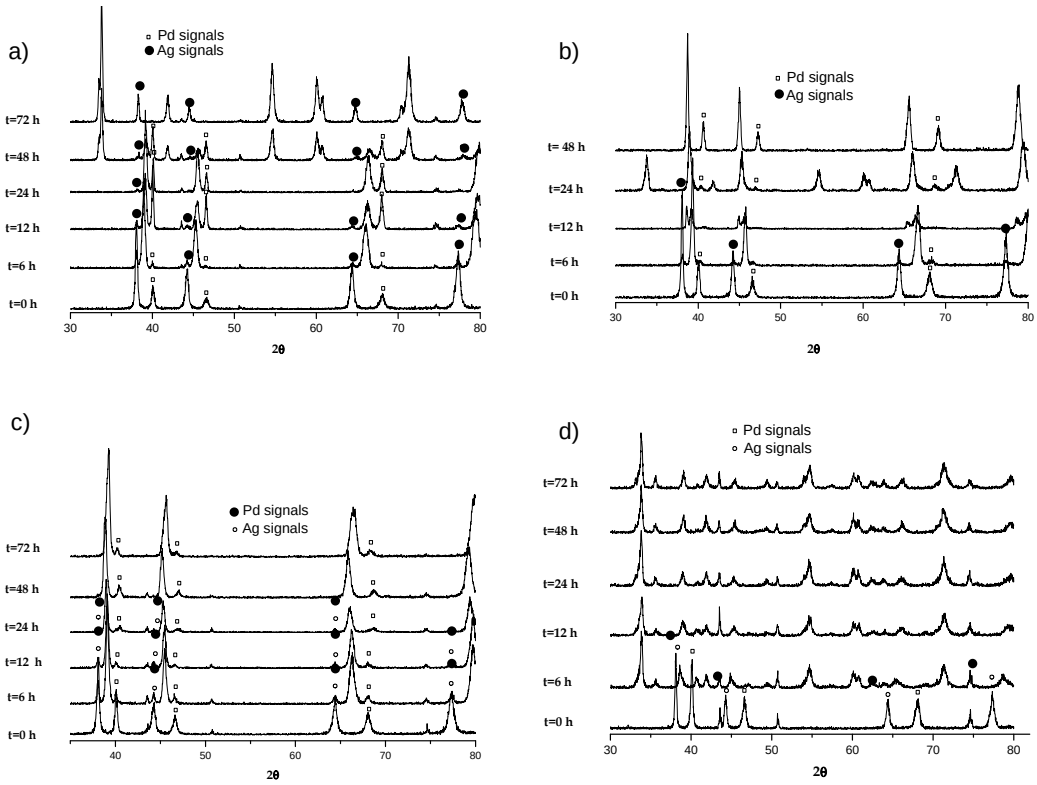

Figure 2: X-ray diffraction patterns of Pd-Ag membranes prepared in several conditions: Sequential deposition with thermal treatment at 500 ºC (a), 700 ºC (b), 600 ºC (c) and co-deposition with thermal treatment at 600 ºC (d).

Similar experiments were carried out for preparing Pd-Cu membranes over PSS supports. Figure 3 shows SEM photographs of the surface after sequential plating of Pd-Cu and Cu-Pd and simultaneous deposition of both (co-deposition). In this case, the composition of the plating baths of Pd and Cu are very different between them. This fact provokes that co-deposition of both metals was unfeasible being the sequential plating the most suitable alternative for the membrane preparation. Moreover, EDX analysis of the samples shows that Cu is extracted and re-dissolved by typical palladium plating baths. Thus, in this bimetallic alloy is necessary to incorporate first the palladium and then the copper. In this manner, it was found very difficult to achieve the suitable composition of alloy for maximize the permeation flux of hydrogen ($Pd_{60}Cu_{40}$).

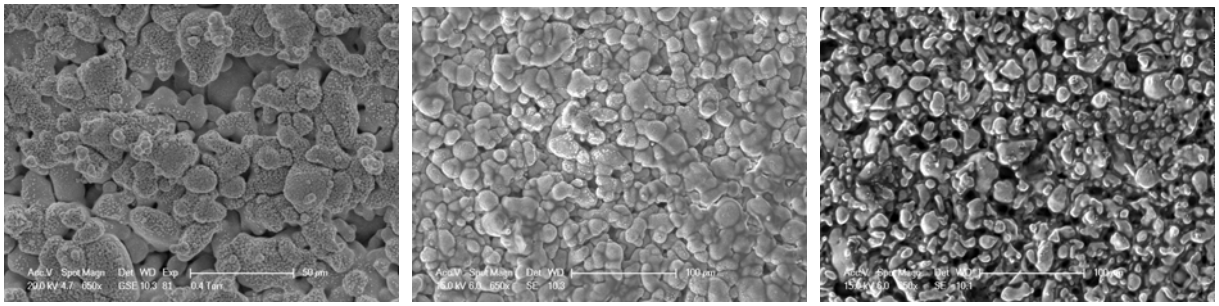

a) b) c)

Figure 3: SEM images of Pd-Cu composite membranes: a) Pd-Cu sequential plating, b) Cu-Pd sequential plating and c) co-deposition.

Figure 4 shows the XRD spectra for each temperature at different times of thermal treatment over Pd-Cu membranes prepared by sequential plating. The spectra at t=0 h (before any thermal treatment) shows the diffraction peaks corresponding to pure metals at 40º, 47º and 68º for Pd and 44º, 51º, and 74º for Cu. As it can be clearly seen, temperature influences significantly in the annealing process in a major grade than Pd-Ag membranes. For Pd-Cu membranes thermal treatment at 500ºC is insufficient for obtaining the alloy until 24 h, although the presence of remaining amounts of Pd and copper even appear after 72 hours. At 600ºc the annealing process is improved, since the signals related to the Pd-Cu alloy between each diffraction peak of both metals appear at relatively low times. However, at higher temperature, as it was mentioned for Pd-Ag membranes, the migration of components of PSS supports to the selective layer of the membrane became relevant, which reduces the application of the membrane for a good hydrogen separation.

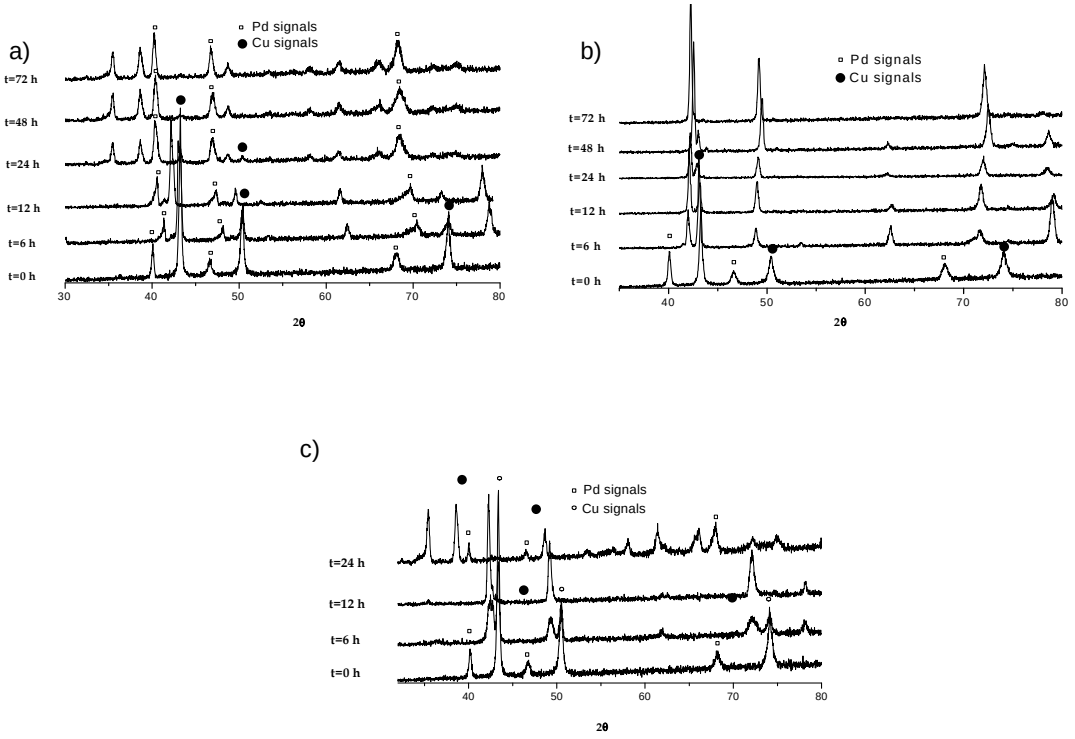

Figure 4: X-ray diffraction analysis of Pd-cu membranes prepared by sequential deposition followed by thermal treatment at 500 ºC (a), 600 ºC (b), 700 ºC (c).

4 Conclusions

Pd-Ag and Pd-Cu membranes can be prepared by electroless plating of these metals on porous stainless steel tubes followed by thermal treatment. Pd and Ag can be incorporated by both sequential plating and co-deposition (simultaneous deposition of both metals) methods, although the composition of the alloy can be adjusted better with the first technique. The homogeneity of the Pd-Ag alloy depends of the preparation method and temperature of the annealing treatment. The co-deposition provokes the generation of clusters of pure metals, reducing the area for contact between Pd and Ag and making the diffusion of metals difficult. Pd-Ag alloy was obtained for sequential plating of both metals although temperature influenced significantly in the time necessary for obtaining the Pd-Ag phase. After 6 h of thermal treatment, characteristic diffraction peaks of Pd-Ag alloy appear independently of the temperature of the process. However, at longer times this phase only was maintained at 600 ºC, appearing new diffraction peaks and/or re-appearing the signals due to both pure Pd and Ag. In this manner, the temperature of 600 ºC was selected for the thermal treatment of annealing on Pd-Ag membranes prepared by sequential plating. On the other hand, it has been determined that Pd and Cu only can be incorporated by sequential plating (firstly Pd and then Cu) making very difficult to achieve the suitable composition of alloy for maximize the permeation flux of hydrogen (60:40 respectively). For these membranes thermal treatment at 500ºC is clearly insufficient for obtaining the alloy until 24 h,

although the presence of remaining amounts of Pd and copper even appear after 72 hours. Higher temperatures improve the annealing process, appearing the signals related to the Pd-Cu alloy between each diffraction peak of both metals at relatively low times. However, very high temperatures can provoke the migration of components of PSS supports to the selective layer of the membrane, reducing their application for a good hydrogen separation. This fact provokes the generation of Pd-Cu alloy phase for long times at 600ºC (72 h) while it can be obtained after times lower than 12 h with thermal treatment at 700ºC. Nevertheless, longer times at this high temperature provoke the apparition of new signals due to several components different of searched alloy.

Acknowledgements

The authors gratefully acknowledge financial support received from the Ministry of Science and Innovation of Spain through projects ENE-2007-66959 and CIT-120000-2008-004.

References

[1] Marban G., Valdes-Solis T., Int. J. Hydrog. Energy 32 (2007) 1625-1637.

[2] Tosti S., Basile A., Bettinali L., Borgognoni F., Gallucci F., Rizzello C., Int. J. Hydrogen Energy 33 (19) (2008) 5098-5105.

[3] Uemiya S., Matsuda T., Kikuchi E., J. Membr. Sci. 56 (1991) 315-325

[4] Paglieri S.N., Way J.D., Sep. Pur. Methods

[5] Okazaki J., Tanaka D.A.P., Tanco M.A.L., Wakui Y., Mizukami F., Suzuki T.M, J. Membr. Sci. 282 (1-2) (2006) 370-374

[6] Bhandari R., Ma Y.H., J. Membr. Sci. 334 (2009) 50-63.

Ceramic-supported Polymer and Carbon Membranes for Hydrogen Separation

Daniel Montané, Catalonia Institute for Energy Research (IREC). Bioenergy and Biofuels Division. Av. Països Catalans, 16. 43007, Tarragona, Spain
Kelly Briceño, **Ricard Garcia-Valls**, Universitat Rovira i Virgili. Departament d'Enginyería Química. Av. Països Catalans, 26. 43007, Tarragona, Spain

1 Introduction

The expansion of hydrogen as energy carrier has generated a growing effort to develop processes that can produce high-purity hydrogen suitable for low-temperature fuel cells (mainly PEMFC). This is the case in steam reforming, where membranes can be used to purify hydrogen but also to increase the yield of the reaction using reformers based on membrane reactors. The latter is a powerful concept but demands high-performance membranes, constructed of materials that may withstand the harsh reaction conditions required for steam reforming (i.e., high temperature and a high partial pressure of superheated steam). Processing the reformer product gas to purify hydrogen at low temperature in membrane units coupled to conventional reformers, is an option that may be implemented more easily because the membranes are operated at less demanding conditions.

In this work we focused on the development of polymeric- and carbon-based membranes supported on ceramic carriers for hydrogen purification. Polyimides are versatile materials that have been used in membranes for the separation of gas mixtures, mainly as hollow fiber membranes and other unsupported arrangements with large specific surface area [1]. They may be supported in other polymers to obtain membranes suitable for pervaporation [2], but the manufacture of supported tubular polyimide membranes has difficulties related to poor reproducibility and crack formation [3]. Additionally, hollow fibres fail in mechanical stability at high temperature under high-pressure drops [2]. Therefore, the use of ceramic carriers for developing supported polyimide membranes offers potential for obtaining efficient and mechanically stable membranes [4]. Additionally, controlled thermal treatment of ceramic-supported polyimide membranes yields supported carbon membranes that have promising characteristics for the separation of gas mixtures [5].

2 Experimental

2.1 Preparation of the supported membranes

The preparation of the polymeric membranes supported on tubular ceramic elements was based on a spinning solution technique. The macroporous ceramic support was a 1 kD ceramic membrane of 7.2 cm length and 10 mm of outer radius (Tami). It was mounted horizontally and rotated at constant speed to distribute a uniform layer of around 3 g of a viscous Matrimid solution. The solution was previously prepared by dissolving 10 to 16% w/w of polymer in N-Methyl-2-pyrrolidone (NMP) for 4 hours with mechanical stirring under

controlled vacuum. After gelification at room temperature, the polymeric membranes were developed by imidization at 110°C for 24 h (Series 1) + 350°C for 2 h (Series 2). Supported carbon membranes were prepared by pyrolysis of the polymeric membranes. They were heated at 1°C/min to 550°C and maintained at this temperature for 5 h, using a flow rate of 30 NmL/min of nitrogen (Series 3).

2.2 Permeation measurement

Single gas permeation was determined for pure gases (H_2, N_2, CH_4, CO_2 and CO) at trans-membrane pressures from 1 to 3 bars and 25°C. The fluxes of single gases were measured by a soap film flowmeter. The ideal selectivity of the membrane was defined as the ratio of hydrogen permeance to the permeance of the other gases, measured at the same transmembrane pressure and temperature. The real selectivity of the membrane was determined in binary mixtures with hydrogen of 50% vol. The composition of the permeate gas was measured with a mass spectrometer. The influence of temperature on the selectivity of the carbon membranes was determined in experiments performed between 25 and 150 °C.

3 Results and Discussion

3.1 Influence of the polymer concentration on the thickness of the polymeric membranes

The viscosity of the Matrimid in NMP solution had a strong influence on the development of the polymer layer on the ceramic carriers by spinning solution. Figure 1 shows surface and transversal ESEM views of the polymeric membranes obtained with 10%, 13% and 16% w/w polymer solutions. At 10% the viscosity of the solution is too low and the polymer penetrates the macroporous structure of the ceramic carrier (Images A and B), while at 16% the viscosity is too high and it favours the formation of an irregular polymer layer with superficial wrinkles and defects (Images E and F). The best results were obtained using a 13% w/w solution. Images C and D in Figure 1 show that a regular layer of polymer was obtained, and that it only presented minor superficial defects in the form of gas bubbles.

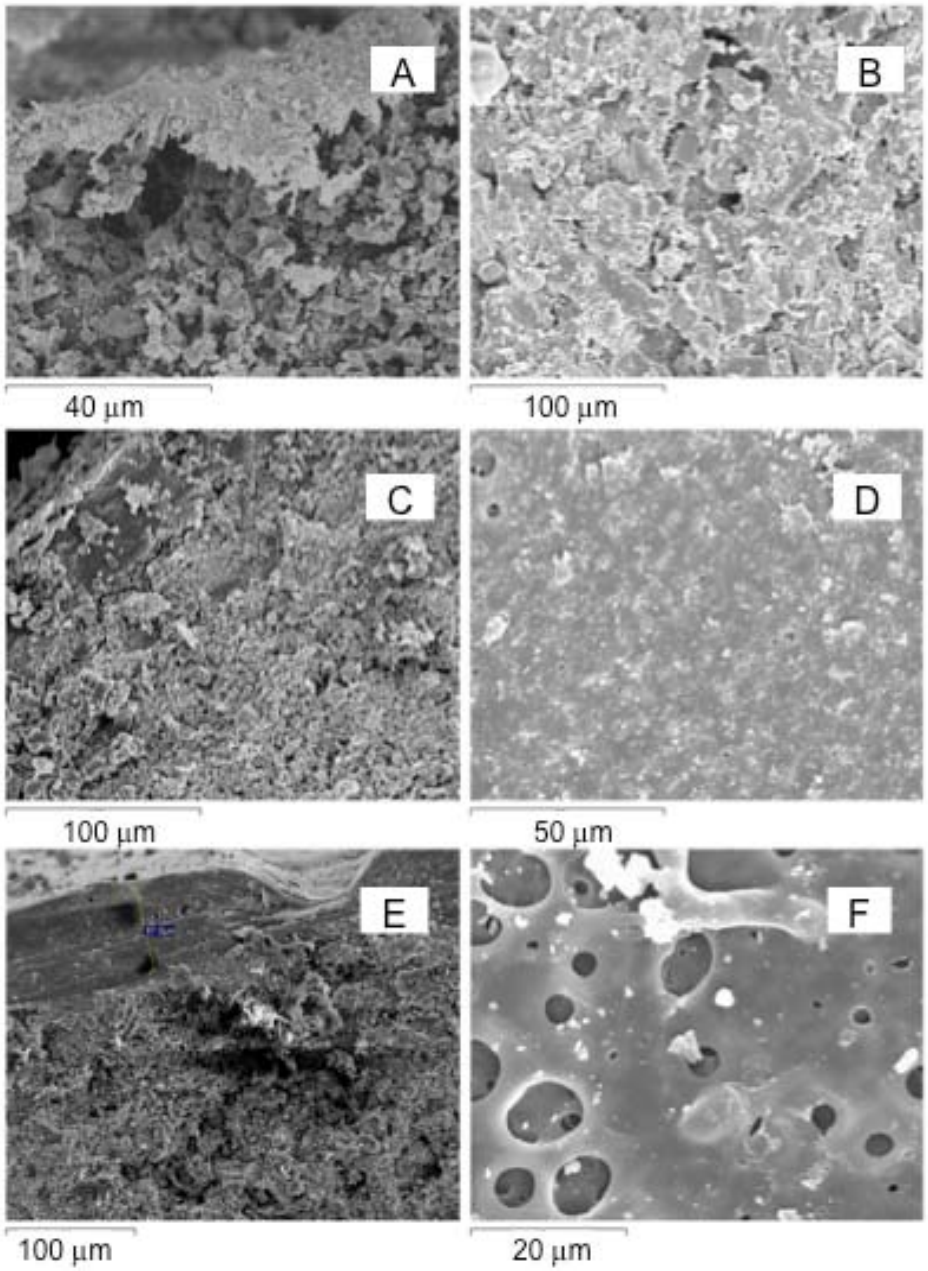

Figure 1: ESEM images of the polymer layers deposited on the ceramic carrier at 10% (A, B), 13% (C, D) and 16% (E, F) w/w of Matrimid in NMP (A, C and E, section view; B, D and F, surface view).

3.2 Influence of the Imidization temperature on the permeation of pure gases.

Imidization temperature plays a determinant role on the permeation properties of pure gases, because it affects the development of the structure of the polymeric membrane. With membranes prepared with the 13% w/w Matrimid solution the small surface defects disappeared completely when the imidization temperature was above 250°C, as shown in Figure 2 where a transversal view of the ceramic support and the deposited and imidized polymer layer are shown.

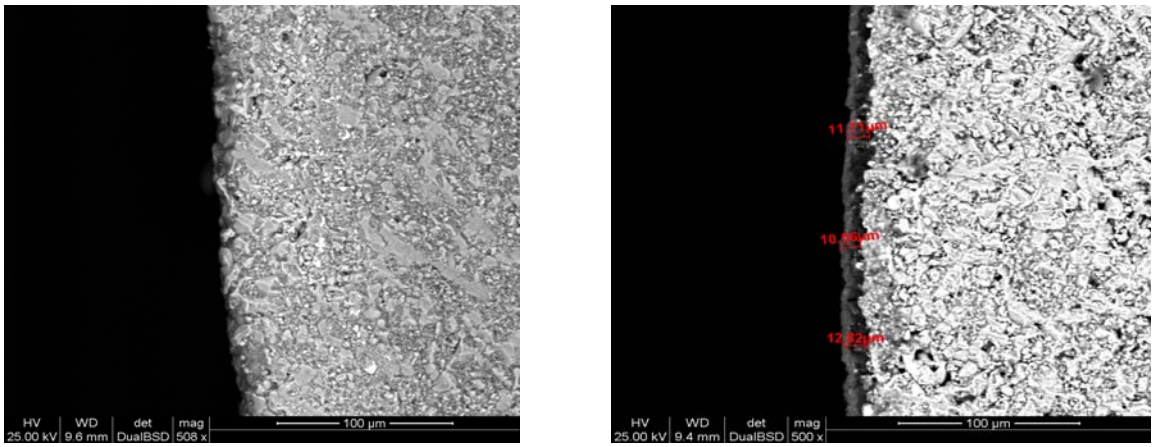

Figure 2: Supported polymer membrane (series 2): ceramic support (left) and supported membrane (right)

Table1 shows that the membranes produced at an imidization temperature of 110°C (Series 1) had lower permeance than those obtained at 350°C (series 2) for all the gases we studied. At the latter temperature permeance diminished in the order H_2>CH_4>CO>CO_2. Estimation of the ideal selectivity (i.e., the ratio of permeance of pure gases) in Table1 shows that it decreased from 2.9 to only 1.9 for H_2/CH_4 and from 4.5 to 2.8 for H_2/CO when imidization temperature was raised from 110 to 350°C, while it remained nearly constant for H_2/CO_2. Real selectivity was determined in experiments using binary gas mixtures with hydrogen containing equimolar proportions, and it was always below the ideal values. In fact, ideal and real selectivities were below those that may be expected if transport through the membrane was governed by pure Knudsen diffusion, which points out to the existence of a fraction of pores with large diameters in the membrane.

Table 1: Average permeance and selectivity of pure gases and binary mixtures with hydrogen in polymer membranes at room temperature and trans-membrane pressure below 2.5 bar.

	H_2	CH_4	CO	CO_2	H_2/CH_4	H_2/CO	H_2/CO_2
Molar mass (g/mol)	2	16	28	44	-	-	-
Kinetic diameter (nm)	0.29	0.38	0.43	0.33	-	-	-
Series 1 membranes							
Permeance (GPU)*	40.0	14.0	8.82	9.62	-	-	-
Ideal selectivity	-	-	-	-	2.9	4.5	4.2
Real selectivity	-	-	-	-	1.8	2.1	1.7
Series 2 membranes							
Permeance (GPU)*	875.	455.	314.	204.	-	-	-
Ideal selectivity	-	-	-	-	1.9	2.8	4.3
Real selectivity	-	-	-	-	1.8	1.8	2.2
Knudsen selectivity	-	-	-	-	2.83	3.74	4.69

*GPU= 10^{-6} cm^3 (STP)/(cm^2·s·cm_{Hg})

3.3 Supported carbon membranes.

Supported carbon membranes (series 3) were obtained by controlled pyrolysis of a Matrimid layer coated on the ceramic carrier. Figure 3 shows that their permeance varied with the inverse of the square root of the molar mass of the gas, which suggests the existence of Knudsen diffusion as the main transport mechanism. However, Figure 4 also shows that permeance was dependent on the trans-membrane pressure, which indicates the existence of viscous flow. The ideal selectivities calculated from the permenaces of pure gases were below those corresponding to a situation in which pure Knudsen diffusivity was the sole transport mechanism (Figure 5), in agreement with the coexistence of viscous flow.

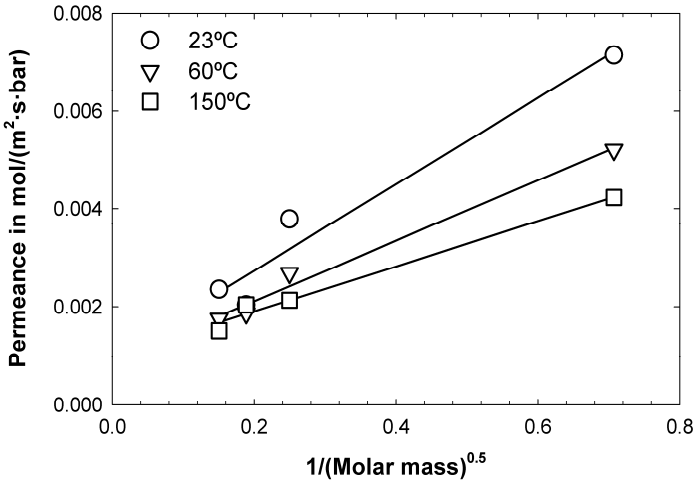

Figure 3: Dependence of pure gas permeances in a carbon membrane (series 3) with the molar mass of the gas at different temperatures and a trans-membrane pressure of 2.0 bar.

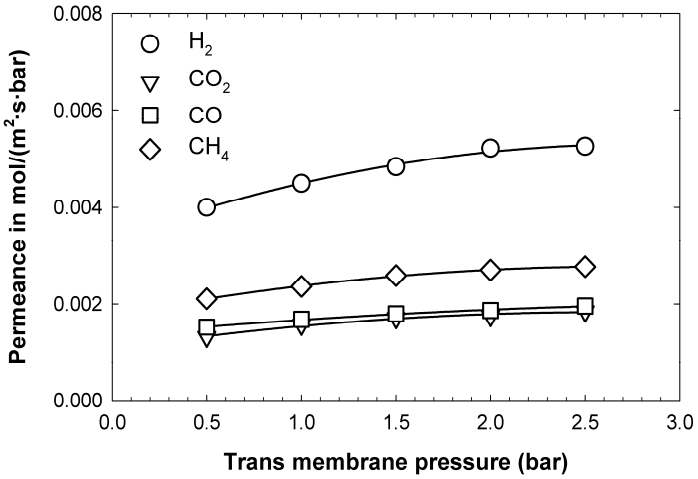

Figure 4: Permeances of pure gases in a carbon membrane (series 3) at a temperature of 60°C.

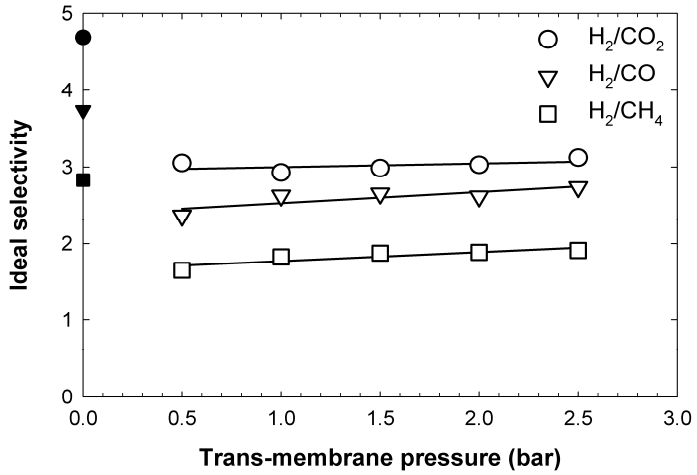

Figure 5: Effect of trans-membrane pressure on the ideal selectivity in a carbon membrane (series 3) at 23°C. Solid symbols correspond to the Knudsen selectivity.

Figure 3 show that temperature decreased the permeance of the carbon membranes, especially for hydrogen. In addition, calculation of the ideal selectivity at several temperatures shows that temperature increased selectivity slightly, except for CO_2/H_2 mixtures that remained independent of temperature (Figure 6). Measurements of the pore size distribution of carbon samples extracted from the membrane by CO_2 adsorption isotherms and the NLDFT model gave an average pore size of 0.50 nm. This value implies that in addition to Knudsen mechanism and viscous flow contribution, the pore size obtained a 550°C is so close to the kinetic diameter of the molecules considered for hydrogen separation that would imply existence of additional transport mechanisms.

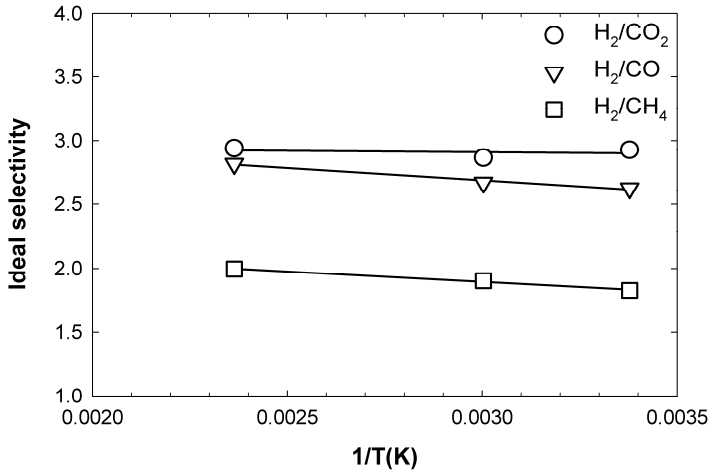

Figure 6: Effect of temperature on the ideal selectivity in a carbon membrane (series 3) at 1 bar.

Gas transport in carbon membranes is a complex interaction of several mechanisms, as already reported by Haraya et al [6], and for pore sizes below 1 nm activated diffusion is also present [7].

4 Conclusions

Supported polymer and carbon membranes were formed in the outer surface of tubular ceramic carriers by a spinning coating method. Imidization temperature plays an important role in the change of permeation values for polymeric membranes, but not in their ideal selectivity. By controlled pyrolysis of the supported polymer membranes, carbon membranes with smooth surfaces and absence of cracks were obtained. Characterization of the membrane at different trans-membrane pressures indicated that a fraction of pores with large diameters is present, which reduced the selectivity of the membranes. The pore diameters in carbon membrane are close to the kinetic diameter of the gas molecules we tested, which may favour activated diffusion.

Acknowledgments

This research was supported by the Ministry of Science and Innovation of the Spanish Government (project CTQ2008-02491/PPQ), and the Catalan Regional Government (2009SGR-00237).

References

[1] E.P. Favvas, G.C. Kapantaidakis, J.W. Nolan, A.Ch. Mitropoulos, N.K. Kanellopoulos. J. Mater. Proc. Technol. 186 (2007) 102-110.

[2] R. Kreiter, D.P Wolfs, Ch.W.R. Engelen, H.M. van Veen, J.F Vente. J. Mem. Sci. 319 (2008) 126-132.

[3] B. S. Liu, N. Wang, F. He, J. X. Chu. Ind. Eng. Chem. Res. 47, (2008) 1896-1902.

[4] N. Itoh, K. Haraya. Catalysis Today 56 (2000) 103-111.

[5] K.Haraya, K.Obata, N. Itoh, Y. Shndo., T. Hakuta, H. Yoshitome. J. Membrane Sci. 41 (1989) 23-35.

[6] K. Haraya, K. Obata, T. Hakuta, H. Yoshitome. J. Chem. Eng. Japan 19 (1986) 431-436.

[7] Rao M.B, Sircar S. J. Membrane Sci. 110 (1996) 109-118.

Reforming Performance of Hydrogen Production Modules Based on Membrane on Catalyst

Yasuhiro Takagi, **T. Shimamori**, **H. Shigaki**, **H. Hikosaka**, **H. Tanak**, NGK Spark Plug Co., Ltd., Japan
T. Nishii, **H. Kurokawa**, **Y. Shirasaki**, **I. Yasuda**, Tokyo Gas Co., Ltd., Japan

1 Introduction

Demand of pure hydrogen for fuel will rapidly increase due to spread of fuel cell for vehicles, houses and power stations. One of the most promising pathways to produce and supply hydrogen in near to mid-term future is on-site production from natural gas, because of its high overall energy efficiency and substantial reduction of greenhouse gas emissions. On the other hand, some hydrogen production methods by using renewable energy such as solar energy are researched actively; however they are far from practical use level. A membrane reactor system is an efficient hydrogen production system. This is because in a membrane reactor steam reforming reaction of hydrocarbon fuels (natural gas, etc.) and hydrogen separate process proceed in a single reactor simultaneously. Tokyo Gas has developed and operated a 40 $Nm^3/h\text{-}H_2$ class membrane reactor system, and demonstrated its high efficiency of 81.4 % (HHV) at a hydrogen refuelling station for fuel cell vehicles in Tokyo [1]. However, more compact and inexpensive MRF systems are required for commercialization. In these few years, we have successfully developed a new type of hydrogen production and separation module which we call MOC (Membrane On Catalyst) module [2-4]. It requires no separate catalyst parts, and can make a membrane reactor system more compact and inexpensive. More to say, MOC is designed to have a membrane of palladium-based alloy prepared on the surface of the tubular structured catalyst that has catalytic activity for steam reforming reaction, thermal expansion matching with the membrane material, proper porosity and so on. We also have reported some MOC properties [5-6]. For example, our electroless plating membrane of less than 10 μm thick showed hydrogen permeability of over 30 $Ncc/min/cm^2$ and conversion of methane was higher than the equilibrium conversion under the same temperature. In this work, duration properties of hydrogen permeation and hydrogen production were especially focused.

2 Configuration of the MOC Module

The structure of MOC is schematically shown in Figure 1 as compared with the conventional membrane reactor module. The conventional module consists of reforming catalyst and hydrogen separation membrane on a porous support as shown in Figure 1 (A). Hydrogen produced from reforming of methane and steam in the catalyst layer permeates the membrane and passes through the porous support. In contrast, the MOC module consists of hydrogen separation membrane on porous support which has catalytic activity and requires no separate catalyst layers as shown in Figure 1 (B). Feedstock gases, i.e. methane and steam, are reformed and converted to hydrogen, carbon monoxide and carbon dioxide in the

catalytic porous support and only hydrogen permeates the membrane to produce highly-pure product hydrogen. The MOC module has four favourable characteristics. Firstly, it is more compact than the conventional module because the porous support has catalytic activity and requires no separate catalysis layers. Secondly, it may be durable because no friction of membrane with catalyst will occur. Thirdly, it can offer higher hydrogen permeability because plating technology can be applied to prepare a thin film membrane on the porous support. Lastly, manufacturing cost may be significantly reduced because well-established mass production technology can be applied to produce the porous supports, and because the amount of expensive rare metals, i.e. palladium and silver, can be reduced by plating thin membranes.

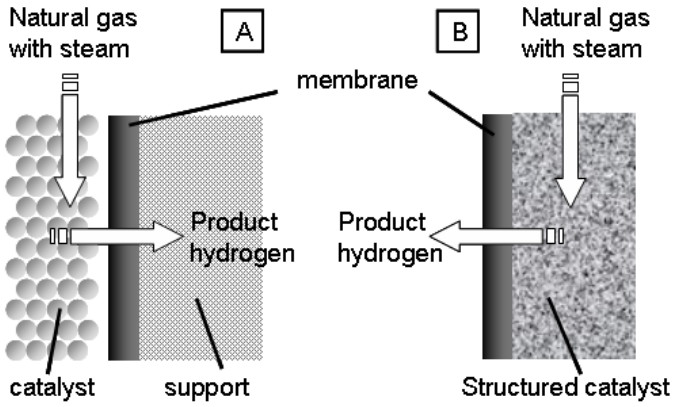

Figure 1: Structure of the conventional module and catalyst (A) and the MOC module (B).

3 Experimental

The fabrication process of the MOC module is roughly divided into three steps; production of porous support, coating of barrier layer and plating of palladium alloy membrane. Figure 2 shows the cross-section of the MOC module.

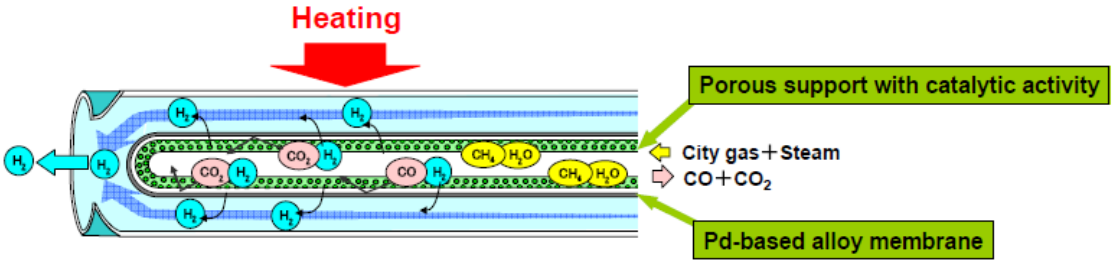

Figure 2: Cross-section of the MOC module and schematic flow of several gases.

NiO and 8YSZ (8 mol % Y2O3-ZrO2) powders were blended at the weight ratio of 60:40 and formed into a tube by an extrusion molding method. The porous support was produced by sintering the tube in air at 1673 K. A slurry of 8YSZ was dip-coated on the outer surface of

the support and fired to form a barrier layer. The barrier layer is 20-60 μm in thickness and prevents interdiffusion of palladium and silver in the membrane and Ni in the catalytic support. The hydrogen permeation membrane was formed on the support coated with barrier layer by electroless plating of palladium and silver and subsequent heat treatment for alloying of them. The thickness of the membrane was 6-20 μm. The module was heat-treated in H_2 atmosphere at 873 K for three hours to reduce NiO in the support into Ni. The size of MOC module was 10 mm in outside diameter and 100 mm or 300 mm in length.

Hydrogen permeation and reforming tests were conducted with the 100 mm and 300 mm long MOC modules. The MOC module was kept at 823 K and inlet gases, i.e. pure hydrogen for permeation test and natural gas and steam for reforming tests, were introduced into the inside of the module (process side). The pressure of process side and permeation side were 0.1 MPaG and 0.0 MPaG in hydrogen permeation test, and 0.8 MPaG and -0.06 or 0.0 MPaG, in reforming tests, respectively. The schematic flow diagram of the experimental apparatus for hydrogen permeability and reforming tests for the MOC modules is shown in Figure 3. A flow of hydrogen or city gas and steam was controlled by mass flow controller and fed into the MOC module after heated in a pre-heater. The MOC module was placed in a chamber and heated to a given temperature. Test gases were introduced into inside of MOC module (process side) and hydrogen permeates through the membrane to the outside of MOC module (permeation side). The amount of permeated hydrogen flux was measured by a wet gas flow meter and the amount of off gas which was not-permeated hydrogen and residual gases from reforming reaction was also measured by a wet gas flow meter. The composition of off gas was measured by a gas chromatography. The gas pressure of the process side was regulated by a back pressure valve located after the MOC module and that of the permeation side was atmospheric pressure or under ambient pressure. The long-term hydrogen permeation test was conducted with pure hydrogen at 0.1 MPaG of process side pressure at 823 K. The reforming performance tests were carried out with natural gas and steam at 0.8 MPaG of process side pressure from 773 to 823 K, and the long-term reforming test at 823 K.

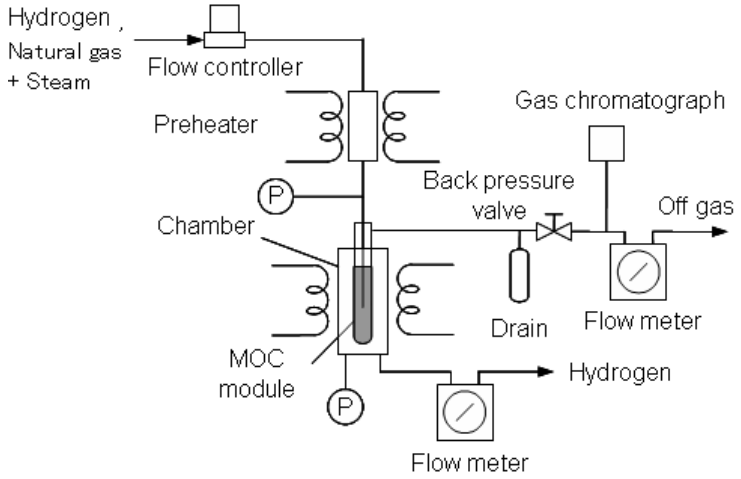

Figure 3: Schematic flow diagram of the reforming test apparatus.

4 Results and Discussions

4.1 Long-term hydrogen permeation test

Figure 4 shows permeated hydrogen flux or leakage of helium gas versus time. Quick increasing of permeated hydrogen flux occurred in the early several ten hours and hydrogen permeation increased up to 37 Ncc/min/cm^2 slowly until 1000 hour and maintained 37-38 Ncc/min/cm^2 through 3000 hour. This result indicated that hydrogen permeability for palladium alloy membrane (by electroless plating) has a long-term durability for at least 3000 hours. On the other hand, leakage increased gradually, because some pin-holes were formed by reaction between palladium and metal like particulates on the membrane. The particles should be removed in the gas flow system in the membrane reactor system to avoid formation of pinholes in long-time operation.

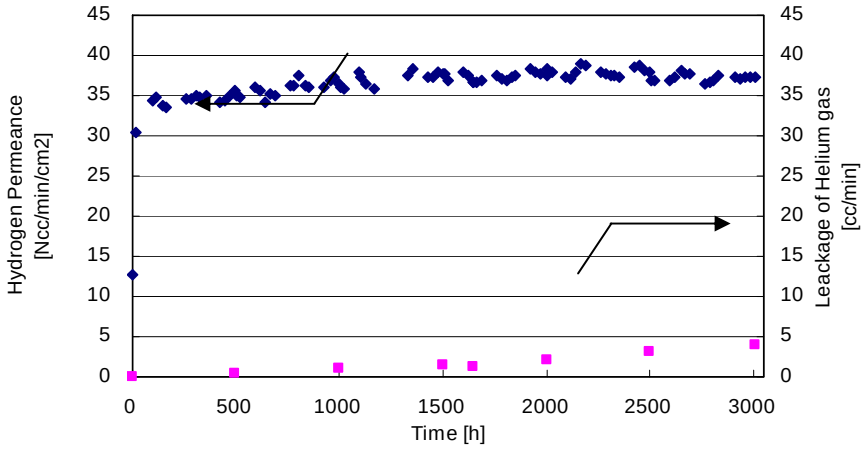

Figure 4: Hydrogen permeability of a 100 mm long MOC module at 823 K.

4.2 Reforming performance

Figure 5 shows the reforming temperature dependence of hydrogen product, conversion and hydrogen recovery at the pressure of process side, 0.8 MPaG. S/C (Steam/Carbon) was 3.0. Figure 4 (A) and (B) indicated the results at the pressure of the permeation side 0.0 MPaG and -0.06 MPaG, respectively. Hydrogen recovery was defined as the ratio of permeated hydrogen to all hydrogen generated by reforming reaction. It was found that the conversion was higher than equilibrium conversion in all temperature range and the effect was greater at elevated temperature. This is because the hydrogen permeation and the equilibrium conversion increased at elevated temperature in both test conditions. However, hydrogen recovery showed different behaviour. Only when the pressure of the permeation side was -0.06 MPaG, hydrogen recovery did not decrease at lower temperatures. Different rate limiting steps in both conditions were suggested. Figure 6 shows the result of long-term reforming test using another MOC module. Hydrogen product maintained constant (4.6 - 4.9 Ncc/min/cm^2) up to near 750 hours as well as the conversion (50 -55 %). These indicated

that not only hydrogen permeation but also catalytic activity did not degrade for 750 hours at least.

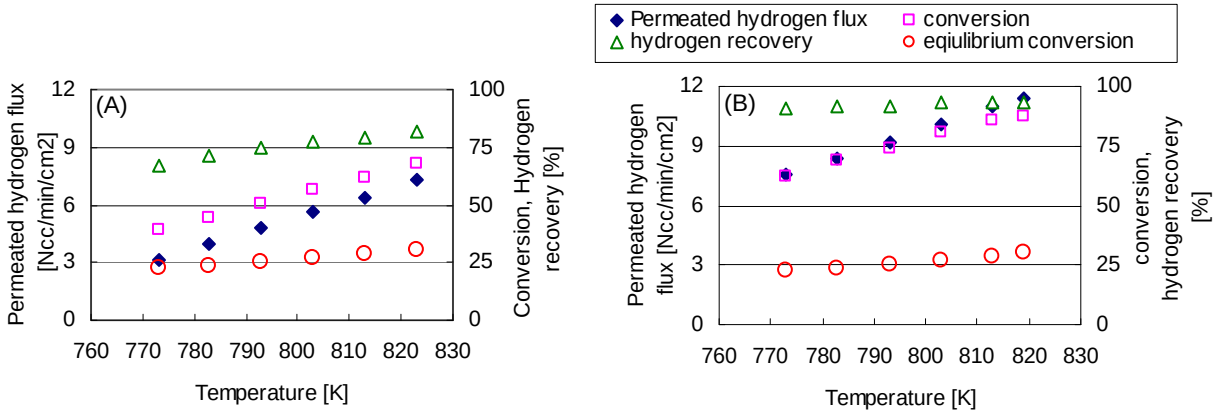

Figure 5: Reforming temperature dependence of permeated hydrogen flux, conversion and hydrogen recovery at the permeation side pressure of 0.0 MPaG (A) and of -0.06 MPaG (B).

5 Conclusions

We conducted hydrogen permeation or reforming tests using MOC modules at 823 K. Hydrogen permeability of membrane and catalytic activity were both demonstrated to have a long-term stability. However, pin-holes were formed and some leakages were observed. We will solve this problem and aim to have more durability for 8000 hours.

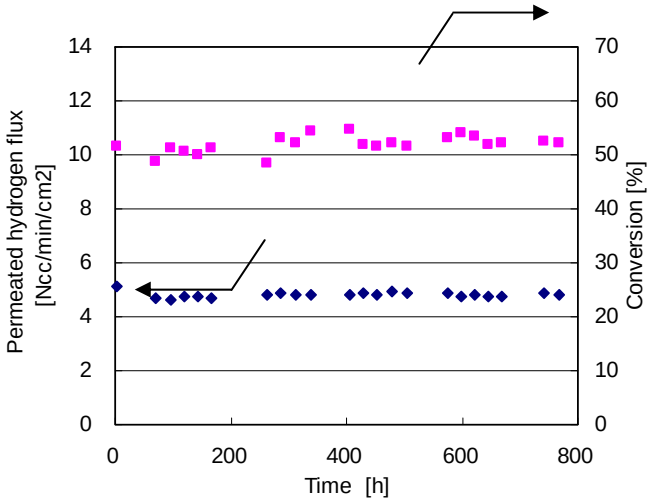

Figure 6: Long-term reforming test of a 100 mm long MOC module at 823 K.

Acknowledgements

This work was supported by the New Energy and Industrial Technology Development Organization (NEDO). The authors acknowledge their financial and technical supports.

References

[1] Y. Shirasaki, T. Tsuneki, Y. Ota, I. Yasuda, S. Tachibana, H. Nakajima, K. Kobayashi, Int. J. Hydrogen Energy 34, p4482-4487, 2009.

[2] I. Yasuda, T. Tsuneki, Y. Shirasaki and T. Shimamori, presented at Fuel Cell Seminar 2005, Parm Springs, November 2005.

[3] T. Tsuneki, Y Shirasaki, I. Yasuda, T. Shimamori, H. Shigaki, H. Tanaka, presented at 9th International Conference on Inorganic Membranes, Lillehammer, June 2006.

[4] H. Kurokawa, T. Tsuneki, Y. Shirasaki, I. Yasuda, T. Shimamori, H. Shigaki, H. Tanaka, K. Mitsuya, presented at Fuel Cell Seminar 2007, San Antonio, October 2007.

[5] T. Nishii, T. Tsuneki, H. Kurokawa, Y. Shirasaki, I. Yasuda, T. Shimamori, H Shigaki, H. Tanaka, K. Mitsuya, presented at Fuel Cell Seminar 2008, Phoenix, October 2008.

[6] T. Nishii, Y. Shirasaki, H. Kurokawa, I. Yasuda, T. Shimamori, Y. Takagi, H Shigaki, H. Hikosaka, H. Tanaka, K. Mitsuya, presented at 9th International Conference on Catalysis in Membrane Reactors, Lyon, July 2009.

The Effect of Hydrogen on Transport Properties of Highly Permeable Metal Membranes

Christian Zillich, **Jürgen Roes**, **Angelika Heinzel**, University Duisburg-Essen, Germany

1 Introduction

Highly permeable metal membranes for hydrogen separation in fuel cell systems have the potential to reduce system complexity and increase system efficiency. The mechanism of hydrogen permeation leads to almost ideal selectivity of metal membranes. Within this mechanism diffusion of hydrogen through the metal, which is generally considered being Fickian type diffusion, is often regarded to be the limiting step. Under high hydrogen loads this functional representation is not sufficient. Hydrogen interactions within the metal lead to a concentration dependent diffusion coefficient and hydrogen induced stresses have to be taken into account as part of the chemical potential of hydrogen. By permeation experiments with a palladium silver capillary membrane we show the influence of hydrogen on permeation rate and develop a model that fully accounts for the effects mentioned above and explains the unusual permeation characteristic of this membrane.

2 Experimental Procedure

Hydrogen permeation rates through a palladium silver (PdAg) capillary membrane were measured at temperatures between 200 °C and 500 °C. Experiments were carried out using pure (99.999 %) hydrogen. High feed pressures of up to 9 bar were applied on the outside of the membrane. After permeating through the capillary wall hydrogen left only through one end of the capillary at approximately atmospheric pressure. Hydrogen flow was measured with a bubble flow meter. The other end of the capillary was kept closed while the membrane was allowed to expand freely under high hydrogen loads.

3 Experimental Results

As can be seen in Figure 1 permeation rates show a large increase between 200 °C and 250 °C and a strong change in dependence on feed pressure. At temperatures between 300 °C and 380 °C permeation rates do not change within experimental error. At higher temperatures permeation rates show a low increase with increasing temperature.

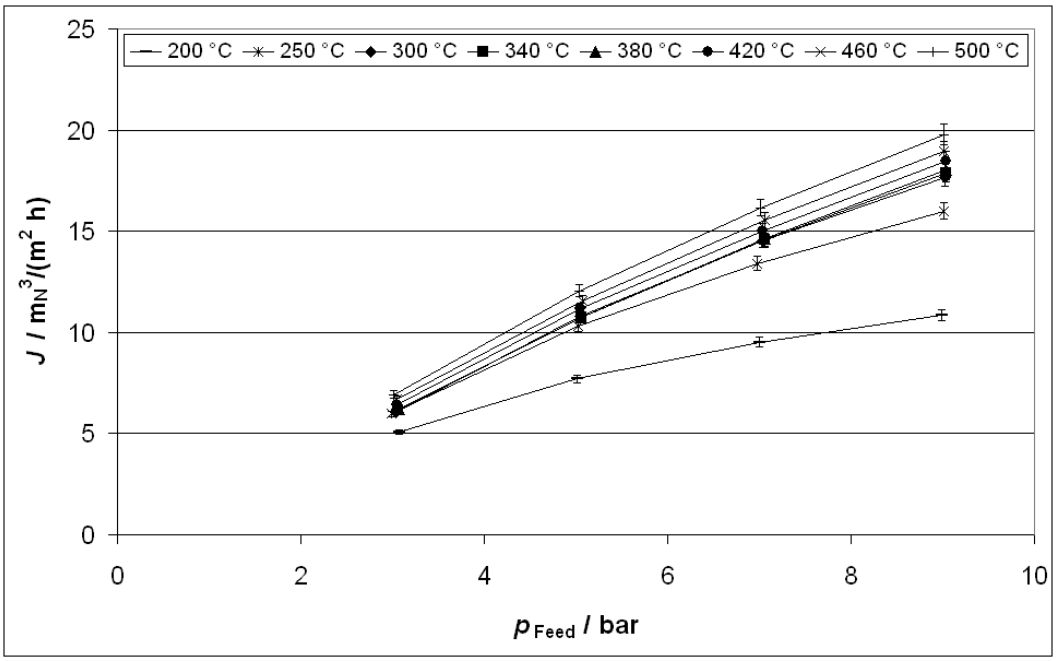

Figure 1: Permeation rates through the capillary PdAg membrane.

4 Model Development

To investigate the cause of this permeation behaviour a permeation model for PdAg was developed based on a well known model by *Ward and Dao* [1] for pure Pd that takes into account all transport steps of the hydrogen permeation mechanism through metals.

Using hydrogen partial pressures on the feed and permeate side and membrane temperatures that were applied during the experiments permeation rates were calculated using the new model. However the results did neither match the experimental values nor could explain the origin of the unusual permeation characteristic. Measured permeation rates were higher than the calculated fluxes up to a temperature of 420 °C. Calculations showed that hydrogen permeation through the capillary should be mainly limited by diffusion through bulk metal above about 250 °C.

The diffusion flux is represented by a Fickian type diffusion equation in the model. But hydrogen diffusion in metals especially under high hydrogen concentrations is more accurately represented by

$$J = -M(c)c\nabla\mu \ , \tag{1}$$

where $M(c)$ is the mobility of hydrogen atoms which can be related to the macroscopic diffusion coefficient, c is the hydrogen concentration in the metal an μ is the chemical potential of hydrogen in the membrane. To adequately model the diffusion flux of hydrogen through PdAg under high hydrogen concentration the concentration dependent diffusion coefficient (the mobility) of hydrogen must be known as well as the chemical potential gradient in the membrane.

To calculate the diffusion coefficient it has to be taken into account that hydrogen diffusion takes place via activated jumps between interstitial sites. Whether a jump between a starting interstitial site *i* and a target interstitial site *j* takes place is mainly dependent on

- the jump frequency of hydrogen atoms,
- the probability that a hydrogen atom occupies interstitial site *i*,
- the probability that interstitial site *j* is not occupied,
- the probability that *j* is a next neighbour site of *i*,
- the probability that the hydrogen atom is capable of overcoming the activation energy of the jump due to its thermal energy and
- the interaction between hydrogen atoms and between hydrogen atoms and the host metal.

A solubility model of hydrogen in PdAg that is able to cover the thermodynamic aspects of diffusion (site occupancy, interactions) was taken from *Salomons et al.* [2]. A diffusion model for hydrogen in a binary alloy that is compatible to the solubility model was taken from *Brouwer et al.* [3] and modified to describe hydrogen diffusion in face centered cubic binary alloys via octahedral sites, namely palladium silver. It turned out to be essential that hydrogen diffusion through PdAg is mainly governed by jumps through Pd-rich sites as stated by *Züchner et al.* [4]. We found that taking into account only diffusion through octahedral sites with six or five Pd atoms leads to reasonable results which is in agreement with the findings of *Züchner et al.* [4] for a $Pd_{90}Ag_{10}$ alloy.

Values of the diffusion coefficient at negligible hydrogen concentrations depending on the silver concentration in the alloy were calculated and compared to literature data from *Holleck* [5] between 300 °C and 600 °C. The calculated values agree well with the values of *Holleck* [5] up to an Ag concentration of 30 %. At higher silver contents and lower temperatures the modelled values deviate somewhat from the measured values. However since PdAg alloys with Ag contents above 30 % are not regarded to be suitable alloys for membranes used for hydrogen separation the model was considered to be sufficiently accurate.

Additionally concentration profiles in a $Pd_{77}Ag_{23}$ membrane at 150 °C and high hydrogen feed concentrations have been calculated. The profiles show a strong dependence on feed concentration and agree very well with profiles that have been calculated by *Wang et al.* [6].

To include the total influence of the chemical potential gradient of hydrogen in the membrane, the hydrostatic stress gradient has to be taken into account. This gradient is generated by the non-uniform hydrogen induced expansion of the capillary in radial direction due to the concentration gradient in the metal.

The hydrostatic stress component σ_h in a freely expanding cylindrical membrane can be calculated by

$$\sigma_h = -\frac{2}{9}\frac{V_H E\, n}{(1-\nu)}\left(c(r)-\bar{c}\right) \tag{2}$$

where V_H is the partial molar volume of hydrogen in the metal (1,81 x 10^{-6} m^3/mol_H), E is young's modulus (120 GPa), n is the number of metal atoms per volume, ν is the Poisson ratio (0,39), c(r) is the hydrogen concentration in the membrane and $\overline{C}$ is the mean concentration of hydrogen.

5 Discussion of Model Results

To show the influence of high hydrogen concentrations on hydrogen transport through the PdAg capillary permeation rates were calculated using experimental parameters and assuming equilibrium between hydrogen in the gas and in the membrane on the feed and permeate side. For temperatures of 200 C and 250 °C these permeation rates exceed experimental values by about 30 %, however show a similar increase with temperature and a similar change in pressure dependence. It can be assumed that this deviation exists because the assumption of linear elastic material behaviour does not apply under high hydrogen concentration and stresses that presumably existed in the metal. For temperatures between 300 °C and 500 °C relative deviations of the calculated permeation rates from the experimental values are shown in Figure 2. The dashed lines represent the experimental error.

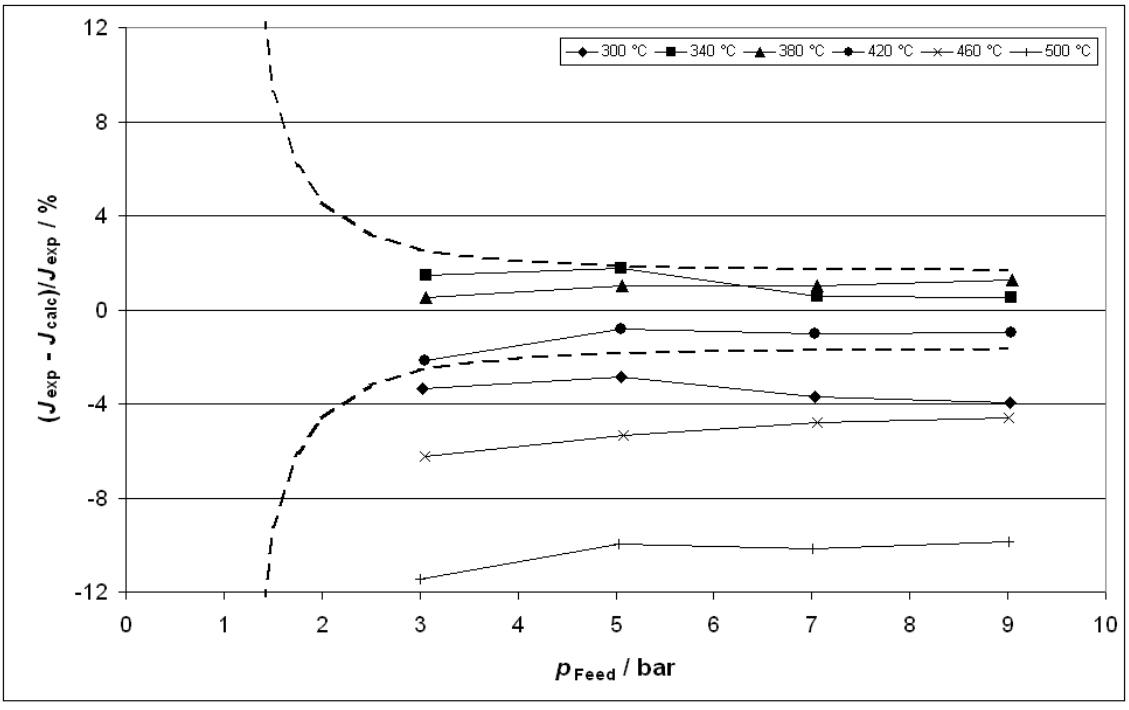

Figure 2: Relative deviations of measured and modelled permeation rates between 300 °C and 500 °C.

It can be seen that between 340 °C and 420 °C the model values coincide with the experimental values within the experimental error. At 300 °C the measured permeation rates are about 4 % lower than the calculated values. Above 420 °C the increase of modelled permeation rates tends to be higher than the increase of the measured ones, which is

probably caused by an over-prediction of hydrogen concentrations in the metal by the solubility model of *Salomons et al*. [2]. No parameters were used to fit modeling data to experimental results.

For a hydrogen partial feed pressure of 9 bar hydrostatic stresses in the capillary were calculated. On the feed side the metal is under compressible stresses between about –600 MPa and –200 MPa. Calculated hydrostatic tensile stresses on the permeate side reach as high as 800 MPa at 250 °C. These large tensile stresses probably exceed the yield stress of the metal. Further investigation is needed to explain why the membrane was not severely damaged under these conditions.

Although hydrogen solubility at 200 °C is higher than at 250 °C maximum stresses occur at 250 °C due to an increasing overall concentration gradient in the membrane between 200 °C and 250 °C that also causes the large increase of permeation rates in this temperature range.

6 Conclusions

A freely expanding capillary membrane shows unusual permeation behaviour between 200 °C and 500 °C at elevated hydrogen partial feed pressures up to 9 bar. To explain this permeation behaviour a detailed permeation model was set up that fully accounts for all transport steps of the hydrogen permeation mechanism through metals. Calculations with this model show that permeation through the capillary was limited by diffusion, however fails to explain the permeation characteristic. By developing a model for the concentration dependent diffusion coefficient of hydrogen through PdAg and taking into account the effect of hydrostatic stress gradient on permeation the permeation model was improved. Calculations show that the unusual permeation characteristic of the capillary can be explained by hydrogen interactions within the metal and the stress gradient generated by hydrogen induced expansion of the metal. The gradient of hydrostatic stress improves hydrogen permeation in freely expanding cylindrical membranes. The permeation model can also be used to predict hydrogen induced stresses in PdAg.

References

[1] *Ward, T and Dao, T*: Model of hydrogen permeation behaviour in palladium membranes. Journal of Membrane Science, 153, 1999, 211-231

[2] *Salomons, E, Hemmes, H and Griessen, R*: Hydrogen spectroscopy of $Pd_{1-y}Ag_y$ and $Pd_{1-y}Cu_y$ alloys. Journal of Physics: Condensed Matter, 2, 1990, 817-834

[3] *Brouwer, R, Salomons, E and Griessen, R*: Diffusion of hydrogen in Nb1-yVy alloys. Physical Review B, 38 (5), 1988, 10217-10226

[4] *Züchner, H, Barlag, H and Majer, G*: The existence of more than one jump process of hydrogen in palladium-silver alloys – an NMR study. Journal of Alloys and Compounds, 330-332, 2002, 448-453

[5] *Holleck, G*: Diffusion and solubility of hydrogen in palladium and palladium-silver alloys. The Journal of Physical Chemistry, 74 (3), 1970, 503-511

[6] *Wang, D, Flanagan, T and Shanahan, K*: Diffusion of H through Pd-Ag alloys (423 – 523 K). Journal of Physical Chemistry B, 112, 2008, 1135-1148

Hydrogen System Assessment: Recent Trends and Insights

Joan M. Ogden

Abstract

The potential role of hydrogen in the world's future energy system has been analyzed in many assessments and remains a topic of vigorous, ongoing debate. A hydrogen economy involves not only new types of vehicles, but a new fuel infrastructure and development of low carbon primary resources. Given the number of possible configurations for a future hydrogen economy, systems analysis plays a key role in informing decision-makers in government and industry about the best hydrogen strategies and the prospects for hydrogen as compared to alternatives such as electricity, biofuels or fossil-derived liquid fuels.

While early assessments presented a vision of an "end-state" hydrogen economy, recent analyses have focused more on transitions: what is required to move toward widespread use of hydrogen energy starting from today's energy system. To understand the dynamics of transitions, analysts are using increasingly sophisticated tools: models of consumer choice and decision-making, infrastructure design models including spatial optimization and regional geographic data, and energy system modeling including interactions with the rest of the energy system. Lifecycle assessment is an important method for comparing the societal benefits of hydrogen to other fuels, considering the entire system, across multiple dimensions.

In this paper, I present an overview of recent trends in hydrogen system modeling and results from hydrogen systems assessments. In the last section, I propose a multi-attribute framework for evaluating hydrogen and other future fuels with respect to technical performance, cost, energy use, infrastructure development and greenhouse gas (GHG) emissions, while considering air pollution, energy security and reliability, water use, land use, and materials requirements. The goal is to illuminate hydrogen transition pathways that are viable across a wide range of economic and sustainability constraints, and to compare to other energy pathways.

Utilisation of Excess Wind Power for Hydrogen Production in Northern Germany

Christoph Stiller, Jan Michalski, Ludwig-Bölkow-Systemtechnik GmbH, Germany

1 Introduction

With more than 20 GW of installed wind power capacity in Northern Germany and more to come due to the expansion of offshore wind power there are periods when the available wind power exceeds the capacity of the electricity grid or even the electricity demand within reach. This excess wind power could be utilized for the electrolytic production of hydrogen, which can be stored and used as a transportation fuel, as a feedstock for the chemical industry, or even for power production in times of low renewable generation.

This paper will first review the current framework of the German electricity generation. Then, based on the expected electricity generation and demand, the amount of excess power available for hydrogen production will be estimated. This will be followed by a discussion of operation models for hydrogen electrolysis, rounded off by a discussion of required storage demand and possible uses of the hydrogen.

2 General Framework of the German Electricity Generation

Since 1990, electricity production in Germany has only increased by about 0.8% p.a. on average, and almost the entire surplus has been covered by renewable electricity [1].

Due to the age structure of the power plant park and in view of the planned nuclear phase-out, currently a large number of new fossil power plant projects (especially hard coal) are in the planning phase; yet, it needs to be mentioned that partially, the realization is uncertain. In addition, the nuclear phase-out will most likely be postponed by the new German government.

The share of renewables for electricity production in Germany has increased from 10 to 15% in only three years (2005-2008); highest shares being achieved in the North (e.g., in Schleswig-Holstein, renewable energy generation, mainly wind power, exceeds 40% of the electricity demand). Specifically in regions with high intermittent renewable capacities installed, already today grid capacity issues occur and wind turbine power need to be cut off temporarily in order not to cause grid breakdown (regulated in the renewable energy law as “feed-in management”) [2]. Further extensive renewable potentials lie within repowering of onshore wind farms and the build-out of offshore wind energy use in the North and Baltic Sea.

By 2020, according to the “Lead scenario 2009” [3], 33 GW from onshore and 9 GW from offshore wind power are expected to be fed into the German grid. The offshore feed-in is expected to grow to 24 GW by 2030. Since all offshore capacity is landed in Northern Germany (mainly in Schleswig-Holstein and Lower Saxony) where also the density of onshore generation is high, this will at times cause massive excess power production. This implies grid reinforcement and extension to transmit the power to neighboring regions;

however, even Germany-wide power production may exceed the demand and export capacities at times of low load and high wind.

Possible remedies are the temporal shift of loads by demand-side management and battery electric vehicles; however, potentials are limited both with respect to quantities and time periods over which the loads can be bridged [4]. Therefore, large-scale electricity storage will be urgently required in order to more easily integrate the further increase in intermittent renewable electricity generation into the grid.

3 Availability of Excess Power for Hydrogen Production

In order to analyse the potentials of hydrogen production from excess renewable electricity, the quantities of power surplus have to be estimated. In this sense “excess power/electricity” will be defined as the portion of power/electricity which cannot be utilised in times of high generation (renewable+fossil+nuclear) and low demand as well as export capacities of a region. In such cases the renewable generation will have to be cut off in order to assure grid stability. The quantity of excess power production depends mainly on the following four factors:

- Installed capacity of intermittent renewables, especially wind power. The feed-in of photovoltaics is less relevant in this context as it provides electricity during daytime with comparatively high demand.
- Installed capacity of conventional power plants, especially base load plants. In particular, lignite and nuclear power plants are operated at high load also in times of high winds increasing the excess power. For example, during the night of October 4th, 2009, high wind volume and low electricity demand resulted in the negative spot market price of -0.50 €/kWh. Since at this time German nuclear power plants still operated at an average load of 77%, lignite at 65%, hard coal at 12% and natural gas at 9% [5] we assume this capacity utilization as the minimum practical part load of conventional plants during situations with excess electricity.
- Electricity demand and demand profile of the region. In general, the excess electricity can be reduced either by demand-side management or by an increased demand for a given level of power supply.
- Export capacity to neighbour regions. This is not only limited by the available transfer capacities, but also by the fact that adjacent regions are meteorologically linked. In this sense, excess wind power generation may occur not only in Northern Germany but also in other regions with own wind parks. In consequence, extension of grid capacity alone is not always effective to reduce excess power.

For the calculation of the excess power, specific assumptions regarding the capacity of energy generation per type and demand curves had to be made. The minimum generation of dispatchable power plants was derived from the estimated available capacity and the minimum part load numbers mentioned above. Onshore wind power curves were based on scaled Germany-wide production curves of the reference year 2008. Wind speed data from FINO platforms in the North and Baltic Sea were used in order to calculate the offshore power curves based on the characteristics of a 5 MW turbine. To estimate the electricity demand, hourly data from 2008 provided by UCTE / ENTSOE [6] were scaled to the

respective future demand. Due to metrological linkages between adjacent regions, electricity export to neighbour countries was not considered as a way to use excess electricity. From the comparison of resulting generation and demand, the excess power generation could be estimated as shown in Figure 1.

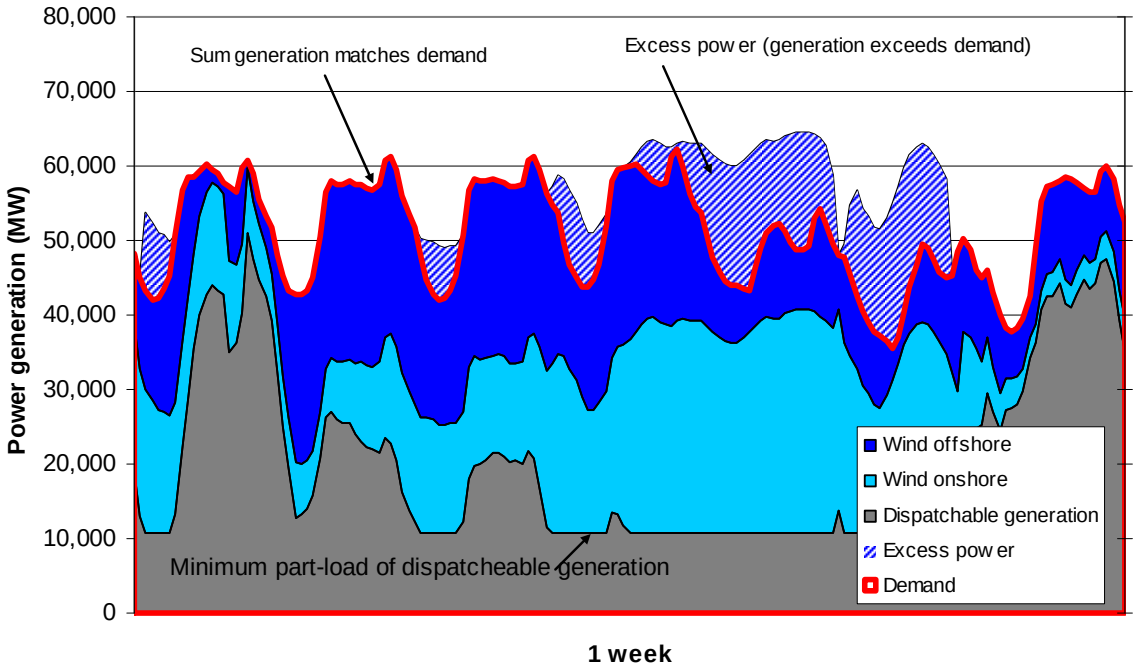

Figure 1: Methodology to determine excess power (1 week displayed).

With this methodology, the excess electricity was estimated for different scenarios based on the generation and demand projections of the “Lead scenario 2009” [3]. Two variations from the lead scenario were considered: a scenario where 15 GW nuclear generation capacity would remain online (compensated by lower capacities of hard coal and natural gas), and an extreme scenario where the 2008 values for fossil and nuclear generation capacity and demand were frozen and the onshore and offshore generation capacity ramped up as in the Lead scenario (33 GW onshore + 9 GW offshore by 2020, and 36 GW onshore + 24 GW offshore by 2030). Figure 2 shows the resulting excess power generation per year in Germany until 2030. In the lead scenario, only up to 9 TWh of excess electricity accrue until 2030 due to the consequent phase-out of fossil power plants. Retaining nuclear capacities will strongly increase excess electricity, and assuming that the power plant park of 2008 is retained while ramping up renewables, huge amounts of excess electricity will accrue until 2030. According to this estimation, by 2020 between 1.1 and 13 TWh of electricity (corresponding to 1.1-13% of overall wind power generation) cannot be used when they accrue and will therefore be available for energy storage in the form of hydrogen. For comparison, other authors with similar approaches have concluded that for whole Europe, 16 to 260 TWh excess power would accrue by 2020 [7]. Wietschel et al. [8] found that for Germany, 9 TWh excess power would accrue with 38.3 GW wind power installed, increasing to 28 TWh with 48.3 GW wind power installed.

4 Operation Model for Hydrogen Production

Northern Germany is generally an ideal location for hydrogen production from renewables and large-scale storage due to the high concentration of wind power capacity and the geologic conditions facilitating the construction of underground salt caverns suitable for hydrogen storage. With the aim to develop a sound operation strategy for hydrogen production based on the use of excess electricity while at the same time unstraining the grid in the most economic way, the location of electrolysers as well as the economics of purchasing electricity (i.e. the connection to the electricity market) are the main criteria to be addressed.

In general there are three major options for the allocation of electrolysers: directly at the larger on- and offshore wind farms, at the end user location (e.g., an industrial sites or a hydrogen refuelling station) or at grid hubs of the high or ultra-high voltage grid in the areas with the highest wind loads and the heaviest loads on the grid (e.g., along the west coast of Schleswig-Holstein). Placement directly at the wind farms helps to unstrain the electric grid regionally and super-regionally, but hydrogen production is dispersed and the distribution to the consumers is comparatively complex, especially from offshore locations. Placement directly at the consumer site omits the transportation of hydrogen, but does not unstrain the electric grid between the wind farm and the consumer. Furthermore, access to large-scale storage caverns for longer-term storage of hydrogen cannot be provided easily in either of the distributed placement strategies. Therefore we assume that placing larger electrolysis plants at grid hubs in areas with high wind power capacity is most beneficial, since this concept effectively unstrains the electric grid, efficient access to large-scale storage and efficient distribution of the produced hydrogen. The maximum electrolysis capacity installed at the grid hubs should be limited to a certain share of the upstream wind power.

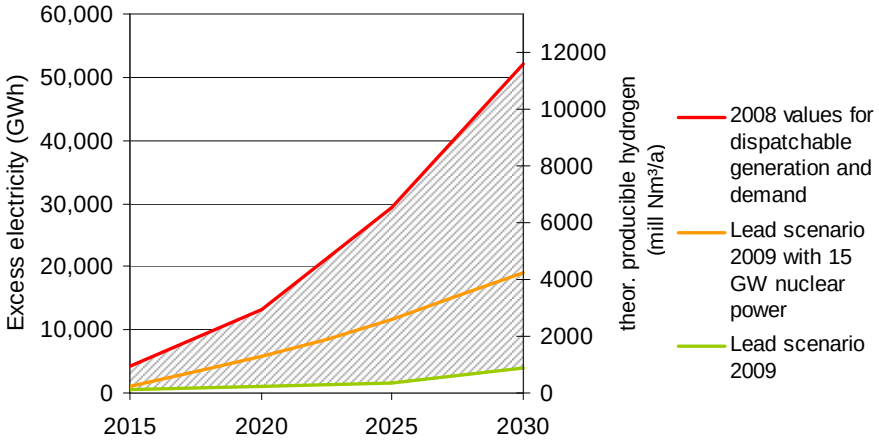

Figure 2: Resulting excess power generation in Germany through 2030.

As a price basis for the required electricity, either the feed-in tariffs for renewable electricity, or the day-ahead spot market hourly price curve of the European Energy Exchange (EEX) are reasonable. The latter can be interpreted either as purchasing the power at the EEX or directly from the wind farm operators, who otherwise would trade at EEX. Today, most wind

power is fed in according to the fixed feed-in tariffs regulated by the German Renewable Energy Law. However, it can be expected that by 2020 most wind power will be directly traded at the spot market due to the declining tariffs. Moreover, the spot market price represents the balance between electricity demand and supply: in times of low demand and high renewable energy generation the spot market price will be low, and vice versa. Hence, taking the spot market price as a base for electricity purchases ensures the operation of electrolysers in a way which indirectly unstrains the grid by using the excess electricity at low costs. As a simple operation strategy, electrolysers may be operated at full load during hours when the price is below a certain threshold, and may be kept in warm stand-by mode when the price is above the threshold. The number of operation hours per year and the average electricity price paid then depend on the price threshold set.

Further revenues for hydrogen producers can result from control reserves since electrolysers represent a controllable load within the power grid. An electrolyser can be turned off or switched on upon request in order to providing positive or negative control reserve. The provision of the so-called “minute reserve” is tendered jointly by the transmission system operators (TSO) in Germany in 4-hour blocks for the following day. It is important to mention that the pure provision of control power (without actually being called) is already compensated by a per-MW rate. While tendering for control reserve brings additional revenues to the hydrogen production, it also increases the administration effort; since the control reserve is awarded at 10:00 AM for the next day, and the day-ahead spot market auction is at noon, the operator has to rely on a forecast of the spot market price in order to decide whether the electrolyser should be operated during every 4 hour block (i.e. tender positive control reserve), or not (i.e. tender negative control reserve). Once control reserve has been awarded, the electrolyser must be operated according to the plan, even if electricity prices differ from the forecast. Therefore and due to the implication to operate in 4-hour blocks, the average electricity price levels will be somewhat higher if control reserve is to be provided.

A further benefit for the hydrogen producers can be achieved by utilising wind power from turbines temporarily cut down under “feed-in management”. The opportunity losses for wind parks caused by such incidents have to be fully compensated by the TSO according to the Renewable Energy Law. Provided that there are no grid restrictions between the wind turbines and the electrolysers, the balance could be used for hydrogen production at marginal costs. However, since the TSOs are obliged to reinforce the power grid in order to avoid such events the potential benefits from this strategy are limited and uncertain.

5 Required Storage Demand and Options for Usage of the Hydrogen

A strategy as described above will lead to varying electrolyser utilisation with a tendency to higher production in the winter time with high wind power feed-in. In order to optimally level out the seasonal variations in production and facilitate a constant delivery of hydrogen to the end customers we found that a hydrogen storage capacity of approximately 700 full load hours is needed. If the hydrogen consumption can be adapted to the availability (higher consumption in winter than in summer), the storage capacity can be lower; on the other hand, if the hydrogen consumption is inflexible and peaks in summer, the storage capacity

will need to be higher. The economic optimum of design storage capacity will be a trade-off between storage costs and timely flexibility of electrolysis operation (leading to savings in electricity costs). In the case of large-scale storage in salt caverns, the storage only contributes a minor part to the overall costs; however, if storage in e.g. aboveground pressure vessels or liquid hydrogen dewars is chosen, then the costs will be a multiple of the electrolysis costs.

A viable use of the renewable hydrogen is partial or complete substitution of hydrogen generated from natural gas for uses in chemical and process industry. Besides saving fossil primary energy for hydrogen production by reforming, this has the potential to reduce the greenhouse gas emissions of the industries, improving their carbon footprint and avoiding costs of CO_2 certificates.

Hydrogen in road transportation will be an emerging market in the mid term. Offering hydrogen from renewables at the refuelling stations to be erected is an interesting option, especially when considering the fact that the consumers might prefer “green hydrogen” and could also be forced by legislation (California has already implemented a law that 33% of all hydrogen for transportation will need to be renewable).

The hydrogen could further be used for power generation (so-called re-electrification) in combined cycle gas turbines. Co-firing with natural gas at flexible shares is technically feasible. Re-electrification is a way to stabilise the electric grid by not only taking away power in times of excess renewable electricity but also compensate lack of renewable generation, e.g. in times of low wind.

6 Conclusion

The paper showed that due to the ongoing build-out of intermittent renewable generation capacity and limited part-load ability of dispatchable power plants, significant amounts of excess electricity will accrue in the German electricity system in the future. This excess energy may be used to generate hydrogen, which can then be economically stored in large-scale salt caverns and utilized in industry and transportation sector or for electricity generation at times of low feed-in of renewables. An operation model based on central electrolysis plants at grid hubs, the spot market as a price basis for electricity purchases and a threshold-price strategy can yield minimum overall hydrogen production costs and at the same time facilitate effective unstraining of the grid. Northern Germany is an ideal location for storage of hydrogen from renewables in caverns since huge capacities of onshore and offshore wind energy are expected to be installed during the coming decade posing local challenges to the electric grid and furthermore since the geologic conditions are favorable for hydrogen storage in salt caverns.

References

[1] Arbeitsgemeinschaft Energiebilanzen e.V.: Electricity generation by energy carriers 1990 to 2008 (in TWh) Germany, Status 27 May 2009; http://www.ag-energiebilanzen.de/viewpage.php?idpage=65

[2] Act Revising the Legislation on Renewable Energy Sources in the Electricity Sector and Amending Related Provisions – Renewable Energy Sources Act (EEG 2009) –

official document, Federal Law Gazette (Bundesanzeiger) 2008 I No. 49, Bonn, 31 October 2008, p. 2074.

[3] German Federal Ministry for the Environment, Nature Conservation and Nuclear Safety: Lead scenario 2009. http://www.bmu.de/files/pdfs/allgemein/application/pdf/leitszenario2009.pdf

[4] Klobasa, M.; Nachfrageseitige Regelungsmöglichkeiten im Energiesystem; in: EnInnov 08, 10. Symposium Energieinnovation. Energiewende: 13.-15. Februar 2008; TU Graz: Verlag der TU Graz, 2008; ISBN: 978-3-902465-94-8, S. 89-90

[5] EEX Transparency data, power plant information (visited October 2009). http://www.eex.com/en/Transparency/Power%20plant%20information

[6] European Network of Transmission System Operators for Electricity: Hourly load values of a specific country for a specific month; http://www.entsoe.eu/index.php?id=92, visited October 2009

[7] C. Hoffmann, M. Greiner, L. Von Bremen, K. Knorr, S. Bofinger, M. Speckmann, K. Rohrig: Design of transport and storage capacities for a future European power supply system with a high share of renewable energies. IRES Conference 2008, Berlin, 24-25 November 2008.

[8] M. Wietschel, U. Hasenauer, N. Juncà Vicens, M. Klobasa, P. Seydel: Ein Vergleich unterschiedlicher Speichermedien für überschüssigen Windstrom. Zeitschrift für Energiewirtschaft 30 (2006) 2, p. 103-114.

Techno-economic and Market Assessment of Decentralised Hydrogen Production Technologies for Early Markets in the UK

Marcello Contestabile, Imperial College London, UK

1 Overview

The early phases of the mass market uptake of hydrogen as an energy vector in both transport and stationary applications will require the availability of decentralised hydrogen production technologies that satisfy the technical, economic and environmental requirements of these markets as they rapidly grow. Decentralised technologies that are closest to commercial viability are reforming of natural gas and of liquid bio-derived fuels, and water electrolysis. However, costs still need to come down and technical barriers remain; significant R&D activity is devoted internationally to addressing these problems by developing innovative systems, subsystems and components for hydrogen production and purification.

The recently funded, £5M UK EPSRC project “Delivery of Sustainable Hydrogen” focuses on the development and integration of innovative membranes and catalysts for hydrogen production and purification using fossil fuels, biomass and electricity as feedstock. As part of the project, a rigorous techno-economic, environmental and market assessment of these technologies is also being carried out. This paper will present preliminary results of the assessment, which uses a bottom-up, techno-economic modelling approach to investigate the potential role of improved decentralised hydrogen production technologies in enabling the developing of early mass markets.

The analysis is based on case studies, where specific market, geographic, policy and resource aspects are accounted for. The first case study will be based on London and more case studies will follow for other key locations in the UK. This provides a realistic approach to estimating the market potential of technologies and to defining minimum technical and economic targets for their initial commercialisation. Preliminary results from the London case study will be presented at the conference.

2 Methodology

The methodology used for the analysis is graphically represented in the Figure.

Demand scenarios are built based on current and future planned demonstration projects in London and likely follow-ups. The scenarios are developed by combining local policy and market drivers and barriers with technology development scenarios. Local policy and market drivers and barriers are investigated by means of interviews with key stakeholder as well as analysing relevant information and data available in the public domain. Technology development scenarios on the other hand are developed aided by the use of a simulation model originally described in [1] and also used in [2]. In particular, for the purposes of the present study the model is used to simulate endogenous learning in hydrogen fuel cell

powertrains technologies driven by the global uptake of hydrogen fuel cells in niche markets outside transport as well as in early transport markets and particularly urban buses.

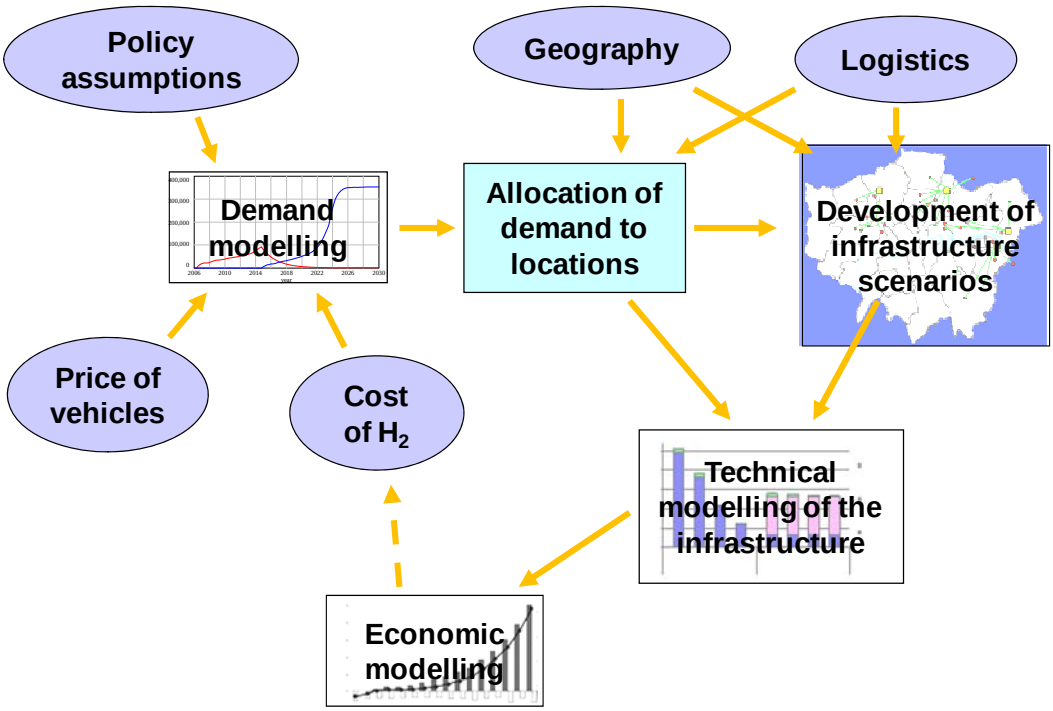

Figure: **Schematic representation of the methodology used for the techno-economic, environmental and market analysis of innovative decentralised hydrogen production technologies (adapted from [3]).**

The demand scenarios so obtained, characterised over both space and time, drive the development of local infrastructure scenarios. Possible hydrogen infrastructure options are considered, encompassing centralised, decentralised and on-site hydrogen production; however, only those options that are technically compatible with the hydrogen demand scenarios considered are selected and translated into detailed infrastructure build-up scenarios for further analysis. Choice of viable infrastructure scenarios is also informed by previous work carried out at Imperial College on hydrogen infrastructures for London, and particularly [4].

The subsequent techno-economic, environmental and financial analysis involves:

1. Detailed technical and economic characterisation of existing as well as prospective hydrogen production, purification and delivery technologies. Existing technologies are characterised based on techno-economic data available from the literature and, where possible, also on data acquired directly from industry; potential for technological learning and economies of scale is also assessed. Prospective technologies, and particularly those based on the innovative systems, subsystems and components being developed as part of the project “Delivery of Sustainable Hydrogen”, are characterised based on a combination of complementary methods,

encompassing basic scaling-up methods applied to laboratory-scale systems as well as Delphi-type surveys.

2. Development of a bottom-up hydrogen infrastructure techno-economic model and its use in the evaluation of technical, economic, environmental and financial performance and requirements of decentralised hydrogen production technologies under the demand and infrastructure scenarios previously discussed.

The bottom-up hydrogen infrastructure model is a spreadsheet scenario model which uses as main inputs the spatial and temporal hydrogen demand scenarios and also the techno-economic data of all the hydrogen production and delivery technologies that are relevant to the infrastructure scenarios considered. The model allows building a number of specific hydrogen production delivery-pathways that meet the demand for hydrogen over space and time; for each one of these pathways the model calculates key cost, emission and financial metrics for the various infrastructure components considered as well as for the cost of the hydrogen delivered, and can also be used to estimate minimum techno-economic parameters that individual production and delivery technologies need to meet in order to be commercially viable. As an example, keeping all techno-economic input data as constant, financial metrics such as Net Present Value, Payback Time and Internal Rate of Return of specific infrastructure components can be calculated. However, where uncertainty in technical input data is high, as is the case of prospective technologies, the levelised cost of hydrogen production can be set as constant, and cost and performance targets for the development of specific technologies can be explored using the model.

Finally, the results of the techno-economic, environmental and financial analysis carried out based on the infrastructure model will feedback into the demand and infrastructure scenarios, thus allowing to:

- estimate potential windows of opportunity for commercialisation of the decentralised hydrogen production technologies that are being developed as part of the project “Delivery of Sustainable Hydrogen”;
- define key technical and economic targets that, if achieved, would allow the technologies to maximise their market potential;
- estimate environmental benefits associated with the use of decentralised hydrogen production technologies as opposed to centralised options.

Work is still in progress and scenarios, techno-economic input data used in the model as well as preliminary results of the analysis will be available for presentation at the conference.

References

[1] Contestabile, M. (2006). The possible future development of a market for PEM fuel cell road vehicles – a System Dynamics based analysis within an EC-funded project. International Conference of the System Dynamics Society. Njimegen, The Netherlands.

[2] Contestabile, M. (2009). "Analysis of the market for diesel PEM fuel cell auxiliary power units onboard long-haul trucks and of its implications for the large-scale adoption of PEM FCs." Energy Policy doi:10.1016/j.enpol.2009.03.044.

[3] Joffe, D. (2005). "Scenario modelling of hydrogen infrastructure for London", EPSRC Project Workshop, Islington Business Design Centre, London, 5th May 2005.

[4] Shayegan, S., P. J. G. Pearson, et al. (2009). "Hydrogen for buses in London: A scenario analysis of changes over time in refuelling infrastructure costs." International Journal of Hydrogen Energy 34(19): 8415-8427.

Performance and Economic Competitiveness Comparison of Advanced Hydrogen Production Processes

Christine Mansilla, CEA, DEN, I-tésé, France
Pierre Baurens, Isabelle Noirot, CEA, LITEN, DTH, France
Philippe Carles, CEA, DEN, DPC, France
Jean Duhamet, Jean Leybros, Anne Saturnin, CEA, DEN, DTEC, France
Thierry Gilardi, Sabine Poitou, CEA, DEN, DTN, France
François Le Naour, CEA, DRT, DPSE, France
Jean-Charles Robin, Pascal Yvon, CEA, DEN, DDIN, France

1 Introduction

Hydrogen demand is already strong. It should significantly increase in the next few years due to the refinery industry growing needs and new applications such as synthetic fuel or biofuel production. To meet the demand advanced processes are developed throughout the world in a sustainability context. The most studied ones are thermochemical cycles: the sulphur-iodine and hybrid-sulphur cycles, and high temperature steam electrolysis. In order to compete with available technologies – alkaline water electrolysis is the only process that could enable sustainable massive hydrogen production today – advanced processes need to demonstrate their economic potential. Based on recent progress, a thorough study was carried out at CEA, from the flowsheet development to the final hydrogen production cost assessment. The methodology is first presented. Then the sulphur-iodine and hybrid-sulphur cycles coupled to a high temperature nuclear reactor are assessed. High temperature steam electrolysis also underwent a detailed study in order to identify the cost drivers.

2 Methodology

The methodology implemented at the CEA is divided into several steps (cf. Figure 1):

- a flowsheet is first developed from the experiments that are carried out at the CEA (thermodynamic data collection, corrosion test, cf. [1] for instance);
- the components are then designed and the energy consumption is assessed from the flowsheet and the process simulation;
- the investment cost is therefore evaluated based on material selection [2] as are other cost items;
- finally, the hydrogen production cost is estimated through a levelized production cost model. A common set of assumptions is of course used for the different processes that are examined.

This techno-economic model was selected because it enables quite simple production cost estimates, by limiting the number of needed assumptions, especially as regards the plant financing (contrary to the H2A model for instance, for which equity and debt shares should be provided [3]). Only one major parameter is necessary: the discount rate, the impact of

which can be assessed through a sensitivity study. Consequently, this model is a relevant tool to identify the main cost drivers for advanced processes.

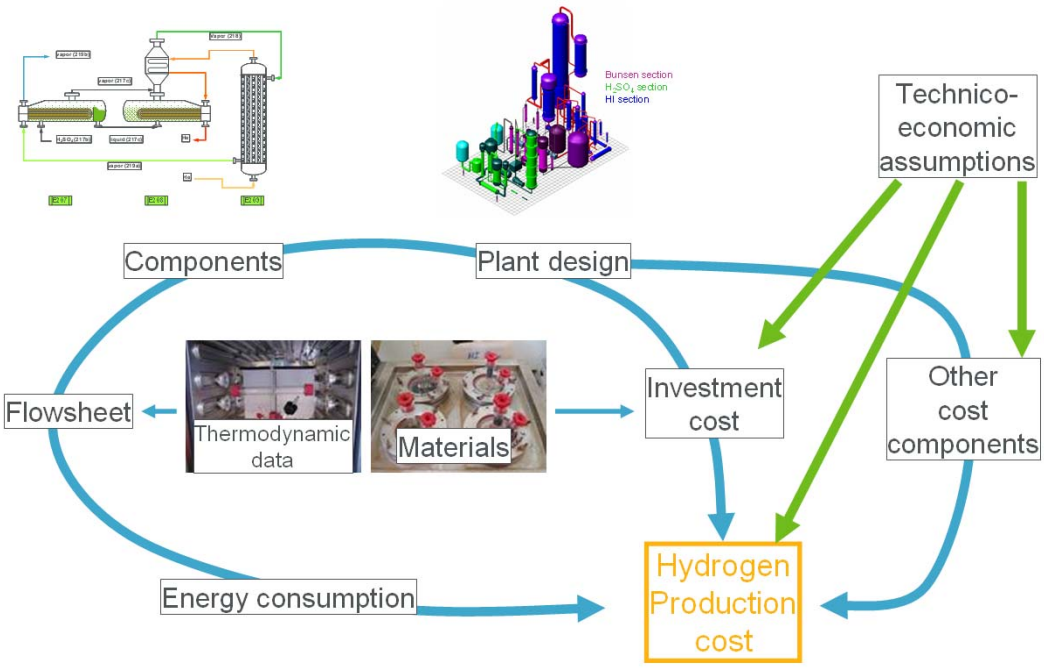

Figure 1: Methodology.

3 Considered Processes and Performance Comparison

Three processes are studied here:

- the sulphur-iodine cycle (S/I) [4],
- the hybrid-sulphur cycle (HyS) [5],
- high temperature steam electrolysis (HTSE) [6].

For space matters, they will not be detailed hereafter. One could refer to the provided references if needed.

We first examine their performances in terms of energy consumption cost. The energy consumption is assessed from a detailed flowsheet and is then not restricted to theoretical needs.

To produce 2 kg_{H2}/s, the energy demand is the following, depending on the considered process:

- 600 MW_{th} and 66 MW_e for the S/I process;
- 410 MW_{th} and 118 MW_e for the HyS process;
- 79 MW_{th} and 255 MW_e for the HTSE process.

Let us mention that the HTSE electricity consumption should be increased to consider the electrolyser performance degradation along time. To assess the energy consumption cost, 40 €/MWh_e was assumed and the thermal energy cost was calculated based on the electricity cost and the heat-to-electricity efficiency. The previous hypotheses lead to an energy consumption cost of 2 €/kg_{H2} for the S/I process and 1.8 €/kg_{H2} for HyS. Contrary to

these thermochemical cycles, HTSE does not require high temperature heat when being operated in the autothermal mode. Therefore, low cost heat can be supplied to the process. The energy consumption amounts to approximately 1.8 €/kg$_{H2}$ when including the degradation of the electrolyser performances.

From these results it appears that efficiency still needs to be improved to compete with available mature processes. The mere energy consumption cost is quite high.

4 Main Cost Drivers

The cost drivers are very different according to the considered process.

First let us consider the S/I thermochemical cycle. Given the model that was implemented, the hydrogen production cost was evaluated at 12.0 €/kg [4]. Let us recall that the energy consumption cost was estimated at 2.0 €/kg$_{H2}$. If the investment was reduced by 30%, for instance through learning effects, the production cost would be reduced to about 9 €/kg. These facts highlight the impact of the plant investment. It is related to the material selection (for the components but also the pipes): highly-resistant materials are selected (e.g. Nb-Zr liners), in order to stand the high-temperature, corrosive environment.

As a result from the high investment, the maintenance cost accounts for half the O&M cost and parameters such as the load factor or the discount rate influence quite significantly the production cost (cf. Figure 2).

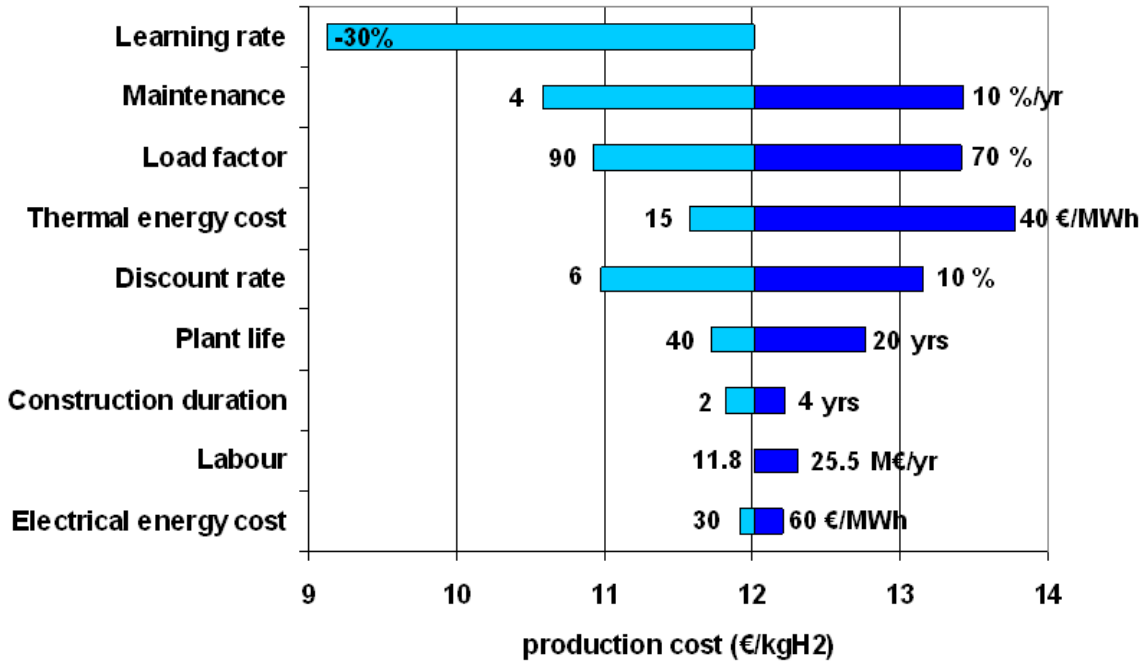

Figure 2: Parametric study around the S/I cycle production cost [4].

As regards the HyS process, the influence of the electrolyser on the final production cost should be underlined (cf. Figure 3). The electrolyser investment was based on alkaline electrolyser data and specific characteristics of HyS electrolysers (catalyst, membrane). Therefore it is quite uncertain. If the electrolyser price was increased by 50%, its investment

cost would amount to about 0.7 €/kgH2 but the total production cost would be increased by 0.5 €/kg. Besides, given its high price, if sooner replacement was needed, the hydrogen production cost would rise significantly.

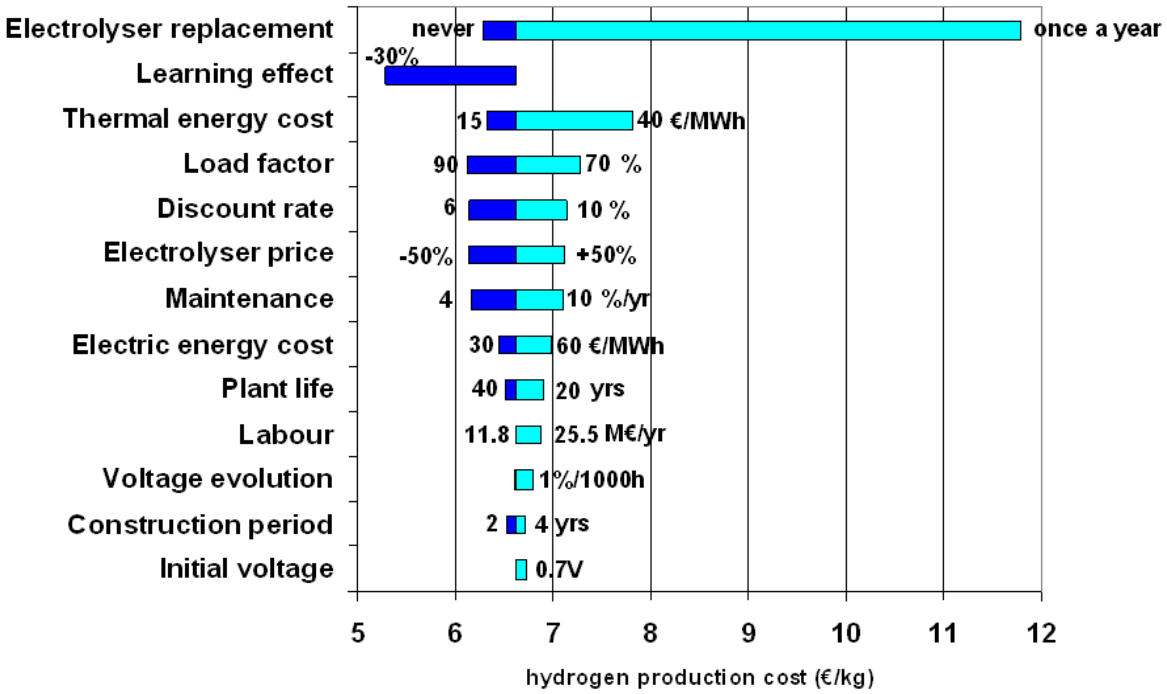

Figure 3: Parametric study around the HyS cycle production cost [5].

HTSE is an electrolysis process. Contrary to the above mentioned thermochemical cycles, an electrolyser forms the process heart. Therefore and quite logically, the electricity consumption is a major cost factor and performances should be optimised. This means that a minimum voltage should enable satisfactory current density (i.e. hydrogen production) but also that this voltage needs not to dramatically increase during operation. The other major cost driver of the process is stack replacement. Indeed, electrolysis is performed at high temperature and regular replacement should be expected. As it can be seen on Figure 4 and due to discounting, stack replacement has a high impact for 3-year lifespans (or shorter). From 3 to 5 years, its influence is mitigated. For longer lifespans, it can hardly make a difference. This could provide R&D targets.

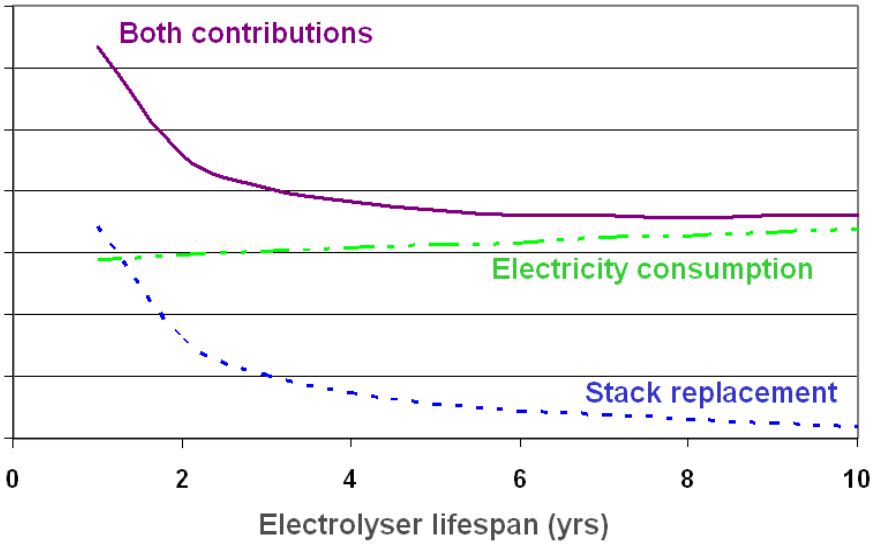

Figure 4: Impact of the electrolyser lifespan on HTSE cost items.

5 Conclusion

Economic assumptions are characterised by many uncertainty sources: raw material prices, accuracy of the cost method, high temperature thermal energy cost, only to name a few. Besides, advanced hydrogen production processes have different specificities and cost drivers: high investment cost for S/I, thermal energy consumption cost for processes appealing to high temperature heat (S/I and HyS), electrolyser performance and durability for hybrid or electrolysis processes (HyS and HTSE). Comparing hydrogen production costs, even with a common model, is then tricky. One should not focus on final figures which very much depend on the model assumptions, but use such assessments to identify trends and R&D priorities.

References

[1] D. Doizi, V. Dauvois, JL Roujou, V. Lorin, P. Fauvet, B. Larousse, et al. Experimental study of the vapour–liquid equilibria of HI–I2–H2O ternary mixtures, part 1: experimental results around the atmospheric pressure. Int J Hydrogen Energy 2009;34(10):4275–82.

[2] T. Gilardi, G. Rodriguez, A. Gomez, J. Leybros, J.M. Borgard, P. Carles, P.Anzieu. Influence of material choice on cost estimation of some key components of the Sulfur Iodine thermochemical process. In: 16thWorld Hydrogen Energy Conference,WHEC 16, Lyon, France; 2006-06-13-2006-06-16; 2006.

[3] DOE H2A. Production analysis, http://www.hydrogen.energy.gov/h2a_production.html.

[4] J. Leybros, T. Gilardi, A. Saturnin, C. Mansilla, P. Carles. 2010. Plant sizing and evaluation of hydrogen production costs from advanced processes coupled to a nuclear heat source. Part I: Sulphur-Iodine cycle. International Journal of Hydrogen Energy 35(3) 1008-1018.

[5] J. Leybros, A. Saturnin, C. Mansilla, T. Gilardi, P. Carles. 2010. Plant sizing and evaluation of hydrogen production costs from advanced processes coupled to a nuclear heat source. Part II: Hybrid-Sulphur cycle. International Journal of Hydrogen Energy 35(3) 1019-1028.

[6] R. Rivera-Tinoco. 2009. Etude technico-économique de la production d'hydrogène à partir de l'électrolyse haute temperature pour différentes sources d'énergie thermique. PhD report. Ecole Normale Supérieure des Mines de Paris.

Hydrogen Vehicle Deployment and Required Policy Support for Roll-out Scenarios in the Dutch THRIVE Project

Bart Hoevenaars, **Marcel Weeda**, **Paul Lebutsch**, **Bram v.d. Broek**, ECN - Energy Research Centre of the Netherlands, The Netherlands

Abstract

The work presented is part of the Dutch THRIVE project which centers on dynamic simulation of joint roll-out of a hydrogen refuelling infrastructure and a hydrogen vehicle fleet. The simulation tool enables modelling of fuel supplier and car manufacturer strategies, and consumer attitude towards hydrogen. A car cost model is used in the THRIVE project for the post-processing of roll-out simulation results to determine type and level of possible policy support necessary that make FCEVs cost-competitive.

1 Introduction

The Dutch THRIVE project addresses the use of hydrogen as a fuel for passenger cars in the Netherlands during the commercialisation phase. Its objective thereby is the identification of plausible rollout scenarios for both a hydrogen refuelling infrastructure as well as for a hydrogen car fleet. Attention was paid to the preferences of the motorists and the influence of the availability and visibility of both hydrogen cars as hydrogen refuelling opportunities. The methodology applied in the THRIVE project consists mainly of two steps. The first step consist of running model-simulations that generate plausible roll out scenarios for both hydrogen cars and an hydrogen infrastructure, under the assumption of level playing field conditions. The input data is bounded by coherent sets of assumptions around different levels of policy ambition regarding the stimulation of hydrogen fuelled auto mobility. During the second step, the output of the model-simulations is analysed in terms of quantitative market development, well-to-wheel efficiency and emissions and effects of policy measures. In this report, particular focus is on the analysis of the consequences of the level playing field assumption in terms of required policy support for vehicle retail prices.

2 Cost Gap Analysis

The objective of the cost gap analysis is to come to sound estimations on the amount of investment that is required to ensure the level playing fields condition. We applied the learning curve methodology which describes the fuel cell car costs as a function of the cumulative number of produced of fuel cell vehicles.

2.1 Methodology: scaling

The roll out simulations realised in the THRIVE project generate, among others, fuel cell car sales numbers in the Netherlands. Sales numbers can be translated to cumulative production numbers. Yet, the cumulative production numbers required for estimating fuel cell car cost developments should be global and not national. To estimate global cumulative production numbers, a straightforward multiplication factor of 100 has been determined which indicates

the scale of the Dutch car-fleet compared to the global car-fleet. History has shown that the introduction of new drive-train technology doesn't necessarily pick up at the constant same rate in the Netherlands as it may do in the rest of the world: after 10 years, the penetration of the ICE-hybrid in the Dutch car-fleet accelerated to a rate double to that of the global average. The general interpretation of this shift of rates is explained here by the fact that the Netherlands are generally progressive when it comes to cleaner energy technologies, yet since they do not have their own car-industry, it takes a while before the trend gains momentum. It is assumed this mechanism holds for FCEVs too. The global cumulative production numbers as derived from the simulated penetration of hydrogen vehicles in the Dutch national car fleet, for the three scenarios low, medium and high, are given in figure 1. Also the global cumulative production curve as it was estimated by the European HyWays project is plotted in the same graph.

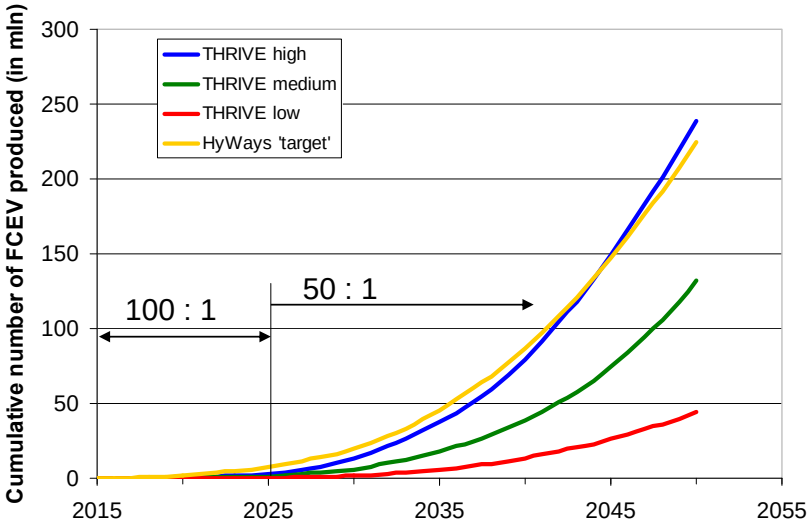

Figure 1: Global cumulative hydrogen car production numbers as derived form the THRIVE simulation results. The "high" scenario does not deviate very much from the HyWays estimations. The arrows with the ratio's indicate the interval in time over which a certain ratio is assumed.

2.2 Methodology: learning curve methodology

To estimate the future price development of hydrogen cars, a learning curve approach is applied which describes the relation between cost price and total cumulative number of units produced:

$$I(C) = I_0 * (C/C_0)^{-(\ln(pr)/\ln(2))}$$

*With **I** = cost price fuel cell vehicle, **C** = cumulative number of vehicles produced,*
***I₀** = cost price fuel cell vehicle at t = 0, **C₀** = cumulative number of vehicles produced at t = 0,*
***Pr** = progress ratio.*

We assume here that the cost price of hydrogen vehicles equals the cost price of conventional ICE vehicles minus the costs of an ICE drive-train plus the costs of a fuel cell drive-train. The drive-train consists of a fuel cell system, a hydrogen storage tank, an electromotor and a battery-pack. These three subparts differ in technological maturity. Furthermore it is assumed that learning will flatten out at a bottom cost price after 1 million vehicles produced. The values of the progress ratio for each of the subparts are given in table 1. Progress ratio **pr** is here assumed to represent the lumped sum of learning by doing, learning by searching and economy of scale. [1].

Table 1: Progress ratios, initial costs and production numbers for the subparts of a fuel cell drive-train system [2,3,4].

C_0 = 2000 (in 2013)	80 kW FC system	H_2 tank	E-motor	Battery
I_0 (€)	28 000	7 000	4 000	2 750
pr	0.80	0.90	0.90	0.90
pr after 1 mln cars	0.90	0.95	0.95	0.95

2.3 Methodology: reference car

The ICE hybrid is chosen as the benchmark for the FCEV in terms of cost price. In contrast to the fuel cell drive train, the ICE drive train will increase in price as a result of technological changes that are required to meet emission legislations, reaching it's maximum increase at around 2800,-euro [5]. The forecasted development of the cost-price of both the ICE hybrid drivetrain as well as the FC drivetrain is plotted in figure 3.

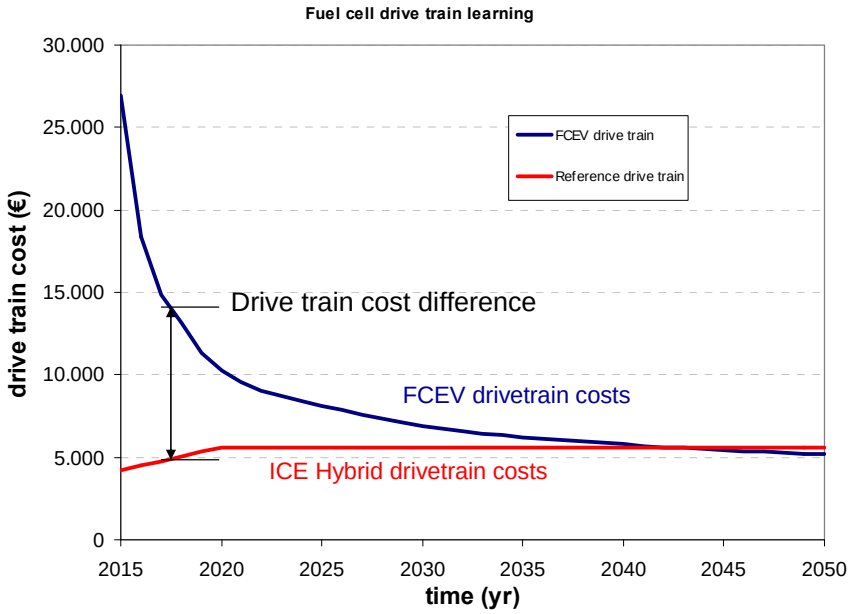

Figure 2: The expected cost price development of an 80kW fuel cell vehicle compared to that of the reference car, an 80kW ICE hybrid.

The difference between the costprice of the FCEV and the ICE hybrid in year X is the basis for calculating the cost gap in year X. The total cost-gap of a future transition equals the summation of all the annual cost-gaps over the whole transition-period 2015-2050.

3 Calculations

The annual cost-gap is calculated for the three scenario's based on low, medium and high policy ambition. The result is shown in figure 3. To get a feeling for when the FCEV cost-price is within a close range of the cost-price of the ICE hybrid, the orange crosses in figure 4 indicate when in time the FCEV costs still only 10% more than the ICE hybrid.

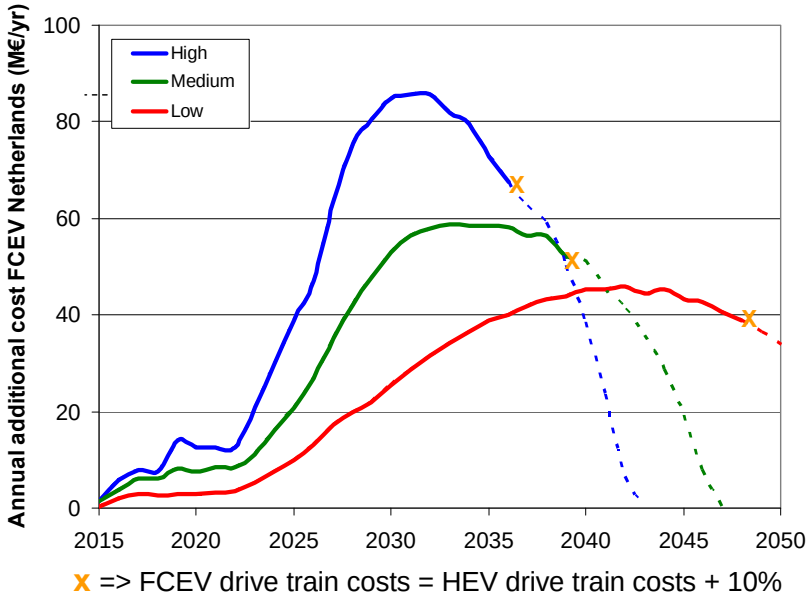

Figure 3: The annual cost-gap for the three different scenario's based on low, medium and high policy ambition.

4 Discussion

4.1 The order of magnitude of the cost-gap

The analysis performed in this study gives an indication of the range of investment required to bridge the cost-gap between FCEV's and reference cars, ICE-hybrids. Yet in order to get a feeling for the relative size of the total investment, the yearly cost-gap has been divided over the sales of non fuel cell vehicles. For the three scenarios built on low, medium and high policy level, the resulting costs per non-FCEV sold are plotted in figure 4. The figure reveals that the amount of required investment in the Dutch car-market, would translate to about 75 to 160 euro per non-FCEV car.

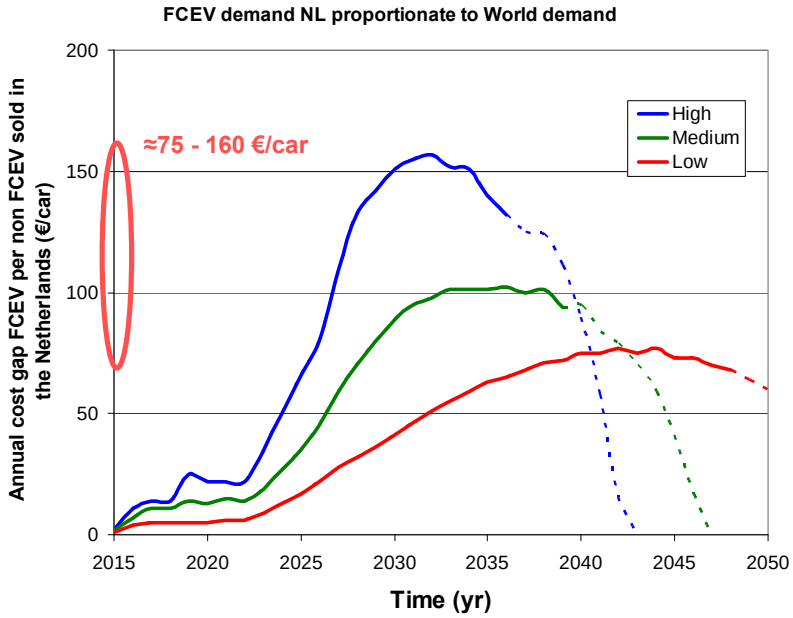

Figure 4: The annual cost gap divided by the total amount of non-FCEV's per year.

4.2 The influence of cost-reduction rates induced by different progress ratios

So far, little attention has been payed to the influence of the chosen progress ratios **Pr**. History has shown that for new technologies, progress ratios of 0.8 are rather typical and achievable. Yet the progress ratio **Pr** cannot be predicted, as it is an empirical methodology; the value for **Pr** can "officially" only be established in hindsight. Yet, an alternative approach is to establish a value for **Pr** that should be achieved, in order to keep a market situation which is competitive for FCEV's. In other words, if a **Pr** value is monitored real-time and it shows a deviation of the target **Pf** that was established as the necessary value, this can be interpreted as an indicator for the viability of FCEV's on the market. Figure 5 presents plots for different combinations of values of the progress ratio **Pr**. As was mentioned earlier, it is logical to assume that the Pr values will not be constant over time but will show flattening over time. In our calculations, we introduced two transition points in time on which the progress ratio changes: after 1 million and after 20 million cars globally produced.

4.2.1 Case I

In case I, the optimal 'default' case is analysed, this is the case that follows the **Pr** values for the different parts such as is given in table 1. This also translates to only 1 **Pr** transition after 1 mln cars and no further transition after 20 mln cars. The annual additional costs of FCEV's for the default case is one of the three curves displayed in figure 5. The figure shows that for the default case, the annual additional costs do not exceed the 100 M€ and are reduced to 0 €/year around the year 2043.

4.2.2 Case II

To analyse the influence of the progress ratio **Pr** on the annual additional costs, the value for **Pr** has been varied. The first variation on the default case is based on an increased value of **Pr** for only the fuel cell system during the first million cars. The input looks as given in table 2.

Table 2: Input for the case II scenario: Pr > 0.8 during the first million FCEV's produce. Deviations from the default case are printed in bold.

Progress Ratios	Fuel Cell	H_2 tank	E-motor	Battery
Phase I	**0.85**	0.90	0.90	0.90
Phase II > 1mln cars	0.90	0.95	0.95	0.95

In figure 5, the Case II scenario is represented by the graph named “Reduced FC cost decrease”. The sensitivity of the annual additional costs for the progress ratio **Pr** is made clear once the default case (Case I) and the “reduced FC cost decrease” (Case II) are compared. Case II leads to maximum annual additional costs of around 350 M€, whereas the maximum annual additional costs in the default case do not exceed 100 M€. Furthermore, whereas the annual additional costs have decreased to 0€ around the year 2043 in the default case, the annual additional costs in Case II are in decline after the year 2043 but still around 300 M€ in 2050. This difference is significant and already indicates the need for continuous R&D efforts to keep the progress ratio **Pr** at a minimum of 0.8 and preferably lower.

4.2.3 Case III

The third case considered, is the case which is identical to Case I up to 20 million cars. After 20 million cars however, there is a transition to higher values for the progress ratio Pr for not just the fuel cell system, but also the hydrogen tank, the electromotor and the battery pack. The input for case III is as given in table 3.

Table 3: Input for the case III scenario. After 20 million cars, the following values are introduced: Pr(fuel cell system) = 0.95, Pr(H2 tank) = 0.98, Pr(e-motor) = 0.98, Pr(battery) = 0.98. Deviations from the default case are printed in bold.

Progress Ratios	Fuel Cell	H_2 tank	E-motor	Battery
Phase I	0.80	0.90	0.90	0.90
Phase II > 1mln cars	0.90	0.95	0.95	0.95
Phase III >20mln cars	**0.95**	**0.98**	**0.98**	**0.98**

In figure 5, Case III is represented by the curve “Further decrease rate of cost reduction > 20 mln”. The annual additional costs in Case III do not exceed 175 M€, which is half the maximum annual additional costs of Case II. Yet, Case III like Case II shows a much longer period of annual additional costs than the default case, Case I. From the comparison of Cases I, II and III it can be concluded that the influence of the progress ratio Pr is much more significant in the initial stages (< 1 million cars) than in later stages. Furthermore, figure 5

indicates that in order to keep the time-interval in which annual additional costs are a reality short, it is recommended to especially keep the progress ratio **Pr** for the fuel cell system at around 0.8 or lower. This can only be achieved by continuous and sustaining R&D efforts.

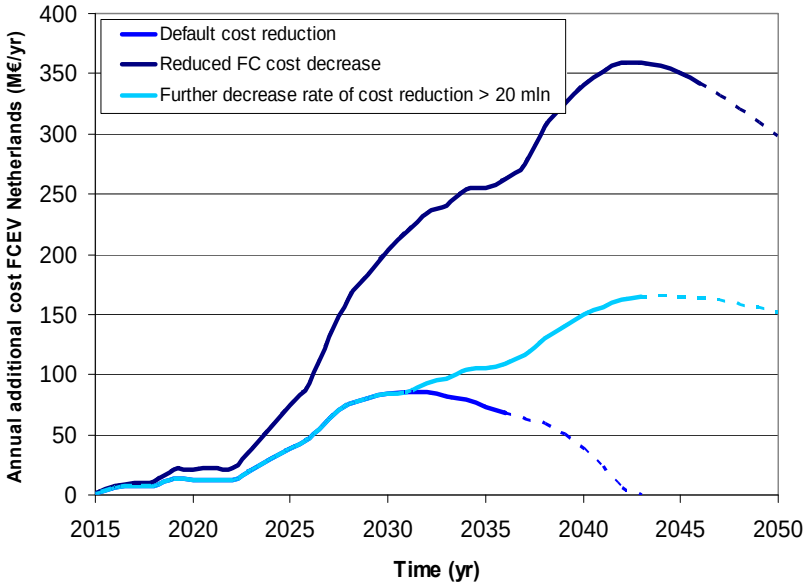

Figure 5: The annual additional costs for Case I, II and III.

5 Conclusions

This study intended to create insight in the mechanisms which shape the market for hydrogen vehicles in the Netherlands.

Calculations on the basis of estimations for input data showed that the implementation of FCEV's seems feasible. Plausible scenarios indicate annual additional costs of maximally 40 – 80 M€ which would translate to an order of magnitude of 160€ per non-FCEV sold on the Dutch car market.

In order to achieve these 'low' annual costs however, strong R&D efforts remain required in order to further decrease fuel cell system costs.

It is not the intention of this study to give accurate predictions of cost developments. There are many parameters involved, and the development of these parameters in time are uncertain: thus, uncertainty accumulates easily in the calculations. Slight perturbations in the progress rates have large consequences for long term cost developments. However, reverse reasoning allows us to explain which conditions minimally need to be fulfilled in order to make fuel cell vehicles competitive. If these conditions were to be absurd, this would lead to the conclusion that fuel cell vehicles will not be able to compete decently with mainstream alternatives.

Furthermore, there are antagonist forces when it comes to the introduction of FCEV's in the Netherlands. The Dutch car market is about 1/100 x the size of the global car-market. The

influence that the Dutch market can have on the globally induced fuel cell system cost reduction is tiny and insignificant. From that perspective, the Netherlands have an interest to be a follower, rather than an early adopter. Yet because of the integration of the European market and road-network, the Netherlands do have an interest to keep up with for example neighbouring country Germany.

References

[1] Schoots, K., Kramer, G.J., Van der Zwaan, B.C.C, Technology learning for Fuel Cells: an assessment of past and potential cost reduction, proceedings of the InternationalEnergy Workshop, Venice 2009

[2] Well-to-wheel analysis of future automotive fuels and powertrains in the European context, TANK-TO-WHEELS report Version 3, October 2008

[3] DRIVE – The future of Automotive Power, McKinsey&Company 2006

[4] HyWays D3.22 final report Socio/Economic analysis – phase II, European Commission – DG Research, May 2007

[5] Transport, Energy and CO_2 – Moving towards sustainability, IEA 2009

The Prospects of Clean and Green Hydrogen in Japan

Hiromichi Kameyama, **Hideto Kurokawa**, **Isamu Yasuda**, Tokyo Gas Co., Ltd., Japan
Gert Jan Kramer, Shell Global Solutions International, The Netherlands

1 Introduction

Because of Japan's limited opportunities for geological CO_2 storage and its high population density which limits the availability of indigenous renewable energy, transition towards a "low-carbon society" in Japan poses special challenges. Here we explore the challenges and opportunities for the production and use of clean and green hydrogen for the Japanese transport sector. In this study, clean hydrogen is produced through natural gas reforming with CO_2 capture and storage (CCS), and green hydrogen is produced by wind power and water electrolysis at suitable locations, e.g. Patagonia. As transoceanic hydrogen transport systems, liquid hydrogen (LH_2) shipment and liquid organic hydrogen carrier (LOHC) shipment are considered. Imported LH_2 and LOHC are distributed to hydrogen station and produce hydrogen at the station.

Four energy systems are compared in this study. Case 1 is clean hydrogen transported by LH_2, Case 2 is clean hydrogen transported by LOHC, Case 3 is green hydrogen transported by LH_2 and Case 4 is green hydrogen transported by LOHC. We estimated the cost and CO_2 emission intensity of each case. The hydrogen supply cost in Case 2 (clean hydrogen with LOHC) is estimated as 6.5 $/kg and is positioned as the most economically reasonable energy system, while the CO_2 emission is 5.7 kg-CO_2/kg-H_2. The CO_2 emission intensity in Case 3 (green hydrogen with LH_2) is as low as 0.7 kg-CO_2/kg-H_2 and is positioned as the least CO_2 emission energy system, while the cost of hydrogen is estimated as 10.5 $/kg.

Starting from usage of domestically produced hydrogen, then importing clean hydrogen, and finally importing green hydrogen will be a realistic approach for realization of the hydrogen society in Japan,

2 Premises and Assumptions

It has been attempted to give this feasibility study as much as possible a real-world setting. The starting point for this was to envision implementation of hydrogen production and retail in the Tokyo metropolitan area in the 2015-2020 timeframe, in accordance with the assumptions of METI for hydrogen vehicle rollout. A total fleet of 900,000 hydrogen vehicles is foreseen at that time, consuming a grand total of 150 ton per day (tpd) hydrogen. We assumed a 50 tpd "central liquid" production by natural gas steam reforming without CCS. This case is called "domestic production". The cost of this hydrogen production and delivery pathway was estimated as 5.6 $/kg and CO_2 emission intensity was estimated as 11.6 kg/kg [1], [2], [3]. These numbers are as a reference against which the cost of further CO_2 reductions of Cases 1 through 4 are measured.

Figure 1 shows a hydrogen energy chain including the four energy systems (clean hydrogen with LH_2, clean hydrogen with LOHC, green hydrogen with LH_2 and green hydrogen with LOHC). For the study of hydrogen production through natural gas reforming with CCS, LH_2

distribution and supply at a forecourt station is evaluated. For the study of hydrogen production by wind power, we assumed 45% operating rate and 900 $/kw each for wind turbine, transmission construction and electrolyzer. For the study of hydrogen importing, we assumed LH_2 case and LOHC case. The LH_2 case was evaluated based on WE-net project, which was done by NEDO in Japan. For the LOHC case, we assumed a Very Large Crude oil Carrier (VLCC) oil tanker to carry decalin and naphthalene as the hydrogen carrier. The assumed distance is 5,000 km.

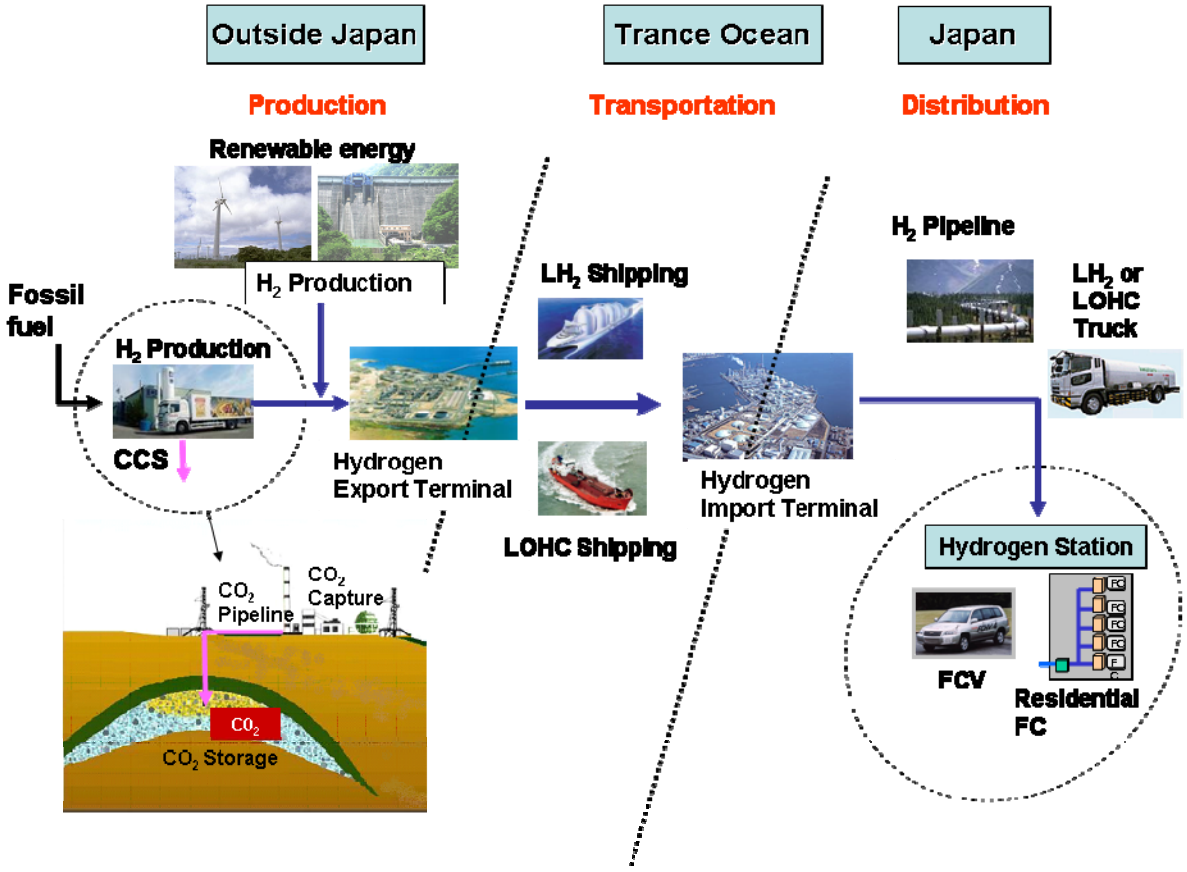

Figure 1: Hydrogen energy chain including the four energy systems (Case 1: clean hydrogen transported by LH_2, Case 2: clean hydrogen transported by LOHC, Case 3: green hydrogen transported by LH_2 and Case 4: green hydrogen transported by LOHC.)

3 Results and Discussion

Table 1 shows the results from our estimation. The cost of clean hydrogen with LOHC (Case 2) is estimated as 6.5 $/kg and is positioned as the most economically reasonable energy system, while the CO_2 emission is 5.7 kg-CO_2/kg-H_2 [4] The CO_2 emission intensity of green hydrogen with LH_2 (Case 3) is estimated as low as 0.7 kg-CO_2/kg-H_2 and is positioned as the least CO_2 emission energy system, while the cost of hydrogen is estimated as 10.5 $/kg.

Table 1: Hydrogen cost, CO_2 Emission Intensity and CO_2 Avoided cost of each case.

	Hydrogen Cost	CO_2 Emmision Intencsity	CO_2 Avoided Cost
1. NG+CCS LH_2	8.0 $/kg	5.1 kg/kg	152 $/t-CO2
2. NG+CCS LOHC	6.5 $/kg	5.7 kg/kg	154 $/t-CO2
3. Renewable LH_2	10.5 $/kg	0.7 kg/kg	450 $/t-CO2
4. Renewable LOHC	8.9 $/kg	4.5 kg/kg	453 $/t-CO2

CO_2 reduction cost analysis is one of the important methods to assess the CO_2 reduction potential and the public financial burden. RITE (Research Institute of Innovative technologies for the Earth) presented their analysis, and the image of their estimation is shown in Figure 2 [5]. The CO_2 reduction cost for the previous government's midterm target in Japan (-15% CO_2 reduction by 2020 comparing with 2005) is calculated as \$151/t-CO_2. The CO_2 reduction cost for the present government's midterm target in Japan (-25% CO_2 reduction by 2020 comparing with 1990) is calculated as \$476/t-CO_2. Nuclear power facilities and CCS technologies are not included in this analysis because of uncertainty in availability of these technologies in that time frame. The CO_2 avoidance cost of clean hydrogen with LOHC (Case 2) is 154 \$/t-CO_2, which is similar to the CO_2 abatement cost of the previous government's target in Japan. The CO_2 avoidance cost of green hydrogen with LH_2 (Case 3) is 450 \$/t-CO_2, which is a littlie bit lower than the CO_2 abatement cost of the present government's target in Japan.

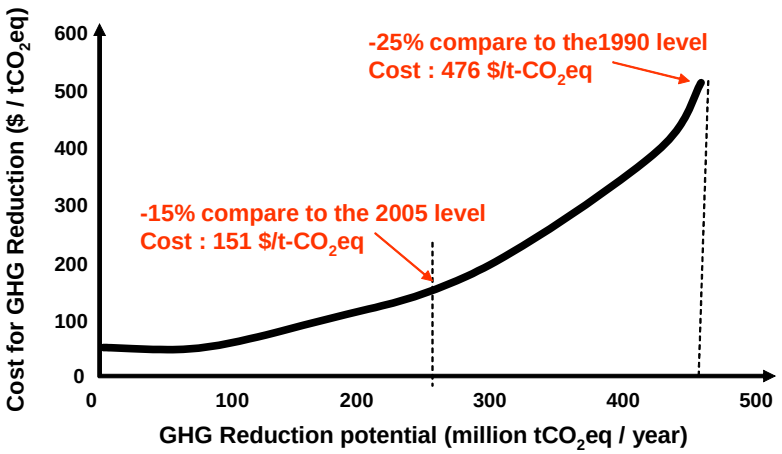

Figure 2: CO_2 reduction cost curve of Japan (by RITE) [6].

Figure 3 shows the breakdown of hydrogen cost estimated here. Comparing the hydrogen cost transported by LOHC (Case 2 and 4), cost for production has big difference. It means, we should try to decrease the cost of hydrogen production by wind power to reduce the cost of green hydrogen. The cost of hydrogen production by wind power consists of fixed cost for wind turbine, construction of transmission and electrolyzer. The variable costs are not

significant because all required energy can be supplied by electricity produced by free wind. Large-scale wind power is rapidly spreading these days, and the cost of wind turbine and construction of transmission will significantly go down in future. R&D for economical large-scale electrolyzer will be needed for further reduction of hydrogen production cost by wind power.

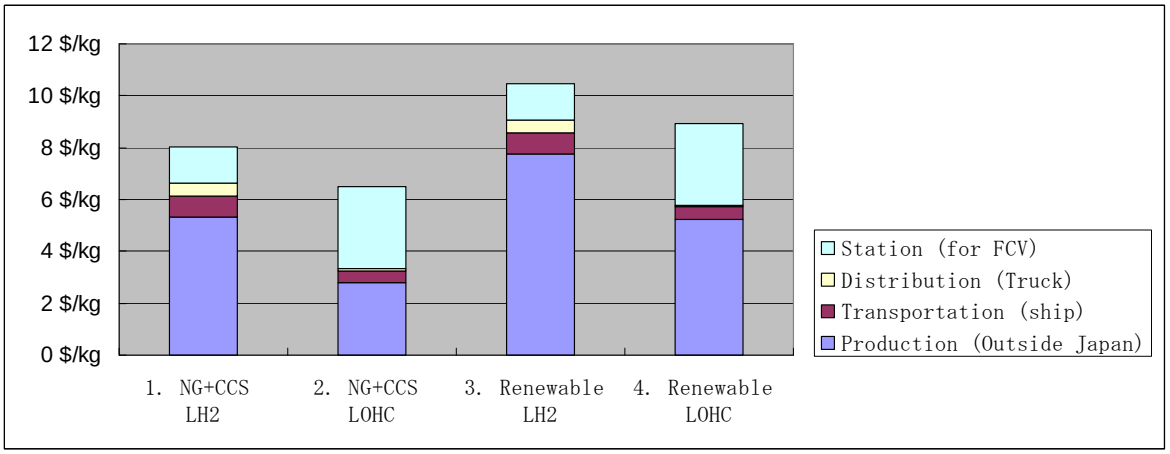

Figure 3: Breakdown of hydrogen cost.

Figure 4 shows the breakdown of CO_2 emission intensity estimated here. Over 90% of CO_2 is emitted at the station in both green hydrogen cases (Case 3 and 4). When LH_2 is used for hydrogen carrier, all CO_2 emission at the station is attributed to electricity consumption. When LOHC is used for hydrogen carrier, most CO_2 emission at the station is attributed to natural gas consumption for de-hydration. Case 3 needs most of energy at production and is supplied by CO_2 free electricity. Case 4 needs most of energy at station and required heat for heating the de-hydration reactor is supplied by natural gas burning without CCS. If the CO_2 emission intensity of heat source for case 4 becomes lower, the CO_2 emission intensity of case 4 becomes lower. Waste heat from CHP or solar heating can be considered for such heat sources.

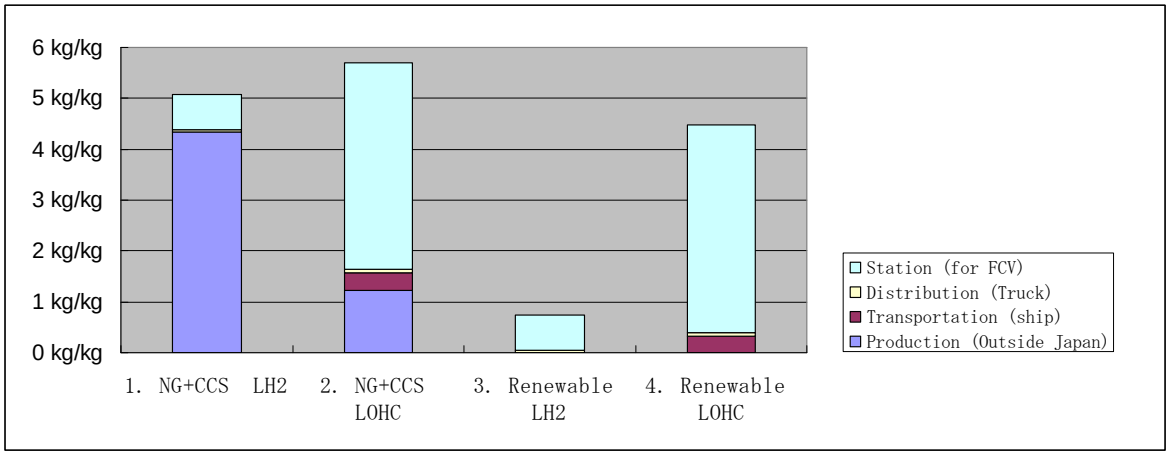

Figure 4: Breakdown of CO_2 emission intensity.

Figure 5 shows Well to Wheel CO_2 emission intensity of H_2-FCV comparison with gasoline vehicles. CO_2 emission intensity of gasoline vehicle and FCV's efficiency is assumed based on the study by JHFC [6]. Well to wheel CO_2 emission intensity of FCV depends on hydrogen source. When FCV is fueled by domestically produced hydrogen without CCS, the CO_2 intensity becomes around 1/2 comparing with that of gasoline ICE. When FCV is fueled domestically produced clean hydrogen or is fueled by imported clean hydrogen transported by LOHC, the CO_2 emission intensity becomes around 1/4 comparing with that of gasoline ICE. When FCV is fueled by imported green hydrogen transported by LH_2, CO_2 emission intensity becomes less than 1/30 comparing with that of gasoline ICE.

Importing clean and green hydrogen will contribute to transition towards a "low-carbon society" in Japan without handling CO_2 in Japan. But, we should remember that hydrogen importing needs enough hydrogen demand. If a VLCC continuously carries LOHC for hydrogen importing, over 2 billion Nm^3/yr (490 tpd) of hydrogen will be imported to Japan, and will require over 2 million FCVs to consume that amount of hydrogen. Spreading domestically produced hydrogen in Japan ahead of hydrogen importing is very important to create hydrogen demand in Japan. When hydrogen demand becomes large enough, hydrogen importing will start as LNG importing started in Japan 40 years ago.

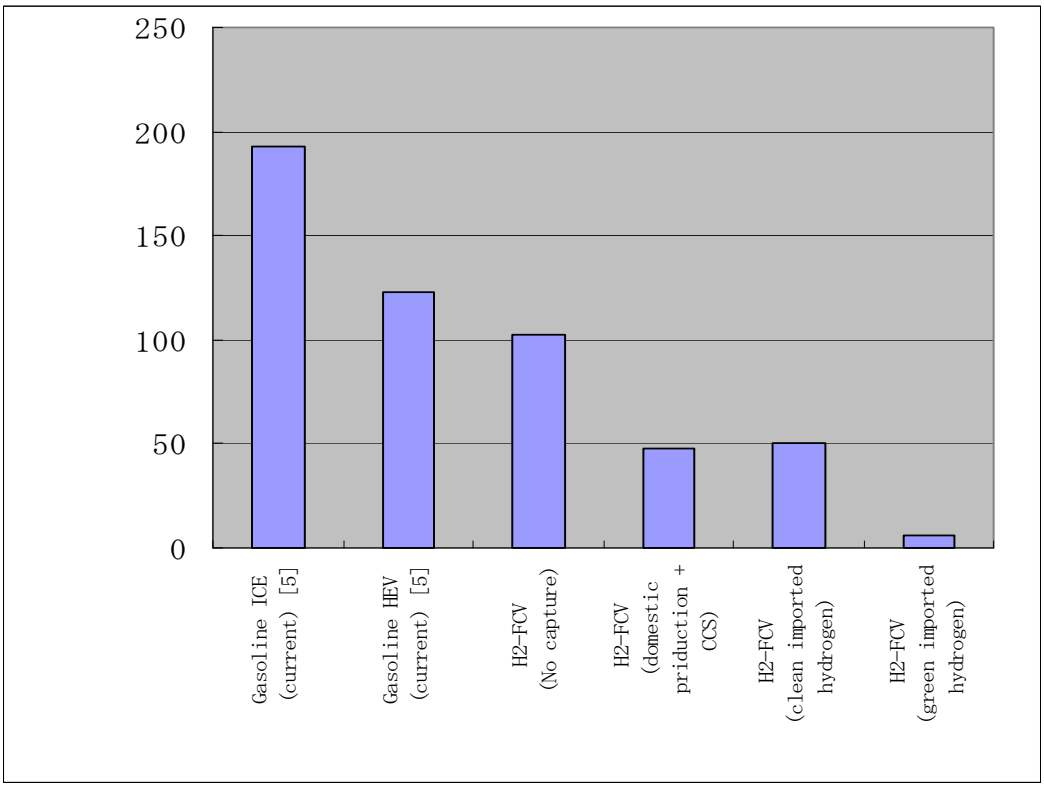

Figure 5: Well to Wheel CO_2 emission intensity of H_2-FCV comparison with gasoline vehicles.

4 Conclusion

In this paper we have explored the challenges and opportunities for the production and use of clean and green hydrogen for the Japanese transport sector. In this study, clean hydrogen

is produced through natural gas reforming with CO_2 capture and storage (CCS), and green hydrogen is produced by wind power and water electrolysis. Four energy systems (clean hydrogen with LH_2, clean hydrogen with LOHC, green hydrogen with LH_2 and green hydrogen with LOHC) are compared in this study.

The hydrogen supply cost of clean hydrogen transported by LOHC is estimated as 6.5 $/kg and is positioned as the most economically reasonable energy system, while the CO_2 emission is 5.7 kg-CO_2/kg-H_2. The CO_2 emission intensity of green hydrogen transported by LH_2 is as low as 0.7 kg-CO_2/kg-H_2 and is positioned as the least CO_2 emission energy system, while the cost of hydrogen is estimated as 10.5 $/kg. The CO_2 avoidance cost of clean hydrogen transported by LOHC is estimated as 154 $/t-$CO_2$, and is similar to the CO_2 abatement cost of previous government's midterm target in Japan (-15% CO_2 reduction by 2020 comparing with 2005). This is an important finding as it shows that the cost importing of clean hydrogen is within the range of abatement costs that Japan is expected to face, and it thereby opens up opportunities for international clean energy trade which have so far been underexplored.

Using importing clean hydrogen as fuel for FCV, CO_2 emission will be around 1/4 comparing with gasoline ICE. Using importing green hydrogen, CO_2 emission will become less than 1/30. Considering importing hydrogen needs over 2 billion Nm^3 of hydrogen demand in a year (around 2 million FCVs is required to consume the hydrogen), starting from usage of domestically produced hydrogen, then importing clean hydrogen, and finally importing green hydrogen will be a realistic approach for realization of the hydrogen society in Japan.

References

[1] G. J. Kramer, J. Huijsmans and D. Austgen, "Clean and green hydrogen", Proceedings of 16th World Hydrogen Energy Conference, CD-ROM. June 2006, Lyon, France.

[2] Isamu Yasuda, Makoto Arakawa, Satoshi Takahira, Gert Jan Kramer, Ajay Madgavkar, Shilpa Damle-Mogri, Yasuhiro Koide, Joep Huijsmans, "A Case Study of Hydrogen Fuel Production in the Greater Tokyo Area", Proceedings of World Hydrogen Technologies Convention, CD-ROM. November 2007, Montecatini Terme, Italy.

[3] Isamu Yasuda, Makoto Arakawa, Satoshi Takahira, Gert Jan Kramer, Ajay Madgavkar, Shilpa Damle-Mogri, Joep Huijsmans", Proceedings of 17th World Hydrogen Energy Conference, CD-ROM. June 2008, Brisbane, Australia.

[4] Faysal Benaskar, *Liquid Organic Hydrogen Carriers as a means to deliver "Clean Hydrogen" to Japan*, MSc thesis, Technical University of Eindhoven (2008), unpublished.

[5] Presentation by Keigo Akimoto (RITE) at "Innovative Environmental Technology Symposium" November 4 2009, Japan

[6] JHFC study about total efficiency, March 2006 http://www.jhfc.jp/data/report/2005/pdf/result_main.pdf

Process Integration Analysis of an Industrial Hydrogen Production Process

Laurence Tock, **François Maréchal**, **Christian Metzger**, Industrial Energy Systems Laboratory (LENI), EPFL, Switzerland
Philippe Arpentinier, AIR LIQUIDE, Research center Claude-Delorme, France

Abstract
The energy efficiency of an industrial hydrogen production process using steam methane reforming (SMR) combined with the water gas shift reaction (WGS) is analyzed using process integration techniques based on heat cascade calculation and pinch analysis with the aim of identifying potential measures to enhance the process performance. The challenge is to satisfy the high temperature heat demand of the SMR reaction by minimizing the consumption of natural gas to feed the combustion and to exploit at maximum the heat excess at low temperature by producing valuable steam or electricity or by performing cogeneration. By applying a systematic methodology based on energy-flow models, process integration techniques and a multi-objective optimization procedure, the process performances defined by the specific natural gas consumption and the specific steam or electricity production is optimized and analyzed for different operating conditions (i.e. air preheating, pre-reforming/reforming, WGS temperature) and process modification options like pre-reformer integration. Identified measures are to increase the production of exportable steam by consuming the entire waste heat and optimizing the steam production pressure level, and to reduce the natural gas consumption by adjusting process parameters. By these measures the performance can be varied between 0.53-0.59 kmol natural gas/kmol H_2 for the specific total natural gas consumption and 1.8-3.7 kmol steam/kmol H_2 for the specific steam production.

Keywords: Hydrogen, Steam methane reforming, Multi-objective optimization, Process integration, Thermo-economic modeling

1 Introduction

In order to satisfy the worldwide hydrogen demand, hydrogen has to be produced industrially. On an industrial scale hydrogen is synthesized mainly by chemical conversion of hydrocarbons. Due to economic reasons only a small percentage is produced by electrochemical processes being more energy-intensive. Thermal, thermochemical, biochemical and photochemical processes have so far not found many industrial applications [2]. In this study an industrial hydrogen process generating H_2 by steam methane reforming (SMR) combined with water gas shift reaction (WGS) and H_2 purification is analyzed with regard to the energy efficiency. In terms of energy performance, the challenge consists in satisfying the heat demand from the reforming reaction at high temperature and valorizing at maximum the heat excess at lower temperature. The objective of this study is to analyze the energy efficiency of the present configuration and to identify potential measures to enhance the process performance. Different process layouts with different operating conditions are

evaluated, compared and optimized systematically by applying a consistent methodology based on process flowsheeting, energy integration techniques and multi-objective optimization [1, 5, 6].

2 Process Description

The process energy flow diagram described in Figure 1 represents the process unit operations that are relevant for the energy analysis. Natural gas and steam are heated up to produce syngas ($CO+H_2$) according to the endothermic SMR reaction Eq.1. To increase the chemical conversion and accordingly the energy efficiency, the reaction is performed at different temperatures in a pre-reformer (T_{preref}) and reformer (T_{ref}) unit. After the reforming two different H_2 purification routes are followed. In the first route, the process gas is cooled down before entering the water-gas-shift reactor where the CO is converted into CO_2 and additional H_2 according to the exothermic WGS reaction Eq.2. After pressure swing absorption (PSA) highly pure H_2 (99.99%) is released. In the other route, the process gas is cooled down, separated and purified resulting in several pure streams; CO_2 stream after chemical absorption with amines (MDEA), CO stream, water stream and enriched H_2 stream (98%). Table 2 reports common operating ranges.

SMR: $CH_4 + H_2O \xrightarrow{\Delta\tilde{h}_R^0 = 206\frac{kJ}{mol}} CO + 3H_2$ Eq. 1

WGS: $CO + H_2O \xrightarrow{\Delta\tilde{h}_r^0 = -41\frac{kJ}{mol}} CO_2 + H_2$ Eq.2

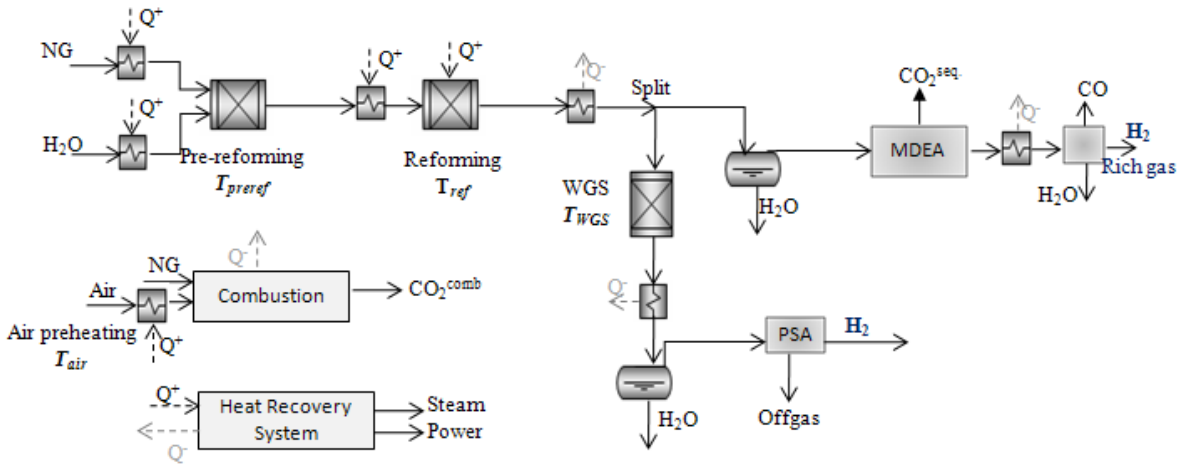

Figure 1: Process energy flow diagram.

3 Process Modeling

3.1 Method

The process is optimized by using simultaneously an energy-flow model and a separate energy integration model as described in [1]. Using a multi-objective framework, the process

operating conditions are defined in order to minimize the specific natural gas consumption and to maximize the specific steam production.

3.2 Thermodynamic model

The energy-flow model represented in Figure 1 computes the chemical and physical transformations and the associated heat transfer requirements using the commercial flowsheeting software Belsim-Vali [1]. The model being a representation of the current industrial process is developed based on the industrial process operating conditions.

3.3 Energy-integration model

The energy-integration model determines the optimal heat recovery and computes the combined heat and power production using heat cascade constraints and a linear programming model. The energy consumption of the process is minimized by calculating thermodynamically feasible energy targets and achieving them by optimizing heat recovery systems, energy supply methods and operating conditions. The energy integration model is based on the definition and identification of the hot and cold streams and their minimum approach temperature ΔT_{min} to allow heat transfer and the calculation of the heat cascade as explained in [1, 3]. A $\Delta T_{min}/2$ contribution of 4 is assumed for the gas streams.

The hot and cold composite curves illustrated in Figure 2 represent the heat needs of the process. Outside the shaded area representing the potential heat recovery, the process needs have to be satisfied by a hot utility delivering heat to the process at higher temperatures and by a cold utility dissipating heat from the process at lower temperatures.

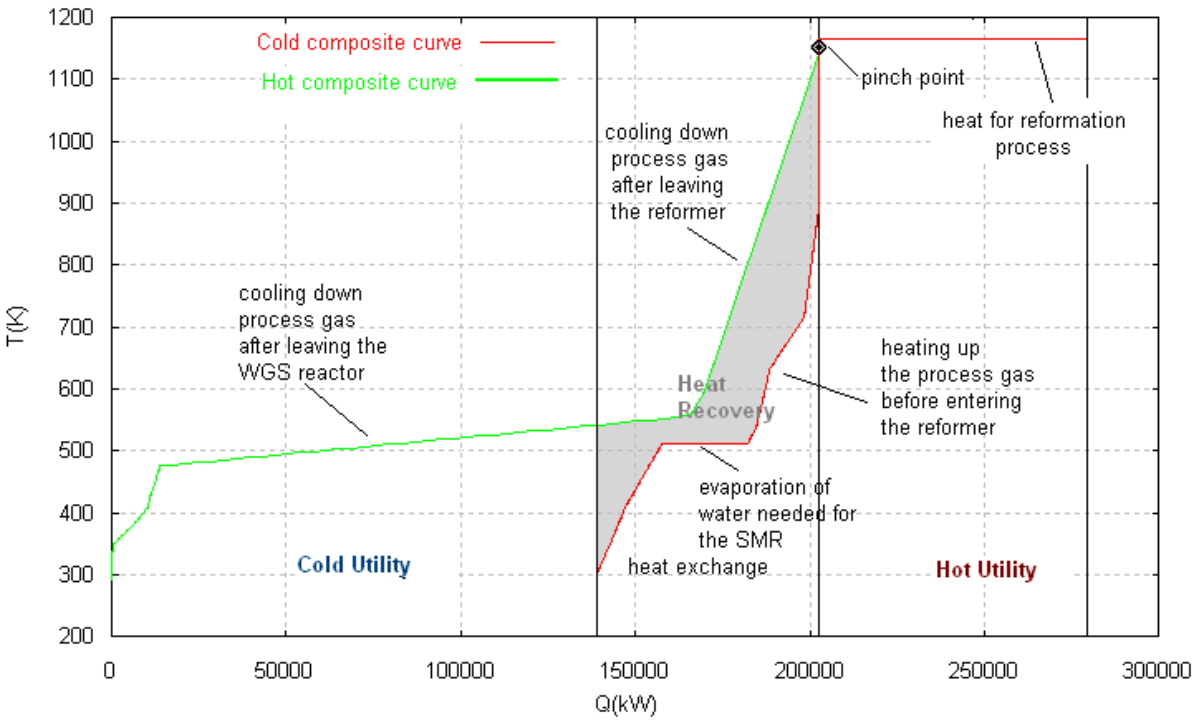

Figure 2: Hot and cold composite curves of the industrial hydrogen process.

The grand composite curve with the integrated utilities represented in Figure 3 visualizes the process energy integration.

Above the pinch point the heat required by the endothermic reforming process is satisfied by the combustion of natural gas and optionally depleted hydrogen streams (hot utility). The applied combustion model considers radiative and convective heat transfer of the flue gas, as well as the preheating of the air feeding the combustion. Below the pinch point the process is a heat source and heat has to be dissipated from the process. A stream of cooling water (cold utility) can satisfy these process demands as illustrated by the case without steam exportation on Figure 3.

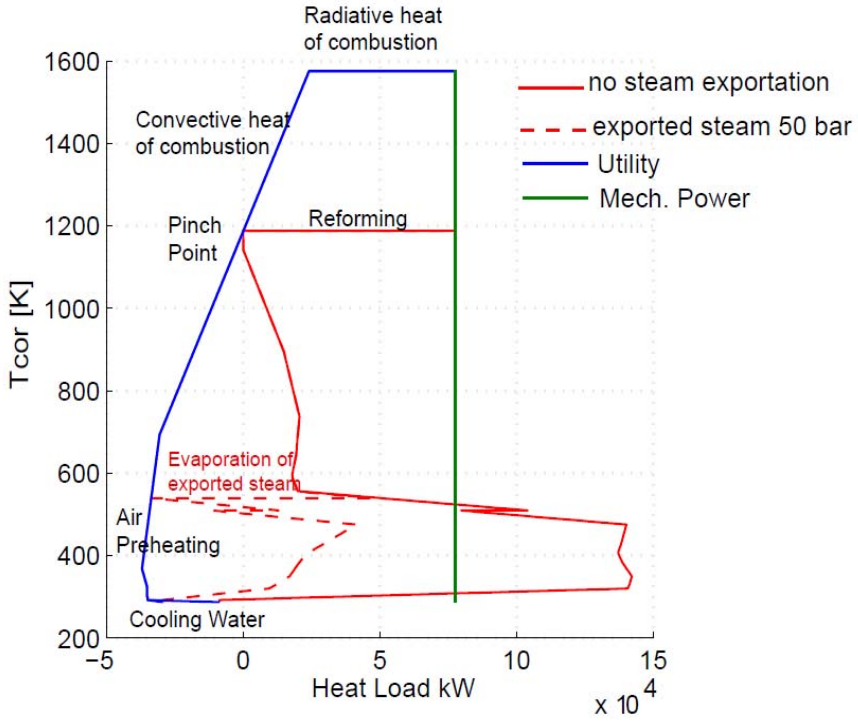

Figure 3: Grand composite curve of the process with integrated utilities.

However different possibilities to exploit the exergy value of the heat excess at low temperature can be considered in order to improve the performance of the examined process. These measures are steam export or combined electricity production that are introduced as utilities in the energy integration model. The influence on the energy integration is illustrated for the production of exportable steam at a pressure of 50 bar and a temperature of 550 K on Figure 3.

4 Process Performance

4.1 Performance indicators

In order to compare the influence of the different measures a set of performance indicators is defined:

- Specific total natural gas consumption:

$$C_{natgastot}^{specific} = \frac{total\ natural\ gas\ consumption\ \left[\frac{kmol}{s}\right]}{H_2\ production\ \left[\frac{kmol}{s}\right]}$$

The total consumption of natural gas is referring to the part of the natural gas which is used to feed the combustion and to the part consumed for the hydrogen production itself.

- Specific steam production:

$$P_{steam}^{specific} = \frac{exportable\ steam\ production\ \left[\frac{kmol}{s}\right]}{H_2\ production\ \left[\frac{kmol}{s}\right]}$$

$$P_{steam}^{specific} = \frac{exportable\ steam\ production\ \left[\frac{kmol}{s}\right]}{H_2\ production\ \left[\frac{kmol}{s}\right]}$$

- Specific exergy of produced steam:

$$B_{steam}^{specific} = \frac{exportable\ steam\ exergy\ [MW]}{H_2\ production\ \left[\frac{kmol}{s}\right]}$$

- Specific electricity production:

$$P_{electricity}^{specific} = B_{electricity}^{specific} = \frac{electricity\ production\ [MW]}{H_2\ production\ \left[\frac{kmol}{s}\right]}$$

The specific production of electricity is based on the assumption that the turbines feature a mechanical efficiency of 99% and an isentropic efficiency of 70%. The specific exergy of the electricity production equals the specific electricity production, since electric power is pure exergy.

4.2 Performance improvement

To improve the process performance several measures aiming at maximizing the exploitation of excess heat below the pinch point and minimizing natural gas consumption for the combustion are analyzed.

Measures to exploit the heat excess

For the exploitation of the excess heat below the pinch the influence of different parameters on the process performance is analyzed by a sensitivity analyses under the constraint that $C_{natgastot}^{specific}$ remains constant. Table 1 summarizes the different results. The variation of the

steam pressure level (i.e. evaporation temperature) shows that the maximal flowrate of exportable steam at 550 K is reached for a steam pressure of 38.6 bar. Instead of exporting steam, electricity can be generated by a steam network valorizing the heat excess. A steam network consisting of three headers (850 K / 150 bar, 503 K / 27 bar and 293 K / 0.02 bar) and two turbines features the best performance. However, compared to the production of exportable steam, the generation of electricity results in a lower specific exergy export. Another interesting alternative is the cogeneration of steam and electricity. The idea is to define a steam network generating electricity and performing the evaporation and the condensation at a temperature level that is settled above the production of the exported steam. By changing the condensation level pressure a trade-off is observed between the electricity and the steam production competing for a limited amount of waste heat.

Table 1: Performance indicators for different process configurations.

Configuration	$C_{natgastot}^{specific}$ $\frac{kmol\ natural\ gas}{kmol\ H_2}$	$P_{steam}^{specific}$ $\frac{kmol\ steam}{kmol\ H_2}$	$E_{steam}^{specific}$ $\frac{MW}{\frac{kmol}{s} H_2}$	$E_{electricity}^{specific}$ $\frac{MW}{\frac{kmol}{s} H_2}$
No steam exportation	0.59	-	-	-
Exported steam @50 bar	0.59	3.1	58	-
Exported steam @38.6 bar	0.59	3.8	70	-
Electricity generation	0.59	-	-	45
Cogeneration P_{cond}=37 bar	0.59	1.82	33.6	9.1
Cogeneration P_{cond}=45 bar	0.59	1.85	34.2	8.0

Multi-objective optimization

The influence of the operating parameters on the process performance is analyzed in a multi-objective optimization [6]. The fixed objectives are to minimize the natural gas consumption for the combustion and to maximize simultaneously the steam production by varying appropriate decision variables. Table 2 presents the chosen process parameters; T_{air}, T_{preref}, T_{ref} and T_{WGS} and their respective variation range. The steam for export is generated at the optimal conditions of 550K and 38.6bar and no additional natural gas consumption just to satisfy the heat demand of the steam production is accepted.

The generated Pareto plot in Figure 4 represents the optimal trade-off between the objectives in the case of the maximum steam export production. An increased specific steam production goes in pair with an increase of the specific natural gas consumption. Using the full range of the process parameters the performance can be varied between 0.53-0.59 kmol natural gas/kmol H_2 for the specific total natural gas consumption and 1.8-3.7 kmol steam/kmol H_2 for the specific steam production. Table 3 summarizes the influence of the different operating parameters on the objectives. Relative to these results there are opportunities to enhance the current process performance.

Table 2: Decision variables for the multi-objective optimization.

Parameter	Abbreviation	Variation Range
Pre-Reforming T	T_{preref}	439-650°C
Reforming T	T_{ref}	581-700°C
WGS T	T_{WGS}	206-227°C
Air preheating T	T_{air}	400-627°C

Table 3: Influence on process performance.

T_{air} ↗ T_{preref} ↗ T_{ref} ↗	$C_{natgastot}^{specific}$ ↘	$P_{steam}^{specific}$ ↘
T_{WGS} ↗	$C_{natgastot}^{specific}$ ↗	$P_{steam}^{specific}$ ↗

Compared to a ordinary steam generator with a boiler efficiency of η=0.95 and producing steam with a steam to natural gas ratio of 14.9 $kmol_{steam}/kmol_{naturalgas}$, the supplementary production of steam within this industrial process is a favorable option. As illustrated in Figure 4, between point 6 and point 4 the curve has a slope of

$$\frac{\Delta P_{steam}^{specific}}{\Delta C_{natgastot}^{specific}} = 63.5 \frac{kmol\ steam}{kmol\ natural\ gas}$$

and between point 4 and point 5 of

$$15.4 \frac{kmol\ steam}{kmol\ natural\ gas}.$$

Above point 4 there is a need to buy an additional amount of natural gas to satisfy the demands and export additional steam, while from point 6 to 4 the steam production is based on excess heat. Similar optimizations with and without a pre-reforming step and including the variation of the steam to carbon ratio allow to study the benefit for steam export and the trade-off between steam and electricity production.

5 Conclusion

The energy analysis based on process integration techniques identified several measures to enhance the performance of an industrial hydrogen process. Measures identified are to use the maximal amount of available heat excess by increasing the production of steam for export by adjusting the pressure and temperature levels according to the peculiarities of the process, and to reduce the natural gas consumption for combustion without interfering with the specific steam production by adjusting the process parameters. The assessed efficiency of the steam production within this process reaching 64 or 15.4 $kmol_{steam}/kmol_{naturalgas}$ depending on the process configuration is higher than the one of an ordinary steam generation unit (14.9 $kmol_{steam}/kmol_{naturalgas}$). This study is the basis for a future thermo-economic analysis designing the process to perform with the highest energy and economic performance.

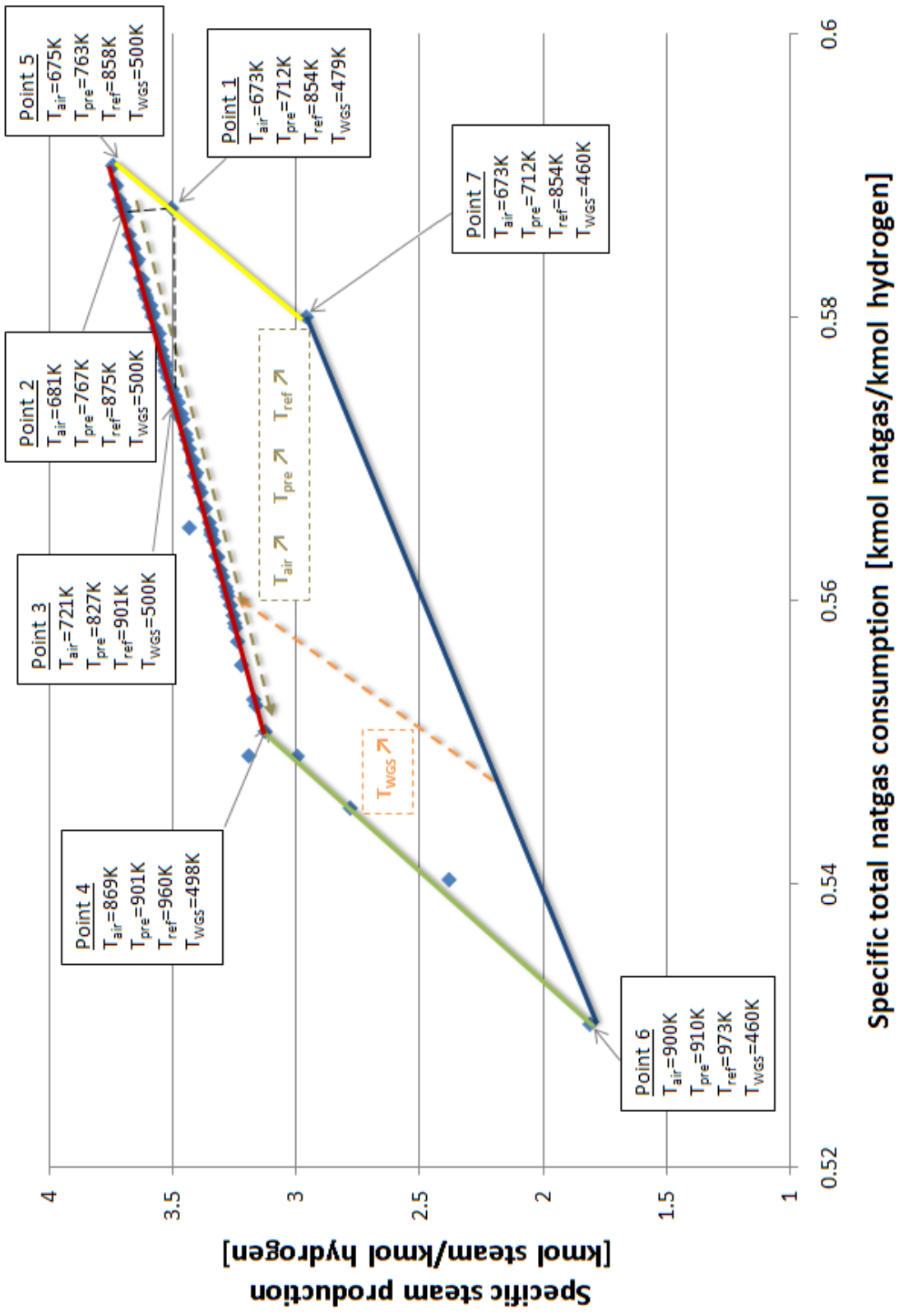

Figure 4: Optimal solutions in the Pareto domain for variation of the process parameters.

Acknowledgments

The authors wish to acknowledge Air Liquide for collaboration by providing process data and the Belsim Vali flowsheeting and data reconciliation software for their support (www.belsim.com).

References

[1] Belsim S.A. (last visited 01.2010). URL http://www.belsim.com/.

[2] Gassner, M., & Maréchal, M. (2009). Methodology for the optimal thermo-economic, multi-objective design of thermochemical fuel production from biomass. Computers & Chemical Engineering 33 (3) , 769-781.

[3] Häussinger, P., Lohnmüller, R., & Watson, A. (2000). Hydrogen. Ullmann's Encyclopedia of Industrial Chemistry. Wiley-VCH.

[4] Maréchal, F., & Kalitventzeff, B. (1998). Process integration: Selection of the optimal utility system. Computers & Chemical Engineering 22 , 149-156.

[5] Palazzi, F.; Maréchal, F.; Godat, J. & Favrat, D. (2005), Thermo-Economic Modelling and Optimisation of Fuel Cell Systems, Fuel Cells, 5, 5-24

[6] Molyneaux, A; Leyland, G & Favrat, D. (2010), Environomic multi-objective optimisation of a district heating network considering centralized and decentralized heat pumps, Energy 35(2) 751-758.

Resources of Fossil and Non-Fossil Hydrogen in the Middle East Can Make Fuel Cells an Attractive Choice for Transportation: A Survey Study

Hussein Abdel-Aal, M.Bassyouni, Shereen M.-S. Abdel-Hamid and Maha Abdelkreem, Department of Chemical Engineering, Higher Technological Institute, Tenth of Ramadan, Egypt

1 Introduction

With substantial investments and growing interest in fuel cell technology, exciting new market opportunities are opening up for hydrogen. Nowhere is this potential more significant than in the transportation market, where numerous organizations are developing light-duty vehicles, heavy-duty transit buses, and a host of niche vehicle products powered by hydrogen fuel cells [1, 2]. Fuel cells provide the most efficient conversion device for converting hydrogen and possibly other fuels into electricity. Hydrogen and fuel cells open the way to integrated open energy and environmental challenges. A major challenge, however for the widespread use of hydrogen fuel cells is the source of hydrogen itself. In this presentation, two avenues are explored as far as the resources available in the Arab World. These are: fossil hydrogen and non fossil hydrogen.

The earth's potential energy resources are enormous; however the limitations in the access to energy are mainly caused by the uneven distribution. In general, in order to get useful information for the energy resources available in the Middle East, in particular the Arab countries, one divides the primary energy resources into two categories. They are:

(a) Fixed (stored) "capital", fossil sources.

(b) Continuous "income", non-fossil sources.

A survey of the natural gas reserves is carried out first, for potential Arab countries indicating which resources are "sweet gas" and which are "sour". Fossil hydrogen is produced next by the thermo-chemical reforming of "sulfur-free" natural gas which is the current technology employed for the production of synthesis gas (hydrogen/ carbon monoxide). Solar energy on the other hand, is regarded by many as the only ideal energy source especially for countries in the Middle East located around the so called "solar belt". Data on the surface area, solar intensity flux and sunshine hours for Arab countries are reported. Harnessing the power of the sun under these conditions would lead to a remarkable source of renewable energy to be utilized in the production of hydrogen.

2 Production of Fossil Hydrogen

2.1 Natural gas resources in the Middle East (Arab countries)

Arab countries are endowed with large reserves of hydrocarbons including oil, natural gas. The vast resources of untapped hydrocarbons mean that much development is focused there. Looking at the natural gas reserves by country, it is found that a total of 51,200 trillion cubic meters is credited to the Arab countries. It represents about 30 % of the world gas reserves [3]. If we consider Qatar as an example, we find that Qatar's offshore north field, estimated to have 25 trillion cubic meters (9.0×1014 cu ft) of gas in place.

2.2 Basis and assumptions used for fossil hydrogen production

1. The gas reserves for the selected Arab countries considered in this study, is estimated to be: 51,200 trillion cubic meters.
2. Gas reserves could last for 200 years, at optimum production levels.
3. The average total annual production of natural gas will be: 51,200 Trillion cubic meters/ 200 years = 256 trillion cubic meter/year.
4. Only 1 % of the annual production will be committed for hydrogen production using catalytic reforming for sweet natural gas; while non-catalytic partial oxidation (NCPO) is recommended for sour natural gas reserves.
5. In the steam reforming process of natural gas (represented by methane) as given by the equation: $CH_4 + 2H_2O \rightarrow CO_2 + 4H_2$
   1 lb mole of methane [which occupies 359 cubic feet @ standard conditions of 32 °F & 14.7 psia] would yield 8 lb of hydrogen, at 100 % conversion. Assuming 50% conversion, the yield would be 4 lb hydrogen.
   In other words: 359 cubic feet (10.73 cubic meters) of Natural gas @ SC → 4 lb Hydrogen

2.3 Output of hydrogen production

Based on the above, 1% of the annual natural gas production would yield:
{1/100 x 256 TCM]/ 10.73 x 4 x 1/2000 = **477×10^6 Tons of Hydrogen**

2.4 Current practice for hydrogen production

Current technology employed to manufacture hydrogen or synthesis gas (hydrogen/ carbon monoxide) from natural gas is based on one of three major thermo-chemical-reforming techniques:

1. Steam reforming of methane (SRM)
2. Partial oxidation (PO)
3. Auto thermal reforming (ATR)

These are catalytic processes, which necessitates a sulfur-free feedstock of natural gas to avoid catalyst poisoning. Acidic gas removal is a pre-request step for this process, which is a costly operation involving the use of amine solvents with subsequent regeneration. Today, almost all hydrogen is produced via steam reforming of natural gas. The process referred to

as steam methane reforming (SMR) is the most common method of producing commercial bulk hydrogen as well as the hydrogen used in the industrial synthesis of many chemicals. The main reactions are:

$$CH_4 + H_2O \rightarrow CO + 3\ H_2$$

This is followed by the shift reaction:

$$CO + H_2O \rightarrow CO_2 + H_2$$

Thus, the final net reaction is:

$$CH_4 + 2H_2O \rightarrow CO_2 + 4H_2$$

Separation of CO_2 represents the very final step in the production of hydrogen.

2.5 Novel trends in reforming sour natural gas

About a third of the world's natural gas reserves contain high concentrations of contaminants and so are termed 'sour gas' [4].The defining chemicals are often hydrogen sulphide (H_2S) and carbon dioxide (CO_2) though in some cases other sulfur compounds such as carbonyl sulfide (COS) and mercaptans are also found. All producing countries in the Middle East are stepping up their efforts to exploit sour gas, often in partnership with western energy companies, reversing the trend for hydrocarbon production in the region to concentrate on oil. Now a key target is to efficiently process sour gas to improve recovery of both liquids and natural gas. In this respect, non catalytic partial oxidation (NCPO) process is introduced for handling sour natural gas. The process was proposed by Abdel-Aal & co-workers [5, 6] as a means for the direct production of synthesis gas from **sour** natural gas. It involves the combustion of sour natural gas under partial oxidation conditions in the absence of catalysts. The following reactions are cited:

$$CH_4 + 1/2\ O_2 \rightarrow CO + 2H_2 \quad (1)$$

$$H_2S + 3/2\ O_2 \rightarrow SO_2 + H_2O \quad (2)$$

The NCPO process of sour natural gas is exemplified by the schematic diagrams shown in Figures 1 & 2.

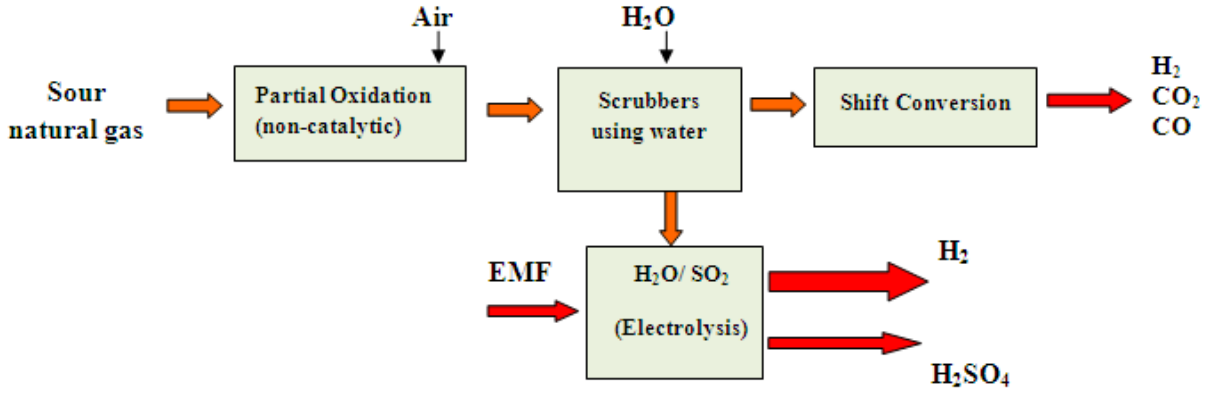

Figure1: NCPO of Sour Natural Gas producing Hydrogen and Sulfuric Acid.

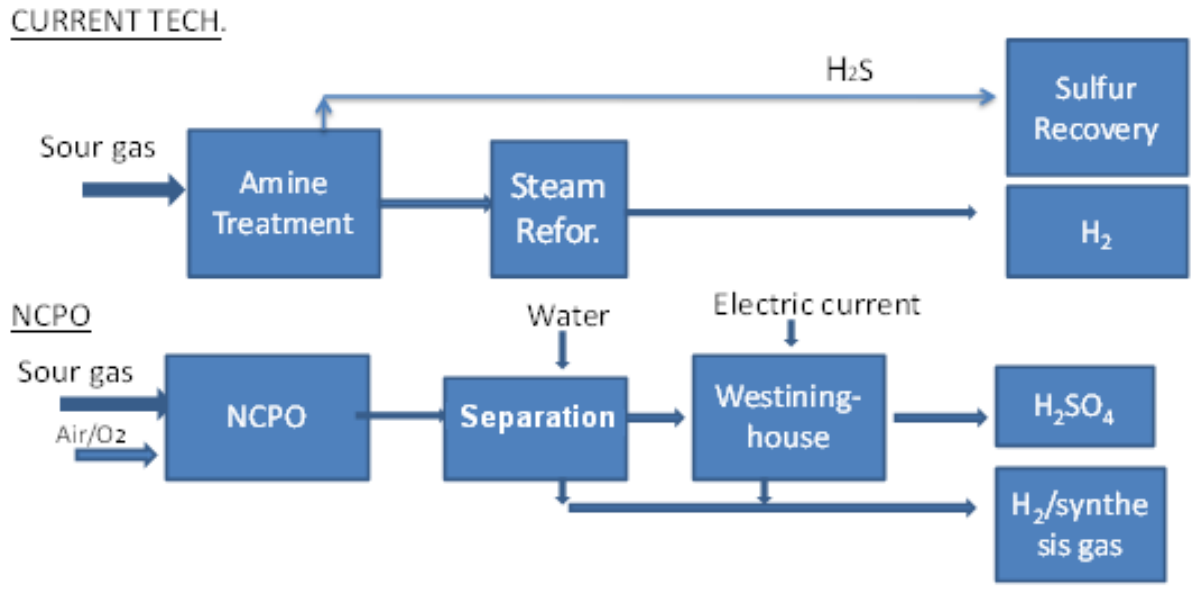

Figure 2: Current Tech. Vs NCPO for Hydrogen Production.

The merits of NCPO as compared to the SRM are as shown in table 1:

Table 1: Comparison between NCPO and STR of Sour Methane.

Parameters	SRM	NCPO
1. Treatment of raw gas to remove H_2S	Requires amine solvents	Not required
2. Recovery of S from H_2S	Claus process is applied	Not required
3. Manufacture of synthesis gas		
a) use of steam b) use of catalyst	Yes Yes	No No
4. Separation of SO_2 from synthesis gas	No	Yes
5. Production of sulfuric acid	present technology is applied: Start with S➔SO_2➔SO_3 ➔ H_2SO_4	direct production by electrolysis : H_2SO_3 (apply electric current)➔ H_2SO_4 + H_2
6. Final end products	Synthesis gas	Synthesis gas, Hydrogen and Sulfuric acid

3 Production of Non-fossil Hydrogen

3.1 The role of solar energy

Solar energy provides electricity via photovoltaic cells. Sunlight reaching the land surface of our planet can produce the equivalence of 1,600 times the total energy consumption of the world; the amount of solar energy derived from the sun's radiation on just one square

kilometer is about 4,000 megawatts, enough to light a small town. Many of the Arab countries have all practical futuristic possibilities of supplying at a significant proportion of the total world energy demand of 20 TW (electric) by 2050, from their vast solar rich deserts, by erecting solar farms on them to generate power which could be used for hydrogen production. The strategic proximity of the Arab countries to many European, Asian, African and other countries would be of crucial advantage in this respect. Recently, countries such as Saudi Arabia and Qatar and organizations such as UNESCO have initiated numerous solar energy projects although the history of large-scale solar energy use dates back to the first solar power station connected to a national grid in Adrawo, Sicily. In the wake of the first Gulf War, the US Army assessed Saudi Arabia's solar energy resource potential in a classified effort to determine how oil fires had affected the region. The results were clear and surprising. In addition to being a vast petroleum repository, the desert nation was also the heart of the most potentially productive region on the planet for harvesting power from the sun. In other words, Saudi Arabia was the Saudi Arabia of solar energy. Sitting in the center of the so-called Sun Belt, the country is part of a vast, rainless region reaching from the western edge of North Africa to the eastern edge of Central Asia that boasts the best solar energy resources on Earth [7]. With the cost of oil skyrocketing, this belt is attracting the attention of a growing number of European leaders, who are embracing an ambitious proposal to harvest this solar energy for their nations.

3.2 Basis and assumptions used for non-fossil hydrogen production

(a) The average solar intensity flux = 700 Watt/m²

(b) The average sunshine hours is 3000 annually

(c) The total land area of the Arab countries considered in the survey for producing non-fossil hydrogen = 11.34 x 106 Km2 ≈ 11 x 106 Km² [8]

(d) Only 1% of total land area is utilized for solar power generation

(e) The efficiency of solar conversion is 10%

(f) The efficiency of hydrogen production is 30%

(g) One cubic meter of hydrogen produces 3 Kw.hr (thermal) [9]

3.3 Output of hydrogen production

Based on the above, the following calculations are presented:

1. The total annual Kw.hr received by one m^2 = 0.1x0.7 Kw x 3000 hr/y
   = 210 Kw.hr ≈ 200 Kw.hr
2. The total annual Kw.hr received by land area:
   $0.01 \times 200 \times 11 \times 10^6$ (Km^2)x10^6(m^2/Km^2) = 22×10^{12} Kw.hr
3. The annual hydrogen production:
   $0.3 \times 22 \times 10^{12}$]/3 = 22×10^{11} m^3 = 22×10^{11} x 83.76 (g/m^3) x 10^{-6}(ton/g)
   = 184 x 10^6 Tons of Hydrogen

4 Summary and Conclusions

In this presentation two avenues for producing hydrogen are explored as far as the resources available in the Arab world. These are:

- Fossil hydrogen, to be produced from natural gas
- Non fossil hydrogen, to be produced using solar energy as a primary energy source

A summary of the anticipated hydrogen production by both approaches is presented in Figure 3. Natural gas reserves abundant in the Arab world were cited for a number of countries. These include: Qatar, Saudi Arabia, United Arab Emirates, Algeria, Iraq, Egypt, Kuwait and Libya with a total reserve of 51,200 trillion cubic meters. This represents about 30 % of the global world reserves.

For the production of fossil hydrogen, current technology of steam reforming of natural gas along with novel trends for handling **sour** gas reserves were presented.

For non-fossil hydrogen on the other hand, harnessing the power of the sun would lead to a remarkable source of renewable energy to be utilized in the production of hydrogen. Data on the surface area, solar intensity flux and sunshine hours for Arab countries are reported.

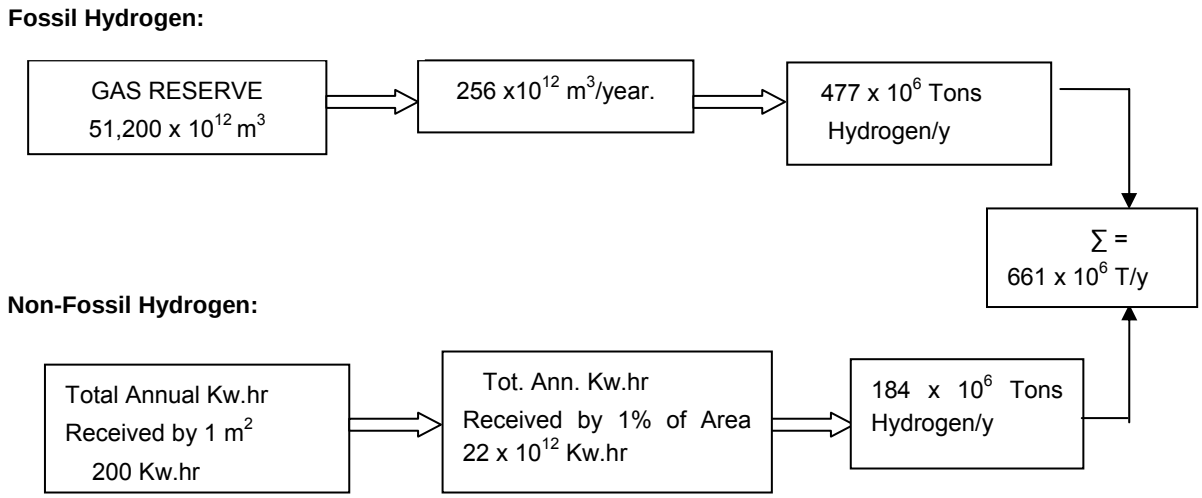

Figure 3: Summary of Hydrogen Production.

The following conclusions are most significant to be presented:

1. The Arab world could participate to supply hydrogen to the international market via the fossil and the non fossil sources. The anticipated annual production is 477 x 10^6tons plus 184 x 10^6 tons respectively to make a total of **661 x 10^6** tons.
2. As far as **sour** natural gas reserves available in the Middle east, big potential is there but technological innovation will be the key to making such reserves viable from technical and financial perspectives.
3. The **NCPO** process for producing hydrogen from sour natural gas could be a promising approach in this regard.

References

[1] World Hydrogen and Fuel Cells Market Status and Predictions, www.reportlinker.com.

[2] Global Market for Fuel Cells and Hydrogen Energy, Published October 20, 2009, www.electronics.ca

[3] CIA, World Factbook, https://www.cia.gov/library

[4] Hydrocarbons-technology.com, product of Net Resources International. Copyright 2009

[5] Abdel-Aal, H.K. and M. A. Shalabi, " Non Catalytic Partial Oxidation of Sour Natural Gas versus Catalytic Steam Reforming of Sweet Natural Gas, Ind .Eng. Chem. Res., 1996, 35, 1785-1787.

[6] Abdel-Aal, H. K., Shalabi, M. A., Al-Harbi, D.K. and Hakim T. "Simulation of the Direct Production of Synthesis Gas from Sour Natural Gas by None Catalytic Partial Oxidation (NCPO): *Thermodynamics and Stoichiometry*, *Ind .Eng. Chem. Res.,* 1999, 38, 1069-1074.

[7] AMEinf.com

[8] Middle East at a Glance: Includes Middle Eastern countries and Arab countries of North Africa.www.mideastweb.org/countries.htm.

[9] T. Ohta, editor, "Solar-Hydrogen Energy Systems", Pergamon Press, 1979

Comparative Analysis of Photovoltaic Power Storage Systems by Means of Batteries and Hydrogen in Remote Areas of the Amazon Region in Brazil

André Luis Furlan, Cristiano da Silva Pinto, School of Mechanical Engineering - FEM/UNICAMP, Campinas, São Paulo, Brazil
Newton Pimenta Neves Jr., Laboratory of Hydrogen - IFGW/UNICAMP, Campinas, São Paulo, Brazil

Abstract
This study analyzes the photovoltaic power storage comparing the traditional lead-acid batteries with electrolytic hydrogen where the gas is reconverted to power in a fuel cell. In order to design the two systems a load profile of the Brazilian Amazon communities was used as well as some practical operational data of equipment tested in the laboratory. A mathematical model was developed, implemented in a spreadsheet that considers the several devices and their efficiencies in order to specify and match the systems components. The results were employed to evaluate the economic viability of the two systems in remote communities. Considering the present conditions, it was verified that the battery system is slightly cheaper. However, it was also observed that a minor cost reduction in the electrolyser, as well as in the buffer and fuel cell would make the hydrogen system very competitive, becoming the best option for photovoltaic power storage with important benefits to the environment.

Keywords: Photovoltaic Power, Battery, Hydrogen and Fuel Cell.

1 Introduction

Brazil, a developing country, presents high levels of energy consumption, comparable to that of rich countries. But the access to that energy is not privilege of all. It is estimated that there are about 12 million people without electricity, most of them living in rural communities and small villages in isolated areas [1].

The main characteristic of those communities is that they are disconnected from the existing Interconnected Electrical Systems in Brazil. The generation of electricity in places like that is generally made by diesel generators, whose diesel fuel is subsidized [2].

Traditionally systems based on photovoltaic panels used to attend isolated communities require a battery bank to store electricity during daylight and to supply electricity either at night or during low incidence of sunlight. However, the operational conditions of the panels and the battery bank are not always optimal, and even in the best cases the use of a large number of batteries is mandatory.

Other ways of storing energy generated by photovoltaic panels can be more interesting from the viewpoint of system optimization. In this study, a system composed of photovoltaic

panels connected to a water electrolyser to produce hydrogen is considered. The gas is stored in a reservoir to be used in a standard PEM fuel cell whenever necessary.

2 The Mathematical Model to Assess the Energy Systems

To dimension the systems based on photovoltaic panels, it is initially necessary to know the solar radiation of the site and the characteristics of energy consumption to be met. The optimal design is the balance between the available energy and the consumption, taking into account the efficiency of the different equipment involved in the transformation [4].

As the study takes into account the profile of demand load over 24 h, it was considered the average hourly incident solar radiation during the day (4,75 kWh/m^2) [5]. The characteristic energy demand used belongs to the rural community of Vila Campinas/AM. Based on a study involving the community [3], a single system is proposed to attend a school, a community center, a health center and three houses totaling an electric power consumption of 10.4 kWh/day.

The mathematical model was developed using a Microsoft Excel spreadsheet where the main characteristics associated with solar radiation, equipment operation and electricity consumption profile were introduced. Some of the most important input parameters are: i) average solar radiation per hour; ii) electricity consumption of each appliance; iii) equipment efficiency; and iv) equipment minimum and maximum operational limits (voltage, pressure, etc.). The spread sheet can provide as output data the amounts of used, stored, and wasted energy over 24 hours per day, by each piece of equipment as well as the whole system. Figures 1 and 2 show the arrangement of the complete systems to be analyzed.

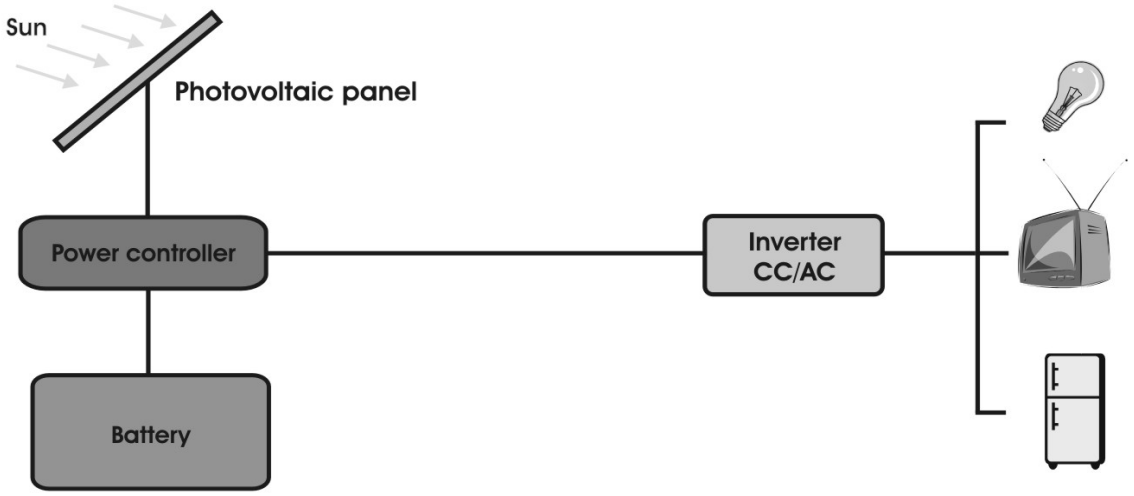

Figure 1: Array of photovoltaic system with energy storage in batteries.

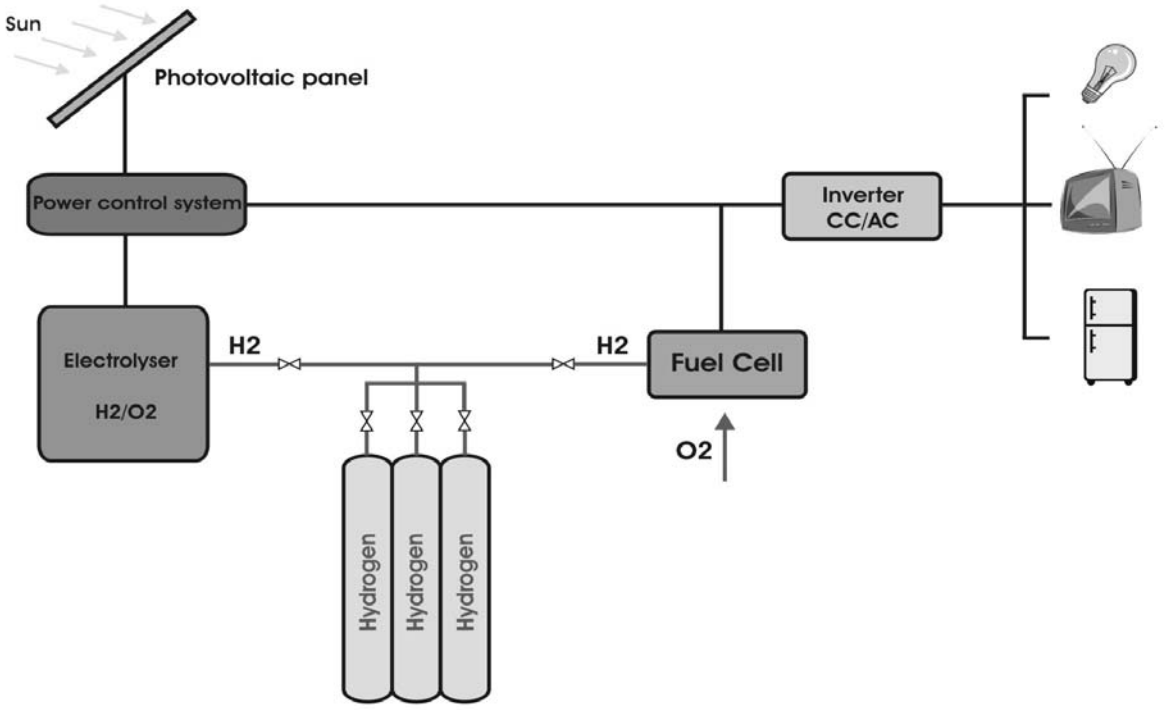

Figure 2: Array of photovoltaic system with storage of energy as hydrogen.

3 Results and Discussion

3.1 Photovoltaic panels

According to calculations, the photovoltaic system with hydrogen storage requires a larger amount of photovoltaic panels than the system using batteries, 58 and 24 respectively. This difference is related to the minimum energy required for the operation of the electrolyser (1 kWh), below which the electrolyser does not operate. On the other hand, the batteries do not require a minimum amount of energy to start the storage process, when its state of charge is below its full capacity.

3.2 Production, storage and conversion of hydrogen

Unlike a photovoltaic system that uses batteries as electrical energy storage, the system that uses hydrogen needs more devices to perform the functions fulfilled by batteries. Therefore, the batteries should be replaced by a device capable of: i) converting the electrical energy from the photovoltaic panels into hydrogen, i.e. an electrolyser; ii) a reservoir to store the hydrogen; iii) a device to convert hydrogen into power, i.e. a fuel cell.

An immediate comparison between the two systems includes:

Lifetime: The lifetimes of the devices replacing the batteries (electrolyser, hydrogen storage vessel, fuel cell) are respectively 20, 20 and 6 years, while the batteries lifetime, considering daily loading/unloading, do not exceed 4 years. So, the conventional system would require 66 batteries and 4 replacements, totalizing 330 batteries along its lifetime.

Efficiency: The overall efficiency of the hydrogen system, considering an efficiency of 80% for the electrolyser [7] and 50% for the fuel cell [6], is 40%, while the battery reaches 80% [8]. The lower efficiency of the photovoltaic-hydrogen system is due to the combined efficiency of the various devices required to substitute the battery pack.

Environmental: Lead-acid batteries contain lead and sulfuric acid, and consequently need special care to be disposed of, as they may cause environmental damages. This aspect is quite important in isolated communities where logistics for batteries' replacement and disposal is difficult. In the hydrogen system, the useful life of its main components is longer and the rate of replacement is much lower. Therefore, the equipment has reduced chances of causing environmental damages.

3.3 Energy produced, surplus and autonomous systems

An important feature to be considered in these systems is the amount of energy produced and stored. Figure 3 shows the typical production profile of an electric power system with photovoltaic panels and batteries, and the consumption of electricity by an isolated community in a typical day. If the batteries bank reaches its maximum state of charge and the photovoltaic panel exceeds demand, the surplus energy will not be used. This is shown at the 14 and 15 hours in the figure. In this system the energy surplus was 0.378 kWh/day.

Figure 4 presents the amount of energy stored in the form of hydrogen over the period of 24 hours, which considered the high heating value (HHV) of hydrogen to transform the quantity of gas into energy. The same approach can be made for the surplus energy, which in this case is around 0.993 kWh/day.

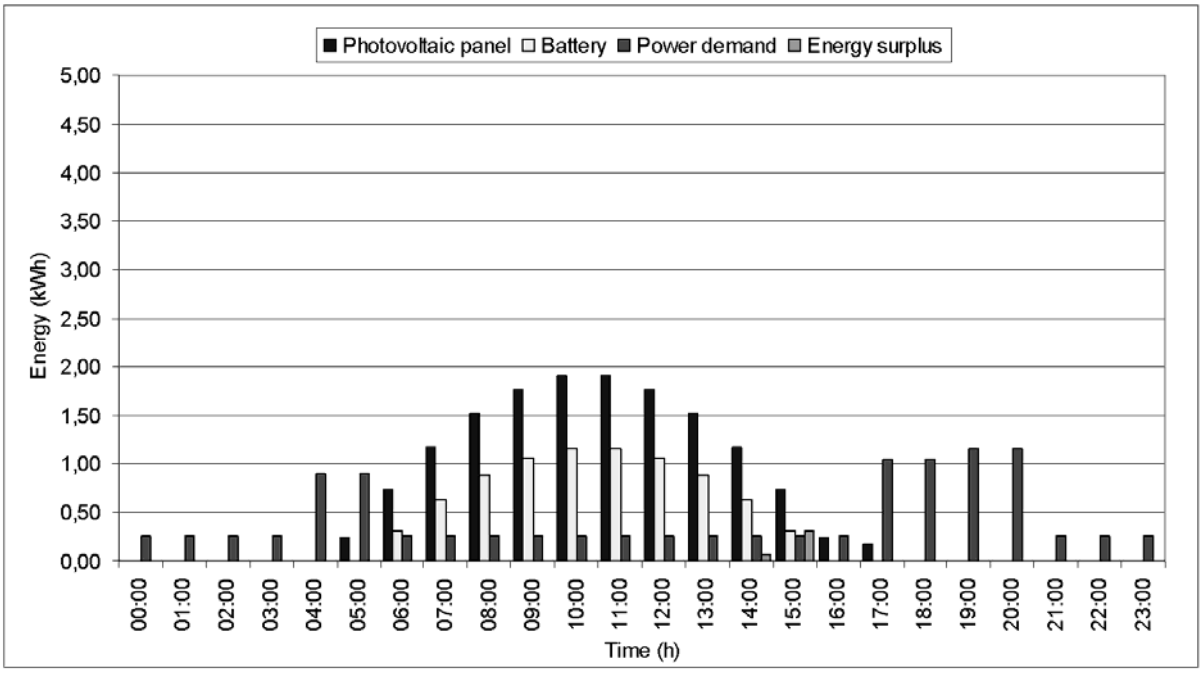

Figure 3: Typical profile of photovoltaic system with energy storage in batteries.

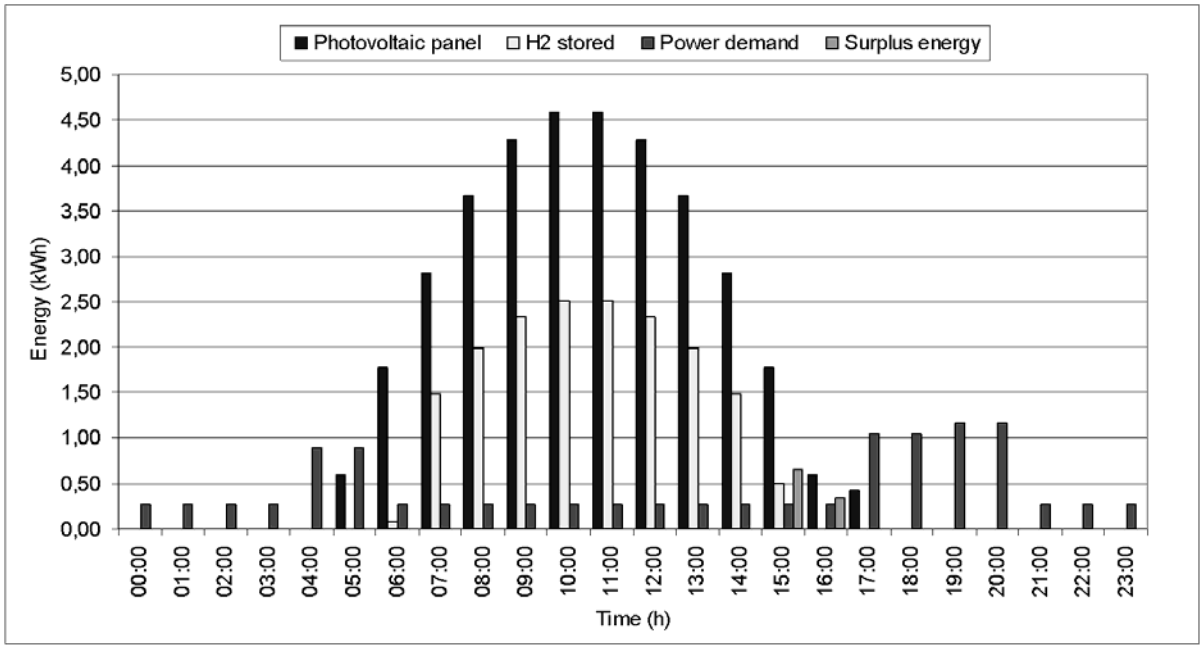

Figure 4: Typical profile of photovoltaic system with storage energy in hydrogen.

4 Conclusions

In both systems, the photovoltaic panel is the equipment that most contributed to the initial investment. Thus the total cost of the photovoltaic system with the battery was US$ 139,560.00 and with hydrogen storage US$ 168,056.00, or 20% higher. A reduction of approximately 35% in the costs of the electrolyser/hydrogen storage vessel/fuel cell makes this system economically comparable to the battery pack system. The capital cost of photovoltaic power system with batteries seems more competitive in relation to the photovoltaic system for hydrogen storage, but when a thorough consideration is done concerning environmental aspects, it can be said that the hydrogen storage system is potentially much less aggressive to the local environment than the battery system.

Therefore, using as a criterion the comparative cost of electricity produced by each system, it is possible to conclude that the photovoltaic system with battery pack still seems to be the most economically competitive than the hydrogen storage system. The expectation, however, is that with the increase in scale of production of fuel cells and electrolysers, there will be a drop in their market prices to the point of making such system viable. To support this expectation it is interesting to remember that although the PEM fuel cells have only recently reached the stage of commercialization, they are successfully replacing batteries in applications such as back-up power in telecommunication antennas, and forklifts.

Acknowledgements

To Laboratory of Hydrogen and Energy Company of Minas Gerais (CEMIG).

References

[1] IBGE, Instituto Brasileiro de Geografia e Estatística, Censo 2000. Available at www.ibge.gov.br.

[2] Souza, C. R. Planej. suprimento de eletricidade de sistemas isolados na Amazônia. FEM/UNICAMP, 2000.

[3] Cartaxo, E. F, Análise técnica de um sistema híbrido solar/diesel, FEM/UNICAMP, 2000.

[4] Castaner, A. Consideraciones sobre el diseño de sistemas fotovoltaicos. 1985. p. 158–162.

[5] Tiba, C. et al, “Atlas Solarimétrico do Brasil. UFPE, Recife/PE, 2000.

[6] PLUGPOWER, Fuel Cell products for backup power. Available at www.plugpower.com.

[7] PIEL, Hydrogen and Oxygen Generators. Available at www.digital.sm/piel-ilt/eng/index.htm.

[8] MOURA Acumuladores. Available at www.moura.com.br/.

Cost Estimation of Transported Hydrogen, Produced by Overseas Wind Power Generations

Tomofumi Watanabe, Kenji Murata, The Institute of Applied Energy, Japan
Dr. Shoji Kamiya, Kawasaki Heavy Industries, Ltd., Japan
Prof. Dr. Ken-ichiro Ota, Yokohama National University, Japan

1 Introduction

Japan is striving to spread the use of nuclear and renewable energy, yet still continues to be highly dependent on fossil fuel. This sort of energy supply-demand structure carries significant risks from foreseeable future resource and environmental restrictions. Therefore, it will be very important in the future to establish a social system that can consistently import or produce a set amount of resource supplies without green house gas emissions. In this study, we developed a concept for a global hydrogen energy system using wind power generation as a hydrogen source, investigated its economic efficiency, compared it with power generating fuels used at existing thermal power plants, and examined the feasibility of the global hydrogen energy system.

2 System Concept

Figure 1 shows a conceptual diagram of a system to import wind power generated in overseas regions with favorable climatic conditions into Japan.

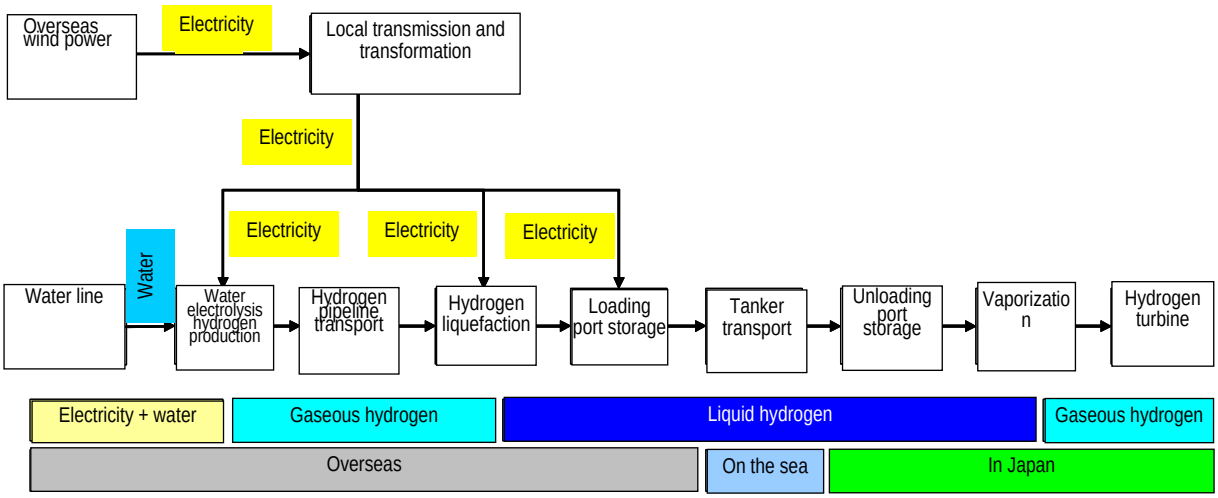

Figure 1: Conceptual diagram of overseas wind-hydrogen system.

Overseas wind energy will fuel domestic steam power plants. Component systems leading to domestic electricity power supply are shown in Figure 1. “Local transmission and transformation” is a system which supplies electricity for “water electrolysis hydrogen production,” “hydrogen liquefaction” to liquefy gaseous hydrogen transported, and utility “loading port storage” at a liquid hydrogen loading and storage base. “Water line” is a system which supplies water from nearby rivers to use as hydrogen source material in “water

electrolysis hydrogen production." "Hydrogen production" and "hydrogen liquefaction" are connected via hydrogen pipelines. Liquid hydrogen will be loaded on to tankers, shipped to Japan, and supplied to domestic power plants. This system leading to domestic hydrogen supply is similar to importing liquefied natural gas (LNG).

3 Feasibility Study of Overseas Wind Energy Import

3.1 Cases to study

As shown in Table 1, three cases were examined.

Table 1: Cases to study.

	Equipment Scale	**Energy Efficiency**
Case (1)	Existing equipment	Present case
Case (2)	Larger equipment	Present case
Case (3)	Larger equipment	Future case

Existing equipment is assumed to have capacities that are already being utilized as products in the world (e.g. storage tank capacity estimated at 3,000m^3). Larger equipment is assumed to have larger capacity, to take cost advantages into account (e.g. storage tank capacity estimated at 80,000m^3).

Present cases of energy efficiency assume the electric power consumption rate for water electrolysis hydrogen production and hydrogen liquefaction to be at present levels. Future case assume an improved electric power consumption rate over present levels.

3.2 Assumed wind power plant construction site

Based on the report [1] prepared by the investigation team of the Hydrogen Energy Systems Society of Japan (HESS), it is predicted that the overseas wind power station would be constructed north of the city of Pico Truncado, in the state of Santa Cruz in Southern Patagonia, Argentina.

In Southern Patagonia, it is assumed that windmills can be used in 50% of its 469,000km^2 area. Its wind energy potential is said to be ten times Japan's electricity demand [2, 3]. For the purpose of this study, the domestic transmission side electric energy was set to approx. 10% (8.9 ×1010kWh/year) of the electricity sold by ten Japanese power companies in FY2006. To cover this much electricity in Patagonia, 340 billion kWh/year for present cases (at current levels of electric power consumption rate for water electrolysis hydrogen production and hydrogen liquefaction) or 265 billion kWh/year for future cases needs to be generated, which would account for 3 to 4% of the 9.6 trillion kWh/year potential electricity generated in Patagonia.

3.3 Overseas wind power generation

(1) Annual Capacity Factor

The HESS investigation report [1] estimates that the capacity factor of wind power generation in Santa Cruz will be 49%, taking into account maintenance outages and miscellaneous losses. In this study, the annual capacity factor was set to 50% as shown in Equation (1).

$$\text{Annual capacity factor (\%)} = \frac{\text{Annual output} \times 100}{\text{Rated output} \times 8{,}760} \quad (1)$$

(2) Unit Price and Number of Windmills Installed

The unit price of windmill construction was calculated based on the data published by the U.S. National Renewable Energy Laboratory (NREL) [4, 5]. According to NREL published data, the construction unit price of a windmill at 1.5MW rated output, 70m rotor diameter, and 65m hub height is calculated at US$981/kW. The maximum rated output is 5MW [6] for current commercial windmills. In this study, however, it is assumed that Case (1) will use a windmill at 3MW rated output, 99m rotor diameter, and 65m hub height, while Case (2) or (3) will use a windmill at 5MW rated output, 99m rotor diameter, and 65m hub height. Based on the NREL unit price.

As a result, the construction unit price of the 3MW windmill for Case (1) was estimated at US$1,031/kW, and the 5MW windmill for Cases (2) and (3) at US$859/kW.

By using Equation (1), the rated power generating capacities, the number of windmills installed, and their construction costs were obtained as shown in Table 2 for the wind farm to be constructed in Patagonia.

Table 2: Rated power generating capacities, windmills, and construction costs for wind power generation.

	Capacity (MW)	Windmills (Units)	Construction Cost (million US$)
Case (1)	77,500	25,800	80,000
Case (2)	77,500	15,500	66,600
Case (3)	60,400	12,100	51,900

3.4 Local transmission and transformation

For a wind farm to supply wind energy for “water electrolysis hydrogen production,” “hydrogen liquefaction,” and “loading port storage,” a rated electric power of approx. 1,500MW and 500 windmill units are required for Case (1), and 300 units for Cases (2) and (3).

The number of wind farms to construct and the scale of each location are shown in Table 3.

Table 3: Number of wind farms to construct and scale of each location wind farms.

	Wind Farms (Locations)	At Right Angle to Wind Direction (km)	Parallel to Wind Direction (km)
Case (1)	52	15	10
Case (2)	52	9	10
Case (3)	41	9	10

Using the substation construction unit price presented in the Electric Technology Research [7], as well as Reference 9 [8] of the Working Group on Electric Power Equipment and Electromagnetic Fields for reference, the cost for local transmission and transformation per wind farm was estimated at US$500 million. The total construction cost for local transmission and transformation was calculated at US$26.4 billion for Case (1), US$25.6 billion for Case (2), and US$20.2 billion for Case (3).

3.5 Examination of Electric Power Required and Capacity Factor

(1) Relationship between Rated Output and Capacity Factor

The relationship between rated output and capacity factor was calculated based on the following assumptions:

Assumption 1: All output from wind power generation will be used for “water-electrolysis hydrogen production,” “hydrogen liquefaction,” and “loading port storage.”

Assumption 2: The amount of liquefied hydrogen reflects losses that may occur before produced hydrogen arrives for liquefaction.

Equations (2) and (3) can be worked out from Assumption 1, and Equation (4) from Assumption 2.

When the relationship between Gt×G, Lt×Lm, and Wt×Wm is obtained based on the above relational Equations, Equations (2) and (3) can be worked out.

$$Gt \times Gm = \alpha/(\alpha + \beta(1 - \delta)) \times (1 - \gamma) \times Wt \times Wm \quad (2)$$

$$Lt \times Lm = \beta(1 - \delta)/(\alpha + \beta(1 - \delta)) \times (1 - \gamma) \times Wt \times Wm \quad (3)$$

Where,

Wt: Rated output from wind power generation (kW)

Gt: Rated power for water electrolytic hydrogen production (kW)

Lt: Rated power for liquefaction (kW)

Wm: Capacity factor of wind power generation (%)

Gm: Capacity factor of water electrolytic hydrogen production (%)

Lm: Capacity factor of hydrogen liquefaction (%)

α: Electric power consumption rate for hydrogen production (kWh/Nm3)

β: Electric power consumption rate for liquefaction (kWh/Nm3)

δ: Loss until arrival for liquefaction/hydrogen produced by water electrolysis

γ: Electric power used for loading port storage/generated output ( )

(2) Percentages of Generated Output Used for Water Electrolysis Hydrogen Production and Hydrogen Liquefaction

The percentages of generated output used for water electrolysis hydrogen production Pg (%) and hydrogen liquefaction Pl (%) can be obtained by Equations (4) and (5), based on Equations (2) and (3).

$$Pg = (Gt \times Gm)/(Wt \times Wm) \times 100 = \alpha/(\alpha + \beta(1-\delta)) \times (1-\gamma) \times 100 \quad (4)$$

$$Pg = (Gt \times Gm)/(Wt \times Wm) \times 100 = \alpha/(\alpha + \beta(1-\delta)) \times (1-\gamma) \times 100 \quad (5)$$

The percentages of generated output used for hydrogen production and liquefaction are independent of the scale and capacity factor of wind power generation.

Next, assuming that the electric power consumption rates of hydrogen production and liquefaction are for present cases (applicable to Cases (1) and (2)) [9] and for future cases (applicable to Case (3)) [10], the percentages of generated output used for hydrogen production and liquefaction are shown in Table 4.

Table 4: Percentages of generated output by electric power consumption rate.

	Present Case	**Future Case**
Hydrogen production power consumption rate	4.77 kWh/Nm^3	4.05 kWh/Nm^3
Hydrogen liquefaction power consumption rate	1.20 kWh/Nm^3	0.6 kWh/Nm^3
Pg	79.2%	86.3%
Pl	19.8%	12.7%

3.6 Water line

Water used for water electrolysis hydrogen production will be taken from the Desead River, near the wind farm construction site. The water line will be composed of a main pipe to supply water from the water source, and branch pipes within the farm. The length and bore diameter of the main pipe will be approx. 213km and 1,400mm respectively for Case 1, and 153km and 1,400mm for Cases 2 and 3. Assuming that the length of a branch pipe is approx. 10km, the total length and bore diameter of branch pipes will be 515km and 500mm respectively for Cases 1 and 2, and 406km and 500mm for Case 3. Based on interviews with experts, the ratio of material costs, ancillary equipment including pumps, and installation costs was assumed to be 30:30:40. The water line construction cost was estimated at approx. US$1,540 million for Case (1), US$1,260 million for Case (2), and US$1,140 million for Case (3).

3.7 Water electrolysis hydrogen production

Based on the annual total hydrogen production of 54 billion Nm^3/year and hydrogen production capacity of approx. 13.5 million Nm^3/h is required for Cases (1) and (2), and 13.0 million Nm^3/h for Case (3).

3.8 Hydrogen pipeline transport

The arrangement of the hydrogen pipelines installed between the water electrolysis hydrogen production systems.

Table 5: Length and construction cost of hydrogen pipelines.

	Pipeline Length (km)	Construction Cost (US$-in million)
Case (1)	1,290	640
Case (2)	980	490
Case (3)	770	390

3.9 Hydrogen liquefaction

The maximum capacity of existing liquefaction equipment is approx. 50 to 60 tons/day. The per-unit liquefaction capacity was set at 51 tons/day for Case (1). Since the larger equipment for Cases (2) and (3), would require an enormous liquefaction capacity (approx. 16,400 tons/day), the per-unit liquefaction capacity was set to 300 tons/day based on the conceptual design [11] implemented by the World Energy Network (WE-NET). Based on the estimation [12] performed by a European liquefaction equipment manufacturer, the construction cost of a 300 tons/day unit was calculated at approx. €199.5 million (approx. US$245 million using the exchange rate of US$1.23 to an Euro), with a 51 tons/day unit calculated at approx. US$75 million using the 2/3 power law. As a result, it was estimated that 322 units would be required for Case (1) at construction cost of approx. US$24.3 billion while 55 units would be required for Cases (2) and (3) at construction cost of US$13.5 billion.

3.10 Loading port storage and unloading port storage

Storage facilities will be constructed at liquid hydrogen loading and unloading bases. Assuming the loading port can hold 1/24th or 14 day's worth of the annual liquid hydrogen discharge amount, and the unloading port can hold 1/12th or 30 day's worth of domestically generated electricity, a storage capacity of approx. $2.6\times10^6 m^3$ will be required at the loading port and $5.0\times10^6 m^3$ at the unloading port. Since the largest liquid hydrogen storage facility (held by NASA) is approx. $3{,}000 m^3$, the capacity of a single tank for Case (1) was set to $3{,}000 m^3$. For Cases (2) and (3) involving larger equipment, it was set to $80{,}000 m^3$/unit, based on the conceptual design of a $50{,}000 m^3$-class liquid hydrogen storage system implemented by WE-NET.

After consulting with experts, the construction unit price of an 80,000m3 unit was estimated at US$240 million, and we estimated the price of a 3,000m3 unit at US$27 million using the 2/3 power law.

It was ultimately estimated that for Case (1), 866 units would be required at the loading port at construction costs of US$23.300 billion, while 1,670 units would be required at the unloading port at construction costs of US$44.9 billion. For Cases (2) and (3), 33 units will be required at the loading port at construction costs of US$7.9 billion, while 63 units will be required at the unloading port at construction costs of US$15.1 billion.

3.11 Tanker transport

The shipping distance from the loading storage base to the unloading storage base is approx. 20,000km. Liquid hydrogen may be transported in containers, barges, or tankers, but shipping liquid hydrogen has not yet been commercialized. Therefore, we had to estimate tanker capacity at 12,000m³/tanker for Case (1) and 63,000m^3/tanker for Cases (2) and (3), using the liquid hydrogen tanker conceptual design [11] based on WE-NET LNG tanker technology as reference. Assuming that the construction unit price of a 63,000m^3 tanker is US$248 million, the price of a 2,000 m^3 tanker was calculated at US$82 million using the 2/3rds law. Assuming tanker speed of 19.5 knots (approx. 36.1km/h) at 7 round trips per year, it is estimated that 807 tankers will be required for Case (1) at construction cost of US$66.3 billion, while 154 tankers will be required for Cases (2) and (3) at construction cost of US$38.2 billion.

3.12 Vaporization

It is estimated that a vaporization capacity of approx. 12 thousand tons/day will be required, based on the annual total hydrogen vaporization capacity of 4.3 million tons/year. Assuming that the same capacity is applicable for Cases (1) through (3), the carburetor capacity and capacity factor were calculated at 8 tons/h and 80%, respectively. The construction unit price was calculated at US$1.4 million/unit based on the DOE review [13]. As a result, it was estimated that 24 units would be required at construction cost of US$109 million.

3.13 Hydrogen turbine power generation

In order to achieve 60% generating efficiency (HHV), WE-NET examined major components of the hydrogen turbine, such as turbine blades and rotors. Specifications for turbine capacity, equipment cost, generation-side efficiency, and capacity factor were drawn up based on WE-NET achievements [11]. For Cases (1) through (3), it is estimated that a total of 33 turbines will be required at a total rated output of to 16.5 GW (500MW x 33 units) and construction costs of US$15.4 billion.

4 Prerequisites for Feasibility Study

The operating period will be 30 years and the equipment will continue to be used even after the statutory depreciation period (e.g. 17 years for wind power generation). For water electrolysis hydrogen production and hydrogen liquefaction, however, the equipment will be upgraded once (in Year 16). Table 6 shows the statutory service life of each component system.

Table 6: List of annual expenses of each component system.

Component System	Statutory Service Life (years)	Repair Expenses (%)
Overseas wind power generation	17	1.0
Local transmission / transformation	22	2.0
Water line	18	2.0
Water electrolysis hydrogen production	10	2.0
Hydrogen pipeline transport	22	2.0
Hydrogen liquefaction	10	3.0
Loading port storage	10	3.0
Tanker transport	15	2.0
Unloading port storage	10	3.0
Vaporization	15	2.0
Hydrogen turbine	15	4.0

5 Feasibility Study Results

5.1 Total cost

Figure 2.1 show the total costs for Cases (1) and Figure 2.2 show the total costs for Cases (3). The total costs were obtained by Equation (6).

Total cost = construction cost with interest + 30-year variable expenses (15)

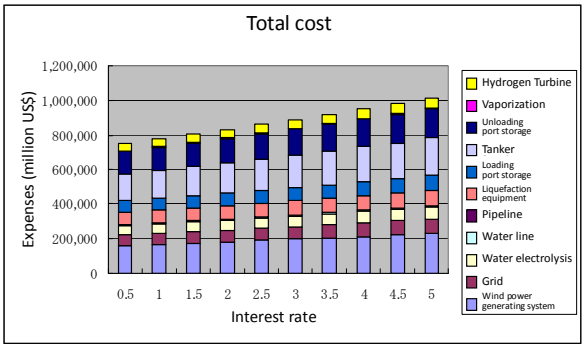

Figure 2.1: Construction cost (case (1)).

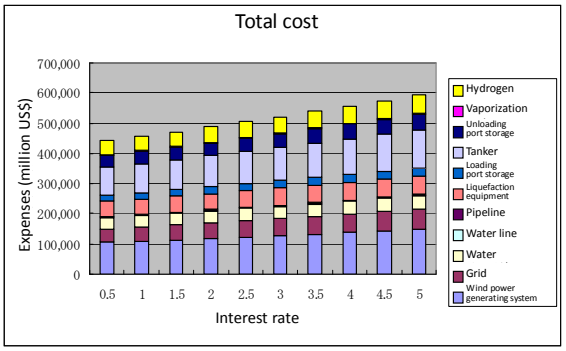

Figure 2.2: construction cost (case (3)).

The construction cost in Case 1 was estimated at approx. US$750 billion with a 0.5% interest and approx. US$1 trillion with a 5% interest. However in Figure 5.1.2, the construction cost in Case 3 was estimated to be much lower at approx. US$ 450 billion with a 0.5% interest and approximately US$ 600 million with a 5% interest.

5.2 Electricity Price

(1) Electricity Price by Case

The plant transmission side electricity price (cent/kWh) for electricity fueled by hydrogen from overseas wind power generation was calculated, with results shown in Figure 3.1 and Figure 3.2.

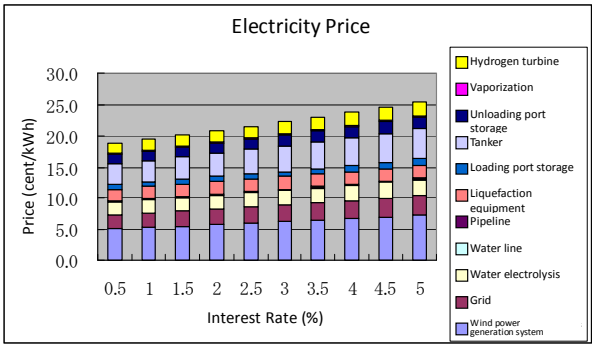

Figure 3.1: Electricity price (case (1)).

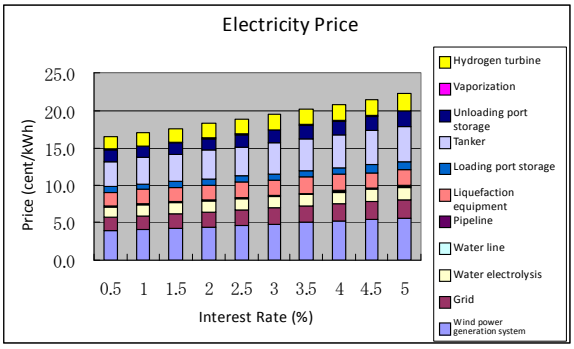

Figure 3.2: Electricity price (case (3)).

(2) Comparison of Unit Electricity Price with Thermal Power Plant

The prices of fossil fuels were obtained by dividing the fuel import CIF prices (monthly average) published in the Trade Statistics of Japan [14] by their respective calorific values (heavy oil: 41.9MJ/liter, LNG: 54.6MJ/kg, coal: 25.7MJ/kg) [15]. Figure 4 shows the relationship between the hydrogen turbine plant transmission side electricity price of hydrogen turbine power generation calculated in 5.2 and the fuel expenses of the existing thermal power plant.

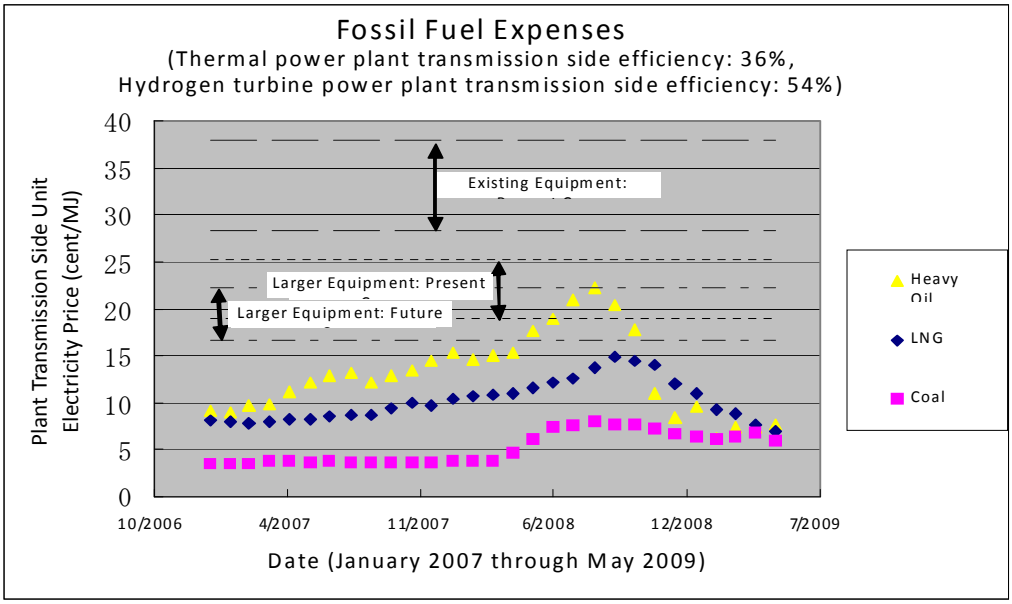

Figure 4: Calorimetric comparison of hydrogen from overseas wind power generation and fossil fuels.

It was found that the construction of a new hydrogen turbine plant would be economically justified when import prices for heavy oil and LNG were close to the 2008 peak values. During that period, the monthly CIF price was US$ 850 to 930 /kl for heavy oil and US$660 to 810/ton for LNG, while the WTI value averaged US$100 to 133/barrel. The Energy Supply and Demand Subcommittee of the Advisory Committee for Natural Resources and Energy recalculated its long-term energy supply and demand outlook, estimating crude oil prices would be US$ 121/barrel in 2020 and US$ 169/barrel in 2030 [16]. This study suggests that electricity stemming from overseas wind power generation may have economic efficiency compared with existing thermal power generation by around 2020 to 2030.

6 Conclusion

It is difficult for hydrogen stemming from overseas wind power generation to show economic efficiency in terms of calorific value compared to present fossil fuel prices. It has sufficient economic efficiency over byproduct hydrogen produced at factories. It is suggested that in the future, it would be more effective to decommission existing oil-fired thermal power plants and construct new hydrogen turbine plants.

Finally, we would like to extend our appreciation to those who provided their wisdom and advice on this study.

References

[1] NEDO; Investigation Report on the “Investigation on Hydrogen Production Using South American Renewable Energy,” (2006)

[2] Yukio Suguro; Potential of Windmill Utilization in Argentina, 6th Wind Energy Utilization General Seminar of Ashikaga Institute of Technology (2006)

[3] Kenji Murata: Patagonia in Argentina Famous for Wind, Seasonal Report, Institute of Applied Energy, Vol. 29, No. 2 (2006), 98-106

[4] NREL; Baseline Cost of Energy (Date of Access: 2008.4.14) http://www.nrel.gov/wind/coe.html

[5] The following sheets contained in 4) were used: - Example COE Projection Sheet - Annual Energy Production Calculator (MS Excel 253KB)

[6] REpower; WEB (Date of Access: 8/5/2008) http://www.repower.de/index.php?id=1&L=1

[7] Electric Technology Research; “Technologies to Expand the Dissemination of 20kV-class/400V Distribution Systems,” Electric Technology Research Vol. 56, No. 3, (2000), 287

[8] Nuclear and Industrial Safety Subcommittee, Subcommittee on Electric Power Safety; “Working Group on Electric Power Equipment and Electromagnetic Fields,” Reference 9, (2008), NEDO, Fuel Cell and Hydrogen Technology Development Department; 2005 Fuel Cell and Hydrogen Technology Development Roadmap, (2006)

[10] DOE Hydrogen Program; Well-to-Wheels Analysis, 39.

[11] NEDO; International Clean Energy System Technology Using Hydrogen Subtask 3 Total System Conceptual Design, (1999)

[12] E4tech; The Economics of a European Hydrogen Automotive Infrastructure, A study for Linde AG, (2005)

[13] DOE; 2008 DOE Hydrogen Program Review Hydrogen Delivery Infrastructure Analysis, (2008), 6

[14] Trade Statistics of Japan Homepage; http://www.customs.go.jp/toukei/info/index.htm (Date of Access: 2009.8.17)

[15] Agency for Natural Resources and Energy; Standard Calorific Value Review Results and Revised Values Applicable in and after FY2005, (2007)

[16] Energy Supply and Demand Subcommittee, Advisory Committee for Natural Resources and Energy; Long-Term Energy Supply and Demand Outlook (Recalculated) (Draft), (2009)

Water Splitting and Electricity with Semiconducting Silicides in Sunight

Martin Demuth, Max-Planck-Institut für Bioanorganische Chemie, D-45413 Mülheim an der Ruhr, Germany and H2 Solar GmbH, D-79541 Lörrach, Germany
Klaus Kerpen, Andriy Kuklya, Marc-Andre Wüstkamp, Max-Planck-Institut für Kohlenforschung, D-45470 Mülheim an der Ruhr, Germany

Abstract
Generation of hydrogen and oxygen from water is described using mainly the semiconductor titanium disilicide as catalyst and halogen light which closely mimics solar radiation. The reactions are carried out under non-aerobic conditions, i.e., under nitrogen. High efficiencies are reached at 1.1-1.2 bar pressure. In the first phase of these reactions the catalytically active centers are built up. During this phase of reaction the kinetics of the water splitting process is growing in and leads to a linear dependence in the further course of the reactions which consists of >96% water splitting to yield hydrogen and oxygen in a 2:1 ratio. Hydrogen is partially and reversibly stored physically, depending on temperature. Oxygen behaves differently since it is stored entirely under the applied reaction conditions (50-80 ^{o}C and light) and can be liberated from storage upon heating the slurries in the dark. This allows convenient separation of hydrogen and oxygen. The stability of titanium disilicide has been positively tested over several months. This material is abundant and inexpensive besides that it absorbs most of the solar radiation. Further, XRD and XPS studies show that titanium disilicide is 80% crystalline and the oxide formation is limited to a few molecular layers in depth. By using labeled water it was shown that labeled dioxygen appears in the gas phase of such reactions, this showing definitively that hydrogen evolution occuring here stems from photochemical splitting of water.

Further, water splitting is part of a project which involves photoelectrochemistry and in which the silicides are used as light-receiving electrode and transition metal-coated anodes serve to split water.

Key words: Solar hydrogen and oxygen; water splitting; semiconductor photocatalysis; titanium disilicide; oxygen storage; hydrogen storage, photoelectrochemistry.

1 Water Splitting, i.e. Hydrogen and Oxygen Evolution from Water Using Silicide Catalysts as Powders and Solar Light

Hydrogen and oxygen production from water with semiconductors and light is an important issue in the exploitation of solar radiation[2] as a sustainable energy. However, a major drawback of most of the research in this field relates to the fact that appropriate semiconductors either are not readily accessible, absorb solar radiation inefficiently,[3-8] or produce hydrogen in a sacrificial manner only. We present here the use of titanium silicides, Ti_5Si_3 and $TiSi_2$, as prototypes for a promising new class of semiconductors which so far have not been used for the title application. These materials are inexpensive and abundant, and

they absorb solar radiation efficiently. A major point concerns the stability of these alloys in water, which could have been questioned a priori.[9,10] However, we anticipated that sufficiently effective passivation of the titanium silicides by a finite oxide layer might be the clou to render this project successful.[11]

The absorption characteristics of these materials are ideal for solar application: broad band reflectance measurements show a band gap range from 3.4 eV (ca. 360 nm) to 1.5 eV (ca. 800 nm) for $TiSi_2$. This is atypical of semiconductors since these materials usually exhibit little band gap spreads. Determination of the quasi-Fermi level of electrons at pH 7 afforded a value of -0.43 eV and -0.41 eV for both silicides before and after reaction, respectively.[12]

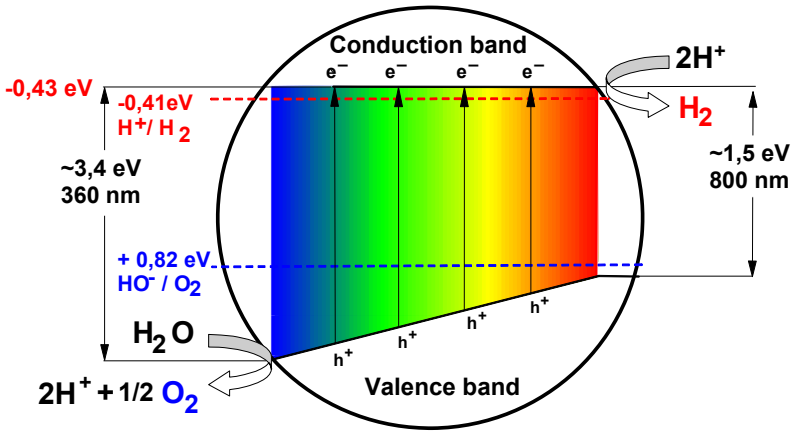

Figure 1: Band-gap range of the titanium silicide photocatalysts employed in this work.

Suspensions of titanium silicide alloys in either tridistilled or tap water, both giving identical results, at pH 7 were irradiated at 50 to 60 °C in round-bottomed flasks or cylindrical glass vessels which were equipped with a gently stirring magnetic bar and which were either closed or connected to a gas burette (*standard conditions*). In both cases non-aerobic conditions were applied, i.e., the reactions were run under nitrogen after purging the water with nitrogen. Externally positioned halogen lamps with wavelength emissions closely mimicking solar radiation served as light source with an emission range of 310-800 nm (main range at 380-780 nm). The resulting gas evolution (hydrogen and dioxygen) was monitored by gas chromatography (gc; TCD detector; column: Rt-Msieve 13X, 30 m, S-40); nitrogen served as reference gas. The gas partial pressure of the closed reactions was normalized at intervals. The majority of the reactions was run with $TiSi_2$ (2 g,[13] supplier *Alfa*; in 150 ml water), 100% light absorption and 26 cm^2 surface of irradiation); Ti_5Si_3 showed lower catalytic activity and was therefore used for exploratory experiments only.

Two rates for hydrogen evolution are observed at 55-60 °C: One for the *thermally driven reduction/addition of water to the titanium silicide giving limited amounts of sacrificially formed hydrogen* according to

$$Ti_xSi_y + 2(x+y)H_2O \rightarrow Ti_xS_y\text{oxides} + 2(x+y)H_2 \qquad (1)$$

during the initial phase A (Figure 2). This process is in part responsible for the in situ formation of the catalytically active domains (see discussion below) at both, the silicon and titanium of the alloy. Its rate depends strongly on the quality of the catalyst, temperature and pH.[14] The second rate (phase B) stands for oxygen and hydrogen formation in the *light-driven water splitting process*

$$2H_2O + h\nu + Ti_xSi_y(cat.) \rightarrow \frac{1}{2} O_2 + 2H^+ + 2e^- \qquad (2)$$

together with the exothermic *reduction of the protons* formed in *(2)*:

$$2H^+ + 2e^- \rightarrow H_2 \qquad (3)$$

Hydrogen. Phase A of hydrogen evolution (Figure 2) starts at time = 0 with conc.(H_2) = 0 and shows a non-linear grow-in dependence. Phase B is characterized by the linear part of the hydrogen evolution curve. We interprete the time dependence of hydrogen evolution as a consequence of simultaneously occuring reactions *(1)-(3)* [for illustration of the processes *(1)-(3)*, see Figure 4]. The thermal reaction *(1)* alone has initially a similar dependence but it levels off and does not yield the linear part of phase B which has been verified by dark reactions under the same conditions. At 55-60 ^oC under nitrogen phase A is distinctly replaced by phase B (Figure 2). This shows the existence of at least two processes being responsible for hydrogen production. According to our interpretation the catalytically active domains for water splitting are built up within phase A via *(1)* together with the growing-in processes *(2)* + *(3)* being essential for the activity of the catalytic domains; these are seemingly not formed in dark reactions (see above). Only minor water splitting is found in phase A (cf. run 1 in Table 1 yielding a minor amount of oxygen only) besides major sacrificial hydrogen formation via *(1)* which ceases at the end of phase A. Notably, the initially formed volume of sacrificial hydrogen remains unchanged, within exptl. error, thereafter (cf. runs 2-5 in Table 1) and >96% pure water splitting controls phase B. In a parallel run at 50 ^oC under nitrogen (Figure 3) the change of kinetics is not as significant as at 55-60 ^oC since the rate of formation of sacrificial hydrogen is lower. The limited growth of the catalytically active domains is controlled by temperature and pH.[14]

A significant increase of the water splitting rate is found at higher gas pressure as shown in Figure 3 (standard conditions, closed vessel) reaching energy conversions (η) of 4% (at rates β and ***γ*** in Figure 3).

A technically important aspect of titanium silicide semiconductors is the capacity for reversible physical hydrogen storage (for oxygen storage, see below). The hydrogen storage capacity of, e.g., ca. 20 ml H_2/g $TiSi_2$ at 30 ^oC and ca. 5-7 ml H_2/g $TiSi_2$ at 50 ^oC is certainly lower than the one encountered for other inorganic materials forming metal hydrides which, however, are technically more demanding and require higher reaction temperatures.[15] Nevertheless the hydrogen storage capacity of $TiSi_2$ is sufficient for short term storage and it minimizes undesired overpressure during reaction.

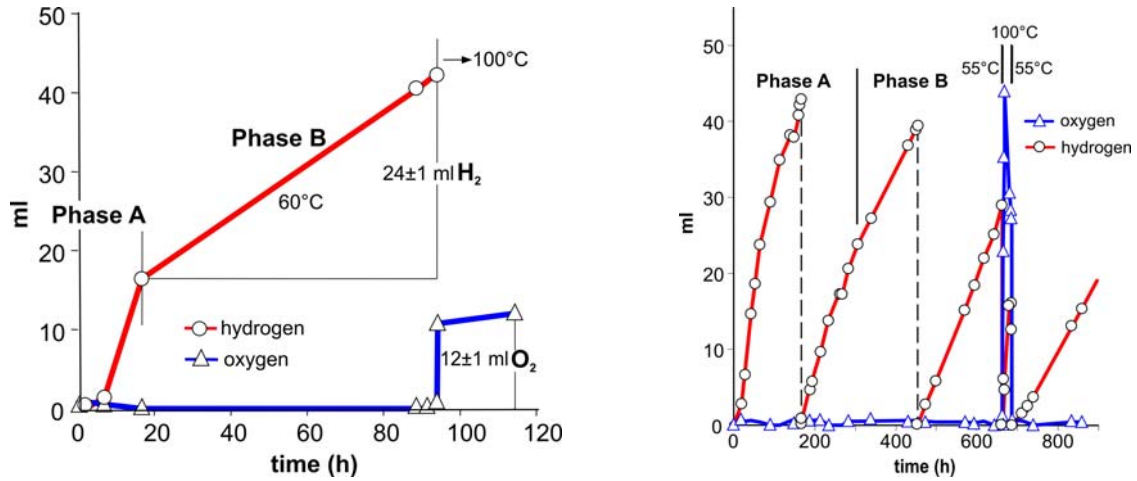

Figure 2: **Representative reactions at 60 (a) and 55 °C (b) under nitrogen. Phase-A hydrogen evolution (red): formation of the catalytic domains (cd, Figure 4) and growing in of the water splitting kinetics (2) + (3). Dashed lines: pressure release and flushing the gas phase with nitrogen (scale shift of hydrogen concentration to 0). Phases B: hydrogen evolution from water splitting (>96% by comparison with dark reactions) showing linear kinetics. Liberation of dioxygen (blue) from storage upon heating to 100 °C in the dark [cf. (a), (b) and runs 3, 5 in Table 1, respectively.**

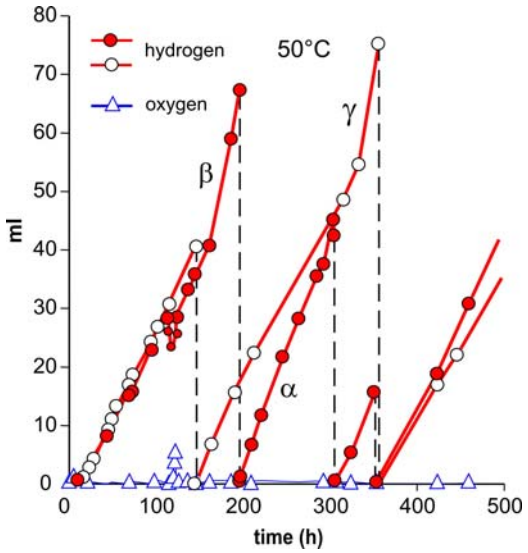

Figure 3: **Pressure dependent efficiency of water splitting as determined by hydrogen evolution measurement (reactions under nitrogen). Dashed lines: pressure release and flushing the gas phase with nitrogen (scale shift of hydrogen concentration to 0). Efficiency (η) = 4 % (at rates β and γ). β and γ rates are obtained at 1.1-1.2 bar. The reactions were run at 50 °C and in one example oxygen was released from storage in phase A after ca. 125 h by short heating to 100 °C in the dark (4x amplification of peak intensity; cf. run 1 in Table 1); thereafter the reaction was continued at 50 °C.**

Oxygen. The evolution of oxygen requires further comment since in routine runs at constant temperature only hydrogen is found in the gas phase, and dioxygen does not appear. Also there is no hydrogen peroxide detected in either gas and liquid phase. As it turned out, oxygen is stored efficiently by the titanium silicide catalyst and the conditions for its release from storage are different from those of hydrogen. A quantitative release of dioxygen sets in rapidly when reaction slurries are heated to ≥100 ^{o}C in the dark (see Figures 2, 3 and Table). An H_2/O_2 ratio of 2:1 for the water splitting process in phase B results, which is compatible with our claim that phase B-hydrogen and -dioxygen production is catalytic. This result exemplifies for the first time liberation of stored dioxygen from a semiconductor surface.[16]

A mechanistic picture regarding this particular behaviour of oxygen is still open to speculation. It could have been argued that oxygen is stored at the site where water splitting occurs, i.e., in the catalytic oxide domains [(cd) in II and III in Figure 4)]. However, these catalytic domains are unlikely the storage site for oxygen from *(2),* since its uptake by the catalyst occurs very efficiently from time = 0.[17] In this connection it is of interest to compare our result with a recent study of the adsorption of oxygen in the course of its photoreduction at a TiO_2 surface, employing ab initio calculations based on infrared data.[18] It was concluded that desorption of (ionized) oxygen is hardly possible from the surface of such a gas-solid system. Another investigation supports our finding in that a high storage capacity of TiO_2 for oxygen (25 wt%) is found upon high-temperature treatment;[16] an equilibrium between TiO_2 and a lower oxide is proposed as oxygen trap in analogy to CeO_2.[19] We favor the idea that in our system water-solubilized dioxygen leaves the catalytic domain after photolytic water splitting (III in Figure 4) and is stored thereafter under irradiation in clusters (IV in Figure 4) at the oxide layer of the catalyst formed upon oxygen addition to titanium silicide from moisture prior to submersion in water (I in Figure 4). The clusters would then release dioxygen at 100 ^{o}C.

Table 1: Analysis of the gas phase by gaschromatography.

Run	H_2 (total in the gas phase, ml)	O_2 (evolved from storage, ml) [a]	H_2 [thermal from (*1*)](ml) [b]	H_2 [from water splitting *(2)* + *(3)*] (ml) [c]
1	6	< 3 d,e	< 6	< 6
2	24	5 e	14	10
3	40	12 e	16	24
4	42	15 e	12	30
5	112	48 e	16	96

[a] Gas phase + 3 ml dissolved in water; [b] H_2 (total) - H_2 (splitting); [c] calc: ml O_2 x 2; [d] below detection limit in gas phase; [e] unloaded from storage upon heating to 100 ^{o}C in the dark. Exptl. error 5-10 %.

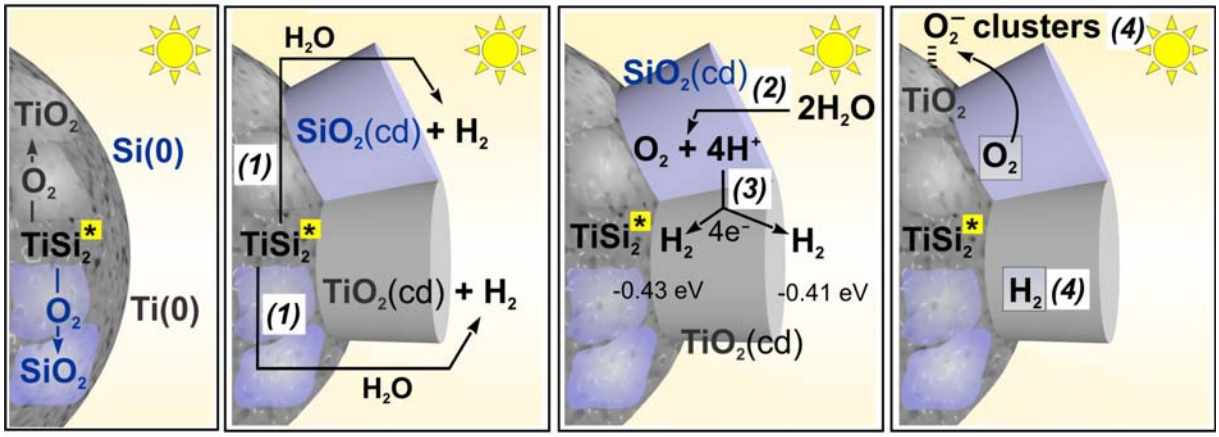

I: Dark-grown oxide layers and activation of TiSi2 with light

II: Build-up of catalytic domains (cd)

III: Water splitting (2) and reduction of protons (3)

IV: Storage of oxygen and hydrogen (reversible)

Figure 4: Proposed mechanistic events. $TiSi_2$*: electronically excited $TiSi_2$ by solar radiation (mimicked in this work by halogen light), surface partially covered by TiO_2 and SiO_2 layers originating from oxidation of $TiSi_2$ by moisture prior to water contact under irradiation (I); build up of catalytically active domains in water (1) under irradiation and nitrogen at 50-60 °C (thermal and photochemical) (II); (2) water splitting ($\rightarrow O_2 + 4H^+$) (photochemical); (3) reduction of $2H^+ \rightarrow 2H\bullet \rightarrow H_2$ (thermal) (III); (4) reversible storage of H_2 and O_2 (thermal) and formation of O_2^- clusters (photochemical) (IV).

***XRD and XP Spectroscopy*.** The aforementioned slight decrease of the reduction potential of the titanium silicides to 4.1 ± 0.1 eV at pH 7 during reaction points to the formation of titanium oxide layers or domains the potential of which is comparable with the one of TiO_2[20] (Figure 4). X-ray powder diffraction (XRD) and X-ray photoelectron spectroscopy (XPS) of the structural changes of $TiSi_2$ in

water and upon irradiation revealed intricate insights An average sample of $TiSi_2$ shows 80% crystalline and 20% amorphous phase as determined by XRD. No changes of the XRD pattern are detectable even after longer reaction times of the catalyst. Also the XPS relative peak intensities of the $TiSi_2$ samples remain constant after reaction times of 100-200 h. Both composite regions of the $TiSi_2$ are covered in part by an oxide layer and, interestingly, even after extended reaction times Ti(0) and Si(0) domains remain detectable by XPS. The oxide layers and domains, as measured for both titanium and silicon by XPS sputtering technique, are limited to a few molecular layers in depth.

In conclusion we consider the *in situ* grown catalytic domains TiO_2(cd) on the $TiSi_2$ binary alloy being responsible for hydrogen formation and the corresponding catalytic domains SiO_2(cd) for the water splitting process (see II and III in Figure 4). Under the applied reaction conditions $TiSi_2$ does not show detectable instability during phase-B water splitting over several months; hence long-lasting stability can be predicted. The hydrogen production by water splitting under the non-optimized laboratory conditions described, amounts to 20-25 ml per 26 cm^2 irradiated area at 1.1-1.2 bar and per 24 h using low-power halogen lamps, the

light intensity of which is 3-50 times lower than the total of diffuse and direct solar radiation. This corresponds to an energy conversion (η) for hydrogen formation of 4% wherein the expected high energy content of the compactly stored oxygen is not yet included.[21] The important result concerning reversible photoadsorption of oxygen at low temperatures allows beneficially convenient separation of the two product gases based on their different physisorption properties.

2 Water Splitting via Photoelectrochemistry – the Silicides Serve as Cathodes

Further, silicides are being explored as photoelectrodes for water splitting and production of electricity via electrochemical photovoltaics [1b]. A prototype of a *photoelectrochemical cell for water splitting* (TriplePowerCell, Picture 1) has been realized, consisting of a silicide cathode and a transition metal counter electrode (e.g. IrO_2). The cathode (silicide for reduction of protons to hydrogen) is the light-receiving electrode and is prepared by sputtering of the silicides on titanium sheets. The counter electrode (transition metal coating of titanium sheets serve for water splitting) is prepared by dipping method. The electrodes are inserted into an electrolyte and are separated by a Nafion membrane for selective proton exchange and for separation of the product gases hydrogen and oxygen. This device (Picture 1, below) can in the future also serve the production of electricity upon proper choice of the electrode potentials and is able to collect residual thermal energy. It is important to note that the silicide materials and counter electrodes employed for the photoelectrochemical applications are thermally (up to at least 300 °C) and mechanically stable besides being corrosion resistant.

Picture 1: TriplePowerCell assembly which adopts a silicide cathode as light receiver and a transition metal anode and is filled with an electrolyte (e.g., water - sulfuric acid or a base or salts). The system is able to a) split water into hydrogen and oxygen under acidic conditions where the product gases can be separated by a membrane, and b) the system allows to collect additionally or separately electricity, and c) the TriplePowerCell allows to collect residual thermal energy by way of a heat exchanger.

Acknowledgment

We thank the *Max Planck Society (Germany)* for generous financial support of this work.

References

[1] a) Patent: Demuth, M.; Ritterskamp, P., Generation of Hydrogen and Oxygen from Water and Storage thereof with Silicides, no 10 2005 040 255.0 (Germany) and PCT/EP2006/008333. b) German patent application no 10 2008 021 489.2: Demuth, M., Kerpen, K. Kuklya, A., Silicides for Photoelectrochemical Water Splitting and/or Production of Electricity (2008). c) Ritterskamp, P; Kuklya, A.; Wüstkamp, M.-A.; Kerpen, K.; Weidenthaler, C.; Demuth, M. Angew. Chem. Int. Ed. 2007, 119, 7917-7921.

[2] Bard, A. J.; Fox. M. A. Acc. Chem. Res. 1995, 28, 141-145.

[3] Fujishima, A.; Honda, K. Nature 1972, 238, 37-38.

[4] Kato, H.; Kudo, A. J. Phys. Chem. B 1972, 106, 5029-5034.

[5] Sayama, K.; Mukasa, K.; Abe, R.; Abe, Y.; Arakawa, H. Chem. Comm. 2002, 2416-2417.

[6] Maeda, K.; Takata, T; Hara, M; Saito, N; Inoue, Y; Kobayashi, H; Domen, K. J. Am. Chem. Soc. 2005, 127, 8286-8287.

[7] Maeda, K.; Teramura, K.; Takata, T.; Hara, M.; Saito, N.; Toda, K.; Inoue, Y.; Kobayashi, H.; Domen, K. .J. Phys. Chem B 2005, 109, 20504-20510.

[8] Maeda, K.; Teramura, K.; Lu, D.; Takata, T.; Saito, N., Inoue, Y.; Domen, K. Nature 2006, 440, 295.

[9] a) Murarka, S. P. Ann. Rev. Mater. Sci. 1983, 13, 117-137. b) Silicides – Fundamentals and Applications, Miglio, L.; d'Heurle, F. (eds.), World Scientific (Singapore, New Jersey, London, Hong Kong) (2000).

[10] Murarka, S. P. Annu. Rev. Mater. Sci. 1983, 13, 117-137.

[11] Holleman, A. F.; Wiberg, E.: Lehrbuch der Anorganischen Chemie/Holleman-Wyberg, de Gruyter (Berlin, New York), 101st ed., pp. 890ff (1995).

[12] We thank Professor H. Kisch and Dipl.-Chem. J. Eberl, Dept. of Inorganic Chemistry, University of Erlangen-Nürnberg, Germany, for helpful discussions and the measurements of the quasi-Fermi levels.

[13] The relatively large amount of TiSi2 is chosen to provide for sufficient oxygen storage during irradiation. For catalytic purposes alone 20% of this amount is sufficient to overcome the slow water-gas exchange processes at the heterogeneous catalytic site.

[14] Results to be published and work in progress.

[15] Bellosta von Colbe, J. M.; Schmidt, W.; Felderhoff, M.; Bogdanovic, B.; Schüth, F. Angew. Chem Int. Ed. 2006, 45, 3663-3665.

[16] Cf. a literature claim of reversible dioxygen storage, not substantiated by experiment except in an indirect disclosure where hydrocyrbons are oxidized by oxygen-enriched TiO2: Sinel'niko, V. V.; Tolkachev, N. N.; Stakheev, A. Y. Kinetics and Catalysis 2005, 46, 550-554 and refs. 10-14 cited therein.

[17] This has been verified by runs under air wherein oxygen uptake under irradiation is constant and fast even from time = 0, i.e., at the onset of formation of the catalytically active domains.

[18] a) Mattioli, G.; Filipponi, F.; Bonapasta, A. M. J. Am. Chem. Soc. 2006, 126, 13772-13780. b) Gerischer, H.; Heller, A. J. Electrochem. Soc.1992, 139, 113-118.

[19] Kaspar, J.; Fornasiero, P.; Hockey, N. Catal. Today 2003, 77, 419.

[20] Carp, O.; Huisman, C. L.; Reller, A. Progress in Solid State Chemistry 2004, 32, 33-177.

[21] This result compares favorably with the efficiencies reported for other semiconducting materials used for water splitting with visible light, all having so far drawbacks: One example of 2.5 % efficiency evidently works for short reaction times and within a narrow wavelength range of solar radiation only (ref. 8); all others lie <1 % (refs 7, 22). Further improvement of the photo-electrocatalytic Grätzel multicomponent system (ref. 23) which employs dyes for sufficient light absorption and electrolytes, both being photodegradable, achieves 8 % efficiency (ref. 24).

[22] Sayama, K.; Mukasa, K.; Abe, R.; Abe, Y.; Arakawa, H. Chem. Commun. 2005, 2416-2417.

[23] Grätzel, M. Nature 2001, 414, 338-344.

[24] http://www.hydrogensolar.com/november24.html.

IrO_2 Nanoparticle-decorated Water Oxidation Catalysts for Semiconductor Photoanodes

Klaus Hellgardt, Dept of Chemical Engineering, Imperial College London, UK
P. Bumroongsakulsawat, S. Dennison, G.H. Kelsall, Dept of Chemical Engineering, Imperial College London, UK

Hydrogen has applications as a fuel for both vehicle and stationary power generation. It is very conveniently, if expensively, produced by electrolysis of water. If electrolysis could be driven by solar energy, hydrogen becomes the ultimate “green” fuel, with low environmental impact in both production and consumption.

Solar photoelectrolysis of water, in which one or both electrodes in an electrolyser are powered by solar photons to split water into hydrogen and oxygen, has been investigated intensively, since the original publication [1] using a TiO_2 photo-anode. Most photoelectrochemical studies in water splitting have focused, for stability reasons, on the development of oxygen evolving photoanodes. These operate according to the reaction scheme (1-3) below:

$$SC + h\nu \rightarrow SC(h^+_{VB}, e^-_{CB}) \quad (1)$$

$$2H_2O + 4h^+_{VB} \longrightarrow O_2 + 4H^+ \quad (2)$$

$$2H_2O + 2e^-_{CB} \longrightarrow H_2 + 2OH^- \quad (3)$$

The absorption of a photon of energy greater than the band gap energy of the semiconductor generates an electron-hole pair in process (1). The space charge field in the semiconductor causes separation of the generated charge carriers. Holes are driven to the electrode surface, where they oxidise water to oxygen by reaction (2). Conversely, electrons are driven via an external circuit to a cathode at which water is reduced to hydrogen by reaction (3).

The photoanode should be an oxide in order to withstand the strongly oxidising conditions of oxygen evolution. However, most oxides are wide band gap semiconductors, and thus not well-matched to the solar spectrum. Advances in materials engineering have enabled materials better matched to the solar spectrum, but intrinsically less efficient, to be considered as potential photoelectrodes [2-4]. Their absorption of visible light has attracted interest in Fe_2O_3 (E_g ca. 2.2 eV, threshold absorption < 565 nm) and WO_3 (2.6 eV, threshold absorption = 475 nm). However, both Fe_2O_3 and WO_3 are poor oxygen evolution catalysts, which limit the overall kinetics and therefore the efficiency of water splitting. One approach to improve the water splitting efficiency is to modify the semiconductor with suitable electrocatalysts that increase oxygen evolution kinetics. Recently, this has been achieved with Fe_2O_3, using a cobalt-phosphate (Co-Pi) catalyst [5]. Transition metal oxides, such as IrO_2 and RuO_2 are known to be active oxygen electrocatalysts [6] and can be produced as

nanoparticles, which would enable decoration of surfaces with catalyst layers sufficiently thin to permit unhindered photon absorption by the semiconductor.

We report results of decorating Fe_2O_3 photoanode surfaces with IrO_2 nanoparticles, deposited by means of an electrochemical process [6, 7].

1 Experimental

Fe_2O_3 thin films, doped with tin, were deposited by spray pyrolysis from an ethanol solution of $FeCl_3$ and $SnCl_2$ (Sn/Fe = 0.05-0.6%) onto fluorine-doped tin oxide-coated glass heated to 450 °C on a hotplate. Details of the spray pyrolysis process and film growth will be described elsewhere [8]. IrO_2 was electrodeposited onto the Fe_2O_3 films from two solutions:

1. Oxalate-stabilised IrO_2 at +1.4 V vs. SCE [7].
2. Hydroxide-stabilised IrO_2 at +1.0 and +1.4 V vs. SCE [6].

Electrodeposition was carried out for times ranging from 1 ms to 100 s to achieve a range of IrO_2 coverage. The photoelectrochemical behaviour of Fe_2O_3, before and after IrO_2 decoration, was measured in 0.1 mol dm^{-3} NaOH, using standard techniques. A silver wire was used as a quasi-reference electrode (QRE) in the photoelectrochemical experiments. The QRE potential was regularly measured against a saturated calomel (SCE) as +0.125 V (SCE) to determine the stability of the QRE potential. All electrochemical measurements were made using an Eco Chemie Autolab 320N potentiostat.

2 Results and Discussion

Fig. 1 shows the typical response of untreated Fe_2O_3 in 0.1 M NaOH. In the dark, the current remains in a range ±2 $\mu A\ cm^{-2}$, for potentials between -0.5 and +0.5 V (QRE). At potentials > +0.5 V (QRE) a rapid increase in current occurred due to oxygen evolution by reaction (2). This behaviour was observed for a range of Fe_2O_3 films with different $SnCl_2$ doping levels (0.05 to 0.6% in precursor solution) and thicknesses (200-500 nm) Fe_2O_3 was stable when cycled to potentials above +1.4 V (QRE), resulting in a significant rate of oxygen evolution. However, they were very sensitive to the negative potential limit of the potential cycle, undergoing irreversible reduction at potentials below approximately -0.6 V (QRE).

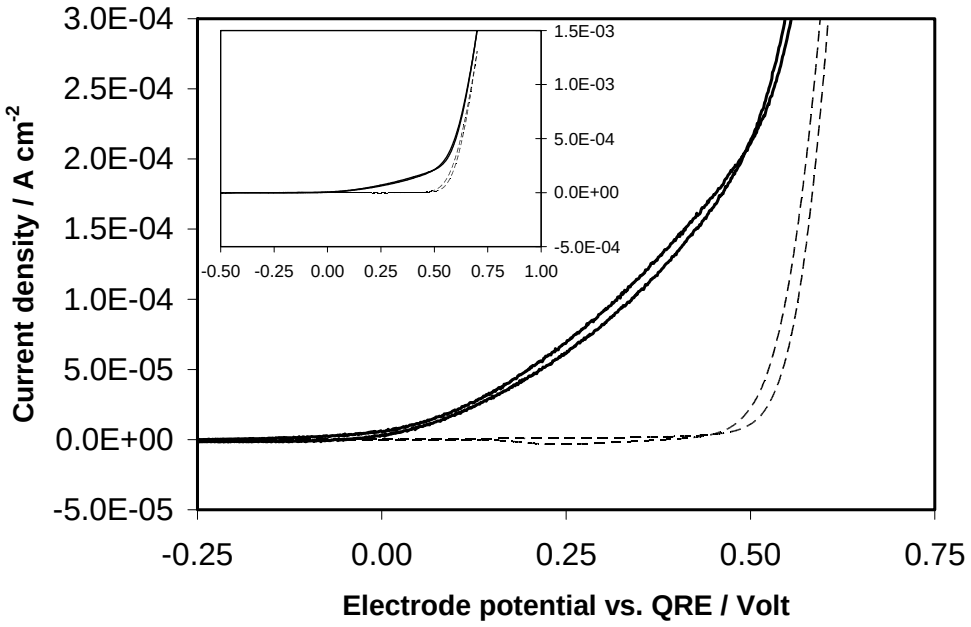

Figure 1: Current-potential response for a Fe_2O_3 electrode in 0.1 M NaOH: dashed line: dark current; solid line: white light illumination (20 W m^{-2}). Potential scan rate: 0.01 V s^{-1}. Inset shows the full response between -0.5 and +0.75 V (QRE).

Upon illumination with white light, the photocurrent onset potential was ca. 0 V (QRE). Under continuous illumination, the photocurrent did not reach a limiting value before the onset of light-independent oxygen evolution occurred. However, using chopped light and phase-sensitive detection, the photocurrent-potential response shown in Fig. 2, exhibiting a plateau. These reflect more closely the expected form of the photocurrent-potential behaviour for a semiconductor-electrolyte interface.

Fig. 2 also shows the effect of depositing ca. 0.2 monolayer of IrO_2 for 10 ms at +1.4 V vs. SCE onto the surface of the Fe_2O_3. The limiting photocurrent increased and there was a -0.2 V shift in the photocurrent onset potential when IrO_2 was present on the Fe_2O_3 surface. This indicated that the deposited IrO_2 catalysed the water oxidation reaction (2) by photogenerated holes in the Fe_2O_3. The catalytic effect of the IrO_2 was also highlighted by the decrease in the photocurrent for the IrO_2-decorated Fe_2O_3 at +0.5 V (QRE). This was due to an increase in the light-independent oxygen evolution reaction rate, which increased rapidly and prevented accurate subtraction of the photocurrent.

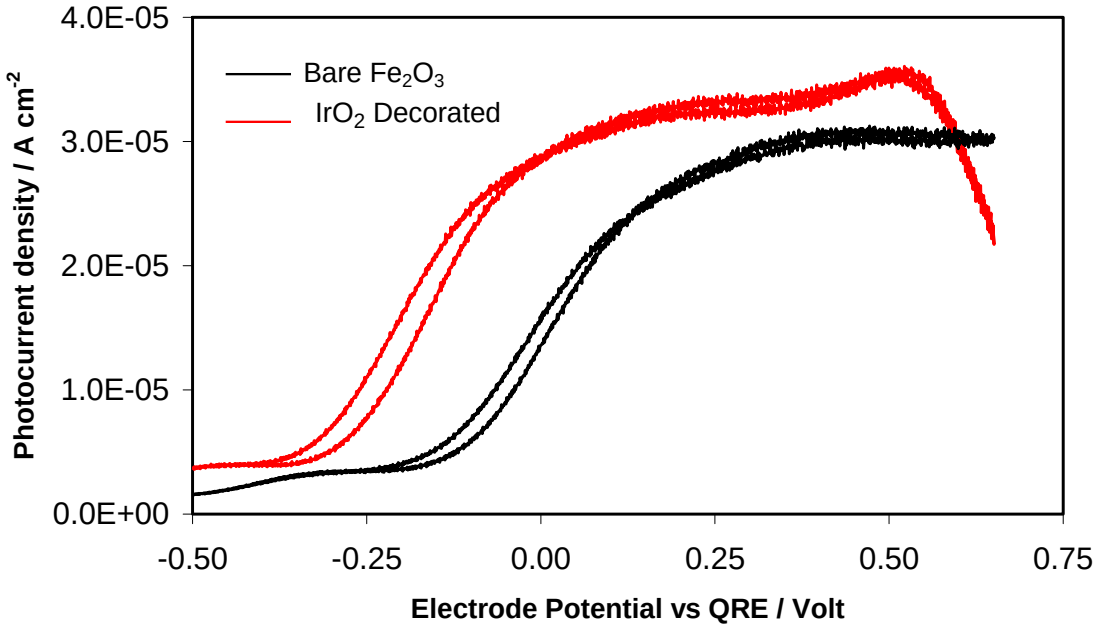

Figure 2: Photocurrent-potential response of Fe_2O_3: no IrO_2 (black); after 10 ms IrO_2 deposition at +1.4 V vs. SCE (red). Light chopped at 87 Hz; potential scan rate: 0.01 V s^{-1}.

The coverage of the Fe_2O_3 by IrO_2 deposited in the 10 ms was estimated to be ca. 0.2 of a monolayer of IrO_2, assuming that each IrO_2 had a molecular radius of 135 pm and required 1 electron per molecule for deposition. The effect of IrO_2 coverage on the photocatalytic activity was investigated further by depositing IrO_2 for both shorter and longer times. During these experiments, it was evident that, although there was an initial enhancement of the Fe_2O_3 photo-response, this was quite short-lived. In the case of short deposition times (0.1-100 ms), the enhanced activity due to IrO_2 persisted for only 2 - 3 potential cycles under illumination. Following these cycles, the photo-response returned to the same level as before IrO_2 deposition.

The IrO_2 deposition was investigated further using a hydroxide-stabilised solution of IrO_2 nanoparticles. Although the current density – potential behaviour of this deposition process was different, the same result was observed, with initial enhancement of photo-response decreasing over three potential cycles to that observed before IrO_2 deposition. However, if IrO_2 was deposited for 100 s, an initial decrease in photo-response was observed. Further potential cycling resulted in a slight increase in photo-response, which gradually tended towards that before IrO_2 deposition.

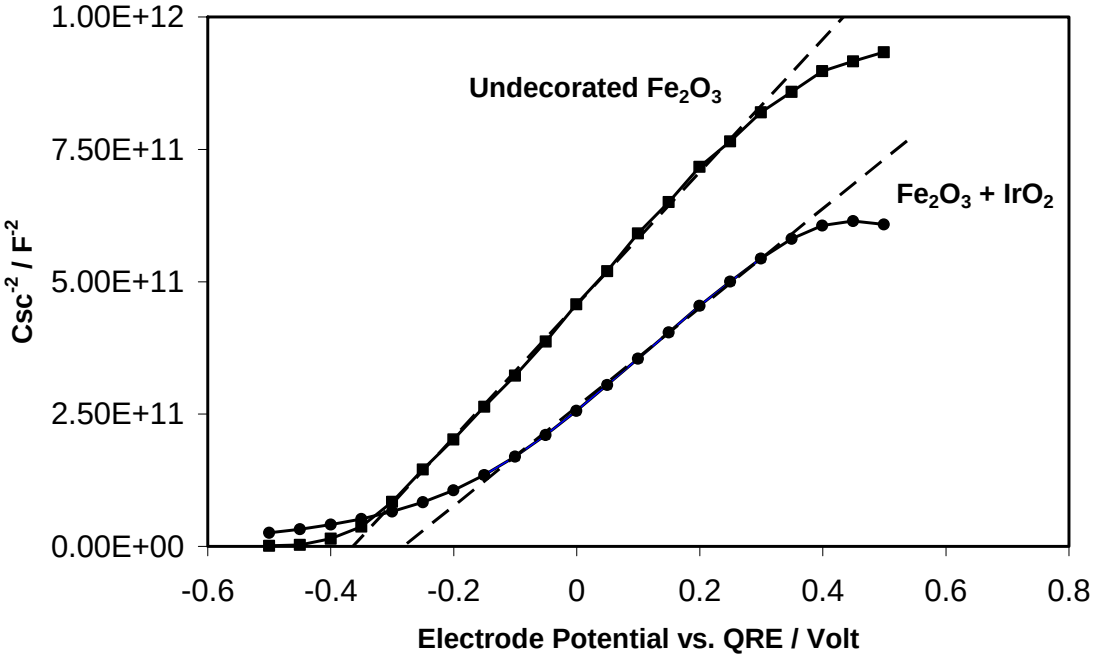

Figure 3: Mott-Schottky plots of Fe_2O_3 electrodes in 0.1 M NaOH. a) undecorated Fe_2O_3 (squares); b) Fe_2O_3 after IrO_2 deposition for 10 s at +1.4 V vs. SCE.

Further analysis of Fe_2O_3 before and after IrO_2 deposition was carried out using electrochemical impedance spectroscopy to determine the flat band potential and dopant density of the semiconductor, using the Mott-Schottky relationship. Fig. 3 shows Mott-Schottky plots for Fe_2O_3, before and after coating with IrO_2. For the undecorated Fe_2O_3, the flat band potential was found to be -0.35 V (QRE), in the range of previously determined values for Fe_2O_3. On depositing IrO_2, the flat band potential shifted slightly to ca. -0.3 V (QRE), apparent doping density increased, corresponding to a lower gradient in Fig.3, and no irreversible damage to the semiconducting properties of the Fe_2O_3 was apparent.

These results show that the photocurrent onset potential was very close to the flat band potential. This shows that the catalysis was efficient for as long as the IrO_2 catalyst persisted on the surface, since photocurrent was generated under conditions of low band bending. IrO_2 deposition on Fe_2O_3 enhanced the usually slow surface kinetics [9], decreasing photocurrent onset potentials by several tenths of a volt.

Analysis of the electrolyte for dissolved iridium species is being undertaken to determine whether loss of photocatalytic activity was (improbably) due to dissolution of the IrO_2.

3 Conclusions

These results demonstrated that IrO_2, at sub-monolayer coverage, enhanced the photo-response of Fe_2O_3 photoanodes, lowering the onset potential for photocurrent (oxygen evolution) by 0.2 V compared to the un-catalysed surface. However, the effect of the IrO_2 deposit was transient, usually persisting for only a few minutes on potential cycling. The deposition of IrO_2 did not appear to affect Fe_2O_3 irreversibly, suggesting that this approach to enhancing photo-response should be extended to other photoanode materials.

Further work is required to determine why the effect of IrO_2 lasts only for a short time, since it is known to be stable to oxygen evolution under similar conditions on metallic electrodes.

References

[1] A. Fujishima and K. Honda, Nature, 1972, 238, 37.

[2] B. O'Regan and M. Grätzel, Nature, 1991, 353, 737.

[3] A. Kay, I. Cesar and M. Grätzel, J. Amer. Chem. Soc. 2006, 128, 15714.

[4] K. Sivula, F. Le Formal and M. Grätzel, Chem., Mater. 2009, 21, 2862.

[5] D.K. Zhong, J. Sun, H. Inamaru and D.R. Gamelin, J. Amer. Chem. Soc. 2009, 131, 6086.

[6] T. Nakagawa, C.A. Beasley and R.W. Murray, J. Phys. Chem. C, 2009, 113,12958

[7] S.A.M. Marzouk, Anal. Chem. 2003, 75, 1258.

[8] S. Dennison, K. Hellgardt, G.H. Kelsall, in preparation.

[9] M.P. Dare-Edwards, J.B. Goodenough, A. Hamnett and P.R. Trevellick, J.C.S. Faraday Trans. 1983, 79, 2027.

Double Surfactants-assisted Hydrothermal Synthesis of $Cd_{1-x}Zn_xS$ Solid Solution as an Efficient Visible-light-driven Photocatalyst for Hydrogen Production

Maochang Liu, Liejin Guo, Xi'an JiaoTong University, Xi'an, China

1 Introduction

Photocatalytic hydrogen production from water splitting under visible light by semiconductor has attracted increasing attention for its many advantages [1-4]. In view of practical application of photocatalytic hydrogen production technique, reduction of the photocatalyst cost is one of the key issues. CdS, as one of the most well-known semiconductor photocatalysts, has been used for water splitting due to its proper band gap of approximately 2.4 eV and good absorption properties of visible light [5, 6]. However, CdS is prone to produce photocorrosion in aqueous solution under light irradiation. Lots of efforts have been made to improve the stability of metal sulfide, for example, by loading noble metal (Pt, Ru et al.) [7, 8], incorporating the nanoparticles of metal sulfides into the interlayer photocatalysts [9-11], and compound with oxide, for example, TiO_2 [12]. It has been reported that CdS could also be modified by ZnS to form a solid solution, resulting in enhanced stability and photoactivity. This method required no noble metal loading, which means low cost [13-16]. Thus, active photocatalysts free of noble metal like $Cd_{1-x}Zn_xS$ is valuable in this consideration. However, the activity of $Cd_{1-x}Zn_xS$ prepared by traditional methods is still far from being satisfactory for commercial utilization. Development of new approach for the preparation of $Cd_{1-x}Zn_xS$ with improved activity and stability is thus highly valued.

In present work, a series of nano-$Cd_{1-x}Zn_xS$ solid solution were prepared by a double surfactants-assisted hydrothermal method. Results showed that the as-prepared photocatalysts had a very high activity for hydrogen production under visible light from Xe lamp. The factors for this high activity were investigated and the amount of catalyst for the photocatalytic reaction was optimized.

2 Experiment

2.1 Preparation of photocatalysts

The details are as follows: NaOH aqueous solution (4 M, 10 mL), SDS (0.1 M,10 mL), SDBS (0.025 M, 9 mL) were sequently spilled into a aqueous solution (20 ml) containing stoichiometric $Cd(Ac)_2 \cdot 2H_2O$ and $Zn(Ac)_2 \cdot 2H_2O$ (n(Cd)+n(Zn)=0.02 mol), then thioacetamide (0.025 mol) were added to the previous mixture. The whole process was carried out under magnetic stirring. The reaction mixture was stirred for 20 min, and then was sealed in a 60mL capacity Teflon-lined stainless steel autoclave. Mixtures of different molar ratio for Cd and Zn were heated under autogenous pressure at 130℃ for 24 h; mixtures of the molar ratio 1:1 for Cd and Zn were heated under temperatures of 130℃, 150℃, 170℃, 180℃, 190℃, 210℃ and 230℃ for 24h, respectively. After cooling, the products were separated by

centrifugation, washed with deionized water and ethanol several times, and dried at 80 ℃ for 5 h in a vacuum oven.

2.2 Characterization

These as-prepared $Cd_{1-x}Zn_xS$ photocatalysts were characterized by X-ray diffraction (XRD) confirmed by an X'Pert PRO diffractometer using Cu Ka irradiation; diffuse reflectance UV-vis spectra measured on a Hitachi U-4100 instrument employed with a lab-sphere diffuse reflectance accessory; and a JEOL JSM-6700F field emission scanning electron microscopy (SEM). Surface areas were determined by a Beckman Coulter SA3100 instrument.

2.3 Photocatalytic reaction

Photocatalytic reactions of hydrogen production from water were conducted in a gas-closed system with a side irradiation Pyrex cell. The effective area for the cell is 12.56 cm2. The photocatalyst powder (0.2 g) was dispersed by a magnetic stirrer in an aqueous (200 mL) containing Na_2S (0.35 M) and Na_2SO_3 (0.25 M) as electron donors. The photocatalysts were irradiated with visible light (λ≥ 430 nm) through a cutoff filter from a 350 W Xe lamp. The amount of H_2 gas was determined using online thermal conductivity detector (TCD) gas chromatography (NaX zeolite column, TCD detector, N_2 carrier). Apparent quantum yields defined by eq 1 were measured using a 425 nm band pass filters and an irradiatometer.

$$\text{A.Q.Y}(\%) = \frac{\text{The number of reacted electrons}}{\text{The number of incident photons}} \times 100$$
$$= \frac{\text{The number of evolved } H_2 \text{ molecules} \times 2}{\text{The number of incident photons}} \times 100 \qquad (1)$$

3 Results and Discussion

3.1 Crystal structure and morphology of nano-$Cd_{1-x}Zn_xS$

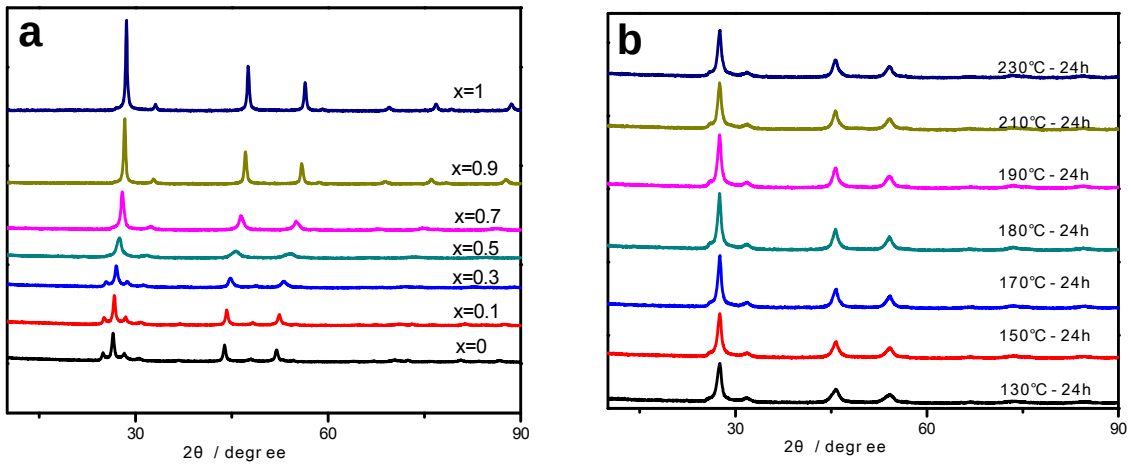

Figure 1: XRD patterns of nano-$Cd_{1-x}Zn_xS$ solid solution. a) $Cd_{1-x}Zn_xS$ solid solution of different molar ratio for Cd and Zn prepared at 130 ℃. b) $Cd_{0.5}Zn_{0.5}S$ prepared under different temperature.

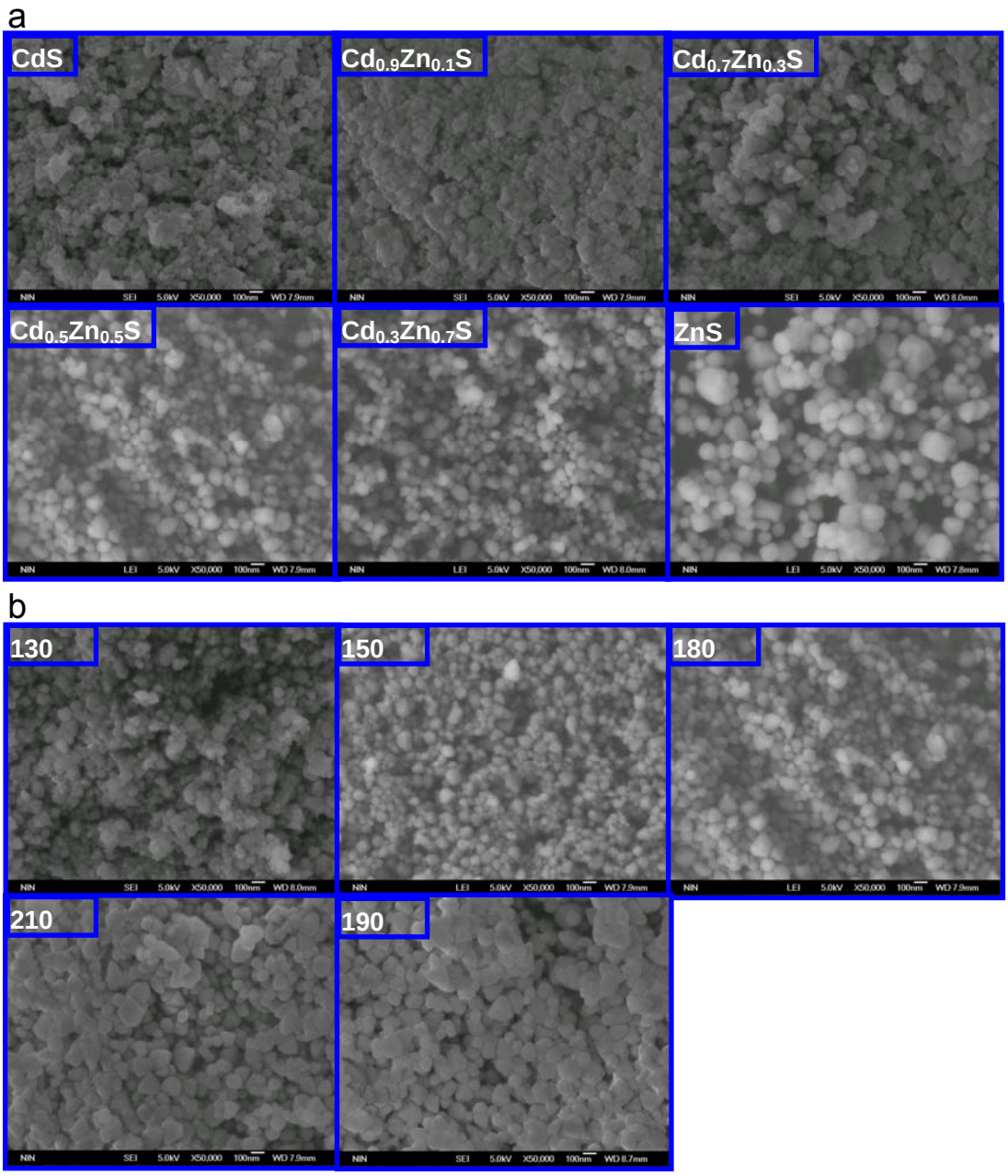

Figure 2: **SEM patterns of nano-$Cd_{1-x}Zn_xS$ solid solution. a) Cd1-xZnxS solid solution of different molar ratio for Cd and Zn prepared at 130 ℃ for 24h. b) $Cd_{0.5}Zn_{0.5}S$ prepared under different temperature.**

The crystal structure of $Cd_{1-x}Zn_xS$ photocatalysts was investigated by X-ray diffraction as shown in Figure 1. As shown in Figure 1(a), it is found that the peaks are gradually shifted to a higher-angle side with the increase of Zn concentration from hexagonal CdS to cubic ZnS. Similar phenomenon had also been reported by Zu [17] and Nien [18]. This successive shift indicates that CdS and ZnS a not mechanically mixed but formed a solid solution. The radii of Zn^{2+} ion (0.74 Å) is smaller than Cd^{2+} ion (0.97 Å), so Zn^{2+} ion could easily insert into the CdS Lattice or enter its interstitial sites [19-21]. Moreover, the electronegativities of Cd (1.69) and Zn (1.65) are very close to form a solid solution [22]. The interplane spacing of $Cd_{1-x}Zn_xS$

solid solution became smaller with the increase of Zn concentration for the smaller radii of Zn^{2+} ion than Cd^{2+} ion, which means a decrease in crystal lattice parameters (a, b, c). As a result, the peaks are shifted to the higher-angle side with the increase of Zn concentration. It is also found that the intensity of the peaks is enhanced by the increase of Zn concentration, which indicated that, from CdS to ZnS, more cubic crystals with better crystallization are formed. The temperature has little impact on the photocatalysts' X-ray diffraction property as shown in Figure 1(b). The SEM pictures of the as-prepared photocatalysts are shown in Figure 2. As shown in Figure 2(a), Well-crystallized particles with estimated particle sizes of ~100nm are observed. Interestingly, the surface morphology of the crystals is a mixture of polyhedrons and near-nano-sphere; moreover, the higher content of Zn, the more sphere-like crystals obtained. So it can be inferred that the formation of these near-nano-spherical particles is mostly because of the existence of the cubic phase, while the formation of nano-polyhedron particles is a result of hexagonal phase. The nano-particles, with uniform size, shape, will enhance the separation of electrons and holes, increase the transfer rate of electrons, and decrease their body composite [23]. So the activity of the photocatalyst can be greatly increased. Temperature is another important factor that impacts the growth of the crystals. As shown in Figure 2(b), the crystals grow with the increase of temperature, indicating better crystallinity.

3.2 Optical properties of nano-$Cd_{1-x}Zn_xS$ solid solution

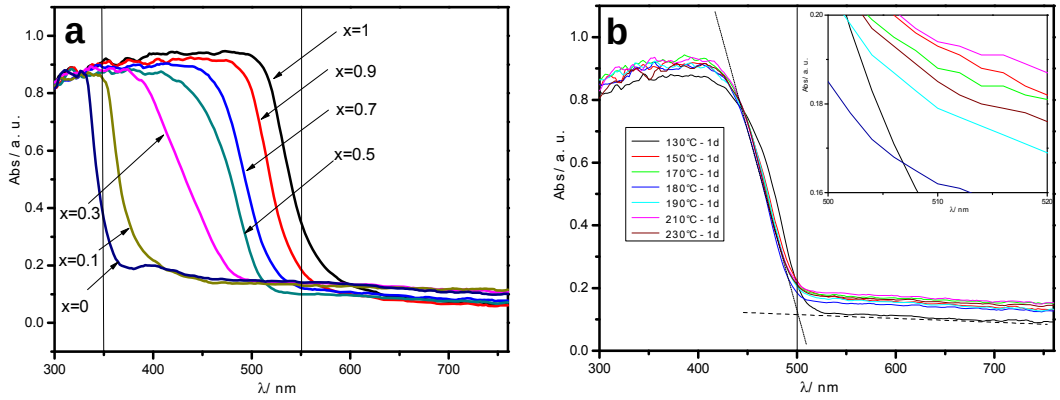

Figure 3: UV-Vis spectrum of nano-$Cd_{1-x}Zn_xS$ solid solution. a) $Cd_{1-x}Zn_xS$ solid solution of different molar ratio for Cd and Zn prepared at 130 ℃ for 24h. b) $Cd_{0.5}Zn_{0.5}S$ prepared under different temperature.

Figure 3 shows the UV-Vis absorption spectra of nano-$Cd_{1-x}Zn_xS$ photocalalysts. As shown in Figure 3(a) the absorption edges are gradually red shift with the increase of x, from about 350 nm to about 560 nm, which also prove that CdS and ZnS have formed a solid solution. Figure 3(d) shows the nearly same absorption spectra of $Cd_{0.5}Zn_{0.5}S$ photocatalysts prepared at different temperatures, indicating that synthesized temperature has little influence on band structures of the as prepared photocatalysts. The band structures of solid solution are schematically shown in Figure 4. The band gap size of $Cd_{1-x}Zn_xS$ solid solution shift monotonously in energy (from 2.2eV to 3.5eV, calculated by the UV-Vis absorption spectra with the Kubelka-Munk method [24]). This variation in the band structure of the solid solution

is a result of Cd^{2+} ion, which offers a lower conduction band, incorporated in the Zn Lattice. The sharp absorption curve indicates the absorption almost purely due to the band-gap transition of electrons.

3.3 Photocatalytic activity of nano-$Cd_{1-x}Zn_xS$

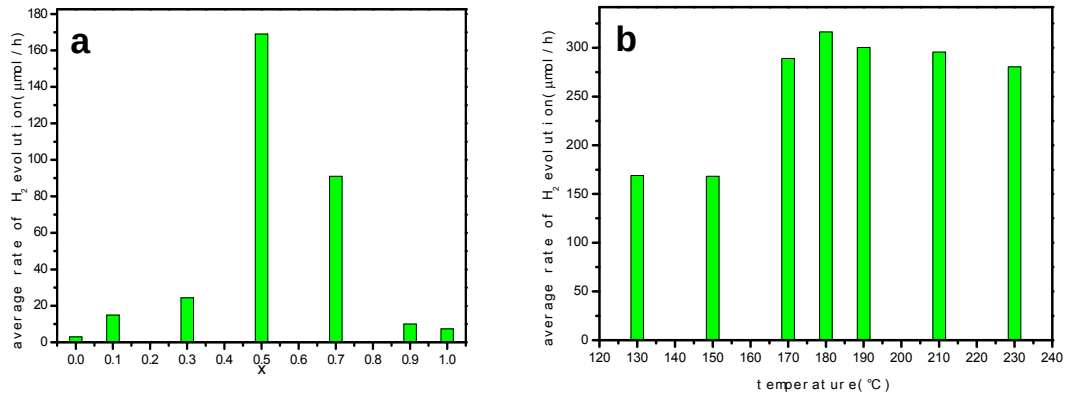

Figure 4: Rate of H_2 evolution by nano-$Cd_{1-x}Zn_xS$ solid solution. a) $Cd_{1-x}Zn_xS$ solid solution of different molar ratio for Cd and Zn prepared at 130 ℃ for 24h. b) $Cd_{0.5}Zn_{0.5}S$ prepared under different temperature.

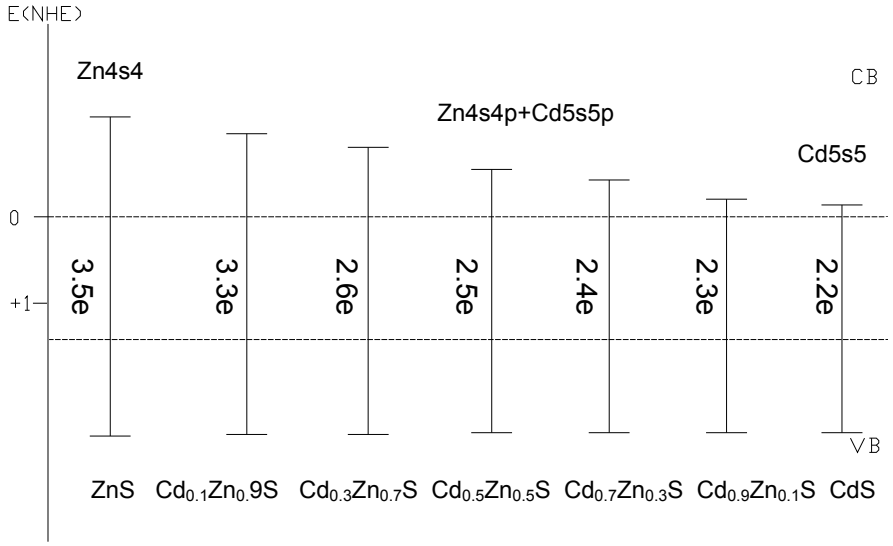

Figure 5: Band structure of nano-$Cd_{1-x}Zn_xS$ solid solution

It was found that the nano-$Cd_{1-x}Zn_xS$ solid solution prepared by precipitate-hydrothermal method showed a good activity for water splitting hydrogen production under visible light. As shown in Figure 6(a), $Cd_{0.5}Zn_{0.5}S$ had the highest activity for hydrogen production. The band gap energy can be increased with the increase of Zn content, along with the elevation of the conduction band position, which will enhance the mobility of the photogenerated carriers, thus promoted the photocatalytic activity [19]. However, the ability of absorbing and the

utilizing photons by the catalysts will be decreased. So an appropriate Zn or Cd content could balance the two factors to gain a good solid solution with the highest-activity. As we can see, the critical concentration of Zn is 50% in molar ratio. The crystallinity is another important factor for the photocatalytic activity. As analysed above, better crystallinity can be obtained at higher temperature. $Cd_{0.5}Zn_{0.5}S$ photocatalysts prepared at different temperatures were used to investigate the impact of temperature. It is found that the photocatalytic activity increases with the temperature rised as shown in Figure 5(b). When the temperature got to 180 ℃, the rate of hydrogen production under visible light reached the highest, 316 μmol/h, without loading noble metal. And the apparent quantum yield of it at 425 nm reached 30%. Go on increasing the temperature will not promote the activity. As we known, crystallinity will be better when temperature increased. However, the surface area of the crystal will be decrease in this process, which is not favorable for photocatalytic reaction. Thus a critical temperature for the synthesis of nano-$Cd_{1-x}Zn_xS$ solid solution is needed to balance the conflict of crystallinity and surface area to gain the highest photocatalytic activity.

In summary, a series of nano-$Cd_{1-x}Zn_xS$ solid solution were synthesized by a precipitate-hydrothermal method. The visible-light-driven catalysts exhibited a very high activity for hydrogen production by water splitting. The activity of the solid solution was greatly influenced by Zn content, which attributed to its impact on the crystallinity, conduction band and light absorption and electron transferred ability associated to changes in band gap, etc. The photocatalytic activity of the photocatalyst reached the highest when x=0.5 ($Cd_{0.5}Zn_{0.5}S$) and prepared at 180 ℃, corresponding to the average rate 316 μmol/h for hydrogen production under visible light without loading noble metal, and the apparent quantum yield at 425 nm reached 30%, which is one of the highest quantum efficiencies reported in the literature for naked photocatalyst without loading noble metal to the best of our knowledge.

Acknowledgements

This work was financially supported by the National Natural Science Foundation of China (Contracted No. 50521064) and the National Basic Research Program of China (Contracted No. 2009CB220000).

References

[1] Osterloh, F. E., Inorganic Materials as Catalysts for Photochemical Splitting of Water. *Chemistry of Materials* 20 (2008), 35-54.

[2] Maeda, K.; Teramura, K.; Lu, D.L.; Takata, T.; Saito, N.; Inoue, Y.; Domen, K., Photocatalyst releasing hydrogen from water. *Nature* 440 (2006), 295.

[3] Jing, D.; Zhang, Y.; Guo, L., Study on the synthesis of Ni doped mesoporous TiO_2 and its photocatalytic activity for hydrogen evolution in aqueous methanol solution. *Chem. Phys. Lett*. 415(2005) 74-78.

[4] Kudo, A., Development of photocatalyst materials for water splitting. *Int. J. Hydrogen Energy* 31(2006), 197-202.

[5] Matsumura, M.; Furukawa, S.; Saho, Y.; Tsubomura, H., Cadmium sulfide photocatalyzed hydrogen production from aqueous solutions of sulfite: effect of crystal structure and preparation method of the catalyst. *J. Phys. Chem*. 89(1985), 1327-1329.

[6] Reber, J.F.; Meier, K., Photochemical hydrogen production with platinized suspensions of cadmium sulfide and cadmium zinc sulfide modified by silver sulfide. *J. Phys. Chem.* 90(1986), 824-834.

[7] Li, Y.X.; Lu, G.X.; Li, S.B., Photocatalytic reduction of Rhodamine B over Pt-TiO2. *Appl. Catal. A* 15(2001), 287-290.

[8] Li Y.X.; Du J.; Peng S.Q.; Xue D.; Lu G.X.; Li S.B., Enhancement of photocatalytic activity of cadmium sulfide for hydrogen evolution by photoetching. *Int. J. Hydrogen Energy* 33(2008), 2007-2013.

[9] Shangguan, W.; Yoshida, A., Synthesis and photocatalytic properties of CdS-intercalated metal oxides. *Solar Energy Mater Solar Cells* 69(2001), 189-194.

[10] Tawkaew, S.; Fujishiro, Y.; Yin, S.; Sato, T., Synthesis of cadmium sulfide pillared layered compounds and photocatalytic reduction of nitrate under visible light irradiation. *Colloids Surfaces A: Physicochem Eng Aspects* 179(2001), 139-144.

[11] Fujishiro, Y.; Uchida, S.; Sato, T., Synthesis and photochemical properties of semiconductor pillared layered compounds. *J. Inorg. Mater.* 1(1999), 67-72.

[12] Xing, C.; Jing, D; Liu, M.; Guo, L., Photocatalytic hydrogen production over $Na_2Ti_2O_4(OH)_2$ nanotube sensitized by CdS nanoparticles. *Materials Research Bulletin* 44(2009), 442-445.

[13] Xing, C.; Zhang, Y.; Guo, L., Band structure-controlled solid solution of $Cd_{1-x}Zn_xS$ photocatalyst for hydrogen production by water splitting. *International Journal of Hydrogen Energy* 31(2006), 2018-2024.

[14] Zhang, X.; Jing, D.; Liu, M.; Guo, L., Efficient photocatalytic H_2 production under visible light irradiation over Ni doped $Cd_{1-x}Zn_xS$ microsphere photocatalysts. *Catalysis Communications* 9 (2008), 1720-1724.

[15] Zhang, K.; Jing, D.;Xing, C.; Guo, L., Significantly improved photocatalytic hydrogen production activity over $Cd_{1-x}Zn_xS$ photocatalysts prepared by a novel thermal sulfuration method. *International Journal of Hydrogen Energy* 32 (2007), 4685 – 4691.

[16] Liu, G.; Zhao, L.; Ma, L.; Guo, L., Photocatalytic H_2 evolution under visible light irradiation on a novel $Cd_xCu_yZn_{1-x-y}S$ catalyst. *Catalysis Communications* 9 (2008) 126-130.

[17] Zu, S.; Wang, Z.; Liu, B.; Fan, X.; Qian, G., Synthesis of nano-$Cd_xZn_{1-x}S$ by precipitate-hydrothermal method and its photocatalytic activities. *Journal of Alloys and Compounds* 476(2009), 689-692.

[18] Nien, Y.; Chen, P.; Chen, I., Synthesis and characterization of $Zn_{1-x}Cd_xS$:Cu, Cl red electroluminescent phosphor powders. *J. Alloys Compd.* 462 (2008), 398-403.

[19] del Valle, F.; Ishikawa, A.; Domen, K. et al., Influence of Zn concentration in the activity of $Cd_{1-x}Zn_xS$ solid solutions for water splitting under visible light. *Catalysis Today* 143 (2009), 51-56.

[20] Nayeem, A.; Yadaiah, K.; Vajralingam, G.; Mahesh, P.; Nagabhooshanam, M., Structural characterization of co-precipitated $Cd_{1-x}Zn_xS$:Cu crystals. *International Journal of Modern Physics B: Condensed Matter Physics, Statistical Physics, Applied Physics* 16(2002), 481-496.

[21] Cherin, P.; Lind, E.L.; Davis, E.A., Preparation and crystallography of cadmium zinc sulfide solid solutions. *J. Electrochem. Soc.* 117 (1970), 233-236.

[22] Dean, J.A., Lange's Handbook of Chemistry, *McGraw-Hill Book Co. Beijing* 1999.

[23] Sebastian, M.T.; Krishna, P. The discovery of a 2H-6H solid state transformation in zinc cadmium sulfide ($Zn_xCd_{1-x}S$) single crystals. *Solid State Commun.* 48 (1983), 879-882.

[24] Morales, A. E.; Mora, E. S.; Pal, U. Use of diffuse reflectance spectroscopy for optical characterization of un-supported nanostructures. *Revista Mexicana de Fisica S* 53 (2007), 18–22.

Latex-supported, Dye-sensitised, TiO_2 Core Shell Spheres, for the Photocatalytic Generation of Hydrogen from Water

Costanzo Lorenzo, Thomas Maschmeyer, Anthony F. Masters, University of Sydney, Australia

A sustainable method of hydrogen production for use as a fuel for energy generation is one area of research aimed at reducing carbon emissions from fossil fuels. Photo-catalytic hydrogen generation from water is attractive from an environmental perspective as harvesting solar energy and converting it into chemical energy is a sustainable natural process (photosynthesis). The facile release of energy stored in the H−H bond upon reaction with oxygen, yielding water as the only chemical product of the reaction, makes hydrogen an attractive, clean energy carrier and a possible, ideal solution for energy- related issues in the long-term [1].

Conventional electrolysis of water requires the generation of electricity in a separate process, leading to gross overall inefficiencies of the reaction system. Direct water splitting avoids this issue.

TiO_2-based materials are expected to play an important role as photocatalysts [2], both for the removal of organic pollutants from water and for the photocatalytic generation of hydrogen from water. An issue that needs to be overcome is the fact that TiO_2 predominantly absorbs ultra-violet light, which constitutes only 4% of the solar spectrum. For this reason it is necessary to sensitise crystalline titania towards visible wavelengths, an aim that can be achieved either by doping [3,4] the crystalline structure or coating its surface with organic [5,6] or metallorganic dyes [7,8]. The issues with these enhancements are that firstly, the insertion of dopant into the crystalline structure can create defects which become good recombination sites for the electron and hole pair formed by the absorption of a photon, and secondly, dyes could be desorbed from the surface of the TiO_2.

Here we report a novel core-shell TiO_2 structure, containing a dye supported on a polymeric sphere, enabling direct evolution of H_2 gas from an aqueous solution using light of visible wavelengths.

The basis of this concept is to covalently bind a dye-sensitiser to a support and the support/dye combination is then encapsulated by a thin layer of TiO_2, which serves as both the photocatalyst and as a physical barrier, preventing desorption of the dye.

Two different configurations of sensitised TiO_2 structures were prepared. In the first configuration, polystyrene latex spheres were synthesised using emulsion polymerisation with 4,4'-azobis(4-cyanovaleric acid) as the initiator. This process leaves carboxylic acid groups on the surface of the latex sphere (diameter: ~500 nm) [9]. These carboxylic acid groups were then functionalised with an organic dye (Rhodamine B isothiocyanate) through NHS/EDC (NCS=N-hydroxysuccinimide; EDC=1-Ethyl-3-[3-dimethylaminopropyl]carbodiimide hydrochloride), coupling [10]. Subsequently these latex spheres were suspended in dry butyl-1-methylpyrrolidinium bis-triflamide [11], under inert

atmosphere, to which titanium isopropoxide was added. The Ti-precursor was then hydrolysed at 80 °C upon addition of water. This hydrolysis reaction although at low temperature, allows the synthesis of nanocrystalline anatase TiO_2 (studies were performed at different temperatures in the range 60□100 °C, Fig.2). A second ruthenium dye (N3) was then adsorbed onto the surface of the titania crystals. For the second configuration the polystyrene spheres were functionalised with the ruthenium dye (N3), with a similar procedure followed for the organic dye and then the TiO_2 layer was hydrolysed onto the dye-functionalised polystyrene surface, again in the presence of the pyrrolydinium ionic liquid. The crystals were then platinised (0.5 wt.% Pt to TiO_2).

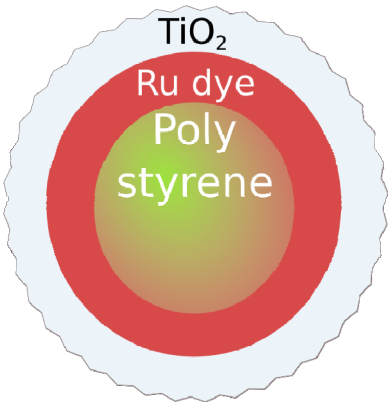

Figure 1: (a) Schematic illustrating of the core shell structure.

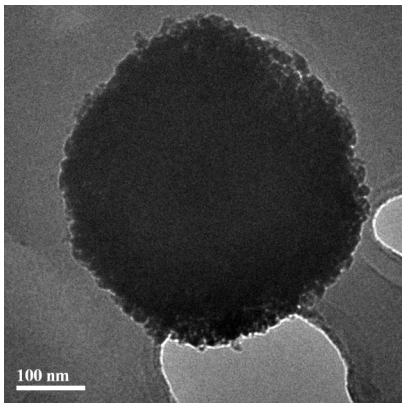

Figure 1: (b) TEM micrograph of a polystyrene sphere coated with TiO_2 nanocrystals.

The coating of the polystyrene sphere with TiO_2 in the ionic liquid was required to obtain a crystalline structure without the need for calcination at 450 °C, which would have destroyed both the polystyrene substrate and the organic sensitisers.

Photochemical testing of the materials for hydrogen generation was performed in a double walled quartz reactor, thermostated to 25 °C. The catalyst was suspended in a water:methanol (10:1) solution and deoxygenated with nitrogen before irradiation with a mercury lamp (350 W, Oriel) equipped with a water filter and cut-off filters (305, 395, 430 nm). Argon was used as a carrier gas to convey any hydrogen produced into an online GC for quantification with a TCD detector.

The preliminary studies for the synthesis of TiO_2 at low temperatures, allowed the formation of crystalline titania even at temperatures as low as 60 °C (Fig. 2), significantly lower than the ones previously reported in the literature [11].

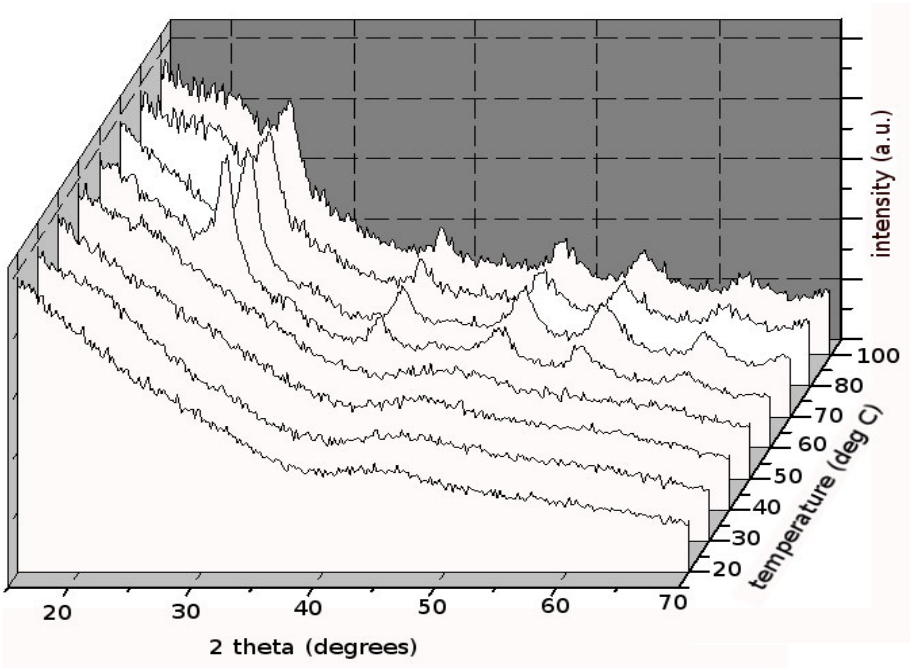

Figure 2: XRD diffractograms of TiO_2 hydrolysed at different temperatures.

The coating of the polystyrene spheres was performed in a buffered solution at pH 7.4 (phosphate buffered saline), after activation with NHS/EDC, ethylendiamine was added to the suspension in order to obtain an amino terminated chain, which could readily react with isothiocyanate groups present onto the rhodamine B dye. Confocal microscopy images confirm the presence of the dye on the surface of the PS spheres, before (Fig. 3a) and after coating with the TiO_2 layer (Fig. 3b). The second image shows that although the spheres are almost uniformely coated, the dye underneath is still capable of absorbing visible light.

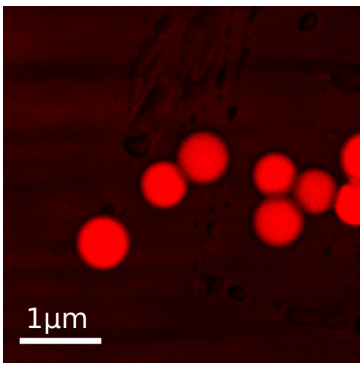

(a) before coating with TiO_2.

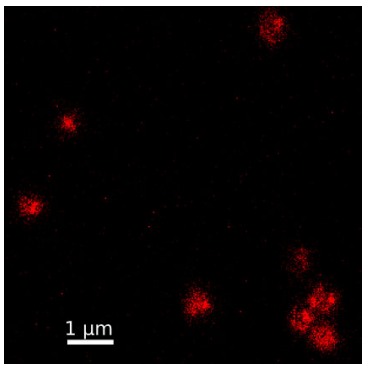

(b) after coating with TiO_2.

Figure 3: Confocal microscopy images under irradiation at 530 nm.

The expected spherical morphology of the TiO_2 coated spheres was confirmed by TEM (Fig. 1b) and the crystallinity of the titania was verified by X-ray diffraction analysis. The diameter of the composite was slightly larger than of the uncoated spheres (~500 nm), showing a layer

roughly 20□30 nm thick. Occasionally larger agglomerates of TiO_2 crystals were observed to protrude from the surface of the beads.

Tests for photochemical hydrogen production show that the visible light sensitised structure is still active under irradiation at 430 nm (Fig. 4) , in contrast with the standard P25 which is active only in the UV region.

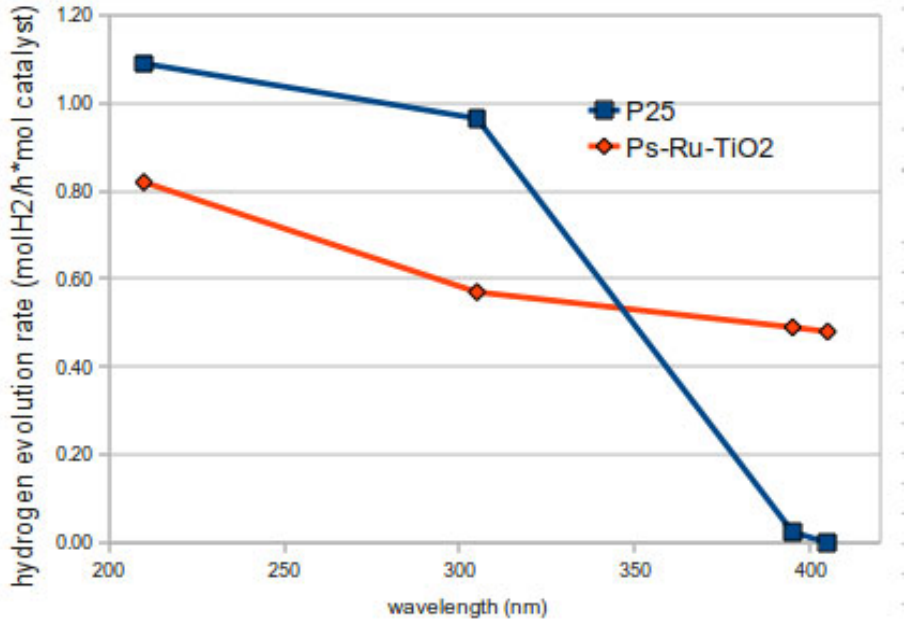

Figure 4: Hydrogen evolution rate of P25 and the N3 sensitised PS-dye-TiO_2 structure.

In conclusion, the step-wise process allowed the synthesis of supported, dye-sensitised TiO_2 core shell structures, which benefit from both crystallinity and dye encapsulation for photo-catalytic hydrogen production.

The TiO_2 structures will have to be further optimised and then tested for recyclability and stability of the dyes to photo-degradation. A newly acquired solar simulator will be used for more accurate testing of the catalyst.

References

[1] Bockris, J. O. International Journal of Hydrogen Energy 27, 731-740.

[2] Fujishima A. ScienceDirect - Journal of Photochemistry and Photobiology C: Photochemistry Reviews : Titanium dioxide photocatalysis.

[3] Zhu, J.; Deng, Z.; Chen, F.; Zhang, J.; Chen, H.; Anpo, M.; Huang, J.; Zhang, L. Applied Catalysis B: Environmental 2006, 62, 329-335.

[4] Tsai, C.; Teng, H. Applied Surface Science 2008, 254, 4912-4918.

[5] Li, Y.; Xie, C.; Peng, S.; Lu, G.; Li, S. Journal of Molecular Catalysis A: Chemical 2008, 282, 117-123.

[6] Abe, R.; Hara, K.; Sayama, K.; Domen, K.; Arakawa, H. Journal of Photochemistry and Photobiology A: Chemistry 2000, 137, 63-69.

[7] Park, H.; Bae, E.; Lee, J.; Park, J.; Choi, W. The Journal of Physical Chemistry B 2006, 110, 8740-8749.

[8] Bae, E.; Choi, W. The Journal of Physical Chemistry B 2006, 110, 14792-14799.

[9] Pham, B. T. T.; Nguyen, D.; Ferguson, C. J.; Hawkett, B. S.; Serelis, A. K.; Such, C. H. Macromolecules 2003, 36, 8907-8909.

[10] VanDelden, C.; Bezemer, J.; Engbers, G.; Feijen, J. JOURNAL OF BIOMATERIALS SCIENCE-POLYMER EDITION 1996, 8, 251-268.

[11] Al Zoubi, M.; Farag, H.; Endres, F. Aust. J. Chem. 2008, 61, 704-711.

A Novel One-step Hydrothermal Method for the Preparation of $Cd_{1-x}Zn_xS$/Titanate Nanotubes Composites for Photocatalytic Hydrogen Production

Yubin Chen, **Liejin Guo**, State Key Laboratory of Multiphase Flow in Power Engineering, School of Energy and Power Engineering, Xi'an Jiaotong University, China

Photocatalytic water splitting over semiconductors has attracted much attention as a promising route for hydrogen production [1-3]. Taking the solar spectrum into account, it is indispensable to develop visible-light-driven photocatalysts. One of the most well-known semiconductor photocatalyst, CdS, has been widely used for hydrogen evolution. However, pure CdS is usually not very active and prone to photocorrosion. Combining CdS with the wide band gap semiconductor ZnS to form the solid solution $Cd_{1-x}Zn_xS$ is demonstrated to be an effective way to solve the above problems [4-6]. By adjusting the value of x, the conduction band and the band gap of $Cd_{1-x}Zn_xS$ can be modified to well meet the requirement of the photocatalytic reaction. Thus the efficient photocatalytic hydrogen production is achieved over $Cd_{1-x}Zn_xS$ photocatalyst even without cocatalyst loaded. As known, CdS has been extensively used to form nanocomposite photocatalysts with other semiconductors so that the efficient charge separation can occur [7-9]. And yet the nanocomposites of $Cd_{1-x}Zn_xS$ are not common, partly because it is difficult to exactly control the metal compositions of Cd and Zn and to obtain the intimate contacts between two components in the composites.

In 1998, Kasuga et al [10] developed a simple method to prepare nanotubes by the hydrothermal treatment of TiO_2 powder in 10 M NaOH solution, which are generally considered as titanate nanotubes (TNTs) [11]. Titanate nanotubes combine many properties of conventional TiO_2 nanoparticles with their distinguishing feature of one-dimension nanostructure, large surface-to-volume ratio, high sedimentation rate and ion-exchangeable ability. These interesting properties make TNTs suitable to form efficient composite photocatalysts with other semiconductors [12,13].

Here, a novel one-step hydrothermal method was developed to prepare series of $Cd_{1-x}Zn_xS$/titanate nanotubes(TNTs) composite photocatalysts, where the exact metal compositions of Cd and Zn were obtained. Meanwhile, it was discovered that the $Cd_{1-x}Zn_xS$ nanoparticle with high crystallinity was surrounded by a network of well-developed TNTs in the nanocomposites, resulting in the well dispersed $Cd_{1-x}Zn_xS$ nanoparticles and the intimate multipoint contacts between $Cd_{1-x}Zn_xS$ and TNTs. The activity was evaluated by photocatalytic hydrogen evolution from aqueous solution containing Na_2SO_3/Na_2S as sacrificial reagents under visible light irradiation. In detail, the photocatalytic reaction was performed in a side irradiation Pyrex cell with stirring. The efficient irradiation area for the cell was 15.90 cm^2. 190 mL of aqueous solution containing 0.2 g of catalyst, as well as 0.25 M Na_2SO_3/0.35 M Na_2S as sacrificial reagents, was added into the cell. A 500 W Xe lamp

equipped with a cut-off filter (λ > 430 nm) was used as the light source, and the irradiation power after the filter was monitored by an irradiatometer to be 55 mW cm^{-2}. In the research, the value of x was optimized, and compared with the single $Cd_{1-x}Zn_xS$, the composite photocatalysts showed much higher activity for hydrogen production.

Table 1 summarizes series of $Cd_{1-x}Zn_xS$/TNTs photocatalysts with various compositions. It can be seen that the metal compositions of Cd and Zn in each composite catalyst didn't change much compared to its stoichiometric ones. During the process of preparation, $Cd_{1-x}Zn_xS$ nanoparticles were first formed, which could successfully avoid the loss of the metal compositions.

Table 1: The composition of $Cd_{1-x}Zn_xS$/TNTs.

Photocatalyst	The stoichiometric composition	The composition
a	$Cd_{0.1}Zn_{0.9}S$/TNTs	$Cd_{0.12}Zn_{0.88}S$/TNTs
b	$Cd_{0.3}Zn_{0.7}S$/TNTs	$Cd_{0.34}Zn_{0.66}S$/TNTs
c	$Cd_{0.5}Zn_{0.5}S$/TNTs	$Cd_{0.57}Zn_{0.43}S$/TNTs
d	$Cd_{0.7}Zn_{0.3}S$/TNTs	$Cd_{0.74}Zn_{0.26}S$/TNTs
e	$Cd_{0.9}Zn_{0.1}S$/TNTs	$Cd_{0.91}Zn_{0.09}S$/TNTs

Fig. 1 shows the XRD patterns of various photocatalysts. The XRD traces of single TNTs were similar to those of alkali or hydrogen titanates, which exhibited an orthorhombic structure [14]. For the composite photocatalysts, XRD patterns of TNTs and crystalline $Cd_{1-x}Zn_xS$ appeared. It can be discovered that the diffraction peaks assigned to TNTs in all the composites were the same. However, the diffraction peaks of $Cd_{1-x}Zn_xS$ changed a lot. As the value of x increased, the diffraction peaks shifted to higher angles indicating that the crystals obtained were not simple physical mixture of CdS and ZnS but the $Cd_{1-x}Zn_xS$ solid solutions. Further analysis revealed that the $Cd_{1-x}Zn_xS$ solid solutions exhibited both cubic phase and hexagonal phase, which can be clearly seen through the XRD pattern of $Cd_{0.5}Zn_{0.5}S$. And with the increase of x, the major crystal structure of the solid solution changed from the hexagonal wurtzite structure to the cubic zinc-blende one [5].

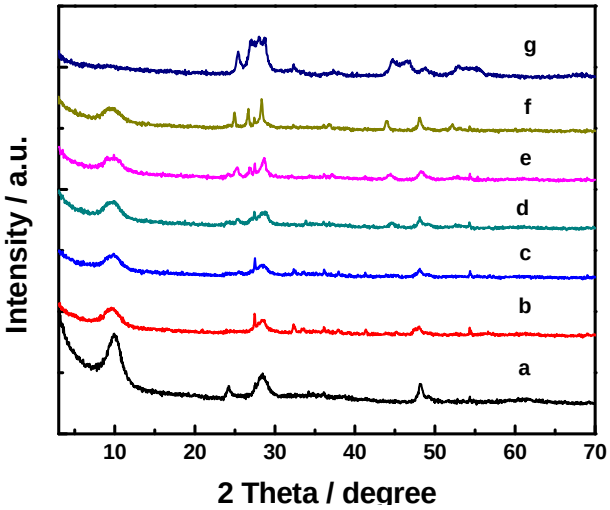

Figure 1: **The XRD patterns of photocatalysts: (a) TNTs, (b) $Cd_{0.1}Zn_{0.9}S$/TNTs, (c) $Cd_{0.3}Zn_{0.7}S$/TNTs, (d) $Cd_{0.5}Zn_{0.5}S$/TNTs, (e) $Cd_{0.7}Zn_{0.3}S$/TNTs, (f) $Cd_{0.9}Zn_{0.1}S$/TNTs, (g) $Cd_{0.5}Zn_{0.5}S$.**

Fig. 2 shows the TEM images of the obtained products. As shown in Fig. 2a, titanate nanotubes have been successfully synthesized and presented uniform distribution, in accordance with the literature [11]. Fig. 2b showed the TEM image of $Cd_{0.5}Zn_{0.5}S$/TNTs prepared by our one-step hydrothermal method. Interestingly, $Cd_{0.5}Zn_{0.5}S$ nanoparticles of ca. 100nm were well dispersed and enwrapped by the network of titanate nanotubes tightly in the composites. This unique architecture successfully avoided the agglomeration of $Cd_{0.5}Zn_{0.5}S$ nanoparticles and finally led to the intimate multipoint contacts between the $Cd_{0.5}Zn_{0.5}S$ primary particle and the surrounding titanate nanotubes (Fig. 2c). During the hydrothermal treatment, titanate nanotubes were obtained by transformation of TiO_2 nanoparticles and $Cd_{0.5}Zn_{0.5}S$ nanoparticles grew further. Some titanate nanotubes would grow along the $Cd_{0.5}Zn_{0.5}S$ nanoparticle. Hence, CdS and TNTs well accreted in the hydrothermal process and the intimate lattice contacts between the nanocrystallines were achieved.

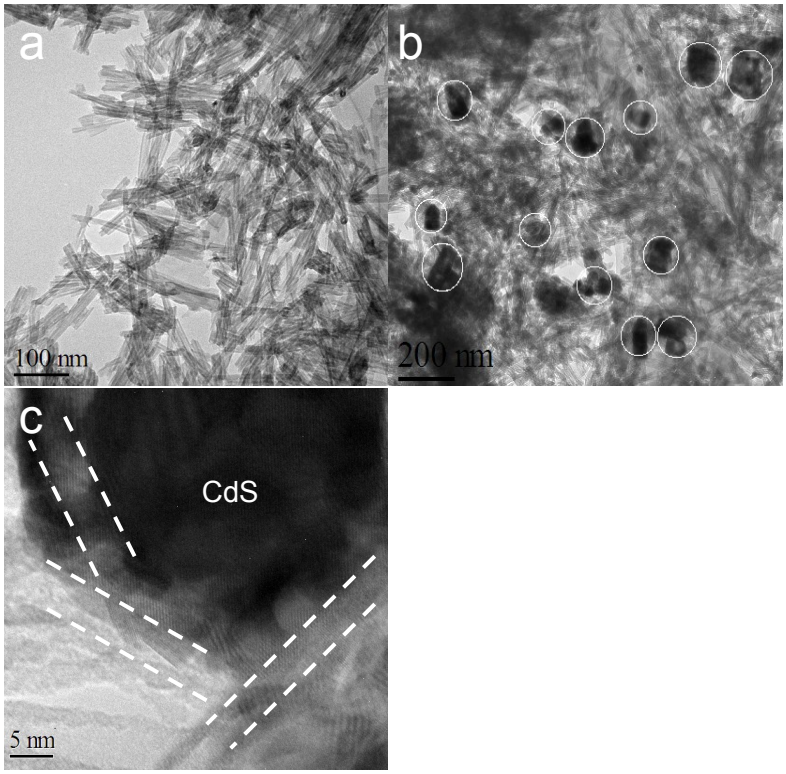

Figure 2: TEM images of various samples: (a) TNTs, (b) $Cd_{0.5}Zn_{0.5}S$/TNTs, (c) the multipoint contacts between $Cd_{0.5}Zn_{0.5}S$ and TNTs.

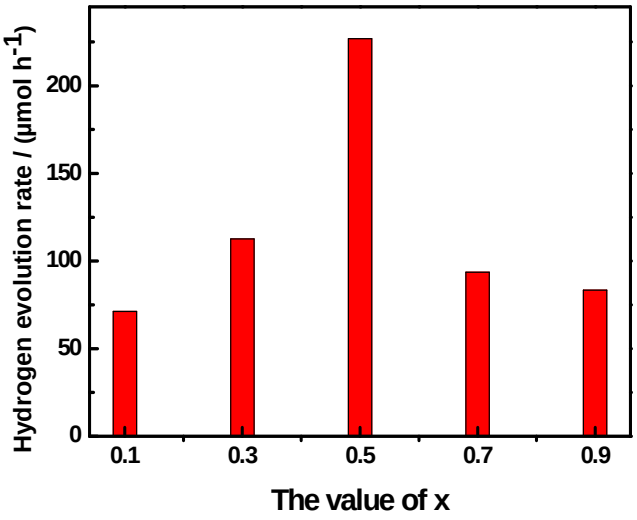

Figure 3: Photocatalytic H_2 evolution over different $Cd_{1-x}Zn_xS$/TNTs samples.

Fig. 3 shows the photocatalytic H_2 evolution over different $Cd_{1-x}Zn_xS$/TNTs samples. With the increase of x, the hydrogen production rate initially increased and then underwent a decrease. $Cd_{0.5}Zn_{0.5}S$/TNTs displayed the best photocatalytic activity, probably due to the suitable band gap and the favorable conduct- ion band of $Cd_{0.5}Zn_{0.5}S$. XRF analysis result

confirmed that the content of $Cd_{0.5}Zn_{0.5}S$ in the $Cd_{0.5}Zn_{0.5}S$/TNTs sample is as small as 8.7 wt%. This is important from an environmental point of view because of the toxicity of Cd^{2+}. The comparison between the photocatalytic activities of single $Cd_{0.5}Zn_{0.5}S$ and $Cd_{0.5}Zn_{0.5}S$/TNTs have been displayed in Fig. 4. Corresponding to the unit gram of $Cd_{0.5}Zn_{0.5}S$, $Cd_{0.5}Zn_{0.5}S$/TNTs exhibits significantly higher activity.

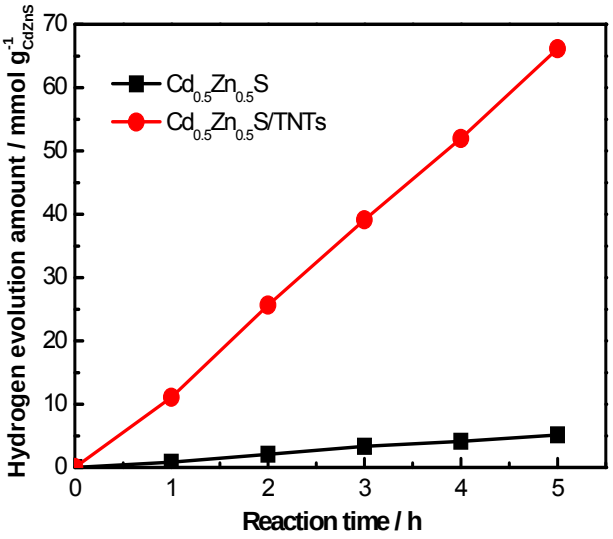

Figure 4: The time courses of hydrogen evolution over $Cd_{0.5}Zn_{0.5}S$/TNTs and $Cd_{0.5}Zn_{0.5}S$.

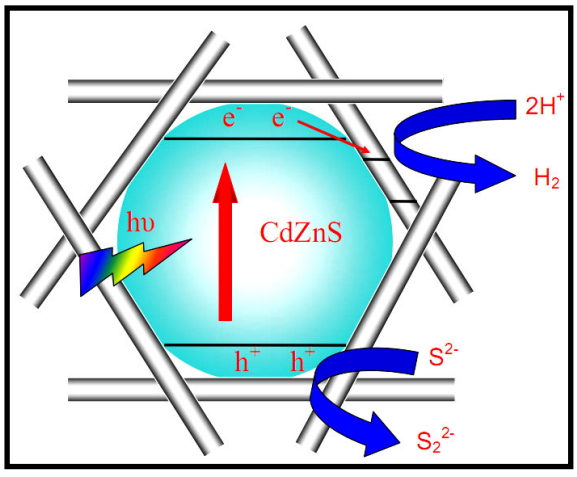

Figure 5: The schematic model of charge seperation in $Cd_xZn_{1-x}S$/TNTs composites.

For a photocatalyst to be highly active, the separation of photoinduced electrons and holes should be effective. As illustrated in Fig. 5, the $Cd_{1-x}Zn_xS$ nanoparticle was surrounded by a network of titanate nanotubes in $Cd_xZn_{1-x}S$/TNTs composites, which could avoid the agglomeration of $Cd_{1-x}Zn_xS$ nanoparticles and lead to the intimate multipoint contacts. The appropriate dispersion of $Cd_{1-x}Zn_xS$ nanoparticles could reduce the recombination of photogenerated charges, contributing to the highly efficient charge separation. The multipoint

contacts mean that when $Cd_{1-x}Zn_xS$ nanoparticle was irradiated with light, more paths could be used to transfer photogenerated electrons to the surrounding TNTs, and more efficient charge separation could be achieved. In addition, the one-dimensional tubular structure of titanate nanotubes was beneficial for enhanced mobility of electrons transferred from CdS, and their large surface area could offer more photocatalytic active sites to facilitate the photoexcited electrons reacting with the water molecule for hydrogen evolution. In summary, the efficient composite photocatalysts have been achieved through the novel one-step hydrothermal method. Both the conclusions drawn from this research and the novel preparation method itself can be extended to the preparation of other composite photocatalysts with even higher efficiency.

Acknowledgments

The authors gratefully acknowledge the financial support of the National Natural Science Foundation of China (Grant No. 50821064) and the National Basic Research Program of China (Grant No. 2009CB220000).

References

[1] Z. Zou, J. Ye, K. Sayama, H. Arakawa, Nature 2001, 414, 625.

[2] D. Lu, T. Takata, N. Saito, Y. Inoue, K. Domen, Nature 2006, 440, 295.

[3] A. Kudo, Y. Miseki, Chem. Soc. Rev. 2009, 38, 253.

[4] C. Xing, W. Yan, Y. Zhang, L. Guo, Int J Hydrogen Energy 2006, 31, 2018.

[5] K. Zhang, D. Jing, C. Xing, L. Guo, Int J Hydrogen Energy 2007, 32, 4685.

[6] L. Wang, W. Wang, M. Shang, W. Yin, S. Sun, L. Zhang, Int J Hydrogen Energy 2010, 35, 19.

[7] D. Jing, L. Guo, J. Phys. Chem. C 2007, 111, 13437.

[8] L. Wu, J. C. Yu, X. Fu, J. Mol. Catal. A: Chem. 2006, 244, 25.

[9] W. F. Shangguan, A. Yoshida, J. Phys. Chem. B 2002, 106, 12227.

[10] T. Kasuga, M. Hiramatsu, A. Hoson, T. Sekino, K. Niihara, Langmuir 1998, 14, 3160.

[11] D. V. Bavykin, J. M. Friedrich, F. C. Walsh, Adv. Mater. 2006, 18, 2807.

[12] L. Wang, M. Xiao, X. Huang, Y. Wu, J. Hazard. Mater. 2009, 161, 49.

[13] M. Hodos, E. Horváth, H. Haspel, á. Kukovecz, Z. Kónya, I. Kiricsi, Chem. Phys. Lett. 2004, 399, 512.

[14] J. Yang, Z. Jin, X. Wang, W. Li, J. Zhang, S. Zhang, X. Guo, Z. Zhang, J. Chem. Soc. Dalton. Trans. 2003, 14, 3898.

Study of ZnO-ZnS Composite as Photocatalyst in the Water Splitting Reaction

Donna Chen, Anthony F. Masters, Thomas Maschmeyer School of Chemistry, The University of Sydney, NSW, Australia

The combined influences of global warming and declining oil reserves have meant that alternative energy resources that are much more environmentally friendly and sustainable are being explored. Hydrogen has always been a favoured candidate of green and renewable energy resources as combusting hydrogen produces mainly energy with water as a by-product. Hydrogen can be generated from water in the presence of a photocatalyst, which harnesses solar energy as illustrated in Figure 1. With light of appropriate wavelengths, electrons can be excited from the valence band to the conduction band of a photocatalyst. These excited electrons then migrate to the surface of the catalyst reducing protons to form hydrogen.

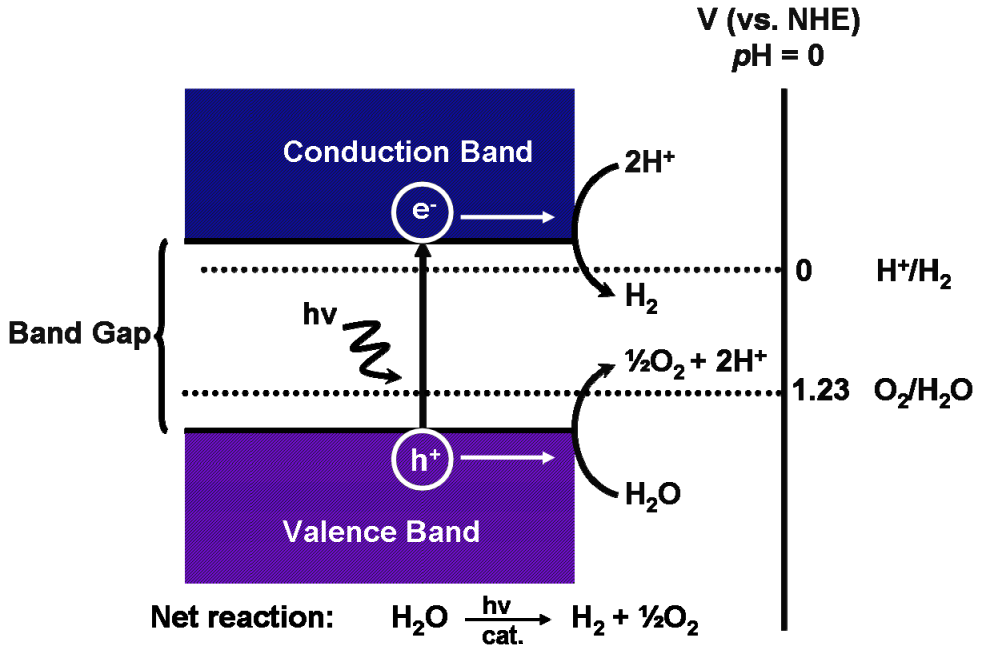

Figure 1: The basic principal of generating hydrogen from water photocatalytically.

Over the last few decades, a large amount of research has been conducted to produce hydrogen photocatalytically from aqueous solution. Recently, investigations have been carried out to utilize a ZnO-ZnS composite as a catalyst for water splitting and organic mineralization [1–3]. Both zinc oxide and zinc sulfide are cheap, widely available and relatively non-toxic to the environment. Even though they are large band gap semiconductors, the band gap of the resulting composites could be smaller and hence absorb a greater fraction of the solar spectrum. The composite materials can be synthesized

by adding aqueous $Zn(NO_3)$ [2] into a vigorously stirred solution of NaOH and Na_2S.[1] Subsequent heat treatment of the washed white precipitate in nitrogen at 400 °C would yield a yellow material. The synthesized composite materials were screened for hydrogen activities using the experimental set-up as illustrated in Figure 2.

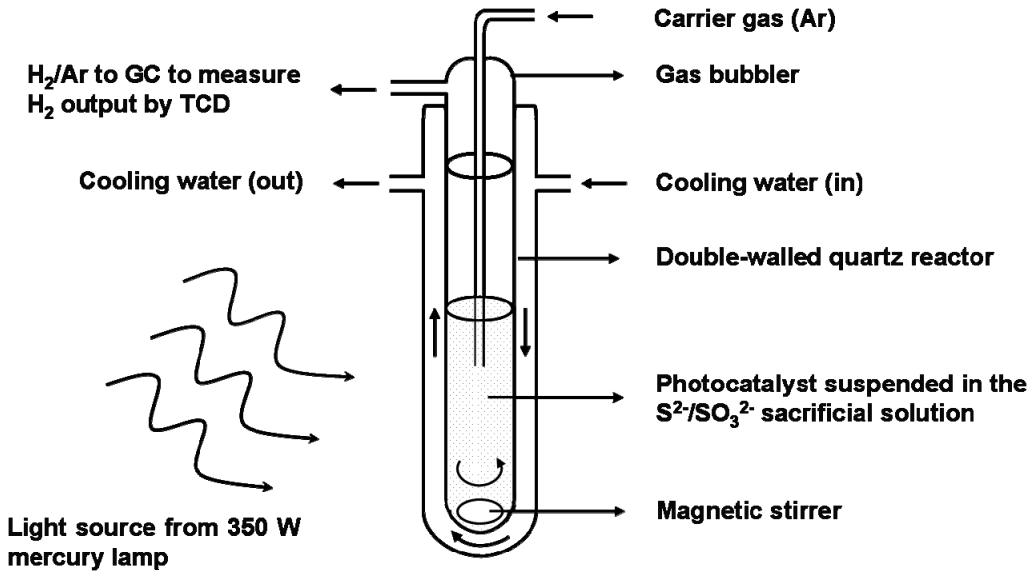

Figure 2: Schematic diagram of the photolysis set-up.

From the solid state UV-Vis analysis, the absorption band edges of the resulting composite materials are shifted to longer wavelengths as compared to both ZnO and ZnS. Characterising the materials using XRD revealed that the synthesized material exists as a mixture of two different phases, which can be assigned as wurtzite ZnO and cubic ZnS. At present, it is suggested the observed red shift in the absorption band edges is due to the presence of defects in the material. This suggestion will be tested by other characterisation techniques such as Photoluminescence.

As for the hydrogen activities, it is found that the composite materials photocorrode, possibly because of the instability of ZnO upon UV illumination. Preliminary results showed that ZnO barely produced any hydrogen in the presence of the S^{2-}/SO_3^{2-} sacrificial solution. However, an increase of hydrogen activities was observed with prolonged exposure of UV light. The XRD patterns of the photolysed ZnO sample exhibited an increase in intensity with photolysis duration of impurity peaks that can be attributed to elemental Zn and cubic ZnS. An intense S K_α peak observed in the EDX spectrum of the photolyzed ZnO sample further supported the XRD result. It is therefore suggested that during photolysis, ZnO photocorroded to form Zn^{2+}, which either reacted with S^{2-} from the sacrificial solution to form ZnS with a concomitant increase in hydrogen evolution, or was reduced to elemental Zn.

Both XRD and EDX-FESEM techniques were employed to examine a series of the composite materials with different molar ratios of ZnO to ZnS, before and after photolysis. Overall, no distinct peaks of wurtzite ZnO were observed from the XRD patterns of the photolyzed composite materials, except the sample with the most ZnO. As mentioned earlier,

ZnO is not stable under the given experimental condition, and thus it is reasonable that no wurtzite ZnO XRD pattern was detected from the photolyzed samples. Generally, all of the photolyzed composite materials exhibited more of the crystalline phase of cubic ZnS by comparison with non-photolyzed samples.

A change of surface morphology of the composite material is apparent after photolysis as illustrated in the FESEM images in Figure 3. The composite material lost its dendritic features after the photocatalysis reaction. The observation implied that the dendritic feature consists of mostly ZnO. And since ZnO photocorrodes, it is reasonable that the dendritic feature is not being observed from the photolyzed samples anymore. In addition, the observed decrease in the intensity of the Zn K_α peak relative to that of the S K_α from the EDX spectrum suggests an increase in S content in the composite material after photolysis. The analysis result implied that excess ZnS was formed during photolysis which complemented the XRD result.

a) b)

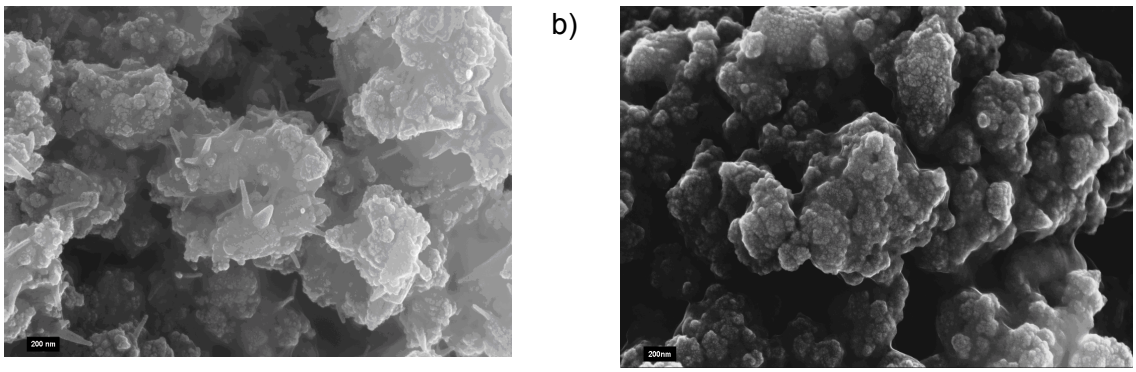

Figure 3: FESEM images of the composite material with ZnO(75):ZnS(25) (a) before and (b) after photolysis.

In conclusion, the composite materials are active in generate hydrogen generation, using light mainly in the UV region. With the insertion of a 395nm cut-off filter, there is no activity observed from ZnS whereas there is still traceable activity from the composite materials. This is most likely due to the effective shifting of the band edge towards longer wavelength that can be attributable to the presence of defects in the materials. Further investigations are to be carried out to explore the reason behind the extended absorption band edge of the composite materials to the region of longer wavelengths, as well as correlating the physical properties and activities of the composite materials with different synthetic conditions.

References.

[1] C. Kim, S.J. Doh, S.G. Lee, S.J. Lee, H.Y. Kim, *Appl. Catal., A* **2007**, 330-127-133.

[2] Y. Li, S. Ki, *Appl. Catal., A* **2009**, 363, 180-197.

[3] J.S. Jang, C.J. Yu, S.H. Choi, S. M. Ji, E.S. Kim, J.S. Lee, *J. Catal.* **2008**, 254,144-145.

Study on the Optical Properties, Crystal Growth and Photocatalytic Activity of Ni-doped TiO_2 Nanoparticles

Penghui Guo, State Key laboratory of Multiphase Flow in Power Engineering, Xi'an Jiaotong University, China
Liejin Guo,State Key laboratory of Multiphase Flow in Power Engineering, Xi'an Jiaotong University, China

TiO_2, as a widely used material for photocatalysis, is attracting more and more attention [1-5]. Up to date, a great deal of methods are under research to enhance its photocatalytic activity, for example, doping TiO_2 with metal ion or nonmetal ion [6, 7], loading TiO_2 with expensive metals [8, 9], sensitizing TiO_2 with dyes [10-12] or other methods [13, 14] etc. Ni is a low-price metal and of high activity in industrial catalysis, and it is also used in photocatalytic reactions to lengthen the absorption band of catalysts [15]. Nevertheless, systematic experimental studies regarding the influence of the doping ion to the main body TiO_2 are still lacking, especially the photoexcited carriers changing. In the present work, a series of porous and nano-structured Ni-doped TiO_2 with anatase structure are synthesized by ultrasonic sol-gel method. The structure, photophysical and photochemical properties are well discussed in this paper. What's more, the photoluminescence spectra were used to compare the photo charge carries transfer before and after Ni doping.

All chemicals used were of analytical grade without further purification. Firstly TBOT was dispersed in methanol with PEG-6000 and proper glacial acetic acid. Then the sol was dropped into acetic acid aqueous solution along with ultrasonic under room temperature. As for the Ni-TiO_2, the $Ni(NO_3)_2{\cdot}2H_2O$ were added into the aqueous solution to give doping level from 0%-10%. The mixture was evaporated in a water bath under 343K after 3h ultrasonic reaction. The gel was dried in vacuum at 343K for 8h. The product was finally heated in air at 723K for 4h.X-ray diffraction patterns of the samples were obtained from a PANalytical X'pert Pro diffractometer using Cu Kα irradiation. N_2 adsorption-desorption isotherms at 77K were measured using a Beckman Coulter SA 3100 instrument. Uv-vis adsorption spectra were determined by Hitachi U-4100 UV-vis-near IR spectrophotometer with $BaSO_4$ as the reference. Fluorescence emission and excitation spectra were got from PTI QM4 fluorescent photometer using a 75W Xe lamp as the exciting light resource and a filter is used to cut off the scattering light between the sample and detector.Photocatalytic hydrogen evolution was tested in a side-irradiation pyrex cell. A 350 W Xe lamp was used as the light source. Hydrogen evolved was analyzed by an on-line thermal conductivity detector (TCD) gas chromatograph (NaX zeolite column, nitrogen as a carrier gas). In all experiments, 200ml of 20 vol% aqueous methanol solution containing 0.1g catalyst was added into the cell.

N_2 adsorption-desorption results for Ni-TiO_2 with Ni doping of 5% and 0% are shown in Fig.1. Actually all the samples give typical H_1-type N_2 adsorption-desorption isotherms with obvious hysteresis loops proving the mesopores of large size. The small figuration shows that the pore sizes are smaller than 20nm compared with after Ni doping. The BET surface area of samples increased from 127 m^2/g to 148m^2/g when the amount of Ni doping increased from

0% to 5%, while the BET surface area for Ni doping of 10% is 144m^2/g. The total pore volume decreased from 0.51ml/g to 0.34 ml/g when the doping amount increased from 0% to 10%.

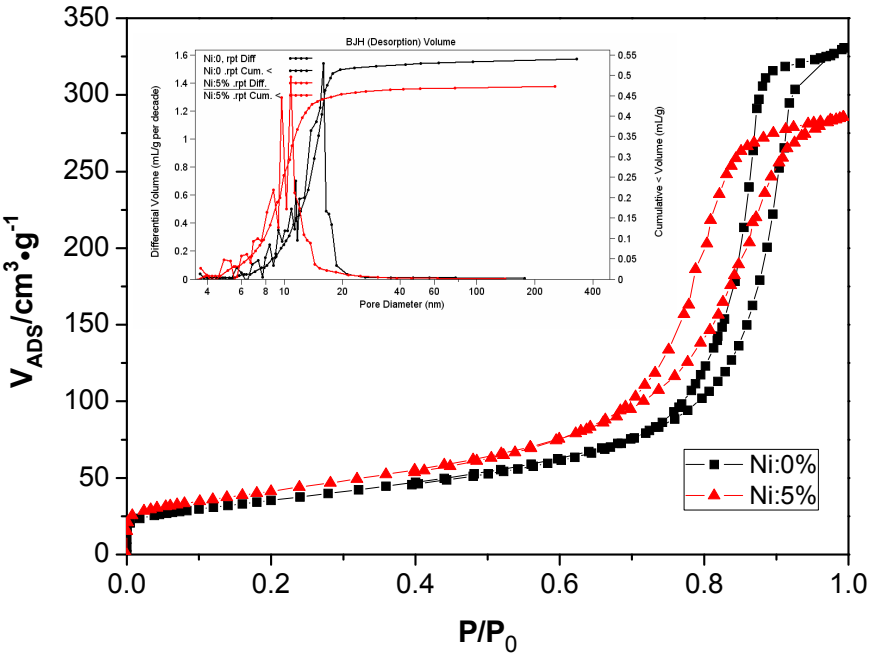

Figure 1: N_2 adsorption-desorption isotherms at 77K for Ni-TiO_2 with Ni^{2+} doping of 5% and 0% respectively.

TEM images for TiO_2 with Ni^{2+} doping of 0% and 5% are shown in Fig.2. The TiO_2 with or without Ni are both very homogenous particle distribution due to the dispersing role of ultrosonication. Considering the particle shape, both samples are anatase of cubic nanoparticles. It can also be seen that the particle size of Ni-TiO_2 is smaller than TiO_2 without Ni doping under high resolution transmission electron microscopy. Giving the result of the EDS, the grains we see from TEM are polycrystals. However, the TEM images also show that the product is not mesopore structure as the N_2 adsorption-desorption isotherms indicate. It is supposed that the crystals are growing uniformly because of ultrasonic process and piled up forming pores.

Fig.3 shows the XRD patterns of TiO_2 with various Ni doping calcined at 723K. It can be seen only the sample with 10% Ni doping is not pure anatase. The peak at 2θ=43.2°, which only can be seen when the doping amount increases to 10%, is identified as the characterized peak of cubic NiO (h=2, l=k=0). The mean size of the crystallites in samples can be estimated by the FWHM of the XRD peak at 2θ=25.3° using the Debye-Scherrer equation. Although the further crystallization of TiO_2 particles is a main process at a lower annealing temperature [16], the crystallite size decreases from 11nm to 9nm with increasing Ni doping from 0% to 5%, which may cause by the Ni-O bond distance (1.87 Å) shorter that the Ti-O bond distance(1.94 Å) [17]. On condition that, we can say that Ni has entered the framework of TiO_2 crystals. Combined with N_2 ads-des isotherms and XRD results, it can be concluded

that Ni doping can restrain the particle growth and inhibit the formation of rutile crystallites in the matrix of mesoprous TiO_2 at a higher calcination temperature before NiO appears. It also indicates that the ultrasonic method can have a larger doping amount than other methods [15].

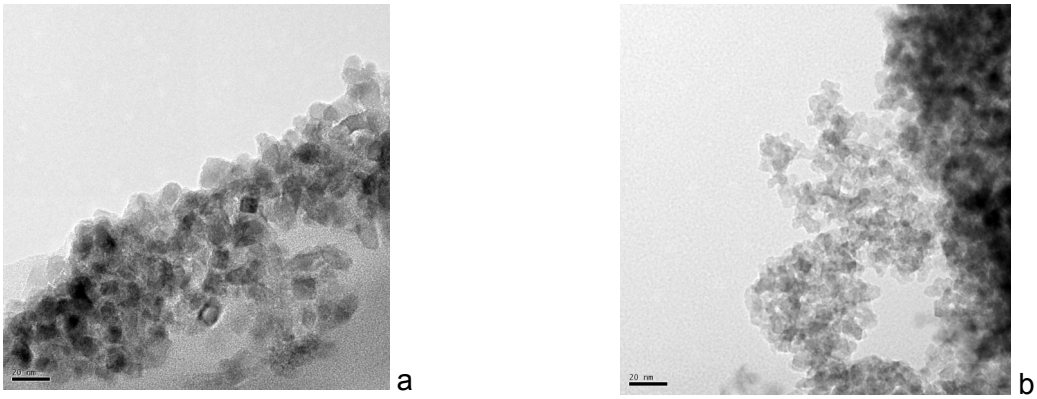

Figure 2: TEM images of TiO_2 with Ni^{2+} doping of 0% and 5%. (a: TiO_2; b: Ni-TiO_2).

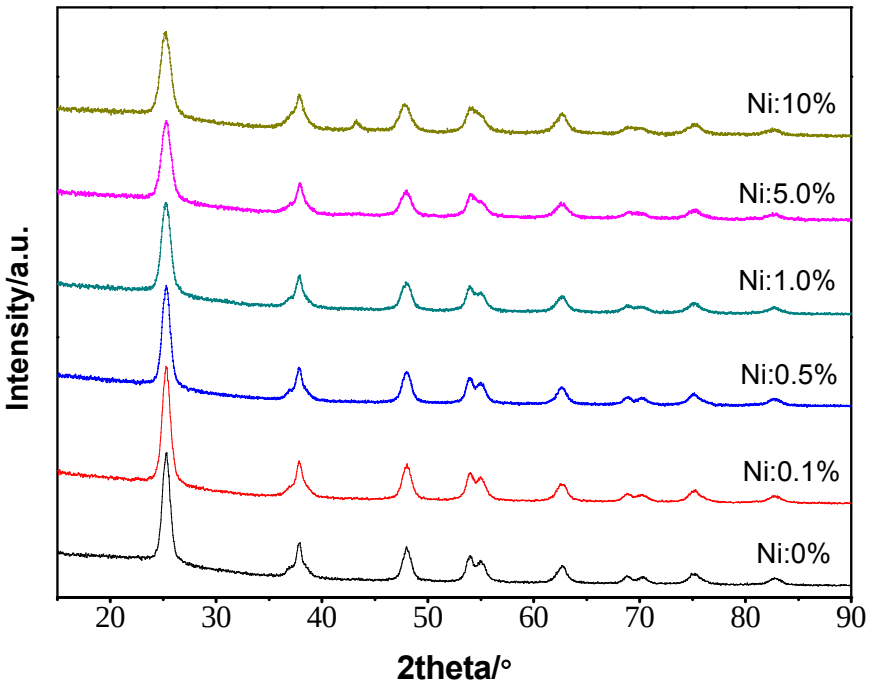

Figure 3: XRD diagram of various TiO_2 with increasing doping; all samples were calcined at 723K.

Raman scattering is a more sensitive detection technique of nanocrystal structure characterization. Five peaks showed in the spectra are attributed to the antase phase Raman scattering model of $A_{1g}+2B_{1g}+3E_g$. The Raman scattering did not detect the NiO of TiO_2 with a doping amount of 5%. We can say that by using this ultrasonication method a large

amount of Ni^{2+}, as a substitution for Ti^{4+}, were successfully synthesized, incorporating into the matrix of TiO_2. The bands of TiO_2 with Ni doping are 123cm^{-1}(E_g), 177cm^{-1}(E_g), 374cm^{-1}(B_{1g}), 497cm^{-1}(A_{1g}, B_{1g}), 621cm^{-1}(E_g), have a small red shift and broadening change distinguished from the TiO_2 without Ni doping, whose peaks are 125cm^{-1}(E_g), 179cm^{-1}(E_g), 376cm^{-1}(B_{1g}), 498cm^{-1}(A_{1g}, B_{1g}), 622cm^{-1}(E_g). Compared to the P25 (commercial TiO_2 with a surface area of 55 m^2/g), the Raman scattering bands of all the TiO_2 samples prepared by ultrasonication method have an obvious red shift and broadening. This shift and broadening are caused by photon relaxation due to the defects or oxygen vacancies of the nanocrystals, the same results as our former research[18].

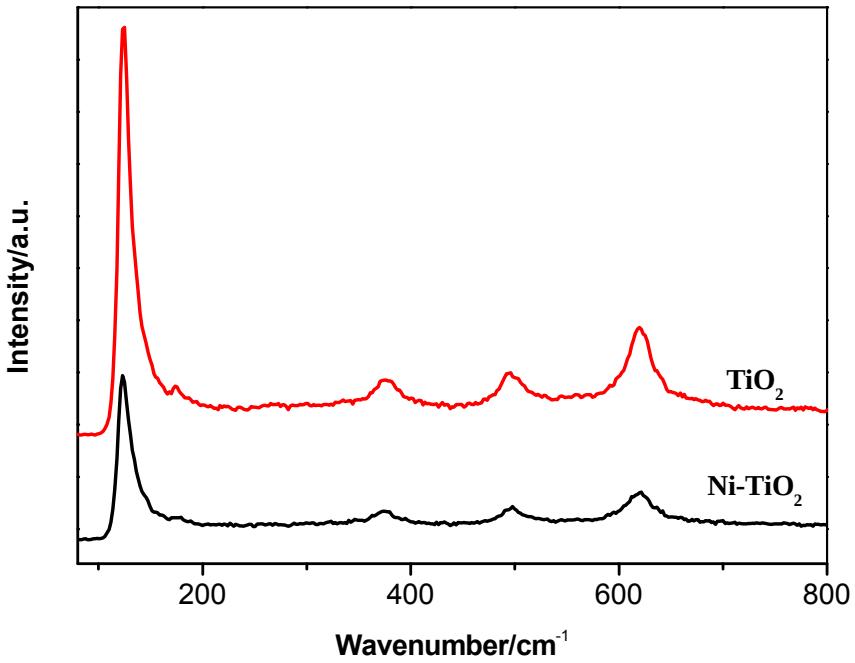

Figure 4: Raman of TiO_2 and TiO_2 with 5% Ni doping.

Fig.5 shows the UV-VIS-NIR absorbance of Ni-TiO_2. The bands at near infrared area for all the samples are due to bending and symmetric or asymmetric stretching vibration modes of the H_2O molecules adsorbed on the surface of the samples [19]. TiO_2 with Ni doping has a visible light response due to the formation of impurity energy level. The absorption band around 750nm is supposed to be due to the oxygen vacancies formation in virtue of the imbalance of charges caused by Ni doping. The band gap energy of the pure TiO_2 is 3.28eV calculated by K-M equations, a little bigger than reported, which may be caused by the quantum size effect as the particle size is around 10nm more or less with the Bore radius of TiO_2 [20].

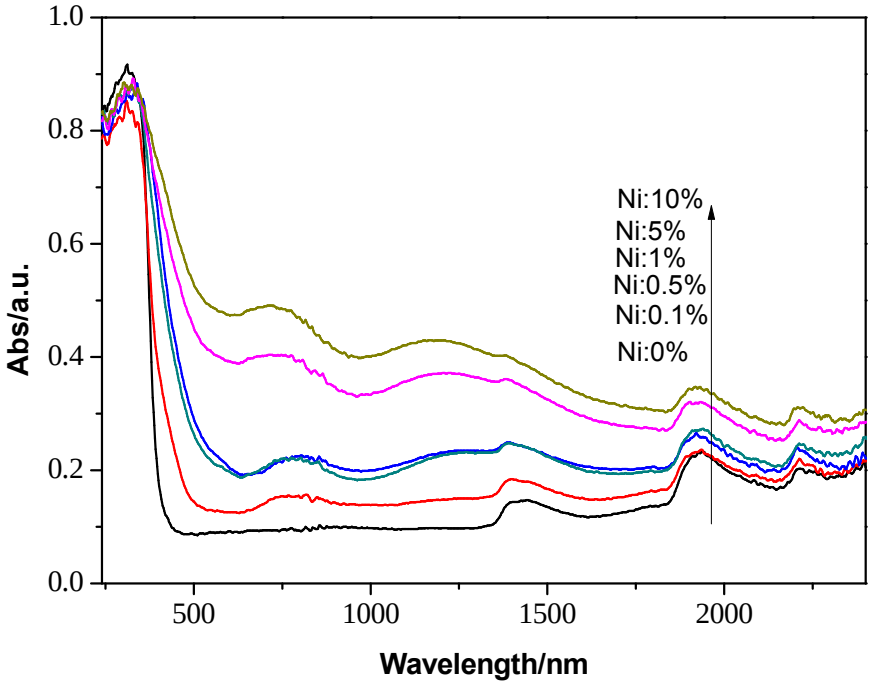

Figure 5: UV-VIS-NIR absorbance spectra of Ni doped TiO_2.

There are three Gaussian-type peaks at 358, 378, 394 showed in PL excitation spectrum. The 378nm peak is engendered by electron transition from valence band to conduction band on base of the band gap energy. The other two peaks may be caused by the vibration energy level in the CB and VB or free exciton absorption band around CB and VB [21]. Stokes shift is obviously observed because of indirect transition and the vibration energy level in energy band. Based on the symmetry property of excitation and emission, the 436nm emission band stems from conduction band to valence band direct recombination. The emission band observed in fig.6 (b) around 825nm is supposed to be caused by the intrinsic defects of anatase TiO_2 [22]. When Ni is doped in the frame of TiO_2, the quantum-size effect makes the emission band a little blue-shift, and this is in accordance with the crystal growth results.

It is very interesting that when TiO_2 has a very small doping amount of Ni, it hardly emits, which is probably resulted from that Ni^{2+} dispersed in the TiO_2 trapped the excited electron and relaxed them through a non-radiative way. But the amount is limited so the photocatalytic activity decreased a little. As the amount of Ni increasing, the impure energy levels generate, as we can see from the fig.6(d), it emits along with the conduction band of TiO_2 for the emission band is blueshifting. The optimal amount exists because the excessive Ni would become trapping center of photo excited holes. The hydrogen evolution amount has a same tendency with the PL emission spectra. It is supposed that Ni has two roles in doping TiO_2. One is when Ni is dispersed in TiO_2 bulk with very small amount, excited electrons are trapped by Ni and then relaxed non-rediatively, so the electrons can't migrate to the TiO_2 surface and reduce H^+. But this influence is not big enough for the Ni amount limited. The other role is the excited electrons are transiently trapped by the level and then released to transfer to TiO_2 surface when Ni has an abundant amount to generate new impure energy level in TiO_2. The Ni-doped TiO_2 has visible light absorption but no photocatalytic hydrogen

production activity under visible light. One reasonable possibility is that a deep energy level is yielded in TiO_2 with Ni doping. The location of the impure energy level will be discussed in next work.

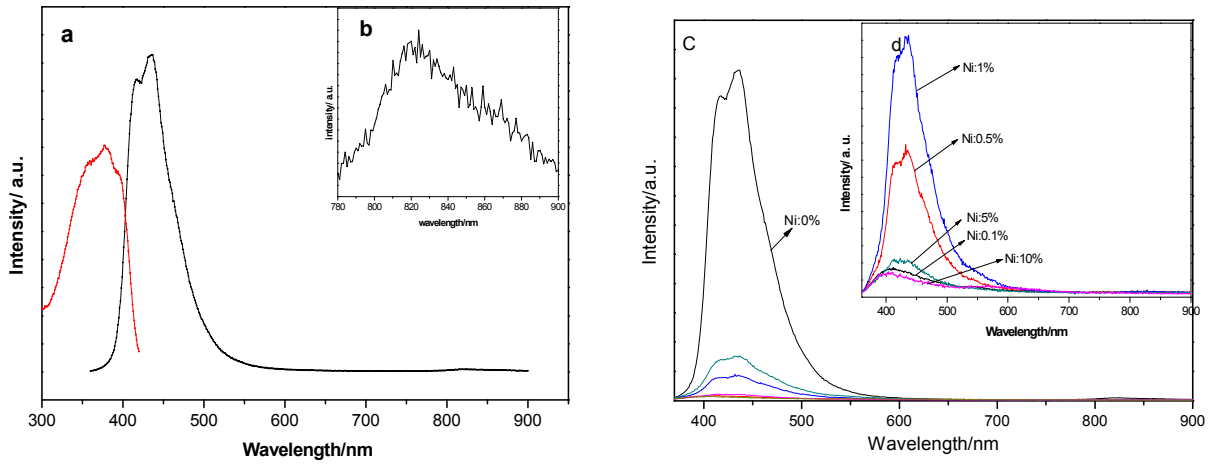

Figure 6: Fluorescence excitation and emission spectra of TiO_2 (all the PL emissions are excited by 340nm with a cut-off filterλ≥350nm and the PL excitations are collected with a band-pass filter at λ=441.6nm. a: nondoped TiO_2, b: the enlarged figuration from 700nm to 900nm; c: TiO_2 doped with different amount of Ni; d: the enlarged figuration of Ni doping TiO_2).

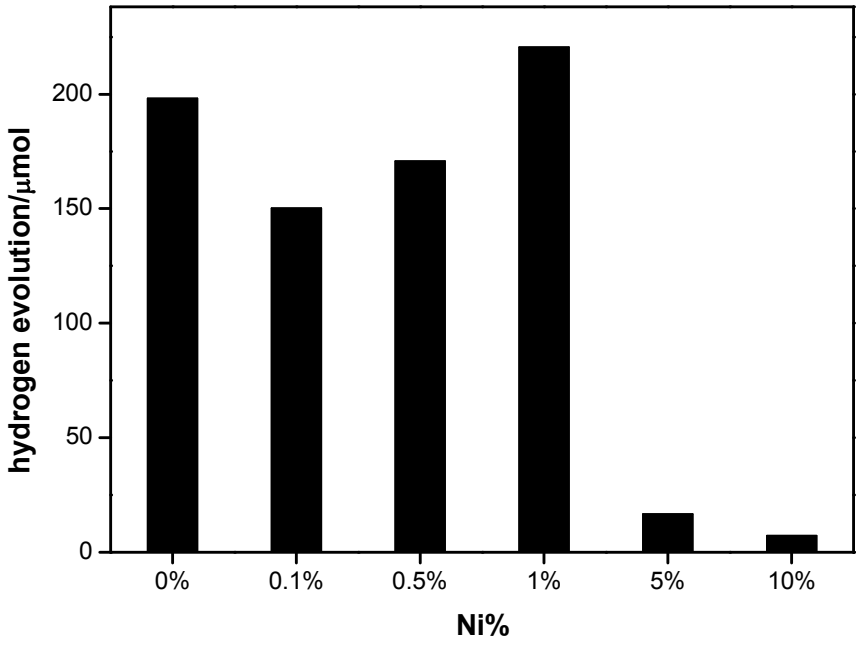

Figure 7: Hydrogen evolution of all the samples under 350W Xe lamp irradiation.

Acknowledgements

This research was financially supported by the National Basic Research Program of China (Grant 2009CB220000).

References

[1] Hu X.L., Li G.S., and Yu J.C., Design, Fabrication, and Modification of Nanostructured Semiconductor Materials for Environmental and Energy Applications. Langmuir, 2010. 26(5): p. 3031-3039.

[2] Serrano E., Rus G., and Garcia-Martinez J., Nanotechnology for sustainable energy. Renewable & Sustainable Energy Reviews, 2009. 13(9): p. 2373-2384.

[3] Mor G.K., et al., A review on highly ordered, vertically oriented tio2 nanotube arrays: Fabrication, material properties, and solar energy applications. Solar Energy Materials and Solar Cells, 2006. 90(14): p. 2011-2075.

[4] Hashimoto K., Irie H., and Fujishima A., TiO2 photocatalysis: A historical overview and future prospects. Japanese Journal of Applied Physics Part 1-Regular Papers Brief Communications & Review Papers, 2005. 44(12): p. 8269-8285.

[5] Guo L.J., et al., Solar hydrogen production and its development in China. Energy, 2009. 34(9): p. 1073-1090.

[6] Yu J.C., et al., Effects of F- doping on the photocatalytic activity and microstructures of nanocrystalline tio2 powders. Chemistry of Materials, 2002. 14(9): p. 3808-3816.

[7] Choi W.Y., Termin A., and Hoffmann M.R., the Role of Metal-ion Dopants in Quantum-sized TiO2 - Correlation between Photoreactivity and Charge-carrier Recombination Dynamics. Journal of Physical Chemistry, 1994. 98(51): p. 13669-13679.

[8] Wan B., et al., Preparation of Ag/TiO2 Nanotube and Its Photocatalytic Performance. Rare Metal Materials and Engineering, 2009. 38(11): p. 2012-2016.

[9] An H.Q., et al., Deposition of Pt on the stable nanotubular TiO2 and its photocatalytic performance. Catalysis Communications, 2009. 11(3): p. 175-179.

[10] Li Y.X., et al., Formation of multilayer-Eosin Y-sensitized TiO2 via Fe3+ coupling for efficient visible-light photocatalytic hydrogen evolution. International Journal of Hydrogen Energy, 2009. 34(14): p. 5629-5636.

[11] Jin Z.L., et al., 5.1% Apparent quantum efficiency for stable hydrogen generation over eosin-sensitized CuO/ TiO2 photocatalyst under visible light irradiation. Catalysis Communications, 2007. 8(8): p. 1267-1273.

[12] Chatterjee D., Effect of excited state redox properties of dye sensitizers on hydrogen production through photo-splitting of water over TiO2 photocatalyst. Catalysis Communications, 2010. 11(5): p. 336-339.

[13] Liu Y.L., et al., A composite visible-light photocatalyst for hydrogen production. Journal of Power Sources, 2006. 159(2): p. 1300-1304.

[14] Yang H.H., et al., A novel composite photocatalyst for water splitting hydrogen production. Journal of Power Sources, 2006. 159(2): p. 1305-1309.

[15] Jing D.W., Zhang Y.J., and Guo L.J., Study on the synthesis of Ni doped mesoporous TiO2 and its photocatalytic activity for hydrogen evolution in aqueous methanol solution. Chemical Physics Letters, 2005. 415(1-3): p. 74-78.

[16] Zhang W.F., Zhang M.S., and Yin Z., Microstructures and visible photoluminescence of TiO2 nanocrystals. Physica Status Solidi a-Applications and Materials Science, 2000. 179(2): p. 319-327.

[17] Wang Y.W., et al., Polyol-Mediated Synthesis of Ultrafine TiO2 Nanocrystals and Tailored Physiochemical Properties by Ni Doping. Journal of Physical Chemistry C, 2009. 113(21): p. 9210-9217.

[18] Ma L.J. and Guo L.J., Study on the thermo-Raman spectrum of TiO2 prepared with different precursors. Acta Chimica Sinica, 2006. 64(9): p. 863-867.

[19] Takeuchi M., et al., Investigations of the structure of H2O clusters adsorbed on TiO2 surfaces by near-infrared absorption spectroscopy. Journal of Physical Chemistry B, 2005. 109(15): p. 7387-7391.

[20] Kormann C., Bahnemann D.W., and Hoffmann M.R., Preparation and Characterization of Quantum-size Titanium-dioxide. Journal of Physical Chemistry, 1988. 92(18): p. 5196-5201.

[21] Yu J.G., et al., The effect of calcination temperature on the surface microstructure and photocatalytic activity of TiO2 thin films prepared by liquid phase deposition. Journal of Physical Chemistry B, 2003. 107(50): p. 13871-13879.

[22] Jianying S., et al., Photoluminescence characteristics of TiO2 and their relationship to the photoassisted reaction of water/methanol mixture. Journal of Physical Chemistry C, 2007. 111(2): p. 693-699.

Photocatalytic Hydrogen Production with Nanocomposite Photocatalysts

Satoshi Kaneco, **Takuya Miwa**, Department of Chemistry for Materials, Faculty of Engineering, Mie University, Tsu, Mie 514-8507, Japan
Suresh Chand Verma, **Kunihiro Sugihara**, Chubu Electric Power Co. Inc., Midori-ku, Nagoya 459-8522, Japan

Hydrogen, which has potential as a clean energy fuel, can be extracted from water, biomass, natural gas and other carbon sources [1]. Methanol has been recommended as the best source for hydrogen fuel among the high energy density liquid fuels [2]. Methanol can be converted to hydrogen by several reactions, containing methanol steam reforming [3,4], partial oxidation of methanol [5,6], oxidative methanol reforming [7], methanol decomposition and photocatalytic oxidation [8,9]. The photocatalytic hydrogen production with the methanol decomposition appears to be very promising method for the practical and low-cost technologies in the hydrogen-based energy system.

Titanium dioxide (TiO_2) is considered as a good photocatalyst for hydrogen generation because of its excellent resistance to chemical and photochemical corrosion in aggressive aqueous environments and due to its activity towards both light and aqueous solutions such as water and methanol. Nobel metal loading onto TiO_2 have been widely investigated for hydrogen generation, and have been presented to be very effective to enhance TiO_2 photocatalytic activity since it can contribute to efficient electron-hole separation. However, considering the high costs incurred by the consumption of novel metals, it is very significant to fabricate a highly efficient and cost-effective photocatalyst, meanwhile, converting them into environment-friendly products. Because copper-containing TiO_2 is cost-effective compared with noble metal loaded TiO_2, its utilization has been energetically studied for the photocatalytic hydrogen production. Sreethawong and Yoshikawa have described that copper-loaded TiO_2 gave about two fold higher hydrogen generation activity compared with the optimum value of the Ni loaded case. Wu and Lee have studied hydrogen generation with TiO_2 with deposited copper, and proven that oxidation of metal copper occurred during reaction induced high hydrogen generation activity. Bandara et al. and Choi el al. have fabricated TiO_2 photocatalysts loaded with CuO, and found that hydrogen production was drastically enhanced by CuO relative to pure TiO_2. However, little information on the photocatalytic hydrogen production with the nanocomposite composed of three components containing TiO_2 and CuO.

The present work deals mainly with the photocatalytic hydrogen production from aqueous methanol solution with $CuO/Al_2O_3/TiO_2$ nanocomposite. Furthermore, the photocatalytic activities of ZnO/TiO_2, SnO/TiO_2, CuO/TiO_2 and Al_2O_3/TiO_2 nanocomposites were evaluated for the comparison with the nanocomposite composed of three components.

TiO_2 P25 photocatalyst was purchased from Degussa Co. Ltd., Germany (anatase 75%, rutile 25%, BET specific surface area 48 m^2/g, mean particle size 25nm). Nanopowders

(ZnO, SnO, CuO and Al_2O_3) were obtained from Sigma□Aldrich. The mean diameter and specific surface area were 50~70 nm and 15~25 m^2/g for ZnO, 18 nm and 47 m^2/g for SnO, 33 nm and 29 m^2/g for CuO and 40~47 nm and 35~40 m^2/g for Al_2O_3. Methanol (99.8%, Nacalai Tesque, Inc., Japan) was used as received without further purification. Laboratory pure water was obtained from an ultrapure water system (Advantec MFS Inc., Tokyo, Japan) resulting in a resistivity > 18 MΩ cm.

A mechanical mixing method was used for the preparation of nanocomposite photocatalyst. The oxide powders were mixed with the mortar. An electric furnace (Koyo Box Furnace, KBF828N, Nara, Japan) was used for sintering at 500 ^oC under an air atmosphere. The furnace was heated from ambient to the final sintering temperature of 500 ^oC at a rate of 4.7 ^oC/min and then the temperature was kept constant for 3 h.

The surface areas of nanocomposite photocatalysts were determined by the three points BET method with di-nitrogen at 77 K (Autosorb-1-C, chemisorption and physisorption analyzer, Qnantachrome Instruments, USA). The structure and crystalline phases of nanocomposite photocatalysts were characterized by X-ray diffractometer (XRD, RIGAKU Ultima IV, sample horizontal type) with Cu K_α radiation (λ=0.15406 nm) at 40 kV and 50 mA. The diffraction patterns were taken over the 2θ angle range from 10^o to 80^o with a scan speed of 4^o/min and a stepsize of 0.02^o. The microstructure and morphology of the nanocomposite photocatalysts were analyzed by transmission electron microscope (TEM, Hitachi H-7000, 125 kV accelerating voltage).

The pyrex column vessel reactor (inner volume: 55.6 mL) was used for the photocatalytic production of hydrogen from aqueous methanol solution. The pyrex glass cuts off all wavelength below 300 nm. Typically, 20 mg of the nanocomposite photocatalysts were added to 30 mL of 10 vol% methanol solution in the photoreactor. A 15 W black light (Toshiba Lighting & Technology Corp) with a maximum emission of ~352 nm was applied as light source, which was positioned on the side of photoreactor. The light intensity was measured by a UV radio meter with a sensor of 320 to 410 nm wavelengths (UVR-400, Iuchi Co., Osaka, Japan), and the value was 1.0 mW/cm^2. The nanocomposite photocatalysts were continuously dispersed in the aqueous methanol solution by a magnetic stirrer during the irradiation. The temperature of the suspension in the photoreactor was kept constant by the water bath. The irradiation time was 3 h. The hydrogen product from the aqueous methanol solution was analyzed by gas chromatography (GL Sciences, GC□3200) with thermal conductivity detector (TCD). The stainless column (4 m long, 2.17 mm i.d.) packed with Molecular Sieve 5A was used for the separation. The carrier gas was high purity argon gas. The temperature conditions of GC were 50 ^oC for injection, column and detector.

The quick recombination of photogenerated electrons (e^-) and holes (h^+) decreases the photocatalytic efficiency of TiO_2. The use of a charge transfer catalyst (CTC) to prepare a binary photocatalyst is an alternative way to achieve better photocatalytic activities because the charge transfer catalyst is able to trap the photogenerated electrons (e^-) and holes (h^+) in its domain. Therefore, the effect of metal oxide cocatalysts on the photocatalytic hydrogen production over TiO_2 was investigated for the simple mixing preparation methods. The photocatalytic hydrogen production over TiO_2 tended to increase in the addition of metal oxide cocatalysts, compared with those in the absence of them. The optimum contents were

1.5, 0.5, 1.0 and 0.5 wt% for ZnO, SnO, CuO and Al_2O_3 cocatalysts, respectively. The photocatalytic activity for hydrogen formation increased in the order ZnO, SnO, CuO and Al_2O_3. The Al_2O_3/TiO2 photocatalytic activity was approximately 6 times better than that obtained with TiO_2. Wu et al. have studied the photocatalytic hydrogen evolution over Cu□deposited TiO_2 from the aqueous methanol solution (42%), and presented that the optimum Cu loading was approximately 1.2 wt%. The incident radiation produces electrons from the valence band to the conduction band, the band gap energy being lowered by copper incorporation. A photo-induced electron reduces water to hydrogen while methanol, the sacrificial reagent for hole, gets oxidized. Because the CuO conduction band is located below that of TiO_2, electron transfer to the conduction band of CuO is possible. The phenomenon becomes important when a part of incident radiation has wavelength in the UV range. The hole transfer from the valance band of TiO_2 to that of CuO is also allowable for the same reason. The combined effects of CuO with TiO_2 are responsible for the enhanced hydrogen evolution.

When the electron–hole (e–h) pair is formed by the UV light, the activated energy is large enough to excite the photogenerated electron ($e^{\square}$) from the TiO_2 band (3.2 eV) into the Al_2O_3 band (>5.0 eV). Nevertheless, the photogenerated hole (h^+) in the TiO_2 cannot shift the Al_2O_3 region energetically. Therefore, the recombination of the photogenerated electron (e^-) and hole (h^+) pair is hindered by the separation. Hence, the estimated phenomenon may be attributable to the enhanced hydrogen formation.

An increase in the lifetime of photogenerated electron–hole pairs in the coupled oxides, due to the hole and electron transfer between the two coupling oxides, seems to be very critical to the catalytic activity enhancement for the hydrogen production. Therefore, the photocatalytic hydrogen production with the nanocomposite composed of three components, TiO_2, CuO and Al_2O_3, were investigated in the aqueous methanol solution. When the Al_2O_3 doping concentration was 0.2 wt%, the maximum hydrogen formation was obtained in the doping concentration of CuO 0.4 wt%. As the doping concentration of Al_2O_3 increased to 0.3 and 0.4 wt%, the optimal doping concentrations for CuO shifted to 0.2 wt%. On the CuO doping concentration of 0.2 wt%, the best hydrogen production was observed with 0.3 wt% Al_2O_3 doping concentration. With increasing the CuO doping concentration, the peak of convex curves moved to the lower Al_2O_3 content. Therefore, the photocatalytic hydrogen production proved a close relationship between the CuO and Al_2O_3 doping concentrations. The maximum hydrogen formation (1200 μmol $g^{\square 1}$·cat) was obtained using 0.2 wt% CuO/0.3 wt% Al_2O_3/TiO_2 nanocomposite photocatalysts. Wang et al. have fabricated $ZnO/TiO_2/SnO_2$ mixtures with the molar ratio of $ZnO:TiO_2:SnO_2$ = 4:1:1 from the component oxide powders ZnO, TiO_2 and SnO_2 by solid-state reaction at elevated temperature. In the photocatalytic degradation of methyl orange, the mass photocatalytic activity of $ZnO/TiO_2/SnO_2$ mixture was 2.0 times that of TiO_2, 16.4 times that of SnO_2 and 0.92 times that of ZnO, i.e. $ZnO/TiO_2/SnO_2$ composite was photocatalytically more active than the pure TiO_2 and SnO_2 but less active than ZnO. In the present work, the photocatalytic activity for hydrogen production was approximately ten times that of pure TiO_2.

Little information of the temperature effect on the photocatalytic hydrogen production from the aqueous solution has been presented. Therefore, the effect of reaction temperature on the photocatalytic hydrogen formation from the aqueous solution with $CuO/Al_2O_3/TiO_2$

nanocomposites was investigated in the range of 40 to 70 ^{o}C. Formic acid potassium supporting electrolyte was added into the aqueous methanol solution for the enhancement of hydrogen production. The H_2 yield increased gradually with increasing in the reaction temperature. The hydrogen production yield at 70 ^{o}C was about three times that near room temperature (40 ^{o}C). Korzhak et al. have reported the influence of temperature on the quantum yield of photocatalytic hydrogen production in the presence of TiO_2/Cu nanocomposites. In the study, the quantum yield was proportional to the temperature, and it could be postulated that the temperature dependences of quantum yield (hydrogen production) originate from the thermal activation of desorption of acetaldehyde which was the oxidation product from a sacrificial reagent ethanol. In the present work, the affect of temperature on the photocatalytic hydrogen production may similarly be attributable to the thermal activation of desorption of formaldehyde which was produced by the oxidation of methanol. Consequently, it was found that the reaction temperature is a significant factor for the photocatalytic hydrogen formation from the aqueous solution.

In summary, it was found that the deposition of CuO and Al_2O_3 into TiO_2 greatly enhance the photocatalytic activity of TiO_2 toward hydrogen production from aqueous methanol solution. The photocatalytic activity with 0.2 wt% CuO/0.3 wt% Al_2O_3/TiO_2 for hydrogen production was about 10 times that of pure TiO_2. Methanol dehydrogenation has application in indirect methanol fuel cells, where methanol is first reformed to hydrogen in an energy-consuming step. Photocatalytic dehydrogenation of methanol has the advantage of supplying the reforming energy from sunlight.

References

[1] Kulprathipanja A, Falconer JL., Applied Catalysis A: General, 2004;261(1):77–86.

[2] Ou TC, Chang FW, Roselin LS., Journal of Molecular Catalysis A: Chemical, 2008;293(1-2):8-16.

[3] Shishido T, Yamamoto Y, Morioka H, Takehira K., Journal of Molecular Catalysis A: Chemical, 2007;268(1-2):185-94.

[4] de Wild PJ, Verhaak MJFM., Catalysis Today, 2000; 60(1-2):3-10.

[5] Cubeiro ML, Fierro JLG., Applied Catalysis A: General, 1998;168(2):307-322.

[6] Agrell J, Hasselbo K, Jansson K, Järås SG, Boutonnet M., Applied Catalysis A: General 2001;211(2):239-50.

[7] Murcia-Mascarós S, Navarro RM, L. Gómez-Sainero L, Costantino U, Nocchetti M, Fierro JLG., Journal of Catalysis, 2001;198(2):338-347.

[8] Wu G-S, Wang L-C, Liu Y-M, Cao Y, Dai W-L, He-Yong He, Fan K-N., Applied Surface Science, 2006;253(2): 974-82.

[9] Yoong LS, Chong FK, Dutta BK., Energy 2009;34(10),1652–61.

Electronic Structures and Optical Absorption Properties of Ni-doped Anatase TiO_2 for Photocatalysis from First-Principles Calculation

Maochang Liu, Zhaohui Zhou, Mingtao Li, Liejin Guo[*], State Key Laboratory of Multiphase Flow in Power Engineering, School of Energy and Power Engineering, Xi'an Jiaotong University, 28, Xianning Street, Xi'an, Shaanxi 710049, China

From the viewpoint of photocatalysis, it is the anatase form of TiO_2 that is most important. Ti ions in the lattice were substituted by Ni ions to form Ni-doped TiO_2 which has been applied successfully for degradation of hazardous organic compounds or production of hydrogen or oxygen gas [1-4]. Therefore, a DFT calculation for the band structures and optical absorption spectra with varying Ni concentration in anatase TiO_2 models was conducted, in order to explore the effects of Ni doping on the band structure, photocatalytic property, and optical absorption spectrum.

The plane-wave pseudopotential method, implemented by CASTEP package [5], has been used to optimize crystal geometries, obtain the corresponding band structures and simulate the optical absorption spectra.

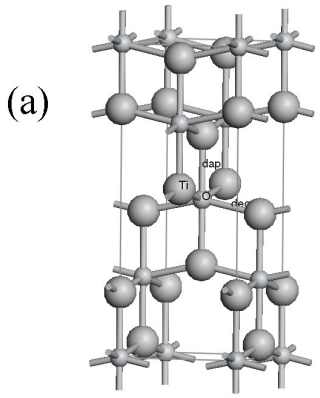

Figure 1: The crystal structure of pure TiO_2 (Model a).

2×1×1, 2×2×1, and 2×2×2 supercells with one Ti atom replaced by one Ni atom were denoted as Model (b), (c), and (d) to simulate doping concentration of 0.125, 0.062, and 0.031, respectively. Pure TiO_2 denoted as Model (a) was also calculated for comparison, as shown in Figure 1.

The optimized structural parameters of *a, c* and *u* ($u = d_{ap}/c$, d_{ap} is the apical Ti-O bond length) for pure anatase TiO_2 were listed in Table 1, which showed good consistence with

[*] Corresponding author, email address: lj-guo@mail.xjtu.edu.cn.

experimental [6] and theoretical results [7]. Six Ti-O bonds were contained in the distorted TiO_6 octahedron: d_{ap}=2.001Å and d_{eq}=1.941 Å, while d_{ap}=1.898Å and d_{eq}=1.919 Å in NiO_6 octahedron for Model (c) and (d). The local symmetry D_{2d} for the NiO_6 octahedron was remained in Ni doped TiO_2 with low Ni concentration. Mulliken population analysis [8] showed that the charge on the Ni ion was about 0.88, independent of its concentrations in the crystal and smaller than the charge (1.33) on the original Ti ion in this site. The adjacent six oxygen ions at vertices of the NiO_6 octahedron were slightly reduced. The charges on them were -0.61 in Model (c) and (d), while the charges on oxygen ions of the TiO_6 octahedron were -0.66.

Table 1: Structural parameters of anatase TiO_2.

	This work	Experimental [6]	FPLAPW [7]
a (Å)	3.785	3.782	3.692
c (Å)	9.718	9.502	9.471
u	0.206	0.208	0.206

Band structure plots for pure (Model a) and doped (Model c) TiO_2 were shown in Figure 2. It was indicated from Figure 2a that pure TiO_2 was an indirect band gap semiconductor with a minimum band gap of 2.13eV. The top of valence bands was near M point and the bottom of conduction bands was at G point. The underestimated band gap (3.2eV for experimental value) was well known for DFT method. After Ni doping, two dopant bands which were marked with solid squares (Figure 2c) appeared in the band gap of TiO_2. These bands were unoccupied, so they would be acceptor levels upon visible light excitation.

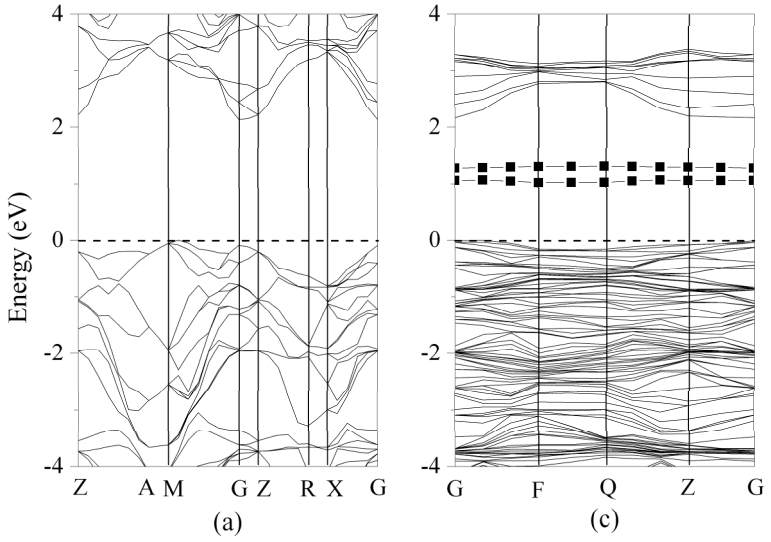

Figure 2: Band structure plots for pure (Model a) and doped (Model c) anatase TiO_2. The top of the valence band was denoted as zero.

Partial density of states (PDOS) plots calculated for TiO_2 with different concentrations of Ni impurity were presented in Figure 3. For pure TiO_2 in Figure 3(a), the upper valence bands showed a strong hybridization between O 2p and Ti 3d orbitals. The top of the valence bands was dominated by the O 2p orbitals, while the conduction bands, especially the bottom, contained significant contributions from the Ti 3d orbitals. It was obvious from Model (b), (c) and (d) in Figure 3 that the doped Ni 3d orbitals substantially contributed to the valence bands and the impurity bands. Two narrow bands (band I and II as shown in Figure 3c) were located in the middle of the band gap for Model (c) and (d). As Wang et al. [9] clarified for V doped TiO_2, the D_{2d} symmetry caused the three-fold degenerate t_{2g} ($3d_{xy}$, $3d_{xz}$, and $3d_{yz}$) and two-fold degenerate e_g ($3d_{x^2-y^2}$ and $3d_{z^2}$) of a transition metal cation to further split; the t_{2g} split into a two-fold degenerate level of both $3d_{yz}$ and $3d_{xz}$ and a level of $3d_{xy}$ while the e_g split into two levels of $3d_{x^2-y^2}$ and $3d_{z^2}$. Through a further examination of the orbital wavefunction contour maps of band I and II, the orbital contours for band I and band II showed the σ anti-bondings between O p_x or p_y orbital and Ni $d_{x^2-y^2}$ orbital and between O p_z orbital and Ni d_{z^2} orbital.

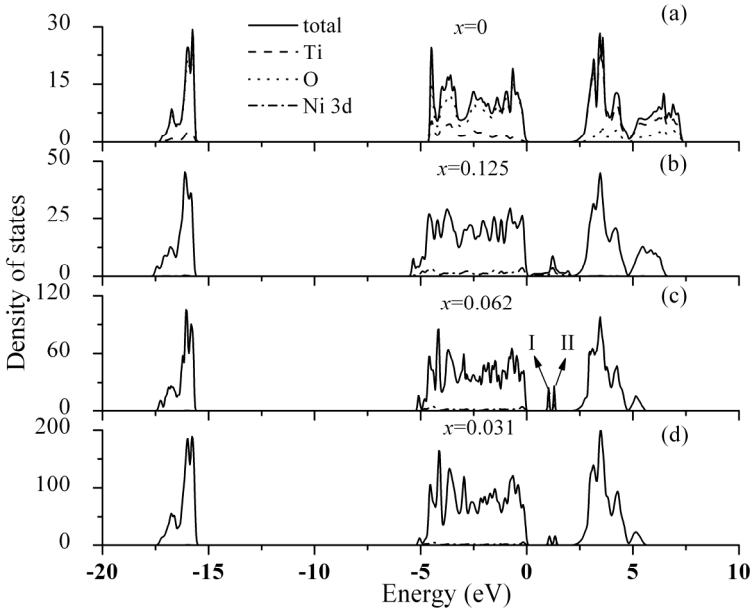

Figure 3: Partial density of states plots for different concentrations of Ni impurity in anatase TiO_2. The unit for density of states is electrons/eV, *x*: doping concentration.

In addition, Optical absorption spectra were calculated for different concentrations of Ni-doped anatase TiO_2 and the results were shown in Figure 5. The curve (a) for pure TiO_2 was calculated as a benchmark for comparing the results for Ni-doped TiO_2. For lower Ni impurity concentrations, curve (c) and (d) were very similar in the overall shape. The absorption for visible light with the characters of the shoulders around 450 nm and the tails reaching 700 nm was observed.

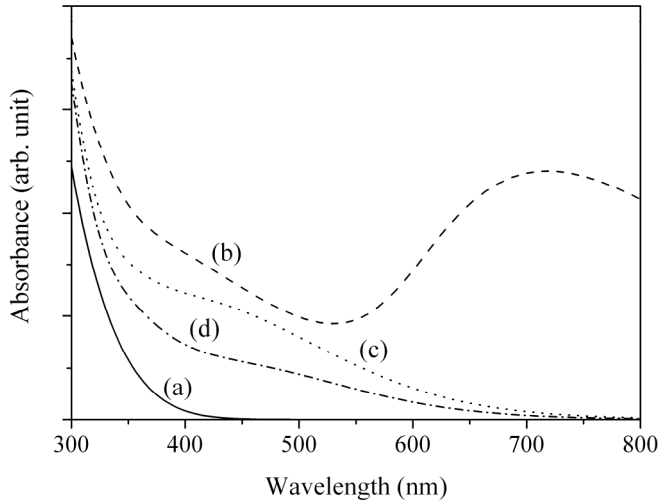

Figure 4: The optical absorption spectra for different concentrations of Ni impurity in anatase TiO_2 of the polycrystalline powder.

In summary, Ni doping had significant effect on electronic structure, optical absorption, and even photocatalytic property of anatase TiO_2. By introducing deep localized acceptor levels in the band gap, the response for visible light can be realized and the optical absorption spectra show the characters of the shoulder around 450 nm and the tail reaching 700 nm when Ni concentration approaches the experimental value. A schematic diagram of the band structure for Ni-doped anatase TiO_2 vs. normal hydrogen electrode (NHE) potential was drawn, as shown in Figure 5. This type of band structure was reasonable for the interpretation for various experimental phenomena.

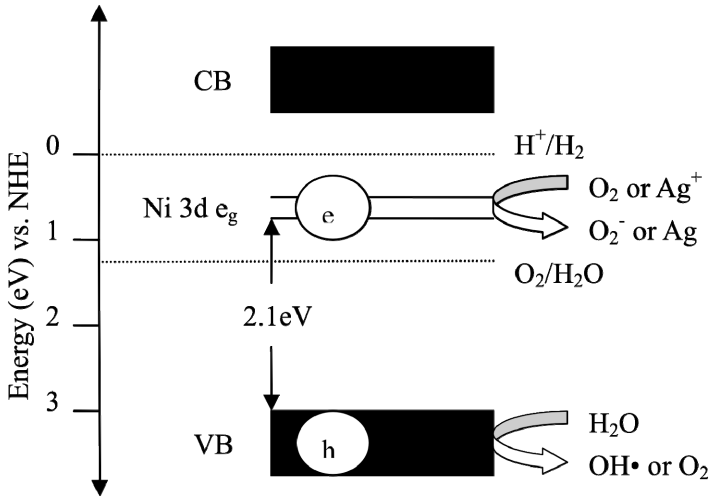

Figure 5: Schematic band structure diagram for Ni doped anatase TiO_2 vs. NHE potential.

Acknowledgments

The authors gratefully acknowledge the financial supports from the National Natural Science Foundation of China (Contracted No. 50821064), the National Basic Research Program of China (Contracted No. 2009CB220000) and the calculation resource supports from the molecular simulation computing platform in Xi'an Jiaotong University.

References

[1] S.D. Sharma, D. Singh, K.K. Saini, et al, Appl. Catal. A 314 (2006), 40-46.

[2] D.W. Jing, Y.J. Zhang, L.J. Guo, Chem. Phys. Lett. 415 (2005), 74-78.

[3] H. Yamashita, M. Harada, J. Misika, et al, Photoch. Photobio. A 148 (2002), 257-261.

[4] R. Niishiro, H. Kato, A. Kudo, Phys. Chem. Chem. Phys. 7 (2005), 2241-2245.

[5] M.D. Segall, P.L.D. Lindan, M.J. Probert, et al, J. Phys.: Condens. Matter 14 (2002), 2717-2744.

[6] J.K. Burdett, T. Hughbandks, G.J. Miller, et al, J. Am. Chem. Soc. 109 (1987), 3639-3646.

[7] R. Asahi, Y. Taga, W. Mannstadt, et al, Phys. Rev. B 61 (2000), 7459-7465.

[8] M.D. Segall, R. Shah, C.J. Pichard, et al, Phys. Rev. B 54 (1996), 16317-16320.

[9] Y. Wang, D.J. Doren, 136 (2005), 142-146.

Construction of Z-scheme Using $XTiO_3$:Pt (X = Ca, Sr, Ba) in Combination with WO_3 and BiV_5O_{14} for Hydrogen Production from Water

Michal Ludwiczak, Macin Wlodarczak, Marek Laniecki, A. Mickiewicz University, Poland

1 Introduction

Modern civilization has grown greatly dependent on technology and in consequence on energy. Continuous and stable energy supplies are the basis for economic growth of every country. Most of energy used today is derived from fossil fuels. It creates many environmental problems, like acid rains or speeding up the greenhouse effect. Abundance of fossil fuels can only be found in few regions of the world. It makes other regions energetically vulnerable. Another problem is limited amount of these energy sources. In this situation, there is a great need for alternative energy sources. We need not only new energy sources but also energy carriers. Among many possible candidates, hydrogen seems like the most promising one [1].

There are many industrial methods for hydrogen production, like steam reforming of natural gas, water gas shift reaction, electrolysis of water, etc. However neither of them can be used to produce environmentally clean hydrogen because they use energy form burning of fossil fuels.

There is a great need for an efficient, clean and inexpensive method of hydrogen production. Photocatalytic splitting of water is a very promising solution. There are numerous reports of photocatalytically active transition metal oxides and sulfides capable of generating hydrogen from water [2]. Most of them absorb radiation in UV region. Ultra-violet radiation constitutes for only 4% of total radiation reaching surface of the Earth. Therefore there is a necessity for a photocatalytic system working under solar radiation. In recent years, systems based on artificial photosynthesis became studied with more interest. Many researchers attempted to create photocatalytic system based on Z scheme [3-4]. My work focuses on synthesis and characterization of perovskite based photocatalysts, modified with platinum. The perovskite structure has been chosen with regard to its versatility and ease of manipulating physical and chemical properties. This work focuses on three perovskites, $CaTiO_3$, $SrTiO_3$ and $BaTiO_3$. A sol-gel method has been selected for preparation of perovskites. It was expected to produce higher surface area compared to solid state reaction method. High surface area, although not directly important in photocatalysis, can provide high platinum dispersion and in consequence create many photocatalytically active sites. For oxygen generating photocatalysts WO_3 and $BiVO_4$ have been chosen.

2 Experimental

Synthesis under acidic conditions

$CaTiO_3$, $SrTiO_3$ i $BaTiO_3$ were prepared by sol-gel method. As precursors $Ti[OCH(CH_3)_2]_4$ and $X(OOCH_2CH_3)_2$ (where X = Ca, Sr, Ba) were used. An exact amount of a metal acetate was dissolved in acetic acid – water solution. The ratio of acetic acid and water has been chosen to get pH value near 2. Next , the solution was added to previously prepared solution of titanium (IV) isopropoxide in isopropanol, with intense stirring. The solvents were then evaporated with continuous heating, until gel formed. The gel was aged in 70-90^oC and then dried in 120^oC. Prepared powders were calcined at different temperatures to give product.

Synthesis in melted stearic acid

$CaTiO_3$ was prepared by reaction between $Ti[OCH(CH_3)_2]_{40}$ and calcium stearate in melted stearic acid. Firstly, $[CH_3(CH_2)_{16}COO]_2Ca$ was dissolved in stearic acid melted at 80^oC. Next, titanium (IV) isopropoxide was added and the solution was stirred until gel was formed. The obtained gel was left to cool down naturally. The perovskite precursor was then calcined in temperatures between 500^oC to 600^oC.

Synthesis under alkaline conditions

In this method the first step was to produce gel using the same method as described in acidic synthesis paragraph. The prepared gel was then put into a stainless steel autoclave with teflon inlay. Autoclave was filled with water and pH was adjusted to 12 using KOH. Next, the autoclave was heated to 200^oC for 6 hours. After that, the autoclave was allowed to cool down naturally. The prepared suspension was rinsed with methyl alcohol and water and centrifuged. Samples were dried in 120^oC.

Preparation of WO_3

Tungsten oxide (VI) was prepared by thermal treatment of H_2WO_4 in air atmosphere.

Preparation of bismuth vanadate

The first phase of preparation was a solid state reaction between V_2O_5 and K_2CO_3, which were mixed in molar ratio 3:5. The mixture was heated to 430^oC for 5 hours. The prepared $K_3V_5O_{14}$ was suspended in $Bi(NO_3)_3$ water solution and stirred for 72 hours. The precipitate was rinsed with water and dried at 120^oC.

Catalysts surface modification

Perovskites surface was modified with different amounts of platinum, using incipient wetness impregnation technique.

Sample characterization

The thermogravimetric analysis was peroformed on Thermogravimeter Setaram Setsys 12 (TGA/DSC), in air atmosphere. A temperature from 17^oC to 1000^oC was used (10^oC/min temperature bear). Powder X-ray diffraction was done on Bruker AXS D8 Advance diffractometer, with 20^o do 70^o 2θ range and using 0,02^o/s measure rate. CuK_α (wavelength = 1,5406 Å) was used as radiation source. Surface area was determined using full adsorption/desorption isotherm performed at Micromeritics Sorptometr ASAP 2010. The presented values of surface area were calculated with BET theory. The average pore

diameter was calculated using BJH method, based on desorption isotherm. The range of radiation absorbed by photocatalysts was measured with UV-VIS Varian Carry 100 spectrophotometer. Catalytic tests were performed in a pyrex glass reactor, illuminated with four Ultra-Vitalux lamps imitating solar radiation. The reactor was coupled with Varian CP-3800 gas chromatograph in order to measure the amount of produced hydrogen.

3 Results

In order to evaluate optimal calcination temperature a thermal gravimetry technique was used. The TG curves were similar to all samples synthesized under acidic conditions. A weight loss below 200°C was caused by evaporation of moisture. A massive weight loss accompanied by big exoenergetic effect in 300-400°C range can be associated with oxidation of organic compounds like acetate and isopropyl groups. Around temperatures between 600-750°C a third weight loss can be observed. It is consistent with pyrolysis of residual organic derivatives. Last weight loss, related to formation of perovskite structure, was usually observed in temperature above 800°C.

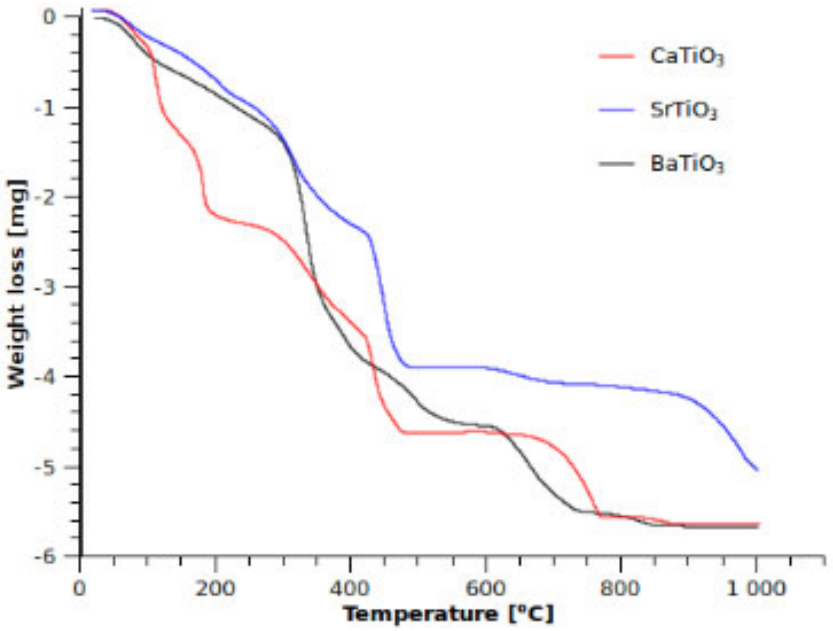

Figure 1: TG curves of $CaTiO_3$, $SrTiO_3$ and Ba TiO_3 dried gels.

The XRD patterns of samples calcined at different temperatures show, that for all three perovskites the $XTiO_3$ crystalline structure is created in 800°C and higher. At low calcination temperatures additional reflexes are present, which can be associated to trace amounts of TiO_2 (rutile) and XCO_2. At calcination temperatures above 1000°C additional phases are still visible but very weak.

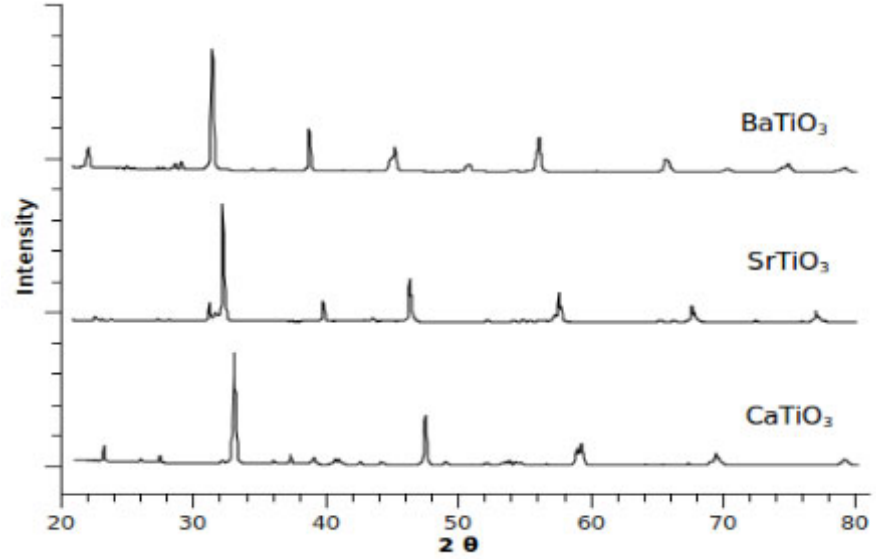

Figure 2: XRD patterns of perovskites prepeared under acidic conditions, calcined at 1000 °C.

Adsorption/desorption data shows that surface areas of samples produced by all three methods are higher compared to perovskites prepared using solid state reaction. The highest surface area was achieved for $CaTiO_3$ prepared by synthesis in melted stearic acid - 87 m^2/g.

Table 1: Surface areas for samples prepeared under various conditions.

		Surface area [m^2/g]	Average pore volume [nm]
Acidic synthesis	$CaTiO_3$ 900°C	12,2	9,5
	$SrTiO_3$ 900°C	4,5	13,7
	$BaTiO_3$ 900°C	7,9	13,9
Stearic acid	$CaTiO_3$ 500°C	87,6	15,9
	$CaTiO_3$ 600°C	42,8	16,8
	$BaTiO_3$ AUTOCLAVE	23,1	7,7

In general, surface area decreases rapidly with increasing calcination temperature. Table 1 presents a comparison of surface areas of perovskites synthesized by all three methods.

Table 2 shows selected results of catalytic tests. All results are presented in μmol/h and calculated for 1 g of photocatalyst.

Table 2: Hydrogen production after 1 h of reaction using 1 g of catalyst.

		Calcination temperature [°C]	Amount of Pt [% wt.]	Hydrogen produced [µmol/h]
$CaTiO_3$	Prepared under acidic conditions	900	0,1	46,5
$CaTiO_3$		900	0,05	64,2
$SrTiO_3$		1000	0,1	62,5
$BaTiO_3$		800	0,1	46,9
$BaTiO_3$		800	0,05	40,6
$CaTiO_3$	Prepared in melted stearic acid	600	0,1	110,7
$CaTiO_3$		500	0,1	253,1

4 Conclusions

All prepared photocatalysts have higher surface areas than perovskites produced by traditional method. High loss of surface area with increasing calcination suggests need for optimizing the gelation process to make calcination at lower temperatures possible. $CaTiO_3$ produced by synthesis in melted stearic acid is most active of all photocatalysts. The absorption band of all photocatalysts starts at aproximately 400 nm which should make catalysis under Solar radiation possible.

References

[1] Goltsov, V.A., International Journal of Hydrogen Energy, 31 (2006) 153 – 159

[2] Shangguan, W., Science and technology of advanced materials, 2007 (8) 76-81

[3] Kato, H., Chemistry Letters, Vol.33, No.10 (2004)

[4] Sasaki, Y., Journal of Catalysis, 259 (2008) 133–137

Mesoporous SnO_x/TiO_2 Materials as Photocatalyst for Water Splitting Reaction

M. Stodolny, A. Mikołajczak, M. Łaniecki, A. Mickiewicz University, Poland

1 Introduction

Transformation of solar energy towards other storable form of energies is a big challenge both for science and academia. There are two ways of solar energy transformations: direct and indirect. In the first one, solar energy in photocells is directly transformed into electric energy. The main disadvantage of wider application is related with low energy density accumulated this way. An alternative energy carrier can be based on hydrogen. This energy carrier seems to be ideal from environmental reasons because the only “ash” is represented by water. Moreover, hydrogen is easy in storage and transport. It can be produced from water either by photocatalytic splitting of water or electrolysis but only in those countries with the surplus of hydroenergy. First photocatalytic way of splitting of water was demonstrated by Fujishima and Honda in 1972 [1]. Since that time significant efforts were directed towards search of new photocatalytic materials. At the beginnings it seemed that TiO_2 will be the best photocatalyst for numerous applications. However, relatively high value of band gap of TiO2 prompted many research groups for search of new semiconducting materials [4-6]. Among these new materials modified or non-modified perovskites, inorganic sulfides, nitrides and oxonitrides represented the best properties for photcatalytic reactions. Simultaneously, the research related with modification of already mentioned materials started to flourish. The main methods of photocatalysts modification are summarized below:

- modification of the oxide surface with noble metals (Pt, Au, Ag, Ni) [7],
- formation of semiconducting composites (eg. $CdS\text{-}TiO_2$) [8],
- sensibilisation of the surface (TiO_2 with adsorbed $[Ru(dcpy)_2(dpq)]^{2+}$ [9],
- doping with metals [10] or anions [11]
- modification of photocatalyst morphology via synthesis of nanostructured materials.

This paper describes the influence of deposition of SnOx on porous TiO2 and mesoporous SBA-15 on photocatalytic activity in water splitting.

2 Experimental

2.1 Preparation of photocatalysts

Method I

SBA-15 was prepared according to the procedure described by Zhao et al. [12]. For this synthesis an appropriate amount of block co-polymer PLURONIC -123 , tetraothoxysilan and hydrochloric acid were heated in autoclave at 383 K for 20 hours. After removal of template by burning organic substances at 823 K.

The modified titanium –tin sol was prepared by hydrolysis of titanium isopropoxide for 6 hours at 348 K. Next, to such sol an appropriate amount of tin oxide (II) was added providing

TiO_2-SnO ratio as 1.5. After 5 minutes in ultrasound bath this sol solution was introduced to dry SBA-15. The content of TiO_2 in newly prepared SBA-15/ titania structure was 16 wt. %. Final calcinations of these samples were performed at 675 K.

Method II

Titanium isopropoxide was applied during synthesis of mesoporous titania. In standard synthesis the Ti(OC3H7)4 dissolved in ethanol and aged with glucose and HCl for 12 hours. Then, SnO was introduced into obtained gel while vigorously stirring. This procedure was followed by ultrasonification. After drying on air samples were calcined at 606 K.

Method III

Here, 1g of block copolymer of Pluronic 123 was dissolved in ethanol. Than to this solution TiCl4 was added dropwise and finally appropriate amount of SnO. The obtained sol was gelated for 7 days in air and calcined at 773 K for 5 hours.

2.2 Photocatalytic measurements

Photocatalytic reactor consisted from Quickfit® round bottom bulb equipped with reflux. The 0.1 g of photocatalyst was placed in 250 cm^3 of water containing 5 cm^3 of methanol. Four Vitalux bulbs from Osram served as the source of light (spectral characteristic close to the sunlight). The amount of photogenerated hydrogen was measured chromatografically (Varian 388 equipped with carbon column and TCD).

All samples were characterized with thermogravimetry, low-angle and regular XRD spectroscopy, DRIFT and DRUV spectroscopies. Occasionally TEM and SEM micrographs were recorded. For surface area and porosity measurements low temperature adsorption of nitrogen (77K) was performed.

3 Results and Discussion

The results of surface area, porosity of pure supports and those with supported SnO are presented in Table 1.

Table 1: Characteristic of the applied supports.

Materials	Surface area [m^2/g]	Pore volume [cm^3/g]	Pore diameter [nm]
SBA-15	821	1,03	6,1
SBA16zolSnO	610	0,80	5,8
TiO_2/SnO glu.	118	0,15	5,2
TiO_2/SnO	108	0,25	7,2

The drop in surface area and porosity after deposition of titania-SnO sol shows that majority of this sol is located inside the porous structure of SBA-15. Adsorption-desorption isotherms of N_2 (see Figure 1) clearly confirm this assumption.

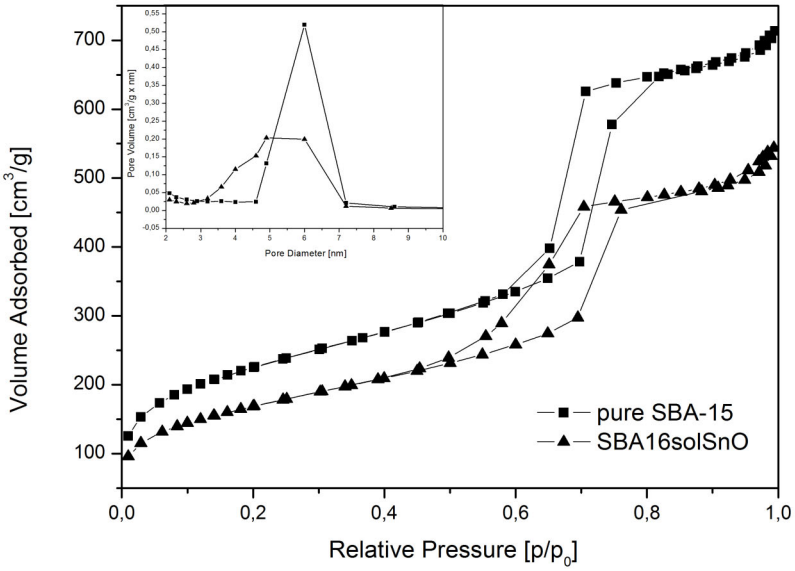

Figure 1: Adsorption-desorption isotherms of N2 at 77K.

In both cases (pure and modified siliceous material) the presence of mesopores is demonstrated by hysteresis loop in the range of p/p_0 equal 0.5 to 0.8. Moreover, the microporous system remained almost untouched after deposition of SnO. This property provides excellent diffusion in the system both liquid as well as evolved gases.

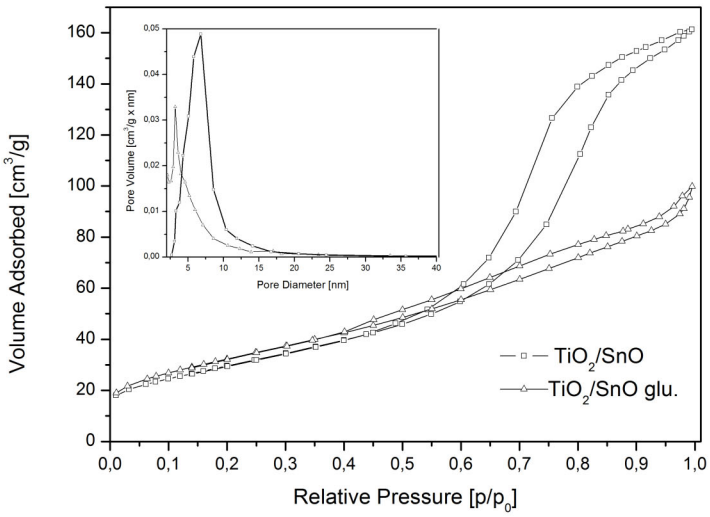

Figure 2: Adsorption –desorption isotherms of N_2 ay 77 K for TiO_2 based materials.

Completely different situation can be observed when titania, instead of SBA-15, was applied as the support for SnO. The shape of isothers as well as the results of surface area values clearly indicate that deposited SnO will represent different character than in SBA-15.

The DRUV-vis spectra of the studied systems are shown on Figure 3. It is obvious that each system is characterized by different ability of electron excitation and in consequence the value of the band gap is different for each studied photocatalyst.

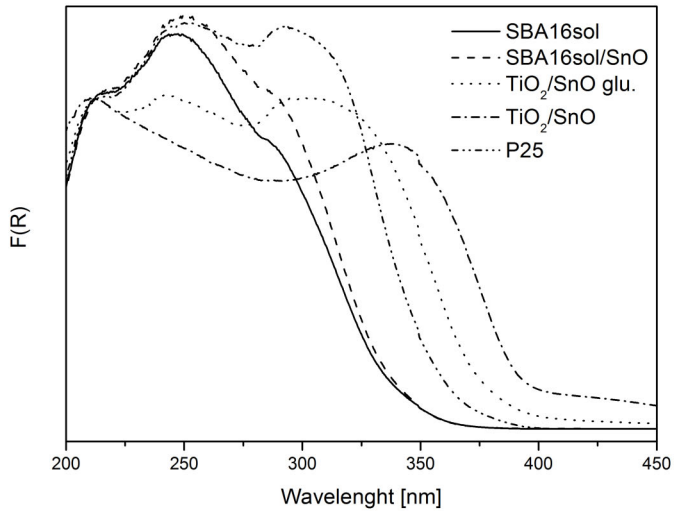

Figure 3: DRUV-vis spectra of the studied photocatalysts.

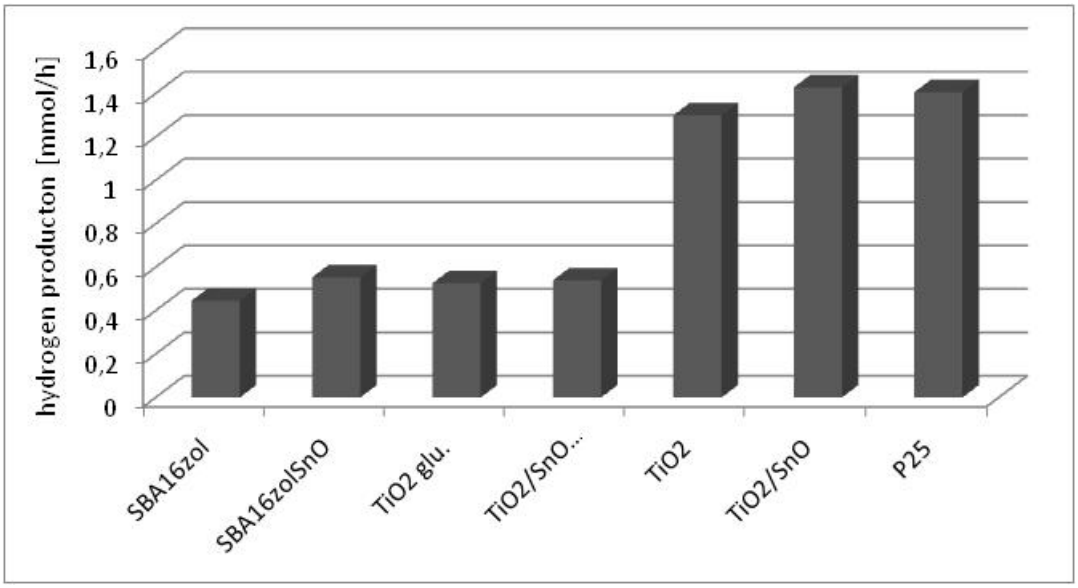

Figure 4: Hydrogen generated over different photocatalysts.

Results presented on Figure 4 show that attempts to increase photocatalytic activity only in one case were successful. Sample prepared according to the method III show the best activity and addition of SnO slightly increase the amount of generated hydrogen. An addition of Sn2+ ions influences the ability of light absorption at higher wavelength values. Samples

prepared according to method III show constant progress in hydrogen evolution and an increase of SnO concentration can improve the yield of the studied process.

Acknowledgements

Authors are indebted to MNiSW for financial support (grant N204 031 32/0793)

References

[1] A. Fujishima, K. Honda, Nature 238 (1971) 37

[2] B. Kraeutler, A.J. Bard, J. Am. Chem. Soc. 99 (1977) 7729

[3] F.T. Wagner, S. Ferrer, G.A. Somorjai, Surf. Sci. 101 (1980) 462

[4] M. Ashokkumar, Int, J. Hydrogen Energy 23 (1998) 427

[5] A.L. Linsebigler, G. Lu, J.T. Yates Jr., Chem. Rev. 95 (1995) 735

[6] A. Milles, S. La Hunte, J. Photochem, Photobiol. A: Chem. 108 (1997) 1

[7] K. Sayama, H. Arakawa, J. Photochem. Photobiol, A: Chem. 77 (1994) 243

[8] W.W. So, K.J. Kim, S.J. Moon, Int. J. Hydrogen Energy 29 (2004) 229

[9] K.B. Dhanalakshmi, S. Latha, S. Anandan, P. Maruthamuthu, Int. J. Hydrogen Energy 26 (2001) 669

[10] E.C. Butler, A.P. Davis, J. Photochem. Photobiol. A: Chem. 70 (1993) 273

[11] D. Zhao, Q. Huo, J. Feng, B.F. Chmelka, G.D. Stucky, J. Am. Chem. Soc. 120 (1998) 6024

[12] S. Brunauer, P.H. Emmett, E. Teller, J. Am. Chem. Soc. 60 (1938) 309

[13] E.P. Barrett, L.G. Joyner, P.P. Halenda, J. Am. Chem. Soc. 73 (1951) 373

[14] M.l. Pena, V. Dellaroca, F. Rey, A. Corma, S. Coluccia, L. Marchese Micro. Mesopor. Mater. 44-45 (2001) 345

[15] B.L. Newalkar, J. Olanerwaju, S. Komareni Chem Mater. 13 (2001) 552

[16] G.N. Vayssilov Catal. Rev. Sci. Eng. 39 (1997) 209

[17] S. Gontier, A. Tuel, Zeolites 15 (1995) 603

Modified Titanate Perovskites in Photocatalytic Water Splitting

M. Włodarczak, M. Ludwiczak, M. Laniecki, A. Mickiewicz University, Poland

1 Introduction

The present world is energy dependant as never it was before. The continuous demand for increased energy production results in significant depletion of the environment. Almost 80 % of generated energy comes from fossil fuels [1]. The significant amounts of greenhouse gases, contamination of air, generation of all kinds of wastes and generation of tremendous amounts of ashes are the final effects of application fossil fuels and to some extent also nuclear energy. One of the possible solutions to minimize and to avoid this scenario is the application of hydrogen as the energy carrier – a universal and ecological fuel [2,3]. Presently, except for electrolysis hydrogen is generated basically from fossil fuels. The photocatalytic splitting of water one day can become the alternative solution to the traditional methods. Since the early seventies of XX century significant efforts have been directed towards extension of this method. Different photocatalysts and their modifications were tested under different conditions both in laboratories and under natural sunlight illumination. Titania and simple perovskites became the well known photocatalysts but their activity is limited only to ultraviolet part of the solar spectrum. Energy required for electron excitation in these materials is relatively high (3.2 eV). Typical perovskites can be obtained in different ways but the most popular is based on reaction of titania and other oxides or carbonates in solid state reactions at high temperatures (>1200 °C). This method provides significant amounts of the required product with uniform dimensions of particles [4]. The main drawback of this method relay on low surface area of the obtained solids; usually close to 1 m^2/g. Low surface area of such perovskites is an obstacle in good dispersion during deposition of platinum or nickel and in consequence leads towards low quantum yield during splitting of water. Thanks to the method of synthesis of perovskites applied in this paper, the obtained solids posses much higher surface area. This effect was attained by lowering significantly temperature of the synthesis. Moreover, the applied method is much simple than in other methods, eg. MBE [5,6] or CVD [7].

2 Experimental

Synthesis performed in this paper represents the modification of synthesis proposed by McLaren and Ponton [8]. The procedure initially proposed for synthesis of barium titanate was also applied for formation of strontium and calcium titanates. Here, for the synthesis barium, strontium or calcium acetates (Sigma-Aldrich), titanium isopropoxide (Ti-isoPrOH) and 1M solution of the organic base (tetramethyl hydroxylamine –TMHA from Sigma Aldrich) were applied.

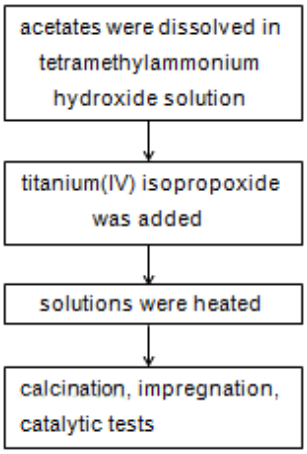

Figure 1: Experimental procedure.

Scheme from Figure 1 shows the basic steps in preparation procedure. In the first step an appropriate acetate was dissolved at room temperature in water solution of TMHA. The ratio of OH- ions to metal ions in all cases was equal 4:1. In the next step the titanium ispropoxide was added while continuously stirring. The molar ratio of Ti-isoPrOH to acetate was like 1:1. After 5 minutes the suspension was heated up to 80 °C and kept at this temperature for 4 hours. After filtration the obtained white powders were washed with distilled water, dried at room temperature and finally calcined. The minimum of calcinations temperature (500 °C) was established on the basis of thermogravimetric measurements.

Samples after characterization with XRD and adsorption-desorption of N_2 at minus 196 °C were impregnated with chloroplatinic acid. Three different concentration of chloroplatinic acids provided 0.5, 0.1 and 0.01 wt. % of platinum on the surface of the perovskites. The incipient wetness method was applied for impregnations.

Photocatalytic test in splitting of water were carried out in photoreactor (from Pyrex glass) with capacity of 250 cm^3. The water-methanol mixture (molar ratio 50:1) with suspended catalyst (0.1 g) was illuminated with 4 Vitalux bulbs from Osram. Temperature of the reaction was 50 °C. The amount of evolved gases was determined applying gas chromatography (Varian 3800 equipped with CarboPlot capillary column).

3 Results

Thermogravimetric experiments with air-dried samples showed that 500 °C is the lowest possible temperature for calcinations. Water, acetic acid and carbon oxides were the main gaseous products during temperature increase. Above 500 °C no further decomposition occurs and this was demonstrated by essential lack of the weight loss. Surface area (BET) of the obtained perovskites is high in comparison with those observed for ceramic method. Pore volume (BJH), except calcium titanate is rather small. Data presented in Table 1 summarize surface properties of the obtained materials.

Table 1: Surface area of received samples.

	Area [m^2/g]	Pore volume [cm^3/g]	Pore diameter [nm]
Sample	Calcination 500°C		
$CaTiO_3$	109.1	0.31	10.9
$SrTiO_3$	23.9	0.08	17.3
$BaTiO_3$	25.7	0.06	10.7
Sample	Calcination 700°C		
$CaTiO_3$	37.9	0.21	25.7
$SrTiO_3$	18.6	0.07	17.7
$BaTiO_3$	12.6	0.05	20.0

Crystal structure of the obtained perovskites was determined with powder XRD technique. In the case of calcium titanate it was found that calcination at 500 °C is not sufficient to create the appropriate structure of perovskite (see Figure 2). The other two materials showed the structure of regular perovskite after calcinations at this temperature. For calcium titanate the appropriate pervoskite type structure appeared after calcination at 700 °C. Here, the presence of reflexes at 33°, 48° and 59° of 2 θ indicates formation of $CaTiO_3$ with slightly increased dimensions of crystals, when compared to standard.

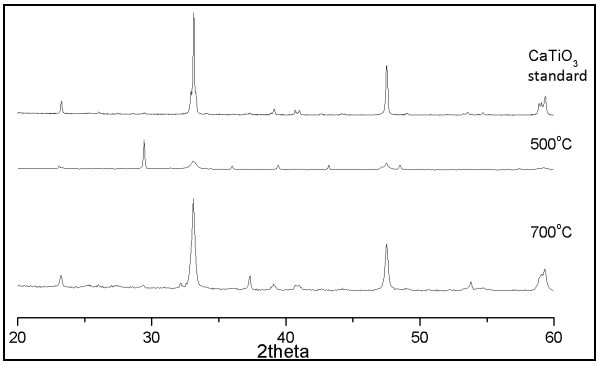

Figure 2: Powder X-ray diffraction pattern, $CaTiO_3$.

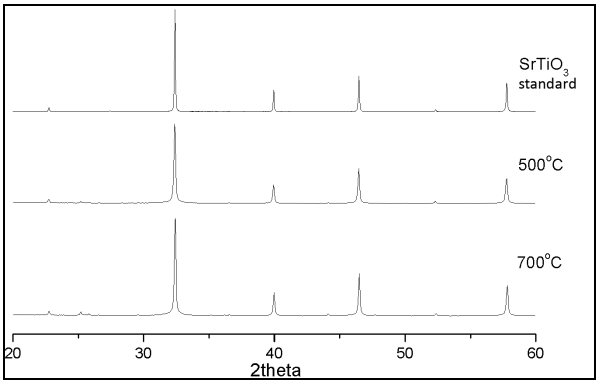

Figure 3: Powder X-ray diffraction pattern, $SrTiO_3$.

Diffraction patterns for strontium titanate shown on figure 3 indicate that appropriate structure of perovskite is already present after calcination at 500 °C. Well defined, narrow reflexes are indicative for small, well crystallized material. The X-ray diffraction patterns of $BaTiO_3$ (see Figure 4) are also well defined after calcination at 500 °C, however, less precise than in the case of $SrTiO_3$.

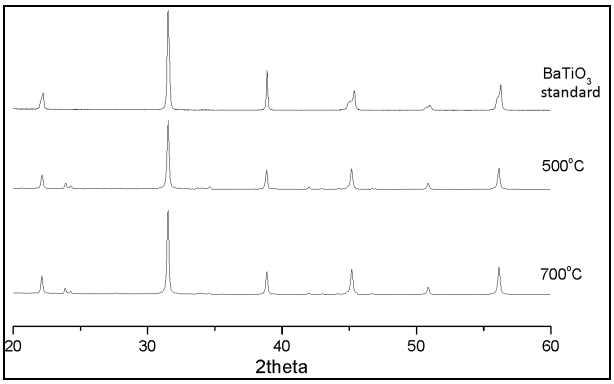

Figure 4: Powder X-ray diffraction pattern, $BaTiO_3$.

The confirmation of the results obtained during XRD measurements In part can be confirmed by SEM microphotographs.

All SEM micrographs (Figure 5) show the same shape and dimensions for the obtained materials. Small dimensions of the obtained semiconductors can be very useful in photocalytic processes while working with suspensions.

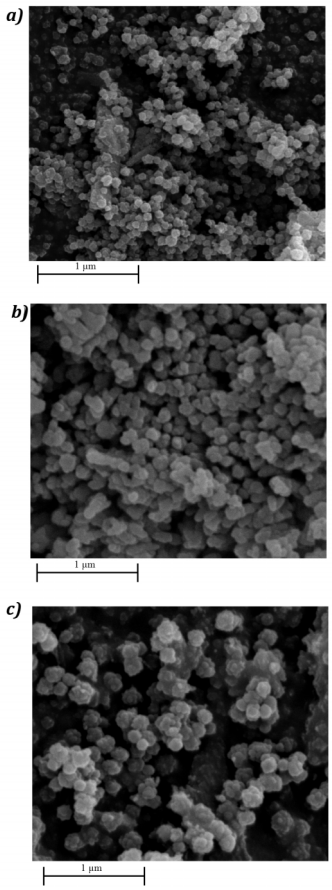

Figure 5: SEM images of perovskites: a) $CaTiO_3$, b) $BaTiO_3$, c) $SrTiO_3$; calcined in 700°C.

In all studied photocatalysts with deposited noble metal the dispersion of these metals was measured. Data for materials containing 0.5 wt. % of platinum and calcined at 700 °C are shown in Table 2. Here, the dispersion was the highest for $CaTiO_3$, and lower for two other. The influence of surface area is here easily observable.

Catalytic activity in water splitting was observed in all studied cases but the best activity was obtained for samples calcined at 700 °C and containing 0.1 wt. % of platinum. Calcium perovskites showed the best performance.

Table 2: Dispersion of platinum (0.5% Pt, calcination 700°C).

Sample	**$CaTiO_3$**	**$SrTiO_3$**	**$BaTiO_3$**
Dispersion [%]	55.6	44.5	38.9

The results for one series of non-modified perovskites are shown on Table 3. These data indicate that performance of calcium titanate containing 0.1 wt. % of platinum is the best. Samples activated at 500°C showed photocatalytic activity, but the amounts of generated hydrogen were much smaller. It was found that for presented perovskites the amount of deposited platinum should be 0.1 wt. %. Too high concentration leads towards formation of large platinum clusters and in consequence a screening effect can be involved.

Table 3. Platinum content and hydrogen evolution.

Sample	**Amount of Pt [% of weight]**	**H_2 [µmol · h^{-1} · g_{cat}^{-1}]**
$CaTiO_3$	0.5	443
	0.1	481
	0.02	371
$SrTiO_3$	0.5	262
	0.1	110
	0.02	102
$BaTiO_3$	0.5	106
	0.1	197
	0.02	trace

4 Summary

Received materials have structure of perovskite, what was shown by XRD diffraction patterns. Perovskite structure is present in all samples with strontium, barium and one sample with calcium. Moreover, received barium and strontium titanate are very similar to pattern materials. XRD results show, that temperature 500°C is too low to create perovskite structure in $CaTiO_3$. However, it is high enough in case of $SrTiO_3$ and $BaTiO_3$. One regularity is obvious, surface area increases for samples calcined in lower temperature. There is a connection between surface area and dispersion of platinum. Both of them reach the greatest value to the calcium titanate.

Catalytic activity was shown by all of received samples. Measurable values were received to samples calcined in 700°C. Calcium titanate had the best catalytic activity, both an amount of

hydrogen and a ratio of hydrogen to platinum. There is one regularity to all samples, the ration of hydrogen to platinum increase when amount of platinum decrease.

References

[1] Energy Information Administration (EIA), International Energy Outlook 2008, available from: http://www.eia.doe.gov/oiaf/ieo/pdf/0484(2008).pdf

[2] P. Moriarty, D. Honnery, International Journal of Hydrogen Energy, 34 (2009) 31-39

[3] M. Ball, M. Wietschel M., International Journal of Hydrogen Energy, 34 (2009) 615-627

[4] Khamman O., Wongmaneerung R., Chaisan W., Yimnirun R., Ananta S., Journal of Alloys and Compounds, 456 (2008) 492-497

[5] Rinaldi, F. Basics of Molecular Beam Epitaxy (MBE). http://www-opto.e-technik.uni-ulm.de/forschung/jahresbericht/2002/ar2002_fr.pdf

[6] Yang G. Z., Lu H. B., Chen F., Zhao T., Chen Z. H., Journal of Crystal Growth, 227-228 (2001) 929-935

[7] Suzuki K., Kijima, Vacuum, 80 (2006) 519-529

[8] A MacLaren I., Ponton C. B., Journal of European Ceramic Society, 20 (2000) 1267-1275

1. **Einsatz von multispektralen Satellitenbilddaten in der Wasserhaushalts- und Stoffstrommodellierung – dargestellt am Beispiel des Rureinzugsgebietes**
von C. Montzka (2008), XX, 238 Seiten
ISBN: 978-3-89336-508-1

2. **Ozone Production in the Atmosphere Simulation Chamber SAPHIR**
by C. A. Richter (2008), XIV, 147 pages
ISBN: 978-3-89336-513-5

3. **Entwicklung neuer Schutz- und Kontaktierungsschichten für Hochtemperatur-Brennstoffzellen**
von T. Kiefer (2008), 138 Seiten
ISBN: 978-3-89336-514-2

4. **Optimierung der Reflektivität keramischer Wärmedämmschichten aus Yttrium-teilstabilisiertem Zirkoniumdioxid für den Einsatz auf metallischen Komponenten in Gasturbinen**
von A. Stuke (2008), X, 201 Seiten
ISBN: 978-3-89336-515-9

5. **Lichtstreuende Oberflächen, Schichten und Schichtsysteme zur Verbesserung der Lichteinkopplung in Silizium-Dünnschichtsolarzellen**
von M. Berginski (2008), XV, 171 Seiten
ISBN: 978-3-89336-516-6

6. **Politikszenarien für den Klimaschutz IV – Szenarien bis 2030**
hrsg.von P. Markewitz, F. Chr. Matthes (2008), 376 Seiten
ISBN 978-3-89336-518-0

7. **Untersuchungen zum Verschmutzungsverhalten rheinischer Braunkohlen in Kohledampferzeugern**
von A. Schlüter (2008), 164 Seiten
ISBN 978-3-89336-524-1

8. **Inorganic Microporous Membranes for Gas Separation in Fossil Fuel Power Plants**
by G. van der Donk (2008), VI, 120 pages
ISBN: 978-3-89336-525-8

9. **Sinterung von Zirkoniumdioxid-Elektrolyten im Mehrlagenverbund der oxidkeramischen Brennstoffzelle (SOFC)**
von R. Mücke (2008), VI, 165 Seiten
ISBN: 978-3-89336-529-6

10. **Safety Considerations on Liquid Hydrogen**
by K. Verfondern (2008), VIII, 167 pages
ISBN: 978-3-89336-530-2

11. **Kerosinreformierung für Luftfahrtanwendungen**
    von R. C. Samsun (2008), VII, 218 Seiten
    ISBN: 978-3-89336-531-9

12. **Der 4. Deutsche Wasserstoff Congress 2008 – Tagungsband**
    hrsg. von D. Stolten, B. Emonts, Th. Grube (2008), 269 Seiten
    ISBN: 978-3-89336-533-3

13. **Organic matter in Late Devonian sediments as an indicator for environmental changes**
    by M. Kloppisch (2008), XII, 188 pages
    ISBN: 978-3-89336-534-0

14. **Entschwefelung von Mitteldestillaten für die Anwendung in mobilen Brennstoffzellen-Systemen**
    von J. Latz (2008), XII, 215 Seiten
    ISBN: 978-3-89336-535-7

15. **RED-IMPACT**
    Impact of Partitioning, Transmutation and Waste Reduction Technologies on the Final Nuclear Waste Disposal
    SYNTHESIS REPORT
    ed. by W. von Lensa, R. Nabbi, M. Rossbach (2008), 178 pages
    ISBN 978-3-89336-538-8

16. **Ferritic Steel Interconnectors and their Interactions with Ni Base Anodes in Solid Oxide Fuel Cells (SOFC)**
    by J. H. Froitzheim (2008), 169 pages
    ISBN: 978-3-89336-540-1

17. **Integrated Modelling of Nutrients in Selected River Basins of Turkey**
    Results of a bilateral German-Turkish Research Project
    project coord. M. Karpuzcu, F. Wendland (2008), XVI, 183 pages
    ISBN: 978-3-89336-541-8

18. **Isotopengeochemische Studien zur klimatischen Ausprägung der Jüngeren Dryas in terrestrischen Archiven Eurasiens**
    von J. Parplies (2008), XI, 155 Seiten, Anh.
    ISBN: 978-3-89336-542-5

19. **Untersuchungen zur Klimavariabilität auf dem Tibetischen Plateau - Ein Beitrag auf der Basis stabiler Kohlenstoff- und Sauerstoffisotope in Jahrringen von Bäumen waldgrenznaher Standorte**
    von J. Griessinger (2008), XIII, 172 Seiten
    ISBN: 978-3-89336-544-9

20. **Neutron-Irradiation + Helium Hardening & Embrittlement Modeling of 9%Cr-Steels in an Engineering Perspective (HELENA)**
by R. Chaouadi (2008), VIII, 139 pages
ISBN: 978-3-89336-545-6

21. **in Bearbeitung**

22. **Verbundvorhaben APAWAGS (AOEV und Wassergenerierung) – Teilprojekt: Brennstoffreformierung – Schlussbericht**
von R. Peters, R. C. Samsun, J. Pasel, Z. Porš, D. Stolten (2008), VI, 106 Seiten
ISBN: 978-3-89336-547-0

23. **FREEVAL**
Evaluation of a Fire Radiative Power Product derived from Meteosat 8/9 and Identification of Operational User Needs
Final Report
project coord. M. Schultz, M. Wooster (2008), 139 pages
ISBN: 978-3-89336-549-4

24. **Untersuchungen zum Alkaliverhalten unter Oxycoal-Bedingungen**
von C. Weber (2008), VII, 143, XII Seiten
ISBN: 978-3-89336-551-7

25. **Grundlegende Untersuchungen zur Freisetzung von Spurstoffen, Heißgaschemie, Korrosionsbeständigkeit keramischer Werkstoffe und Alkalirückhaltung in der Druckkohlenstaubfeuerung**
von M. Müller (2008), 207 Seiten
ISBN: 978-3-89336-552-4

26. **Analytik von ozoninduzierten phenolischen Sekundärmetaboliten in *Nicotiana tabacum* L. cv Bel W3 mittels LC-MS**
von I. Koch (2008), III, V, 153 Seiten
ISBN 978-3-89336-553-1

27. **IEF-3 Report 2009. Grundlagenforschung für die Anwendung**
(2009), ca. 230 Seiten
ISBN: 978-3-89336-554-8

28. **Influence of Composition and Processing in the Oxidation Behavior of MCrAlY-Coatings for TBC Applications**
by J. Toscano (2009), 168 pages
ISBN: 978-3-89336-556-2

29. **Modellgestützte Analyse signifikanter Phosphorbelastungen in hessischen Oberflächengewässern aus diffusen und punktuellen Quellen**
von B. Tetzlaff (2009), 149 Seiten
ISBN: 978-3-89336-557-9

30. **Nickelreaktivlot / Oxidkeramik – Fügungen als elektrisch isolierende Dichtungskonzepte für Hochtemperatur-Brennstoffzellen-Stacks**
von S. Zügner (2009), 136 Seiten
ISBN: 978-3-89336-558-6

31. **Langzeitbeobachtung der Dosisbelastung der Bevölkerung in radioaktiv kontaminierten Gebieten Weißrusslands – Korma-Studie**
von H. Dederichs, J. Pillath, B. Heuel-Fabianek, P. Hill, R. Lennartz (2009), Getr. Pag.
ISBN: 978-3-89336-532-3

32. **Herstellung von Hochtemperatur-Brennstoffzellen über physikalische Gasphasenabscheidung**
von N. Jordán Escalona (2009), 148 Seiten
ISBN: 978-3-89336-532-3

33. **Real-time Digital Control of Plasma Position and Shape on the TEXTOR Tokamak**
by M. Mitri (2009), IV, 128 pages
ISBN: 978-3-89336-567-8

34. **Freisetzung und Einbindung von Alkalimetallverbindungen in kohlebefeuerten Kombikraftwerken**
von M. Müller (2009), 155 Seiten
ISBN: 978-3-89336-568-5

35. **Kosten von Brennstoffzellensystemen auf Massenbasis in Abhängigkeit von der Absatzmenge**
von J. Werhahn (2009), 242 Seiten
ISBN: 978-3-89336-569-2

36. **Einfluss von Reoxidationszyklen auf die Betriebsfestigkeit von anodengestützten Festoxid-Brennstoffzellen**
von M. Ettler (2009), 138 Seiten
ISBN: 978-3-89336-570-8

37. **Großflächige Plasmaabscheidung von mikrokristallinem Silizium für mikromorphe Dünnschichtsolarmodule**
von T. Kilper (2009), XVII, 154 Seiten
ISBN: 978-3-89336-572-2

38. **Generalized detailed balance theory of solar cells**
by T. Kirchartz (2009), IV, 198 pages
ISBN: 978-3-89336-573-9

39. **The Influence of the Dynamic Ergodic Divertor on the Radial Electric Field at the Tokamak TEXTOR**
von J. W. Coenen (2009), xii, 122, XXVI pages
ISBN: 978-3-89336-574-6

40. **Sicherheitstechnik im Wandel Nuklearer Systeme**
von K. Nünighoff (2009), viii, 215 Seiten
ISBN: 978-3-89336-578-4

41. **Pulvermetallurgie hochporöser NiTi-Legierungen für Implanat- und Dämpfungsanwendungen**
von M. Köhl (2009), XVII, 199 Seiten
ISBN: 978-3-89336-580-7

42. **Einfluss der Bondcoatzusammensetzung und Herstellungsparameter auf die Lebensdauer von Wärmedämmschichten bei zyklischer Temperaturbelastung**
von M. Subanovic (2009), 188, VI Seiten
ISBN: 978-3-89336-582-1

43. **Oxygen Permeation and Thermo-Chemical Stability of Oxygen Permeation Membrane Materials for the Oxyfuel Process**
by A. J. Ellett (2009), 176 pages
ISBN: 978-3-89336-581-4

44. **Korrosion von polykristallinem Aluminiumoxid (PCA) durch Metalljodidschmelzen sowie deren Benetzungseigenschaften**
von S. C. Fischer (2009), 148 Seiten
ISBN: 978-3-89336-584-5

45. **IEF-3 Report 2009. Basic Research for Applications**
(2009), 217 Seiten
ISBN: 978-3-89336-585-2

46. **Verbundvorhaben ELBASYS (Elektrische Basissysteme in einem CFK-Rumpf) - Teilprojekt: Brennstoffzellenabgase zur Tankinertisierung - Schlussbericht**
von R. Peters, J. Latz, J. Pasel, R. C. Samsun, D. Stolten
(2009), xi, 202 Seiten
ISBN: 978-3-89336-587-6

47. **Aging of ^{14}C-labeled Atrazine Residues in Soil: Location, Characterization and Biological Accessibility**
by N. D. Jablonowski (2009), IX, 104 pages
ISBN: 978-3-89336-588-3

48. **Entwicklung eines energetischen Sanierungsmodells für den europäischen Wohngebäudesektor unter dem Aspekt der Erstellung von Szenarien für Energie- und CO_2 - Einsparpotenziale bis 2030**
von P. Hansen (2009), XXII, 281 Seiten
ISBN: 978-3-89336-590-6

49. **Reduktion der Chromfreisetzung aus metallischen Interkonnektoren für Hochtemperaturbrennstofzellen durch Schutzschichtsysteme**
von R. Trebbels (2009), iii, 135 Seiten
ISBN: 978-3-89336-591-3

50. **Bruchmechanische Untersuchung von Metall / Keramik-Verbundsystemen für die Anwendung in der Hochtemperaturbrennstoffzelle**
von B. Kuhn (2009), 118 Seiten
ISBN: 978-3-89336-592-0

51. **Wasserstoff-Emissionen und ihre Auswirkungen auf den arktischen Ozonverlust**
Risikoanalyse einer globalen Wasserstoffwirtschaft
von T. Feck (2009), 180 Seiten
ISBN: 978-3-89336-593-7

52. **Development of a new Online Method for Compound Specific Measurements of Organic Aerosols**
by T. Hohaus (2009), 156 pages
ISBN: 978-3-89336-596-8

53. **Entwicklung einer FPGA basierten Ansteuerungselektronik für Justageeinheiten im Michelson Interferometer**
von H. Nöldgen (2009), 121 Seiten
ISBN: 978-3-89336-599-9

54. **Observation – and model – based study of the extratropical UT/LS**
by A. Kunz (2010), xii, 120, xii pages
ISBN: 978-3-89336-603-3

55. **Herstellung polykristalliner Szintillatoren für die Positronen-Emissions-Tomographie (PET)**
von S. K. Karim (2010), VIII, 154 Seiten
ISBN: 978-3-89336-610-1

56. **Kombination eines Gebäudekondensators mit H2-Rekombinatorelementen in Leichwasserreaktoren**
von S. Kelm (2010), vii, 119 Seiten
ISBN: 978-3-89336-611-8

57. **Plant Leaf Motion Estimation Using A 5D Affine Optical Flow Model**
by T. Schuchert (2010), X, 143 pages
ISBN: 978-3-89336-613-2

58. **Tracer-tracer relations as a tool for research on polar ozone loss**
by R. Müller (2010), 116 pages
ISBN: 978-3-89336-614-9

59. **Sorption of polycyclic aromatic hydrocarbon (PAH) to Yangtze River sediments and their components**
by J. Zhang (2010), X, 109 pages
ISBN: 978-3-89336-616-3

60. **Weltweite Innovationen bei der Entwicklung von CCS-Technologien und Möglichkeiten der Nutzung und des Recyclings von CO_2**
Studie im Auftrag des BMWi
von W. Kuckshinrichs et al. (2010), X, 139 Seiten
ISBN: 978-3-89336-617-0

61. **Herstellung und Charakterisierung von sauerstoffionenleitenden Dünnschichtmembranstrukturen**
von M. Betz (2010), XII, 112 Seiten
ISBN: 978-3-89336-618-7

62. **Politikszenarien für den Klimaschutz V – auf dem Weg zum Strukturwandel, Treibhausgas-Emissionsszenarien bis zum Jahr 2030**
hrsg. von P. Hansen, F. Chr. Matthes (2010), 276 Seiten
ISBN: 978-3-89336-619-4

63. **Charakterisierung Biogener Sekundärer Organischer Aerosole mit Statistischen Methoden**
von C. Spindler (2010), iv, 163 Seiten
ISBN: 978-3-89336-622-4

64. **Stabile Algorithmen für die Magnetotomographie an Brennstoffzellen**
von M. Wannert (2010), ix, 119 Seiten
ISBN: 978-3-89336-623-1

65. **Sauerstofftransport und Degradationsverhalten von Hochtemperatur-membranen für CO2-freie Kraftwerke**
von D. Schlehuber (2010), VII, 139 Seiten
ISBN: 978-3-89336-630-9

66. **Entwicklung und Herstellung von foliengegossenen, anodengestützten Festoxidbrennstoffzellen**
von W. Schafbauer (2010), VI, 164 Seiten
ISBN: 978-3-89336-631-6

67. **Disposal strategy of proton irradiated mercury from high power spallation sources**
by S. Chiriki (2010), xiv, 124 pages
ISBN: 978-3-89336-632-3

68. **Oxides with polyatomic anions considered as new electrolyte materials for solid oxide fuel cells (SOFCs)**
by O. H. Bin Hassan (2010), vii, 121 pages
ISBN: 978-3-89336-633-0

69. **Von der Komponente zum Stack: Entwicklung und Auslegung von HT-PEFC-Stacks der 5 kW-Klasse**
von A. Bendzulla (2010), IX, 203 Seiten
ISBN: 978-3-89336-634-7

70. **Satellitengestützte Schwerewellenmessungen in der Atmosphäre und Perspektiven einer zukünftigen ESA Mission (PREMIER)**
von S. Höfer (2010), 81 Seiten
ISBN: 978-3-89336-637-8

71. **Untersuchungen der Verhältnisse stabiler Kohlenstoffisotope in atmosphärisch relevanten VOC in Simulations- und Feldexperimenten**
von H. Spahn (2010), IV, 210 Seiten
ISBN: 978-3-89336-638-5

72. **Entwicklung und Charakterisierung eines metallischen Substrats für nanostrukturierte keramische Gastrennmembranen**
von K. Brands (2010), vii, 137 Seiten
ISBN: 978-3-89336-640-8

73. **Hybridisierung und Regelung eines mobilen Direktmethanol-Brennstoff-zellen-Systems**
von J. Chr. Wilhelm (2010), 220 Seiten
ISBN: 978-3-89336-642-2

74. **Charakterisierung perowskitischer Hochtemperaturmembranen zur Sauerstoffbereitstellung für fossil gefeuerte Kraftwerksprozesse**
von S.A. Möbius (2010) III, 208 Seiten
ISBN: 978-3-89336-643-9

75. **Characterization of natural porous media by NMR and MRI techniques: High and low magnetic field studies for estimation of hydraulic properties**
by L.-R. Stingaciu (2010), 96 pages
ISBN: 978-3-89336-645-3

76. **Hydrological Characterization of a Forest Soil Using Electrical Resistivity Tomography**
by Chr. Oberdörster (2010), XXI, 151 pages
ISBN: 978-3-89336-647-7

77. **Ableitung von atomarem Sauerstoff und Wasserstoff aus Satellitendaten und deren Abhängigkeit vom solaren Zyklus**
von C. Lehmann (2010), 127 Seiten
ISBN: 978-3-89336-649-1

78. **18th World Hydrogen Energy Conference 2010 – WHEC2010 Proceedings**
Speeches and Plenary Talks
ed. by D. Stolten, B. Emonts (2010)
ISBN: 978-3-89336-658-3

78-1. **18th World Hydrogen Energy Conference 2010 – WHEC2010 Proceedings**
Parallel Sessions Book 1:
Fuel Cell Basics / Fuel Infrastructures
ed. by D. Stolten, T. Grube (2010), ca. 460 pages
ISBN: 978-3-89336-651-4

78-2. **18th World Hydrogen Energy Conference 2010 – WHEC2010 Proceedings**
Parallel Sessions Book 2:
Hydrogen Production Technologies – Part 1
ed. by D. Stolten, T. Grube (2010), ca. 400 pages
ISBN: 978-3-89336-652-1

78-3. **18th World Hydrogen Energy Conference 2010 – WHEC2010 Proceedings**
Parallel Sessions Book 3:
Hydrogen Production Technologies – Part 2
ed. by D. Stolten, T. Grube (2010), ca. 640 pages
ISBN: 978-3-89336-653-8

78-4. **18th World Hydrogen Energy Conference 2010 – WHEC2010 Proceedings**
Parallel Sessions Book 4:
Storage Systems / Policy Perspectives, Initiatives and Cooperations
ed. by D. Stolten, T. Grube (2010), ca. 500 pages
ISBN: 978-3-89336-654-5

78-5. **18th World Hydrogen Energy Conference 2010 – WHEC2010 Proceedings**
Parallel Sessions Book 5:
Stategic Analysis / Safety Issues / Existing and Emerging Markets
ed. by D. Stolten, T. Grube (2010), ca. 530 pages
ISBN: 978-3-89336-655-2

78-6. **18th World Hydrogen Energy Conference 2010 – WHEC2010 Proceedings**
Parallel Sessions Book 6:
Stationary Applications / Transportation Applications
ed. by D. Stolten, T. Grube (2010), ca. 330 pages
ISBN: 978-3-89336-656-9

Schriften des Forschungszentrums Jülich
Reihe Energie & Umwelt / Energy & Environment

78 Set (7 Bände)

18th World Hydrogen Energy Conference 2010 – WHEC2010 Proceedings
eb. by D. Stolten, T. Grube, B. Emonts (2010)
ISBN: 978-3-89336-657-6

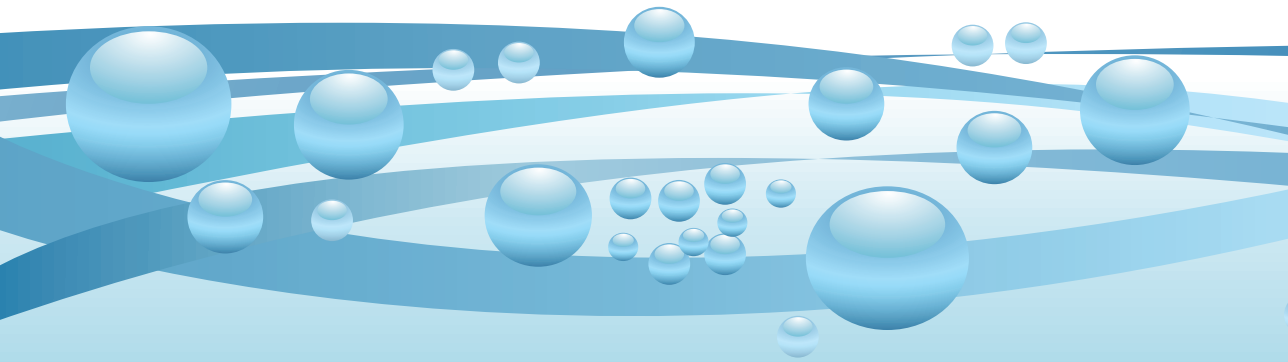

Energy & Environment
Volume 78-3 Book 3

Vol. 78	ISBN 978-3-89336-658-3
Vol. 78-1 Book 1:	ISBN 978-3-89336-651-4
Vol. 78-2 Book 2:	ISBN 978-3-89336-652-1
Vol. 78-3 Book 3:	**ISBN 978-3-89336-653-8**
Vol. 78-4 Book 4:	ISBN 978-3-89336-654-5
Vol. 78-5 Book 5:	ISBN 978-3-89336-655-2
Vol. 78-6 Book 6:	ISBN 978-3-89336-656-9
Vol. 78 Set (complete book series):	ISBN 978-3-89336-657-6

JÜLICH
FORSCHUNGSZENTRUM